

UCLA

UCLA Electronic Theses and Dissertations

Title

Development of Fiber Bragg Grating Strain, Thermal, and Magnetic Sensors for Smart Structure Applications

Permalink

<https://escholarship.org/uc/item/3825817p>

Author

Emmons, Michael

Publication Date

2012

Peer reviewed|Thesis/dissertation

UNIVERSITY OF CALIFORNIA

Los Angeles

Development of Fiber Bragg Grating Strain, Thermal, and
Magnetic Sensors for Smart Structure Applications

A dissertation submitted in partial satisfaction of the requirements
for the degree Doctor of Philosophy
in Mechanical Engineering

by

Michael Christian Emmons

2012

© Copyright by
Michael Christian Emmons
2012

ABSTRACT OF THE DISSERTATION

Development of Fiber Bragg Grating Strain, Thermal, and
Magnetic Sensors for Smart Structure Applications

by

Michael Christian Emmons

Doctor of Philosophy in Mechanical Engineering

University of California, Los Angeles, 2012

Professor Gregory P. Carman, Chair

Optical fiber Bragg gratings offer great potential for sensing pertinent phenomena in a wide range of applications. Such range is demonstrated in this dissertation with the utilization of fiber Bragg gratings (FBGs) in two different fields of research. Both of these fields are encompassed by an overarching goal of developing smart structures capable of providing necessary feedback to enhance performance and safety. FBGs are employed in the field of structural health monitoring by measuring strain and detecting damage when embedded within AS4/3501-6 quasi-isotropic composites. The grating sensors are also utilized in the field of ferroic materials to explore novel methods of coupling external phenomena to the optical fiber reflection signal. The desire to create smart structures is carried out by developing the Bragg grating measurements system created by NASA Dryden Flight Research Center. This development involves studying the validity of strain measurements provided by embedded Bragg gratings and expanding the

capabilities of the measurement system by coupling the sensors to additional types of external phenomena such as magnetic fields.

Theoretical and experimental work is carried out for both phases of the dissertation. In the strain sensing phase, photoelasticity, electromagnetic wave propagation, and coupled mode theory are applied to understand the theoretical behavior of FBGs. Mechanical loads are applied to composite specimens with embedded FBGs to monitor the response of the reflection signal. Finite element analysis is then performed to further clarify how the load is transferred from the host composite to the embedded fiber. In the thermal and magnetic sensing phase, a description is given for the fabrication and experimental results of coating FBGs with thin film ferroic materials. Next, a more extensive electromagnetic wave propagation theory is described in the context of manipulating various fiber characteristics for magnetic field coupling. A FBG magnetometer is then fabricated and a magneto-optic coupling is demonstrated experimentally with an externally applied magnetic field.

The dissertation of Michael Christian Emmons is approved.

Pei-Yu Chiou

Christopher S. Lynch

Oscar M. Stafsudd

Gregory P. Carman, Committee Chair

University of California, Los Angeles

2012

To Erin

TABLE OF CONTENTS

CHAPTER 1: INTRODUCTION	1
1.1 Case Study	1
1.2 Smart Structure Applications	2
1.2.1 Structural Health Monitoring	2
1.2.2 Magnetic Field Sensing	4
1.3 Sensor Type	5
1.4 Scope and Flow of the Dissertation	7
1.4.1 Breadth of Research	7
1.4.2 Flow of the Dissertation	9
CHAPTER 2: FIBER BRAGG GRATINGS	12
2.1 Synopsis.....	12
2.1.1 Optical Fibers	12
2.1.2 Fiber Bragg Gratings	13
2.2 Fabrication.....	15
2.2.1 Optical Fiber Drawing.....	15
2.2.2 Photosensitivity	16
2.2.3 Writing Techniques	17
2.2.4 Concluding Remarks	20
2.3 Light Propagation in Optical Fibers	20
2.3.1 Solving Maxwell’s Equations for Optical Fibers	21
2.3.1.1 DERIVING THE WAVE EQUATION	21
2.3.1.2 SEPARATION OF VARIABLES.....	22
2.3.1.3 SOLUTION IN TERMS OF z AND t	24
2.3.1.4 DIFFERENCE BETWEEN β AND k	26
2.3.1.5 SOLUTION IN TERMS OF φ	26
2.3.1.6 SOLUTION IN TERMS OF r	27
2.3.1.7 BOUNDARY CONDITIONS	29
2.3.1.8 TRANSCENDENTAL EQUATION	32
2.3.2 Modes of Propagation	34
2.3.3 Concluding Remarks	39
2.4 Bragg Reflection.....	39
2.4.1 Coupled Mode Theory	40
2.4.2 Reflected Wavelength Spectrum	46
2.4.3 Concluding Remarks	47
2.5 Sensing Phenomena.....	48
2.5.1 Defining the Sensor	48
2.5.2 Strain Sensing - Photoelasticity.....	49
2.5.2.1 OPTICAL INDICATRIX.....	51
2.5.2.2 STRAIN-OPTIC COEFFICIENTS	57
2.5.2.3 PHOTOELASTICITY IN FIBER BRAGG GRATINGS - BIREFRINGENCE.....	59
2.5.2.4 UNIAXIAL STRAIN SENSING	62
2.5.3 Thermomechanical Sensing – Ferroelasticity	63
2.5.3.1 FERROELASTIC NITI.....	64

2.5.3.2 THERMO-OPTIC EFFECTS.....	66
2.5.3.3 THERMO-OPTIC RESPONSE OF NITI COATED FBG	67
2.5.4 Magnetic Field Sensing – Magnetostriction and Magneto-Optics.....	68
2.5.4.1 STRAIN-BASED APPROACH.....	69
2.5.4.2 INDEX-BASED APPROACH.....	70
2.5.5 Concluding Remarks.....	72
2.6 NASA Dryden Fiber Optic Interrogation Device.....	73
2.6.1 FOID Data Processing.....	73
2.6.2 FOID Data Collection	76
2.6.3 Concluding Remarks.....	77
2.7 Summary.....	78
CHAPTER 3: COMPOSITE STRAIN SENSING	79
3.1 Synopsis.....	79
3.2 Literature Review.....	79
3.2.1 FBG Sensing Background.....	80
3.2.2 FBG Strain Sensing – Early Years.....	82
3.2.2.1 FBG SENSING ONSET.....	83
3.2.2.2 METHODS TO RELATE λ_B CHANGES TO STRAIN	84
3.2.2.3 DEMODULATING TEMPERATURE AND STRAIN	85
3.2.2.4 SURFACE-MOUNTED FBGS.....	86
3.2.2.5 EMBEDDED FIBER SENSORS.....	87
3.2.2.6 EMBEDDED FBGS.....	90
3.2.2.7 NONUNIFORM STRAIN.....	92
3.2.2.8 TRANSVERSE LOADING/SENSITIVITY.....	94
3.2.2.9 CURE MONITORING.....	95
3.2.2.10 DUAL-GRATINGS	96
3.2.3 FBG Strain Sensing – Current Years	97
3.2.3.1 STRAIN TRANSFER	98
3.2.3.2 TRANSVERSE LOADING.....	99
3.2.3.3 CURE MONITORING AND RESIDUAL STRAINS.....	100
3.2.3.4 EMBEDDED FBGS.....	102
3.2.3.5 CRACKS	105
3.2.4 FBG Strain Sensing – Reviews	107
3.2.5 FBG Strain Sensing – Applications	111
3.2.5.1 COPV	111
3.2.5.2 BRIDGE MONITORING	112
3.2.5.3 OTHER APPLICATIONS	114
3.2.6 Concluding Remarks.....	116
3.3 Fabrication, Experimental Setup, and FEA Models.....	117
3.3.1 Fiber Characterization.....	117
3.3.2 Composite Lay-Up.....	125
3.3.3 Composite Mechanical Load Testing.....	132
3.3.4 Fiber Optic Interrogation Device	135
3.3.5 Finite Element Model.....	143
3.3.5.1 MODEL GEOMETRIES.....	144

3.3.5.2 MATERIAL PROPERTIES	147
3.3.5.3 LOADING AND BOUNDARY CONDITIONS	152
3.3.5.4 MESH REFINEMENT	154
3.3.6 Concluding Remarks	157
3.4 Experimental Results	157
3.4.1 0°/0° Sample	158
3.4.2 0°/90° Sample	163
3.4.2.1 PROBLEM INTRODUCTION	164
3.4.2.2 CURING EFFECTS	165
3.4.2.3 COMPRESSIVE OPL	169
3.4.2.4 TENSILE IPL	171
3.4.2.5 CROSS-PLY CRACKING	176
3.4.2.6 CONCLUDING REMARKS	179
3.4.3 90°/90° Sample	180
3.4.3.1 PROBLEM INTRODUCTION	180
3.4.3.2 CURING EFFECTS	183
3.4.3.3 COMPRESSIVE OPL	185
3.4.3.4 TENSILE IPL	189
3.4.3.5 CROSS-PLY CRACKING	190
3.4.4 Concluding Remarks	193
3.5 Finite Element Analysis Results	195
3.5.1 Strain Transfer	196
3.5.2 2-D Model Validation	211
3.5.3 Non-Experimental Parameter Variation	215
3.5.4 Experimental Parameter Variation	221
3.5.5 Comparison with Experimental Results	225
3.5.6 Concluding Remarks	228
3.6 Summary	230
CHAPTER 4: FERROIC THIN FILM COATINGS	233
4.1 Synopsis	233
4.2 Literature Review	233
4.2.1 Ferroic Materials	234
4.2.2 Alternative FBG Sensors	237
4.2.3 Concluding Remarks	240
4.3 Fabrication and Experimental Setup	240
4.3.1 FBG Preparation	240
4.3.2 Thin Film Deposition	242
4.3.2.1 GENERAL SPUTTERING DEPOSITION	242
4.3.2.2 FBG SPUTTERING TECHNIQUE	243
4.3.2.3 ANNEALING	245
4.3.3 Thin Film Characterization	245
4.3.4 Sensor Testing	246
4.3.4.1 NICKEL TITANIUM COATING	247
4.3.4.2 TERFENOL-D	248
4.3.5 Concluding Remarks	250

4.4 Results	250
4.4.1 NiTi Coated FBG	251
4.4.1.1 FILM CHARACTERIZATION RESULTS	251
4.4.1.2 THERMAL TESTING RESULTS	254
4.4.2 Terfenol-D Coated FBG	261
4.4.2.1 BULK TESTING	261
4.4.2.2 THIN FILM TESTING	268
4.4.3 Concluding Remarks	273
4.5 Summary	274
CHAPTER 5: MAGNETO-OPTIC COUPLING	276
5.1 Synopsis	276
5.2 Literature Review	276
5.2.2 Evanescent Field Coupling.....	278
5.2.3 Magnetic Sensors	280
5.3 Theoretical Calculations	285
5.3.1 Theoretical Analysis.....	286
5.3.2 Computational Program	295
5.3.2.1 EFFECTIVE INDEX RELATIONSHIP	296
5.3.2.2 REFLECTED WAVELENGTH DETERMINATION	300
5.3.2.3 MODE SHAPE CALCULATION	302
5.3.3 Examples	304
5.3.3.1 RADIUS	305
5.3.3.2 OUTER INDEX	310
5.3.3.3 COMBINATION.....	314
5.3.3.4 MODES	317
5.3.4 Experimental Sensitivity	327
5.3.5 Concluding Remarks	329
5.4 Fabrication and Experimental Setup	330
5.4.1 Design Iterations	330
5.4.1.1 ITERATION 1: TAPERED FIBER	331
5.4.1.2 ETCH RATE CHARACTERIZATION.....	335
5.4.1.3 ITERATION 2: MONITORED TAPERED FIBER	338
5.4.1.4 ITERATIONS 3-5: DIRECTIONALITY WITH BUCKLING	341
5.4.1.5 ITERATION 6: DIRECTIONAL DROP ETCHING.....	342
5.4.1.6 ITERATION 7: DIRECTIONAL BATH ETCHING	352
5.4.2 Experimental Setup	354
5.4.2.1 APPARATUS.....	354
5.4.2.2 HYDROFLUORIC ACID ETCHING PROCESS	358
5.4.2.3 ETCHING EVALUATION.....	362
5.4.2.4 MAGNETIC FIELD TESTS	363
5.4.3 Concluding Remarks	369
5.5 Experimental Results	369
5.5.1 Etch Results.....	370
5.5.2 Etch Evaluation	376
5.5.3 Ferromagnetic Particles Evaluation	384

5.5.4 Magnetic Field Test Results: Fiber-1	387
5.5.5 Magnetic Field Test Results: Fiber-2 & 3	398
5.5.6 Concluding Remarks	406
5.6 Summary	407
CHAPTER 6: CONCLUSION	409
6.1 Summary	409
6.2 Future Work	411
CHAPTER 7: APPENDIX	414
7.1 Appendix A: Luna FBG Specifications	414
7.2 Appendix B: Hexcel Composite Material Properties.....	417
7.2.1 AS4 Carbon Fiber Properties	417
7.2.2 3501-6 Epoxy Matrix Properties	419
7.3 Appendix C: MATLAB Program for Rotation Matrices.....	423
7.4 Appendix D: Creation of the 8x8 [Ω] Components.....	426
7.4.1 Electric and Magnetic field components	426
7.4.2 Boundary Conditions.....	427
7.4.3 Matrix Assembly	430
CHAPTER 8: LIST OF REFERENCES	433

LIST OF FIGURES

Figure 1-1: Multidisciplinary approach to developing the sensor system for smart structure applications.....	8
Figure 2-1: A depiction of how total internal reflection leads to light propagation.	13
Figure 2-2: Qualitative reflection characteristics of FBGs.	14
Figure 2-3: Interference technique for writing FBGs.	17
Figure 2-4: Manner in which writing technique influences the type of grating.....	19
Figure 2-5: Form of the Bessel functions used to calculate the radial dependence of the magnitude of the propagating EM wave.	29
Figure 2-6: Influence of V parameter on the effective index for various modes of light propagation.....	35
Figure 2-7: Various EM wave mode shapes in the cross section of the fiber.....	38
Figure 2-8: The variation of fiber effective IOR as a function of length along a fiber.....	41
Figure 2-9: A comparison of theoretically and experimentally obtained wavelength reflection spectra.....	47
Figure 2-10: The basis used to represent light propagation in this research.....	50
Figure 2-11: Demonstration that light propagating down a fiber in the fundamental mode can be approximated as being linearly polarized.....	51
Figure 2-12: Un-deformed optical indicatrix with eigenvectors and eigenvalues identified...	54
Figure 2-13: Deformed optical indicatrix with new eigenvectors and eigenvalues identified.	56
Figure 2-14: Plane used to cut through optical indicatrix defined as intersecting the origin and being orthogonal to the direction of propagation.	60
Figure 2-15: Shape memory behavior of NiTi undergoing stress and temperature change.....	65
Figure 2-16: Shape memory behavior of NiTi undergoing a thermal cycle.	66
Figure 2-17: Magnetostrictive behavior of Terfenol-D.	69
Figure 2-18: Laser tuning of the FOID system used to collect a reflection signal for the entire Bragg fiber.....	74
Figure 2-19: Data processing method for separating the contribution of individual FBGs to the fiber reflection signal.	75
Figure 3-1: Plot of the values associated with the transcendental equation whose zeros provide effective IOR values over a range of wavelengths.....	121
Figure 3-2: OFDR processing steps to calculate the peak and centroid of the reflected wavelength spectrum of each individual FBG.	123
Figure 3-3: Comparison of peak and centroid methods for calculating reflected wavelength along the length of the Bragg fiber.....	124
Figure 3-4: Orientation of individual plies relative to loading direction (0°) making up the composite laminate.....	126
Figure 3-5: Picture of the lay-up process involving the use of a heat gun to prevent the layers from slipping during stacking.	127
Figure 3-6: Schematic of the positioning of the five Bragg fibers within the composite panel to be cut into smaller, rectangular samples.	128
Figure 3-7: Input and measured curing parameters.....	129
Figure 3-8: Pictures of the composite panel before and after cutting.	129
Figure 3-9: Orientation of the embedded optical fiber relative to nearby structural carbon fibers.....	130

Figure 3-10: Original and altered x-ray images to demonstrate the positioning of the optical fiber for alignment with the surface-mounted electrical resistance strain gauge shown in the camera photograph.	131
Figure 3-11: Drawing of the final composite samples to be tested.	132
Figure 3-12: Instron load frame mechanical test set-up.	133
Figure 3-13: Schematic diagram of the flow of measurement data during mechanical load testing.	134
Figure 3-14: Correlation between applied pump pressure and stress applied to tabs by the Instron grips.	135
Figure 3-15: Picture of the FOID system and grounded computer used to run the system. ..	136
Figure 3-16: Tools used for splicing fibers together.	138
Figure 3-17: Test setup for calibrating the FOID system's strain-optic coefficient.	139
Figure 3-18: Results of the strain-optic coefficient validation comparing the stiffness measurements of nine FBGs with an ESG.	140
Figure 3-19: Depiction of the FBG processing technique where the wavelength range must be known in order to determine the value of the reflected wavelength.	141
Figure 3-20: Shift in the peak data point as the starting wavelength of the sweep is changed.	142
Figure 3-21: Pertinent features and dimensions of a cross-section of the 2-D IPL model. ...	146
Figure 3-22: Images depicting the dimensions of the model reduced from the experimental composite samples.	147
Figure 3-23: Method for calculating elasticity matrix for each ply orientation by rotating about a particular axis depending on whether the rotation is for a 2-D or 3-D model.	151
Figure 3-24: Boundary conditions of the 2-D IPL and OPL models.	153
Figure 3-25: Images depicting the mesh refinement in the far field of the composite and in the near field of the embedded optical fiber.	154
Figure 3-26: Mesh refinement results indicating the necessary finesse of the mesh in order to achieve a converged calculation.	156
Figure 3-27: Sample configuration for the 0°/0° sample.	159
Figure 3-28: Comparison of FBG and ESG data measuring the stress-strain relationship in a 0°/0° sample.	160
Figure 3-29: Strain profile within the 0°/0° sample at various load levels.	161
Figure 3-30: Comparison amongst ESG, FBG, and FEA results for a particular load applied to the 0°/0° sample.	162
Figure 3-31: Microscope images of the lenticular resin rich regions adjacent to the optical fiber.	164
Figure 3-32: Stress-strain behavior of the surface-mounted ESG and embedded FBGs for the 90°/90° sample under IPL conditions.	165
Figure 3-33: Reflected wavelength spectra of one non-embedded and four embedded FBGs in the 0°/90° sample.	166
Figure 3-34: Reflected wavelength spectra indicating birefringence increase with OPL conditions in the tab region (FBG-27) of the 0°/90° sample.	170
Figure 3-35: Increase in TSD in FBG-27 with the application of OPL.	171
Figure 3-36: Reflected wavelength spectra indicating stagnant birefringence with IPL conditions in the far field region (FBG-15) of the 0°/90° sample.	172
Figure 3-37: Evolution of TSD in FBG-15 during IPL.	173

Figure 3-38: Comparison of stress-strain behavior in the 0°/90° composite as measured by ESG and FBG-15.	175
Figure 3-39: Behavior of the peak and centroid of the reflected wavelength spectrum of FBG-15 during IPL.	176
Figure 3-40: Optical microscope images of cross-ply cracks in the 0°/90° sample after loads up to 6000 $\mu\epsilon$ were applied.....	177
Figure 3-41: Effects of cross-ply cracking and nonuniform strain on the reflected wavelength spectrum of FBG-15 during IPL.	178
Figure 3-42: Strain profile of a 90°/90° sample under IPL.....	181
Figure 3-43: Strain-strain plot for the ESG and the FBG embedded between the collocated strain gauges.	182
Figure 3-44: Reflected wavelength spectra of a non-embedded, embedded 0°/90°, and two embedded 90°/90° FBGs under no mechanical load.....	184
Figure 3-45: Sample configuration for application of OPL.	186
Figure 3-46: Evolution of the reflected wavelength spectra under compressive OPL for FBG-3 in the 90°/90°a and 90°/90°b samples.	187
Figure 3-47: Change in TSD for FBG-3 in the 90°/90°a and 90°/90°b samples under OPL.	188
Figure 3-48: Evolution of TSD and birefringence during IPL for FBG-3 in the 90°/90°a and 90°/90°b samples.....	189
Figure 3-49: Optical microscope images of the region near the optical fibers embedded in the 90°/90° samples.....	191
Figure 3-50: Opening of the cross-ply crack during IPL and OPL conditions which effectively creates a FBG surface-mounted to the crack plane.	192
Figure 3-51: Summary of the experimental results observed in IPL and OPL testing.	193
Figure 3-52: FEA strain in the loading direction for a 90°/90° sample under IPL.	197
Figure 3-53: FEA strain in the composite's out-of-plane direction for a 90°/90° sample under IPL.....	198
Figure 3-54: FEA strain in the direction of the embedded optical fiber for a 90°/90° sample under IPL.....	199
Figure 3-55: Depiction of the three cut lines in the IPL model along with which FEA strains will be plotted.....	200
Figure 3-56: Plot of strains in the coordinate directions along Cut Line 1 in the model under IPL conditions.	201
Figure 3-57: Plot of strains in the coordinate directions along Cut Line 2 in the model under IPL conditions.	202
Figure 3-58: Plot of strains in the coordinate directions along Cut Line 3 of the model under IPL conditions.	203
Figure 3-59: FEA strain in the 0° direction for a 90°/90° sample under OPL.....	204
Figure 3-60: FEA strain in the direction of the embedded optical fiber for a 90°/90° sample under OPL.	205
Figure 3-61: FEA strain in the composite's out-of-plane direction for a 90°/90° sample under OPL.	206
Figure 3-62: Depiction of the three cut lines in the OPL model along with which FEA strains will be plotted.....	207
Figure 3-63: Plot of strains in the coordinate directions along Cut Line 1 in the model under OPL conditions.....	208

Figure 3-64: Plot of strains in the coordinate directions along Cut Line 2 in the model under OPL conditions.....	209
Figure 3-65: Plot of strains in the coordinate directions along Cut Line 3 of the model under OPL conditions.....	210
Figure 3-66: Validation of 2-D IPL model by comparing strains transverse to the embedded optical fiber with the 3-D IPL model.	212
Figure 3-67: Validation of 2-D IPL model by comparing the TSD of the embedded optical fiber with the 3-D IPL model.	213
Figure 3-68: Validation of 2-D OPL model by comparing strains transverse to the embedded optical fiber with the 3-D OPL model.....	214
Figure 3-69: Validation of 2-D OPL model by comparing the TSD of the embedded optical fiber with the 3-D OPL model.....	215
Figure 3-70: Variation of coating thickness in the FEA study.	216
Figure 3-71: Variation of TSD in 2-D IPL and OPL models while varying coating thickness.	217
Figure 3-72: Variation of TSD in 3-D IPL and OPL models while varying coating thickness.	218
Figure 3-73: Variation of resin pocket length in the FEA study.....	219
Figure 3-74: Variation of TSD in 2-D IPL and OPL models while varying resin pocket length.	219
Figure 3-75: Variation of de-adhesion angle in the FEA study.	221
Figure 3-76: Variation of crack propagation in the FEA study.	221
Figure 3-77: Variation of TSD in 2-D IPL and OPL models while varying de-adhesion angle and crack propagation.	222
Figure 3-78: Variation of TSD in 3-D IPL and OPL models while varying de-adhesion angle and crack propagation.	223
Figure 3-79: Variation of strains transverse to the optical fiber in 3-D IPL and OPL models while varying de-adhesion angle and crack propagation.	224
Figure 3-80: Evolution of TSD and birefringence during IPL for FBG-3 in the 90°/90°a and 90°/90°b samples.....	226
Figure 3-81: Stress transmission across the extremely compliant material used to model the crack.	228
Figure 4-1: Various forms of energy which can be coupled.....	234
Figure 4-2: Sulfuric acid etching resulting in coated and uncoated regions of fiber.	241
Figure 4-3: Custom DC magnetron sputtering system.....	242
Figure 4-4: Fiber holder and rotator apparatus within the sputtering chamber.	243
Figure 4-5: Plasmas developing within the sputtering chamber during deposition of NiTi and Terfenol-D.	244
Figure 4-6: Experimental setup for thermal testing of NiTi coated FBGs.....	247
Figure 4-7: Magnetic field test schematic for experiment with Terfenol-D coated FBGs. ...	249
Figure 4-8: DSC results demonstrating phase transition temperatures in thin film NiTi, indicating the deposition parameters are satisfactory for coating an optical fiber.....	252
Figure 4-9: Lateral and cross-sectional SEM images of a NiTi coated FBG.....	253
Figure 4-10: XRD data demonstrating the thin film NiTi coating the optical fiber is crystalline.	254
Figure 4-11: Length domain plot of the NiTi coated Bragg fiber reflection signal.....	255

Figure 4-12: Bragg wavelength shift profile along the NiTi coated Bragg fiber at various temperatures.	256
Figure 4-13: Comparison of Bragg wavelength shift in a polyimide coated FBG and the NiTi coated FBG at the 3 cm mark along the fiber.	257
Figure 4-14: Comparison of Bragg wavelength shift in a polyimide coated FBG and the NiTi coated FBG at the 5 cm mark along the fiber.	259
Figure 4-15: Difference between NiTi and polyimide Bragg wavelengths during heating and cooling resulting in a hysteresis characteristic of ferroelastic materials.	260
Figure 4-16: Comparison of a free FBG with a FBG surface-mounted to a bulk Terfenol-D sample when a magnetic field is applied.	262
Figure 4-17: Time domain response of a bonded FBG, free FBG, and magnetic field.	263
Figure 4-18: Frequency domain response of a bonded FBG, free FBG, and magnetic field.	265
Figure 4-19: Comparison of a free FBG with a FBG surface-mounted to a bulk Terfenol-D sample when a small magnetic field is applied.	266
Figure 4-20: Time Domain response of a bonded FBG, free FBG, and magnetic field for low AC magnetic field strength.	267
Figure 4-21: Frequency domain response of a bonded FBG, free FBG, and magnetic field at low AC magnetic field strength.	268
Figure 4-22: Time domain data of four different AC magnetic field frequencies.	270
Figure 4-23: Frequency domain data of magnetic fields oscillating with four different frequencies.	271
Figure 4-24: Time domain response of the bonded FBG when four different AC magnetic field frequencies are applied.	272
Figure 4-25: Frequency domain response of the bonded FBG when four different AC magnetic field frequencies are applied.	272
Figure 5-1: Schematic diagram of the 2- and 3-layer fibers analyzed in this research.	289
Figure 5-2: Plot indicating combinations of effective IOR and V parameter values which cause the sign of the determinant of $[\Omega]$ to be positive and negative.	298
Figure 5-3: Plots showing the curves representing the dependence of effective IOR on V parameter.	299
Figure 5-4: Re-parameterization of the effective IOR scale.	300
Figure 5-5: Re-parameterization of the V parameter which leads to two curves representing a supported fiber mode and the satisfaction of the Bragg condition. The intersection of the curves represents the FBG reflected wavelength.	301
Figure 5-6: Change in the n - V relationship when the cladding radius is altered.	302
Figure 5-7: Mode shape of the fundamental HE_{11} mode.	303
Figure 5-8: Arrow plot indicating the direction of the electric field in the cross-section of the optical fiber for the HE_{11} mode.	304
Figure 5-9: Relationship between core radius and effective IOR in a 2-layer fiber.	306
Figure 5-10: Change in mode shape when core radius is altered in a 2-layer fiber.	307
Figure 5-11: Relationship between cladding radius and effective IOR in a 3-layer fiber.	308
Figure 5-12: Change in mode shape when cladding radius is altered in a 3-layer fiber.	309
Figure 5-13: Relationship between cladding IOR and effective IOR in a 2-layer fiber.	310
Figure 5-14: Change in mode shape when cladding IOR is altered in a 2-layer fiber.	311
Figure 5-15: Relationship between surrounding material IOR and effective IOR in a 3-layer fiber.	312

Figure 5-16: Change in mode shape when surrounding material IOR is altered in a 3-layer fiber.	313
Figure 5-17: Variation of effective IOR with change in core radius and cladding IOR in a 2-layer fiber.	315
Figure 5-18: Variation of effective IOR with change in cladding radius and surrounding material IOR in a 3-layer fiber.	316
Figure 5-19: Altering the core radius to shift the V parameter to a higher value in order to have more modes intersect the Bragg condition curve.	318
Figure 5-20: Variation of effective IOR for three different modes with change in cladding radius and surrounding material IOR in a 3-layer fiber.	319
Figure 5-21: Mode shape for two different modes under two sets of cladding radius and surrounding material IOR values.	320
Figure 5-22: Arrow plot indicating the approximately linearly polarized nature of the propagating light for the given mode and fiber parameter combinations.	322
Figure 5-23: Altering the lower bound of the wavelength sweep in order to have more modes intersect the Bragg condition curve.	323
Figure 5-24: Variation of effective IOR for three different modes with change in cladding radius and surrounding material IOR in a 3-layer fiber.	324
Figure 5-25: Mode shape for two different modes under two sets of cladding radius and surrounding material IOR values.	325
Figure 5-26: Arrow plot indicating the approximately linearly polarized nature of the propagating light for the given mode and fiber parameter combinations.	326
Figure 5-27: Shift in effective IOR due to a +0.005 change in surrounding material IOR as a function of initial surrounding material IOR and cladding radius. The noise level cutoff is represented with the black plane.	328
Figure 5-28: Shift in reflected wavelength for FBGs which were etched for different times along two different fibers.	332
Figure 5-29: Response of the FBGs along Fiber-2 when moved from air to either IPA or benzene.	334
Figure 5-30: Schematic of the removal of optical fibers dipped in HF acid for etch rate characterization.	336
Figure 5-31: Dependence of fiber radius on etching time for two sets of 10 fibers.	337
Figure 5-32: Shift in λ_B during the etching process for 11 FBGs etched for various amounts of time.	339
Figure 5-33: Apparatus for maintaining the directionality of an etched fiber.	341
Figure 5-34: Fiber with directionality maintained at closer fixed points.	341
Figure 5-35: Tape used to loosely fix the fiber in place to avoid the problem of buckling. ...	342
Figure 5-36: Iteration for maintaining the directionality of the thinned optical fiber while allowing for the buckling problem to be resolved.	343
Figure 5-37: Microscope image demonstrating the length required to taper down to the final fiber diameter.	344
Figure 5-38: Change in λ_B when the FBG is immersed in IPA from air and evolution of reflected wavelength spectrum as the number of etches increases.	345
Figure 5-39: Response of an etched FBG when immersed in IPA and then ferrofluid with a magnetic field applied.	347
Figure 5-40: Progression of error in the λ_B measurement for the various states.	348

Figure 5-41: Images depicting the ferrofluid sticking to the fiber apparatus and the uneven surface of the thinned fiber.....	349
Figure 5-42: SEM images of a fiber dipped in ferrofluid and subsequently rinsed in IPA in an attempt to remove the ferric oxide particles.....	350
Figure 5-43: Increased taper rate by immersing part of the optical fiber which is still coated within the HF droplet.	351
Figure 5-44: Poor etching results due to the small volume of HF used for thinning the fiber.	352
Figure 5-45: Final design of the fiber holding apparatus.....	354
Figure 5-46: Alteration of the mechanical splice.....	356
Figure 5-47: Schematic of the plastic structure of the apparatus.....	356
Figure 5-48: Schematic demonstrating that the amount of glue used should give the fiber enough height so that the glass tube will lay flat on the plastic mount.....	357
Figure 5-49: Translational positioning of the fiber relative to the apparatus.....	358
Figure 5-50: Final steps of gluing the glass tube and Teflon tube in place.	358
Figure 5-51: Drawing depicting how far the fiber apparatus should be dipped in a bath of HF.	359
Figure 5-52: Broadening of the end reflection peak during the etching process.	360
Figure 5-53: Mitigation of the buckling problem by pulling the fiber taut after etching and gluing the fiber to the Teflon tube egress point.	362
Figure 5-54: Pictures of the fiber apparatus placed in a vial containing ferric oxide particles.	364
Figure 5-55: Pictures of the electromagnet used to apply the magnetic field during testing and a close-up image of the fiber apparatuses between the electromagnet's yokes.	365
Figure 5-56: Schematic diagram showing the application of an external magnetic field and how much of the fiber apparatus is buried in ferric oxide particles.....	367
Figure 5-57: Change in reflected wavelength of FBG#2 and #3 on Fiber-1 during etching.	371
Figure 5-58: Shift in λ_B of FBG#2 and #3 on Fiber-1 toward the end of etching and when the apparatus is removed from the HF bath and rinsed in IPA.	372
Figure 5-59: Change in reflected wavelength of FBG#2 and #3 on Fiber-2 during etching.	373
Figure 5-60: Change in reflected wavelength of FBG#2 and #3 on Fiber-3 during etching.	375
Figure 5-61: Reflected wavelength at each of the six etch evaluation states for FBG#2-4 in Fiber-1.	376
Figure 5-62: Reflected wavelength spectra in each of the six etch evaluation states for FBG#3 on Fiber-1.	378
Figure 5-63: Reflected wavelength at each of the six etch evaluation states for FBG#2-4 in Fiber-2 and -3.	379
Figure 5-64: Reflected wavelength spectra in each of the six etch evaluation states for FBG#3 on Fiber-2.	380
Figure 5-65: Reflected wavelength spectra in each of the six etch evaluation states for FBG#3 on Fiber-3.	381
Figure 5-66: SEM images of Fiber-2 after magnetic field testing used to determine the diameter of the optical fiber.	383
Figure 5-67: SEM images of Fiber-3 after magnetic field testing used to determine the diameter of the optical fiber.	384
Figure 5-68: SEM images of the ferric oxide particles to determine their size.	385

Figure 5-69: SQUID magnetometer results for a sample of ferric oxide particles.	386
Figure 5-70: Shift in reflected wavelength for FBG#2 and #3 for Fiber-1 while the electromagnet test setup is being cooled.	388
Figure 5-71: Penetration of the end reflection peak into the reflection signal of FBG#4 on Fiber-1.	389
Figure 5-72: Real-time monitoring of the reflected wavelength shift of FBG#2 and #3 on Fiber-1 during the On/Off magnetic field test.	390
Figure 5-73: Shifts in reflected wavelength of FBG#2-4 on Fiber-1 calculated from peaks of the reflected wavelength spectra during the On/Off magnetic field test.	391
Figure 5-74: Reflected wavelength spectra of FBG#3 on Fiber-1 during the On/Off magnetic field test to evaluate how far the signal is above noise.	392
Figure 5-75: Real-time monitoring of the reflected wavelength shift of FBG#2 and #3 on Fiber-1 during the Magnetic Saturation test.	393
Figure 5-76: Shifts in reflected wavelength of FBG#2-4 on Fiber-1 calculated from peaks of the reflected wavelength spectra during the Magnetic Saturation test.	394
Figure 5-77: Normalized behavior of ferric oxide particles and of λ_B shifts in FBG#3 on Fiber- 1 during the Magnetic Saturation test.	395
Figure 5-78: Reflected wavelength spectra of FBG#3 on Fiber-1 during the Magnetic Saturation test to evaluate how far the signal is above noise.	396
Figure 5-79: Real-time monitoring of the reflected wavelength shift of FBG#2 and #3 on Fiber-1 during the Magnetic Saturation test at higher magnetic field values.	397
Figure 5-80: Shift in reflected wavelength for FBG#2 and #3 of Fiber-2 and -3 while the electromagnet test setup is being cooled.	398
Figure 5-81: Length domain reflection signals of Fiber-2 and -3 to determine the influence of noise.	399
Figure 5-82: Reflected wavelength spectra of FBG#3 on Fiber-2 and -3 before and after cooling the electromagnet test setup.	400
Figure 5-83: Shifts in reflected wavelength of FBG#2-4 on Fiber-2 and -3 calculated from peaks of the reflected wavelength spectra during the On/Off magnetic field test.	401
Figure 5-84: Reflected wavelength spectra of FBG#3 on Fiber-2 during the On/Off magnetic field test to evaluate how far the signal is above noise.	402
Figure 5-85: Shifts in reflected wavelength of FBG#2-4 on Fiber-2 and -3 calculated from peaks of the reflected wavelength spectra during the Magnetic Saturation test.	403
Figure 5-86: Reflected wavelength spectra of FBG#3 on Fiber-2 during the Magnetic Saturation test to evaluate how far the signal is above noise.	404
Figure 5-87: Shift in λ_B for FBG#3 and #4 in Fiber-2 corrected by subtracting the shifts measured in FBG#3 and #4 in Fiber-3.	405
Figure 5-88: Normalized behavior of ferric oxide particles and of the corrected λ_B shifts in FBG#3 on Fiber-2 during the Magnetic Saturation test.	406
Figure 7-1: Page 1 of the FBG specifications sheet.	414
Figure 7-2: Page 2 of the FBG specifications sheet.	415
Figure 7-3: Page 3 of the FBG specifications sheet.	416
Figure 7-4: Page 1 of the AS4 carbon fibers material properties.	417
Figure 7-5: Page 2 of the AS4 carbon fibers material properties.	418
Figure 7-6: Page 1 of the 3501-6 epoxy matrix material properties.	419
Figure 7-7: Page 2 of the 3501-6 epoxy matrix material properties.	420

Figure 7-8: Page 3 of the 3501-6 epoxy matrix material properties. 421
Figure 7-9: Page 4 of the 3501-6 epoxy matrix material properties. 422

LIST OF TABLES

Table 2-1: Notation consolidation from two indices to one.....	58
Table 3-1: Summary of various topics on FBG strain sensing covered by relevant review papers.	110
Table 3-2: Peak data points for several FBG reflection spectra as the starting sweep wavelength is shifted.	143
Table 3-3: Mechanical properties of isotropic materials utilized in FEA models.	148
Table 3-4: Comparison of Voigt and COMSOL contracted notation.	149
Table 3-5: Material properties of both composite phases used in a rule of mixtures calculation to determine lamina properties.	150
Table 3-6: Measured reflected wavelengths and calculated TSD in a non-embedded FBG and several FBGs embedded in the 0°/90° sample.	167
Table 3-7: Measured reflected wavelengths and calculated TSD in a non-embedded FBG and FBGs embedded in either the 0°/90° or 90°/90° samples sample.	185
Table 5-1: Demonstration of the Bessel functions that describe the EM wave behavior in the three different fiber layers.	290
Table 5-2: Input parameters for calculating and plotting the n - V relationship in an optical fiber.	297
Table 5-3: Bragg wavelength shifts between relevant pairs of states in the etch evaluation process.	382

ACKNOWLEDGEMENTS

I would first like to thank Professor Greg Carman and Dr. Lance Richards. Their balance in providing guidance and independence and their generous financial support were invaluable to my success as a graduate student. Their approach to management and research provided lessons I will carry with me for the rest of my professional career and I am very grateful for the privilege to work for them.

I must thank the many current and former members of the Active Materials Lab. Thank you to Lenka Stepan and Marie Tieck for introducing me to the lab as an undergraduate and making my first exposure to life as a graduate student researcher a positive experience. Thank you to Sunny Karnani and Stefano Trono for helping with my work at the beginning of graduate school so I could hit the ground running with my research. Thank you to Kotekar Mohanchandra and Scott Keller for being invaluable resources and helping me work through the many bumps along the road through my research. Thank you to Youngjae Chun, Hyungsuk Kim, Scott Strutner and Alexander Bur for the various forms of assistance which were necessary for my success. Thank you to all the other members of the lab who have made my time in school such a great experience.

The team at NASA Dryden and the AERO Institute has been very helpful and a great resource for information. Thank you to Anthony (Nino) Piazza, Allen Parker, and Hon (Patrick) Chan for so graciously incorporating me into your group.

I also would like to thank my family for their unwavering support. Sean, Alyssa, and Matt have been tremendous siblings and friends throughout my life. My extended family, Nancy, Jan, Lee, Janet, John, Clint, Kristen, Adam, Larry, and Heather have displayed nothing but overwhelming and flattering pride. My parents, Jeanne and Kent Emmons, have provided in my upbringing a solid foundation from which all of my future successes are based. They have encouraged my problem-solving nature, taught me balance in life, and provided innumerable opportunities. No group of people brings me greater joy than my family. Thank you all so much.

Lastly, I would like to thank my divine wife, Erin. I could easily write a second dissertation on all the ways she has shown me love and support throughout college and graduate school. She has taught me so much and made me a better person. As this work comes to a close, I am excited to move into the next stage of our lives together. I truly could not have done this dissertation without you. I love you. This is for you.

Sincerely,

Mike

VITA

Education

2007 B.S., Mechanical Engineering
University of California
Los Angeles, California

2010 M.S., Mechanical Engineering
University of California

Employment

2006-2007 Laboratory Assistant
Active Materials Lab
University of California
Los Angeles, California

2007-2010 Graduate Student Researcher
Active Materials Lab
University of California
Los Angeles, California

2010-2011 PhD Intern
NASA AERO Insitute
Palmdale, California

Publications and Presentations

- M. C. Emmons**, H. K. D. Kim, G. P. Carman, and W. L. Richards, “Magneto-optic field coupling in optical fiber Bragg gratings,” *Optical Fiber Technology* (2012). (Accepted)
- M. C. Emmons**, S. Karnani, S. Trono, K. P. Mohanchandra, W. L. Richards, and G. P. Carman, “Strain measurement validation of embedded fiber Bragg gratings,” *International Journal of Optomechatronics*. vol. 44, no. 1, pp. 22-33, 2010.
- M. C. Emmons**, G. P. Carman, K. P. Mohanchandra, and W. L. Richards, “Characterization and birefringence effect on embedded optical fiber Bragg gratings,” San Diego, CA, USA, 2009, 72950C-1-11.
- M. C. Emmons**, S. Karnani, K. P. Mohanchandra, G. P. Carman, S. Trono, W. L. Richards, “Characterization of optical fiber Bragg gratings as strain sensors considering load direction,” Ellicott City, MD, USA, 2008, pp. 1-5.
- K. P. Mohanchandra, S. Karnani, **M. C. Emmons**, W. L. Richards, and G. P. Carman, “Thin film NiTi coatings on optical fiber Bragg sensors,” *Applied Physics Letters* vol. 93, no. 3, pp. 031914-031914-3, 2008.
- K. P. Mohanchandra, **M. C. Emmons**, S. Karnani, G. P. Carman, and W. L. Richards, “Response of optical fiber Bragg sensors with a thin film shape memory alloy

- coating,” Ellicott City, MD, USA, 2008, pp. 85-89.
- Y. Chun, H-Y. Chang, P-Y. Lin, K. P. Mohanchandra, **M. C. Emmons**, M. Seong, D. S. Levi, A. W. Tulloch, C. Kealy, D. A. Rigberg, P. F. Lawrence, and G. P. Carman, “Computational modeling and experimental characterization of hyperelastic thin film NiTi for neurovascular microstent applications,” Philadelphia, PA, USA, 2010, pp. 869-873.
- Y. Chun, P-Y. Lin, H-Y. Chang, **M. C. Emmons**, K. P. Mohanchandra, D. S. Levi, and G. P. Carman,, “Modeling and experimental analysis of the hyperelastic thin film nitinol,” *Journal of Intelligent Material Systems and Structures*, vol. 22, no. 17, pp. 2045-2051, 2011.
- T. Wu, **M. Emmons**, A. Bur, J. Sorge, and G. P. Carman, “Magnetolectric laminate composites with prestress consideration,” San Diego, CA, USA, 2010, pp. 764415-1-10.
- T. Wu, **M. Emmons**, T-K. Chung, J. Sorge, and G. P. Carman, “Influence of mechanical load bias on converse magnetolectric laminate composites,” *Journal of Applied Physics*, vol. 107, no. 9, pp. 09D912-09D912-3, 2010.
- R. M. Tieck, **M. C. Emmons**, and G. P. Carman, “Alternative evaluation criteria of piezoelectric motors,” *Journal of Intelligent Material Systems and Structures*, vol. 18, no. 11, pp. 1215-1221, 2007.

Patents

- G. P. Carman, K. P. Mohanchandra, M. C. Emmons, and W. L. Richards, “Magneto-optic field coupling in optical fiber Bragg gratings,” 2011, DRC-011-002 (Provisional)
- M. C. Emmons, S. Karnani, K. P. Mohanchandra, W. L. Richards, and G. P. Carman, “Smart material coated fiber Bragg grating sensor,” 2009, DRC-009-013 (Provisional)

CHAPTER 1:

INTRODUCTION

1.1 Case Study

In June, 2003, a National Aeronautics and Space Administration (NASA) High Altitude Long Endurance Remote Operated Aircraft (also known as Helios) was flown over Hawaii. The observed aircraft was a propeller driven flying wing used to demonstrate and analyze the viability of particular emerging technologies. In flight, a large amount of turbulence was experienced, resulting in a dihedral wing shape which was too large to be sustained. The aircraft eventually crashed as a result of the inability to monitor and adapt to such turbulence. In the report of the mishap later published by NASA, it was noted that an ability to detect wing shape in real-time during aircraft flight would aid in avoiding such a disaster. It was therefore a necessary requirement for safe operation of the vehicle [1].

This case study provides a compelling example that justifies the need to develop structural systems which mimic the human nervous system whereby information received by sensors (nerves) feeds back into a decision-making computer or operator (brain) for corresponding actuator systems (muscles) to react. A wing shape detection system would provide feedback to on-board flight control and on-ground operators so that necessary measures would be taken to prevent such a disaster. Measures, 2001 describes the need for creating intelligent, adaptive structures that sense external stimuli and process the data with a neural network in a manner that allows for an actuation system to correspondingly adapt [2]. The work presented in this dissertation specifically addresses the creation of smart structures by developing sensor technology.

Relating this back to the Helios aircraft, the development of a system which monitors the wing shape will satisfy the sensing component of creating an intelligent, adaptive structure. A strain sensing system would have to be implemented in order to gather the necessary information for obtaining the wing deflection; however, no strain sensing system at the time could satisfactorily and reliably be implemented to gather the required information. This problem establishes a clear motivation for the work performed in this research developing a fiber optic sensing system for smart structure applications.

This introductory chapter will provide additional examples and motivation behind the pursuit of smart structures. Subsequently, the choice of sensor system along with its advantages over other options will be described. Lastly, the scope and lay-out of the dissertation will be provided to demonstrate the breadth of fields applicable to this work and the various methods used to carry out the research.

1.2 Smart Structure Applications

This section describes several more motivational examples for the development of smart structures. The examples specifically fall within two main categories. The first is structural health monitoring which requires sensors for measuring phenomena such as strain, stress, structural damage, and thermal loading. The second category specifically addresses the need for developing magnetic field sensors for navigation and the detection of foreign objects.

1.2.1 Structural Health Monitoring

Structural health monitoring (SHM) is a burgeoning field drawing much attention from research, military, and commercial entities. The three main motivating factors that nourish structural health monitoring are improving safety, decreasing economic costs, and improving performance. At the heart of this field is the desire to obtain reliable, pertinent information upon which decisions can be made. Obtaining more information on a structure affords better metrics

for evaluating performance and determining when failure may occur. Such feedback can be extremely valuable if it helps to save lives and if it aids in determining how to utilize structures in a cost-efficient manner.

The ability to monitor stresses, vibrations, fatigue behavior, and other phenomena which contribute to the degradation of a structure is a critical component to ensuring safety and efficient operation. An adequate SHM system, for example, could greatly aid in the decision making capabilities of authorities whose job it is to ensure the structural integrity of bridges and tunnels [3]. Additionally, monitoring the cyclic thermo-mechanical loads applied to aircraft from cabin pressurization and depressurization, take-off and landing, and temperature changes between high altitude and ground level can aid in decision making criteria for when certain components of the aircraft must be replaced. Cars are becoming more and more efficient and safe thanks to the dearth of sensors which are utilized, for example, to optimize fuel consumption and to deploy airbags. There is no end in sight to the demand for more information to resolve the safety, efficiency, and performance of smart structures.

A relevant trend in the field of structural health monitoring is the increased use of composite materials in advanced structures. The high stiffness-to-weight ratio and the ability to tailor the composite's properties based on lay-up are two fundamental advantages over single-phase materials such as aluminum. The disadvantages, however, lie in detecting damage such as cross-ply cracking and delamination. The ability of a sensor to detect impairment and maintain functionality despite such damage is an important design consideration. In order to carry this out, the sensor system must not simply be designed for surface mounting on a structure, but must be able to successfully be embedded and incorporated within the structure. This is akin to transitioning from a human only being able to sense stimuli on the surface of their skin to being able to feel internal phenomena, such as stomach aches or broken bones. In the portion of this research devoted to developing a reliable structural health monitoring system (Chapter 3), composite material will be tested and analyzed.

1.2.2 Magnetic Field Sensing

The examples given are aligned with the analogy of developing a human nervous system by detecting damage (pain), wing-shape (limb position), and thermal loading (hot or cold). We can extrapolate the sensor system to monitor phenomena that humans do not have the ability to sense, but other biological organisms do. One such example is detecting magnetic fields. There are several biological species which have demonstrated the ability to detect the Earth's magnetic field. One specific mode of such sensing is to have an internal compass which can be used, for example, in migratory animals to determine if their movement is aligned (North-South) or unaligned (East-West) with the Earth's field. In contrast to a navigational mode, non-migratory animals such as certain species of lobsters and newts have the ability to detect the Earth's local magnetic signature [4]. This vicinal mapping mode utilizes magnetic signatures characteristic to a specific geographical area [5].

The ability to create a sensor which is sensitive to the Earth's magnetic field could come in great use in many applications. Military vehicles could navigate based on the Earth's magnetic field rather than global positioning satellites which may be susceptible to attack from an enemy. Such monitoring of the terrain's magnetic signature additionally means that disturbances to it can be tracked. The ability to detect magnetic signatures from underwater submarines rather than using sonar is one possibility. Another specific example is when two helicopters attempting to deploy ground troops in a location where sand or other material is swept up and impedes visibility. With the ability to magnetically detect one another, the troops in each helicopter could safely deploy in closer proximity, decreasing the vulnerability during the time required for the troops to rendezvous from two separate landing sites.

These examples provide background and relevant examples substantiating the need for smart structures. A significant portion of this research (Chapters 4 and 5) is devoted to designing, fabricating, and testing novel magnetic sensors which could be implemented in a smart structure. These examples provide ample motivation for developing a sensor system. In the next section,

the type of sensor will be identified which offers the potential for providing means for achieving the desired sensing capabilities.

1.3 Sensor Type

The choice of sensor type is a critical component which will heavily influence the effectiveness of the sensory system. Based on the applications listed above, we can begin to list certain design constraints which will play into the choice of sensor. The first consideration is to have a sensor which negligibly impedes the functionality of the structure. Therefore, a lightweight sensor miniaturized to reduce geometric profile is an obvious solution to such a constraint. Aircraft, for example, must be able to maximize their payload and aerodynamic efficiency, so a light system which is easily structurally integrated is ideal. The sensory system should also be distributed in order to maximize the amount of pertinent information captured by the sensors.

Optical fiber Bragg grating (FBG) sensors are a good option because they are lightweight (made of glass) and have a very small geometric profile. The fiber diameter is comparable to that of a typical human hair. Additionally, FBGs are capable of being multiplexed, meaning that thousands of gratings (i.e. sensor locations) can be written onto a single strand of optical fiber. This provides a distributed sensing system with high spatial resolution. Electrical resistance strain gauges are a heavily used strain sensor which provides a good point of comparison to emphasize the benefits of FBGs. Each sensing location for electrical strain gauges (ESGs) requires two separately insulated metal wires for measuring resistance. This sensing method would obviously get very heavy very quickly. Thus, ESGs are not an attractive choice for many smart structure applications [6].

An additional advantage of optical fiber often touted in literature is the immunity of the propagating light signal to electromagnetic interference. This is beneficial for strain and temperature sensors, but not for the proposed magnetic sensor. As will be seen later, FBGs can

be altered by replacing the optical medium, fused silica, which is relatively inert in magnetic fields with a magneto-optically active material.

In addition to the physical characteristic advantages, there are two compelling logistical arguments which make FBGs an attractive choice. The first is that this research is able to build upon a broad foundation of research already performed due to the wide applicability of FBGs. Since the advent of optical fiber Bragg gratings in 1978, a great deal of work has gone into developing this technology for various purposes [7]. FBGs have been developed for applications in photonics included providing distributed feedback for waveguide lasers and creating optical filters. They have also been vastly developed for sensing many types of external stimuli such as acoustic, chemical, current, voltage, and pressure signals in addition to the strain, thermal, and magnetic fields explored in this research.

The second argument is the ever-rising popularity of optical fiber technology in the telecommunications industry. Because of its popularity, much work has gone into developing the peripheral equipment such as lasers, photodetectors, couplers, etc. required to perform work on FBGs. The availability of commercial off the shelf equipment which supports FBG testing has driven down costs and complexity in experimental setup and has shortened the hurdles which must be overcome to perform research in the field.

Fiber Bragg gratings are therefore the sensor of choice for providing the sensory feedback necessary to create a smart structure. Before this research began, NASA had already gone to great lengths developing a structural health monitoring system which utilizes FBGs to monitor strain [8]. This system, called the fiber optic interrogation system (or FOID), is particularly good at accurately and reliably monitoring strain with high accuracy and spatial resolution when surface-mounted onto a structure. The researchers have demonstrated the performance of the system with various experiments. For example, wing shape was monitored during flight of a Predator drone undergoing various maneuvers. This measurement system will be utilized and developed in this research.

In the next section, the various aspects of this research will be tied together in order to provide perspective on the breadth of expertise which is required to develop reliable sensors. Additionally, the flow of the dissertation will be outlined.

1.4 Scope and Flow of the Dissertation

The overarching theme conveyed in this introduction is that the intention of this research is to develop and to create optical fiber Bragg grating based sensors which will improve and expand the capabilities of the NASA FOID system used for creating smart structures. In order to accomplish this, expertise must be developed over a broad range of fields and technical areas. These technical areas will be described first and followed by a description of the flow of the dissertation.

1.4.1 Breadth of Research

Figure 1-1 below demonstrates the various fields which this work incorporates. The field of mechanics will be employed with elasticity theory to understand the various strain states on embedded versus surface-mounted optical fibers experiencing mechanical loads. Additionally, the subject of strain transfer to the optical fiber sensor from the host material will be analyzed. Behavior unique to the field of composites will be explored. The effects of specific types of lay-ups, residual strains from the composite curing process, and cross-ply cracks will be studied. An understanding of material behavior is essential, for instance, in utilizing ferroic materials to transduce energy from one form into another. This transduction creates a mechanism for coupling external phenomena to the FBG signal. Exploring such coupling phenomena will aid in expanding the capabilities of the system to measure fields in addition to strain (for example, magnetism). Comfort with the field of optics must be obtained to fully understand the behavior of light propagating in a fiber in addition to the mechanism of reflection from the FBG. Optical anisotropy will also be studied using photoelastic theory in an excellent example of crossing the

fields of mechanics with optics. In order to understand the output from the FOID system, the process used to collect an optical signal from the FBGs must be known. It is crucial to understand the accuracy limitations of the system as well as how a large quantity of sensors is measured. This includes an understanding of the software code and the hardware used in the system. Lastly, expertise in sensor development must be established which includes understanding how to evaluate the reliability of a sensor in order to understand its potential and its limitations. The coupling mechanism used to relate external phenomena to the sensor signal must also be fully understood along with how to characterize the coupling relationship.

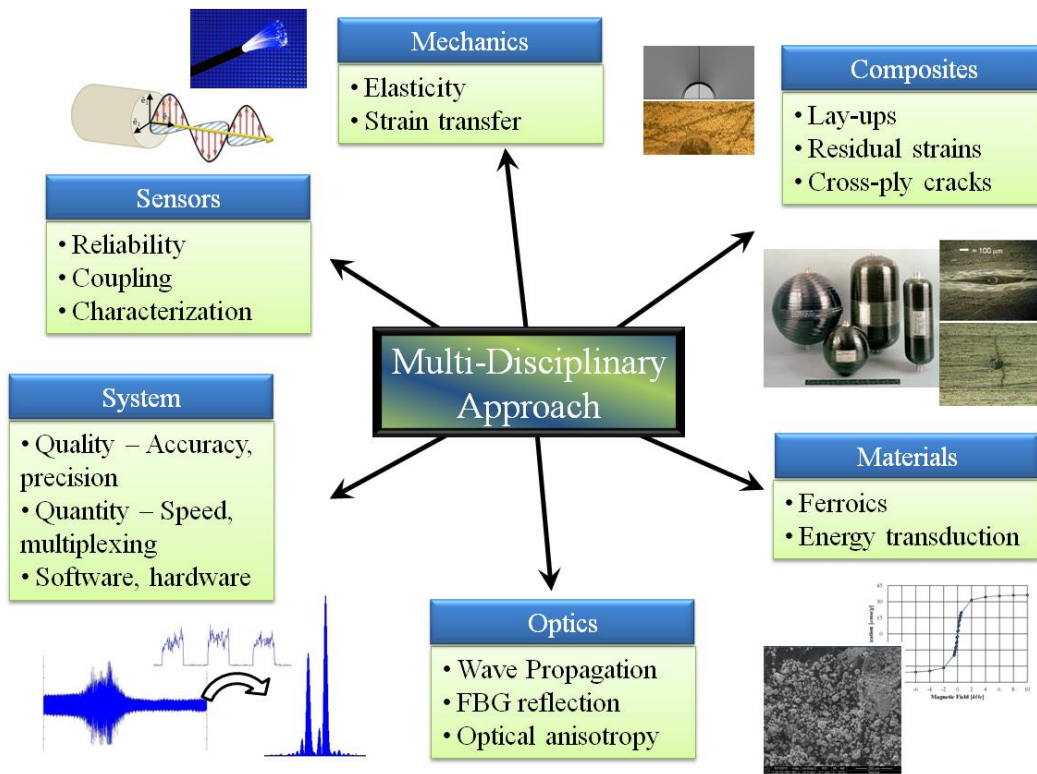


Figure 1-1: Multidisciplinary approach to developing the sensor system for smart structure applications.

In addition to the breadth of technical fields related to this research, various methods of research were performed which included both theoretical and experimental analysis. This included digging through equations to develop expected trends and behavior in the FBG sensor. This included using photoelastic theory to understand the link between changes in optical

properties when a strain state is applied. Additionally, light propagation was analyzed starting with Maxwell's equations to understand how changing various fiber properties (which would occur due to an external phenomenon which is being sensed) will alter the measured optical signal. Lastly, finite element analysis is utilized to understand the behavior of composite materials and the relationship between the composite host's strain state and that of an embedded optical fiber. In addition to the theoretical work, physical experiments were performed and the results were, in many cases, compared to theoretical predictions. These experiments were meticulously designed and often included several steps to characterize the FBG sensor fabrication. Such characterizations included the influence of the composite embedment process on a FBG reflection signal, the crystal structure of thin films coated on a FBG, and how an etching process used to thin a FBG altered the reflection signal. Once these characterizations were carried out, the mechanical, thermal, and magnetic experiments were performed and the data subsequently analyzed.

In essence, breadth was required in this research to successfully tackle the multidisciplinary approach of developing sensors and to explore the behavior of such sensors both theoretically and experimentally. The methods for carrying out this research and the organization of the dissertation will be described next.

1.4.2 Flow of the Dissertation

Five chapters in addition to the introduction will be used to describe this research as follows:

In chapter 2, a general introduction to fiber Bragg gratings will be given. What they are, how they are made, and how they operate are some of the many questions which will be answered. Light propagation in an optical fiber will be analyzed starting with Maxwell's equations and followed up with a derivation of a FBG reflection spectrum based on coupled mode theory. Methods for using FBGs as sensors will be theoretically developed using phenomena such as photoelasticity, thermo-optics, and magneto-optics. The fiber interrogation system will then be described. The purpose of the chapter is to give the reader a solid introductory foundation in

optical fiber Bragg gratings which will be used to explain experimental phenomena seen in subsequent chapters.

Chapters 3, 4, and 5 will each contain its own literature review, as well as fabrication, experimental setup, results, and concluding sections. The topics covered in the three chapters fit into the described overarching theme of the dissertation, but are distinct enough that their literature review, results, etc. are not overlapping.

In chapter 3, the research performed to develop optical fiber Bragg gratings will be described. FBGs perform as reliable surface-mounted strain gauges, but interesting phenomena can be observed when embedded within composite materials. After a comprehensive literature review, the specimens fabricated for testing will be described. Mechanical load testing results will be given and explained using the photoelastic theory developed in chapter 2. These results will be explained with finite element analysis.

In chapter 4, the sensing capabilities of the FBG system will be broadened by introducing active materials coupling strain with other phenomena. Sputter-deposited thin film coatings will be described that couple mechanical strains imparted on the attached optical fiber with thermally induced phase transformations in the case of shape memory alloy nickel-titanium and with magnetically induced strain in the magnetostrictive alloy Terfenol-D. Fabrication issues and experimental results will be described.

In chapter 5, active materials are once again used to provide coupling which expands the FBG sensing system capabilities. This time, however, mechanical, strain-based coupling is avoided. This is accomplished by replacing the optical medium with an active material rather than adhering to the silica. An extension of the electromagnetic wave propagation theory developed in Chapter 2 will be presented to fully understand the behavior of the fiber optic. The various iterations of sensor design will then be described along with the steps for fabricating the final design. Magnetic test results demonstrating a coupling between magnetic fields and the wavelength of light reflected by the FBGs will be illustrated.

The dissertation will be wrapped up with a description of ongoing research and concluding remarks in Chapter 6. Lessons learned and a vision of future endeavors will be described.

CHAPTER 2:

FIBER BRAGG GRATINGS

2.1 Synopsis

The objective of this research is to develop the strain sensing capabilities as well as design, fabricate, and test novel sensors which expand the current sensing capabilities of fiber Bragg gratings (FBGs). In this first section, optical fibers and FBGs are briefly described in order to define the objective in the context of using FBGs as sensors. Subsequently, a section will be devoted to describing the development of FBG fabrication in order to give the reader a history of the origins of FBGs and how they have become readily commercialized. The two sections following will provide a comprehensive theoretical framework for understanding the behavior of FBGs. The manner in which the various material properties and the geometric configuration of the sensor contribute to the reflection signal will be described. Once the pertinent factors contributing to the reflection characteristics of FBGs have been identified, the methods by which external phenomena change those factors and thus, the reflection characteristics will be illustrated. This identifies the strategies used for coupling the optical signal to external phenomena. Lastly, the method for measuring the optical signal will be described to explain how changes in the reflection characteristics of a FBG will be seen and quantified.

2.1.1 Optical Fibers

The most basic version of an optical fiber consists of two cylindrical, concentric layers of silica with slightly differing indices of refraction. The inner and outer layers are called the core and cladding, respectively, and the difference in index of refraction (IOR) is attained by the

introduction of dopants to one or both of the layers. If light, represented with a ray, travels through the core and encounters the core-cladding interface at an angle smaller than the critical angle ($\theta < \theta_c$) as determined by Snell's Law, then a fraction of its intensity will be refracted into the cladding as shown in Figure 2-1. The reflected light will continue to have a fraction of its intensity refracted at every core-cladding interface until eventually the intensity fades. A ray of light that approaches the interface at an angle $\theta > \theta_c$ will experience total internal reflection and remain within the core [9]. The abrupt discontinuity in dopant concentration at the interface causes light with an admissible angle to completely reflect and remain propagating within the fiber. Optical fibers used in this research specifically utilize germanium dopants in the silica core and pure silica in the cladding to create the difference in IOR.

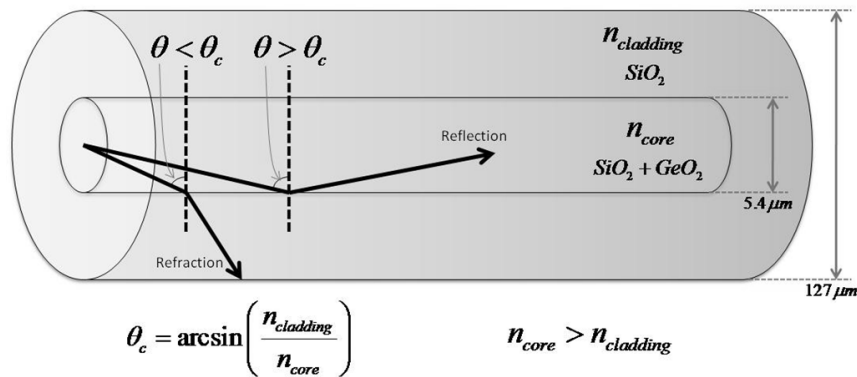


Figure 2-1: A depiction of how total internal reflection leads to light propagation.

2.1.2 Fiber Bragg Gratings

Optical fiber Bragg gratings are essentially a filter which reflects a particular wavelength of light while transmitting others. It is physically an oscillation in the refractive index of the optical fiber core; the peaks of which are represented in Figure 2-2 with bold stripes. The distance between peaks (Λ) plays an essential role in the reflected wavelength.

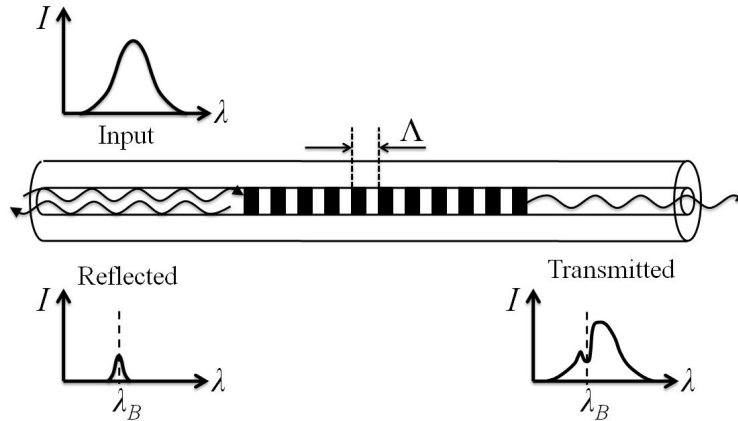


Figure 2-2: Qualitative reflection characteristics of FBGs.

The figure above depicts the result of inputting a distribution of light over a range of wavelengths shown in the intensity (I) vs. wavelength (λ) graph in the upper left corner. A portion of the intensity distribution at what is known as the Bragg wavelength (λ_B) is reflected as shown in the bottom left plot while the rest of the signal is transmitted as shown in the bottom right plot. A particularly important feature to note in Figure 2-2 is that only a fraction of the light signal is reflected. Thus, numerous FBGs can be written onto the same optical fiber without significantly diminishing the propagating signal. The sensors can therefore be multiplexed to develop a distributed sensor system. If, however, multiplexing is not needed, the FBGs can be designed to reflect a larger fraction of light as will be shown later.

Understanding the equation which dictates the wavelength of light reflected by the grating is crucial for understanding how FBGs are utilized as a sensing device. The following is the equation that determines the reflected wavelength:

$$\boxed{\lambda_B = 2n\Lambda} \quad (2.1)$$

This relationship, also known as the Bragg condition, identifies the grating periodicity, Λ , and effective IOR, n , as the main contributors that describe the reflected wavelength. This equation is the most important equation in the dissertation. All endeavors into developing and creating sensors stem from manipulating the reflected wavelength, λ_B by altering the optical (n)

and geometric (Λ) properties of the FBG. This equation will be explored in great depth later in this chapter, but before undertaking the analysis describing how FBGs operate, fabrication techniques will be described.

2.2 Fabrication

A walk-through of how optical fibers and FBGs are fabricated is presented in this section. Historical context is given with respect to landmark publications that led to significant technological advances in the field. The drawing of simple optical fiber is described first followed by the phenomenon known as photosensitivity which gives rise to FBGs. A description of writing techniques that have pushed FBGs into the realm of commercial production wraps up the section. The purpose of this section is to give the reader a foundational knowledge of the physical characteristics of a FBG to better understand the subsequent analysis that will be presented.

2.2.1 Optical Fiber Drawing

A preform, which is essentially a large-scale optical fiber, is created using a vapor phase oxidation technique that allows precise control of dopant concentrations. The fiber is drawn from the heated preform down to a typical diameter of $127 \mu\text{m}$ with a core diameter of $5.4 \mu\text{m}$ for single mode fiber used in this research. For reference, a typical human hair has a diameter between 50 and $100 \mu\text{m}$. The definition of single mode will be provided in a later section. The low tolerances required to create consistent, reliable fiber has triggered extensive research and development through the decades in order to minimize adverse effects such as transmission loss and decreased strength [10]. Diffusion of the dopants during the high temperature drawing process can adversely affect the IOR profile and degrade the quality of the optical fiber. Models have therefore been created to predict and control this effect [11]. Once drawn to the proper diameter, the glass fiber is then coated with a protective material to prevent moisture absorption

which can drive open micro-cracks and fatally deteriorate the fiber strength. The type of coating material depends on the application and cost. Acrylate, for example, is a low-cost material for less demanding environments while polyimide is more durable. Metals such as gold are also used for high-temperature environments which reach several hundred degrees centigrade.

2.2.2 Photosensitivity

Photosensitivity is the phenomenon defined by a change in a material's index of refraction with exposure to a high intensity radiation. The effect was first published in 1978 for Ge-doped silica optical fiber [12]. The peaks of a standing wave created with contra-directionally propagating ultraviolet (UV) light in the fiber core triggered a periodic perturbation of the core IOR. The authors reported the creation of a high quality, narrow-band reflection filter for the application of optical communication systems [13]. This fulfilled their intended goal of coupling forward and backward propagating modes in a periodic optical medium [14]. The authors were specifically interested in creating a distributed-feedback gas laser, but the creation and publication of the first fiber Bragg grating led to the invention becoming relevant in many fields.

A lull in FBG literature followed because it was assumed photosensitivity was a characteristic specific to the fibers used in its discovery. With such a narrow option for optical fibers in which the effect was seen, interest in developing the technology was discouraged. This was later refuted in a paper discussing the strong relationship between GeO_2 dopant concentrations in the fiber core and the successful writing of FBGs [15]. This complements previous work which found the index change in GeO_2 doped fiber to be proportional to the square of the radiation writing power [16]. While the cause of photosensitivity was still unknown, the evidence in these papers and others indicated Ge-Ge and Ge-Si defects were responsible for the effect [17]. This work demonstrated that the types of fibers considered to be photosensitive were more numerous than originally thought. This discovery triggered an increase in interest and the next major accomplishment in FBG fabrication involving a better grating writing method.

2.2.3 Writing Techniques

To this point, Bragg gratings had been written onto optical fibers internally using a standing wave created by green light (488 or 514.5 nm wavelength) sent with an argon ion laser into one end of the fiber and the reflection of that light from the interface at the opposite end. The IOR perturbations are present throughout the entire length of the fiber and the reflected wavelength is restricted to the wavelength of light used to write the grating. These limitations were nullified with the advent of externally written FBGs that allow the EM wave initiating the IOR changes to hit the fiber from the side rather than propagating through the fiber [18]. The method used has become known as the interferometric technique which involves exposing a portion of the optical fiber to two interfering, coherent, UV beams as shown in Figure 2-3. The UV light source of wavelength λ_{UV} is split and guided with reflectors and lenses to the optical fiber. The two beams interfere, creating a standing wave on the fiber core. Locations of constructive interference alter the index of refraction and locations of destructive interference do nothing.

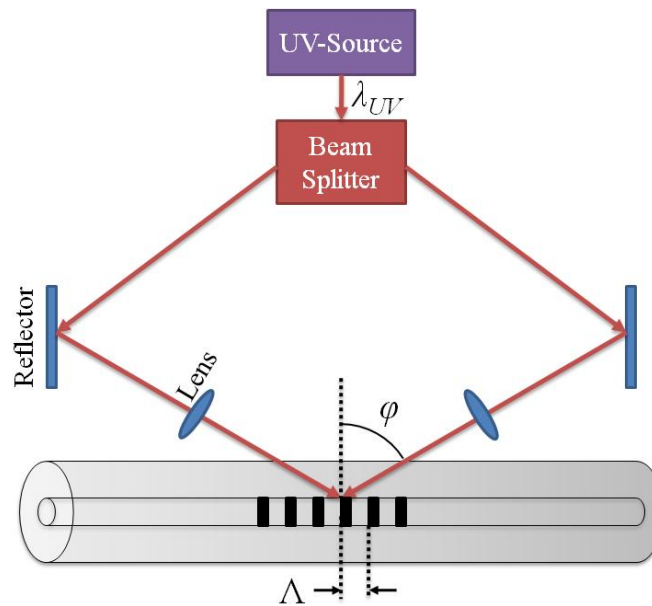


Figure 2-3: Interference technique for writing FBGs.

The UV beams take advantage of the GeO₂ absorption band at a wavelength of 244 nm to induce a periodic change in the index of refraction [19]. The periodicity of IOR change, Λ , is a function of the angle at which the two interfering UV beams strike the fiber as follows:

$$\Lambda = \frac{\lambda_{UV}}{2 \sin(\varphi)} \quad (2.2)$$

Λ is the grating period, λ_{UV} is the ultraviolet wavelength of light used to write the grating, and φ is the half-angle between the two intersecting beams. After a FBG is written onto the core, the optical fiber is translated, the UV exposure resumes, and multiple FBGs are written onto the same fiber [20]. Two factors that heavily contribute to the amount of reflectivity are the length of the FBG and magnitude of index oscillations. The magnitude of index oscillation, Δn , is determined by UV exposure time and intensity [21]. FBG reflection coefficients can range from a fraction of a percent to nearly unity [22]. Manufacturers, therefore, have several tools at their disposal to tailor the properties of FBGs to meet customer and application needs.

Two other methods for writing gratings are the phase-mask and point-by-point techniques which are illustrated in Figure 2-4. The phase-mask is different from the interferometric technique in that rather than splitting the beam in two and recombining to create an interference pattern, a single beam of light is sent through a diffracting phase mask to create the standing UV wave on the fiber optic [23]. This allows more flexibility in designing the standing wave intensity pattern by creating a suitable phase mask. Chirped FBGs, a type of FBG whose grating periodicity is a function of distance along the fiber, $\Lambda = \Lambda(z)$, can be created with such a technique. Chirped FBGs are significant because the reflected wavelength also becoming a function of distance, $\lambda_B = \lambda_B(z)$, and therefore opens up different applications for FBGs.

In the point-by-point technique, each grating plane is written individually with a single, focused pulse from a laser rather than writing an entire FBG at once. This method is much more laborious and time consuming, but allows for manufacturers to create tilted gratings by changing the UV beam's angle of incidence. Such a grating still creates the same transmission signal seen

in Figure 2-2, but the grating will reflect light at an angle which doesn't meet the total internal reflection requirement dictated by Snell's Law. Therefore, no reflected signal will be detected because all the reflected light refracts out of the grating.

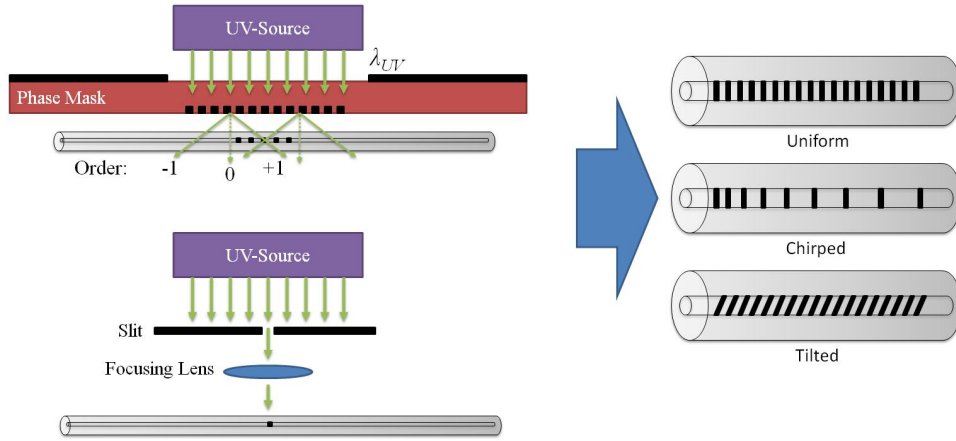


Figure 2-4: Manner in which writing technique influences the type of grating.

The initial shortcoming of side-writing was that the manufactured optical fiber had to be stripped of its coating in order to write the Bragg gratings and subsequently recoated. This hindrance greatly decreased the production speed and also weakened the optical fiber at the writing location due to exposure to ambient moisture. This challenge, however, was overcome with the integration of the writing technique into the drawing process [24]. Due to this development, Bragg gratings are now written onto optical fibers between the drawing and coating steps of production. Advances over the decades such as this have developed the fabrication of optical fiber Bragg gratings into a mature, precise science. FBGs are now commercially available and can address a wide variety of applications.

2.2.4 Concluding Remarks

Describing the development of FBG fabrication processes provides insight into the physical characteristics of FBGs. Though a ray representation of light provides a framework for understanding how optical fibers behave, for instance, the utilization of total internal reflection to promote propagation, it does not tell the whole story. A theoretical framework based on the wave nature of light will be developed in the following sections to expand our understanding of the behavior of light within an optical fiber.

2.3 Light Propagation in Optical Fibers

A forward propagating mode coupling and giving rise to a backward propagating mode via an oscillatory medium such as that found in a FBG is inherently a wave phenomenon. Therefore, in order to understand the behavior of light within an optical fiber, the propagation characteristics of an electromagnetic (EM) wave within a fiber must be analyzed. This begins with a theoretical description of light propagation which is derived from Maxwell's equations. The distribution of electric and magnetic fields in the fiber associated with a propagating EM wave will then be presented. The properties and characteristics of the optical fiber will be seen to play an important role in determining the effective IOR which will in turn directly affect the reflected wavelength. The derivation provided here is a more detailed version of that found in textbooks such as Yariv 1989, Verdeyen 1995, and Yariv 1997 and others addressing electromagnetic theory and light propagation in waveguides [25-27].

The derivation below amounts to creating a partial differential wave equation from Maxwell's equation and solving that differential equation with boundary conditions relevant to optical fiber geometries. Once it is understood how the effective index is calculated, the reader will understand how manipulation of the optical fiber properties will influence the propagating light. This manipulation is the crux for designing FBG sensors found in this research.

2.3.1 Solving Maxwell's Equations for Optical Fibers

The two variables in the Bragg condition described above in Equation (2.1) must be understood in order to grasp how FBGs behave. The Λ term has a straightforward physical meaning and was expanded upon in the previous section describing chirped gratings. The n term, however, is more intricate and is the main focus of this section. It is referred to as an “effective” index of refraction because it is not equal to the core or cladding IOR, but rather a value between. For a typical single mode optical fiber, the difference between core and cladding IOR is small ($\sim 10^{-2}$) compared to their absolute values (~ 1.45), so n can be taken as either layer's IOR without introducing significant error. This will not always be the case in this research, so it becomes important to understand what the effective index is and how it behaves when manipulated by factors such as strain, temperature, and magnetic field.

A mechanical analogy to effective index is the Young's modulus of a composite. The composite Young's modulus is a function of the stiffness of the individual phases and a geometric term, volume fraction. We will find that the effective index is a function of the IOR of the individual phases of the fiber (i.e. the core and cladding) and a geometric term, the radius of the core.

2.3.1.1 DERIVING THE WAVE EQUATION

Maxwell's equations describe the fundamental relationships between electricity and magnetism. These equations play an integral role in describing optical fibers because the light travelling through the fiber is an electromagnetic wave. Equation (2.3) describes how the general form of Maxwell's equations is manipulated for application to optical fibers.

$$\left. \begin{aligned}
\nabla \cdot \mathbf{D} &= \sigma \\
\nabla \times \mathbf{H} &= \mathbf{j} + \frac{\partial \mathbf{D}}{\partial t} \\
\nabla \cdot \mathbf{B} &= 0 \\
\nabla \times \mathbf{E} &= -\frac{\partial \mathbf{B}}{\partial t}
\end{aligned} \right\} \Rightarrow \begin{aligned}
\nabla \cdot e_0 \mathbf{e}_r \mathbf{E} &= 0 \\
\nabla \times \mathbf{H} &= e_0 \mathbf{e}_r \frac{\partial \mathbf{E}}{\partial t} \\
\nabla \cdot \mu_0 \mathbf{I} \mathbf{H} &= 0 \\
\nabla \times \mathbf{E} &= -\mu_0 \mathbf{I} \frac{\partial \mathbf{H}}{\partial t}
\end{aligned} \quad (2.3)$$

The electric flux density vector D is related to electric field vector E with the permittivity tensor \mathbf{e} . The magnetic flux density vector B is analogously related to the magnetic field vector H through permeability tensor $\boldsymbol{\mu}$. The permittivity and permeability of free space is referred to with a “0” subscript while the “ r ” subscript attached to the permittivity term is for the relative permittivity. No relative term is present for permeability because relative permeability at optical frequencies is unity (hence the use of the identity matrix, \mathbf{I}). Additionally, it is assumed that no free charge, σ , or current, j , is present in the material. Bold terms represent second order tensors which are important for anisotropic media, but we can substitute them for scalar constants because both layers of the optical fiber have amorphous crystal structure, making them optically isotropic. In a later section, stress-induced anisotropy is present in the fiber and it becomes necessary to represent permittivity as a second order tensor. Assuming isotropy for now and upon manipulation using vector identities, substitution, and the relation between permittivity and index of refraction, $e_r = n^2$, the governing wave equation is developed as shown in Equation (2.4).

$$\left(\nabla^2 - \frac{n^2}{c^2} \frac{\partial^2}{\partial t^2} \right) \begin{Bmatrix} \mathbf{E} \\ \mathbf{H} \end{Bmatrix} = 0 \quad (2.4)$$

2.3.1.2 SEPARATION OF VARIABLES

The term ∇^2 is the Laplacian operator which will be performed in cylindrical coordinates due to the cylindrical geometry of optical fibers while n and c are the IOR of the material and speed of light, respectively. The ∇^2 term has the following form for cylindrical coordinates:

$$\nabla^2 = \frac{\partial^2}{\partial r^2} + \frac{1}{r} \frac{\partial}{\partial r} + \frac{1}{r^2} \frac{\partial^2}{\partial \phi^2} + \frac{\partial^2}{\partial z^2} \quad (2.5)$$

To solve the wave equation, a separation of variables method will be employed. This splits the function describing the electric and magnetic fields components into three equations multiplied together in the following form:

$$\begin{cases} E_r(r, \phi, z, t) \\ E_\phi(r, \phi, z, t) \\ E_z(r, \phi, z, t) \end{cases} = \begin{cases} F_{Er}(r, \phi) Z_{Er}(z) T_{Er}(t) \\ F_{E\phi}(r, \phi) Z_{E\phi}(z) T_{E\phi}(t) \\ F_{Ez}(r, \phi) Z_{Ez}(z) T_{Ez}(t) \end{cases} \quad (2.6)$$

$$\begin{cases} H_r(r, \phi, z, t) \\ H_\phi(r, \phi, z, t) \\ H_z(r, \phi, z, t) \end{cases} = \begin{cases} F_{Hr}(r, \phi) Z_{Hr}(z) T_{Hr}(t) \\ F_{H\phi}(r, \phi) Z_{H\phi}(z) T_{H\phi}(t) \\ F_{Hz}(r, \phi) Z_{Hz}(z) T_{Hz}(t) \end{cases}$$

Thus, the overall function is composed of a function of r and ϕ , of z , and of t . Note that each separated function ($F_E, Z_E, T_E, F_H, Z_H, T_H$) has three components, r, ϕ , and z . It will be shown shortly that the r and ϕ components of the electric and magnetic field vectors (E_r, E_ϕ, H_r , and H_ϕ) will be entirely dependent on the z components (E_z, H_z). Therefore, the two longitudinal components are determined with the separation of variables technique and subsequently used to calculate the r and ϕ components of the electric and magnetic fields. The separation of variables technique will be shown for the electric field z component as a representative example that can easily be applied to the magnetic field's z component. By plugging the z -direction electric fields from Equation (2.6) into the wave equation, we get the following relationship:

$$\begin{aligned} & \left(\frac{\partial^2 F_{Ez}(r, \phi)}{\partial r^2} + \frac{1}{r} \frac{\partial F_{Ez}(r, \phi)}{\partial r} + \frac{1}{r^2} \frac{\partial^2 F_{Ez}(r, \phi)}{\partial \phi^2} \right) \cdot Z_{Ez}(z) \cdot T_{Ez}(t) \\ & + \frac{\partial^2 Z_{Ez}(z)}{\partial z^2} F_{Ez}(r, \phi) T_{Ez}(t) - \frac{n^2}{c^2} \frac{\partial^2 T_{Ez}(t)}{\partial t^2} F_{Ez}(r, \phi) Z_{Ez}(z) = 0 \end{aligned} \quad (2.7)$$

When this is divided by the original function for the z component of the electric field, the equation simplifies to the following:

$$\frac{1}{F_{Ez}(r, \varphi)} \left(\frac{\partial^2 F_{Ez}(r, \varphi)}{\partial r^2} + \frac{1}{r} \frac{\partial F_{Ez}(r, \varphi)}{\partial r} + \frac{1}{r^2} \frac{\partial^2 F_{Ez}(r, \varphi)}{\partial \varphi^2} \right) + \frac{1}{Z_{Ez}(z)} \frac{\partial^2 Z_{Ez}(z)}{\partial z^2} - \frac{1}{T_{Ez}(t)} \frac{n^2}{c^2} \frac{\partial^2 T_{Ez}(t)}{\partial t^2} = 0 \quad (2.8)$$

The sum of three different terms, each dependent upon a different set of variables, is equal to zero. If any of these terms is brought to the right side of the equation, it becomes clear that because each side must be equal for all values of the variables (none of which are shared by both sides of the equation), both sides must equal a constant. This allows us to solve several simple differential equations rather than one large, complex equation.

2.3.1.3 SOLUTION IN TERMS OF z AND t

By inspection of the previous equation, we only need to solve the following two ordinary differential equations to determine the z and t dependence of the electric field:

$$\frac{\partial^2 Z_{Ez}(z)}{\partial z^2} = C_Z Z_{Ez}(z) \quad (2.9)$$

$$\frac{n^2}{c^2} \frac{\partial^2 T_{Ez}(t)}{\partial t^2} = -C_T T_{Ez}(t) \quad (2.10)$$

The solutions to these equations are simply an exponential of an imaginary number. We now plug in the following proposed solutions:

$$Z_{Ez}(z) = e^{-i\beta z} \quad (2.11)$$

$$T_{Ez}(t) = e^{i\omega t} \quad (2.12)$$

Note that it is more accurate to multiply Equations (2.11) and (2.12) by a constant, but any constant would just get absorbed by the future determination of $F_{Ez}(r, \varphi)$. Therefore, it is ignored here without any loss of validity in the end result. These solutions indicate that $C_Z = -\beta^2$ and $C_T =$

$\omega^2 n^2 / c^2$. All electric and magnetic field components of the propagating wave will have the same oscillatory dependence on the direction of propagation, z , and time, t . Thus, extrapolating the solution to the z -component of the electric field to all other components, we get the following updated solution to the wave equation:

$$\begin{Bmatrix} \hat{E}(r, \varphi, z, t) \\ \hat{H}(r, \varphi, z, t) \end{Bmatrix} = \begin{Bmatrix} \hat{F}_E(r, \varphi) \\ \hat{F}_H(r, \varphi) \end{Bmatrix} e^{i(\omega t - \beta z)} \quad (2.13)$$

The terms ω and β are the EM wave's angular frequency and propagation constant, respectively. Using the solution above, it can be shown using Maxwell's equations that the radial and azimuthal components of the electric and magnetic fields can be written in terms of the longitudinal fields. These relationships are shown in Equation (2.14).

$$\begin{aligned} E_r &= \frac{-i\beta}{\omega^2 \mu e - \beta^2} \left(\frac{\partial E_z}{\partial r} + \frac{\omega \mu}{r \beta} \frac{\partial H_z}{\partial \phi} \right) \\ E_\phi &= \frac{-i\beta}{\omega^2 \mu e - \beta^2} \left(\frac{1}{r} \frac{\partial E_z}{\partial \phi} - \frac{\omega \mu}{\beta} \frac{\partial H_z}{\partial r} \right) \\ H_r &= \frac{-i\beta}{\omega^2 \mu e - \beta^2} \left(\frac{\partial H_z}{\partial r} - \frac{\omega e}{r \beta} \frac{\partial E_z}{\partial \phi} \right) \\ H_\phi &= \frac{-i\beta}{\omega^2 \mu e - \beta^2} \left(\frac{1}{r} \frac{\partial H_z}{\partial \phi} + \frac{\omega e}{\beta} \frac{\partial E_z}{\partial r} \right) \end{aligned} \quad (2.14)$$

As previously stated, it is necessary to solve only for the two independent field components, E_z and H_z , in subsequent differential equation analysis and plug these expressions into Equation (2.14) to determine the rest of the electric and magnetic field components. Thus, the wave equation now takes the following form after plugging in the z component of Equation (2.13) into (2.4):

$$\left[\frac{\partial^2}{\partial r^2} + \frac{1}{r} \frac{\partial}{\partial r} + \frac{1}{r^2} \frac{\partial^2}{\partial \phi^2} + (k^2 - \beta^2) \right] \begin{Bmatrix} F_{Ez}(r, \varphi) \\ F_{Hz}(r, \varphi) \end{Bmatrix} e^{i(\omega t - \beta z)} = 0 \quad (2.15)$$

The newly introduced variable is defined as $k^2 = (\omega n/c)^2$ and represents the wavenumber for light propagating in a particular medium. The exponential term, dependent on z and t , can be divided out of the equation without losing any information in our upcoming pursuit of the form of $F_{Ez}(r,\varphi)$ and $F_{Hz}(r,\varphi)$.

2.3.1.4 DIFFERENCE BETWEEN β AND k

A quick clarification should be made at this point between the propagation constant, β , and wavenumber, k . Both have the same units (m^{-1}) and describe the rate of z component oscillation of a traveling EM wave. The distinction lies in the medium through which the wave propagates. The wavenumber k is used in this analysis to describe the propagation through a single medium, whereas β describes the propagation through a composite medium. In an optical fiber, the EM wave is assigned a propagation constant of β to describe its propagation while being simultaneously present in both the core and cladding layers (each with its own value of k). The simultaneous existence in both layers will be fully demonstrated shortly. If most of the propagating light is present in the cladding, β will be closer to the k value of the cladding. On the other hand, if more light exists in the core, then β will be closer in magnitude to the k value of the core. It will be seen shortly that Equation (2.15) will be split into one equation for the EM wave portion traveling through the core and one in the cladding; two different k values will be used, but the β value will be consistent in both equations.

2.3.1.5 SOLUTION IN TERMS OF φ

After stripping out the influence of z and t in the wave equation by dividing the $e^{i(\omega t - \beta z)}$ out of Equation (2.15), we can perform an additional separation of variables. The separation of F_{Ez} into two separate functions multiplied together will be demonstrated and can easily be extrapolated to find F_{Hz} .

$$F_{Ez}(r, \varphi) = R_{Ez}(r) \Phi_{Ez}(\varphi) \tag{2.16}$$

Plugging this into Equation (2.15), multiplying by r^2 , and dividing by F_{Ez} gives the following:

$$\frac{r^2}{R_{Ez}(r)} \left(\frac{\partial^2 R_{Ez}(r)}{\partial r^2} + \frac{1}{r} \frac{\partial R_{Ez}(r)}{\partial r} + k^2 - \beta^2 \right) + \frac{1}{\Phi_{Ez}(\varphi)} \frac{\partial^2 \Phi_{Ez}(\varphi)}{\partial \varphi^2} = 0 \quad (2.17)$$

Using the same logic for the z and t solutions, we set the second term which is dependent on only φ equal to a constant and solve the ensuing ordinary differential equation. The form of $\Phi_{Ez}(\varphi)$ is an exponential function with multiplicative constant, l :

$$\Phi_{Ez}(\varphi) = e^{il\varphi} \quad (2.18)$$

As was done earlier, Equation (2.18) should be multiplied by a constant for the general solution, but any constant will just get swallowed up in the constant used in the upcoming determination of $R_{Ez}(r)$. A fundamental difference between the φ and z spatial variables must be considered when deciding upon the solution's form. Specifically, the solution must be consistent with the fact that $\Phi_{Ez}(\varphi = 0) = \Phi_{Ez}(\varphi = 2\pi)$. If this requirement is not satisfied, then the function will have two different values at the same location in space which is not physically possible.

2.3.1.6 SOLUTION IN TERMS OF r

Now that the dependence of E_z on φ , z , and t has been determined, the r dependence is established by updating and revisiting the wave equation (Equation (2.4)):

$$r^2 \frac{\partial^2 R_{Ez}(r)}{\partial r^2} + r \frac{\partial R_{Ez}(r)}{\partial r} + \left(r^2 (k^2 - \beta^2) - l^2 \right) R_{Ez}(r) = 0 \quad (2.19)$$

The form of this equation nearly matched the differential equation to which Bessel functions are the solution. In order to obtain a complete match, a change of variable is carried out from r to the unitless variable ρ defined as follows:

$$r = \frac{\rho}{\sqrt{k^2 - \beta^2}} \quad (2.20)$$

Note the following chain rule effects on the differentiation terms:

$$r \frac{\partial R_{Ez}(\rho)}{\partial r} = \frac{\rho}{\sqrt{k^2 - \beta^2}} \frac{\partial R_{Ez}(\rho)}{\partial \rho} \frac{\partial \rho}{\partial r} = \rho \frac{\partial R_{Ez}(\rho)}{\partial \rho} \quad (2.21)$$

$$\begin{aligned} r^2 \frac{\partial^2 R_{Ez}(\rho)}{\partial r^2} &= \frac{\rho^2}{k^2 - \beta^2} \frac{\partial}{\partial r} \left(\frac{\partial R_{Ez}(\rho)}{\partial \rho} \frac{\partial \rho}{\partial r} \right) = \frac{\rho^2}{\sqrt{k^2 - \beta^2}} \frac{\partial}{\partial r} \left(\frac{\partial R_{Ez}(\rho)}{\partial \rho} \right) \\ &= \frac{\rho^2}{\sqrt{k^2 - \beta^2}} \frac{\partial^2 R_{Ez}(\rho)}{\partial \rho^2} \frac{\partial \rho}{\partial r} = \rho^2 \frac{\partial^2 R_{Ez}(\rho)}{\partial \rho^2} \end{aligned} \quad (2.22)$$

After plugging Equations (2.20), (2.21), and (2.22) into Equation (2.19), the differential equation now takes the following form:

$$\rho^2 \frac{\partial^2 R_{Ez}(\rho)}{\partial \rho^2} + \rho \frac{\partial R_{Ez}(\rho)}{\partial \rho} + (\rho^2 - l^2) R_{Ez}(\rho) = 0 \quad (2.23)$$

The equation is now in the requisite form for application of a Bessel function solution. The two features of the equation which dictate the order, type, and kind of Bessel function are the integer value of l and the sign of ρ^2 . The value of l determines the order of the Bessel function. If $\rho^2 > 0$ (i.e. $k^2 > \beta^2$) then the solutions to the equation are Bessel function of the first and second kind. However, if $\rho^2 < 0$ (i.e. $k^2 < \beta^2$), then the solutions to the equation are modified Bessel functions of the first and second kind. The Figure 2-5 below shows the four different Bessel function options in graphical form for integer values of l from zero to two as a function of unitless input, ρ .

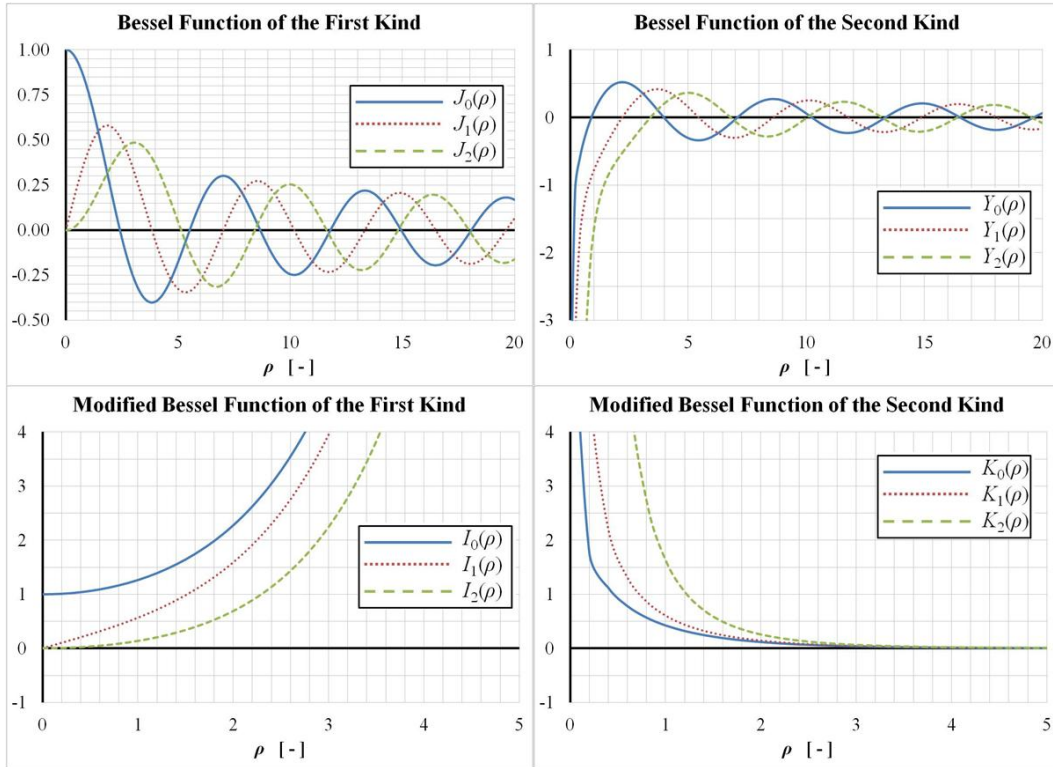


Figure 2-5: Form of the Bessel functions used to calculate the radial dependence of the magnitude of the propagating EM wave.

In summation, the general form for the solution of the z component of the electric field using the separation of variables method is as follows:

$$E_z(r, \varphi, z, t) = R_{Ez}(r) \Phi_{Ez}(\varphi) Z_{Ez}(z) T_{Ez}(t)$$

$$= \begin{cases} \left[AJ_l \left(r\sqrt{k^2 - \beta^2} \right) + BY_l \left(r\sqrt{k^2 - \beta^2} \right) \right] e^{i(\omega t + l\varphi - \beta z)} & k^2 > \beta^2 \\ \left[CI_l \left(r\sqrt{\beta^2 - k^2} \right) + DK_l \left(r\sqrt{\beta^2 - k^2} \right) \right] e^{i(\omega t + l\varphi - \beta z)} & k^2 < \beta^2 \end{cases} \quad (2.24)$$

The multiplicative constants A, B, C, and D contain the previously neglected constants in the solutions to the separated differential equation identifying the φ , z , and t dependence.

2.3.1.7 BOUNDARY CONDITIONS

The first physical characteristic of the fiber imposed so far on the solution is the unchanging properties in the z -direction (i.e. the direction of propagation) which led to the same z and t

dependence as a plane wave solution to the wave equation. The second characteristic is the cylindrical geometry which led us to work in a cylindrical coordinate system. We shall now impose the core and cladding IOR and boundary conditions to finalize our solutions.

The type of optical fiber used in this research is a step-index fiber which is described mathematically as a cylindrical material with IOR equal to n_1 in the fiber core ($r \leq a$) and n_2 in the cladding ($r > a$) where a is the core radius. In order to keep light bound within the waveguide, the EM wave's propagation constant, β , must be defined such that:

$$\begin{aligned} k_1^2 - \beta^2 &= n_1^2 k_0^2 - \beta^2 > 0, & r < a \\ k_2^2 - \beta^2 &= n_2^2 k_0^2 - \beta^2 < 0, & r > a \end{aligned} \quad (2.25)$$

Note the subscript of 1 and 2 on k denotes the wavenumber corresponding to the core and cladding layers respectively and the 0 subscript refers to free space. According to Snell's law, light propagating with the appropriate angle will experience total internal reflection and one would not expect to see any light in the cladding. The presence of the propagating light in both the core and cladding layers is a product of the wave representation of light as opposed to a ray representation. The presence of light in the cladding is very significant to this research because when a sensor is designed that manipulates light propagating through the fiber in a measurable way, it is determined that this can be accomplished by altering the properties of the cladding and not necessarily the core.

Note that the general solution to the wave equation is split into two possibilities (each containing two Bessel functions) depending on whether $k^2 > \beta^2$ or $k^2 < \beta^2$. As seen in Equation (2.25), this corresponds to whether we are analyzing light present in the core or cladding. Thus, the solution can be rewritten as follows:

$$E_z(r, \varphi, z, t) = \begin{cases} \left[AJ_l \left(r\sqrt{k_1^2 - \beta^2} \right) + BY_l \left(r\sqrt{k_1^2 - \beta^2} \right) \right] e^{i(\omega t + l\varphi - \beta z)} & r < a \\ \left[CI_l \left(r\sqrt{\beta^2 - k_2^2} \right) + DK_l \left(r\sqrt{\beta^2 - k_2^2} \right) \right] e^{i(\omega t + l\varphi - \beta z)} & r > a \end{cases}, \quad (2.26)$$

The first boundary conditions considered are that the light intensity remains finite both as $r \rightarrow 0$ and as $r \rightarrow \infty$. From the previous figure showing the Bessel functions, we see that the Bessel function of the second kind approaches $-\infty$ at the center of fiber ($r = 0$) and the modified Bessel function of the first kind approaches $+\infty$ far away from the core ($r \rightarrow \infty$). Neither of these provide physically realistic results, so we determine that $B = C = 0$. Using the same procedure to deal with the longitudinal magnetic field, the z -component of the electric and magnetic fields can be rewritten in the following way before applying the core-cladding interface boundary:

$$\begin{aligned}
r &\leq a \\
E_z(r, \varphi, z, t) &= c_1 J_l(hr) e^{i(\omega t + l\varphi - \beta z)} \\
H_z(r, \varphi, z, t) &= c_2 J_l(hr) e^{i(\omega t + l\varphi - \beta z)} \\
\text{where } h^2 &= k_1^2 - \beta^2 = n_1^2 k_0^2 - \beta^2
\end{aligned} \tag{2.27}$$

$$\begin{aligned}
r &> a \\
E_z(r, \varphi, z, t) &= c_3 K_l(qr) e^{i(\omega t + l\varphi - \beta z)} \\
H_z(r, \varphi, z, t) &= c_4 K_l(qr) e^{i(\omega t + l\varphi - \beta z)} \\
\text{where } q^2 &= \beta^2 - k_2^2 = \beta^2 - n_2^2 k_0^2
\end{aligned} \tag{2.28}$$

Note that the A and D constants from Equation (2.26) have been changed to c_1 and c_3 . The analogous constants for the magnetic field are introduced as c_2 and c_4 . The four constants to be solved with the core-cladding interface boundary conditions are c_1 , c_2 , c_3 , and c_4 . The four boundary conditions we use to determine the four constants are that the electric and magnetic field components transverse to the core-cladding interface are equal (i.e. E_φ , E_z , H_φ , and H_z are continuous across the boundary $r = a$). This is a byproduct of the more general boundary condition that the electric flux and magnetic flux are constant across a boundary. The equations below explicitly state the boundary conditions. Note Equation (2.14) is used to calculate E_φ and H_φ terms.

$$\begin{aligned}
& \boxed{E_\varphi(a^-, \varphi, z, t) = E_\varphi(a^+, \varphi, z, t)} \\
& \Rightarrow \frac{-i\beta}{h^2} \left(\frac{c_1 il}{a} J_l(ha) - \frac{c_2 \omega \mu h}{\beta} \left(\frac{\partial J_l(hr)}{\partial(hr)} \right)_{r=a} \right) \\
& \qquad \qquad \qquad = \frac{i\beta}{q^2} \left(\frac{c_3 il}{a} K_l(qa) - \frac{c_4 \omega \mu q}{\beta} \left(\frac{\partial K_l(qr)}{\partial(qr)} \right)_{r=a} \right) \\
& \boxed{E_z(a^-, \varphi, z, t) = E_z(a^+, \varphi, z, t)} \\
& \Rightarrow c_1 J_l(ha) = c_3 K_l(qa) \\
& \boxed{H_\varphi(a^-, \varphi, z, t) = H_\varphi(a^+, \varphi, z, t)} \\
& \Rightarrow \frac{-i\beta}{h^2} \left(\frac{c_2 il}{a} J_l(ha) + \frac{c_1 \omega e h}{\beta} \left(\frac{\partial J_l(hr)}{\partial(hr)} \right)_{r=a} \right) \\
& \qquad \qquad \qquad = \frac{i\beta}{q^2} \left(\frac{c_4 il}{a} K_l(qa) + \frac{c_3 \omega e q}{\beta} \left(\frac{\partial K_l(qr)}{\partial(qr)} \right)_{r=a} \right) \\
& \boxed{H_z(a^-, \varphi, z, t) = H_z(a^+, \varphi, z, t)} \tag{2.29} \\
& \Rightarrow c_2 J_l(ha) = c_4 K_l(qa)
\end{aligned}$$

The boxed expressions are the general boundary conditions while the unboxed expressions result from plugging Equations (2.27) and (2.28) into the boxed boundary conditions. Note that the following chain rule was applied when taking derivatives of Bessel functions with respect to r :

$$\frac{\partial(J_l(hr))}{\partial r} = \frac{\partial(J_l(hr))}{\partial(hr)} \frac{\partial(hr)}{\partial r} = h \frac{\partial(J_l(hr))}{\partial(hr)} \tag{2.30}$$

2.3.1.8 TRANSCENDENTAL EQUATION

This gives us a system of four equations to solve for the four unknowns. The equations can be gathered into a single matrix equation as follows:

$$\begin{bmatrix} \frac{\beta l}{h^2 a} J_l(ha) & \frac{i\omega\mu_1}{h} J_l'(ha) & \frac{\beta l}{q^2 a} K_l(qa) & \frac{i\omega\mu_2}{q} K_l'(qa) \\ J_l(ha) & 0 & -K_l(qa) & 0 \\ -\frac{i\omega e_1}{h} J_l'(ha) & \frac{\beta l}{h^2 a} J_l(ha) & -\frac{i\omega e_2}{q} K_l'(qa) & \frac{\beta l}{q^2 a} K_l(qa) \\ 0 & J_l(ha) & 0 & -K_l(qa) \end{bmatrix} \begin{Bmatrix} c_1 \\ c_2 \\ c_3 \\ c_4 \end{Bmatrix} = 0 \quad (2.31)$$

$$\text{where } J_l'(ha) = \left. \frac{\partial(J_l(hr))}{\partial(hr)} \right|_{r=a}$$

The system above is represented with a 4x4 matrix multiplied by a column vector, $\{c_1; c_2; c_3; c_4\}$ with the product equaling zero. Equation (2.31) can be restated in the following condensed form:

$$[\Omega_{ij}] \{c_i\} = 0, \quad i, j = 1, 2, 3, 4 \quad (2.32)$$

In order for a nontrivial solution to be found, the determinant of the $[\Omega]$ matrix must equal zero. The result is the following transcendental equation.

$$\boxed{\left(\frac{J_l'(ha)}{haJ_l(ha)} + \frac{K_l'(qa)}{qaK_l(qa)} \right) \left(\frac{n_1^2 J_l'(ha)}{haJ_l(ha)} + \frac{n_2^2 K_l'(qa)}{qaK_l(qa)} \right) = l^2 \left[\left(\frac{1}{qa} \right)^2 + \left(\frac{1}{ha} \right)^2 \right]^2 \left(\frac{\beta_{lm}}{k_0} \right)^2} \quad (2.33)$$

Now obtained is a transcendental equation whose inputs are the core and cladding IORs, n_1 and n_2 , core radius, a , freespace wavelength, λ_0 , and Bessel function order, l . The output is a set of wave propagation constants, β_{lm} , which satisfy the transcendental equation. Note the subscripts, lm , added to the β term in order to denote that there are a finite number of solutions which are able to satisfy the above relation. Each value of β_{lm} corresponds to a different mode of propagation. The relation between a given propagation constant, β_{lm} , and the effective index for that particular mode, n_{lm} , is seen in the following equation:

$$n_{lm} = \frac{\beta_{lm}}{k_0} = \frac{\beta_{lm} \lambda_0}{2\pi} \quad (2.34)$$

To summarize this process of finding the effective index, n_{lm} , we first start out with Maxwell's equations to derive the wave equation. The wave equation is a PDE which was solved in cylindrical coordinates using a separation of variables method. The forms of the z and t dependence are oscillatory just like a plane-wave propagating in the z -direction. The φ dependence is found to be oscillatory as well and the r -dependence is in the form of Bessel functions. Using the boundary conditions that the light intensity must remain finite at the center of the core and far away from the fiber and that the transverse electric and magnetic field components must be continuous across the core-cladding interface, a transcendental equation is derived which is solved for to find the propagation constant, β_{lm} , and in turn, the effective index, n_{lm} .

2.3.2 Modes of Propagation

A finite number of propagation constants will satisfy the transcendental equation. A mechanical analogy to the modes of propagation just derived is the vibration of a circular plate. The out-of-plane vibration of a circular plate can be described as the sum of individual modes shapes. By the same token, light propagating down an optical fiber can be described as the sum of individual modes, each with its own intensity shape. A description of the various mode shapes and how the material properties of the optical fiber inhibit or promote certain modes will now be given.

The input material parameters described above are non-dimensionalized by incorporating them into a single parameter, V , defined as follows:

$$V = \frac{2\pi a}{\lambda} \sqrt{n_1^2 - n_2^2} \quad (2.35)$$

We now have a simplified method for varying the inputs by varying the V parameter and looking at the resulting propagation constants that satisfy the transcendental equation. This relationship is shown in Figure 2-6 below. The horizontal axis is the V parameter and the vertical

axis is the propagation constant divided by freespace wavenumber, k_0 , which equates to the effective index of refraction. Note that the core and cladding IORs (n_1 and n_2) are the upper and lower bounds respectively for the effective index range. Each curve in the graph represents a different mode.

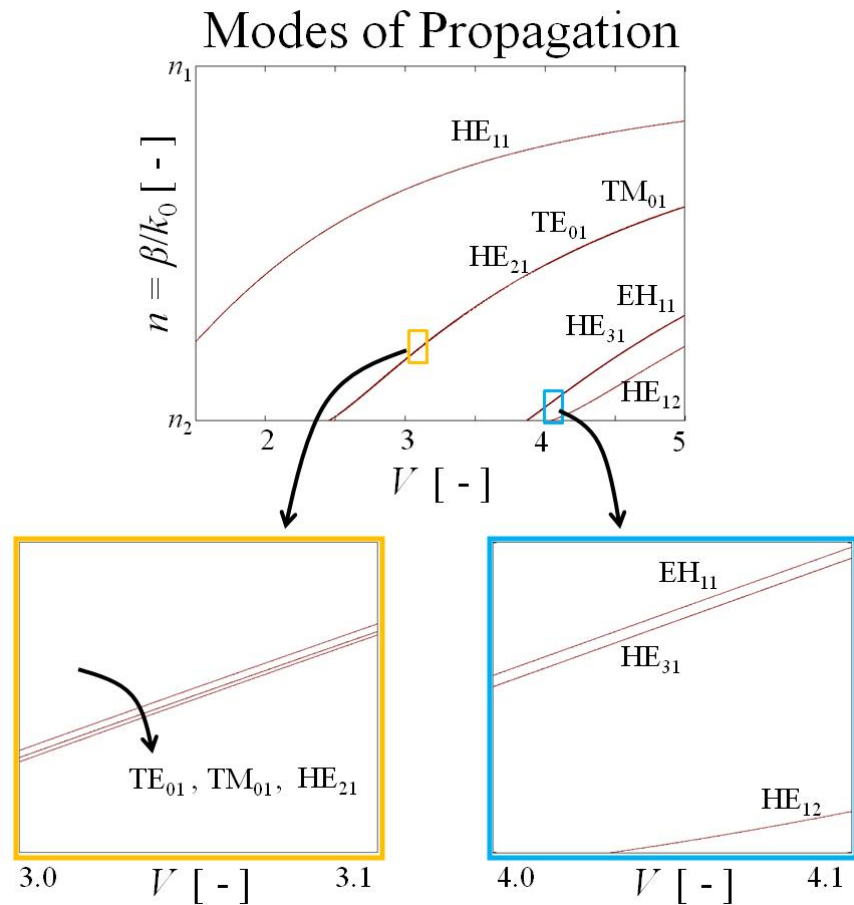


Figure 2-6: Influence of V parameter on the effective index for various modes of light propagation.

To find the modes present in the fiber, draw a vertical line from the x-axis at the V parameter value corresponding to the input parameters of the fiber (n_1 , n_2 , a , λ). The vertical axis coordinate where the drawn vertical line intersects a mode curve corresponds to the effective index for that mode.

Note that the graph above uses four different mode labels (HE, EH, TE, and TM) in addition to the mode number subscripts. The transcendental equation is quadratic in the Bessel function term $J'_l(ha)/haJ_l(ha)$; therefore, solving for the two roots of the quadratic equation results in two different types of modes represented as EH_{lm} and HE_{lm} . Thus, a given input V parameter, Bessel function order, l , and solution number, m , may provide an EH and/or a HE mode propagation constant that satisfies the transcendental equation. In the case of $l = 0$, the longitudinal electric field component vanishes in the HE_{0m} mode, resulting in a purely transverse electric field, or TE_{0m} mode. The magnetic analog is the EH_{0m} mode being referred to as a transverse magnetic, or TM_{0m} mode. Note that below $V = 2.405$, the only mode supported is the HE_{11} mode and the fiber optic behaves as a single-mode fiber. This is beneficial for telecommunications because an EM wave pulse comprised of multiple modes will have its energy distributed into multiple effective IORs. As the pulse propagates, it will spread in time because the different components of the wave's energy will travel at different speeds. This means that pulses cannot be packed together as tightly as in single-mode operation and less information (i.e. fewer pulses representing bits of value 1 or 0) can be sent in the same window of time.

The shape of each mode depends on the values of l and m and whether the mode is HE_{lm} or EH_{lm} . Once a propagation constant is found for a given value of l and m , three of the four c_i multiplication constants can be written in terms of the fourth. The following equations describe the relationships amongst the constants based on Equation (2.31).

$$\begin{aligned} \frac{c_2}{c_1} &= \frac{i\beta l}{\omega a^2} \left(\frac{1}{h^2} + \frac{1}{q^2} \right) \left(\mu_1 \frac{J'_l(ha)}{haJ_l(ha)} + \mu_2 \frac{K'_l(qa)}{qaK_l(qa)} \right)^{-1} \\ \frac{c_3}{c_1} &= \frac{J_l(ha)}{K_l(qa)} \\ \frac{c_4}{c_1} &= \frac{i\beta l}{\omega a^2} \left(\frac{1}{h^2} + \frac{1}{q^2} \right) \frac{J_l(ha)}{K_l(qa)} \left(\mu_1 \frac{J'_l(ha)}{haJ_l(ha)} + \mu_2 \frac{K'_l(qa)}{qaK_l(qa)} \right)^{-1} \end{aligned} \quad (2.36)$$

These values for c_2 , c_3 , and c_4 in terms of c_1 can be plugged into Equations (2.27) and (2.28) in order to determine the z -components of the electric and magnetic fields within a multiplicative constant, c_1 . These in turn are plugged into Equation (2.14) to find the radial and azimuthal components of the EM field. The components of the electric and magnetic fields are explicitly defined in the following equations for $r \leq a$:

$$\begin{aligned}
E_r(r, \varphi, z, t) &= c_1 \left[-\frac{i\beta}{h} J'_l(hr) + \left(\frac{c_2}{c_1}\right) \frac{\omega\mu_1 l}{h^2 r} J_l(hr) \right] e^{i(\omega t + l\varphi - \beta z)} \\
E_\varphi(r, \varphi, z, t) &= c_1 \left[\frac{\beta l}{h^2 r} J_l(hr) + \left(\frac{c_2}{c_1}\right) \frac{i\omega\mu_1}{h} J'_l(hr) \right] e^{i(\omega t + l\varphi - \beta z)} \\
E_z(r, \varphi, z, t) &= c_1 \left[J_l(hr) \right] e^{i(\omega t + l\varphi - \beta z)}
\end{aligned} \tag{2.37}$$

$$\begin{aligned}
H_r(r, \varphi, z, t) &= c_1 \left[-\frac{\omega e_1 l}{h^2 r} J_l(hr) - \left(\frac{c_2}{c_1}\right) \frac{i\beta}{h} J'_l(hr) \right] e^{i(\omega t + l\varphi - \beta z)} \\
H_\varphi(r, \varphi, z, t) &= c_1 \left[-\frac{i\omega e_1}{h} J'_l(hr) + \left(\frac{c_2}{c_1}\right) \frac{\beta l}{h^2 r} J_l(hr) \right] e^{i(\omega t + l\varphi - \beta z)} \\
H_z(r, \varphi, z, t) &= c_1 \left[\left(\frac{c_2}{c_1}\right) J_l(hr) \right] e^{i(\omega t + l\varphi - \beta z)}
\end{aligned} \tag{2.38}$$

And for $r > a$:

$$\begin{aligned}
E_r(r, \varphi, z, t) &= c_1 \left[\left(\frac{c_3}{c_1}\right) \frac{i\beta}{q} K'_l(qr) - \left(\frac{c_4}{c_1}\right) \frac{\omega\mu_2 l}{q^2 r} K_l(qr) \right] e^{i(\omega t + l\varphi - \beta z)} \\
E_\varphi(r, \varphi, z, t) &= c_1 \left[-\left(\frac{c_3}{c_1}\right) \frac{\beta l}{q^2 r} K_l(qr) - \left(\frac{c_4}{c_1}\right) \frac{i\omega\mu_2}{q} K'_l(qr) \right] e^{i(\omega t + l\varphi - \beta z)} \\
E_z(r, \varphi, z, t) &= c_1 \left[\left(\frac{c_3}{c_1}\right) K_l(qr) \right] e^{i(\omega t + l\varphi - \beta z)}
\end{aligned} \tag{2.39}$$

$$\begin{aligned}
H_r(r, \varphi, z, t) &= c_1 \left[\left(\frac{c_3}{c_1} \right) \frac{\omega e_2 l}{q^2 r} K_l(qr) + \left(\frac{c_4}{c_1} \right) \frac{i\beta}{q} K_l'(qr) \right] e^{i(\omega t + l\varphi - \beta z)} \\
H_\varphi(r, \varphi, z, t) &= c_1 \left[\left(\frac{c_3}{c_1} \right) \frac{i\omega e_2}{q} K_l'(qr) - \left(\frac{c_4}{c_1} \right) \frac{\beta l}{q^2 r} K_l(qr) \right] e^{i(\omega t + l\varphi - \beta z)} \\
H_z(r, \varphi, z, t) &= c_1 \left[\left(\frac{c_4}{c_1} \right) K_l(qr) \right] e^{i(\omega t + l\varphi - \beta z)}
\end{aligned} \tag{2.40}$$

In order to determine c_1 , the components are normalized to the input light intensity, I , with the following equation:

$$I = \frac{c n e_0}{2} |\mathbf{E}|^2 \tag{2.41}$$

A few examples of the light intensity distribution in the core of an optical fiber for defined values of l are shown in Figure 2-7. Note that as the mode number increases from the top left to bottom right, more and more radial and azimuthal nodes are present. The modes can be visualized with the aforementioned mechanical analogy comparing light intensity modes to vibrational modes of circular plates.

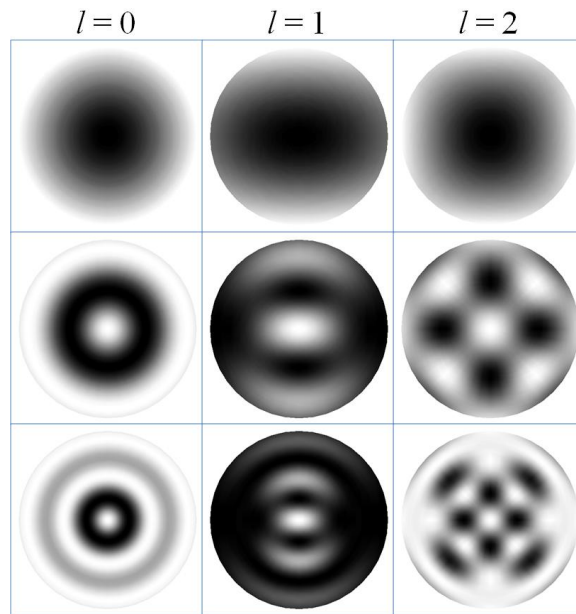


Figure 2-7: Various EM wave mode shapes in the cross section of the fiber.

2.3.3 Concluding Remarks

This temporarily concludes the exploration of effective index which is a main contributor to defining the Bragg condition. The first of two important lessons to be taken from this section are the method for calculating n by solving the wave equation PDE for a cylindrical core and cladding geometry. It is important to understand this because later in the dissertation, the cladding layer will be partially removed and replaced by an active material outer cladding that changes index of refraction in a magnetic field. This complicates the theory because a 3-layer geometry is formed as opposed to the 2-layer geometry just analyzed and we must know how the effective index changes with manipulations in the surrounding material's IOR. The second important lesson involves understanding the variables that go into determining n . For single mode operation where only the HE_{11} mode is present, effective index is a function of input wavelength, core radius, and the core and cladding IORs as follows:

$$\boxed{n = n(\lambda_0, a, n_1, n_2)} \quad (2.42)$$

This effective index in turn determines the reflected wavelength. We shall now take our knowledge of determining n and apply it to a derivation of the Bragg condition which defines the reflected wavelength distribution.

2.4 Bragg Reflection

The theoretical framework describing the fundamental behavior of FBGs is continued here. The previous section dealt with light propagation in an ordinary optical fiber whereas this section introduces a grating into the fiber to explore how the light responds. Coupled mode theory is used to describe the reflected wavelength spectrum of a single FBG. The goal of this section is to continue building upon previous theory to establish the behavior of FBGs and prepare the reader

for the following section when a description will be given of how FBGs are used as sensing devices.

2.4.1 Coupled Mode Theory

Coupled mode theory describes the manner in which perturbations in an optical medium will result in one mode giving rise to additional modes. Specifically for FBGs, the periodic oscillation in core IOR causes a forward propagating mode to couple with and give rise to a backward propagating mode, resulting in light reflection. This is an example of a nonlinear optical phenomenon because, as will be seen, the principle of superposition breaks down for forward and backward propagating light. The wave equation derived from Maxwell's equations will be solved with the assumption that the index of refraction varies along the length, or z-direction, as described in Equation (2.43):

$$n'(z) = n + \Delta n \cos\left(\frac{2\pi}{\Lambda} z\right) \quad (2.43)$$

Note that despite the cladding layer IOR being constant along the entire length of the FBG, an oscillating core IOR will result in a fluctuation of the effective IOR. Figure 2-8 plots the effective index of refraction profile being considered and demonstrates the definitions of grating periodicity, Λ , and index perturbations, Δn , from the effective index, n .

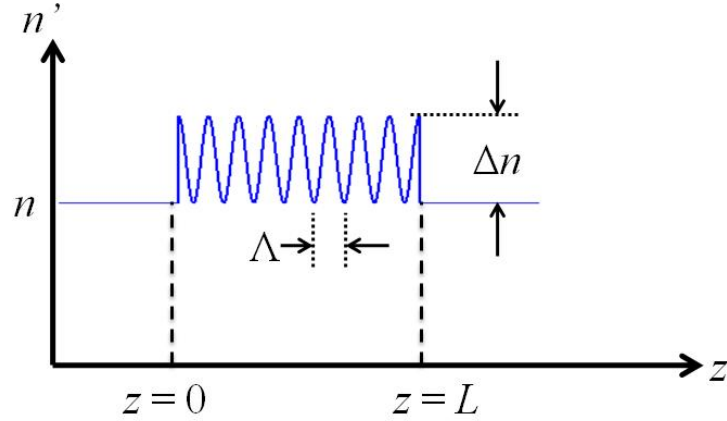


Figure 2-8: The variation of fiber effective IOR as a function of length along a fiber.

The derivation is performed under conditions which allow for the same r , φ , and t dependence as the previous section. The functions describing such dependence of the electric field, $F_E(r, \varphi)$ and $T(t)$, do not depend on z and thus, retain the same form as the previous section. The $Z(z)$ term, however, requires a different form. As before, a solution for the E_z component of the EM wave will be demonstrated. This method is easily extrapolated to determining the H_z component and subsequently, Equation (2.14) is used to determine the other four EM wave components. Rewriting the wave equation seen in Equation (2.4) by incorporating Equation (2.43) leads to the following:

$$\left[\nabla^2 - \left(\frac{n + \Delta n \cos(2pz)}{c} \right)^2 \frac{\partial^2}{\partial t^2} \right] E_z = 0 \quad (2.44)$$

The term $p = \pi/\Lambda$ is used for shortening the notation. The following equation is plugged into the new wave equation in order to carry out a separation of variables technique:

$$\begin{aligned} E_z(r, \varphi, z, t) &= F_{E_z}(r, \varphi) Z_{E_z}(z) T_{E_z}(t) \\ &= F_{E_z}(r, \varphi) Z_{E_z}(z) e^{i\omega t} \end{aligned} \quad (2.45)$$

Note that, as stated before, the form of $T_{Ez}(t)$ is assumed to remain unchanged from the previous section. Equation (2.44) is combined with Equation (2.45) and the variables are separated to get the following equation:

$$\left[\frac{1}{F_{Ez}(r, \varphi)} \left(\frac{\partial^2 F_{Ez}(r, \varphi)}{\partial r^2} + \frac{1}{r} \frac{\partial F_{Ez}(r, \varphi)}{\partial r} + \frac{1}{r^2} \frac{\partial^2 F_{Ez}(r, \varphi)}{\partial \varphi^2} \right) \right] \dots \quad (2.46)$$

$$+ \left[\frac{1}{Z_{Ez}(z)} \frac{\partial^2 Z_{Ez}(z)}{\partial z^2} + \left(\frac{n(z)\omega}{c} \right)^2 \right] = 0$$

There is no overlap in the variables present in each set of brackets. Therefore, the terms in each set of brackets must be set to a constant to obtain a valid solution. This constant will be arbitrarily set to zero because it will still result in a function which satisfies the wave equation. It turns out that taking the specific case where the constant equals zero amounts to assuming that the only source of the backward propagating mode is from coupling with the forward propagating mode. Therefore, this analysis is valid for analyzing a single FBG. This can be extrapolated to the multiplexed FBGs in this research because the reflectivities of the FBGs used are very small. The ordinary differential equation with z as the independent variable created from Equation (2.46) is solved using the following equation:

$$Z_{Ez}(z) = a_f(z)e^{-ipz} + a_b(z)e^{ipz} \quad (2.47)$$

The amplitude terms refer to the forward (a_f) and backward (a_b) propagating waves. Upon plugging this solution into the separated portion of the wave equation, the following equation is found:

$$\left(\frac{\partial^2 a_f}{\partial z^2} - 2ip \frac{\partial a_f}{\partial z} - p^2 a_f \right) e^{-ipz} + \left(\frac{\partial^2 a_b}{\partial z^2} + 2ip \frac{\partial a_b}{\partial z} - p^2 a_b \right) e^{ipz} \dots \quad (2.48)$$

$$+ \left[n^2 + 2n(\Delta n) \cos(2pz) + (\Delta n)^2 \cos^2(2pz) \right] k_0^2 (a_f e^{-ipz} + a_b e^{ipz}) = 0$$

Note the presence of the k_0 term in the place of ω/c . Next, two assumptions are made to eliminate higher order terms in the equation above. The first approximation is that the oscillation of the effective IOR (Δn) is much smaller than the value itself. This is a valid assumption because the order of magnitude of n is 1 whereas that of Δn is 10^{-4} . Thus, the $(\Delta n)^2$ term is neglected. The other assumption is a slowly varying approximation. This amounts to an assumption that over the length of the FBG, the amplitude of the forward and backward propagating modes varies much slower than the magnitude of the wave varies over a wavelength. This is a valid assumption because of the -34 dB reflectivity of the FBGs used in this research as noted in the Luna Innovations specifications sheet seen in the appendix. This means that the amplitude of a forward propagating wave diminished by 0.02 % over the 5 mm length of the FBG. This is compared to the magnitude of the wave undergoing a complete cycle from positive to negative and back over a wavelength on the order of 1 μm . Therefore, the second derivatives of the amplitudes, $\partial^2 a_f / \partial z^2$ and $\partial^2 a_b / \partial z^2$ are neglected. The result is the following equation:

$$\begin{aligned} & \left(-2ip \frac{\partial a_f}{\partial z} - p^2 a_f \right) e^{-ipz} + \left(2ip \frac{\partial a_b}{\partial z} - p^2 a_b \right) e^{ipz} \dots \\ & + \left[\beta^2 + 2\xi \cos(2pz) \right] (a_f e^{-ipz} + a_b e^{ipz}) = 0 \end{aligned} \quad (2.49)$$

Note the β and ξ terms used in the place of nk_0 and $k_0^2 n(\Delta n)$ respectively. The following trigonometric identity is used to help simplify the equation above:

$$2 \cos(2pz) = e^{2ipz} + e^{-2ipz} \quad (2.50)$$

Plugging Equation (2.50) into Equation (2.49), the following equation is developed with terms grouped based on the order of their associated exponential term:

$$\left[-2ip \frac{\partial a_f}{\partial z} + (\beta^2 - p^2) a_f + \xi a_b \right] e^{-ipz} + \left[2ip \frac{\partial a_b}{\partial z} + (\beta^2 - p^2) a_b + \xi a_f \right] e^{ipz} = 0 \quad (2.51)$$

Just as in the case with the separation of variables, in order to have the first two terms equal zero for all values of z , each term in brackets must equal zero. Thus, the separated $Z_{Ez}(z)$ portion of the wave equation is separated further into the following pair of equations:

$$\frac{d^2 a_f}{dz^2} - 2ip \frac{da_f}{dz} + (\beta^2 - p^2) a_f - \xi a_b = 0 \quad (2.52)$$

$$\frac{d^2 a_b}{dz^2} + 2ip \frac{da_b}{dz} + (\beta^2 - p^2) a_b - \xi a_f = 0 \quad (2.53)$$

This demonstrates the nonlinear nature of the optical coupling in FBGs. In a linear system, the principle of superposition applies, meaning forward and backward propagating modes can be treated independently. As demonstrated above, both equations include forward and backward propagating amplitude terms. This means the oscillating effective IOR inextricably links the two modes so they are no longer independent from each other.

The next step is to solve the pair of equations for the backward propagating mode amplitude. This is accomplished by solving Equation (2.53) for a_f as follows:

$$a_f = -\frac{2ip}{\xi} \frac{\partial a_b}{\partial z} - \frac{\beta^2 - p^2}{\xi} a_b \quad (2.54)$$

This result is then plugged Equation (2.52) to create the following differential equation:

$$\frac{d^2 a_b}{dz^2} - \kappa^2 a_b = 0 \quad (2.55)$$

This equation involves a coupling term, κ , which is non-zero and is defined as follows:

$$\kappa^2 = \frac{\xi^2 - (\beta^2 - p^2)^2}{4p^2} = \frac{\left((2\pi/\lambda)^2 n_1 \Delta n \right)^2 - \left(\beta^2 - (\pi/\Lambda)^2 \right)^2}{4(\pi/\Lambda)^2} \quad (2.56)$$

Note the slowly varying amplitude assumption we employed to rid ourselves of second derivative terms will not be applied here. This is because the manipulations performed do not

result in a second derivative term which is much smaller than all other terms (in this case, the $\kappa^2 a_b$ term). The boundary conditions used include the incident EM wave power ($P_f(z=0) = P_0$) and that no backward propagating mode exists at the end of the Bragg grating ($a_b(z=L) = 0$). This is consistent with the fact that we are treating this FBG as the only grating on the fiber. Thus, there is no other source considered in this analysis from which a backward propagating mode can originate. These boundary conditions create a system of two equations to determine the two unknown amplitude terms for the following proposed solution to a_b :

$$a_b = b_1 e^{\kappa z} + b_2 e^{-\kappa z} \quad (2.57)$$

We can eliminate the constant b_2 with the zero amplitude boundary condition at $z = L$. This gives us:

$$\begin{aligned} a_b &= 2b_1 e^{\kappa L} \sinh[\kappa(z-L)] \\ &= 2b_1' \sinh[\kappa(z-L)] \end{aligned} \quad (2.58)$$

The new constant, b_1' absorbs the $e^{\kappa L}$ term. This result for a_b is now plugged into Equation (2.54) to determine the forward propagating amplitude. The result is the following expression:

$$a_f = \frac{2b_1'}{\xi} \left\{ (\beta^2 - p^2) \sinh[\kappa(z-L)] + 2ip\kappa \cosh[\kappa(z-L)] \right\} \quad (2.59)$$

The incident power boundary condition is now employed to find b_1' . This takes the following form:

$$\begin{aligned} P_f(z) &= a_f \cdot a_f^* = \left(\frac{2b_1'}{\xi} \right)^2 \left\{ (\beta^2 - p^2)^2 \sinh^2[\kappa(z-L)] + (2p\kappa)^2 \cosh^2[\kappa(z-L)] \right\} \\ P_f(z=0) &= P_0 = \left(\frac{2b_1'}{\xi} \right)^2 \left[(\beta^2 - p^2)^2 \sinh^2(\kappa L) + (2p\kappa)^2 \cosh^2(\kappa L) \right] \\ \Rightarrow \quad b_1' &= \frac{P_0 \xi^2}{4 \left[(\beta^2 - p^2)^2 \sinh^2(\kappa L) + (2p\kappa)^2 \cosh^2(\kappa L) \right]} \end{aligned} \quad (2.60)$$

This is plugged back into the original equation for the z-component of the electric field as follows:

$$Z_{Ez}(z) = \frac{P_0 \xi}{2} \left\{ \frac{(\beta^2 - p^2) \sinh[\kappa(z-L)] + 2ip\kappa \cosh[\kappa(z-L)]}{(\beta^2 - p^2)^2 \sinh^2(\kappa L) + (2p\kappa)^2 \cosh^2(\kappa L)} \right\} e^{-ipz} \dots$$

$$+ \frac{P_0 \xi^2}{2} \left\{ \frac{\sinh[\kappa(z-L)]}{(\beta^2 - p^2)^2 \sinh^2(\kappa L) + (2p\kappa)^2 \cosh^2(\kappa L)} \right\} e^{ipz} \quad (2.61)$$

This expression, along with the associated expression for $Z_{Hz}(z)$ is plugged back into Equation (2.14) to find the various electric and magnetic field components. This concludes the use of coupled mode theory to determine the field components of the EM wave. This will now be applied to determine the shape of the reflection spectrum.

2.4.2 Reflected Wavelength Spectrum

To get the reflection coefficient, the EM wave power in the backward mode is divided by the incident power at the beginning of the FBG ($P_b(z=0)/P_0$). The reflection coefficient is a function of coupling coefficient and FBG length as follows:

$$R(\kappa L) = \frac{P_b(z=0)}{P_0} = \frac{\xi^2 \sinh^2(\kappa L)}{(\beta^2 - p^2)^2 \sinh^2(\kappa L) + 4p^2 \kappa^2 \cosh^2(\kappa L)} \quad (2.62)$$

or

$$R(\kappa L) = \frac{\left[(2\pi/\lambda)^2 n(\Delta n) \right]^2 \sinh^2(\kappa L)}{\left[\beta^2 - (\pi/\Lambda)^2 \right]^2 \sinh^2(\kappa L) + \left[2(\pi/\Lambda)\kappa \right]^2 \cosh^2(\kappa L)} \quad (2.63)$$

It can be shown that with everything else constant, increasing the length, L , of the FBG will increase R . The same trend is seen with increasing Δn . This theoretical result supports what was stated in the fabrication section of this chapter that increasing the index oscillation amplitude and

length of the FBG will increase the reflectivity. Noting that β and κ are both functions of input wavelength, λ , the reflection coefficient will also be a function of λ . Figure 2-9 displays the dependence of R on λ . The maximum reflection occurs at the phase-matched condition where $\beta = p$, that is:

$$\left. \begin{aligned} \beta = nk = 2\pi n/\lambda \\ p = \pi/\Lambda \end{aligned} \right\} \Rightarrow \frac{2\pi n}{\lambda} = \frac{\pi}{\Lambda} \dots \quad (2.64)$$

$$\Rightarrow \lambda = \boxed{2n\Lambda = \lambda_B}$$

As mentioned earlier, the wavelength of maximum reflection is called the Bragg wavelength and denoted by λ_B . A theoretically calculated reflection spectrum is shown in Figure 2-9 below and compared with an experimentally obtained reflection spectrum to indicate the theory's accuracy.

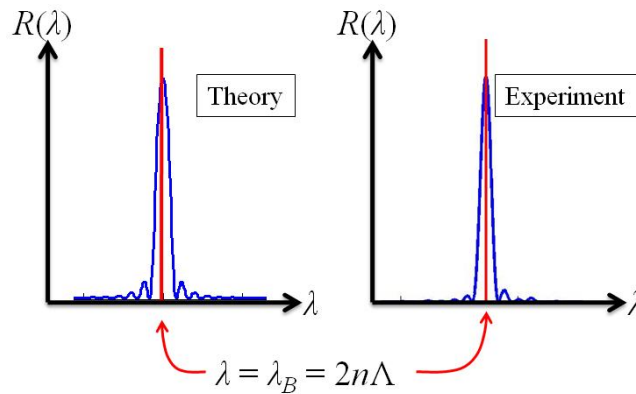


Figure 2-9: A comparison of theoretically and experimentally obtained wavelength reflection spectra.

There is a striking similarity between the shape of the experimental FBG's reflected wavelength spectrum and the theoretically calculated spectrum.

2.4.3 Concluding Remarks

This concludes the work defining the source of light reflection caused by a fiber Bragg grating. The reflection is clearly seen to stem from the wave nature of light. The purpose of this

section is to broaden the reader's understanding of the behavior of FBGs and how the properties of the fiber and grating determine the light propagation and reflection characteristics. Now that a theoretical foundation has been established for light propagation in an optical fiber and reflection from a FBG, we'll begin to explore the methods by which FBGs sense external phenomena.

2.5 Sensing Phenomena

The method of sensing different types of phenomena is characterized by measuring changes in a signal which are caused by an external event. In the case of FBGs, the measured grating reflection signal is manipulated by external fields (e.g. strain, magnetism). This manipulation occurs because various features of the FBG contributing to reflection (e.g. effective IOR) are altered by the external field. Specifically, the method by which strain and magnetic fields influence the properties of the FBG (and subsequently the reflection signal and Bragg wavelength, λ_B) will be explored. The build-up to this section provides a foundation for fully understanding the characteristics influencing a FBG reflection signal while this section describes the correlation between external phenomena and changes in the FBG signal. If the previous two sections of this chapter illustrate the rules of the game, then this section describes how the game is played within those rules.

2.5.1 Defining the Sensor

The method of sensing for FBGs is to apply some external field such as temperature, strain, etc. that produces a shift in the reflected wavelength, λ_B . To demonstrate this, we apply a differential to the Bragg condition, Equation (2.1), as follows:

$$\delta\lambda_B = \delta(2n\Lambda) = 2\Lambda(\delta n) + 2n(\delta\Lambda) \quad (2.65)$$

This indicates that changes in the Bragg wavelength are caused by changes in the effective index, δn , and changes in the grating pitch, $\delta\Lambda$. If this expression is divided by the original Bragg wavelength, we get a variation of the equation:

$$\frac{\delta\lambda_B}{\lambda_B} = \frac{\delta n}{n} + \frac{\delta\Lambda}{\Lambda} \quad (2.66)$$

The term on the left-hand side is measured by the FBG interrogation system while the two terms on the right must be correlated to whatever external stimulus we are trying to measure. Thus, the rest of this section is devoted to establishing links between the external phenomena under consideration, strain, temperature, and magnetism, and the differential terms, δn and $\delta\Lambda$.

2.5.2 Strain Sensing - Photoelasticity

In the case of strain, the $\delta\Lambda/\Lambda$ term is equivalent to a change-in-length divided by the original length which is the longitudinal strain in the direction of the optical fiber. This amounts to Equation (2.66) taking the following form:

$$\frac{\delta\lambda_B}{\lambda_B} = \frac{\delta n}{n} + \varepsilon_3 \quad (2.67)$$

The ε_3 term represents the longitudinal strain in the coordinate system employed in this research. Figure 2-10 below demonstrates the coordinate system for FBGs where the direction of EM wave propagation is defined as the 3-direction, $\{\hat{e}_3\}$. The polarization direction of propagating light can lie anywhere in the 1-2 plane, but the figure below demonstrates light polarized in the 1-direction, $\{\hat{e}_1\}$. The directions of the 1- and 2-axes are dependent upon the properties of the optical fiber. In axisymmetric optical fibers, the orientation is arbitrary; however, when the symmetry is broken the 1- and 2-axes align with principal material directions which will be identified shortly.

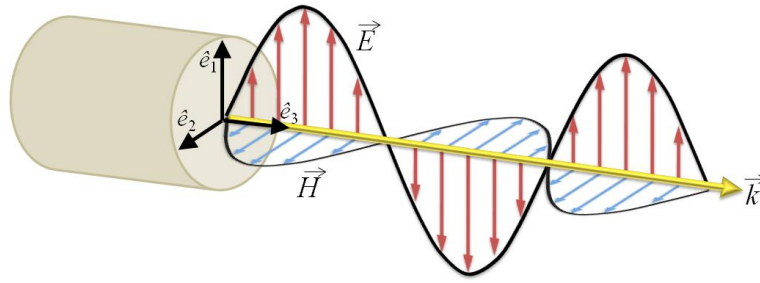


Figure 2-10: The basis used to represent light propagation in this research.

Note that $\{k\}$, $\{E\}$, and $\{H\}$ define an orthonormal basis and the difference in notation between the unit vectors forming the basis, [28], and the components of the permittivity tensor, e_{ij} . The former is a vector with a circumflex above the letter e while the latter is a component of the second order tensor, \mathbf{e} . It may seem counterintuitive that all the work in the section on light propagation was performed in cylindrical coordinates but we are now working with a Cartesian basis. The assumption that light in a fiber can take the form in Figure 2-10 is confirmed when all electric field and magnetic field components of the propagating EM wave are calculated. When the electric field vector $\{E_r, E_\phi, E_z\}$ in the cross section of the fiber is depicted with an arrow plot as shown below in Figure 2-11, it is obvious that the field is overwhelmingly aligned in one particular direction, $\{\hat{e}_1\}$ in this case.

Theoretical E-Field from Maxwell's Equations for Propagating Light

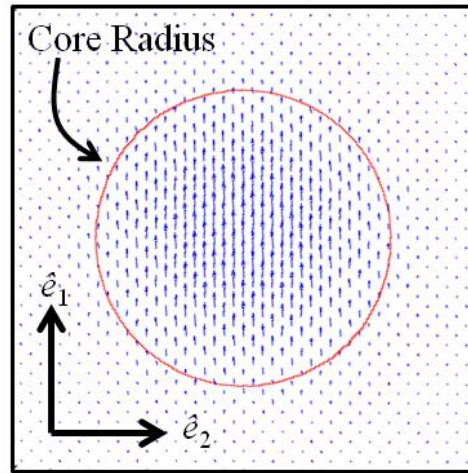


Figure 2-11: Demonstration that light propagating down a fiber in the fundamental mode can be approximated as being linearly polarized.

This electric field behavior above is characteristic of linearly polarized light. Thus, propagating light in the fundamental mode will be treated as being linearly polarized without losing any validity in the results. Now that a coordinate system has been set up and the differential term for grating pitch, $\delta\Lambda/\Lambda$, has already been correlated to strain, the next step is to work on correlating strain to changes in effective IOR, the $\delta n/n$ term. More information can be found on photoelasticity in Nye 1957 and Narasimhamurty 1981 [29, 30].

2.5.2.1 OPTICAL INDICATRIX

Earlier in this section, the term $\delta n/n$ was derived and seen to contribute to shifts in λ_B . While first working with Maxwell's equations earlier in this chapter, it was noted that the index of refraction is related to an optically isotropic material's permittivity, e , through the equation:

$$\frac{e}{e_0} = e_r = n^2 \quad (2.68)$$

The “ r ” subscript refers to the permittivity relative to free space which itself is denoted by the “0” subscript. Permittivity is treated as a second order tensor relating electric field vectors to

electric flux vectors. In general, the electric field maintains nonzero components in every direction. Thus, the entire permittivity tensor will be analyzed beginning in a very general form and subsequently reduced and simplified based on assumptions valid for an optical fiber. Because the silica used to create optical fibers is a nonmagnetic dielectric which is assumed to be lossless over the short distances used in this research, the permittivity tensor is symmetric with real eigenvalues and eigenvectors:

$$\mathbf{e} = \begin{bmatrix} e_{11} & e_{12} & e_{31} \\ e_{12} & e_{22} & e_{23} \\ e_{31} & e_{23} & e_{33} \end{bmatrix} \quad (2.69)$$

In general, \mathbf{e} is not diagonal. However, if the basis chosen to represent \mathbf{e} is aligned with the eigenvectors, the permittivity tensor becomes diagonalized with the components on the diagonal equal to the eigenvalues.

$$\mathbf{e} = \begin{bmatrix} e^{(1)} & 0 & 0 \\ 0 & e^{(2)} & 0 \\ 0 & 0 & e^{(3)} \end{bmatrix} \quad (2.70)$$

In the equation above, the three eigenvalues are $e^{(1)}$, $e^{(2)}$, and $e^{(3)}$ and the three eigenvectors are $\{\hat{e}_1\}$, $\{\hat{e}_2\}$, and $\{\hat{e}_3\}$. When a perturbation is applied to the material via phenomena such as strain or an electric field, the once diagonal matrix now shows extra terms in the diagonal and off-diagonal slots of the matrix:

$$\mathbf{e}' = \mathbf{e} + \delta\mathbf{e} = \begin{bmatrix} e^{(1)} + \delta e_{11} & \delta e_{12} & \delta e_{31} \\ \delta e_{12} & e^{(2)} + \delta e_{22} & \delta e_{23} \\ \delta e_{31} & \delta e_{23} & e^{(3)} + \delta e_{33} \end{bmatrix} \quad (2.71)$$

This effectively rotates the eigenvectors and changes the eigenvalues of the material. Upon re-diagonalizing the matrix, a new set of eigenvalues can be solved for:

$$\mathbf{e}' = \begin{bmatrix} (e^{(1)})' & 0 & 0 \\ 0 & (e^{(2)})' & 0 \\ 0 & 0 & (e^{(3)})' \end{bmatrix} \quad (2.72)$$

The new eigenvalues are $(e^{(1)})'$, $(e^{(2)})'$, and $(e^{(3)})'$ and the new eigenvectors are $\{\hat{e}_1'\}$, $\{\hat{e}_2'\}$, and $\{\hat{e}_3'\}$. Note that Equation (2.71) and Equation (2.72) define (in differing bases) the same permittivity tensor which is not equal to the permittivity tensor described (using differing bases) in Equation (2.69) and Equation (2.70). The IORs change due to the perturbation as follows:

$$n_i = \sqrt{\frac{e^{(i)}}{e_0}} \quad \Rightarrow \quad n_i' = \sqrt{\frac{(e^{(i)})'}{e_0}}, \quad i = 1, 2, 3 \quad (2.73)$$

It is convenient to work with permittivity when trying to calculate index of refraction mathematically. However, a handy method for visualizing the equations above is to work with a material's relative impermeability tensor, which is related to the permittivity tensor as follows:

$$\boldsymbol{\eta} = \left(\frac{1}{e_0} [\mathbf{e}] \right)^{-1} = [\mathbf{e}_r]^{-1} \quad (2.74)$$

A basis which diagonalizes \mathbf{e} will therefore also diagonalize $\boldsymbol{\eta}$. The eigenvalues of the relative impermeability tensor are related to index of refraction as:

$$\eta^{(i)} = \frac{1}{(n_i)^2}, \quad i = 1, 2, 3 \quad (2.75)$$

While at first, dealing with the reciprocal of permittivity seems unnecessarily complicated, the advantage comes in defining an ellipsoid with the following $\{\hat{e}_1\}$ - $\{\hat{e}_2\}$ - $\{\hat{e}_3\}$ coordinate system (i.e. x_1 - x_2 - x_3 coordinates):

$$\eta^{(1)} x_1^2 + \eta^{(2)} x_2^2 + \eta^{(3)} x_3^2 = \frac{x_1^2}{(n_1)^2} + \frac{x_2^2}{(n_2)^2} + \frac{x_3^2}{(n_3)^2} = 1 \quad (2.76)$$

This is represented graphically in Figure 2-12 which was inspired by a figure in Liu, 2005 [31]. This represents the optical indicatrix. The length of each semi-major axis is equal to the index of refraction for light polarized in that direction. For instance, if light is propagating such that $\{k\} \parallel \{\hat{e}_3\}$, then light polarized parallel to $\{\hat{e}_1\}$ will experience an IOR equal to $n^{(1)}$ whereas light polarized parallel to $\{\hat{e}_2\}$ will experience an IOR equal to $n^{(2)}$. Light which is linearly polarized in the $\{\hat{e}_1\}$ - $\{\hat{e}_2\}$ plane but not parallel to either eigenvector can simply be represented as the sum of the light's component which is parallel to each eigenvector. When $n^{(1)} \neq n^{(2)}$, the material is birefringent and linearly polarized light sent into the birefringent material not oriented in the $\{\hat{e}_1\}$ or $\{\hat{e}_2\}$ directions will be circularly polarized.

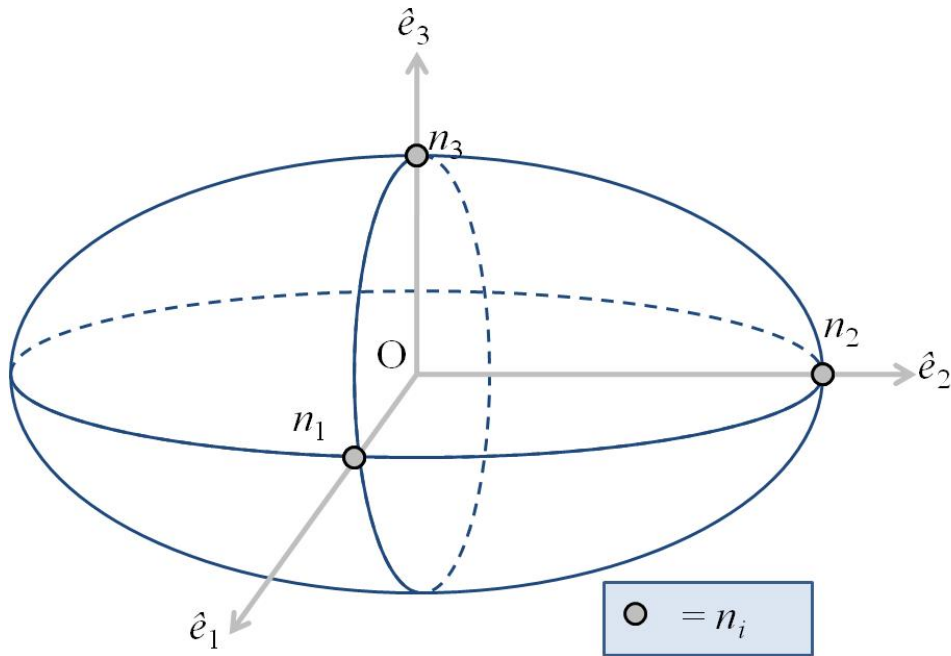


Figure 2-12: Un-deformed optical indicatrix with eigenvectors and eigenvalues identified.

To determine the index of refraction of light traveling in an arbitrary direction, $\{k\}$, you simply cut through the ellipsoid with a plane that intersects the origin and is perpendicular to

$\{k\}$. The locus of points defined by the intersection of the ellipsoid's surface the constructed plane will form a circle or ellipse whose semi-major axes define the principal direction IORs.

If we now take the same perturbation to \mathbf{e} discussed earlier that introduces off-diagonal components, then it is graphically represented as a rotation of the ellipsoid such that the new semi-major axes are defined by the $\{\hat{e}_1'\}-\{\hat{e}_2'\}-\{\hat{e}_3'\}$ basis. This is illustrated below in Figure 2-13. Light polarized parallel to $\{\hat{e}_1\}$ is no longer in a principal direction because the eigenvectors have been rotated. As previously explained, light propagating parallel to $\{\hat{e}_3\}$ after the perturbation which changes the permittivity and impermeability tensors takes place will have different IORs. These principal direction IORs are determined by slicing through the newly rotated ellipsoid with the $\{\hat{e}_1\}-\{\hat{e}_2\}$ plane (i.e. the plane intersecting the origin and perpendicular to $\{\hat{e}_1\}$). The locations of the original $\{\hat{e}_1\}-\{\hat{e}_2\}-\{\hat{e}_3\}$ basis is overlaid along with the original semi-major values, n_i in order to compare with the new $\{\hat{e}_1'\}-\{\hat{e}_2'\}-\{\hat{e}_3'\}$ basis and principal IOR values, n_i' .

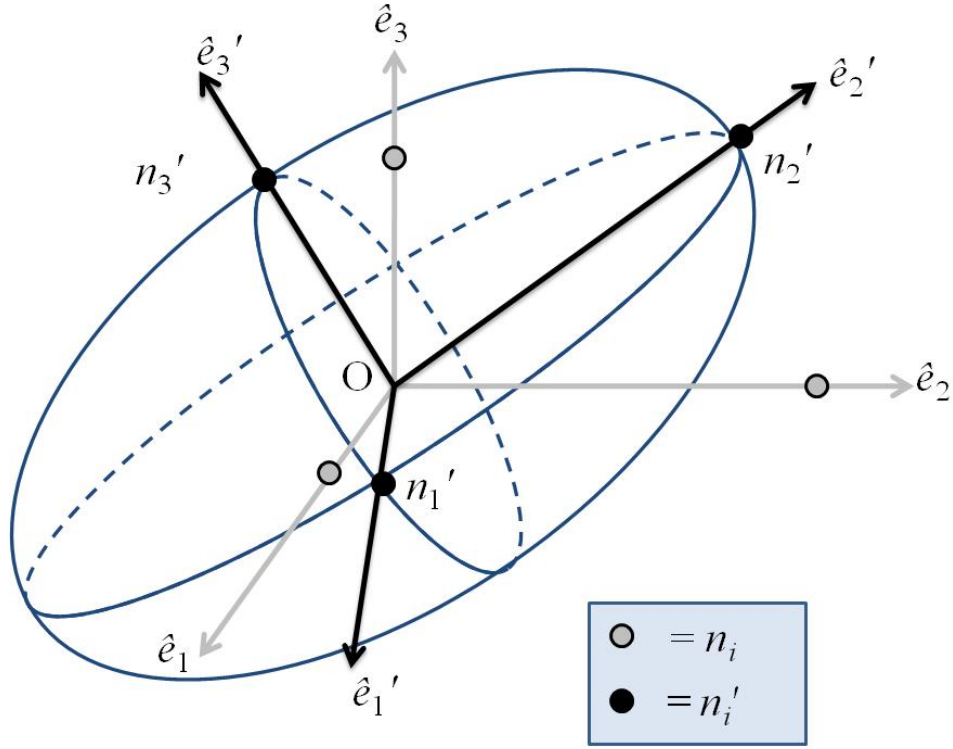


Figure 2-13: Deformed optical indicatrix with new eigenvectors and eigenvalues identified.

The optical indicatrix above can be expressed equivalently in the new coordinate system as:

$$\left(\eta^{(1)}\right)' \left(x_1'\right)^2 + \left(\eta^{(2)}\right)' \left(x_2'\right)^2 + \left(\eta^{(3)}\right)' \left(x_3'\right)^2 = \frac{\left(x_1'\right)^2}{\left(n_1'\right)^2} + \frac{\left(x_2'\right)^2}{\left(n_2'\right)^2} + \frac{\left(x_3'\right)^2}{\left(n_3'\right)^2} = 1 \quad (2.77)$$

Alternatively, the same ellipsoid can be expressed in the original $\{\hat{e}_1\}-\{\hat{e}_2\}-\{\hat{e}_3\}$ coordinate system as:

$$\left(\eta^{(1)} + \delta\eta_{11}\right)x_1^2 + \left(\eta^{(2)} + \delta\eta_{11}\right)x_2^2 + \left(\eta^{(3)} + \delta\eta_{11}\right)x_3^2 + 2\delta\eta_{12}x_1x_2 + 2\delta\eta_{31}x_3x_1 + 2\delta\eta_{23}x_2x_3 = 1 \quad (2.78)$$

Note the absence of off-diagonal terms (e.g. $\delta\eta_{12}$, $\delta\eta_{31}$, $\delta\eta_{23}$) when the ellipsoid is defined with the perturbed eigenvectors. The analogy is that Equation (2.77) is to Equation (2.72) as

Equation (2.78) is to Equation (2.71). We shall now take this theory and apply it to our goal of determining how the $\delta n/n$ term mentioned earlier is related to strain.

2.5.2.2 STRAIN-OPTIC COEFFICIENTS

The relationship between changes in index of refraction, permittivity, and relative impermeability is very important for relating this theory back to our original purpose of relating the $\delta n/n$ term to strain. The relationship is described in the following two equations which relate perturbations in permittivity to impermeability and IOR:

$$\begin{aligned}\delta e_{ij} &= -e_0 n_i^2 n_j^2 \delta \eta_{ij} \\ &\approx -e_0 n^4 (\delta \eta_{ij})\end{aligned}\tag{2.79}$$

$$\begin{aligned}\frac{\delta e_{ij}}{e_0} &= (n_i)^2 - (n_j)^2 = (n_i + n_j)(n_i - n_j) \\ &\approx 2n(\delta n_{ij})\end{aligned}\tag{2.80}$$

These equations employ the two assumptions that differences between IOR in two principal directions and perturbations to IOR are much smaller than the absolute values. This is indeed the case because changes due to strain are on the order of 10^{-4} whereas the absolute values are on the order 1. By combining the two equations above to cancel δe_{ij} , we get the following relationship:

$$\frac{\delta n_{ij}}{n} = -\frac{n^2}{2} (\delta \eta_{ij})\tag{2.81}$$

There is a well-established constitutive relation between strain and changes to relative impermeability through photoelastic coefficients which is illustrated in Equation (2.82) below. The constitutive relation between stress and strain via a stiffness tensor is presented in Equation (2.83) for comparison purposes:

$$\delta \eta_{ij} = p_{ijkl} \epsilon_{kl}\tag{2.82}$$

$$\sigma_{ij} = C_{ijkl} \epsilon_{kl}\tag{2.83}$$

The two analogous relationships aid in understanding the significance of the strain-optic tensor. Just like the stiffness tensor, the photoelastic tensor is fourth order and the number of independent terms can be reduced depending on the symmetry properties of the material. Due to its amorphous crystal structure, silica is both elastically isotropic and photo-elastically isotropic; therefore, the number of independent terms reduces to two. Additionally, symmetry allows us to change our index notation from four letters, each ranging from one to three, to two letters ranging from one to six as described in Table 2-1 below:

Table 2-1: Notation consolidation from two indices to one.

<i>ij</i>	11	22	33	23, 32	13, 31	12, 21
α	1	2	3	4	5	6

The effect on the constitutive equation is that we can now express it as a 6x6 matrix relating the 6x1 impermeability vector to a strain vector:

$$\begin{Bmatrix} \delta\eta_1 \\ \delta\eta_2 \\ \delta\eta_3 \\ \delta\eta_4 \\ \delta\eta_5 \\ \delta\eta_6 \end{Bmatrix} = \begin{bmatrix} p_{11} & p_{12} & p_{13} & p_{14} & p_{15} & p_{16} \\ & p_{22} & p_{23} & p_{24} & p_{25} & p_{26} \\ & & p_{33} & p_{34} & p_{35} & p_{36} \\ & & & p_{44} & p_{45} & p_{46} \\ & \text{symm} & & & p_{55} & p_{56} \\ & & & & & p_{66} \end{bmatrix} \begin{Bmatrix} \epsilon_1 \\ \epsilon_2 \\ \epsilon_3 \\ \epsilon_4 \\ \epsilon_5 \\ \epsilon_6 \end{Bmatrix} \quad (2.84)$$

Now we will add in the effect of isotropy. Just as an elastically isotropic material's stiffness tensor can be written as a function of Young's modulus, Poisson's ratio, and shear modulus (where any one of the three properties can be written in terms of the other two), a photoelastically isotropic material's stiffness tensor can be written as:

$$\begin{bmatrix} p_{11} & p_{12} & p_{13} & p_{14} & p_{15} & p_{16} \\ & p_{22} & p_{23} & p_{24} & p_{25} & p_{26} \\ & & p_{33} & p_{34} & p_{35} & p_{36} \\ & & & p_{44} & p_{45} & p_{46} \\ & \text{symm} & & & p_{55} & p_{56} \\ & & & & & p_{66} \end{bmatrix} \Rightarrow \begin{bmatrix} p_{11} & p_{12} & p_{12} & 0 & 0 & 0 \\ & p_{11} & p_{12} & 0 & 0 & 0 \\ & & p_{11} & 0 & 0 & 0 \\ & & & p_{44} & 0 & 0 \\ & \text{symm} & & & p_{44} & 0 \\ & & & & & p_{44} \end{bmatrix} \quad (2.85)$$

In the matrix above, p_{44} is analogous to shear modulus since it can be written as a function of p_{11} and p_{12} . The theory is nearly concluded when we plug these relationships into the changes to permittivity and index of refraction as follows:

$$\delta e_{\alpha} = -e_0 n^4 (\delta \eta_{\alpha}) = -e_0 n^4 p_{\alpha\beta} \varepsilon_{\beta} \quad (2.86)$$

$$\frac{\delta n_{\alpha}}{n} = -\frac{n^2}{2} (\delta \eta_{\alpha}) = -\frac{n^2}{2} p_{\alpha\beta} \varepsilon_{\beta} \quad (2.87)$$

2.5.2.3 PHOTOELASTICITY IN FIBER BRAGG GRATINGS - BIREFRINGENCE

We will finish this section off by relating the photoelastic theory results back to optical fibers Bragg gratings. An unperturbed FBG will be axisymmetric with equal indices of refraction no matter what direction the light propagating in the 3-direction is polarized. However, upon straining the optical fiber, changes are induced in the relative permittivity which causes the optical indicatrix to rotate and/or distort and the index of refraction will change.

Figure 2-14 shows the optical indicatrix after the distortion. Despite the fact that no pair of the three semi-major axes defines a plane coinciding with the $\{\hat{e}_1\}$ - $\{\hat{e}_2\}$ plane, we remain focused on an EM wave which is still propagating in the $\{\hat{e}_3\}$ direction (i.e. $\{k\} \parallel \{\hat{e}_3\}$). Thus, rather than finding the eigenvector basis for the new ellipsoid, $\{\hat{e}_1'\}$ - $\{\hat{e}_2'\}$ - $\{\hat{e}_3'\}$, we are only concerned with a basis defined by $\{\hat{e}_1''\}$ - $\{\hat{e}_2''\}$ - $\{\hat{e}_3''\}$ which is defined such that $\{\hat{e}_3''\} \parallel \{\hat{e}_3\}$. In the most general case shown in the Figure 2-14, the $\{\hat{e}_1''\}$ - $\{\hat{e}_2''\}$ basis is defined by an appropriate rotation of the $\{\hat{e}_1\}$ - $\{\hat{e}_2\}$ basis and the eigenvalues, n_1'' and n_2'' , change from the

original eigenvalues, n_1 and n_2 . The original basis ($\{\hat{e}_1\}-\{\hat{e}_2\}-\{\hat{e}_3\}$) and eigenvalues (n_1, n_2 , and n_3) are overlaid with the new $\{\hat{e}_1''\}-\{\hat{e}_2''\}$ basis and IORs (n_1'' and n_2'') for comparison purposes.

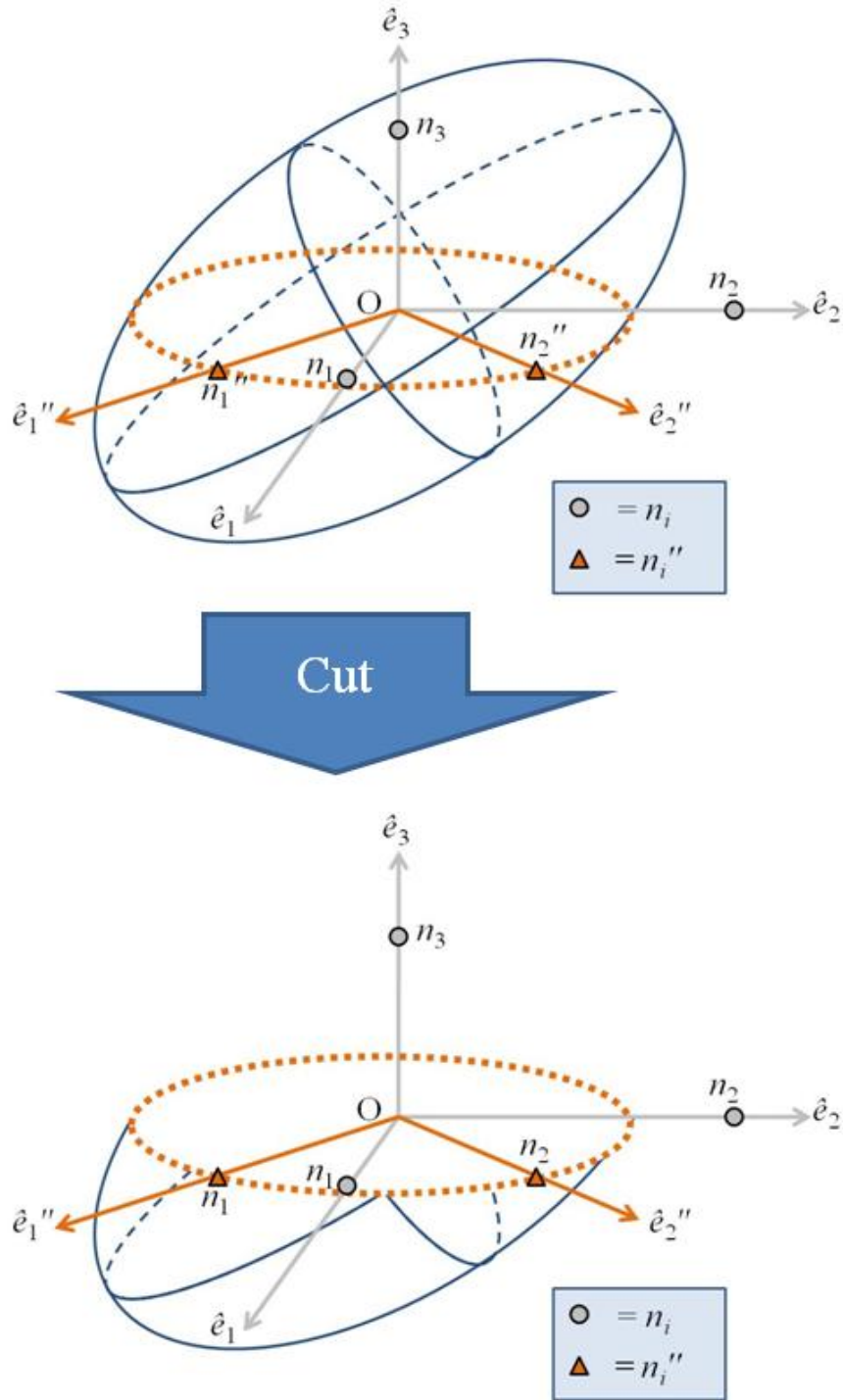


Figure 2-14: Plane used to cut through optical indicatrix defined as intersecting the origin and being orthogonal to the direction of propagation.

Two special cases are (1) when only a rotation occurs to get from $\{\hat{e}_1\}$ - $\{\hat{e}_2\}$ to $\{\hat{e}_1''\}$ - $\{\hat{e}_2''\}$ and the IORs do not change and (2) when the basis does not rotate (i.e. $\{\hat{e}_1\} \parallel \{\hat{e}_1''\}$ and $\{\hat{e}_2\} \parallel \{\hat{e}_2''\}$) but the eigenvalues (and thus, IORs) change. The cases are strictly dependent on how the applied strain state rotates and/or distorts the optical indicatrix. Returning back to Equation (2.66), the Bragg condition is affected by the changes in permittivity due to strain as follows:

$$\left(\frac{\delta\lambda_B}{\lambda_B} \right)_\alpha = \frac{\delta n_\alpha}{n} + \frac{\delta\Lambda}{\Lambda} = -\frac{n^2}{2} p_{\alpha\beta} \varepsilon_\beta + \varepsilon_3 \quad (2.88)$$

The subscript attached to the measured Bragg wavelength corresponds to the direction of polarization. Light polarized in the $\{\hat{e}_1\}$ and $\{\hat{e}_2\}$ directions have the following relationships:

$$\boxed{\begin{aligned} \left(\frac{\delta\lambda_B}{\lambda_B} \right)_1 &= -\frac{n^2}{2} p_{1\beta} \varepsilon_\beta + \varepsilon_3 \\ \left(\frac{\delta\lambda_B}{\lambda_B} \right)_2 &= -\frac{n^2}{2} p_{2\beta} \varepsilon_\beta + \varepsilon_3 \end{aligned}} \quad (2.89)$$

An important result of this analysis is that strain-induced changes in the index of refraction may cause different IORs in the two principal directions of the $\{\hat{e}_1\}$ - $\{\hat{e}_2\}$ plane (i.e. $n_1 \neq n_2$). This will cause the Bragg condition to be dependent upon the polarization of light hitting the FBG:

$$\begin{aligned} (\lambda_B)_1 &= 2n_1\Lambda \\ (\lambda_B)_2 &= 2n_2\Lambda \end{aligned} \quad (2.90)$$

This phenomenon, known as birefringence, plays a pivotal role in the function of FBGs. In the following chapter, the consequences of birefringence with respect to the effectiveness of FBGs as strain sensors will be explored. One interesting calculation that can be made is the transverse strain difference (TSD), which is simply the difference between the two strains transverse to the optical fiber direction. We can arrive at the relationship between TSD and the shifts in reflected wavelength for the two polarization directions by taking the difference between the two relationships in the equation above.

$$\begin{aligned} \left(\frac{\delta\lambda_B}{\lambda_B} \right)_1 - \left(\frac{\delta\lambda_B}{\lambda_B} \right)_2 &= \frac{n^2}{2} (p_{2\beta} - p_{1\beta}) \varepsilon_\beta \\ &= \frac{n^2}{2} (p_{12} - p_{11}) (\varepsilon_1 - \varepsilon_2) \end{aligned} \quad (2.91)$$

This leads to a very useful indicator as to whether or not a TSD is developing due to an applied load. Because the reflected wavelengths are much larger than the changes (1500 nm original λ_B compared to a maximum $\delta\lambda_B$ of 8 nm), it can be approximated that the original wavelength is equal for both polarization states without much loss in accuracy. This turns Equation (2.91) into the following form:

$$\frac{(\delta\lambda_B)_1 - (\delta\lambda_B)_2}{(\lambda_B)_0} = \frac{n^2}{2} (p_{12} - p_{11}) (\varepsilon_1 - \varepsilon_2) \quad (2.92)$$

If the reflected wavelengths associated with each polarization direction shift equally, (i.e. $(\delta\lambda_B)_1 = (\delta\lambda_B)_2$) then the TSD equals zero. It will be seen that this comes in handy for determining the circumstances under which FBGs behave as uniaxial strain sensors.

2.5.2.4 UNIAXIAL STRAIN SENSING

The case where an optical fiber is strained uniaxially in the direction of propagation is relevant for the application of FBGs to strain sensing. It will be shown that this case reduces the relationship between changes in Bragg wavelength and strain to be one dimensional (1-D). In this specific case of uniaxial strain, no shear strains exist and the transverse strains, ε_1 and ε_2 , are equal and related to the longitudinal strain, ε_3 , through Poisson's ratio, ν as follows:

$$\varepsilon_1 = \varepsilon_2 = -\nu\varepsilon_3 \quad (2.93)$$

For a free or surface-mounted FBG, the Poisson's ratio is that of silica, ~ 0.165 . Because this case is axisymmetric, both polarization directions will reflect the same wavelength. The equations above will therefore be reduced as follows:

$$\left(\frac{\delta\lambda_B}{\lambda_B}\right)_1 = \left(\frac{\delta\lambda_B}{\lambda_B}\right)_2 = \frac{\delta\lambda_B}{\lambda_B} \quad (2.94)$$

$$\begin{aligned} \frac{\delta\lambda_B}{\lambda_B} &= -\frac{n^2}{2} p_{1\beta} \varepsilon_\beta + \varepsilon_3 \\ &= -\frac{n^2}{2} p_{11} \varepsilon_1 - \frac{n^2}{2} p_{12} \varepsilon_2 - \frac{n^2}{2} p_{13} \varepsilon_3 + \varepsilon_3 \\ &= \frac{n^2}{2} \nu p_{11} \varepsilon_3 + \frac{n^2}{2} \nu p_{12} \varepsilon_3 - \frac{n^2}{2} p_{12} \varepsilon_3 + \varepsilon_3 \\ &= \left[1 - \frac{n^2}{2} (p_{12} - \nu(p_{11} + p_{12})) \right] \varepsilon_3 \end{aligned} \quad (2.95)$$

We now have an expression for the measured change in wavelength divided by original wavelength as a linear function of longitudinal strain. The expression can be reduced to a pivotal equation at the center of utilizing FBGs as strain sensors:

$$\boxed{\frac{\delta\lambda_B}{\lambda_B} = (1 - p_e) \varepsilon_3} \quad (2.96)$$

In the equation above, $p_e = -(n^2/2) \cdot (p_{12} - \nu(p_{11} + p_{12}))$ and is referred to as the strain-optic coefficient. This is an effective method for relating the change in effective index term to uniaxial strain as:

$$\frac{\delta n}{n} = -p_e \varepsilon_3 \quad (2.97)$$

Now that we have applied FBGs to measuring strain, we will continue the section with describing the relationship between reflected wavelength and temperature.

2.5.3 Thermomechanical Sensing – Ferroelasticity

In Chapter 4, the thermal expansion of an optical fiber will be studied when a layer of thin film NiTi is used to replace the original polyimide coating. The goal will be to observe the ferroelastic properties of the NiTi coating in the optical response of a NiTi coated FBG

undergoing a thermal cycle. This subsection will describe the response of NiTi undergoing a temperature cycle, the optical response of an FBG undergoing a temperature cycle, and what the expected response will be when combining NiTi and FBGs.

2.5.3.1 FERROELASTIC NITI

The ferroelastic behavior of NiTi largely depends on the ratio of Nickel to Titanium used to create the alloy. With certain ratios such as that used in this research, the NiTi will exhibit what is known as the shape memory effect [32]. In this effect, NiTi in a cold-state undergoes a twinned martensite structure reorientation when mechanical stress is applied. This results in plastic deformation of the material. The strain in the specimen will steadily increase until the twin boundary reorientation occurs and a rapid increase in strain takes place. Figure 2-15 below demonstrates the stress-strain behavior. If the stress were to be released, the NiTi would not recover its original state. However, heating the NiTi from the cold state to a hot state will cause a phase transformation from martensite to austenite, the phase encountered when crystallizing NiTi. This negates the previously observed large strain increase and the NiTi is able to recover its original shape.

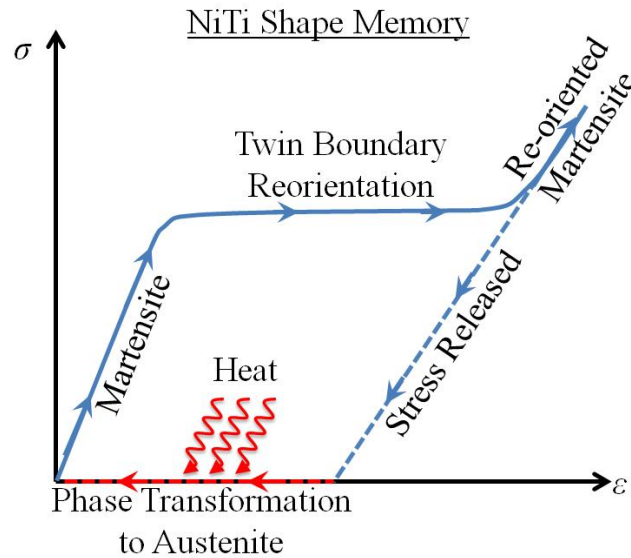


Figure 2-15: Shape memory behavior of NiTi undergoing stress and temperature change.

The temperatures of the hot and cold states are determined by the NiTi mixture ratio in the alloy. In this research, the NiTi is in a martensitic phase at room temperature and a thermal cycle is applied rather than any considerable mechanical stress. The behavior under a thermal cycle is demonstrated below in Figure 2-16. As the NiTi is heated, the red curve takes shape with a steady thermal expansion in the martensitic phase interrupted by a phase transformation into an austenitic phase. Upon cooling, the blue curve illustrates that the austenite phase is depleted as the NiTi returns to a martensitic phase. Note that the phase transformation start and finish temperatures (denoted by black dotted lines as the temperature bounds of the phase transformation) are not the same in heating as in cooling.

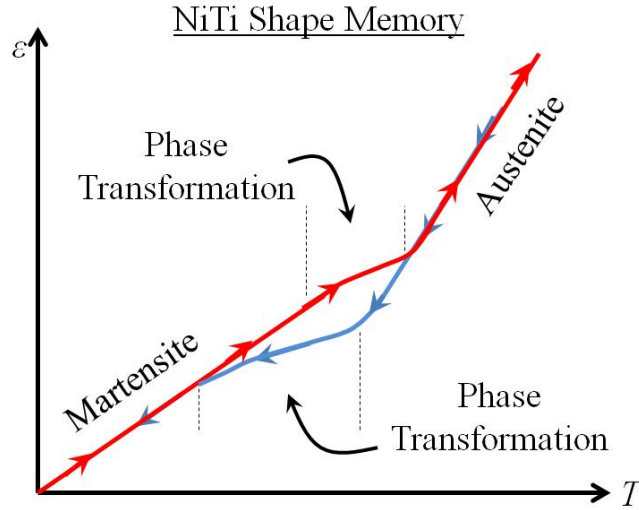


Figure 2-16: Shape memory behavior of NiTi undergoing a thermal cycle.

When heating from the martensite phase to austenite, the temperatures at which the phase transformation begins and ends are known as the austenite start (A_s) and martensite finish (A_f) temperatures respectively. Conversely upon cooling from austenite to martensite, the phase transformation temperature range is bound by the martensite start (M_s) and martensite finish (M_f) temperatures. This concludes the description of the behavior of the NiTi shape memory effect. The influence of temperature on the FBG reflection signal will be described next.

2.5.3.2 THERMO-OPTIC EFFECTS

The Bragg wavelength condition described in Equation (2.1) is differentiated with respect to temperature, multiplied by the temperature change, and divided by the original Bragg wavelength expression as follows:

$$\begin{aligned} \frac{\partial \lambda_B}{\partial T} \Delta T &= 2\Lambda \frac{\partial n}{\partial T} \Delta T + 2n \frac{\partial \Lambda}{\partial T} \Delta T \\ \frac{\partial \lambda_B}{\lambda_B} &= \frac{1}{n} \frac{\partial n}{\partial T} \Delta T + \frac{1}{\Lambda} \frac{\partial \Lambda}{\partial T} \Delta T \end{aligned} \quad (2.98)$$

The term on the left is the measured change in Bragg wavelength divided by the original λ_B . The first term on the right relates index of refraction to temperature changes. The second term on the right relates the mechanical stretching of the FBG to temperature.

In the previous section, tensor notation and changes in eigenvalues and eigenvectors of the permittivity matrix were calculated in order to relate strain to index. This complicated process was needed because strain and permittivity changes are represented as second order tensors. In this case, temperature is simply a scalar value and the thermal response of the optical fiber is taken to be isotropic. Thus, scalar values can be used to describe the thermo-optic effect unlike the vectors and matrices used to describe the photoelastic effect. The change in effective IOR with temperature divided by the original effective IOR can be represented with a single scalar material property, ξ .

As for the change in grating pitch with temperature, the change in Λ with temperature divided by the original Λ is equivalent to longitudinal strain change with temperature. The optical fiber is assumed to be thermo-elastically isotropic, so the thermal expansion in any direction can be represented with a single scalar value. Thus, the $(1/\Lambda) \cdot (\partial\Lambda/\partial T)$ term can be represented with the coefficient of thermal expansion of the fiber, α . Equation (2.98) can therefore be represented with the following equation:

$$\frac{\partial\lambda_B}{\lambda_B} = (\xi + \alpha)\Delta T \quad (2.99)$$

This concludes the description of the thermo-optic effect pertinent to this research. Next, the combination of the NiTi shape memory effect with the optical fiber thermo-optic effect will be described.

2.5.3.3 THERMO-OPTIC RESPONSE OF NITI COATED FBG

An optical fiber with a NiTi coating will exhibit a behavior described by Equation (2.99). However, the material properties, ξ and α must be revisited when comparing the original

polyimide coated FBG to the new, NiTi coated FBG. For both coatings, the medium through which light passes remains silica and germanium-doped silica. Thus, the IOR response of both materials should be equivalent. However, the thermal expansion of NiTi ($6.6 \mu\epsilon/^\circ C$ in martensite phase, $11 \mu\epsilon/^\circ C$ in austenite phase) is different from that of polyimide ($55 \mu\epsilon/^\circ C$). Additionally, the stiffness of NiTi being on the same order of magnitude as the glass compared to the polyimide stiffness being an order of magnitude lower means the influence of the NiTi α on the overall α will be higher. The following equation describes the material properties influencing the coefficient of thermal expansion of the fiber:

$$\alpha_{fiber} = f(\alpha_{silica}, \alpha_{coating}, E_{silica}, E_{coating}, V_f) \quad (2.100)$$

The fiber's coefficient of thermal expansion is dependent on the silica (α_{silica}) and coating ($\alpha_{coating}$) thermal expansion coefficient, the Young's modulus of the silica (E_{silica}) and coating ($E_{coating}$), and the volume fraction (V_f) of the coating.

When the NiTi coating is undergoing a phase transformation, extremely large strains will be transferred to the optical fiber. Thus, the α_{fiber} term will change during the thermal cycle depending on whether the coating is in the martensite phase, the austenite phase, or undergoing a phase transformation.

This concludes the description of how changing thermal fields can alter the reflected wavelength of a FBG. Next, methods for coupling an optical response to a magnetic field will be described.

2.5.4 Magnetic Field Sensing – Magnetostriction and Magneto-Optics

There are two different methods utilized in this research to alter the reflected wavelength with the application of a magnetic field. The first is a strain-based approach involving thin films and macro-scale specimens of magnetostrictive material. The second is an index-based approach which offers a more direct method for manipulating λ_B via IOR changes to the material through which the light is propagating.

2.5.4.1 STRAIN-BASED APPROACH

There is a certain class of materials, known as magnetostrictive materials, in which an externally applied magnetic field induces strain. Examples of ferromagnetic materials which exhibit magnetostriction are Nickel, Terfenol-D, and Metglas. In these materials, an externally applied magnetic field causes the magnetization of micro-scale domains which make up the overall material to change in magnitude and rotate. The aggregate of changes in size and rotation of all the micro-scale domains is what leads to a change in the size and shape of the overall macro-scale material.

This strain based approach simply involves attaching a FBG to a magnetostrictive material so that when a magnetic field is applied, the strain induced in the ferromagnetic material is transferred to the fiber. This strain, as seen in the previous subsection, will result in a shift in the reflected wavelength. Thus, energy is transduced from a magnetic form into a mechanical form which is picked up by the optical reflection signal. Figure 2-17 below demonstrates the qualitative behavior of strain within the magnetostrictive material parallel to the applied magnetic field. Initially, the response is approximately quadratic until it reaches a point when all of the magnetic domains within the material are aligned. At that point, the influence of magnetization on the strain behavior is saturated.

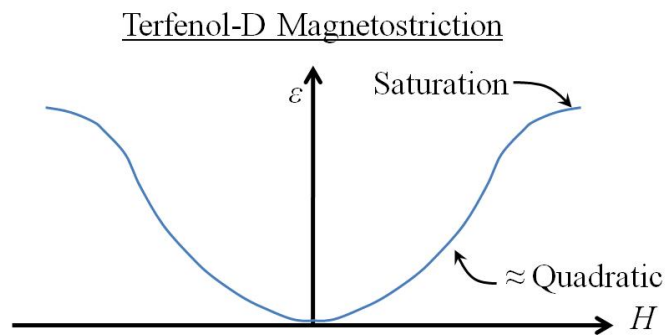


Figure 2-17: Magnetostrictive behavior of Terfenol-D.

Two different methods of mechanically coupling a fiber to a ferromagnetic material are utilized. The first is to take a bulk piece of Terfenol-D and surface-mount an optical fiber to the

ferromagnetic specimen with epoxy. The second is to replace the polyimide coating on a FBG with a thin film of Terfenol-D. For both coupling methods, the relationship between the applied magnetic field and change in reflected wavelength described in the following equation:

$$\frac{\delta\lambda_B}{\lambda_B} = (1 - p_e) \cdot \kappa \cdot \varepsilon(H) \quad (2.101)$$

The change in λ_B on the left side of the equation is measured. The $(1 - p_e)$ term links the measured optical changes to the uniaxial strain applied to the fiber. Both methods of mechanically coupling the fiber to the ferromagnetic material will involve uniaxial strain within the fiber. The $\varepsilon(H)$ term is the relationship between strain in the magnetostrictive material and the applied magnetic field. The form of this function was plotted previously in Figure 2-17. Lastly, the κ term is a mechanical coupling coefficient which determines how much of the strain in the ferromagnetic material is applied to the optical fiber. In the case where the fiber is attached to a bulk piece of Terfenol-D, the κ term will approach unity. In the case where a thin film of Terfenol-D coats the fiber, the ferromagnetic material's volume fraction is significantly reduced; therefore, the κ term will be much smaller.

These strain-based approaches will be explored in Chapter 4 for the purpose of creating novel FBG sensors. Utilizing magnetostriction provides an indirect approach to altering the reflected wavelength. The magnetic field is used to create a strain state in the fiber and the strain state is what manipulated the grating pitch and effective index. An index-based approach will be described next which directly alters the FBG's optical properties with a magnetic field.

2.5.4.2 INDEX-BASED APPROACH

The other approach used for coupling magnetic fields to the optical signal is through a magneto-optic effect. This involves altering only the effective index of the fiber and not the strain state. This means that no change is made to the grating pitch; therefore, the differential

term $\delta\Lambda/\Lambda$ in Equation (2.66) is equal to zero and neglected. The next step is to understand the constitutive relation between index changes and magnetic fields.

Just as strain affects the index of refraction by altering the permittivity tensor as described in photoelasticity, the permittivity tensor is altered by a magnetic field in magneto-optic effects. First-order nonlinear magneto-optic effects include the Magneto-Optic Kerr Effect and the Faraday Effect. In both of these phenomena, an originally diagonalized permittivity tensor has imaginary off-diagonal components introduced as shown in the following equation:

$$\mathbf{e} = \begin{bmatrix} e^{(1)} & 0 & 0 \\ 0 & e^{(2)} & 0 \\ 0 & 0 & e^{(3)} \end{bmatrix} \xrightarrow{H \text{ Applied}} \begin{bmatrix} e^{(1)} & +if(H) & 0 \\ -if(H) & e^{(2)} & 0 \\ 0 & 0 & e^{(3)} \end{bmatrix} \quad (2.102)$$

The off-diagonal components are related to the magnitude of the magnetic field through the function $f(H)$. Higher-order magneto-optic effects include the Voigt Effect and the Cotton-Mouton Effect. Both involve the introduction of birefringence via changes to the diagonal components of the permittivity tensor when the magnetic field is applied perpendicular to the direction of light propagation. Consistent with the coordinate system used in previous sections, the permittivity changes as follows for light propagating in the 3-direction with a magnetic field applied arbitrarily in 1-direction:

$$\mathbf{e} = \begin{bmatrix} e^{(1)} & 0 & 0 \\ 0 & e^{(2)} & 0 \\ 0 & 0 & e^{(3)} \end{bmatrix} \xrightarrow{H \text{ Applied}} \begin{bmatrix} e_p(H^2) & 0 & 0 \\ 0 & e_\perp(H^2) & 0 \\ 0 & 0 & e^{(3)} \end{bmatrix} \quad (2.103)$$

The permittivity for light linearly polarized parallel and perpendicular to the magnetic field change at different rates and depend on the square of the magnetic field because they are higher-order nonlinear optical phenomena. The lower-order phenomena give rise to polarization rotation, but not a change in the effective index of light polarized in a real direction (i.e. with no

imaginary component); therefore, a higher order effect is utilized to change the index of refraction of the fiber.

Magneto-optic effects are very weak in the silica material making up a typical optical fiber; therefore, the fiber material through which light propagates must be changed in order to notice any change in the Bragg wavelength. As noted in Equation (2.42), the effective index is a function of wavelength, the IORs of the various fiber layers, and the radii of those layers. In this research, most of the cladding layer is removed and replaced with a magneto-optically active material. Equation (2.42) is therefore altered into the following form:

$$\begin{aligned}\lambda_B &= 2\Lambda \cdot n(\lambda_0, n_1, n_2, a) \\ \Rightarrow \lambda_B &= 2\Lambda \cdot n(\lambda_0, n_1, n_2, n_3, a, b)\end{aligned}\tag{2.104}$$

The IOR subscripts 1, 2, and 3 correspond to the fiber core, fiber cladding, and magneto-optically active surrounding material respectively. The a and b terms refer to the radii of the fiber core and cladding, respectively. The exact form of the effective index dependence on the properties of a 3-layer fiber as opposed to a 2-layer fiber explored in this chapter will be demonstrated in Chapter 5. By looking at Equation (2.104), it is obvious that if the surrounding material's index of refraction is a function of magnetic field, then the effective index and subsequently, the reflected wavelength will also be a function of magnetic field. The layered functions demonstrating the induction are as follows:

$$\lambda_B = 2\Lambda \cdot n(n_3(H))\tag{2.105}$$

This demonstrates the methodology behind turning a FBG into a magnetic sensor by manipulating the strain or optical properties of the fiber with an external magnetic field.

2.5.5 Concluding Remarks

This section on sensing phenomena is the culmination of the past several sections building up a foundation describing the behavior of FBGs. This foundation serves two purposes. The first

purpose is to successfully understand and interpret signals coming from the FBG sensors during testing or application. This can only be accomplished with a deep understanding of the behavior and functioning of the sensor. The second purpose is to design and create novel sensors which open up avenues to an even wider variety of applications. Without fully understanding the inner workings of the FBG, specifically light propagation, Bragg reflection, and how external phenomena affect optical properties, it would not be clear how to elicit a response in the FBG (i.e. a shift in λ_B) when an external field is applied. The next section gives a summary of the fiber optic measurement system employed in this research to capture the behavior of FBGs.

2.6 NASA Dryden Fiber Optic Interrogation Device

The previous sections focused on the functioning of the FBG itself and how it is manipulated for sensing purposes. This section focuses on the measurements system provided by the NASA Dryden Flight Research Center to measure the reflected wavelength and the FBGs' reflected wavelength spectra.

2.6.1 FOID Data Processing

A description of the hardware which goes into the Fiber Optic Interrogation Device (FOID) such as photodetectors, couplers, broadband reflectors, and reference fibers can be found in Richards 2006 and Froggatt 1996 [8, 33]. The method used by the FOID system to measure and calculate the reflected wavelengths of multiple FBGs on the same fiber is known as optical frequency domain reflectometry (OFDR). More information on the technique can be found in Eickhoff and Ulrich 1981, Kingsley and Davies 1985, and Amano et al. 2005 in addition to the two previous references on the system's hardware [28, 34, 35]. Figure 2-18 below demonstrates the process of collecting data. An optical fiber with multiple FBGs is plugged into the FOID. As shown in the upper graph, a laser signal within the device tunes within a range of wavelengths encompassing the Bragg wavelengths of all the FBGs ($\lambda_{B1}, \lambda_{B2}, \lambda_{B3} \dots \lambda_{Bn}$). For each sweep (where

four sweeps are plotted in the upper graph), the intensity of light reflected back into the system by the FBGs is measured. The result is the plot in the lower graph where the intensity corresponding to noise at the beginning and end of the sweep is lower than near the range of wavelengths where the FBGs are reflecting.

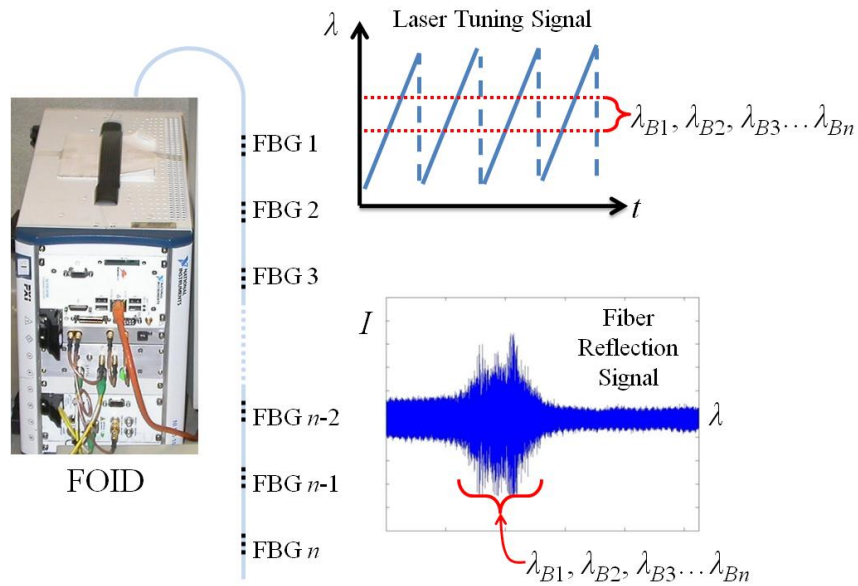


Figure 2-18: Laser tuning of the FOID system used to collect a reflection signal for the entire Bragg fiber.

The next step is to separate the contribution each individual FBG to the fiber reflection signal. The method for doing this is outlined in Figure 2-19 below. Beginning with (a) the fiber reflection signal as a function of wavelength, a Fourier transform is performed on the data to move into the length domain. The length domain plot (b) shows a large intensity peak corresponding to the beginning of the Bragg fiber just before FBG 1, several “top-hats” associated with the reflection of each individual FBG, and a large intensity peak corresponding to reflection of the end of the fiber just after FBG n . Zooming in on the middle of the Bragg fiber, plot (c) is obtained showing alternating regions of consistent reflection and no reflection. Each top-hat corresponds to a 5 mm long FBG and each region with no reflection corresponds to the 5 mm space between gratings where no effective index oscillation occurs. The entire data set at this point is zeroed out with the exception of the data within a specified window encompassing

an individual FBG (the i^{th} grating). An inverse Fourier transform is performed to get the data back into the wavelength domain. Now we have the reflected wavelength spectrum for the individually windowed FBG rather than the entire fiber. The Bragg wavelength, λ_{Bi} , is marked by either the peak or centroid of the distribution depending on the data collection method.

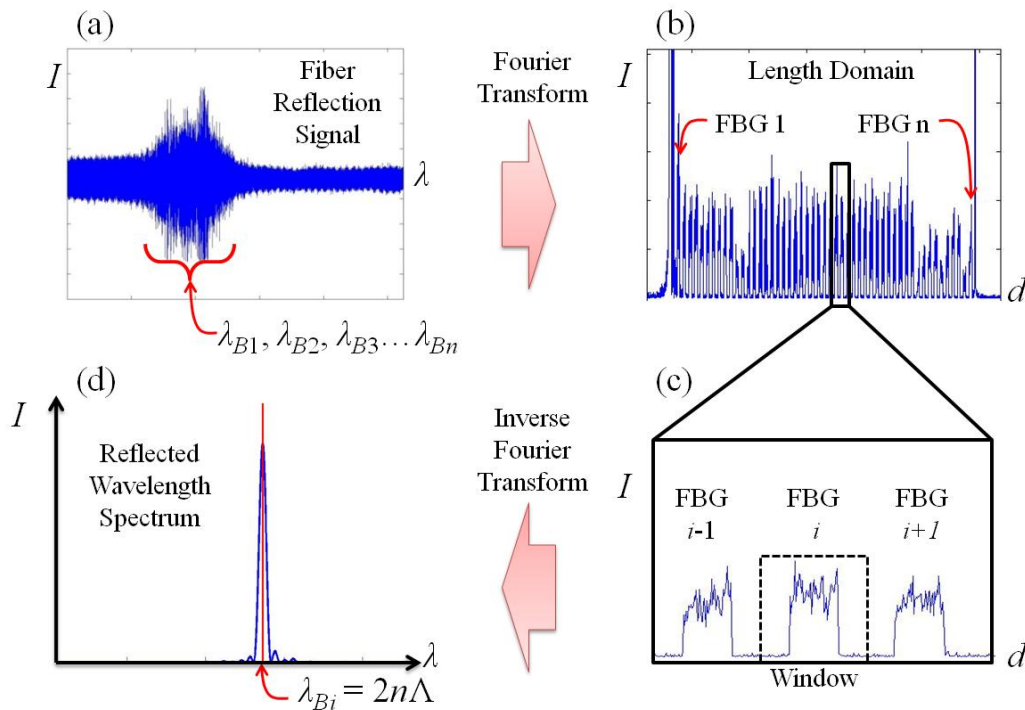


Figure 2-19: Data processing method for separating the contribution of individual FBGs to the fiber reflection signal.

One aspect of this method which should be noted is the domains in which the data is collected. In Figure 2-19 above, it is indicated that the Fourier transform brings the data from the wavelength domain into the length domain and the inverse Fourier transform does the opposite. These units make the data set easy to visualize and give an easily defined physical interpretation. However, the true units are not wavelength and length, but rather time and frequency. It is more difficult to physically interpret the length domain data in units of frequency, but doing so may provide insight which cannot be obtained when interpreting the data as being in the length domain. Further exploration is beyond the scope of this research, but a closer look at optical frequency domain reflectometry can be taken by exploring the references listed on the subject.

Figure 2-19 gives a basic description of the method the FOID system uses for separating the reflected wavelength of individual FBGs from the fiber reflection signal containing contributions from every FBG on the fiber. Depending on the test being run and the type of data desired, different methods of data collection will be used. These methods will be described next.

2.6.2 FOID Data Collection

There are two main ways for collecting data in this research. The first is what is known as “Raw Data” mode. This essentially means that during a test or experiment, a series of fiber reflection signals are collected and will be processed as shown above after the experiment has completed. The data collected from one laser sweep is heretofore referred to as a “raw data snapshot”. The down side of this form of data collection is that the responses of the FBGs are not monitored during the experiment. All results come from post-processing with no feedback as to the progress or success of the experiment until after it has completed. The benefit of this method is the breadth of information recorded and available for analysis. This allows for post-experiment analysis of the behavior of the Bragg fiber in the length domain as well as the study of the reflected wavelength spectrum of each individual FBG. This is particularly helpful for filtering noise out of the signal and for witnessing phenomena such as birefringence by seeing the initial single peak split into two.

The second data collection method involves real-time monitoring of the fiber reflection data. This method performs the transformations of the data as shown in Figure 2-19, but the differences lay in the quantity of data saved and the ability to monitor that data during testing. The advantage of this method is that results are plotted on the computer screen during the experiment. The sampling frequency has improved on more updated iterations of the FOID system, but for the version used in this research, the maximum sampling rate is approximately 18 *Hz*. To the user running an experiment, this is essentially real-time feedback. Thus, the user can witness the progress of the experiment, make necessary changes in the middle of the test, and estimate the success of the experiment while it is still running. The negative aspect of this

method is that rather than collecting an entire reflected wavelength spectrum for each individual FBG for each raw data snapshot, the only data collected is a single, scalar data point for each FBG for each raw data snapshot. This single data point is the shift in λ_B from one raw data snapshot to another for each grating. Thus, neither the reflected wavelength spectrum nor the length domain data can be analyzed after the test.

Within the real-time monitoring method, there are versions known as the “Langley method” and the “Dryden method”. The Langley method is exactly like the method outlined in Figure 2-19. The Dryden method, however, is a variation on the technique with a different windowing procedure among other adjustments to make the processing faster. Thus, a maximum sampling rate of 5-10 *Hz* could be obtained with the Langley method, but 18 *Hz* could be achieved in the Dryden method without losing any accuracy.

In this research, the choices for data collection were Raw Data, Langley, or Dryden mode. Thus, evaluations of the information desired depending on the test were made and the mode was subsequently chosen. In future iterations of the FOID system, multiple methods can be run simultaneously. This means that any limitation of the FOID system stated in this work is specific to the system iteration used and may no longer be consistent with current system design.

2.6.3 Concluding Remarks

This concludes the description of the FOID system provided by NASA Dryden Flight Research Center. The explanations above provide the reader with background knowledge of how data is collected in this research. This background includes a look into the data processing technique known as optical frequency domain reflectometry as well as the various data collection methods employed. In order to develop robust sensors, it is important to understand the method in which data is collected. With this knowledge, appropriate sensor design considerations such as sensitivity can be managed and suggestions for improvements to the measurements system can be made.

2.7 Summary

The purpose of this research is to develop the strain sensing abilities of embedded FBGs in addition to designing and fabricating novel FBG sensors. This chapter provides the necessary background information to understand future chapters describing the research. A short introduction to what fiber Bragg gratings are followed by how they are fabricated was given. From there, theoretical analysis was given on how light propagates within an optical fiber and how a grating elicits a reflection of that light. The various properties of the fiber and grating which contribute to light propagation and reflection were identified. This was followed with a description of the methods by which strain, temperature, and magnetic fields can be measured based on how they affect the reflection properties a fiber and grating. Lastly, the various methods used to monitor and process the optical signal were described

It is important to have a comprehensive understanding of optical fibers and FBGs in order to carry out research developing them as sensors. Extending a previously used analogy, the “Synopsis” section defines the objective of the game, the “Fabrication” section provides the history and origin, the “Light Propagation in Optical Fibers” and “Bragg Reflection” sections define the rules, the “Sensing Phenomena” section identifies the strategy for the game, and the “NASA Dryden Fiber Optic Interrogation Device” section dictates how the score is kept. The next three chapters will provide extended theory and experimental results that make up the body of research performed for this dissertation.

CHAPTER 3:

COMPOSITE STRAIN SENSING

3.1 Synopsis

This chapter describes research in the development of optical fiber Bragg gratings for strain gauge applications. The goal of this chapter specifically is to demonstrate the feasibility of embedded FBGs as uniaxial strain sensors. Certain assumptions dictated in the previous chapter must hold true in order for the uniaxial strain measurements to remain accurate. This chapter aims to identify what situations maintain the uniaxial assumption and which situations invalidate it.

This will be accomplished by embedding FBGs in composite materials in three configurations. The effects of curing residual strains, longitudinal versus transverse loading, strain transfer from the host to the sensor, and cross-ply cracks in the composite will be explored. The chapter will begin first with a literature review to provide the reader with proper context to understand how this work fits into the field of FBG strain sensors.

3.2 Literature Review

Extensive work has been carried out in the realm of FBG strain sensing research. The purpose of this section is to provide the reader with a clear perspective of various areas within FBG strain research and how those specific areas have developed through the years. This development begins with early papers describing the first uses of fiber optic sensors structural applications. This will then be followed with a description of the research performed during the

early years of FBG sensor development from the late 1970s through the mid-1990s. The number of papers published after the year 1997 ballooned heavily and FBG applications went in many different directions. Thus, the literature review is more comprehensive in the early years of FBG strain sensor development and more focused on particular areas pertinent to this research in the current years (after 1997).

The description of the FBG strain sensing field will give proper context to help understand the motivation, direction, and context of the research described in this dissertation. The five areas within FBG strain sensing pertinent to and explored in this research are the effects of strain transfer from a host material to an embedded fiber, the response of a FBG reflection signal to a load transverse to the fiber direction, the role of residual strains developed during the composite curing process, the embedment of FBGs in composites to promote uniaxial strain sensing, and the effects of cross-ply cracking on the sensor signal and response. Each of these five areas will be specifically reviewed for the post-1997 era and the contribution of this work to each of those fields will be explained.

3.2.1 FBG Sensing Background

Fiber optic sensors began to take off in popularity during the 1970s with increased use of fiber optic gyroscopes and acoustic detectors [6, 36]. Dr. Eric Udd, a leading expert in the field of fiber optic sensors, published a comprehensive journal article and book reviewing many types of fiber optic sensors. The sensors described range from intensity based fiber sensors to spectrally based sensors (i.e. Bragg gratings) and interferometric sensors (i.e. Sagnac, Mach-Zender). Methods of multiplexing to obtain distributed sensing and specific applications are also described.

The application of optical fibers to strain sensing has been demonstrated as far back as the late 1970s by Cole et al. 1977 and Butter and Hocker 1978 [37, 38]. Though these papers did not include the use of a fiber Bragg grating, they employed photoelastic theory to relate changes in index of refraction to strain. In the experiments, two optical fibers with different pathlengths

were used to create an interferometer. Cole et al. compared a “sensing” fiber attached to a tank container and a “reference” fiber which was left alone. Butter and Hocker compared one optical fiber cemented to the tension side of a bending cantilever beam to the other fiber on the compressive side. The interference patterns created by combining the light from the ends of the two fibers was seen to change due to a low-frequency acoustic wave applied to the tank and static strain applied to the cantilever beam. The different indices of each fiber altered the relative optical pathlengths in a measurable fashion.

The main issue with such a device is that the sensing region, in practical applications, would include a very long region of the fiber. This poses a limitation because the strain measurement reflects an average strain over the entire length of the sensing region. That is, this method outputs a single average strain measurement over the whole length of fiber attached to the structure rather than distributed strain measurements. This is not desirable for the purpose of obtaining high spatial resolution of measurements in order to calculate wing-shape or detect local damage.

This issue is partially resolved with the extrinsic Fabry-Perot interferometer (EFPI). EFPIs have been extensively researched for SHM as demonstrated by Richards 2006, Wang et al. 1993, and Paul et al. 1993 [8, 39, 40]. An EFPI is essentially a single optical fiber which is cut and separated a small distance on the order of a millimeter. The two fibers are aligned and the gap is enclosed with a glass sleeve which is glued to the two fibers. Reflections off the two ends of the newly formed cavity create the interference pattern which is correlated to strain.

The advantage of this technique is that the sensing region is narrowed down to a very small size to create a localized strain measurement rather than an average strain measurement. Additionally, the output is a true measurement of the strain in the fiber direction which does not change regardless of the direction of loading relative to the EFPI. The two main disadvantages in comparison to FBGs are the increased geometric profile due to the glass sleeve which forms the cavity and the reduced ability to multiplex the sensor. The first disadvantage results in a sensor with a larger geometric footprint which may cause embedment issues in addition to reducing the overall strength and durability of the sensor. The second disadvantage prevents EFPIs from

becoming a distributed strain measurement system due to the need for many more fibers in order to get a satisfactory number of strain measurements.

Fiber Bragg gratings, in comparison to other fiber optic strain measurement methods, provide a suitable method for obtaining a distributed sensing system while maintaining a small geometric footprint. At the moment, the two largest drawbacks to FBG strain sensors are the speed of data acquisition for a multiplexing measurement system and the sensitivity to transverse strain. Though individual FBGs have been demonstrated to be effectively quick dynamic strain sensors on the order of 50 kHz for acoustic wave detection, processing of multiple reflection signals from several FBGs written onto a single fiber optic significantly slows down the data acquisition rate[41]. In the OFDR system utilized in this research, data acquisition is limited to as high as ~18 Hz and newer versions of the same system designed by the NASA Dryden Flight Research Center have pushed this limit to the order of 100 Hz. Though tremendous strides have been taken in speeding up the system, for the time being this limits the ability of a distributed FBG strain sensing system to measure acoustic waves and high-frequency dynamic deformation modes in structures. The sensitivity of FBGs to transverse strain is an interesting problem which is the main focus of the research performed here. Before addressing the specific issues of the influence of transverse strains on embedded FBGs, a review will be provided on the development of FBG strain sensors in the early years of the technology.

3.2.2 FBG Strain Sensing – Early Years

FBG strain sensing became a burgeoning field by the mid 1990's after they were first discovered in the late 1970s and fabrication methods were developed in the early 1980s to expand access to the technology. Various studies were performed to develop the applicability and understand the fundamental behavior of FBGs in situations pertaining to thermomechanical sensing. Interesting methods were introduced for relating strain to changes in reflected wavelength which have since died out in popularity due to survival of the fittest and most successful interrogation systems. Initial studies of FBGs involved techniques for separating the

combined influence of temperature and strain, understanding the role of transverse strain difference (TSD) in birefringence, monitoring of composite curing processes, and calculating strain fields which are nonuniform along the length of a FBG.

3.2.2.1 FBG SENSING ONSET

First FBG strain sensor was proposed in 1978 by Kawasaki et al, the same group of authors who invented FBGs by noticing photosensitivity in germanium doped optical fibers [13]. As mentioned in the previous chapter, however, these initial FBGs extended the entire length of the optical fiber. Any strain measurement, therefore would have been an average measurement over a longer distance rather than a distributed set of measurements, each covering a much smaller distance to provide high spatial resolution. With the exception of utilizing Bragg gratings to form the ends of a Fabry-Perot cavity for interferometric strain sensing, no development of FBGs as direct strain sensors occurred until Meltz et al. 1989 developed and patented a method for side-writing gratings onto a fiber [18, 42-44]. Now that multiple, distinct FBGs could be written on the same fiber, the same group patented the invention of writing multiple FBGs of different reflected wavelengths (i.e. for wavelength division multiplexing) onto the same fiber for the purpose of measuring strain (Meltz et al. 1988, Meltz et al. 1989) [45, 46].

Melle et al. 1993 demonstrated a method for tracking strain by measuring the wavelength emitted by a laser with one of its cavity mirrors being a FBG attached to a cantilever beam [47]. As the beam strained, the cavity properties changed and a different wavelength matching the reflected wavelength of the FBG was emitted from the laser. This same type of setup was used by Kersey and Morey 1993 with four FBGs multiplexed onto the same fiber, essentially creating four laser cavities and thus, four wavelengths emitted by the laser [48]. These papers demonstrate a trend of attempting to increase the multiplexing abilities of FBG sensors.

This trend was continued when Davis et al. 1994 utilized three surface-mounted FBGs with different Bragg wavelengths (i.e. wavelength division multiplexing) to measure vibration modes of a cantilever beam [49]. This work was continued in Davis et al. 1996 with a demonstration of

two sensing modes – one which was “single-sensor locked” to monitor one FBG and the other was a “scanning multi-sensor” mode [50]. The former was used for calculating vibration frequency and the latter was used for mode shape calculations. This demonstrated the trade-off between the quantity of FBGs multiplexed and speed of FBG processed in designing an interrogation system.

3.2.2.2 METHODS TO RELATE λ_B CHANGES TO STRAIN

Davis’ work just described corresponds to directly measuring the reflected wavelength and correlating it to strain. Other methods have been developed which indirectly relate Bragg wavelength changes to strain. For example, LaRochelle et al. 1990 used FBGs as strain sensors for vibration sensing [51]. In this paper, two vibration stress fields imparted on the fiber created a beating pattern which was identified by the reflection power of the FBG. Vengsarkar et al. 1991, created a beating pattern by writing a FBG onto an elliptical core, two-mode optical fiber [52]. The two orthogonal modes experienced slightly different IORs and that difference increased or decreased when strain was applied, thus changing the beat length in a measureable fashion. Using this type of interrogation method, Greene et al. 1992 measured the first two vibration modes of a cantilever beam [53].

A ratiometric processing method was used by Melle et al. 1991 where two FBGs of nearly the same reflected wavelength were employed [54]. One FBG acted as a filter which restricted the intensity distribution of input light to the sensing FBG. Therefore, the intensity of light reflected by the sensing FBG is a function of the overlap between its reflection spectrum and the filter’s. In this method, the filtered intensity of light reflected by the sensing FBG is correlated to reflected wavelength and thus, strain. Melle et al. 1993 used this technique to measure strain in a FBG surface-mounted to an aluminum cantilever beam with results comparable to resistance strain gauges [55]. In this method, the light reflected from a FBG was sent through a wavelength-dependent filter which had a linear relationship between transmission coefficient and

wavelength. This way, only the intensity of the reflection signal needed to be measured. This reflection intensity was correlated to the reflected wavelength and subsequently to strain.

FBGs continued to be used as an interferometric mirror by Kersey and Berkoff 1992 where the pathlength difference between a reference FBG and a sensing FBG exposed to the environment of interest increased as the temperature of the sensing FBG increased [56]. Another common interferometric technique which incorporates FBGs will be described in the next section. It essentially involved the combination of a Fabry-Perot cavity where a FBG represented one reflective surface. These examples represented common and creative methods for relating reflected wavelengths to strain in the early years of FBG strain sensors.

3.2.2.3 DEMODULATING TEMPERATURE AND STRAIN

A common problem with the signal from any strain sensor is the temperature sensitivity. For that reason, there has been a lot of research and many different methods devised for demodulating temperature and strain contributions to a FBG signal.

Arya et al. 1997 used the overlapping reflection signals from a FBG and alternating high and low dielectric index of refraction layers deposited onto the end of the fiber to create a resonant structure [57]. The method was devised by Want et al. 1992 and was similar to the ratiometric method described earlier [58]. The FBG simultaneously served the purpose of a stand-alone strain sensor and a wavelength dependent filter. The resonant structure's reflected wavelength was temperature dependent and the measured reflected intensity was dependent upon the intensity made available by the FBG filter.

Henriksson et al. 1996 decoupled temperature from strain with a combination of using a pulsed light source and two chirped FBGs acting as the ends of a Fabry-Perot cavity [59]. An interferometric method was employed to track the phase difference between the two FBG reflections. By employing chirped FBGs, it was seen that temperature effects became negligible, thus making the strain sensor thermally insensitive.

James et al. 1996 demonstrated a strain-temperature demodulation technique based on splicing two FBGs of equal core and unequal cladding diameters [60]. Under conditions of uniaxial strain or changes in temperature, the two FBGs will respond differently. Thus, a system of two equations to solve for the strain and temperature unknowns was characterized.

Ferreira et al. 1996 came up with a solution which involved comparing a FBG sensitive to both strain and temperature to a nearby FBG surrounded by a cap which prevented strain transfer [61]. The capped FBG was located at the end of the fiber to ensure no strain transfer. The biggest drawback to this setup was that only one thermal-compensating measurement was taken for each Bragg fiber.

Liu et al. 1997 demonstrated a demodulation technique based on a FBG and EFPI in series and in close proximity [62]. This provided two measurements for the two unknowns (i.e. strain and temperature). This was built upon by Rao et al. 1997 by using two sets of a fiber-Fabry-Perot interferometer (FFPI) in series with a FBG where the second set's FBG had a different wavelength reflection from the first set [63]. The interferometric data was utilized to measure temperature, static strain, and dynamic vibration of a piezoelectric transducer.

Song et al. 1997 demodulated strain and temperature by placing two FBGs separated by 1 *cm* within a glass tube [64]. Epoxy was used to attach the ends of one FBG but not the other to the glass tube. In this setup, both FBGs responded nearly equally to temperature but the FBG attached on both ends to the glass tube did not respond when the fiber was strained. It is unclear whether the strain insensitivity was because the glass tube creates additional stiffness and renders any strain negligible or if the FBG glued to the glass tube is provided slack such that a very large amount of strain would have to be provided in order to make the FBG taut and therefore sensitive to strain.

3.2.2.4 SURFACE-MOUNTED FBGS

The simplest application of FBGs for strain measurement is to simply surface mount a Bragg fiber onto a structure. Simonsen et al. 1992 surface-mounted a FBG onto a glass fiber reinforced

plastic (GFRP) composite undergoing a three-point bend test [65]. The FBGs were seen to behave linearly and elastically up to 1.6 % strain with no hysteresis and good agreement with electrical strain gauges.

Magne et al. 1997 demonstrated the successful use of a FBG strain rosette [66]. By placing three FBGs at relative angles of 0°, 60°, and 120° the three in-plane strain components of a metallic plate undergoing a 4-point bend test were calculated. This is a very significant result consistent with demonstrations of surface-mounted FBGs behaving as good uniaxial strain gauges which are insensitive to the substrate's transverse strains. This essentially means, for example, that the strain reading for the 60° FBG is only sensitive to whatever strain is applied in the 60° direction and not anything perpendicular (i.e. -30° and 150°).

3.2.2.5 EMBEDDED FIBER SENSORS

Much background work went into developing the photoelastic theory that relates strain to FBG reflected wavelength changes as described in the previous chapter. Though the early embedment work was not specifically used for FBGs, it was foreseen that embedding optical fiber sensors of some sort in composites was an important and emerging field, so further research in the area was carried out. Sirkis and Haslach 1990, Mathews and Sirkis 1990, and Sirkis and Haslach 1991 developed photoelastic theory pertaining to strain-induced IOR changes in single mode optical fiber [67-69]. Though it was for the application of an interferometric fiber sensor rather than a Bragg grating, the theory was still meaningful for calculating changes to the EM wave's propagation constant, β , and thus, effective index.

A particularly important aspect to consider is whether or not the mechanical properties of a composite are degraded by the presence of an optical fiber. Roberts and Davidson 1991 looked into embedding optical fibers with various cladding and coating diameters, coating materials, load directions, and embedment orientation into unidirectional composites [70]. It was found that for fibers embedded parallel to structural fibers and transverse to the loading direction, coatings with large diameter and high stiffness created stress concentrations that slightly reduced strength

but did not affect stiffness. However, a stiff coating such as polyimide provides more durable adhesion. A polyimide coated optical fiber of diameter $\sim 100 \mu m$ was taken to be the optimal size and material. This type of fiber was embedded in the composite in the four permutations available when aligned parallel or perpendicular to adjacent structural fibers and parallel or perpendicular to load. The only significant reduction in strength was seen when the fiber was embedded parallel to structural fibers and perpendicular to load. These results indicate that in the case of a quasi-isotropic lay-up with a $\sim 140 \mu m$ coating diameter, the composite's cross-ply oriented perpendicular to loading direction may be more susceptible to cracking at the fiber location. However, because these layers are not load bearing (an assumption determined by comparing stiffness with layers that have structural fibers oriented in the loading direction) no significant degradation of composite strength was expected.

Carman et al. 1993 confirmed these results by embedding an optical fiber in a unidirectional composite parallel to structural fibers and perpendicular to loading direction [71]. The uncoated optical fibers decreased the transverse strength by up to 50% for fibers over 100 microns in diameter. Uncoated fibers less than 100 microns in diameter were not experimentally seen to have a significant impact. Optical fibers coated in polyimide achieved better results with a smaller strength reduction of about 23% in the worst case even for large, 250 micron diameter fibers. Carman and Reifsnider 1993 reported that optical fibers with coating properties that closely matched the transverse properties of the host material had the least impact on strength [72]. In addition to coating properties, it was found that the residual strains imparted on the fiber during curing influenced the optimal coating stiffness.

Sirkis and Dasgupta 1990 looked into optimal coating properties for embedding an optical fiber parallel to reinforcing structural fibers [73]. Various factors were theoretically analyzed including the influence of a coating's Poisson's ratio and stiffness on the tangential and radial stress in a fiber. This analysis was carried out for fibers embedded parallel to loading and adjacent to structural fibers. While the results were not experimentally validated and a set of

specific optimal material properties was not named, the paper nevertheless demonstrated the importance of selecting a proper coating material for embedding fiber optics.

Dasgupta et al. in 1990 and Dasgupta et al. 1992 published results exploring the lenticular resin rich region surrounding an optical fiber embedded perpendicular to structural carbon fibers [74, 75]. FEM modeling was carried out to calculate stress concentrations around the optical fiber and also to predict the size of the resin pocket due to curing procedures. This work is very important because the size of the resin pocket greatly influences the residual strain imparted on the optical fiber. Singh et al. 1991 looked into how fiber diameter and coating thickness affected stress concentrations using Moiré Interferometry of the surface during loading [76]. While micro-cracking at the fiber-coating-host interface was a concern, it was concluded that embedded fibers did not degrade the structural integrity as measured by strength and stiffness.

An additional factor considered by de Vries et al. 1995 was whether or not an embedded fiber optic sensor has fatigue properties which are equal to or better than its host [77]. In this study, EFPIs were embedded in steel-reinforced concrete and displacement was measured during fatigue loading. The fiber sensors lasted over 100,000 cycles and still provided good data when compared to strain gauges. The same group, de Vries et al. 1997, did similar NDE testing of concrete structures with embedded EFPIs and described two significant hurdles in embedding fiber [78]. While embedded fiber optic sensors were shown to reliably measure strain through the lifespan of the structure, issues such as selecting a proper coating to deal with the alkaline environment of concrete and devising adequate ingress/egress structures to prevent the fiber from snapping must be addressed.

The detection of damage is another very important area in which fiber optic sensors have shown potential. Damage phenomena that can feasibly be identified include impacts, delaminations, and cracking. Bhatia et al. 1995 embedded EFPIs into a graphite fiber reinforced composite lay-up to monitor delaminations [79]. The responses of four EFPI sensors due to an ultrasonic pulse were monitored before and after loading which induced delamination. The results indicated a large drop in the amplitudes of the sensor responses due to the ultrasonic pulse

which qualitatively indicated damage. The same group, Greene et al. 1995 embedded four EFPIs in CFRP composites to monitor the effects of impact damage [80]. In addition to identifying the presence of impact, the lag amongst the sensor responses was used to accurately calculate the location of impact.

These papers describe basic themes in embedding fiber optics within composites. Such work included the development of photoelastic theory relating index changes to strain, the influence of the fiber and coating presence on the mechanical properties of the host material, the development of a rubric for coating material selection, the fatigue characteristics of the fiber optic sensor compared to the host structure, the ability to accurately monitor strain and damage. Next, we will specifically consider early research on embedded FBGs.

3.2.2.6 EMBEDDED FBGS

The effects of coating were explored either theoretically or by measuring material properties of the host structure, but not with feedback provided by the fiber sensor. The response of embedded FBG sensors was explored when Dockney et al. 1997 performed a 3-point bend test on embedded FBGs parallel to adjacent structural fibers with either no coating or recoated with Acrylate [81]. The strain was compared to theoretical calculations and the response of surface-mounted strain gauges. Bare FBGs had good strain transfer from the host while Acrylate coated FBGs had a reduction of approximately 12%. Bare FBGs seem like the better choice, however, they are more susceptible to damage such as moisture absorption. Polyimide was shown to provide adequate adhesion between embedded FBGs and CFRP composites. In this study, a complete picture was not painted of the reliability of FBG sensors because the reflection signal may have degraded sooner than its structural integrity. The ability of a fiber sensor to maintain its structural integrity as long as or longer than its host structure was explored while considering the sensor's feedback in work by Levin and Nilsson 1996 [82]. The study compared the reliability of surface-mounted and cross-ply composite embedded EFPIs and FBGs. It was found that FBGs had a much higher strain to failure (~0.4 % FBG compared to ~0.18 % EFPI) which

coincided with strain levels inducing matrix cracking. All embedded sensors were parallel to structural plies. Once cracking in the matrix was seen, the FBG signal degraded. This meant that even though the fiber itself did not structurally degrade before the host, its reflection signal did. This indicates that FBG sensors could be very useful for detecting the presence of cracks in composites.

Eaton et al. 1995 studied the interaction of an embedded optical fiber in a cross-ply laminate with finite element analysis [83]. The orientation of the FBG in one model was parallel to adjacent structural fibers and in another model was perpendicular. These results indicated an embedded FBG could lead to premature failure of the composite; however, the strength reduction was not quantified and experiments were not performed to substantiate the finite element model. Additionally, the composite layer thicknesses were set to be very nearly equal to the optical fiber diameter, which could exacerbate stress concentrations.

In addition to the ability of a sensor to last as long as its host, the response of FBG sensors must be compared to well established methods of measuring strain. This generally means embedded FBGs are compared to surface-mounted electrical resistance strain gauges. For example, Foote 1995 reports embedding six FBGs between the 19th and 20th plies (out of 22) in a CFRP composite beam in a quasi-isotropic lay-up [84]. The FBGs survived, but good agreement was not seen amongst embedded FBGs, surface-mounted strain gauges, and analytical predictions with the exception of two locations where strain gauge and FBG data agreed, but analysis did not. This was most likely because the FBGs were placed in locations “so as to measure the largest strain gradient.” The reflected wavelength spectrum, which was not shown, most likely would have indicated the FBGs became chirped in the nonuniform strain field. Rao et al. 1996 demonstrated better results when multiplexing nine FBGs embedded in a CFRP composite similar to Foote’s [85]. The results presented for one of the FBGs matched very well with a surface-mounted strain gauge. The location of this FBG was the same as one of the two in Foote’s work that displayed agreement between FBGs and strain gauges.

FBGs are typically embedded in-plane, but Bullock et al. in 1993 embedded a FBG in the out-of-plane direction of the composite, making the FBG trans-laminar [86]. The sensor tracked what the authors believed to be the strain profile well until failure of the composite, but the result was highly nonlinear and severely influenced by edge effects. In-plane sensors can easily be strategically placed to avoid strain concentrations due to edge effects, but FBGs oriented through-the-thickness cannot.

In addition to CFRPs, extensive work has been performed embedding FBGs in concrete structural components. Ferdinand et al. 1997 surface-mounted and embedded FBGs in a concrete cylinder and compared them to both surface-mounted and embedded extensometers [87]. The FBGs did not always match well with the vibrating wire and inductive sensor, but did always match well with theoretically calculated responses. Davis et al. 1997 embedded several FBGs in different parts of a concrete beam with FRP attached for increased strength on the tension side of the beam [88]. FBGs were first correlated to an electrical strain gauge response and subsequently attached to the surface of the beam in addition to the surface of rebar supports within the beam and within the FRP layers. The FBGs were seen to survive and remain outputting strain data after the beam had been loaded to failure. This work speaks to the survivability of embedded fiber optic Bragg grating strain gauges.

3.2.2.7 NONUNIFORM STRAIN

The research in this dissertation describes FBGs that are assumed to have a uniform strain distribution along the length of the grating; that is, no chirping is present. A significant amount of work has been performed to try and understand the affects that a nonuniform strain distribution along the length of the grating has on the FBG reflection spectrum. Such work could remove the limitation that FBGs must be placed in far field regions of uniform strain.

Le Blanc et al. 1994 demonstrated control over FBG chirping by attaching a fiber to a variable-cross-section cantilever beam while being deflected [89]. Using the strain profile calculated using elasticity theory, the expected wavelength reflection spectrum was calculated

and compared to experimentally measured spectra. The results demonstrated decent agreement for a small amount of chirping. Le Blanc et al. 1995 demonstrated the effects of imparting a large amount of chirping in a FBG glued into a groove which was cut into a piece of aluminum [90]. The nonuniform strain in the FBG due to de-adhesion between the glue and fiber was studied. Using an assumed strain profile, they were able to create a theoretical calculation of the reflected wavelength spectrum that was similar to that found experimentally. This is a very good example of how reflection spectra are affected by large strain gradients.

Huang et al. in 1995 theoretically modeled the reflected wavelength spectrum of a FBG undergoing chirping [91]. Using a transfer-matrix method, the reflection spectrum was studied when grating pitch was a function of FBG length. They also studied the effects of apodized gratings, where the amplitude of index oscillation is a Gaussian function of grating length rather than a constant value or, as in chirped FBGs, linearly increasing. The authors used this method to compare their theoretical calculations with the results of experimentally applied nonuniform strain. While there was good agreement between experiment and theory, this only indicates that strains can be used to calculate the reflected wavelength spectrum. However, in order to create an effective sensor, the reverse must be achieved so that a given reflected wavelength spectrum can be converted into a strain distribution. This concern was addressed by Huang et al. 1996 by taking the phase information from a chirped FBG and going through a set of calculations to obtain the strain as a function of position within the grating [92]. It was found to be most sensitive around regions of higher strain gradient and the method could only be employed for monotonically increasing strain. Le Blanc et al. 1996 also went through the process of taking the reflected wavelength spectrum from a FBG near a circular inclusion in a plate to calculate the strain along the grating length [93]. The results compared favorably with available elasticity solutions, particularly away from the edges of the grating.

3.2.2.8 TRANSVERSE LOADING/SENSITIVITY

One of the crucial issues in embedding FBGs is their sensitivity to transverse strain. As was seen in the theory presented in the last chapter, if two unequal principle strains develop in the plane transverse to the optical fiber, then light polarized in the two directions will experience different effective IORs and thus, reflect at different wavelengths. This phenomenon, known as birefringence, has been studied by applying transverse loading to optical fibers.

Bjerkkan et al. 1997 explored the effect of a transverse load on FBGs with Acrylate and polyimide coatings [94]. As the fiber was laterally compressed, there was Poisson's expansion in the fiber direction. This resulted in the reflected wavelength of both polarization states to increase, but at different rates. Birefringence was seen to increase linearly until it was deemed the polymer coating began to break down and adversely affect strain transfer. This, combined with a nonuniform strain imparted on the polyimide coated fiber due to structural breakdown of the coating, resulted in a nonlinear wavelength shift for the two FBG polarization states.

While the previous research involved lateral compression of a typical, single-mode FBG, Lawrence et al. 1997 performed a similar experiment on a high-birefringence (Hi-Bi) fiber [95]. Hi-Bi fibers are drawn with additional materials on either side of the core such that the residual strains imparted on the core create a transverse strain difference that results in birefringence. This type of fiber is also known as polarization-maintaining (or PM) fiber. Rather than creating a transverse strain difference (TSD) entirely from mechanical loading, the TSD already present was exacerbated and/or rotated by the applied load. If the applied compression was aligned with the residual compressive strain, then the principal strain direction remains. If it is applied at a 45° angle to the residual principal strain directions, however, then the principal residual strain changes in magnitude and orientation. This was quantified by measuring the slope of reflected wavelength change versus applied and plotting it versus applied angle relative to the residual strain orientation. The sensitivity for each polarization state was cyclic, but not in the same sense as a sine or cosine function because the zero points were around -20° and +40° (with error). This

demonstrates the complicated nature of drawing residual strains into an optical fiber and the rotation of principal strain directions when external loads are applied.

3.2.2.9 CURE MONITORING

A necessary aspect in the embedment of FBGs is the effect of curing and residual strains on the FBG after composite fabrication. Researchers have taken this a step further by utilizing FBGs to monitor the progress and phenomena taking place during composite curing. Dunphy et al. 1990 monitored curing progress to calculate the mechanical strains in an embedded FBG [96]. The thermal effects were stripped out of the embedded FBG response by having a second FBG in the autoclave but outside the composite. By including temperature compensation into the embedded FBG's response, the onset of phenomena such as vitrification and residual strains during cooling were observed. The purpose of this test was to demonstrate the usefulness of FBGs to optimize curing procedures.

Dockney et al. 1997 embedded FBGs parallel to adjacent structural fibers in a CFRP composite beam [81]. The effect of coating on the FBG residual strain was explored. The residual strains were calculated to be between 2100 and 2400 $\mu\epsilon$ for bare FBGs and between 1100 and 1700 $\mu\epsilon$ for Acrylate recoated FBGs. The compliant coating layer was therefore seen to reduce residual strains.

Friebele et al. 1994 looked at the result of embedding an optical fiber with 7 FBGs (plus 2 non-embedded reference FBGs) in between the 9th and 10th plies of a 10-ply unidirectional composite. By comparing the reflected wavelengths before and after curing, a strain distribution profile along the length of the composite was calculated. The same experimentally obtained strain profile was taken and compared to a finite element model of the residual strains. The results of the 7 FBGs matched well with finite element analysis [97, 98].

A factor of great importance is whether or not the residual strains imparted on the optical fiber by the composite induce a transverse strain difference and thus, birefringence in the reflection spectrum. While the effect was either seen to be negligible or not mentioned by

previous authors, Sennhauser et al. 1996 demonstrated the inception of birefringence due to curing of a CFRP composite cable meant to replace a steel cable supporting a suspension bridge [99].

The effects of curing on a FBG's reflection signal greatly impacts the signal processing methods when external mechanical strains are imparted on the host. The presence of a split peak could, for example, greatly throw off the ratiometric processing method described earlier in this section. Additionally, residual strains add complexity to the notion of a zero-strain point when it comes to calculating strains within a composite.

3.2.2.10 DUAL-GRATINGS

Dr. Eric Udd, a significant contributor to the field of FBG sensors, has published a body of work on sensing three strain components and temperature with a dual wavelength fiber Bragg grating written in a birefringent optical fiber (Udd et al. 1996, Lawrence et al. 1996, Udd et al. 1997, Nelson et al. 1998, Udd et al. 1999) [100-104]. This is a clever method of retrieving four pieces of information from a single sensing location. This is accomplished by writing two distinct gratings onto the same region of an optical fiber. The result was a FBG that can reflect light near both 1300 nm and 1550 nm, thus providing two data points. Shifts in IOR due to changes in strain and temperature occur at different rates for the two wavelength regimes. In order to turn the two pieces of information into four, a Hi-Bi optical fiber was used so that the reflected wavelengths became polarization dependent. Therefore, four reflected wavelengths of about 1300.0, 1300.6, 1550.0, and 1550.8 nm were measured. A system of four equations that were a function of the four reflected wavelengths was used to solve for the four unknowns (three principal strains and temperature change).

Xu et al. in 1994 used dual-grating FBGs of different wavelengths (~800 and 1200 nm) to provide two measurements that are used to obtain longitudinal strain and temperature [105]. This idea was carried out a couple years earlier than Udd's, but Hi-Bi optical fiber was not used. Patrick et al. 1996 devised a hybrid sensor using FBGs and long period grating for strain and

temperature measurement [106]. The long period FBG was used as a filter for the two short period FBGs which reflected at slightly different wavelengths. The two measurements made are the reflected wavelength of one of the FBGs and the relative reflectivity coefficients of the two short period FBGs.

This concludes the literature review on the early years of FBG strain sensing. Papers in the topics just described go up to the year 1997 because this represents a point where the amount of research on FBG strain sensors greatly expands. From 1996 through 1997, no less than seven review articles on FBG sensors were published, indicating the growing popularity at that point in time. In the next section, we will move on to describe the more current era's work in FBG sensing from 1998 onward.

3.2.3 FBG Strain Sensing – Current Years

The previous section was comprehensive in the scope of topics described pertaining to FBG strain sensing research. The purpose was to give the reader adequate background into the types of research avenues FBGs have inspired for strain sensing and structural health monitoring. At this point, the literature will cover mainly aspects of FBG research that is more closely aligned with the topics addressed in this dissertation. Topics such as nonuniform strain, demodulation of strain and temperature, surface-mounted FBGs, damage involving impact and delamination, and interrogation system developments, for instance, will not be further referenced. The exception to this will be in the next section where several review papers published during both the early and current years will be considered. The review papers will provide adequate starting points for a reader looking to perform their own literature survey on topics not thoroughly investigated in this dissertation. The topics that will be discussed here include (1) strain transfer from a host to an embedded fiber, (2) transverse loading of FBGs to induce birefringence, (3) cure monitoring as it relates to fiber residual strains, (4) general mechanical loading of composite embedded FBGs, and (5) the influence of composite cracking on FBG sensor signals.

3.2.3.1 STRAIN TRANSFER

The transfer of strain from a host material to a FBG is a key aspect of adequately relating host strain to reflected wavelength measurements. There are many factors which contribute such a relationship that have been explored in literature. Yuan and Zhou 1998 explored the transfer of strain from an epoxy host with an optical fiber embedded parallel to the loading direction [107]. In comparing experimental and theoretical results, the length of fiber attached to the epoxy determined the percent of strain transfer. Though this work was performed with an interferometric fiber sensor instead of a Bragg, it could be concluded that the 5 mm long FBGs used in this research must be a couple centimeters from attachment points to experience full strain transfer.

In addition to the length of fiber attached, extensive work has continued on the choice of coating when embedding in a host material. Tang et al. 1999 explored the transfer of strain from an isotropic host material to an embedded fiber theoretically [108]. They found similar results as previous authors that the length of optical fiber attached is an important factor and that the sensor should be located in the far field region away from host edges. Additionally, they calculated an optimal coating stiffness of 1 *GPa* in their model. Duck and LeBlanc 2000 added to this work by providing more theoretical strain work based on elasticity but additionally compared the results to a finite element model [109]. The results indicate the relationship between strain transfer coefficients and factors such as matrix stiffness.

Tao et al. 2000 embedded FBGs in woven composites [110]. When the fiber-coating or coating-host interface was manipulated with an interface polymer, premature de-bonding occurred and was evident with hysteresis in the wavelength shift versus load graph. When no manipulation was performed, the results were linear, indicating adequate strain transfer compared to sensors exhibiting de-bonding characteristics.

3.2.3.2 TRANSVERSE LOADING

A very important phenomenon considered in this research is birefringence in the optical fiber which leads to a split in the FBG reflection spectrum from a single peak to two peaks. The origin of this event arises from unequal transverse loading of an optical fiber. Therefore, understanding the relationship between transverse loads and the distance between peaks is crucial to develop a reliable strain sensor. Bosia et al. 2003 studied the diametrical compression of single-mode (SM) and polarization maintaining (PM) fiber [111]. A linear relationship existed between the birefringence developed and the load applied for SM fiber and for PM fiber when the load was in the direction of the fast or slow axis (note that for SM fiber, the fast and slow axes are equal and can be arbitrarily defined before loading due to the cylindrical symmetry). If, however, the load was applied at an angle that did not line up with the fast or slow axes of the PM fiber, then a nonlinear trend was seen which generates a large amount of complexity. Even when knowing the loading angle, numerical and experimental results did not always match up. This was perhaps due to the inability of one to calculate the exact residual strains in a PM fiber due to the drawing process. Without this knowledge, quantifying the relative effect of additional mechanical loading compared to the initial residual strain effect is impossible. Ye et al. 2002 took a PM fiber and applied a transverse compressive load at various angles relative to the fast and slow axes of the FBG's inherent residual strains [112]. The change in Bragg wavelength divided by the applied load for each axis was cyclic but not in the same fashion as a sine wave. While the load sensitivities of each reflected wavelength was seen to have maxima and minima at 0° and $\pm 90^\circ$, the zero locations were at approximately $\pm 30^\circ$. This is different from the $\pm 45^\circ$ values which would be expected in perfectly sinusoidal behavior.

Prabhugoud and Peters 2006 created a finite element procedure whereby a commercial finite element package was used to calculate the nodal strains within the cross section of an embedded optical fiber [113]. From this point, the strains are fed into a finite element model that calculates changes to the index of refraction and the orientation of principal axes. This process was carried out on a circular core fiber, elliptical core fiber, and PM fiber. The residual strains in the PM

fiber were calculated with the finite element program going through a -800°C temperature change. These results indicate that while it is possible to perform the nonlinear calculations to find the expected birefringence in PM fiber when strains are known, the reverse calculation of finding strains when birefringence is measured is still an unresolved problem.

In addition to transverse loading studies on increases in birefringence, a comparison was made by Melin et al. 1999 between the displacement-field in the core of an optical fiber compared to the surrounding host material [114]. An optical fiber coated with $18\ \mu\text{m}$ of polyimide was embedded parallel to structural fibers in a unidirectional carbon fiber epoxy composite laminate. The sample was compressed in-plane transverse to the fiber direction and the surface displacement field in the load direction was measured using Moiré interferometry. The displacement field was seen to decrease in magnitude in the silica, thus resulting in a decrease in strain imparted on the core. This is a key result in future predictions of the birefringence expected to be seen in the optical fiber based on expected transverse strains of the host.

3.2.3.3 CURE MONITORING AND RESIDUAL STRAINS

In this next part, the thermomechanical effects due to the curing and embedment process will be considered. It has been shown by numerous authors that the fabrication process plays an important role in the resulting reflection spectra of embedded FBGs. Menéndez and Güemes 1999 embedded two FBGs in a quasi-isotropic composite and studied the effects of residual strains on birefringence [115]. The peaks were seen to split upon cooling of the composite during the curing process. Using photoelastic equations and the assumption of in-plane stress, the stresses in the FBG were calculated, but the strains were not. Wavelength shifts were compared to a corresponding longitudinal strain, but it was not said that the optical fiber actually underwent that strain. Menéndez and Güemes 2000 embedded four FBGs in a cross-play CFRP lay-up and used the method described above to actually calculate strains in the FBGs [116]. The authors were able to calculate three unknown residual strains in the optical fiber using the stiffness

constitutive relationship under the assumption that out-of-plane stress was zero. This allowed them to calculate two in-plane stresses from the two reflected wavelengths and using the two stresses to calculate the three strains. A similar method of strain calculation was performed in Güemes and Menéndez 2002 only this time with a FBG embedded in a composite near a hole which causes nonuniform residual strains [117].

Kuang et al. 2001 embedded 3 optical fibers in a laminate made up of unidirectional composite and aluminum plies [118]. The FBG embedded with two parallel adjacent structural plies showed no birefringence whereas the FBG with one parallel and one perpendicular adjacent structural ply exhibited birefringence due to residual strains. Despite the residual strains, both FBGs behaved linearly during tensile loading.

Kang et al. 2002 embedded two hybrid EFPI-FBG sensors in unidirectional, cross-ply, and woven composites [119]. The strain was calculated using the FBGs and thermally compensated with the EFPIs. The first of six sensors was embedded perpendicular to adjacent structural plies, sensors two through 4 were embedded parallel, and sensors five and six were embedded in woven composites. No mention of birefringence was given because the FBG was in the glass capillary of the hybrid sensor. Kang et al. 2003 continued this by monitoring the strains in a non-symmetric cross-ply laminate during curing with two FBGs oriented parallel to the adjacent structural plies of the layers in which they are embedded [120].

Kang et al. 2006 embedded FBGs of different lengths into composite materials and calculated the residual strains imparted on the FBG [121]. Birefringence was seen to be a function of grating length, but this may be a function of the FWHM decreasing as grating length increases, thus making it easier to see the split peaks. Additionally, it is assumed that residual strain in the fiber direction was a linear function of wavelength shift, but this was not the case when considering photoelasticity. The best you can hope to calculate is a transverse strain difference, not any longitudinal strain. Jung and Kang 2007 ignored this when they embedded FBGs within a braided composite and performed compression tests on the specimens after fabrication [122]. After noticing a split in the peaks, a residual strain value is given which was

most likely inaccurate. Jung et al. 2007 embedded FBGs in between woven lamina and measured residual strains [123]. No reflected wavelength spectrum was given nor was birefringence mentioned.

Okabe et al. 2002 embedded three different FBGs parallel with surrounding structural fibers but perpendicular to the structural fibers in an adjacent ply [124]. The residual strains in a bare fiber, polyimide coated fiber, and a polyimide coated small-diameter fiber were experimentally measured and theoretically calculated during curing. The only FBG that exhibited significant birefringence was the bare, normal size FBG. The theoretical calculations performed did not match the experimental reflection spectrum.

Chehura et al. 2005 embedded a Hi-Bi optical fiber in unidirectional composites and an epoxy-only material for a baseline [125]. One Hi-Bi fiber was embedded parallel and another perpendicular to adjacent structural fibers. The transverse strain difference developed was monitored during curing and was seen to vary depending on the host material. Sorensen et al. 2006 embedded FBGs without coating parallel to structural fibers in unidirectional composites [126]. The two polarizations states were seen to split due to curing residual strains and the transverse strain difference was quantified. Lee et al. 2007 embedded two FBGs parallel to adjacent structural fibers but sandwiched between perpendicular structural fibers [127]. A FBG that was stripped and recoated with Acrylate did not exhibit birefringence while a FBG that was stripped and not recoated did exhibit significant split peaks. These papers demonstrate the effects of optical fiber coating on the development of residual strains during the embedment process.

3.2.3.4 EMBEDDED FBGS

Several researchers have looked into validating strain measurements for embedded FBGs undergoing mechanical loading. Wood et al. 2000 embedded FBGs in graphite epoxy laminated composites with $+45^\circ$, -45° , 0° , and 90° plies in a non-quasi-isotropic layup [128]. The FBGs were embedded parallel to the load and 0° plies and were found to agree very well with strain gauges. Kuang et al. 2001 embedded FBGs parallel to loading direction but at various angles

relative to adjacent structural fibers [129]. Birefringence was seen to develop due to curing, but was not exacerbated during loading.

Other authors were able to measure longitudinal strain under certain loading and embedment configurations while avoiding any influence of birefringence. Matrat et al. 2002 embedded FBGs in a rosette configuration with each of the 3 FBGs making up the rosette in between separate layers such that they are all parallel to adjacent structural fibers [130]. When applying tensile, compressive, or shear loading such that the principal strains remained in the 0° and 90° orientation, excellent agreement was seen with surface-mounted strain gauges. Bosia et al. 2002 embedded FBGs in between different layers of 8- and 16-ply cross-ply laminates [131]. The FBGs were oriented parallel to one set of adjacent structural fibers and perpendicular to the others in many cases. No birefringence was shown and the FBGs displayed a linear relationship between strain and height during the 4-point bend test. Bosia et al. 2004 continues the previous research and embeds FBGs in between layers of cross-ply laminates [132]. No birefringence was mentioned, but the sensors tended to perform very well measuring the strain profile in the direction of the optical fiber through the thickness when compared to a 3D finite element model.

Betz et al. 2003 embedded FBGs parallel to adjacent structural fibers in a carbon fiber quasi-isotropic lay-up and performed tensile tests both parallel and perpendicular to the fiber orientation [133]. The results were described to be similar to a finite element model for longitudinal loading, but a significant amount of scatter was reported for the transverse loading. A very thick coating was seen to significantly reduce the creation of an elliptical shape in the optical fiber when loaded transversely. These results however, did not receive much attention in the paper.

Fan and Kahrizi 2005 embedded two FBGs in each of the two cross-ply laminates at different thickness levels in order to remain parallel to adjacent structural fibers [134]. In one laminate, the mid-plane FBG was parallel to the load and perpendicular in the other laminate. Results matched well with surface-mounted strain gauges for FBGs parallel to the load when tested to

over $2100 \mu\epsilon$, but the FBGs oriented perpendicular to the load either stopped responding or departed from strain gauge results at only $-60 \mu\epsilon$.

Luyckx et al. 2007 created a strain sensor made out of two FBGs written on Hi-Bi fiber with one of the FBGs inside a polymer capillary [135]. The purpose of this FBG configuration is to have two separate FBGs which respond differently to equal transverse loading. With this, four reflected wavelengths were obtained (one for each polarization state in each FBG) that can be used to calculate the three principal strains and temperature. The matrix used to convert wavelength changes to strain is calibrated in this work using a longitudinal, transverse, and temperature test. The sensor was tested upon embedment with longitudinal and transverse loading, but the host was not described.

Mulle et al. 2009 embedded four FBGs at different depths in a reinforced quasi-isotropic composite undergoing a three- and four-point bend test [136]. Good agreement was seen between FEM, FBGs, and a digital surface image used to deduce strains in the 4-point test, but not the 3-point test. A significant amount of shear strain was seen by the surface imaging device, but this can be attributed to edge effects that die out in the far field region where the FBGs are embedded.

Emmons et al. 2008 and Emmons et al. 2010 embedded an optical fiber in a graphite epoxy quasi-isotropic lay-up parallel to adjacent structural plies [137, 138]. The optical fiber was multiplexed with several FBGs along its length in order to create a strain profile. The FBG strain profile was compared to both a finite element model and a single surface-mounted strain gauge when the composite was loaded in the fiber direction and showed good agreement

Luyckx et al. 2010 performed a study attempting to relate strains in the far field of a host material to the strains seen by the core of a fiber optic sensor [139]. A 3x3 matrix relating the longitudinal, in-plane transverse, and out-of-plane transverse strains in the fiber to that in the host was populated by applying boundary loads in those three directions of the composite. Longitudinal strains were always seen to be equal to the host, but transverse strains were not. This work was later backed up with experimental data in Voet et al. 2010 with a cross-ply

laminate that had two FBGs (one in a capillary tube shielding the FBG from transverse strains and one not in a capillary tube) [140]. One very interesting and counterintuitive theoretical result was that an out-of-plane compression led to an in-plane transverse compression of the optical fiber. These results were backed up with experimental data. One theoretical result which was not experimentally verified was the ratio of in-plane transverse strain in the fiber optic to be approximately ten times higher than the host in-plane transverse strain when a longitudinal load in the fiber direction is applied. An incorrect statement is made in this paper stating that shear strains will not affect the index of refraction of the fiber, but this is absolutely wrong, as shown in the previous chapter on photoelasticity. However, the loading used in their model did not expose this inaccuracy.

These papers indicate the complex nature of embedding FBGs in a host material undergoing a complex strain state. Some embedding attempts were made with the goal of getting the FBG to behave as a uniaxial strain sensor while other efforts had the goal of fully resolving the strain state of the host material.

3.2.3.5 CRACKS

The effect of cracks in a host material on FBG strain measurements have typically been explored in the context of nonuniform strain fields. Okabe et al. 2000 embedded a FBG in between two cross-ply layers in a CFRP cross-ply laminate which caused some birefringence due to residual strains [141]. The reflected wavelength spectrum was seen to become distorted when cross-ply cracking occurred due to tensile loading in the fiber direction. The cracks were transverse to the optical fiber direction. The results were compared with some theoretically calculated reflection spectra. The cladding diameter was $125\ \mu\text{m}$ and the polyimide coating diameter was $250\ \mu\text{m}$. Satori et al. 2001 performed similar experimental work with a small diameter (cladding/coating was $40/52\ \mu\text{m}$) embedded in the same lay-up [142]. Significant chirping was seen in the reflection spectrum when cracks formed due to nonuniform strain.

In addition to studies linking the effects of nonuniform strain due to cracks with chirped FBGs, other studies have used the observed chirping phenomenon to infer crack density. Takeda 2002 created a theoretical formula to calculate cross-ply crack density in a composite and used FBGs to validate this work [143]. Cracks were seen to affect the FBGs' reflected wavelength spectra and reflectivity due to chirping and sudden strain gradients respectively. It was proposed that the reduction in reflectivity was caused propagating waves turning into leaky EM wave modes from the original fundamental mode. Okabe et al. 2002 performed similar work analyzing the reflection spectra of a small diameter FBG susceptible to cross-ply cracks [144]. It was noted in this work that the reflection spectra did not return to a single peak upon unloading, but did become slightly less chirped. Measurements of the FWHM of the spectra were seen to correlate very well with crack density.

This work was continued by Okabe et al. 2002 by analyzing the strain transfer in the longitudinal direction of the FBG when cracks are present [145]. This was then used to calculate the reflection spectra at various loads for both coated and uncoated FBGs. Okabe et al. 2004 took their work one step further by considering chirped FBGs rather than uniform FBGs [146]. This means that instead of detecting cracks by a single-peak spectrum that broadens and splits into multiple peaks, changes to a consistent, reflected intensity across a range of wavelengths were observed. Because the chirping creates a linear relationship between reflected wavelength and distance along the FBG, changes to the reflection spectrum at particular wavelengths could be mapped as cracks occurring at a specific location along the FBG.

Efforts were later made to quantitatively link reflection spectra to nonuniform strain from cracks. Prabhugoud and Peters 2003 studied the change in reflected wavelength spectra based on whether the FBG is located in the "near-field region" or "far field region" of the crack [147]. A specific case was numerically studied for FBGs at particular distances from a crack in a unidirectional laminate. The effects of micro-bending which contribute to loss in the fiber were taken into consideration as well.

Ussorio et al. 2006 embedded a FBG parallel to the mechanical loading direction and between cross-ply layers of a transparent glass fiber reinforced polymer [148]. The fiber was mostly inside the layer with structural fibers parallel to the FBG. The reflection spectra for the FBG during loading was measured and compared to theoretical calculations when a crack in the adjacent cross-ply developed. Palaniappan et al. 2006 performed a similar embedment process with the FBG between cross plies but mostly within the layer whose structural fibers were parallel to the optical fiber [149]. The FBG was chirped and the reflection spectrum experienced an abrupt change in reflectivity at the wavelength corresponding to the crack location.

A common theme in the existing literature on monitoring cracks within composite materials with FBGs is that a nonuniform strain field develops which breaks the initial single peak into multiple peaks. Some researchers aim to quantify the chirping and nonuniform strain with the FBG's reflection spectrum while others look to calculate crack density to evaluate the amount of damage to the composite. A very interesting result of the work in this dissertation is unique in that a cross-ply crack in certain configurations can result in a FBG initially susceptible to host transverse strains becoming insusceptible and behaving as a uniaxial strain sensor.

This concludes the literature review on a subset of the large body of work involving FBGs. The purpose of this portion of the review is to see how, from the early years to the current years, the utilization of FBGs has evolved into a more precise science when it comes to topics such as strain transfer, cure monitoring, and embedment of FBGs in composite materials. While these individual papers tend to focus on a particular aspect of FBG strain sensing, many review articles have been published providing more comprehensive perspectives of the field of FBG strain sensing.

3.2.4 FBG Strain Sensing – Reviews

Several review papers have been published over the years addressing FBG strain sensing research. A list of 19 review articles published between 1996 and 2011 has been compiled and

the various topics addressed by each paper are displayed in Table 3-1 [7, 17, 150-166]. A quick explanation of the topics is as follows:

Surface-Mounted Strain Sensing: The application of the simple, uniaxial Bragg wavelength-strain relationship as it is applied to surface-mounted strain sensing.

Strain-Temperature Demodulation: The work performed to separate the influence of strain and temperature on the measured shift in Bragg wavelength.

Embedded Strain Sensing: The work performed with FBGs embedded within composite material hosts for the purpose of strain sensing.

Other Sensing Fields: The use of FBGs and other optical fiber sensors to measure alternative fields. Examples include dynamic vibration, magnetic fields, pressure, chemical composition, and rigid body rotation.

Alternative Grating Types: The application and analysis of gratings such as chirped, blazed, or long-period gratings which exhibit reflection spectra unlike typical uniform gratings.

FBG Interrogation & Multiplexing Techniques: The description of methods for measuring the reflected wavelength of a FBG. It also describes how to discern the reflection of a single Bragg grating when multiple gratings on a fiber are simultaneously reflecting light.

Alternative Grating Sensing Configurations: The combination of multiple FBGs or FBGs and EFPIs, for example, in some fashion to obtain a single measurable sensing signal.

Wave Propagation: The influence of light propagation properties on FBG reflection characteristics.

Mode Coupling: The analysis of different modes other than the fundamental mode of propagation in optical fibers.

Reflection Spectra: The spectrum of reflected intensity versus wavelength for various types of FBGs such as chirped gratings and FBGs experiencing nonuniform strain fields.

Photosensitivity & Fabrication: The description of photosensitivity and how it relates to fabrication techniques used to write FBGs on optical fibers.

Damage Detection: The use of FBGs for detecting various forms of damage in composites such as matrix cracking, delamination, and impact.

Applications: Examples given in review papers on specific examples of FBG applications such as monitoring strain in bridges or wings.

Table 3-1: Summary of various topics on FBG strain sensing covered by relevant review papers.

Year	Lead Author	Surface-Mounted Strain Sensing	Strain-Temperature Demodulation	Embedded Strain Sensing	Other Sensing Fields i.e. Magnetics, Pressure	Alternative Grating Types i.e. Chirped	FBG Interrogation & Multiplexing Techniques	Alternative Grating Sensing Configurations	Wave Propagation	Mode Coupling	Reflection Spectra	Photosensitivity & Fabrication	Damage Detection	Applications
1996	Kersey	X	X				X	X						X
1997	Erdogan					X			X	X	X			
1997	Ferdinand	X												X
1997	Hill	X						X	X	X	X			X
1997	Kersey	X	X			X	X	X		X	X			
1997	Othonos	X	X			X	X			X	X	X		
1997	Rao		X		X	X	X	X		X	X	X		
1998	Du	X		X		X					X	X		
1998	Friebele	X										X		X
1999	Rao	X			X		X	X						X
2000	Grattan					X	X	X				X		
2000	Wei			X			X						X	
2002	Zhou	X					X	X					X	
2003	Kuang			X			X	X					X	
2003	Lee	X			X	X	X	X						X
2004	Zhao	X	X				X	X						
2007	Mrad	X		X	X									X
2010	Wang	X			X	X				X		X		X
2011	Luyckx	X	X	X										

3.2.5 FBG Strain Sensing – Applications

This final portion of the FBG strain sensing literature review will cover several papers which describe work using FBGs as strain gauges in specific applications such as bridge monitoring and composite overwrapped pressure vessels (COPVs).

3.2.5.1 COPV

Davis et al. 1996 measured axial and hoop stress in composite-overwrapped concrete cylinders with FBGs embedded within the composite material [167]. When the cylinders were compressed, positive hoop strain up to 1.2 % and negative axial strains down to -3.8 % were measured. The sensors survived up until the cylinder was crushed.

Foedinger et al. 1999 embedded FBGs into the overwrapping composite layers of a COPV [168]. Most FBGs were embedded without manipulation while some were surrounded with a glass capillary to either create a strain-insensitive temperature sensor or a transverse strain-insensitive sensor. The embedded FBGs were studied using micrographs to determine the location of voids which affect strain transfer to the FBGs. Ingress/egress methods were also analyzed. FBGs were embedded parallel to structural fibers in the hoop and helical directions and perpendicular to the hoop plies in the axial direction. Reflected wavelength was measured during curing of the composite and during pressurization. A representative 3D finite element model was created and compared with the embedded FBGs to surface-mounted strain gauges. When comparing resistance strain gauges to FBGs, results were very good (< 2 % error based on average of all embedded FBGs) for hoop, helical, and axial measurements near the middle of the cylinder (i.e. away from the ends). The finite element results agreed for the axial and hoop measurements, but not the helical.

Degrieck et al. 2001 published a methodical study of the embedment of FBGs in the hoop direction of a COPV [169]. Bare optical fiber was first studied followed by FBGs embedded in flat rectangular samples undergoing a 3-point bend test. This was followed by embedding a FBG within the hoop layers of a COPV undergoing pressurization. Hoop strains of approximately 700

$\mu\epsilon$ were applied and a linear relationship existed between applied pressure and measured FBG strain.

Kang et al. 2002 studied surface-mounted FBGs and collocated, electrical strain gauges in the dome and hoop regions of a COPV undergoing up to 1000 *psi* of internal pressure [170]. In the dome region, the FBGs were mounted parallel to the helical wrap. In the hoop wrapped region, most FBGs were mounted parallel to the structural direction while two were mounted in the axial direction perpendicular to structural plies. The FBGs in the dome region did not match very well with strain gauges whereas hoop-oriented FBGs did match well with associated strain gauges. The FBGs mounted on the hoop wrap in the axial direction experienced highly nonuniform strain, thus creating multiple peaks in the reflection spectra.

Grant et al. 2003 embedded FBGs in rectangular composite coupons at various angles relative to the structural fibers and load direction [171]. This was followed by a COPV study utilizing the lessons learned in the coupon testing. The coupon embedded FBGs did not always match up with surface-mounted strain gauge readings due to, according to the authors, a shear lag between the surface and middle of the coupon. FBGs were embedded parallel to hoop and helical plies in the COPV. Three axially oriented FBGs agreed well with each other and the hoop-oriented FBG agreed well with surface-mounted strain gauges up to 1200 *psi* which corresponded to approximately 4000 $\mu\epsilon$.

Kang et al. 2006 embedded FBGs parallel to structural fibers in a COPV which was loaded to failure [172]. FBGs demonstrated strong linearity up to 500 *psi* and showed a significant dependence on embedment depth in the dome region but not in the hoop region. High strain gradients were also observed in the dome region. Several FBGs in the fabrication of multiple COPVs broke due to various reasons such as handling, curing and winding.

3.2.5.2 BRIDGE MONITORING

Measures et al. 1994 and Maaskant et al. 1994 embedded 15-18 FBGs in concrete girders to analyze the relaxation of steel and carbon fiber tendons used to pre-stress and support the girders

[173, 174]. The FBGs were successfully able to measure relaxation in the tendons but issues with proper bonding between the sensor and host material and large strain gradients over the length of the FBGs negatively affected some results. In these papers, strain measurements over several months were provided which indicated a smaller relaxation in composite-reinforced girders. Maaskant et al. 1997 continued this work by reporting additional data points in time for the strain relaxation in addition to reporting strain experienced while a vehicle traversed the bridge [175].

Storøy et al. 1997 placed FBGs on a bridge which was to be loaded to failure [176]. The FBGs were placed in locations which only achieved strains of approximately $1200 \mu\epsilon$ at bridge failure and matched collocated electrical strain gauges very well. Nellen et al. 1999 embedded FBGs inside pre-stressed CFRP wires used to reinforce a 47 m long pedestrian bridge [177]. A complete process of fiber characterization (fiber strength, temperature sensitivity, fatigue strength, etc.) followed by monitoring the CFRP embedment, curing process, anchor cable mounting, and post-installation strain fluctuations was developed and used. This comprehensive process demonstrates both the need to fully characterize FBG sensors and the ability of those sensors to provide a vast amount of data during fabrication and while in service.

Fuhr et al. 1999 published results of embedding FBGs attached to rebar reinforcements in concrete for bridge monitoring [178]. Three processes of embedding the FBGs in an already-constructed bridge were described and the survival of the FBGs was evaluated. Temperature and vibration measurements were taken after embedment. This paper points out the difficulties in embedding optical fibers after a bridge has already been constructed.

Gebremichael et al. 2005 embedded and surface-mounted FBGs on an all-fiber reinforced composite bridge [179]. The original bridge was removed and replaced with the composite version. During construction, which consisted of attaching composite sections together, FBGs were surface-mounted on panels which were subsequently stacked. The FBGs were therefore embedded in the epoxy layer adhering adjacent composite sections. This aided in protecting the FBGs and helped to prevent the effects of birefringence. Strain was monitored while a 30 ton tank was driven across the bridge and subsequently while cars drove across once opened to the

public. The strain reported did not exceed $100 \mu\epsilon$ and provided measurements that matched surface-mounted resistance strain gauges well.

Barbosa et al. 2008 attached several FBGs to wires suspending a circular pedestrian bridge [180]. The FBGs were placed in a stainless steel capillary tube and attached to a thin steel plate. This configuration was created so the FBGs could easily be welded to a metal surface. The strain monitoring system was tested by placing people at different locations on the bridge either evenly spread out or concentrated in particular sections. The strain sensors were utilized to determine the where more people were currently located on the bridge.

3.2.5.3 OTHER APPLICATIONS

Bugaud et al. 2000 embedded FBGs in a glass fiber-polyester composite waterway gate [181]. One temperature and four displacement-monitoring FBGs were utilized and compared to surface-mounted strain gauges. The data drift was monitored while the gate was used in a dock for preliminary investigation. The gate was then put in use at the intended waterway and strain was monitored during operations such as “opening, filling, locking, draining, etc” and while a boat passed nearby. Information on the composite lay-up was not given. The intent of this work was to demonstrate the feasibility of using FBGs to monitor such composite gates and demonstrate the advantages of composite gates over metal gates.

Schroeder et al. 2006 attached several FBGs to wind turbines and successfully monitored strain variations during rotation [182]. The rotations per minute and the effects of wind gusts were observed in the wind turbine rotor blade.

Takeda et al. 2007 provide a review of several of the authors’ publications on FBG applications [183]. Such topics included embedding FBGs for strain monitoring in a CFRP fuselage structure, a cryogenic tank for launch vehicles, for detecting lamb waves in CFRP box structures, and for crack detection in advanced composite grid structures. This work demonstrates several examples which indicate the large breadth of applications for FBG based structural health monitoring.

Dennison et al. 2008 used FBGs as a pressure sensor for measurements inside the intervertebral discs (IVDs) [184]. The fiber optic was glued inside a hypodermic needle which punctured the IVD. The hypodermic needles shielded the fiber optic from transverse stresses, so the only applied stress was from the end tip of the needle. This created an approximately linear strain gradient which broadened the reflection spectrum, thus making the Bragg wavelength tracking more difficult. Actual measurements were taken inside the IVD of a cadaveric porcine (pig).

Dennison et al. 2010 used FBGs for pressure and contact force measurements in the hip joint of two cadavers [185]. The pressure sensor was described in a previous publication while a birefringent optical fiber was used to measure contact force. Rather than exploring the photoelastic equations relating strain components to wavelength shifts, the authors experimentally calibrated wavelength shifts to known contact forces before placing inside the hip joint.

Lee and Hwang 2008 surface-mounted FBGs for dynamic strain measurement on a rotating shaft and blade configuration [186]. This work demonstrated the use of a rotary optical coupler for fiber optic measurements involving rotating structures. It also demonstrated the use of a ratiometric method (described earlier) to deduce strain from multiplexed FBGs all experiencing Bragg wavelength shifts while attached to structures rotating at 1500 *rpm*.

Lee et al. 2010 devised a sensor configuration for attachment to materials which are undergoing corrosive degradation [187]. A pre-strained FBG is attached to the surface of the material under consideration and during corrosion the pre-strain is relaxed in a measurable fashion. Strain in a FBG bonded to a sacrificial metal layer and that in a FBG bonded to an acrylic-coated metal layer immune to corrosion were compared. The measurements were compensated with a strain-insensitive thermal sensing FBG. The difference in wavelength shift of the two FBGs indicated the amount of corrosion quantified by the loss of mass.

Possetti et al. 2009 used long period gratings (LPGs) to monitor the refractive index of fluids for fuel industry applications [188]. Rather than coupling a forward and backward propagating

mode as in a FBG, a LPG couples a forward propagating fundamental mode with forward propagating cladding modes that exit the fiber. Associated grating wavelengths are measured by looking at dips in the transmission spectrum rather than peaks in the reflection spectrum. Because the refractive index of an ethanol-gasoline mixture is dependent upon the relative concentration of both components, the wavelength associated with the dip in reflected wavelength will change with concentration. The results demonstrated the applicability of the sensor to analyze gasoline conformity at commercial gas stations.

He et al. 2010 applied FBGs for measuring the 2D tilt of a plate [189]. The configuration involved an optical fiber attached at three locations around a circular plate separated by 120° and attached to a mass hanging underneath the plate. As the plate tilts, the force distribution on the three segments of fiber will change, thus resulting in shifts in the three reflected wavelengths. One sensor will develop slack due to tilt, so that FBG is used to strip out thermal effects. Tilt angles as small as 0.005° were measured.

Huang et al. 2010 used two FBGs and a piezoelectric acceleration transducer to measure the natural frequencies of vibration of a turbine blade undergoing impact from a hammer [190]. Using two different constraint conditions for the blade, two sets of natural frequencies were observed. The main achievement of this paper was the successful application of techniques for drawing the natural frequencies out of dynamic FBG shifts which were below noise level.

3.2.6 Concluding Remarks

This concludes the description of FBG literature from its invention, through its early development, and into maturity. As mentioned earlier, there are five areas (strain transfer, transverse loading, cure-induced residual strains, embedded FBGs, and crack effects) which specifically relate to this study. The theoretical analysis of photoelasticity in the previous chapter began the analysis which will be continued in this chapter. The focus of this work is to demonstrate the feasibility of using embedded FBGs as uniaxial strain sensors. Additionally, situations will be identified when loading and host strain states result in a breakdown of the

mathematical assumptions used to calculate uniaxial strain. The steps taken to fabricate the composite samples, set up the mechanical load tests, and design finite element analysis (FEA) models is described next.

3.3 Fabrication, Experimental Setup, and FEA Models

This section describes the necessary steps that were performed in order to carry out the experimental tests on the composite samples. This will include methods used for fabricating the composite samples by embedding the optical fiber during the lay-up procedure, processes for setting up the FOID by splicing the embedded fibers into the system and performing the necessary calibrations, and techniques for preparing the samples to apply mechanical loads. In addition to the sample fabrication and experimental setup, the preprocessing steps required to run effective FEA models will be described. The FEA preparation will include creating a suitable geometry, obtaining necessary material properties, applying proper and representative boundary conditions, and checking for the convergence of solutions with a mesh refinement study.

3.3.1 Fiber Characterization

The commercially obtained Bragg gratings used in this work are Luna Innovations' Distributed Sensing System fiber. The provided specifications sheet for the Bragg fiber is shown in the appendix. The fiber came with a $5.4 \mu\text{m}$ diameter core, $127 \mu\text{m}$ diameter cladding, and $7 \mu\text{m}$ thick polyimide coating. The core is silica doped with germanium and cladding is pure silica. Each FBG is 5 mm long and center-spaced every 1 cm . The manufacturer-specified reflected wavelength the gratings written onto the optical fiber is approximately 1546 nm .

For future theoretical work, it will become necessary to calculate the effective index of refraction of the optical fiber. Therefore, the IORs of the core and cladding must be calculated first. Coefficients to the Sellmeier equation relating wavelength to index of refraction have been

published for fused silica which makes up the cladding material. The Sellmeier equation takes the following form:

$$n^2(\lambda) = 1 + \sum_i \frac{B_i \lambda^2}{\lambda^2 - C_i} \quad (3.1)$$

Three terms in the summation will provide satisfactory convergence of the index of refraction. Malitson 1965 provides the coefficients for such terms as follows [191]:

$$\begin{aligned} B_1 &= 0.6961663 \\ B_2 &= 0.4079426 \\ B_3 &= 0.8974794 \\ C_1 &= 0.0684043 \mu m^2 \\ C_2 &= 0.1162414 \mu m^2 \\ C_3 &= 9.896161 \mu m^2 \end{aligned} \quad (3.2)$$

These terms call for λ to be in units of μm when solving the Sellmeier equation above. At the reflected wavelength of 1546 nm , therefore, the calculated index of refraction for the cladding (n_2) is:

$$\begin{aligned} n_2^2 &= 1 + \frac{0.6961663(1.546 \mu m)^2}{(1.546 \mu m)^2 - 0.0684043 \mu m^2} \\ &\quad + \frac{0.4079426(1.546 \mu m)^2}{(1.546 \mu m)^2 - 0.1162414 \mu m^2} + \frac{0.8974794(1.546 \mu m)^2}{(1.546 \mu m)^2 - 9.896161 \mu m^2} \\ &\Rightarrow \boxed{\boxed{n_2 = 1.444}} \end{aligned} \quad (3.3)$$

Note that in this research, the wavelengths of light used are in the range of approximately 1535 nm and 1555 nm . The index of refraction will vary accordingly from 1.44420 to 1.44396 over the specified 20 nm wavelength range. Considering the significant digits of future calculations not yet shown, a constant value of 1.444 will suffice over the specified wavelength

range. This information will be used to calculate the index of refraction of the germanium doped core next.

There are two methods which can be used based on the information provided by the specification sheet to calculate the core IOR (n_1). The first is using the numerical aperture of the optical fiber and the second involves using the cutoff wavelength (i.e. the wavelength that describes when the fiber is no longer single mode). The numerical aperture listed in the specifications sheet is a unitless value of 0.2 (it is actually given a unit of degrees, but this is a typo). If units of degrees were used for the given NA , then the difference between core and cladding IORs would be on the order of 10^{-6} which is far too low for typical single-mode fiber. The following equation relating numerical aperture to the indices of refraction of the core and cladding is used to calculate the core index of refraction:

$$\begin{aligned}
 NA &= \sqrt{n_1^2 - n_2^2} \\
 \Rightarrow n_1 &= \sqrt{(NA)^2 + n_2^2} \\
 n_1 &= \sqrt{(0.2)^2 + 1.444^2} \\
 n_1 &= 1.4577
 \end{aligned} \tag{3.4}$$

The cutoff wavelength given by the FBG specifications sheet is 1290 nm . This wavelength is associated with the cutoff optical fiber V parameter which is related to the optical fiber's core index, n_1 , cladding index, n_2 , cutoff wavelength, λ_{cutoff} , and core radius, a , as follows:

$$V_{cutoff} = \frac{2\pi a}{\lambda_{cutoff}} \sqrt{n_1^2 - n_2^2} \tag{3.5}$$

The V parameter at the cutoff wavelength is the first root of the zero-order Bessel function of the first kind, $J_0(V_{cutoff}) = 0$, which takes a value of 2.4048. Using this along with the specified fiber core diameter of 5.4 μm and the previously calculated cladding index, we can find the core index as follows:

$$\begin{aligned}
n_1 &= \sqrt{\left(\frac{V_{cutoff} \lambda_{cutoff}}{2\pi a}\right)^2 + n_2^2} \\
n_1 &= \sqrt{\left(\frac{(2.4048)(1.290\mu m)}{2\pi(2.7\mu m)}\right)^2 + 1.444^2} \\
n_1 &= 1.4556
\end{aligned} \tag{3.6}$$

The two different methods result in core index values which are different by approximately 0.14 %. The average of the two calculated core indices is used to obtain the following core index of refraction:

$$\boxed{n_1 = 1.457} \tag{3.7}$$

At this point, we can now calculate the effective index for the optical fiber over the relevant wavelength range of 1535 to 1555 nm. This is accomplished by using the calculated values of n_1 and n_2 , the specified value of a , and the given range of relevant λ_0 values to solve the transcendental equation for the propagation constant, β , as described in the previous chapter and shown again here:

$$\begin{bmatrix}
\frac{\beta l}{h^2 a} J_1(ha) & \frac{i\omega\mu_1}{h} J_1'(ha) & \frac{\beta l}{q^2 a} K_1(qa) & \frac{i\omega\mu_2}{q} K_1'(qa) \\
J_1(ha) & 0 & -K_1(qa) & 0 \\
-\frac{i\omega e_1}{h} J_1'(ha) & \frac{\beta l}{h^2 a} J_1(ha) & -\frac{i\omega e_2}{q} K_1'(qa) & \frac{\beta l}{q^2 a} K_1(qa) \\
0 & J_1(ha) & 0 & -K_1(qa)
\end{bmatrix}
\begin{Bmatrix}
c_1 \\
c_2 \\
c_3 \\
c_4
\end{Bmatrix} = 0 \tag{3.8}$$

The equation was also written in an alternative, compact form:

$$[\Omega_{ij}] \{c_i\} = 0, \quad i, j = 1, 2, 3, 4 \tag{3.9}$$

The determinant of $[\Omega]$ must equal zero to have a nontrivial solution. Finding the values of β which provide nontrivial solutions is performed numerically in MATLAB by bringing all terms transcendental equation (created by setting $|\Omega| = 0$) to the left side of the equation and equating

the result to a term, $Z(\lambda_0, n)$. For the specific case of the fundamental mode when $l = 1$, this results in the following equation:

$$\left(\frac{J_1'(ha)}{haJ_1(ha)} + \frac{K_1'(qa)}{qaK_1(qa)} \right) \left(\frac{n_1^2 J_1'(ha)}{haJ_1(ha)} + \frac{n_2^2 K_1'(qa)}{qaK_1(qa)} \right) - \left[\left(\frac{1}{qa} \right)^2 + \left(\frac{1}{ha} \right)^2 \right]^2 \left(\frac{\beta}{k_0} \right)^2 = Z(\lambda_0, n) \quad (3.10)$$

The MATLAB program scans through a range of λ_0 and n values (which is equivalent to scanning through a range of β values) to find when $Z(\lambda_0, n) = 0$. We are interested in the wavelength range from 1535 to 1555 nm and we know the effective index must lie between 1.444 (n_2) and 1.457 (n_1). Therefore, a MATLAB program is run to create a surface plot of Z for the relevant two-dimensional λ_0 - n domain and the locations at which $Z = 0$ correspond to solutions. The Figure 3-1 shows such a surface plot of $Z(\lambda_0, n)$ over the 2-D domain:

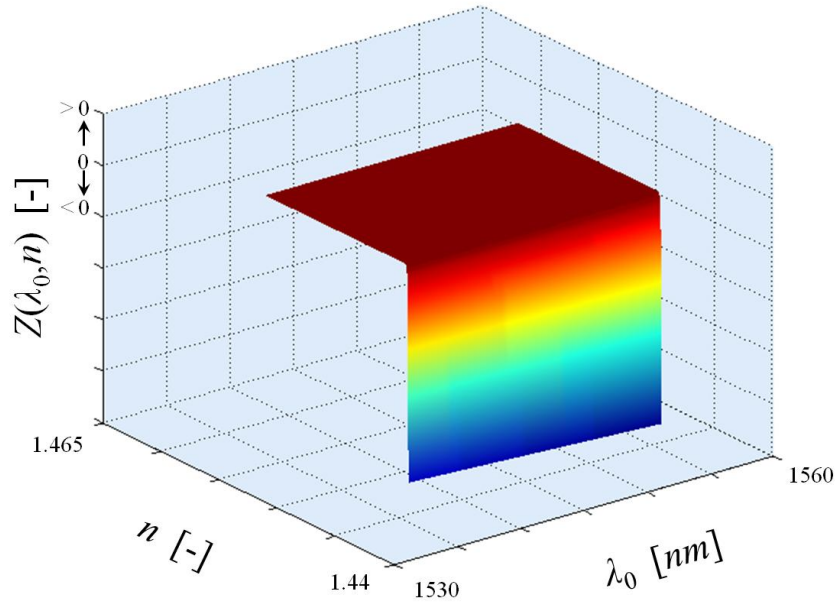


Figure 3-1: Plot of the values associated with the transcendental equation whose zeros provide effective IOR values over a range of wavelengths.

By cutting the surface plot above with the plane defined by $Z = 0$, we obtain the locus of points which satisfy the transcendental equation. It turns out that the effective IOR which garners

a solution to the transcendental equation remains equal to 1.450 (when rounded) over the relevant wavelength range. Therefore:

$$\boxed{n = 1.450} \quad (3.11)$$

The program used to create the figure above and numerically approximate n will be described in greater detail in Chapter 5.

Now that the pertinent index of refraction terms have been calculated, the variation of reflected wavelength along the length of the optical fiber will be determined. This will verify the uniformity of the Bragg wavelengths written on the optical fiber. The length of the Bragg fiber is just over 5 m , which makes sense considering 504 Bragg gratings were seen on the fiber. Six raw data snapshots were taken of the data, each undergoing a Fourier transform followed by the windowing of each individual FBG and subsequent inverse Fourier transforms. The Figure 3-2 below demonstrates one of the six raw data snapshots, the corresponding Fourier transform plot, and an inverse Fourier transform back to the wavelength domain of a representative FBG. Graph (a) is the reflection by the entire 5 m long Bragg fiber versus wavelength in the scanning range of 1542 to approximately 1550 nm . Graph (b) is the Fourier transform which effectively takes the data from the wavelength into the length domain. There is an initial lead-in fiber length which is characterized with noise. The reflections take place over the indicated length of the Bragg fiber. Graph (c) is a zoomed in plot of the length domain data to show the reflection from individual Bragg gratings. Graph (d) is the reflected wavelength spectrum for an individual FBG along the fiber length and represents the approximate shape of the reflection spectrum expected for each FBG. The two vertical lines marking the bottom left graph indicate the peak and centroid values of the spectrum.

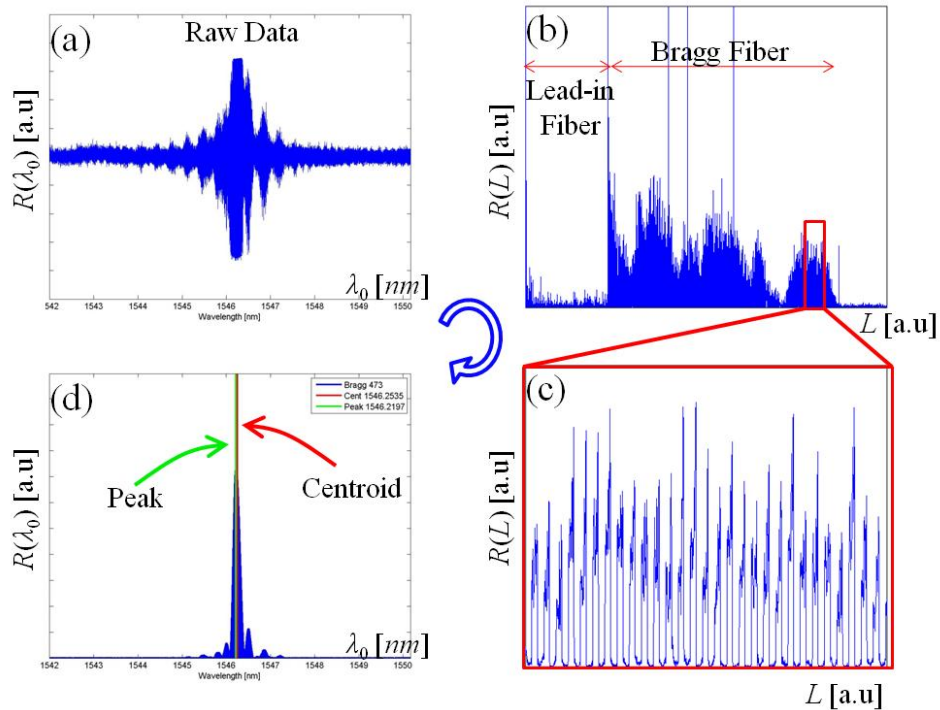


Figure 3-2: OFDR processing steps to calculate the peak and centroid of the reflected wavelength spectrum of each individual FBG.

For a symmetric reflected wavelength spectrum, the peak and centroid values will be equal, but in practice this is not always the case. This will be demonstrated in Figure 3-3 below. The graph in the figure shows the averages and standard deviations of the six snapshot values for each of the 504 FBGs along the length of the optical fiber. The left vertical axis represents the average reflected wavelength for both the peak and centroid data of each FBG while the right vertical axis represents the standard deviation of the six measurements taken for each FBG. The red squares and blue triangles correspond to average centroid and peak values, respectively. The dotted red and solid blue lines correspond to centroid and peak standard deviation data.

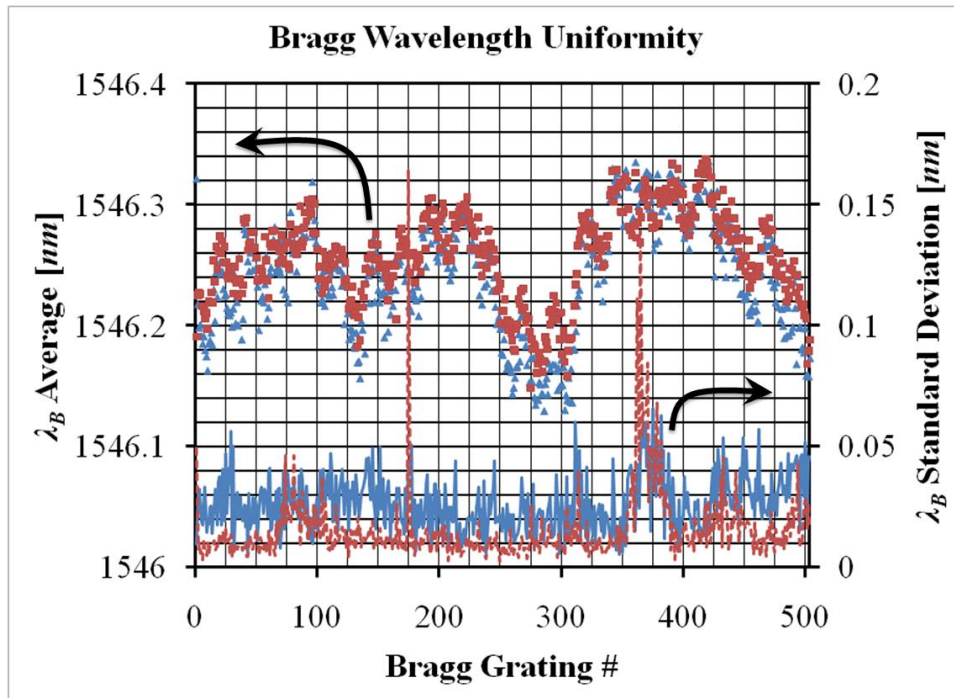


Figure 3-3: Comparison of peak and centroid methods for calculating reflected wavelength along the length of the Bragg fiber.

This plot effectively demonstrates how the reflected wavelength varies along the length of the fiber. The drift in average along the fiber length covers a range of approximately 0.25 nm and is tracked well with both peak and centroid data. The peak and centroid averages are very similar, but not exactly equal. Additionally, the standard deviations of the peak values tend to be higher than that of the centroid values. The only region where this is not true is near the 80th and 370th FBGs. The explanation of this can be seen in the length domain data shown in the upper right hand plot of the previous figure. Due to polarization fading, the region corresponding to the 370th FBG measures hardly any reflection intensity. This causes the reflected wavelength spectra for individual FBGs in that region to be more heavily influenced by noise and thus, cause the centroid to vary more between snapshots. The six snapshots were taken with the lead-in fiber in six different positions which aimed to reduce the influence of polarization fading. While this reduction in polarization fading influence is seen when comparing the averages of peak and centroid data, the reduction in influence is not seen in the standard deviation data.

From the data shown, it can be deduced that the centroid calculation is the less noisy method for calculating the Bragg wavelength. This, however, is the case when neither polarization fading nor birefringence is present. In the presence of polarization fading, the centroid data becomes more heavily influenced by noise compared to the peak data. When birefringence is present, peak data becomes a much more relevant measurement than centroid data because the centroid will drift to whichever peak is dominant or sit between the peaks. In this research, polarization fading is not usually an issue because it takes place in fibers which are several meters long. The longest Bragg fiber in this research is about 0.4 *m* long. Birefringence, on the other hand, will be present in some cases and must be considered when deciding between peak and centroid methods for assigning a λ_B value to a FBG. When manipulating the raw data, peaks will be tracked more often than centroids. This concludes the characterization of optical fiber Bragg gratings to be embedded in a composite material. Next, the embedment process will be described.

3.3.2 Composite Lay-Up

The composite material used in this research is AS4/3501-6, where the AS4 refers to the type of carbon fibers and the 3501-6 refers to the type of resin. From a large spool stored in a freezer near 0 °C, 30 x 30 *cm*² (12" x 12") unidirectional prepregs squares were cut using razor blades for subsequent stacking. The lay-up to be created is quasi-isotropic with a stacking of $([0^\circ/\pm 45^\circ/90^\circ]_s)_3$. Figure 3-4 below demonstrates the four directions of prepregs relative to the eventual loading direction.

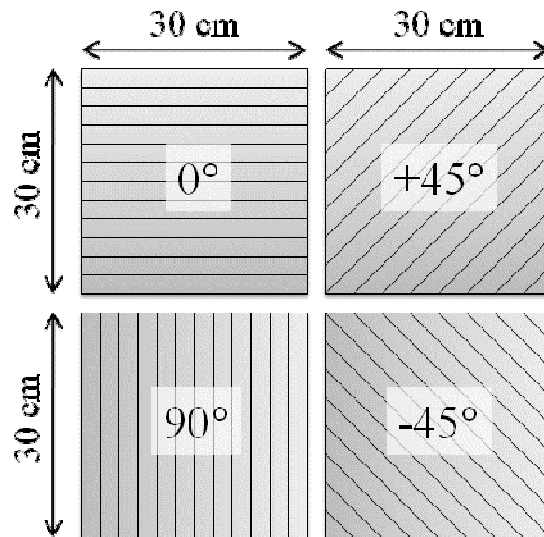


Figure 3-4: Orientation of individual plies relative to loading direction (0°) making up the composite laminate.

Before stacking the prepregs, masking tape was attached to a metal plate in the shape of a 30 x 30 cm^2 square with length measurements written on the tape as shown in Figure 3-5 below. The measurements are meant for accurate positioning of the optical fiber when it comes time to place the fiber on the prepreg. A translucent Teflon sheet was taped down to the plate to provide a non-stick surface for the composite when it is eventually cured. Yellow putty tape was attached to the metal plate encompassing both the masking tape and Teflon sheet for vacuum-bagging the lay-up for storage purposes. At this point, the first 12 layers of composite can be stacked within the area defined by the masking tape. In between layers, a plastic roller and heat gun were used to apply heat and pressure. This creates a small amount of adhesion to prevent slippage between layers during the lay-up process.

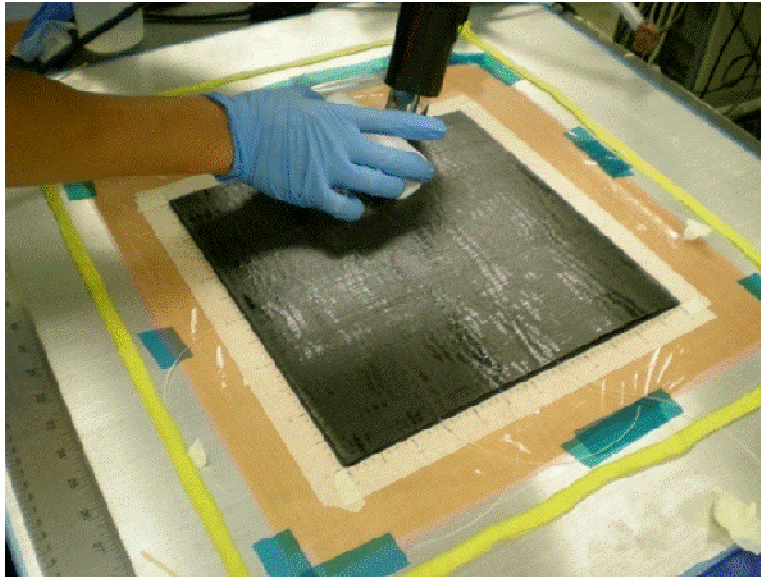


Figure 3-5: Picture of the lay-up process involving the use of a heat gun to prevent the layers from slipping during stacking.

After the first 12 layers are stacked, the five Bragg fibers are laid out across the composite. Figure 3-6 below indicates the lay-out of the optical fibers across the square composite panel. After the embedment and curing processes, the composite will be cut into six $5 \times 30 \text{ cm}^2$ rectangular samples. One of the six rectangular samples will be a reference with no embedded fiber (labeled “Ref” in the figure), three will have an optical fiber oriented in the 0° direction (labeled $0^\circ/90^\circ$), and two will have an optical fiber oriented in the 90° direction (labeled $90^\circ/90^\circ$). The dotted lines indicate where the square sample will be cut. The Bragg fibers indicated in blue will span across each rectangular sample and have 15 cm of length protruding from the composite to allow for splicing into the FOID system. In order to protect the ingress/egress locations, the optical fibers are placed inside a Teflon tube ($875 \mu\text{m}$ outside diameter and $\sim 200 \mu\text{m}$ inside diameter) which penetrates approximately 1.25 cm ($\sim 0.5''$) into the composite. The Teflon tube is represented with thicker red lines intersecting the composite boundary.

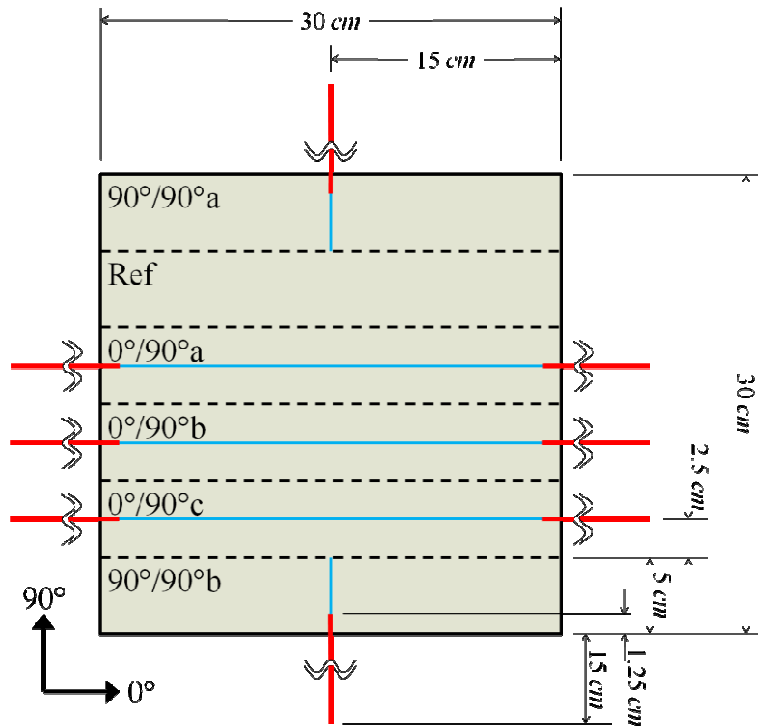


Figure 3-6: Schematic of the positioning of the five Bragg fibers within the composite panel to be cut into smaller, rectangular samples.

A significant problem with using the Teflon tubes to protect the ingress/egress points is the wicking of composite resin. During the curing process, the resin becomes much less viscous and the applied pressure causes the resin to flow into the Teflon tube with the optical fiber. This can cause catastrophic damage to the optical fibers or make them extremely fragile. To prevent this from occurring, a dot of 5-minute epoxy is used to seal the opening and prevent resin wicking. After laying out the fiber, the last 12 layers of prepregs are stacked, making the composite ready for curing. An autoclave at Alliance Spacesystems was used to cure the composite and Figure 3-7 below indicates the input curing parameters and actual measured parameters. The temperature profile rises to 116 °C (240 °F) at a rate of 1.67 °C/min (3 °F/min), holds for one hour, then rises again at the same rate to 177 °C (350 °F), holds for 2 hours 5 minutes, and then drops down to room temperature. The pressure rises at a rate of 34.5 kPa/min (5.0 psi/min) to a level of 310 kPa (45 psi), holds for the entire duration of the cure, and releases back to ambient pressure at the same time the temperature is dropped back to room conditions.

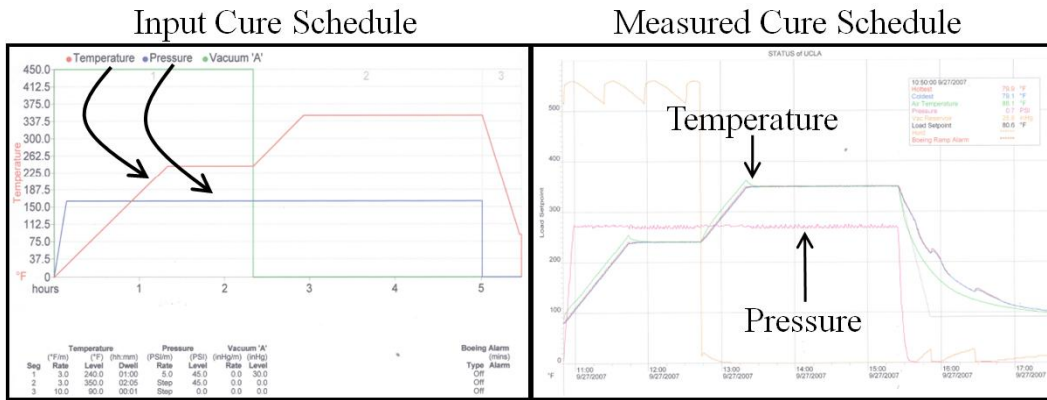


Figure 3-7: Input and measured curing parameters.

Next the square composite coupon will be cut into rectangular samples using a circular tile saw. Figure 3-8 below shows the composite as it was returned from Alliance Spacesystems and a picture of the post-cut specimens.

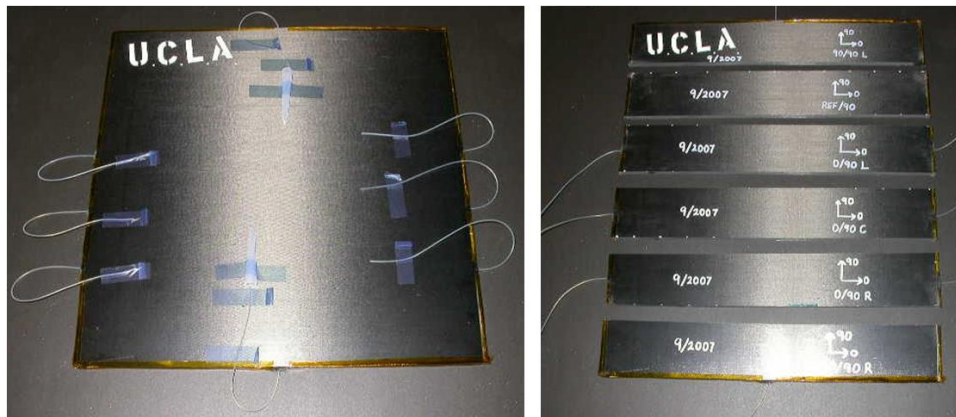


Figure 3-8: Pictures of the composite panel before and after cutting.

The convention used for labeling the composite samples in this research involves two angles, A°/B° , where the first angle indicates the direction of the embedded optical fiber and the second angle refers to the orientation of the mid-plane structural carbon fibers. Both angles are relative to the loading direction (i.e. the 0° direction). Figure 3-9 indicates this relationship by showing the middle eight plies (out of 24) in the lay-up. In both samples, the mid-plane structural fibers are oriented in the 90° direction, but the optical fiber (shown in blue) is in the 0° direction for the $0^\circ/90^\circ$ samples and in the 90° direction for the $90^\circ/90^\circ$ samples. The dimensions provided are

not to scale, but aid in defining the optical fiber's relationship with nearby structural fibers relative to the global $5 \times 30 \text{ cm}^2$ rectangular specimens shown in Figure 3-6 and Figure 3-8.

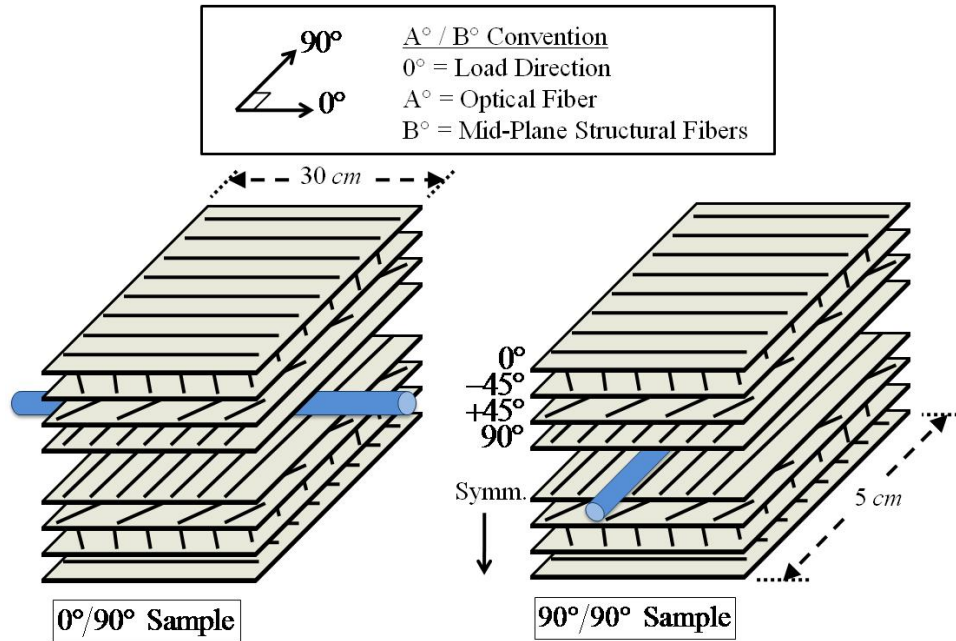


Figure 3-9: Orientation of the embedded optical fiber relative to nearby structural carbon fibers.

The next step is to attach strain gauges above and below the embedded Bragg fiber on the surfaces of the composite. Vishay CEA-06-250UW-120 strain gauges with 120Ω of resistance and a 2.095 gauge factor were used. The strain gauges were centrally located on their respective faces and oriented to measure strain in the longitudinal direction of the embedded optical fibers. The location and orientation of the optical fiber in each sample was verified with an x-ray image such as that shown in Figure 3-10. This figure shows an original and altered x-ray image and a digital camera photograph of a $90^\circ/90^\circ$ sample. The altered x-ray image is intended to aid the reader in seeing the embedded optical fiber because it is very thin. The thicker Teflon tube is easily recognizable and seen to penetrate the intended length into the composite material. Using the Teflon tube outside the composite as a reference, a dotted line is digitally drawn onto the digital camera photograph to indicate where the embedded optical fiber is located. The attached strain gauge is also identified and shown to be located above the embedded optical fiber. An

additional strain gauge is attached to the under-side of the composite at the same location and orientation.

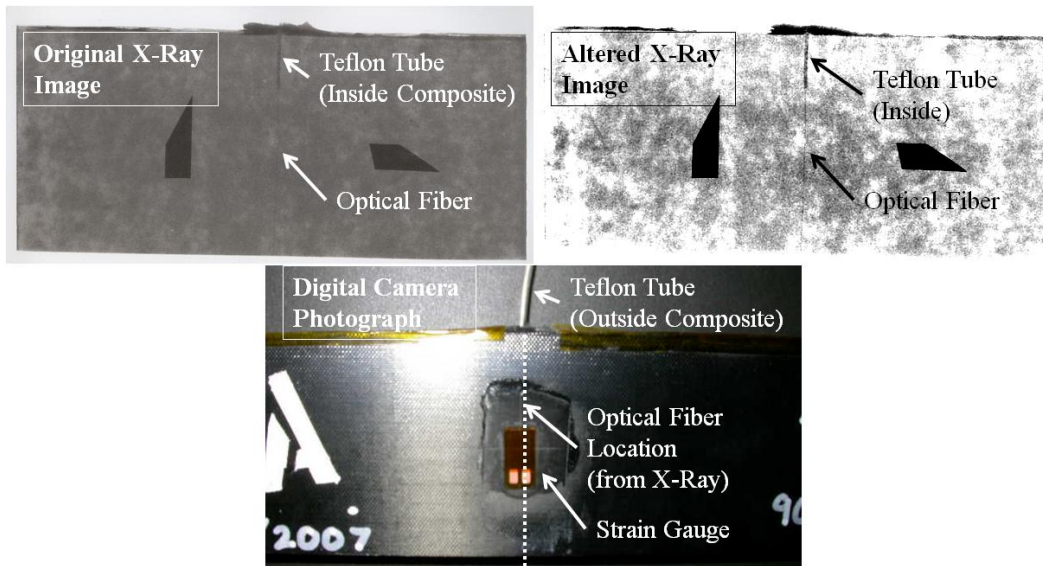


Figure 3-10: Original and altered x-ray images to demonstrate the positioning of the optical fiber for alignment with the surface-mounted electrical resistance strain gauge shown in the camera photograph.

This same process of using an x-ray image to identify the embedded optical fiber location for strain gauge attachment is performed on the other $90^{\circ}/90^{\circ}$ and $0^{\circ}/90^{\circ}$ samples. The final step in sample preparation is the attachment of aluminum tabs to protect the composite during load frame gripping. Square $5 \times 5 \text{ cm}^2$ aluminum plates 3.175 mm ($1/8''$) thick were attached to the ends of the rectangular composite samples with 5-minute epoxy. Figure 3-11 shows the final $0^{\circ}/90^{\circ}$ and $90^{\circ}/90^{\circ}$ specimens with dimensions indicated. Additionally, the top- and bottom-side strain gauges (yellow), aluminum tabs (light grey), and optical fibers (blue) are identified. The composite itself (dark grey) and top-side aluminum tabs were made partially transparent to allow the reader to see the embedded optical fiber and bottom-side strain gauges.

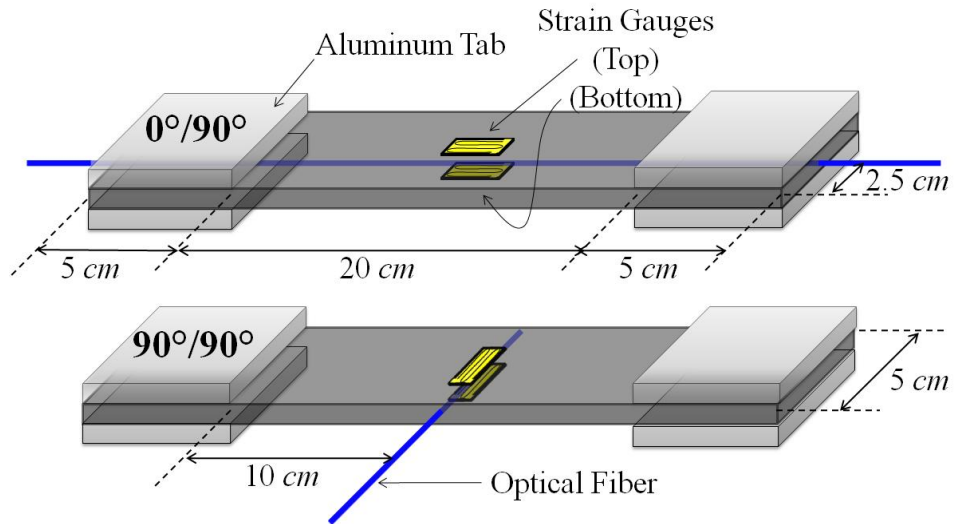


Figure 3-11: Drawing of the final composite samples to be tested.

This concludes the optical fiber embedment and composite fabrication procedures. In the next section the types of mechanical load testing will be described.

3.3.3 Composite Mechanical Load Testing

There are two types of mechanical load tests that will be performed on the rectangular composite samples. The first is in-plane tension and compression and the second is out-of-plane compression. In-plane load (IPL) refers to loading in the previously specified 0° direction while out-of-plane load (OPL) refers to the composite plate's thickness direction. Loads are applied using an Instron 8516 load frame. For IPL, the sample is gripped at the aluminum tabs glued to the composite samples as shown in Figure 3-12. The upper, static grip is used to measure force while the lower dynamic grip is used to apply force and measure total sample displacement. The control panel to the right of the grips is used to input load schedules. A zoomed in picture of the gripped sample shows the lead-in optical fiber and the strain gauge wires which lead from the sample to the data acquisition system.

Instron 8516 Load Frame

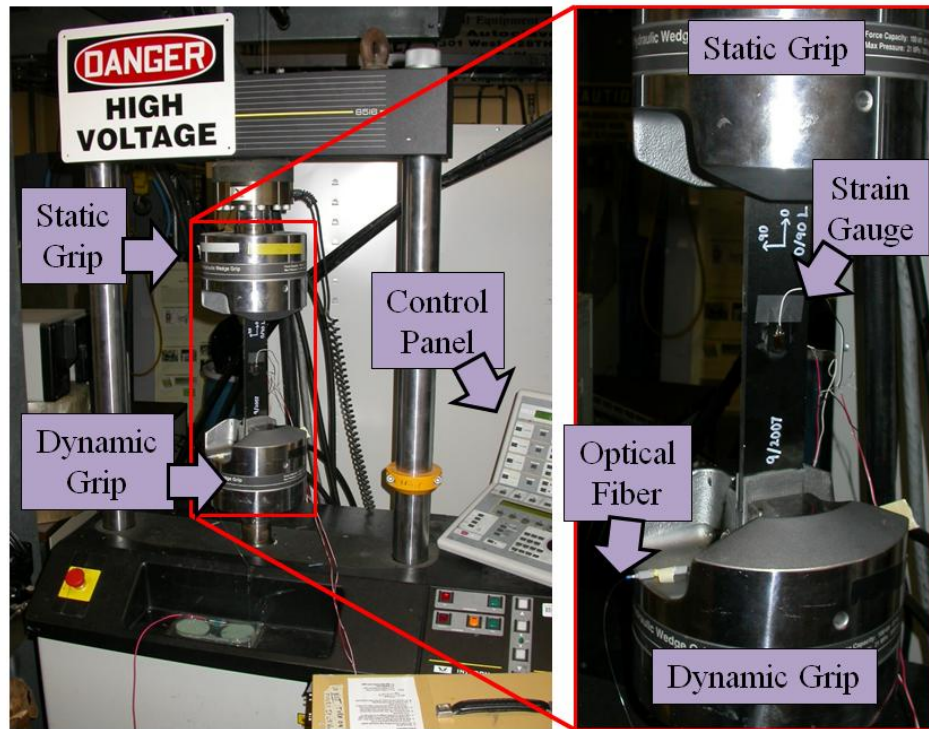


Figure 3-12: Instron load frame mechanical test set-up.

The data acquisition system associated with the IPL tests described above is shown in schematic form in Figure 3-13. From the test sample gripped in the Instron 8516 Load Frame, the Vishay strain gauges will output strain measurements through a Vishay signal conditioning system and into a data acquisition (DAQ) board. Simultaneously, the Instron load cell will output force measurements into the same DAQ board. This data is fed into a LabView program that records and assigns a timestamp to the data. The embedded FBGs reflect particular wavelengths, λ_B , to the FOID system provided by NASA.

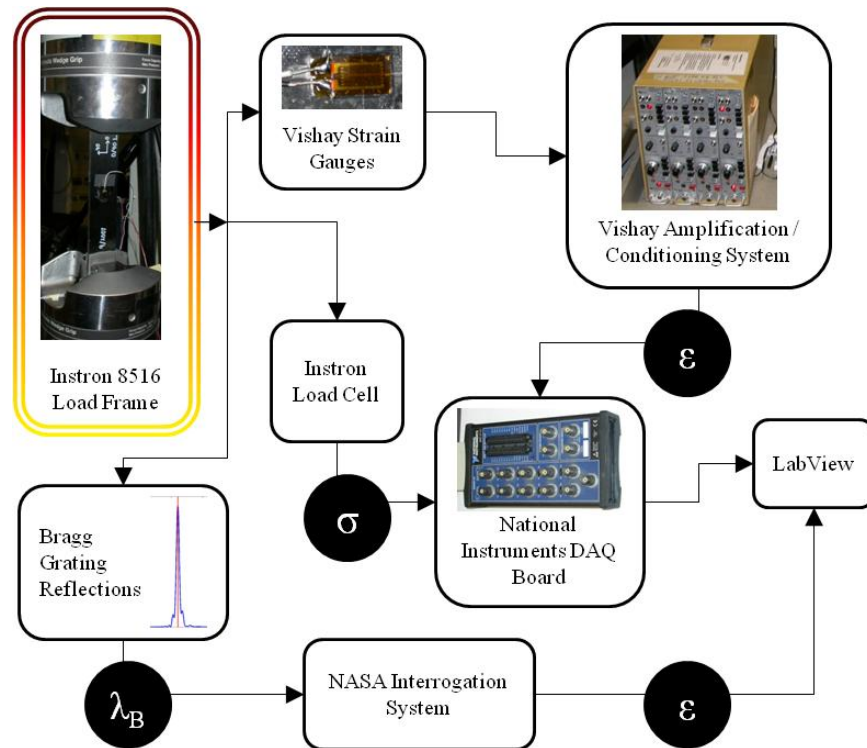


Figure 3-13: Schematic diagram of the flow of measurement data during mechanical load testing.

For out-of-plane loading, the load frame grips apply the compressive force to the composite. For the $0^\circ/90^\circ$ samples, the FBGs between the tabs can be monitored to study the sensor response due to OPL conditions. To apply the load to an optical fiber embedded in a $90^\circ/90^\circ$ sample, however, the strain gauge wires are detached from the samples, aluminum tabs are placed (but not glued) above and below the strain gauge locations, and grip pressure is applied to the unfixed aluminum tabs.

A pressure gauge is used to determine the fluid pressure pumped via a hand crank to grip samples, but this pump gauge pressure does not necessarily correspond to the stress traction applied to the surface of the aluminum tabs. In order to calibrate this, a force transducer is sandwiched between two aluminum tabs and placed between the grips. The force is measured due applied gauge pressures between 0 and 1000 *psi*. The results are shown in Figure 3-14. The horizontal axis displays the measured gauge pressure while the vertical axis displays the measured force divided by the aluminum tab area ($5 \times 5 \text{ cm}^2$). The measured results represented

with diamond symbols are very linear and the mathematical relationship between the applied surface stress and the pump grip pressure is displayed with an equation describing the dotted line.

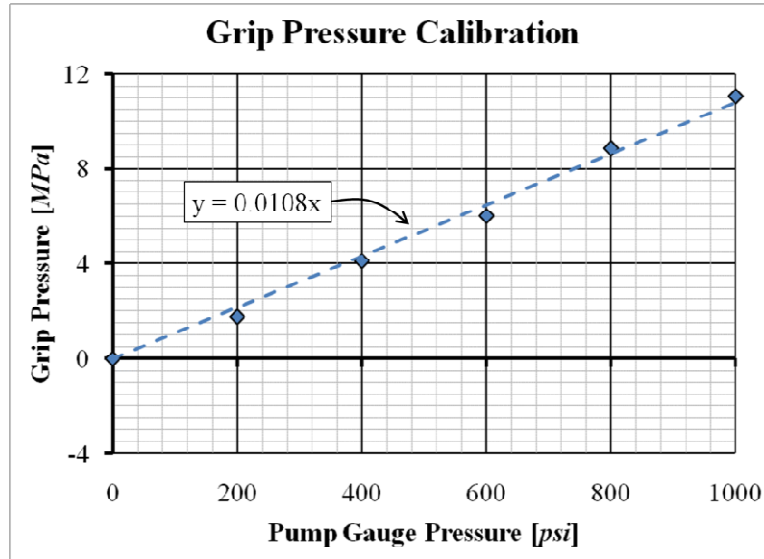


Figure 3-14: Correlation between applied pump pressure and stress applied to tabs by the Instron grips.

The applied pump grip pressure and the reflected wavelengths of the FBG centrally located between the grips are the measured quantities for the out-of-plane loading tests. Next, the NASA FOID system setup will be described.

3.3.4 Fiber Optic Interrogation Device

The fiber Bragg grating interrogation system used is shown in Figure 3-15. The main components of the system are a continuous wave laser with frequency tuning capabilities, an optical circuit consisting of photodetectors, couplers, reference fiber, etc., and an onboard computer. Laser light is sent into the optical circuitry which outputs that light, as indicated in the figure, to a lead-in fiber. This fiber splices into an optical fiber with Bragg gratings. The commands which control the tuning range, sampling rate, etc. of the FOID system are input through a LabView program located in the onboard computer. To access the onboard computer, a

separate desktop computer system (hereafter referred to as the grounded computer) connects to the onboard computer with a remote desktop connection via the Cat 5 ethernet cable shown in the figure. The grounded computer itself contains a LabView program with graphical user interfaces designed to perform additional tasks such as real-time strain monitoring and data recording.

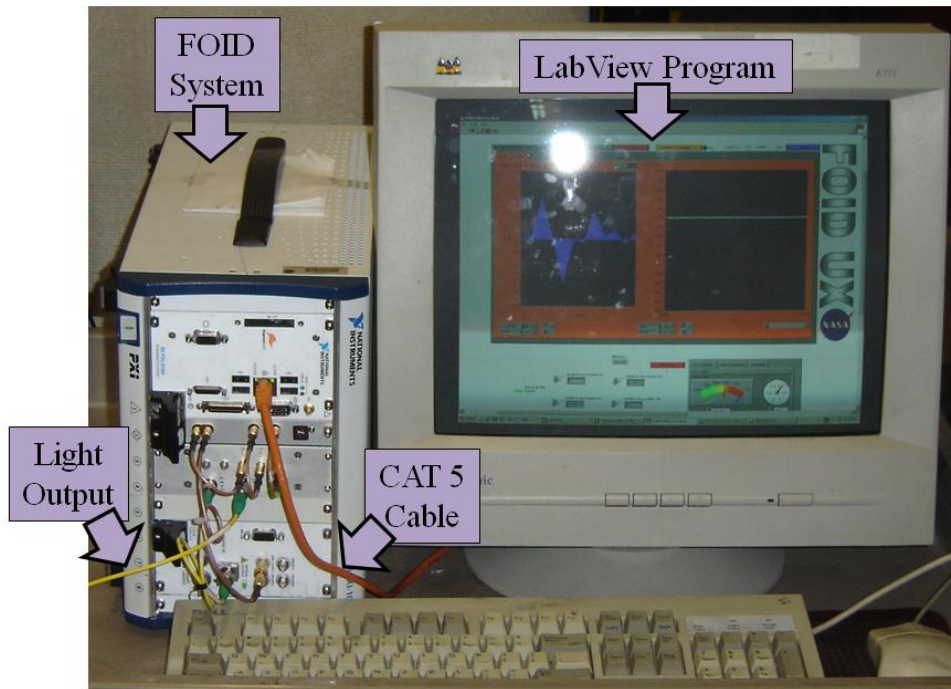


Figure 3-15: Picture of the FOID system and grounded computer used to run the system.

The method of splicing a Bragg fiber into the lead-in fiber connected to the FOID system output will now be described. The two most common methods are fusion splicing and mechanical splicing. For either method, the first step is to cleave the two fibers to create a flat surface which will encourage maximum light transmission. This step typically consists of using a wedge to indent the optical and bending of the fiber to turn the indentation into a propagating crack. For fusion splicing, the cores of two optical fibers are aligned to maximize light transmission from one fiber to the other. Heat is then applied to the optical fiber connection site rapidly using sources such as electric arcs, lasers, or gas flames to fuse the two optical fibers

together. Though fusion splices offer higher reliability and lower insertion losses, it is significantly more costly and not necessary for this research. Therefore, mechanical splicing splices are used.

Mechanical splices simply use a mechanical apparatus to hold two optical fibers together to allow transmission of light. Unlike fusion splicing, this is a temporary splicing method. The necessary steps are shown in Figure 3-16. First, as described earlier, the optical fibers are cleaved to create a flat, pristine surface with the cleaver tool shown in image (a). The mechanical splice, shown in image (b), consists of two entry points with the inserted optical fibers held in place with a plastic cantilever beam tightened by screwing in the two sides. In the middle of the splice is a glass tube housed in a plastic casing. In order to fit the optical fibers in the glass tube, the coating around the last ~ 1 cm of fiber is removed. This is accomplished using one of two different methods dependent upon the coating material. The lead-in fiber is coated with Acrylate, a relatively soft material which can be stripped off the optical fiber using the thermo-mechanical stripper shown in image (c). The stripper heats up the optical fiber, making it easy for the razor blades to indent and wipe off the soft Acrylate as the optical fiber is pulled out. The Bragg fiber is coated with polyimide, a much more durable polymer. To remove this coating, the end of the optical fiber is dipped in sulfuric acid heated on a hot-plate to approximately 80°C as shown in image (d). The acid etches away the polyimide while leaving the glass alone. In some cases, as shown in the figure, the polyimide can melt and flow off of the optical fiber before dissolving.

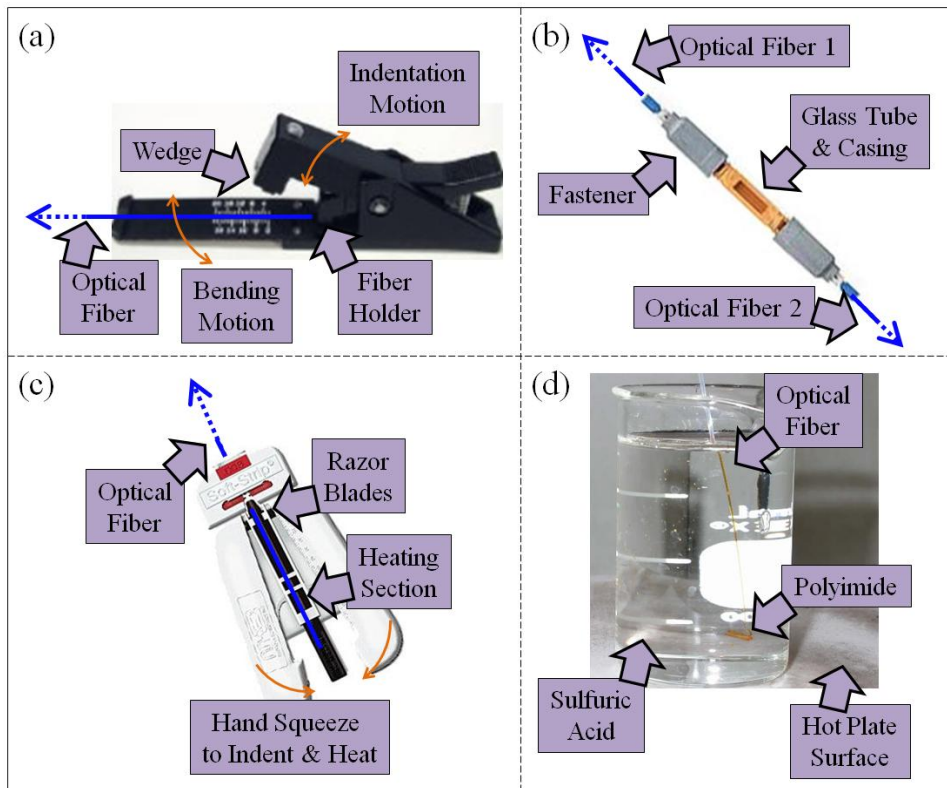


Figure 3-16: Tools used for splicing fibers together.

Despite being cleaved, air pockets at the splice interface can cause a large amount of loss. To minimize this loss, both optical fibers are dipped in index-matching gel so that when they are inserted into the glass tube, those air pockets are replaced by a material whose optical properties are similar to the optical fibers. The final step is to screw both sides of the splice to fasten both optical fibers securely.

Now that the Bragg fiber is hooked into the system with LabView monitoring the reflection, the strain measurements are calibrated. The LabView program is designed to collapse the reflected wavelength spectrum for each individual FBG into a single scalar reflected wavelength. The program linearly relates the shift in λ_B divided by the initial, “zero-strain” λ_B to mechanical strain in the fiber direction via a strain-optic coefficient, $(1-p_e)$. In order to verify that the value given for the fiber is valid, a calibration test is performed by surface-mounting several FBGs to a composite. Figure 3-17 shows the test sample with a Bragg fiber attached to the composite

surface at two locations using 5-minute epoxy. With the given value of $(1-p_e) = 0.8333$, FBG strain results from a tensile load test are compared to a surface-mounted strain gauge.

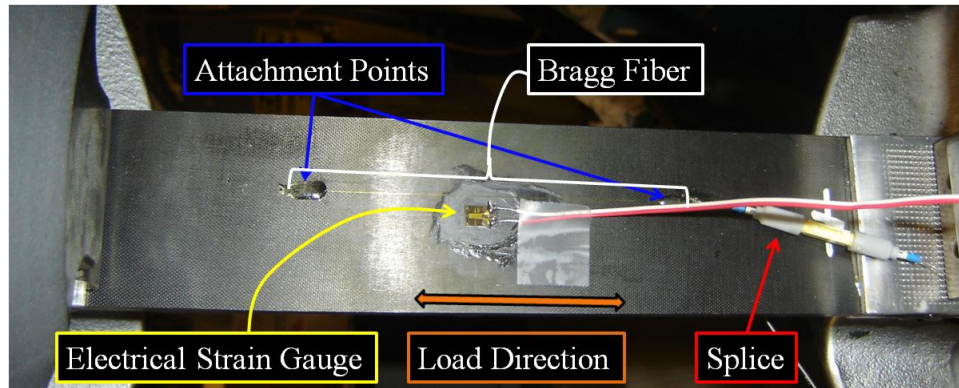


Figure 3-17: Test setup for calibrating the FOID system's strain-optic coefficient.

The results from the test are shown in Figure 3-18 below. The electrical strain gauge (ESG) measurements are linear and indicate a composite stiffness of 49.3 GPa . The signals from the nine FBGs between the two attachment points all display similar nonlinear stress-strain relationships. This is because an initial amount of slack in the fiber must be stretched out (hence the large increase in stress with little increase in strain) before a linear relationship is established. In the linear region above 7 MPa of stress, the average stiffness value of the nine FBGs plus-minus the standard deviation is $49.7 \pm 0.1 \text{ GPa}$.

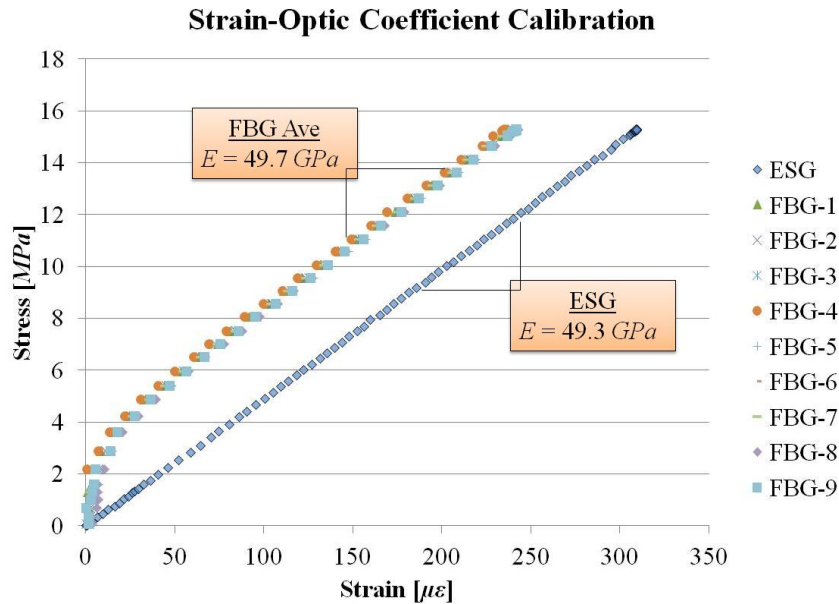


Figure 3-18: Results of the strain-optic coefficient validation comparing the stiffness measurements of nine FBGs with an ESG.

The similar stiffness values validate the given strain-optic coefficient for future tests. The final setup procedure related to the fiber optic interrogation device is to validate the scanned wavelength range displayed in the optical fiber reflection signal. Figure 3-19 describes the need for this step. There are 262,144 data points representing reflected intensity for each wavelength sweep, as indicated in the upper graph of the figure. This information, referred to as a raw data snapshot, represents the reflected wavelength spectrum for the entire optical fiber. Each snapshot provides one strain measurement for every FBG on the Bragg fiber. The raw data is put through a FFT (resulting in the lower graph), windowing procedure, and IFFT (resulting in the graph on the right) to get back to the wavelength domain for each individual FBG. How the data sample range of 1 through 262,144 corresponds to the swept wavelength range needs to be determined.

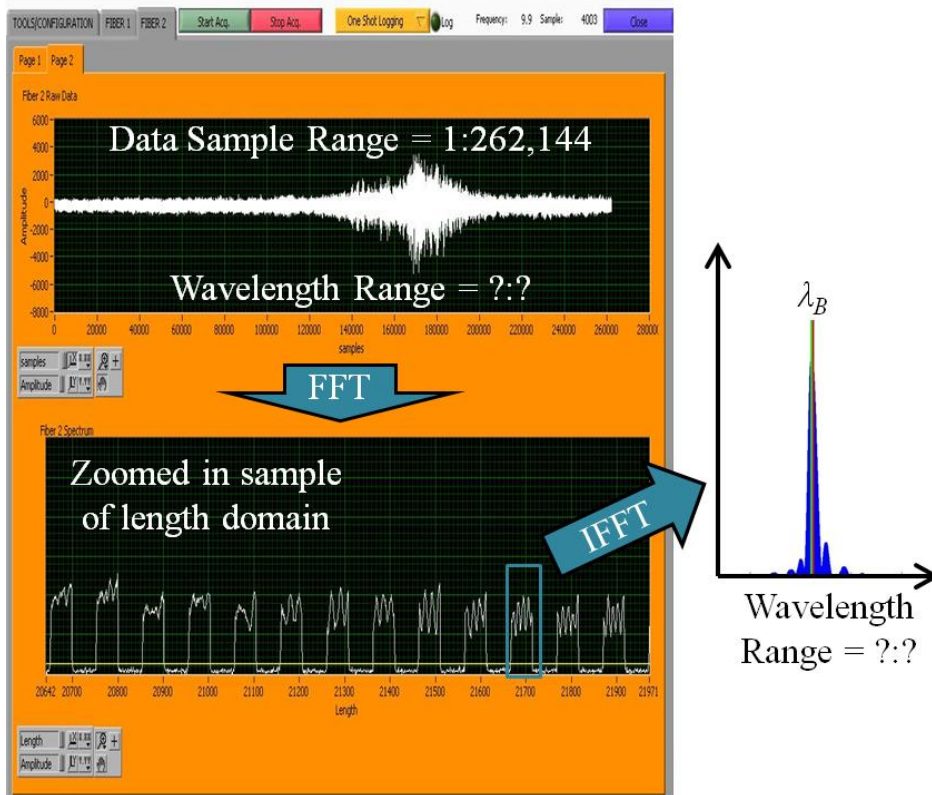


Figure 3-19: Depiction of the FBG processing technique where the wavelength range must be known in order to determine the value of the reflected wavelength.

The mathematical relationship is determined in the following manner. First, a Bragg fiber with 13 FBGs (a number chosen to give an adequate sample size) is plugged into the FOID system. From the previous fiber specifications, we know the FBGs should all have an associated Bragg wavelength near 1546 nm . Therefore, the value of the user command which sets the beginning of the wavelength sweep (i.e. the starting wavelength, λ_{start} , corresponding to the first of 262,144 data points) is set to 1546 nm . The data points which correspond to the peaks of the individual FBG reflection spectra are then recorded. Next, λ_{start} is changed to 1545 nm , thus shifting the peak data point relative to the first data point (which now corresponds to 1545 nm). This process is repeated until the FBGs no longer reflect in the wavelength sweep range. Figure 3-20 demonstrates this process for the first of 13 FBGs on the Bragg fiber. The normalized reflection intensity, input starting wavelength, λ_{start} , and data point at which the peak reflection

occurs are represented with the vertical, left, and right axes respectively. It is easily seen that as the starting wavelength shifts farther from the peak wavelength (i.e. from 1546 to 1539 *nm*), the data point at which peak reflection occurs shifts farther from the first data point (i.e. from 11,512 to 235,902).

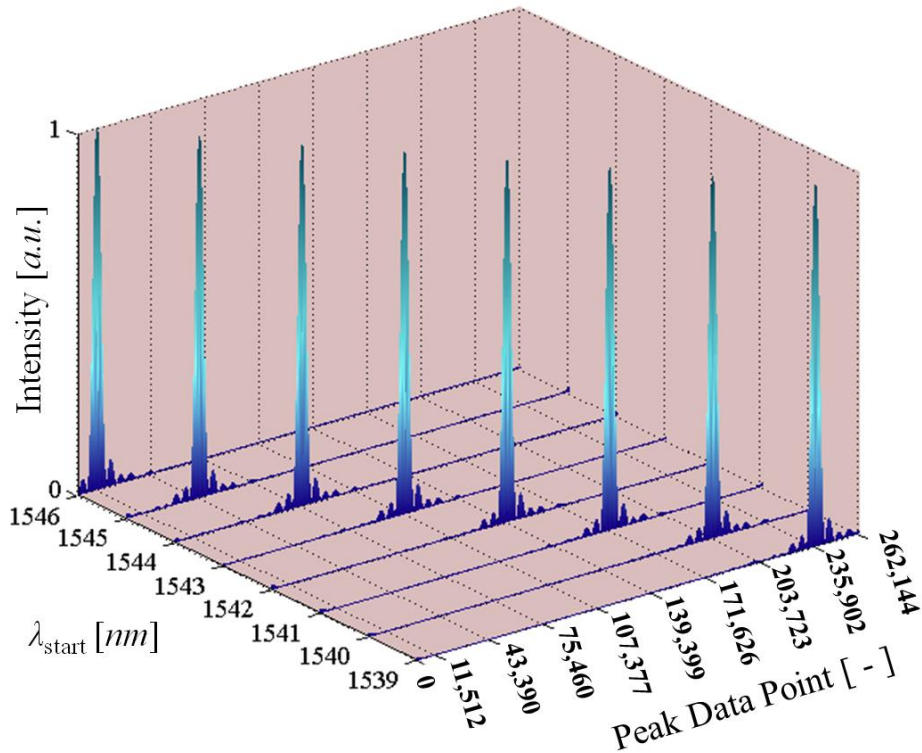


Figure 3-20: Shift in the peak data point as the starting wavelength of the sweep is changed.

A trendline is created for the plot of λ_{start} versus peak data point, the slope of which represents wavelength per data point ratio. The data shown above for FBG-1 indicates a ratio of $3.1193 \times 10^{-5} \text{ nm/data point}$. Multiplying this ratio by the 262,144 data points results in the wavelength range of 8.1770 *nm*. This calculation is performed for all 13 FBGs whose data is shown in Table 3-2 below. Each row corresponds to the FBG while each column corresponds to λ_{start} . The data in the FBG-1 row is seen to match the peak data points in the right axis of Figure 3-20 above. The far right column in the table represents the wavelength range (again, with 8.1770 *nm* displayed for FBG-1 matching the previously described calculation).

Table 3-2: Peak data points for several FBG reflection spectra as the starting sweep wavelength is shifted.

[nm] →	λ_{start}								λ Range
	1539	1540	1541	1542	1543	1544	1545	1546	[nm] ↓
FBG-1	235902	203723	171626	139399	107377	75460	43390	11512	8.1770
FBG-2	235727	203548	171341	139176	107147	75175	43160	11261	8.1746
FBG-3	233270	201091	168925	136801	104874	72793	40887	8865	8.1793
FBG-4	233265	201052	168947	136762	104692	72713	40739	8839	8.1758
FBG-5	233381	201249	169036	136959	104862	72910	40909	8894	8.1750
FBG-6	233114	200908	168769	136618	104568	72636	40635	8600	8.1755
FBG-7	233343	201157	168971	136867	104770	72818	40817	8909	8.1759
FBG-8	233314	201148	169002	136818	104728	72789	40788	8906	8.1756
FBG-9	233341	201109	168976	136812	104821	72816	40828	8840	8.1756
FBG-10	233236	201024	168812	136740	104729	72665	40631	8794	8.1752
FBG-11	233183	201030	168877	136687	104604	72658	40624	8819	8.1758
FBG-12	233538	201372	169303	137042	105050	73026	41044	9251	8.1784
FBG-13	233429	201250	169071	136933	104876	72852	40909	8999	8.1755

Upon averaging the wavelength ranges from the 13 FBGs, we determine the wavelength range to be 8.1761 nm. This range will be used heretofore for the processing of raw data. This concludes the necessary steps in the FOID system setup. In the next part of the setup section, the steps for preparing the finite element program will be described.

3.3.5 Finite Element Model

This section focuses on the design of finite element models used to calculate theoretical results from loading embedded FBGs. The specific configuration modeled is the 90°/90° sample. The purpose behind creating these models is twofold. The first reason is to understand the physical phenomena occurring when the 90°/90° sample is mechanically loaded in order to explain experimental results. The second purpose is to explore design factors which could turn embedded FBGs into uniaxial strain sensors despite a multiaxial strain state existing in the host composite. The finite element analysis software used is COMSOL Multiphysics. Both 2-D and 3-D models were created to analyze strain transfer to an embedded optical fiber. This is because 3-D models take a considerable amount of time and processing power to run. Thus, 2-D models

were created in order to learn general trends so the minimum number of 3-D models would be processed to satisfactorily draw conclusions.

In the model, each ply will be individually modeled as a homogenous material and the optical fiber will be included in the model as well. This poses a challenge in creating a mesh that is fine enough to converge to a solution for features as small as the $7 \mu m$ thick polyimide coating but becomes coarse enough in the composite far field to reduce processing time. COMSOL requires a consistent length unit to be used for all dimensions in the model. In order to satisfactorily describe dimensions as large as 10 cm and as small as $1 \mu m$, units of mm were chosen; henceforth, all dimensions when referring to the finite element model will be expressed in mm rather than cm or μm .

Two types of loading configurations will be studied which resemble the in-plane loading and out-of-plane loading performed experimentally. The studies performed involve exploring the effects of mesh refinement, polyimide coating thickness, lenticular resin rich region size, de-adhesion between fiber optic and composite host, and cross-ply crack propagation. In this section, descriptions will be provided of the geometries of the models, loading and boundary conditions, material properties, and mesh refinement.

3.3.5.1 MODEL GEOMETRIES

In order to reduce the size of the models, the dimensions of the composite were decreased. The size reduction was extensive enough to significantly reduce processing time but minor enough that the optical fiber remained in the far field region of the composite (i.e. sufficiently removed from edge effects). Rather than having in-plane dimensions of $50 \times 300 \text{ mm}^2$ like the experimentally tested samples shown in previous figures, in-plane dimensions of $20 \times 100 \text{ mm}^2$ were used. Additionally, the aluminum tab dimensions modeled were $20 \times 20 \times 2 \text{ mm}^3$ rather than $50 \times 50 \times 3.175 \text{ mm}^3$. The optical fiber diameter, polyimide thickness, and composite ply thickness were not altered.

Figure 3-21 demonstrates a 2-D IPL model zoomed in at various magnifications. Image (a) shows the semi-circular optical fiber with a concentric layer of polyimide. Note that a semicircular geometry is used because a symmetry condition was imposed at the composite's mid-plane where the optical fiber is embedded. The optical fiber radius is 0.0635 mm and the polyimide thickness is 0.007 mm . The optical fiber with polyimide coating is embedded in the mid-plane between 90° layers of the host composite. In image (b), a grid is shown in the near field of the optical fiber. Each row of the grid represents a ply (0.270 mm thick) with the four rows shown representing, from bottom to top layer, 90° , $+45^\circ$, -45° , and 0° layers. The purpose behind creating the grid is to have more control over the mesh size near the embedded optical fiber. Image (c) shows all 12 layers in the top-half of the composite. Each row still represents an individual ply in the composite (0.270 mm each for a total thickness of 3.24 mm). The vertical lines are artificially created in the model to provide more control in meshing the geometry. Image (d) shows the end of the composite to demonstrate the tab dimensions. The composite thickness, tab thickness, and tab length are 3.24 , 2 , and 20 mm , respectively.

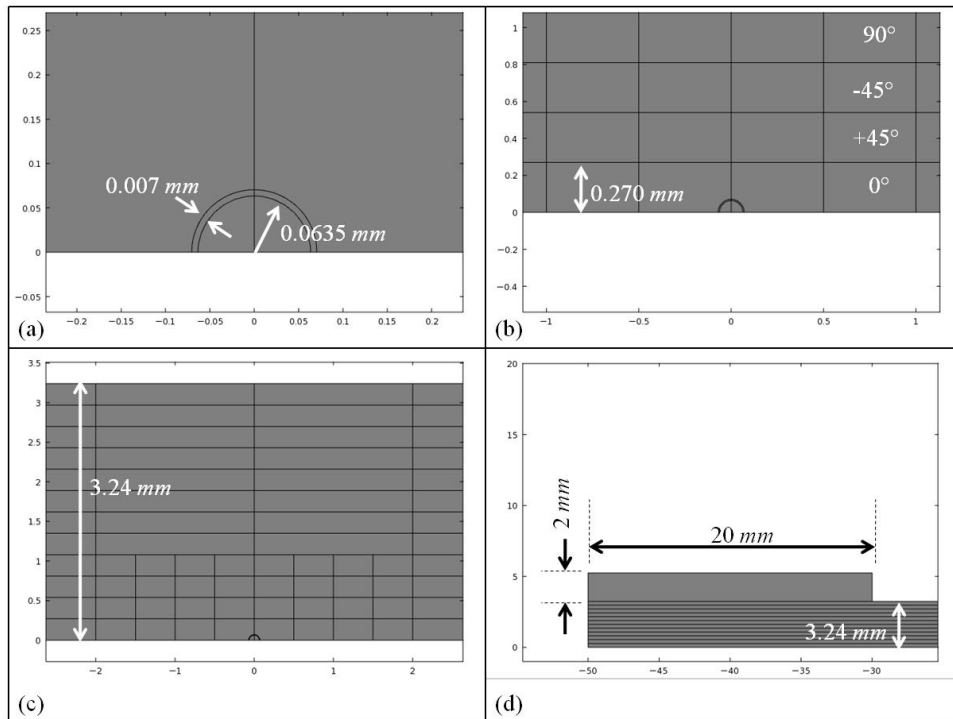


Figure 3-21: Pertinent features and dimensions of a cross-section of the 2-D IPL model.

To provide more clarity and a comparison of 2-D versus 3-D and IPL versus OPL models, Figure 3-22 was created. Image (a) shows a 2-D IPL model that is 100 mm in length with two 20 mm tabs. Image (b) shows a 2-D OPL model that is 40 mm long with one single tab 20 mm long. Images (c) and (d) show the 3-D IPL and OPL models respectively with both 20 mm in width. The 3-D geometry is created simply by taking the 2-D geometries and extruding them.

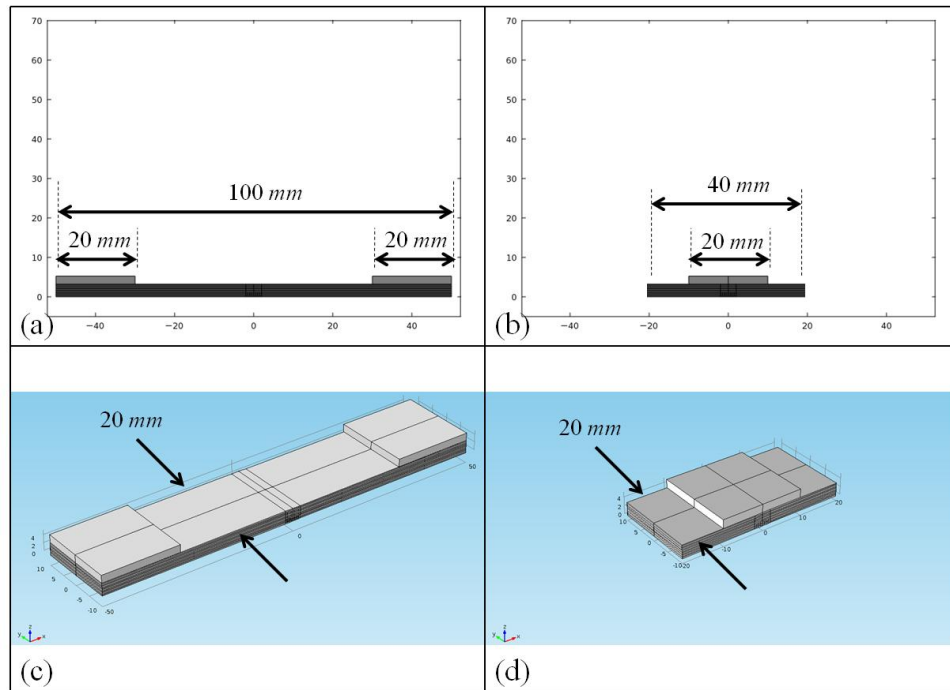


Figure 3-22: Images depicting the dimensions of the model reduced from the experimental composite samples.

One important factor to note is the difference in coordinate axes for 2-D versus 3-D models. This is particularly important when creating anisotropic stiffness matrices for the composite materials which will be described next. In the 2-D models, the x-direction is in the plane of the composite associated with the 0° direction. The y-direction is out-of-plane from the composite. In the 3-D model, the x-direction remains the same, but what was the y-direction in the 2-D model is now the z-direction in the 3-D model. The 3-D y-direction is in the plane of the composite associated with the 90° direction (i.e. parallel to the optical fiber).

3.3.5.2 MATERIAL PROPERTIES

There are five isotropic and four anisotropic materials created for the finite element models. In order to fully define the isotropic stiffness matrices, only the Young's modulus and Poisson's ratio need to be defined. Table 3-3 shows the five isotropic materials along with their associated stiffness and Poisson's ratio. Fused silica makes up the optical fiber, polyimide the coating material, and the tabs are comprised of aluminum. In order to model lenticular resin rich regions,

the matrix material of the composite, 3501-6 resin, must be created as a separate material. Any crack or interface de-adhesion is modeled with a material denoted as “air” with a stiffness orders of magnitude lower than all other materials. The purpose of modeling air as a solid material is to prevent elements surrounding the air from overlapping, which the finite element code has not been set to counteract. A density value is required to be input by COMSOL, though it does not factor into the models considered in this work because all loading is static. Though accurate values are given for all materials, arbitrary values could have been input and the same results would be obtained.

Table 3-3: Mechanical properties of isotropic materials utilized in FEA models.

Material	Young's Modulus [GPa]	Poisson's Ratio [-]	Density [kg/m ³]
Fused Silica	72	0.165	2200
Polyimide	3.2	0.35	1430
Aluminum	70	0.35	2700
3501-6 Resin	4.27	0.34	1265
Air	0.01	0.3	1.25

For an isotropic material, the elasticity matrix, **D**, relating stress to strain in COMSOL is written in terms of Young's Modulus, *E*, and Poisson's ratio, *ν* in the following equations:

$$\begin{Bmatrix} \sigma_{xx} \\ \sigma_{yy} \\ \sigma_{zz} \\ \sigma_{xy} \\ \sigma_{yz} \\ \sigma_{xz} \end{Bmatrix} = [\mathbf{D}] \begin{Bmatrix} \epsilon_{xx} \\ \epsilon_{yy} \\ \epsilon_{zz} \\ \epsilon_{xy} \\ \epsilon_{yz} \\ \epsilon_{xz} \end{Bmatrix} \quad (3.12)$$

$$[\mathbf{D}] = \frac{E}{(1+\nu)(1-2\nu)} \begin{bmatrix} 1-\nu & \nu & \nu & 0 & 0 & 0 \\ \nu & 1-\nu & \nu & 0 & 0 & 0 \\ \nu & \nu & 1-\nu & 0 & 0 & 0 \\ 0 & 0 & 0 & \frac{1-2\nu}{2} & 0 & 0 \\ 0 & 0 & 0 & 0 & \frac{1-2\nu}{2} & 0 \\ 0 & 0 & 0 & 0 & 0 & \frac{1-2\nu}{2} \end{bmatrix} \quad (3.13)$$

Note an important feature of the first equation is the order in which the symmetric, 2nd order stress and strain tensors are represented with contracted notation in a 6 x 1 vector. It is similar to Voigt notation, but has the order of shear terms changed. Table 3-4 indicates the difference with the contraction method used in COMSOL denoted here as the “COMSOL Notation.” While more current versions of COMSOL allow for the user to switch to Voigt notation, this was not available in the version used for this research.

Table 3-4: Comparison of Voigt and COMSOL contracted notation.

Stress, Strain Subscript (x-y-z coordinates)	Stress, Strain Subscript (1-2-3 coordinates)	Voigt Notation	COMSOL Notation
xx	11	1	1
yy	22	2	2
zz	33	3	3
yz	23	4	5
xz	13	5	6
xy	12	6	4

This clearly does not influence the isotropic materials, but the anisotropic composite layers will be affected. The prepregs material used to create the composite is AS4/3501-6 which is composed of unidirectional graphite fibers embedded in a resin matrix. This is a transversely isotropic material system. If a 1-2-3 coordinate system is assigned to the material with the 1-direction aligned with the fibers, a rule of mixture approach can be used to calculate the composite material properties from the individual phases as summarized in Table 3-5. The

volume fraction, V_f , is the volumetric ratio between carbon fibers and matrix. E_1 and E_2 are the longitudinal and transverse stiffness of the structural fibers (note that E_1 and E_2 are equal for the resin which is isotropic). Poisson's ratio, ν_{12} , shear modulus, G_{12} , and density, ρ are also indicated. Material properties were obtained from Hexcel Composites specification sheets provided in the appendix and also from a publication by Soden et al. 1998 [192]. It should be noted that the volume fraction was not measured or specified by the manufacturer, but approximately deduced in order to have a composite laminate whose in-plane stiffness (as calculated using classical lamination theory in Jones, 1999 [193]) would match experimental measurements.

Table 3-5: Material properties of both composite phases used in a rule of mixtures calculation to determine lamina properties.

Material Property	Units	AS4 Fibers	3501-6 Resin	Composite
V_f	[-]	1	0	0.6
E_1	[GPa]	228	4.267	139
E_2	[GPa]	15	4.267	7.48
ν_{12}	[-]	0.2	0.34	0.26
G_{12}	[GPa]	95	1.59	3.88
ρ	[kg/m ³]	1790	1265	1580
ν_{23}	[-]			0.4

The last term in Table 3-5 is the composite ν_{23} which is directly taken from Soden et al. 1998 rather than calculated from the individual phases [192]. The process for calculating the elasticity matrices for each of the four ply angles (0° , 90° , $+45^\circ$, and -45°) that make up the quasi-isotropic laminate is described in Figure 3-23. The \mathbf{D} tensor is calculated and represented with a 6x6 matrix in COMSOL (as opposed to Voigt) notation for a unidirectional ply in the 1-2-3 coordinate system. Next, a 6x6 rotation matrix is derived using a method analogous to the one portrayed in Slawinski, 2010 [194]. The change is that Slawinski derives the rotation matrix in

Voigt notation, but changing to COMSOL notation requires a slight change in the assembly of the rotation matrix. For the 2-D case, the $[D]$ matrix rotation is about the y-axis (or 2-direction of the original coordinate system) whereas the 3-D case involves rotation about the z-axis (or 3-direction of the original coordinate system). Thus, four $[D]$ matrices are created for the 2-D and four for the 3-D cases.

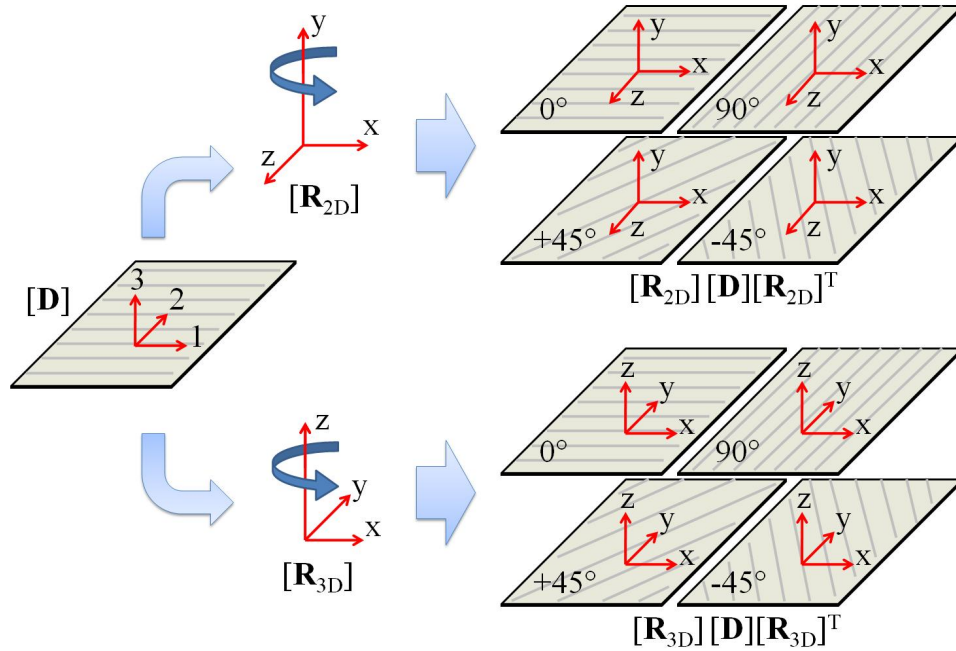


Figure 3-23: Method for calculating elasticity matrix for each ply orientation by rotating about a particular axis depending on whether the rotation is for a 2-D or 3-D model.

A MATLAB program was created requiring the angle of rotation as an input with four elasticity matrices as the output: 2-D and 3-D matrices in Voigt and COMSOL notation. The program is added to the appendix for the reader's reference. The equation for calculating $[D]$ in the original 1-2-3 coordinate system in COMSOL notation is represented in the following equation with the 1-direction representing the axis of symmetry.

$$[\mathbf{D}]^{-1} = [\mathbf{S}] = \begin{bmatrix} \frac{1}{E_1} & -\frac{\nu_{12}}{E_1} & -\frac{\nu_{12}}{E_1} & 0 & 0 & 0 \\ -\frac{\nu_{12}}{E_1} & \frac{1}{E_2} & -\frac{\nu_{23}}{E_2} & 0 & 0 & 0 \\ -\frac{\nu_{12}}{E_1} & -\frac{\nu_{23}}{E_2} & \frac{1}{E_2} & 0 & 0 & 0 \\ 0 & 0 & 0 & \frac{1}{G_{12}} & 0 & 0 \\ 0 & 0 & 0 & 0 & \frac{2(1+\nu_{23})}{E_2} & 0 \\ 0 & 0 & 0 & 0 & 0 & \frac{1}{G_{12}} \end{bmatrix}^{-1} \quad (3.14)$$

The elasticity matrix is simply the inverse of the compliance matrix, $[\mathbf{S}]$, for a transversely isotropic material. Now that the relevant mechanical properties of the isotropic and transversely isotropic materials used in this study have been found, the loading and boundary conditions will be described next.

3.3.5.3 LOADING AND BOUNDARY CONDITIONS

The boundary conditions of the models were applied to simulate the Instron loading method. A symmetry condition was applied in the mid-plane because the composite lay-up is symmetric, the optical fiber is centrally embedded in the mid-plane, and loading is symmetric about the mid-plane. Figure 3-24 demonstrates the loading and boundary conditions for the 2-D IPL and 2-D OPL. For 2-D IPL, the top surface of the left-side tab was fixed from moving left-to-right ($u_x = 0$) but free to move up-and-down. These displacement and symmetry conditions prevent any rigid body motion solutions. A vertical compressive force (F_y) was applied to both tabs to simulate grip pressure while the right-side tab had an additional horizontal tensile force (F_x , pulling the right-side tab from left to right). For 2-D OPL, the same symmetry ($u_y = 0$) condition applies at mid-plane, but to prevent x-direction rigid body motion, the top surface of the tab was

fixed in the x-direction ($u_x = 0$). A vertical compressive force (F_y) was also applied to simulate grip pressure.

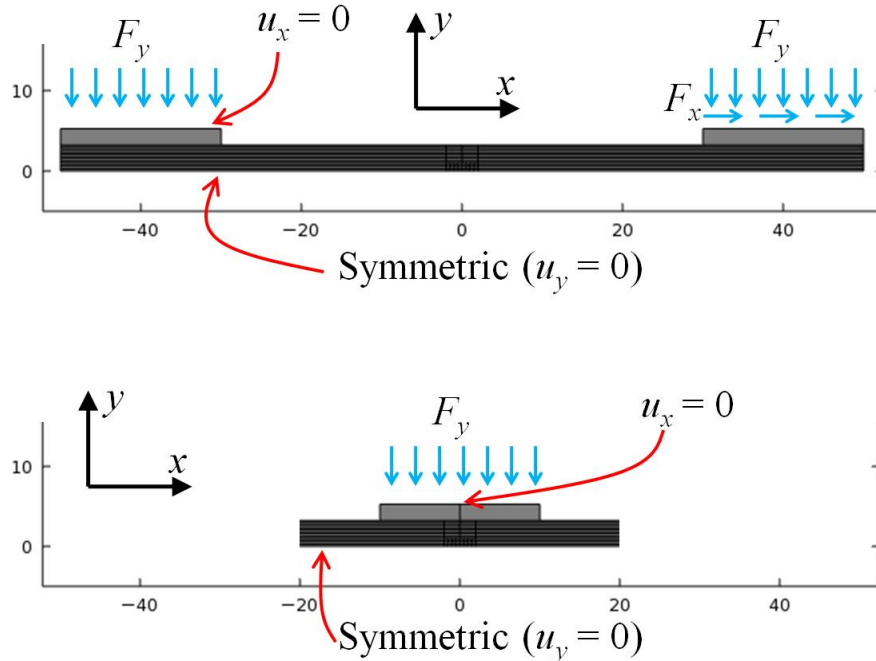


Figure 3-24: Boundary conditions of the 2-D IPL and OPL models.

These boundary conditions can easily be extrapolated to the 3-D cases. The 3-D models are simply an extrusion of the 2-D model, so all constraints seen above will simply be applied to a surface in the 3-D model rather than an edge in the 2-D model. For instance, the mid-plane symmetry condition will be applied to the entire mid-plane of the 3-D model rather than the line representing the mid-plane in the 2-D model. The forces on the tabs will be applied to the planar tab surface in the 3-D model rather than the line representing the tab surface in the 2-D model. Note that the change in coordinate system means the 3-D symmetry condition for the mid-plane is $u_z = 0$ rather than $u_y = 0$ in the 2-D model. The only additional boundary condition in going from 2-D to 3-D modeling is that the top surface of the tabs are prevented from moving in the 3-D coordinate system's y-direction. This simulates the clamping effect of the Instron grips. Now that the geometry, material properties, loading, and boundary conditions have been defined, the preprocessing is complete. The next step is to determine a suitable mesh density.

3.3.5.4 MESH REFINEMENT

The final step in the process is running a few preliminary models with varying mesh refinement. This will help determine how fine or coarse the mesh should be in order to minimize processing time and model size without compromising accuracy. The strain at selected, relevant points will be evaluated with varying mesh refinements in order to determine a suitable mesh size. A very fine mesh is first created in the optical fiber region and becomes coarser in the regions farther and farther from the FBG. Figure 3-25 illustrates this concept in the region of the optical fiber for two mesh densities. In part (a), a coarser mesh is shown magnifying the region near the embedded FBG. In part (b), the same coarse mesh is shown in the composite far field. In part (c), a finer mesh is shown magnifying the region near the embedded FBG. In part (d), the same fine mesh is shown in the composite far field.

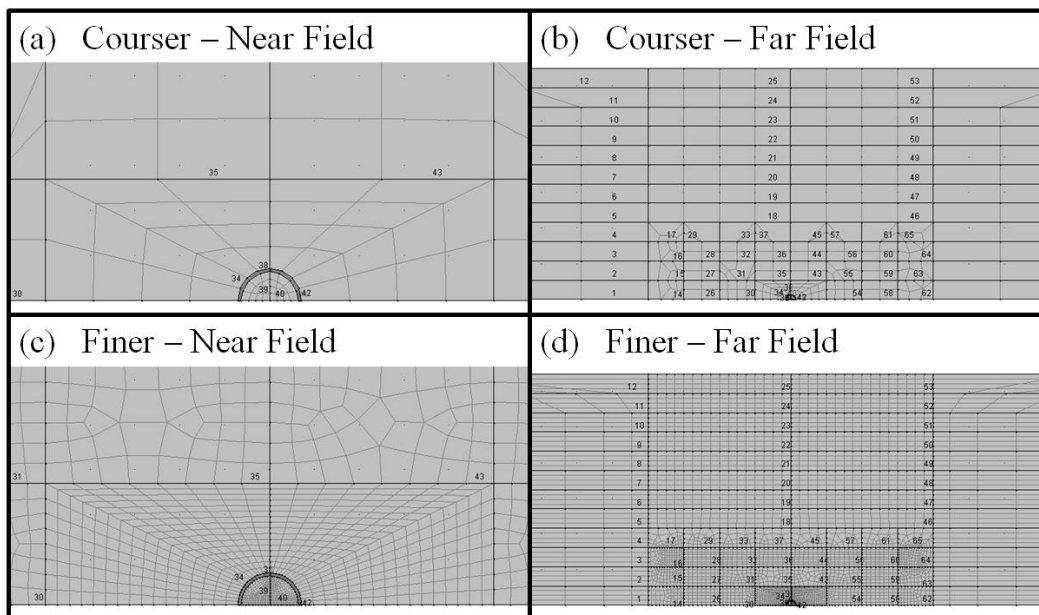


Figure 3-25: Images depicting the mesh refinement in the far field of the composite and in the near field of the embedded optical fiber.

Note that in part (b) and (d), the mesh density decreases away from the FBG located at the bottom (mid-plane) of the composite geometry. Five points will be evaluated at four different

mesh densities to demonstrate a converged solution. Those five points, their labels in the upcoming figure, and their coordinates for an origin located at the FBG's center are:

(1) Core: the center of the FBG [0, 0]

(2) PolyX: The center of the polyimide coating lateral to the optical fiber in the x-direction [0.067, 0]

(3) PolyY: The center of the polyimide coating lateral to the optical fiber in the y-direction [0, 0.067]

(4) CoMid: A composite mid-plane location in the far field suitably far away from both the FBG and the tabs [10, 0]

(5) ESG: The surface of the composite directly above the FBG where an electrical strain gauge would be located in an experiment [0, 3.24].

Figure 3-26 demonstrates the convergence of strain for the mesh refinement procedure. The vertical axis in graph (a) of the figure is the x-direction strain at the aforementioned locations for the various mesh refinements normalized to the x-direction strain with the finest mesh. The horizontal axis is a mesh density variable representative of the mesh refinement throughout the entire geometry. The five data curves represent the five points previously described. Graph (b) of the figure plots the normalized y-direction strain percentage versus mesh density variable.

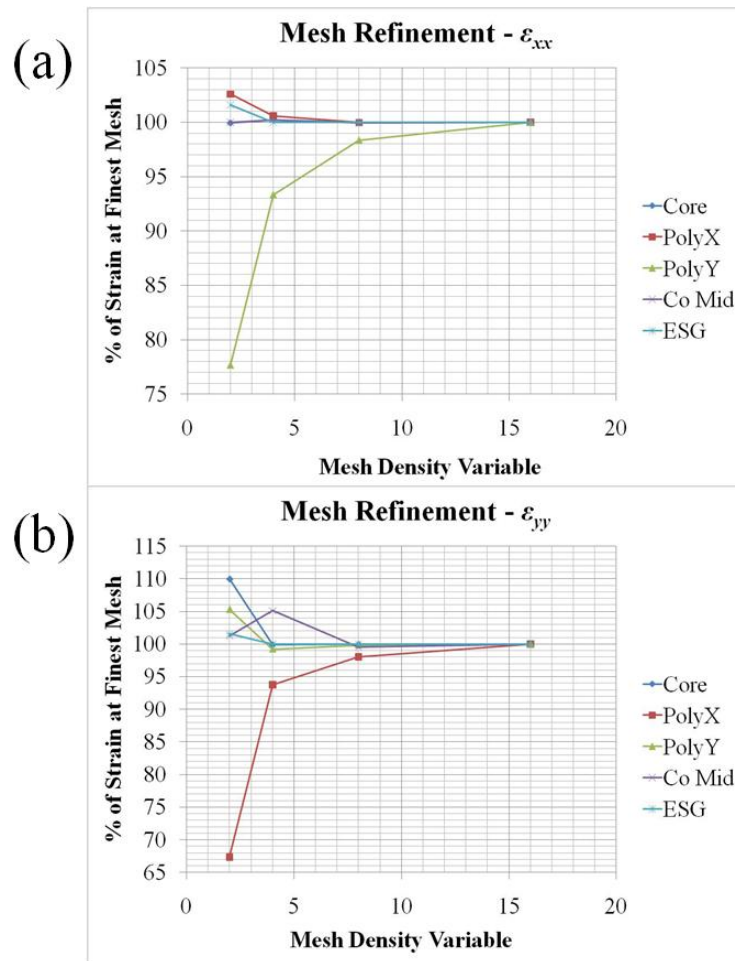


Figure 3-26: Mesh refinement results indicating the necessary finesse of the mesh in order to achieve a converged calculation.

It can be seen that for both plots, the strain within the coating is the slowest to converge whereas the strain in the FBG is the quickest. The benefit of plotting curves for several points within the model is that the mesh density variable can be selectively altered based on location in the model geometry. Thus, the final mesh used in the study can be refined at certain locations more than others depending upon how fast convergence occurs in that location. Based on the figure above, for instance, the mesh density variable in the optical fiber coating region will be heavily refined to a value of approximately 12 to obtain satisfactory convergence whereas the mesh density variable in the optical fiber will be satisfactorily converged at a value of 8. Using this procedure, the mesh can be refined in a manner which minimizes the model size while

maintaining convergence to a sufficiently accurate solution. This methodology is repeated for 3-D models.

3.3.6 Concluding Remarks

This section has focused on describing the necessary, preliminary steps to set up the experimental and theoretical work in addition to the types of experiments and model analyzed. The optical fiber properties were directly obtained and indirectly calculated using specifications from Luna Innovations. Next, the procedure was specified to create the composite lay-up with the optical fibers embedded in the mid-plane along with the steps of taking x-ray photos, attaching electrical strain gauges, and gluing tabs to complete the composite samples. The two types of mechanical load testing were described including the data to be collected and processed. The fiber optic interrogation device was explained including the procedure for splicing optical fibers into the system, verifying the photoelastic coefficient, and obtaining the tuning range for raw data in the wavelength spectrum. Lastly, the finite element model preprocessing was described including the geometry, material properties, load and boundary conditions, and mesh refinement study. The next section will portray and analyze the results of the described tests and models.

3.4 Experimental Results

This section describes the experimental results obtained in testing various composite-embedded FBGs. Past results published of a $0^\circ/0^\circ$ sample will be presented first. This will provide introductory results which frame the idea of the uniaxial assumption for FBGs and what circumstances lead to the assumption breaking down. This will be followed by exploring experimental evidence of $0^\circ/90^\circ$ and $90^\circ/90^\circ$ samples. Both of these composite configurations will be explored in similar fashion. Results from an initial test will lead to interesting questions which should be answered to fully understand the behavior of the FBGs and how the

measurement system turns that behavior into a strain measurement. In order to comprehensively understand the preliminary results, residual strain effects from the curing process will be analyzed. This is followed with mechanical compressive OPL and tensile IPL tests which determine whether or not birefringence is increasing, decreasing, or stagnating. The possible presence of cross-ply cracks will then be determined and used to help understand the observed behavior.

3.4.1 0°/0° Sample

The experimental and finite element work on the 0°/0° sample was mostly carried out by two previous Master's Degree students, Karnani 2007 and Trono 2008 [195, 196]. The work was compiled, analyzed, and published by Emmons et al. 2010 and is a necessary introductory test whose results add context to later testing [137]. This sample was fabricated with the same method as the 0°/90° and 90°/90° samples described earlier. The sample dimensions and fiber orientation are equal to the 0°/90° sample, but the lay-up, while still quasi-isotropic, is different. Simply put, if each composite fiber orientation angle in the 0°/90° sample is rotated by 90° while keeping the optical fiber in place, you get the 0°/0° lay-up. The lay-up, original and altered X-ray images, and sample schematic are shown in Figure 3-27 below analogous to Figure 3-9 through Figure 3-11 for the 0°/90° and 90°/90° samples.

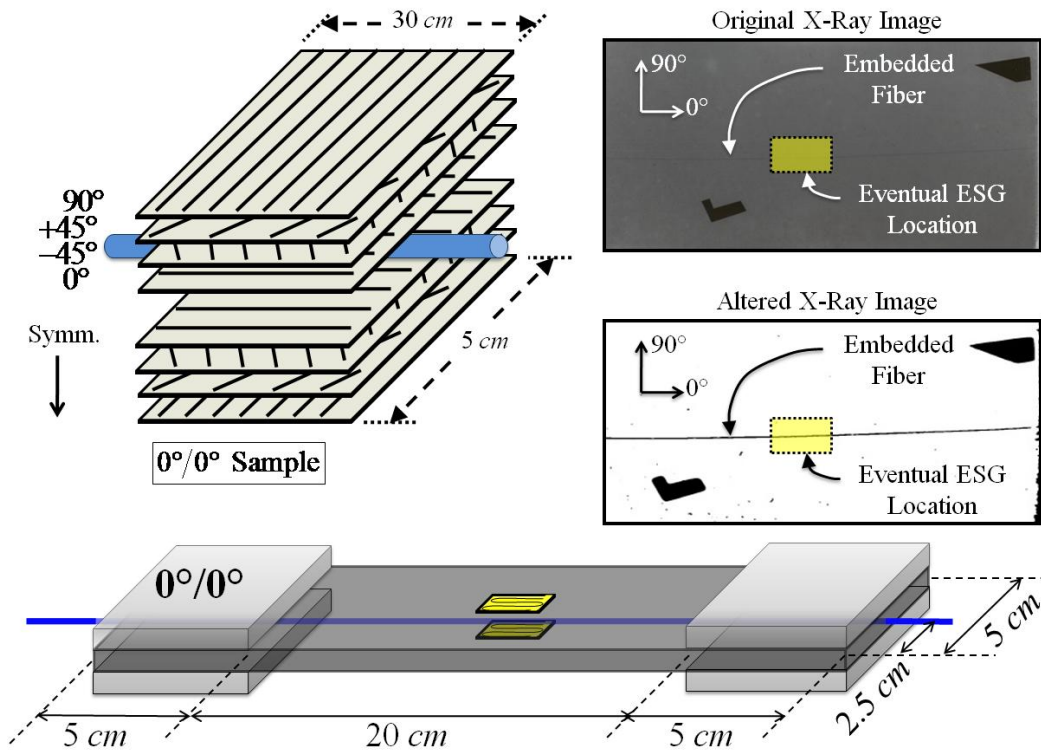


Figure 3-27: Sample configuration for the $0^{\circ}/0^{\circ}$ sample.

An additional difference lies in the finite element modeling of the $0^{\circ}/0^{\circ}$ sample. While modeling the $90^{\circ}/90^{\circ}$ sample in COMSOL, each composite ply is modeled separately with its own anisotropic material properties. In the $0^{\circ}/0^{\circ}$ ANSYS model, however, all 24 layers are represented with a single, homogenous material with quasi-isotropic laminate properties. Additionally, the optical fiber is not incorporated into the model. Instead, the strains inside the composite at the optical fiber location are measured and used to compare with experimental results. Further details of the experimental setup and model can be found in the referenced theses and journal publication.

The first plot shown below in Figure 3-28 for the mechanical tensile load test is a comparison of the strain measurements taken during loading of the surface-mounted, collocated strain gauges and the embedded FBG located between the ESGs. The applied stress in the composite is indicated by vertical axis while the measured strain is indicated by the horizontal axis. The green triangles represent the average at each load value of the two collocated strain gauges to strip out

the effects of bending. The blue circular markers represent the associated FBG strain measurements.

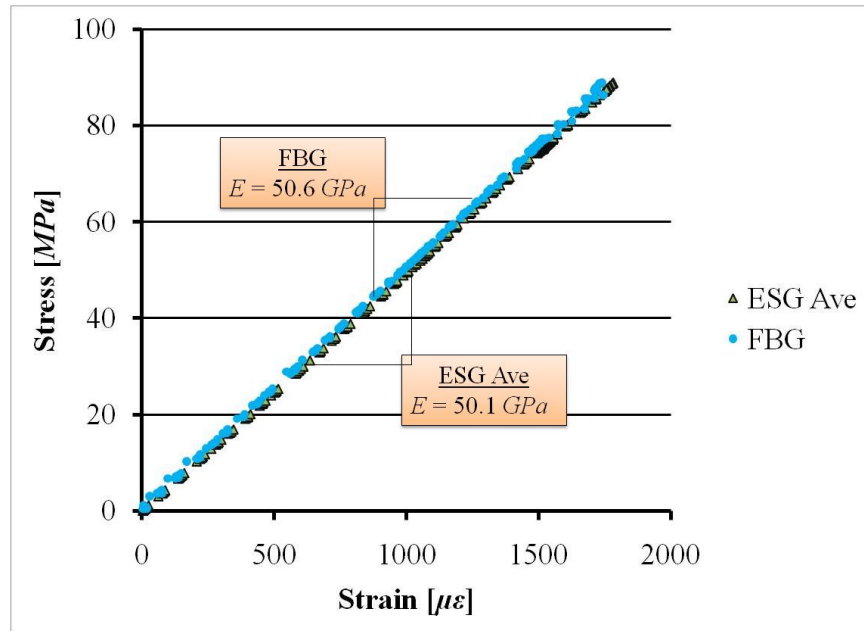


Figure 3-28: Comparison of FBG and ESG data measuring the stress-strain relationship in a 0°/0° sample.

Both data sets agree quite well and indicate a composite Young's modulus of 50.6 *GPa*. This attests to the ability of FBGs embedded parallel to adjacent structural fibers to accurately measure strain in the loading direction. The next graph in Figure 3-29 expands upon the single-location results of the Figure 3-28 by plotting the strain response at specific load levels for all FBGs along the optical fiber. This effectively gives a strain profile for the composite during loading. Strain is represented with the vertical axis while location along the optical fiber is indicated with the horizontal axis. The optical fiber is 38 *cm* in length, but only 30 *cm* are embedded within the composite. Therefore, in Figure 3-28, the length of the composite spans from 0 to 30 *cm* while FBG measurements at locations < 0 and > 30 *cm* are outside the composite. The grip regions are from 0 to 5 *cm* and from 25 to 30 *cm*. The centrally located electrical strain gauges are located at the 15 *cm* point. Strain profiles are plotted every 20 *MPa* from 0 to 80 *MPa* with FBG data at each load level represented with various color and symbol

combinations. The average of the two ESG measurements at each load level is indicated at the 15 cm point by a yellow circular symbol. Data from the ESG Ave and FBG located at 15 cm corresponds to the stress-strain plot in Figure 3-28.

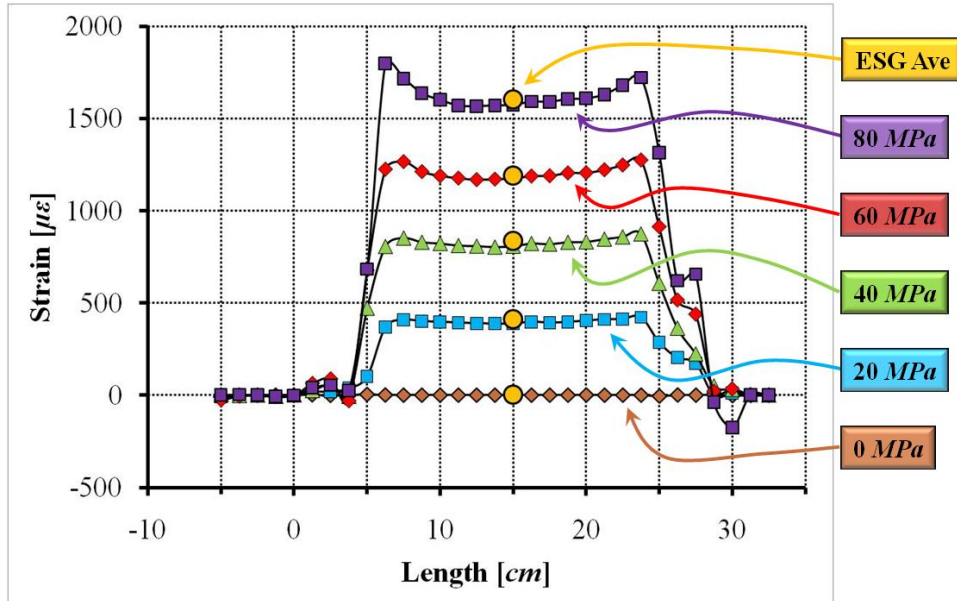


Figure 3-29: Strain profile within the 0°/0° sample at various load levels.

The strain measurements made by FBGs outside the composite (less than 0 and greater than 30 cm) do not change because no strain is being transferred to them. The strain measurements in the grip regions (0-5 and 25-30 cm) are sporadic and unreliable, as will be explained shortly. Away from the gripped region is the far field (8-22 cm) where results are settled and consistent. This region is where the results are most reliable, as shown by the good agreement between the ESG Ave and the far field strain values. This type of plot indicates the much larger quantity of information which can easily be obtained by an optical fiber compared to a strain gauge. Tens of strain measurements are taken from a single optical fiber which weighs considerably less than the metallic wires used for one ESG measurement location.

The final plot for the 0°/0° sample results compares the ESG Ave, FBG strain profile, and FEA results for the particular load level of 87 MPa. In Figure 3-30, the x-axis is taken to be parallel to the loading direction, the y-axis is perpendicular to the load and in the plane of the

composite plate, and the z -axis is the out-of-plane direction (i.e. the direction of grip pressure on the sample's aluminum tabs). The horizontal and vertical axes in the plot are the same as in the previous strain profile graph. The ESG Ave measurement of strain in the x -direction (i.e. ESG ϵ_{xx}) is represented with a yellow circular marker. The profile of FBG strain measurements in the load direction, FBG ϵ_{xx} , is represented with blue diamonds. The three strain components, ϵ_{xx} , ϵ_{yy} , and ϵ_{zz} are represented with green, purple, and red curves respectively.

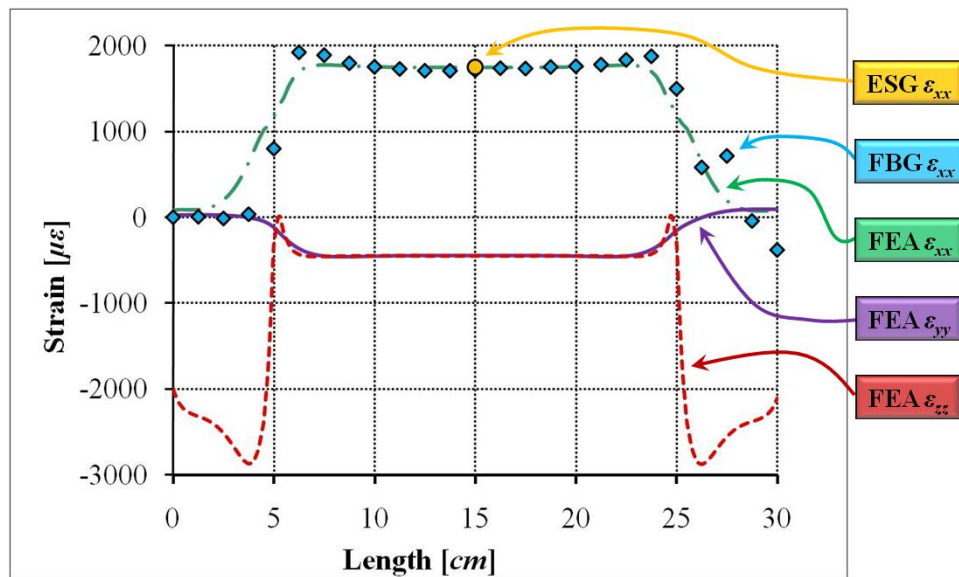


Figure 3-30: Comparison amongst ESG, FBG, and FEA results for a particular load applied to the $0^{\circ}/0^{\circ}$ sample.

From the figure, it can be seen that extremely good agreement exists amongst the three methods of determining strain in the loading direction of the composite. This plot also determines why strain measurements by the FBGs in the grip region are inaccurate and unreliable. The FOID system used to calculate FBG strain assumes uniaxial strain in the fiber direction. This allows the shifts in Bragg wavelength to be associated to strain in the fiber direction via the effective strain-optic coefficient verified in the experimental setup section. A key feature of uniaxial strain is that transverse strains are equal. In the grip region, however, the transverse strains (ϵ_{yy} and ϵ_{zz}) are unequal. This is due to the large compressive grip load (and thus the large negative strain value for FEA ϵ_{zz}). In the far field, however, the transverse strains

are approximately equal and the uniaxial assumption is valid. We would expect to see the single-peak reflection signal for the FBGs in the grip region split into two peaks as birefringence develops due to the increasing TSD. It is expected that the strains transverse to the optical fiber in the host material do not completely match that in the optical fiber due to inadequate strain transfer which will be explored later in this chapter. Despite this, the TSD should still be insignificant in the far field region while very large in the tab regions.

This concludes the results of the $0^\circ/0^\circ$ testing. The lesson taken from this testing is that in order to have a reliable uniaxial sensor, the TSD must not be significantly large (i.e. away from the grip region). This experimental evidence corroborates the theoretical work in the previous chapter on photoelasticity. The goal of this research is to explore the capabilities of FBGs in various load and lay-up configurations to determine whether or not the FBGs will behave as uniaxial strain sensors. The reliability and accuracy of FBGs embedded in $0^\circ/90^\circ$ and $90^\circ/90^\circ$ configurations will be explored in the next section.

3.4.2 $0^\circ/90^\circ$ Sample

This section describes testing of a $0^\circ/90^\circ$ sample. The tensile test results similar to the stress versus strain results in the $0^\circ/0^\circ$ sample will be shown first. This will demonstrate an obvious problem that needs to be resolved by taking a deeper look into the data processing method. Specifically, the reflected wavelength spectra of several FBGs will be analyzed in order to provide insight into the physical phenomena at play.

The curing results will be shown first and followed by compressive out-of-plane and tensile in-plane loading results. A critical lesson from this section will be the necessity for future users of this technology to have a multidisciplinary understanding of optics, composites, and photoelasticity in order to fully understand the responses of FBG sensors.

3.4.2.1 PROBLEM INTRODUCTION

A critical facet of this sample configuration is the orthogonal orientation of the optical fiber relative to the adjacent structural fibers. In order to illustrate this significance, the sample was cut after all testing was performed in order to view the lenticular resin rich region under an optical microscope. A drawing describing the observer's point-of-view and a series of pictures at increasing magnification are shown in Figure 3-31. The total 24-layer composite thickness is 6.5 mm, giving a nominal ply thickness of 270 μm . Thus, the thickness of the two 0° layers in which the optical fiber is embedded is 0.54 mm. The resin rich pockets on both sides are 1.49 mm long and the optical fiber is 127 μm in diameter (not counting the 7 μm thick polyimide coating).

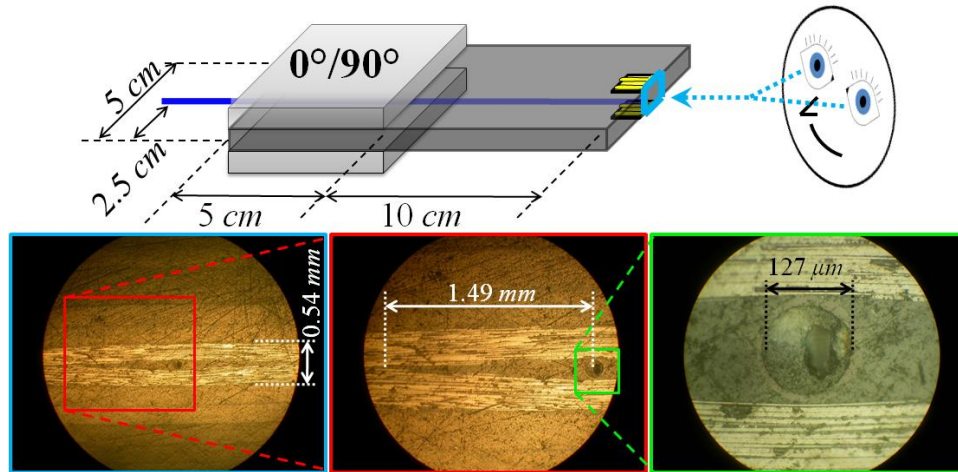


Figure 3-31: Microscope images of the lenticular resin rich regions adjacent to the optical fiber.

The lenticular resin rich region may greatly affect the TSD and thus, birefringence due to the obvious geometric asymmetry and material difference around the optical fiber (i.e. in the microscope images in the figure above, purely resin to the left and right of the FBG and mostly carbon fibers above and below). The results of a preliminary tensile IPL test described in the previous section are shown in the stress-strain plot in Figure 3-32. The green triangles represent the average of the two surface-mounted FBGs. Using the same length scale as the 0°/0° sample, the blue circles represent the FBG at the 15 cm location sandwiched between two surface-

mounted ESGs. The orange squares represent the average strain values of the FBGs at the 14, 15, and 16 cm locations. The ESG average displays a consistent, linear relationship indicating a 51 GPa stiffness which is comparable to the 0°/0° sample. The slight difference originates from the separate composite coupons from which the 0°/0° and 0°/90° samples were cut. The FBG data, on the other hand, displays a nonlinear relationship which cannot be explained with the expected strain response of the host composite.

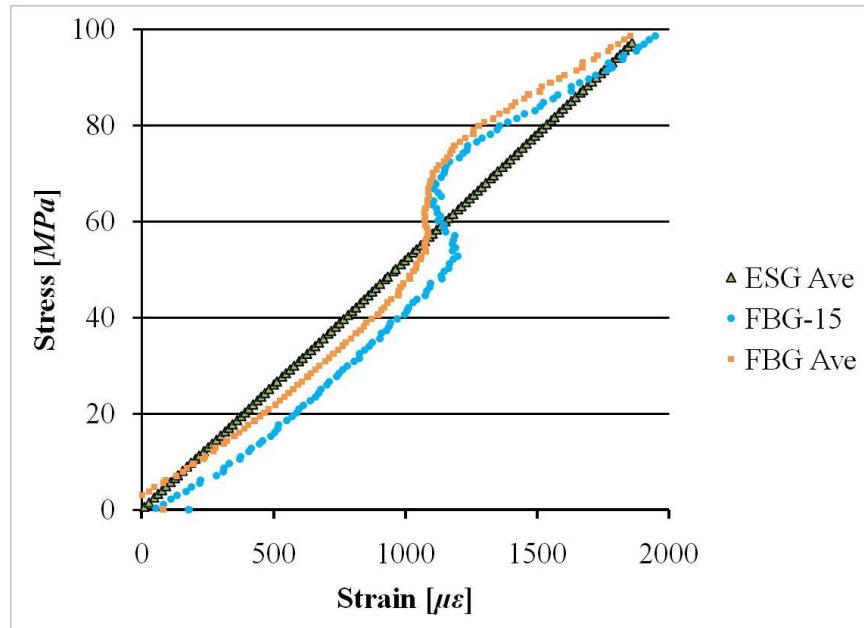


Figure 3-32: Stress-strain behavior of the surface-mounted ESG and embedded FBGs for the 90°/90° sample under IPL conditions.

In order to understand the observed FBG response, the processing method must be methodically stepped through to derive the strain data displayed in the figure above. Before getting straight into the IPL test results though, the influence of curing on the reflected wavelength spectra of a sample of FBGs will be explored.

3.4.2.2 CURING EFFECTS

In order to uncover the reason behind the FBG’s stress-strain relationship above, we will look at the reflected wavelength spectra of selected embedded FBGs. A comparison will be made

between a non-embedded FBG, the three FBGs nearest to the surface-mounted ESG (FBG-14, -15, and -16), and a FBG located between the tabs (FBG-27). The non-embedded FBG is from the same spool as the embedded fiber and therefore, makes for a pre-embedment reference. Note that FBG-14, -15, and -16 were used to calculate the stress-strain data in Figure 3-32. The result is shown in Figure 3-33. The non-embedded FBG clearly shows a single peak around 1546.3 nm whereas each of the four embedded FBGs' reflection spectra shows two reflection peaks. Note that no external mechanical load is applied when obtaining the spectra in Figure 3-33.

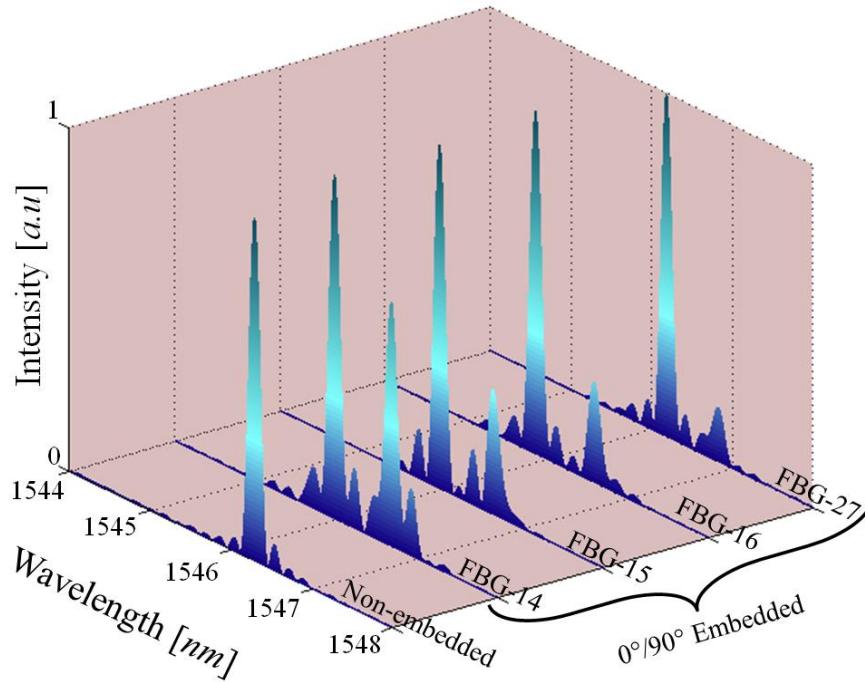


Figure 3-33: Reflected wavelength spectra of one non-embedded and four embedded FBGs in the 0°/90° sample.

By looking at the shift in each embedded FBG's two reflected wavelengths, the TSD can be calculated as described in the previous chapter using the following equation:

$$\varepsilon_1 - \varepsilon_2 = \frac{2}{n^2 (p_{12} - p_{11})} \left[\left(\frac{\delta \lambda_B}{\lambda_B} \right)_1 - \left(\frac{\delta \lambda_B}{\lambda_B} \right)_2 \right] \quad (3.15)$$

Note that none of the individual strain components can be calculated due to only having two pieces of information, $(\lambda_B)_1$ and $(\lambda_B)_2$, to calculate three unknowns, ε_1 , ε_2 , ε_3 (assuming no shear strains in the coordinate system used). The measured reflected wavelengths and calculated TSDs are presented in Table 3-6. The first column indicates the FBG, second and third columns indicate the measured reflected wavelengths associated with the two polarization directions, and fourth column indicates the calculated transverse strain difference.

Table 3-6: Measured reflected wavelengths and calculated TSD in a non-embedded FBG and several FBGs embedded in the 0°/90° sample.

FBG	$(\lambda_B)_1$ [nm]	$(\lambda_B)_2$ [nm]	TSD [$\mu\varepsilon$]
Non-embedded	1546.29	1546.29	0
FBG-14	1546.68	1545.97	3010
FBG-15	1546.63	1545.97	2830
FBG-16	1546.58	1545.86	3090
FBG-27	1546.82	1546.18	2750

Each FBG has a similar TSD, as expected, with slight variations along the length of the fiber ($\pm 6\%$ of the mean TSD for the 4 FBGs). One particularly interesting phenomenon is that the intensity of each peak is not equal. The concise explanation for this is that the photodetector in the FOID is only capable of measuring light in one polarization direction. Light sent to each FBG from the laser source is unpolarized, so both wavelengths will be reflected. However, by the time the reflected light reaches the photodetector, a portion of both wavelengths must have a component of its polarization aligned with the photodetector's orientation to be detected. A more detailed explanation of this will be given at the end of this section, but this is a very influential feature throughout the 0°/90° results.

An additional question to be answered is “Which peak corresponds to which polarization direction?” Due to geometric symmetries when looking at the microscope image of the

embedded optical fiber, we can assume that the principal strain directions in the cross section of the fiber core are aligned out-of-plane and in-plane to the composite sample. Therefore, one wavelength corresponds to a polarization oriented out-of-plane to the composite, while the other wavelength corresponds to an in-plane polarization direction. We will assign the higher wavelength reflection (λ_1) to the in-plane polarization direction and lower wavelength (λ_2) to out-of-plane polarization with the following reasoning:

Consider the residual strains that develop at the end of the curing cycle shown in Figure 3-7 in the fabrication section. The autoclave pressure applied while the resin cross-links results in a compressive out-of-plane force on the composite and thus, the optical fiber. Additionally, a thermal strain mismatch between the host and composite exists as the sample is cooled after the pressure is released. Fused silica has a smaller thermal expansion coefficient ($\sim 0.5 \mu\epsilon/^\circ C$) compared to the composite ($\sim 26 \mu\epsilon/^\circ C$ out-of-plane and $\sim 10 \mu\epsilon/^\circ C$ in-plane). Upon cooling, the composite will want to contract more than the optical fiber in both out-of-plane and in-plane transverse directions. However, the larger thermal expansion coefficient of the composite's out-of-plane direction will cause a larger out-of-plane compressive force on the fiber compared to in-plane.

Consider now the relationship between strain and reflected wavelengths from Chapter 2 and reiterated here:

$$\boxed{\begin{aligned} \left(\frac{\delta\lambda_B}{\lambda_B}\right)_1 &= \left(1 - \frac{n^2}{2} p_{12}\right) \epsilon_3 - \frac{n^2}{2} (p_{11}\epsilon_1 + p_{12}\epsilon_2) \\ \left(\frac{\delta\lambda_B}{\lambda_B}\right)_2 &= \left(1 - \frac{n^2}{2} p_{12}\right) \epsilon_3 - \frac{n^2}{2} (p_{12}\epsilon_1 + p_{11}\epsilon_2) \end{aligned}} \quad (3.16)$$

The longitudinal strain will contribute equally to the shift of both λ_1 and λ_2 but the transverse strains will not. When a much larger compressive strain is applied in either the 1- or 2-direction, the reflected wavelength associated with that direction will be smaller. For example, $-1000 \mu\epsilon$ in

the 2-direction and a $-500 \mu\epsilon$ in the 1- and 3-directions will result in $\lambda_2 < \lambda_1$. Therefore, because we have previously assigned the higher wavelength the 1-direction, this will be associated with the in-plane direction and the 2-direction (associated with λ_2) will be oriented in the out-of-plane direction.

This logic will be corroborated in the next section where a compressive out-of-plane mechanical load will be applied to the embedded FBGs. If our reasoning that higher out-of-plane compressive strain leads to lower wavelengths is true, then the act of applying out-of-plane compression (and simultaneously in-plane Poisson's expansion) will cause the TSD to become exacerbated and the wavelengths will split farther apart.

3.4.2.3 COMPRESSIVE OPL

Next, the results of a compressive OPL applied by the Instron load frame grips will be analyzed. FBG-27 is centrally located between the grips in the tab region. Figure 3-34 demonstrates the reflected wavelength spectrum of FBG-27 when the grip pump pressure is increased in 500 psi increments from zero to 2.5 ksi . Both peaks shift to higher wavelengths, but not at the same rate; thus, birefringence is increasing. Note that the other tab region is not being gripped and thus, the only form of loading is out-of-plane compression.

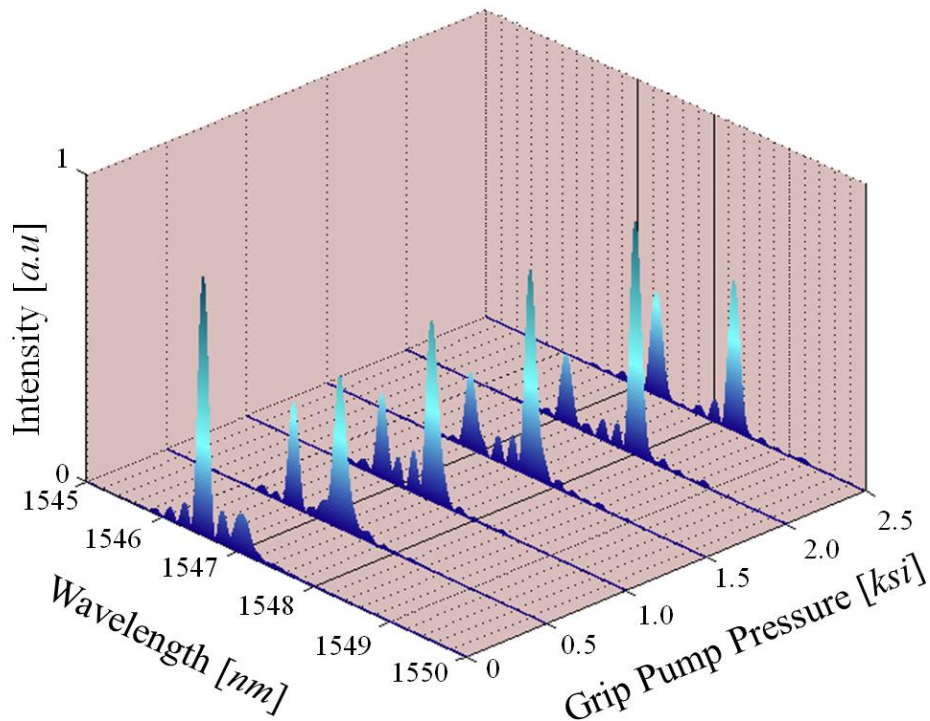


Figure 3-34: Reflected wavelength spectra indicating birefringence increase with OPL conditions in the tab region (FBG-27) of the 0°/90° sample.

When the compressive OPL is applied transverse to the optical fiber, the FBG will experience a Poisson's expansion in the fiber direction. The positive strain in the fiber's longitudinal direction is what causes both peaks to shift to higher wavelengths (i.e. Λ is increasing). However, the load causes compression in one transverse direction to the optical fiber and Poisson's expansion in the other transverse direction. This causes an increase in TSD in the fiber which results in the peaks splitting farther apart. Our reasoning in the previous section appointing the lower wavelength to out-of-plane polarization is correct because the residual TSD becomes exacerbated by the mechanical load.

In a similar fashion as the curing analysis, the TSD can be calculated for each grip pump pressure. Figure 3-35 below show the results. TSD is seen to increase approximately linearly (as expected) with pump pressure. The linear relationship has a correlation coefficient (R) of 0.99.

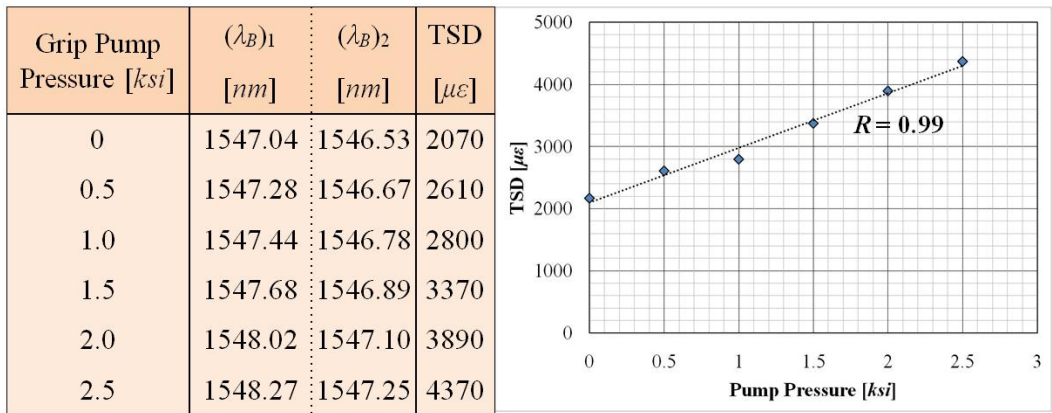


Figure 3-35: Increase in TSD in FBG-27 with the application of OPL.

Note that the TSD shown is calculated using a reference Bragg wavelength of 1546.29, that is, the non-embedded value. This allows us to track the TSD throughout the entire life of the optical fiber from pre-embedment through loading sequences. Now that birefringence has been demonstrated due to curing residual strains and due to out-of-plane compressive mechanical loading, another tensile IPL test will be performed similar to what was shown in Figure 3-32. This time, however, the FOID system will be set to Raw Data mode in order to collect the full reflection spectrum of FBG-15 instead of only the scalar strain value collected in Langley mode.

3.4.2.4 TENSILE IPL

As expected, the lenticular resin rich region affected the residual strain state applied to the optical fiber during curing. This causes an increase in the TSD, thus resulting in birefringence and a split peak reflection spectrum. Embedding FBG strain sensors in the 0°/90° configuration will provide insight into a key issue of whether or not the strain state of the optical fiber is representative of the host strain state. Two plausible hypotheses regarding the effect IPL has on birefringence can be made as follows: (1) The TSD increases because macroscopically, the composite is much stiffer in-plane transverse to the optical fiber (particularly in the plies between which the FBGs are embedded) than in the out-of-plane direction. From this, we can infer that Poisson’s contraction in the two transverse directions due to tensile loading in the optical fiber’s

longitudinal direction will be unequal. (2) The TSD remains the same based upon looking closer at the immediate vicinity of the FBG which includes the resin pocket. The in-plane transverse region surrounding the optical fiber is comprised of solely resin. The presence of a relatively compliant material may cause a “softening” which allows for greater Poisson’s contraction transverse to the optical fiber in-plane. This indicates that the two transverse directions to the optical fiber may be similarly stiff and thus, prevent any change in TSD.

The figure below demonstrates the evolution of the reflected wavelength spectrum of the FBG located between the collocated strain gauges (FBG-15). The stress applied in the 0° in-plane direction increases from 0 to 150 MPa and raw data snapshots were taken every 2.5 MPa; however, increments of 25 MPa are shown in the figure to demonstrate the evolution of the reflected wavelength spectrum during testing. The initial split peaks can be seen at $\lambda_1 = 1546.66$ and $\lambda_2 = 1545.94$ nm and they progress to $\lambda_1 = 1550.17$ and $\lambda_2 = 1549.50$ nm at the maximum load.

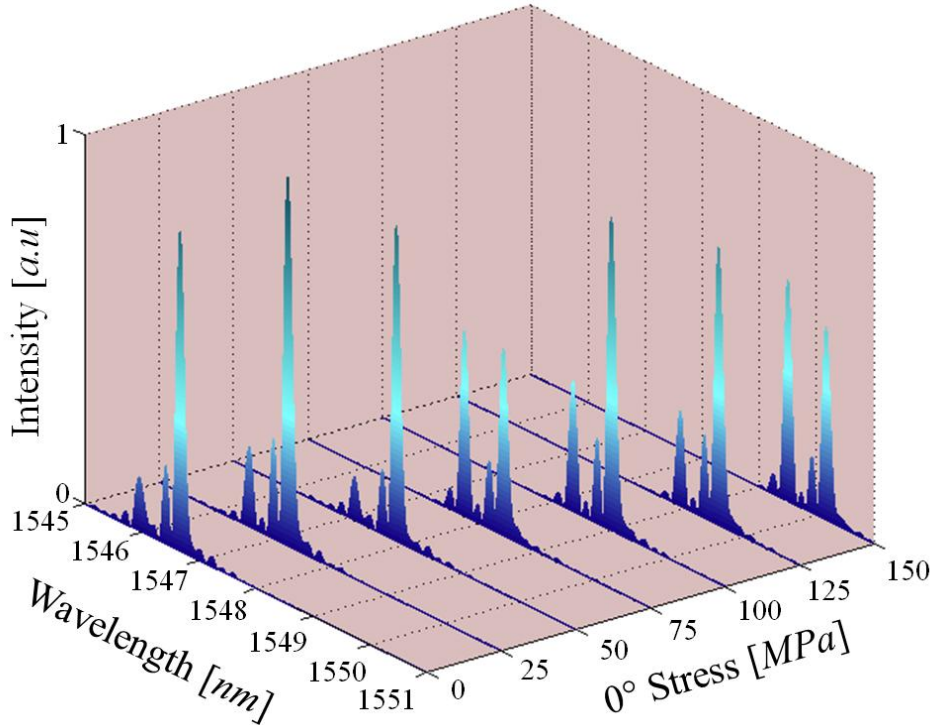


Figure 3-36: Reflected wavelength spectra indicating stagnant birefringence with IPL conditions in the far field region (FBG-15) of the $0^\circ/90^\circ$ sample.

Three important features to note in the figure are (1) due to the longitudinal strain in the fiber direction, both peaks shift to higher wavelengths, (2) both peaks appear to shift equally and indicate a stable TSD, and (3) the relative intensities of the two peaks change during the test. Regarding the first two observations, Figure 3-37 provides the calculated TSD based on the birefringence observed. Note that raw data snapshots were taken during testing every 2.5 MPa; however, only the snapshots corresponding to 25 MPa increments were shown in the wavelength spectra above and in the table within the figure. In contrast, the graph shows TSD data for all of the snapshots. In the plot, the lower horizontal axis represents the composite stress in the loading direction. The upper horizontal axis represents the strain in the loading direction on the surface of the composite as measured by collocated strain gauges. Note that the upper and lower horizontal axes are related by the previously measured Young's modulus for the composite of ~50 GPa.

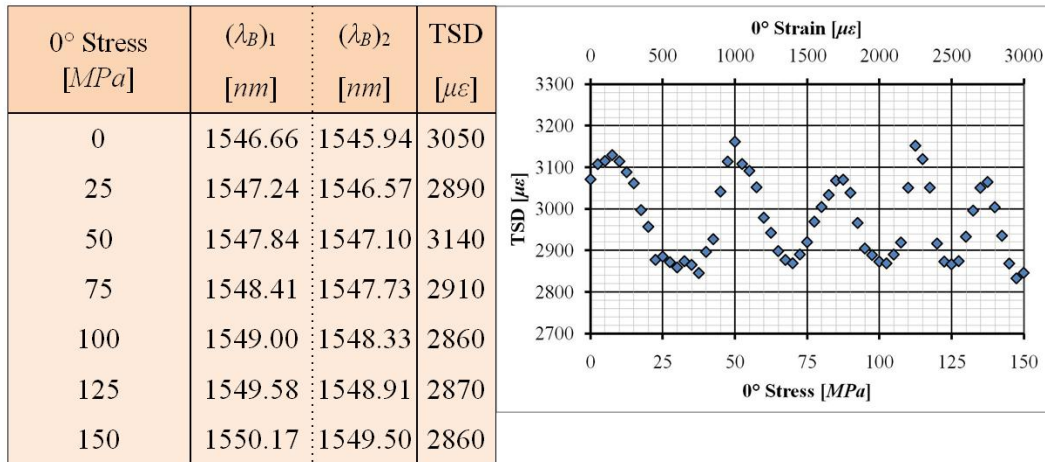


Figure 3-37: Evolution of TSD in FBG-15 during IPL.

While there is some obvious fluctuation in the TSD, it remains within $\pm 6\%$ of the average (2960 $\mu\epsilon$) which indicates that the mechanical load is not causing any change in birefringence. Thus, the source of the birefringence observed during testing is solely due to residual strains. The residual TSD is not exacerbated or diminished due to the in-plane loading. This means that the uniaxial assumption explained in the previous section can be applied to the shifting of the

reflected peaks with strain. Assuming the strain-optic coefficient, p_e , is already known or can be calibrated, the following equation can be used to relate strain to reflected wavelength shifts:

$$\boxed{\frac{\delta\lambda_B}{\lambda_B} = (1 - p_e) \varepsilon_3} \quad (3.17)$$

The third observation regarding the fluctuation in relative peak intensities heavily influences the stress-strain plot shown in Figure 3-32 above and in the IPL retest data shown in Figure 3-38 below. The vertical axis represents the composite stress in the loading direction. Each of the three curves depicting 0° strain is calculated using a different method. The green triangles represent the average of the collocated strain gauges at the 15 *cm* location, the blue circles represent the FBG strain measurement based on a centroid calculation, and the red squares represent the FBG strain measurement based on a peak calculation. This data should be compared with the ESG and FBG strain measurements shown in Figure 3-32. The ESG data remains very linear throughout loading and indicates a 51 *GPa* stiffness as in the previous test. The FBG centroid data shows an initially linear increase followed by a nonlinear departure from agreement with ESG data around the 1000 $\mu\varepsilon$ level which is also similar to previous testing. The FBG peak data is also very linear with the exception of discrete jumps after which the linear trend continues.

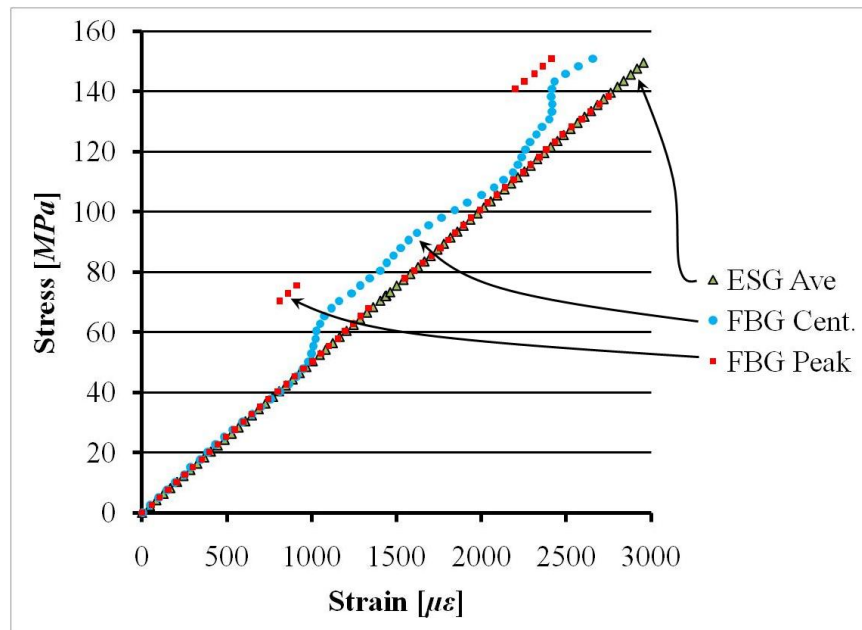


Figure 3-38: Comparison of stress-strain behavior in the 0°/90° composite as measured by ESG and FBG-15.

The origin of the observed nonlinearity is in the FOID system's calculation of the centroid of the reflected wavelength spectrum to assign a λ_B value. Thus, as the two peaks shift equally while simultaneously trading off in intensity, the centroid will gravitate back and forth between whichever peak is dominant. The equal shift in both peaks is also demonstrated in the graph above by the equal, linear slopes of the peak data between discrete jumps in strain data. Figure 3-39 further demonstrates this trend by plotting the reflected wavelength spectrum for FBG-15 at increasing loads during the testing sequence. A blue line marking the centroid and a red line marking the peak location are overlaid on the graphs (with both line colors corresponding to the symbol colors in the stress-strain plot of Figure 3-38). Note that as both peaks shift to higher wavelengths, the blue line traverses back and forth between the two peaks as they trade off in intensity while the red line tracks with and jumps to the dominant peak. The red line can be seen to mostly be centered on the higher-wavelength peak, but jumps for short amounts of time during testing to the shorter wavelengths. This is indicated in the far right plots ($\sigma = 70$ and 150 MPa) on the upper and lower rows of graphs in the figure below and in the discrete jumps from right to left in the red square data in the stress-strain plot above.

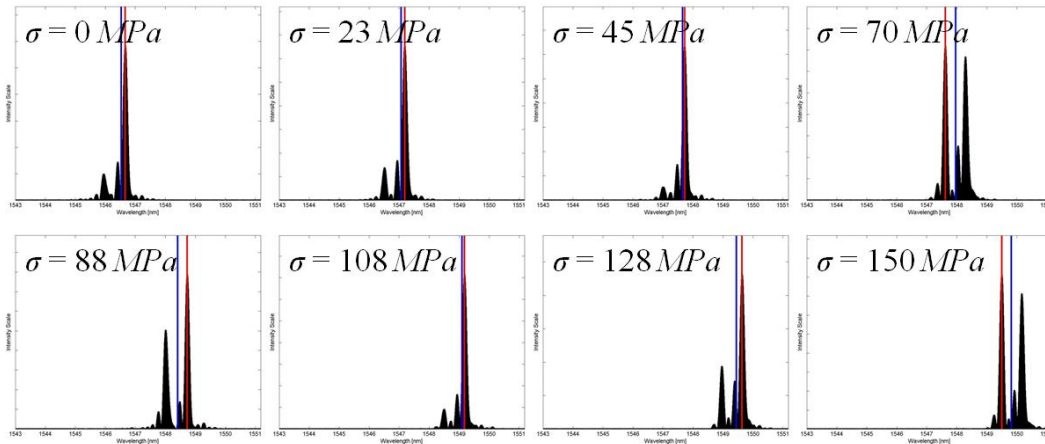


Figure 3-39: Behavior of the peak and centroid of the reflected wavelength spectrum of FBG-15 during IPL.

This nearly concludes the results of the tensile in-plane mechanical load test. We have seen that there is no additional transverse strain difference in the optical fiber due to loading. In the next section, the effects of loading past the point of cross-ply cracking will be shown.

3.4.2.5 CROSS-PLY CRACKING

When the composite is loaded up to a high strain level (thousands of microstrain) the matrix in the plies whose structural fibers are oriented perpendicular to the load may crack. The surface normal to the crack plane will be parallel to the load direction and the crack will propagate through the composite parallel to the structural fibers. The crack terminates at the interface with plies whose structural fibers are oriented more closely with the loading direction (e.g. at the $90^\circ/+45^\circ$ layer interface). This phenomenon is called cross-ply cracking.

The presence of the cracks in layers which are not strong in the loading direction to begin with (i.e. they do not contribute much to the stiffness in the direction of the load which induces cracking) means that the overall stiffness of the composite is not significantly reduced with the advent of cross-ply cracking. The optical fiber in the $0^\circ/90^\circ$ sample is embedded between layers in which cross-ply cracking occurs. This drastically changes the measurement capabilities of the embedded FBGs. Before demonstrating the effects on the FBG reflection signal, the cross-ply

cracks themselves are shown in Figure 3-40. The top picture in the figure is of the $0^\circ/90^\circ$ composite sample after tensile tests up to $6000 \mu\epsilon$. The orange outlined area is a magnified image showing the surface-mounted strain gauge along with the length scale. The blue outlined area is the view under an optical microscope of the side of the composite after polishing. Polishing was performed with a sequence of finer and finer grit sandpaper followed by rubbing a liquid with floating, micron-size, abrasive particles on the surface. Eight cracks are highlighted with red arrows. The bottom images in the figure represent a sequence of increasing magnification in order to better demonstrate the appearance of a cross-ply crack. In the highest magnification (100x), the individual carbon fibers ($\sim 5 \mu m$ in diameter) can be seen. These cracks propagate all the way through the composite, intersecting the embedded optical fiber on its way to the opposite side of the sample.

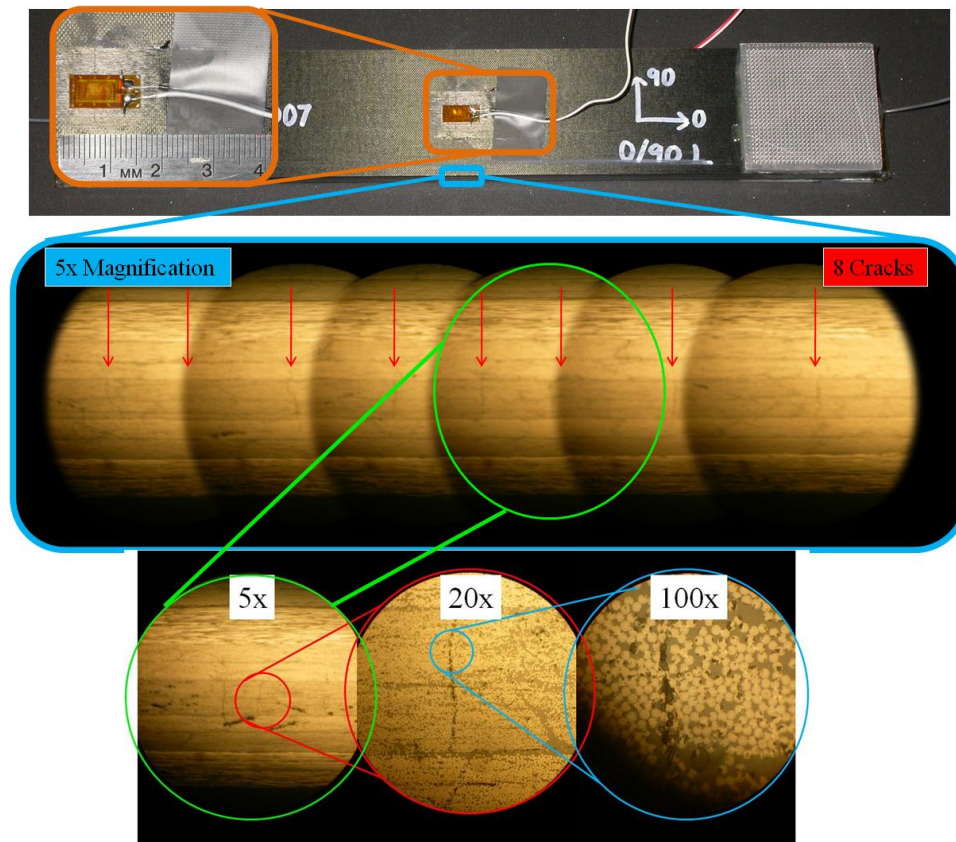


Figure 3-40: Optical microscope images of cross-ply cracks in the $0^\circ/90^\circ$ sample after loads up to $6000 \mu\epsilon$ were applied.

As is common in cross-ply cracking, the cracks are fairly evenly spaced by a distance of approximately three ply widths. A total of 31 cracks were counted spanning a 4 cm distance along the side face of the composite sample. The result is approximately 3 or 4 cracks crossing each 0.5 cm long FBG. Each crack causes a stress concentration which, as mentioned in the literature review, has been seen to cause chirping in the FBG reflection spectrum. The 0°/90° sample testing results so far showed no signs of chirping up to 3000 $\mu\epsilon$ which indicates no cross-ply cracks had yet formed. When the reflected wavelength spectrum is shown at higher strain values, a sudden change occurs as depicted in Figure 3-41. The first three plots below are the reflection spectra for FBG-15 (the same FBG whose reflection spectra appear in previous figures) during the same mechanical load test while the fourth plot is after the load has been released. The sensor responds well up to $\sim 3500 \mu\epsilon$ but above 3750 $\mu\epsilon$, more peaks appear in addition to the two original peaks. This is due to the stress concentrations and the rapidly changing strain gradients across the length of the fiber. The gradient causes the reflected wavelength to vary rapidly along the length of the FBG. Upon unloading to 0 $\mu\epsilon$, the chirping remains and the sensor can no longer perform adequately.

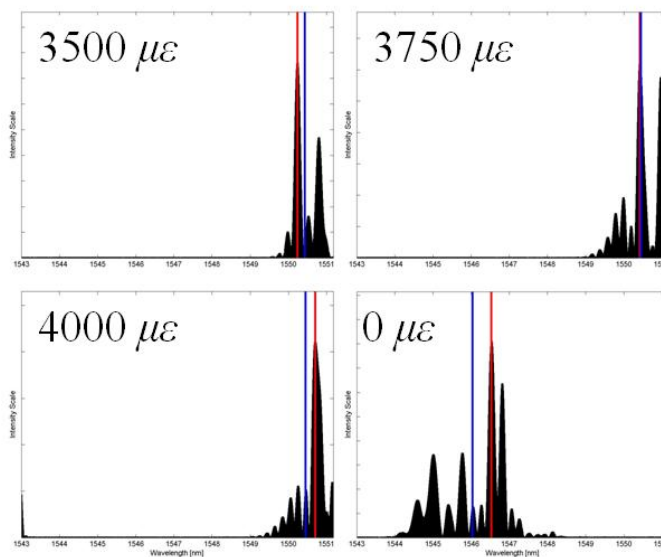


Figure 3-41: Effects of cross-ply cracking and nonuniform strain on the reflected wavelength spectrum of FBG-15 during IPL.

3.4.2.6 CONCLUDING REMARKS

This concludes testing performed on the $0^\circ/90^\circ$ sample. We started this section off with the introduction of a problem which entailed a highly nonlinear response of the FBG to longitudinal strain. In order to understand the behavior occurring, the steps which lead to calculating the measured values of strain were retraced and analyzed to find a plausible explanation. This was done by looking at the raw data to perform a FFT, windowing procedure, and IFFT to witness the wavelength reflection spectra for the embedded FBGs. This spectrum is not recorded or displayed by the FOID system in Langley mode when the original data from Figure 3-32 was collected. Birefringence was found to be present due to the curing step of the composite fabrication. The result was the initial single peak reflection splitting into two peaks. This birefringence was the result of a transverse strain difference which occurred during fabrication, but was seen to remain stable during IPL testing. This means that the uniaxial strain assumption could be applied to the FBG and if each peak is tracked individually, the wavelength shifts can be directly related to mechanical strain in the composite.

In order to utilize embedded FBGs oriented orthogonally to adjacent structural fibers, some form of action must be taken to adjust the FOID system. The trade-off in peak intensity in when birefringence is present throws off the strain sensing abilities of the interrogation system. One option to counteract this is to track an individual peak rather than the centroid; however, if one peak becomes so dominant that the other disappears into noise, this can throw off the accuracy of the sensor. Another option (undertaken by NASA) is to set up photodetectors so that the relative intensity of the peaks remains constant. As explained earlier in this section, the photodetectors are designed to measure one polarization direction. Thus, if the light reflecting from the polarization associated with one of the two wavelengths is rotated as it propagates through the lead-in fiber to an angle orthogonal to the photodetector, then this wavelength will not be detected. NASA has altered the system to measure more than one polarization direction and reconstruct the individual measurements so that the peaks will remain constant in amplitude. Under such circumstances, the centroid calculation would be valid because it would remain

stable between the two reflected wavelengths as they shift equally (in the case of uniaxial strain) rather than drifting back and forth as in the data in this research.

The other lesson learned is the limitation of using embedded FBGs when cross-ply cracking is a factor. The large stress concentrations due to cross-ply cracking cause chirping in the reflection signal and nullify the effectiveness of the sensor. Therefore, FBGs embedded perpendicular to adjacent structural fibers can only be loaded up to strain levels lower than that which generates cross-ply cracking.

3.4.3 90°/90° Sample

This section describes testing of two 90°/90° samples. In similar fashion with the 0°/90° results, a preliminary stress-strain result will be shown in order to introduce an inconsistency to be explained. The phenomena observed will also be explored in a similar fashion, looking at curing residual strains, compressive OPL, and tensile IPL. This work will then be supplemented with finite element models in the following section to provide insight into the photoelastic phenomena occurring and the transfer of strain from the composite host to the embedded FBG.

3.4.3.1 PROBLEM INTRODUCTION

An initial mechanical tensile load test was performed on the sample with the results plotted in the strain profile of Figure 3-42 below. The vertical axis represents strain in the 90° direction (parallel to the embedded optical fiber and perpendicular to the load). The horizontal axis represents the length along the optical fiber with values less than zero corresponding to locations outside of the composite and values greater than zero inside the composite (note the 50mm thickness as described in the experimental setup section). Each set of data with a different type of symbol and color combination corresponds to a different load level. The white circles represent the average strain from the two collocated strain gauges located at the center of the composite (i.e. the 25 mm mark).

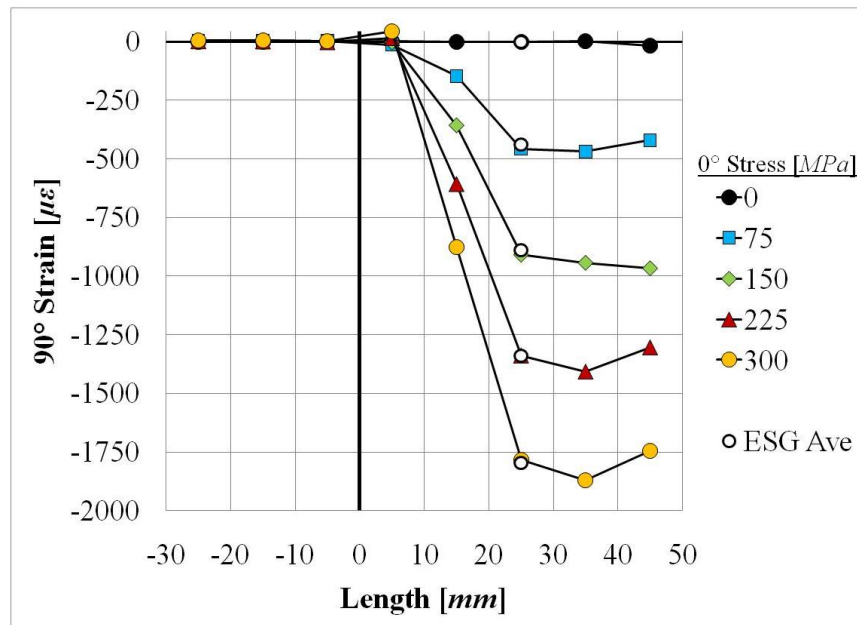


Figure 3-42: Strain profile of a 90°/90° sample under IPL.

As expected, the FBGs outside the composite (in the length region <0 mm) do not respond when a load is applied because no strain is transferred. The first and part of the second FBG (locations 5 and 15 mm) are within the Teflon tube which was partly inserted into the composite in order to protect the fiber optic egress location. This completely inhibits strain transfer in the first FBG and partially inhibits the second. The third and fourth FBGs behave very well while the fifth FBG appears to be somewhat erratic in strain values relative to the fourth FBG which is most likely due to edge effects. There is excellent agreement between the third FBG and the average of the collocated strain gauges in the plot. This is very encouraging for the prospect of utilizing FBGs as a reliable uniaxial strain sensor when loaded laterally in-plane. This agreement is further corroborated in the following strain-strain plot of Figure 3-43 below which takes a look at more strain measurements taken during the same mechanical load test for the FBG and collocated strain gauges at the center of the sample (at the 25 mm mark). The vertical axis represents strain in the 90° direction (parallel to the optical fiber) and the horizontal axis represents strain in the 0° direction (parallel to loading). The black triangles and blue circles

depict the average strain measured by the two collocated FBGs and the FBG between them, respectively.

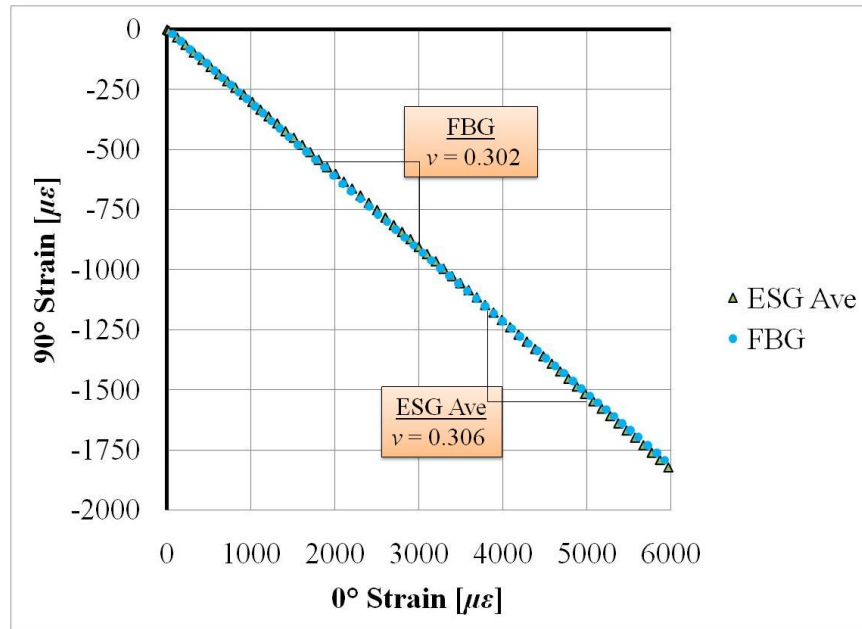


Figure 3-43: Strain-strain plot for the ESG and the FBG embedded between the collocated strain gauges.

The negative of the slopes of the curves above represent the Poisson's ratio with the ESG average and FBG indicating values of 0.306 and 0.302 respectively. The two data sets agree very well (within 1.4 %) which indicates a properly functioning uniaxial strain gauge embedded within the composite. At first glance, one could conclude that the sensor is ready to move on to a more advanced level of testing and that FBGs embedded parallel to adjacent structural fibers will behave as a uniaxial strain sensor when oriented perpendicular to the applied load. However, when birefringence is considered, an inconsistency is apparent. It is expected that the applied tensile load will cause a positive strain in the in-plane direction transverse to the optical fiber and a negative, compressive strain due to Poisson's contraction in the optical fiber's out-of-plane transverse direction. A positive strain in one transverse direction and a negative strain in the other would intuitively cause a TSD which results in split peaks and the possibility of a nonlinear strain response as in the 0°/90° sample.

The objective of this section of composite embedded FBG research is to understand analytically and experimentally why the FBG results above match so well with the ESG data when intuitively, the uniaxial strain assumption is invalid. In a fashion similar to the $0^\circ/90^\circ$ sample, the effects of curing on the reflected wavelength spectrum will be examined and followed by compressive OPL and tensile IPL testing results. Two major differences are that (1) two $90^\circ/90^\circ$ samples of differing load histories will be simultaneously examined and (2) finite element models will be analyzed in order to gain further insight into the physical phenomena at play in the next section.

3.4.3.2 CURING EFFECTS

The effects of residual strain on the reflected wavelength spectrum of FBGs centrally located within two $90^\circ/90^\circ$ samples with different load histories will be described first. The results in Figure 3-42 and Figure 3-43 are for a composite sample that had previously undergone a mechanical test which strained the composite sample to $6000 \mu\epsilon$ in the load direction. This sample will be referred to as $90^\circ/90^\circ$ a. We will compare this to a sample which has undergone mechanical testing to a strain level of only $1500 \mu\epsilon$, which will be referred to as $90^\circ/90^\circ$ b. Figure 3-44 below demonstrates the reflected wavelength spectrum of four different FBGs. The four FBGs are (1) a non-embedded FBG from the same spool as the embedded optical fiber, (2) FBG-15 (out of 30) from the $0^\circ/90^\circ$ sample, (3) the centrally located FBG-3 (out of 5) between the collocated strain gauges in the $90^\circ/90^\circ$ a sample and (4) the centrally located FBG-3 (out of 5) in the $90^\circ/90^\circ$ b sample. The non-embedded and $0^\circ/90^\circ$ FBGs are for comparison purposes.

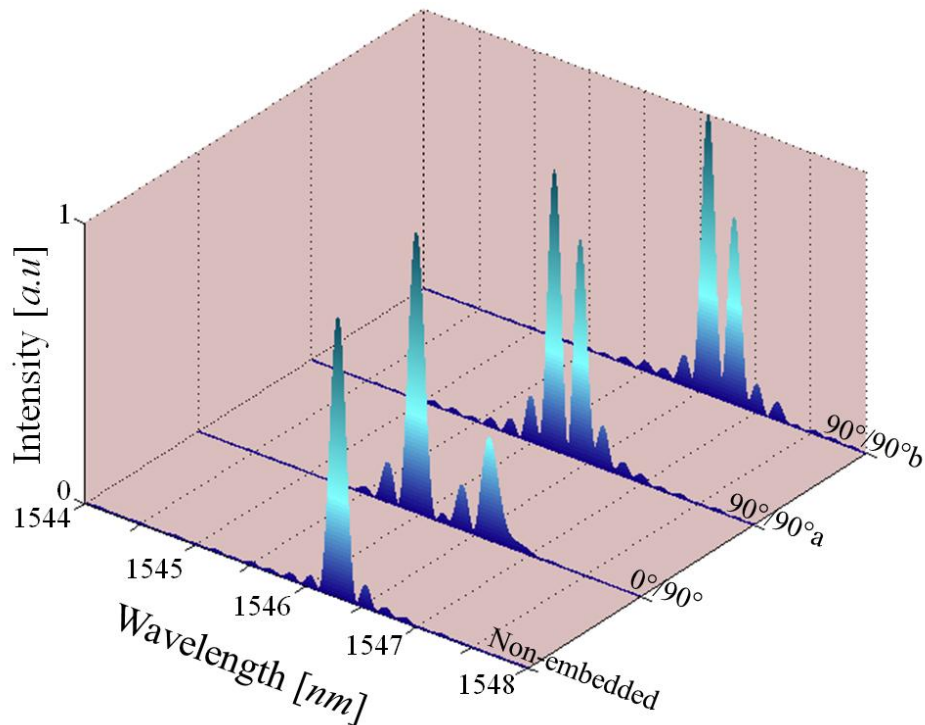


Figure 3-44: Reflected wavelength spectra of a non-embedded, embedded $0^\circ/90^\circ$, and two embedded $90^\circ/90^\circ$ FBGs under no mechanical load.

The $90^\circ/90^\circ$ FBGs show evidence of birefringence just as the $0^\circ/90^\circ$ sample, but to a much smaller degree. This indicates that the $0^\circ/90^\circ$ has a higher residual TSD which can be explained with the lenticular resin rich pockets. The absence of such large pockets around the $90^\circ/90^\circ$ samples results in a much smaller residual TSD. Note that the two $90^\circ/90^\circ$ samples display similar birefringence but are not at the same wavelengths. This indicates that both $90^\circ/90^\circ$ FBGs experience similar residual TSDs, but the $90^\circ/90^\circ$ b sample experiences a larger longitudinal strain; thus, both peaks have shifted to higher wavelengths than in the $90^\circ/90^\circ$ a sample. Note that these reflection spectra were taken after both FBGs were mechanically tested, so it is unknown whether the difference in $90^\circ/90^\circ$ longitudinal strains is due to residual strain only or due to the influence of mechanical load testing. Table 3-7 below demonstrates the reflected wavelengths in addition to the calculated TSD for each FBG.

Table 3-7: Measured reflected wavelengths and calculated TSD in a non-embedded FBG and FBGs embedded in either the 0°/90° or 90°/90° samples

FBG	$(\lambda_B)_1$ [nm]	$(\lambda_B)_2$ [nm]	TSD [$\mu\epsilon$]
Non-embedded	1546.29	1546.29	0
0°/90°	1546.63	1545.97	2830
90°/90° ^a	1546.43	1546.20	1010
90°/90° ^b	1546.81	1546.58	980

Despite the 90°/90°^b FBG reflecting at higher wavelengths, both 90°/90° samples have TSDs that are within 3 % of each other. This analysis so far tells us that despite lacking a lenticular resin pocket, embedding optical fibers parallel to structural fibers can still result in a residual TSD; however, the birefringence will be far less pronounced. The observations so far do not explain why such good agreement was seen in the in-plane tensile mechanical loading of the 90°/90°^a sample, but does provide some insight into the physical phenomena influencing the reflection spectra of embedded FBGs. The next step in the analysis is to apply an out-of-plane compressive load to see whether or not the peaks split farther apart.

3.4.3.3 COMPRESSIVE OPL

An out-of-plane compressive load was applied to the 90°/90° composite samples with the Instron load frame grips in the region of the embedded optical fiber. In order to protect the composite, the aluminum tabs were moved from their locations previously indicated for in-plane tensile loading. Figure 3-45 below demonstrates the sample configuration. Aluminum tabs were placed centrally above and below the optical fiber. This allows for a uniform compressive stress field in the out-of-plane direction in the vicinity of the optical fiber.

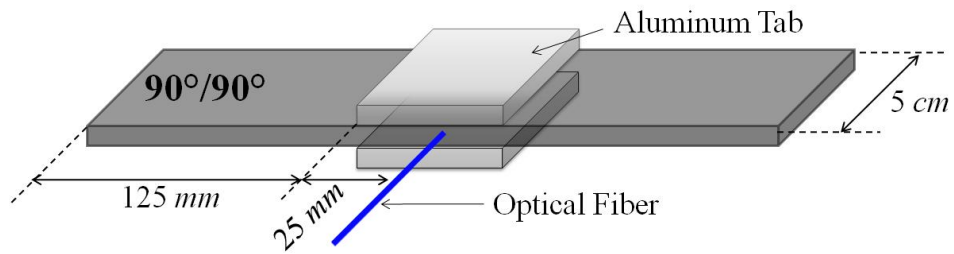


Figure 3-45: Sample configuration for application of OPL.

The response of the reflected wavelength spectra of the two 90°/90° FBGs considered in Figure 3-44 when applying an increasing load are displayed in Figure 3-46 below. Part (a) of the figure plots the results of the 90°/90°^a FBG while part (b) shows that of the 90°/90°^b FBG. The reflected wavelength spectrum is plotted for grip pump pressures between 0 and 2.5 *ksi* in 0.5 *ksi* increments.

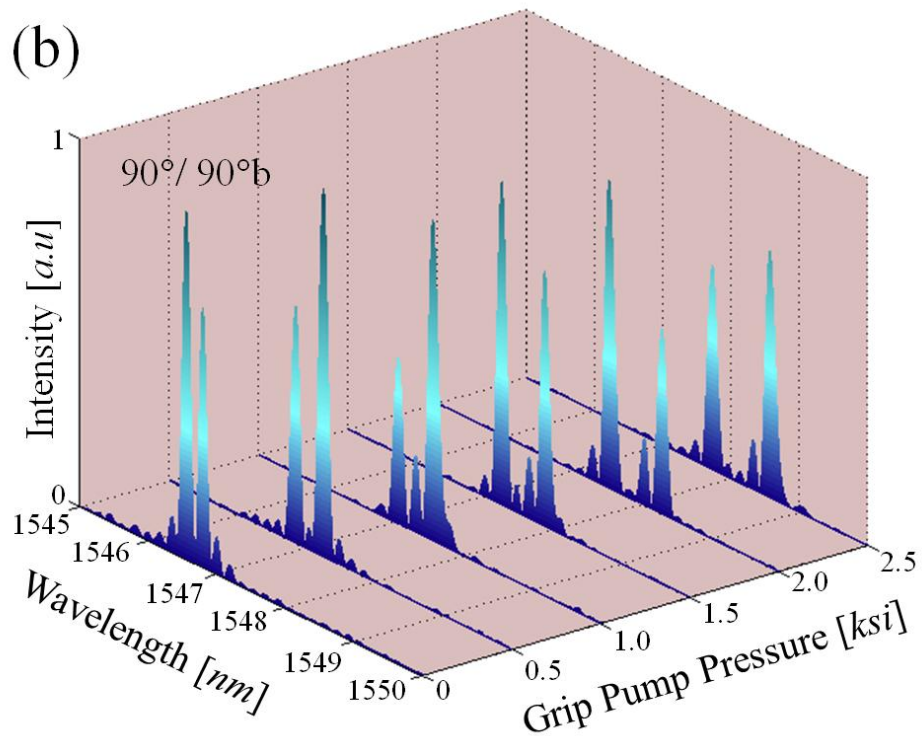
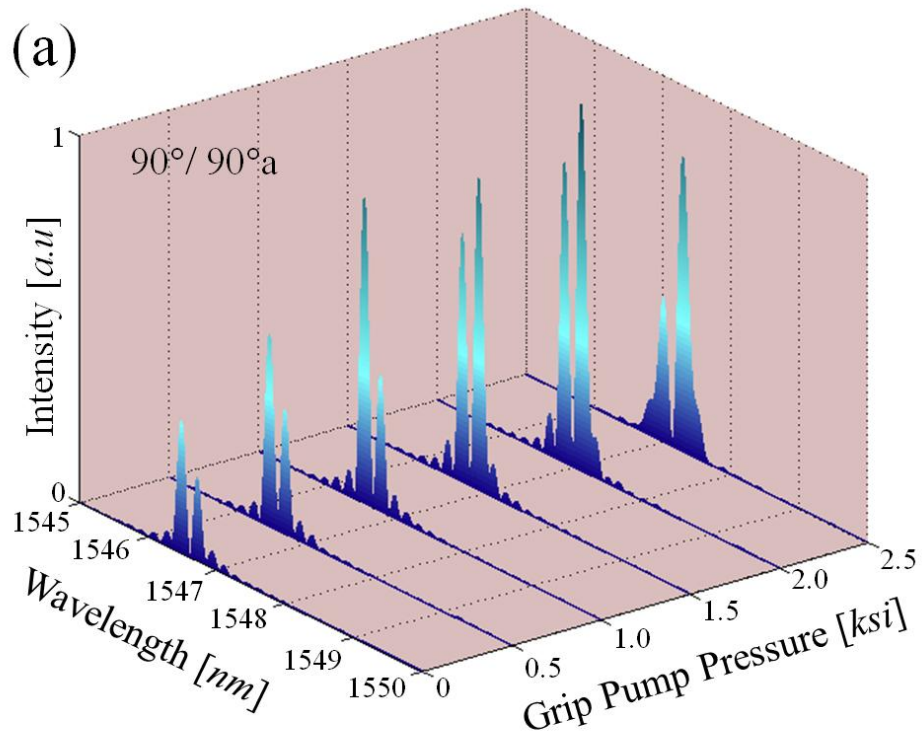


Figure 3-46: Evolution of the reflected wavelength spectra under compressive OPL for FBG-3 in the 90°/90°a and 90°/90°b samples.

Due to the compressive OPL, a Poisson's expansion in-plane in the composite will occur. This causes a longitudinal extension in the optical fiber, thus shifting both peaks to higher wavelengths in both the 90°/90°a and 90°/90°b samples. A noticeable difference in the two samples is that the peaks reflected by the FBG in the 90°/90°a sample do not split farther apart whereas those in the 90°/90°b sample do separate. Figure 3-47 demonstrates the increase in TSD with increasing pump pressure. Both samples start out with very similar TSD values at zero pump pressure. As the pump pressure increases from 0 to 2.5 *ksi*, the 90°/90°a sample's TSD essentially remains flat whereas the 90°/90°b sample's TSD increases approximately linearly. The 90°/90°b response is similar to the out-of-plane compression response of the 0°/90° sample but to a slightly larger degree (a TSD increase of 2590 $\mu\epsilon$ in the 90°/90°b sample compared to an increase of 2300 $\mu\epsilon$ in the 0°/90° sample).

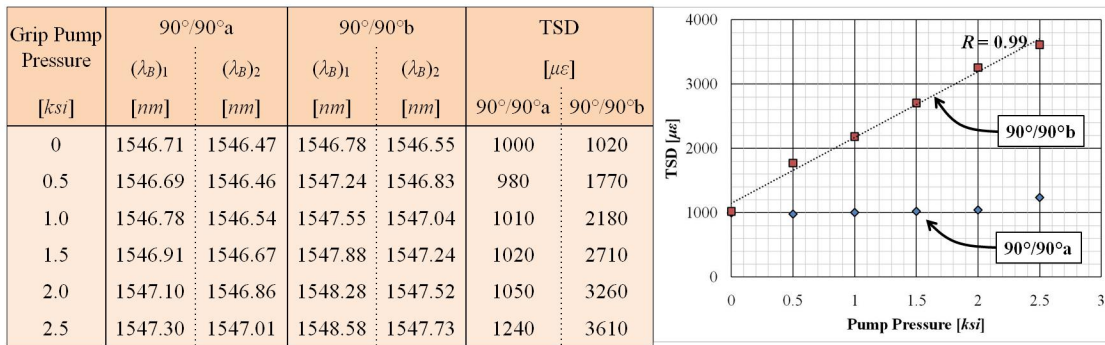


Figure 3-47: Change in TSD for FBG-3 in the 90°/90°a and 90°/90°b samples under OPL.

The out-of-plane compression testing has resulted in one sample which has been heavily loaded to 6000 $\mu\epsilon$ responding differently to a sample loaded only to 1500 $\mu\epsilon$. This evidence corroborates what was seen Figure 3-42 and Figure 3-43 by demonstrating the ability of the FBG in the 90°/90°a sample (heavily loaded) to behave as a uniaxial strain sensor. The next piece of evidence that will be gathered to further understand the response of the embedded FBGs in the 90°/90° samples will be to perform a tensile IPL test as was done previously done. This time, the reflected wavelength spectra will be monitored by setting the FOID system to Raw Data mode.

3.4.3.4 TENSILE IPL

With the aluminum tabs back in their original position at the ends of the composite samples and way from the embedded optical fiber, tensile IPL test was carried out while monitoring the reflected wavelength spectrum of FBG-3 in the 90°/90°a and 90°/90°b samples. The results are shown in the Figure 3-48. The 90°/90°a and 90°/90°b samples were strained in the loading (0°) direction to 3000 $\mu\epsilon$ and 1500 $\mu\epsilon$ respectively. This equates to 150 MPa and 75 MPa of stress in the loading direction (lower horizontal axis), or nearly -900 $\mu\epsilon$ and -450 $\mu\epsilon$ in the optical fiber (90°) direction (upper horizontal axis) respectively. The left vertical axis displays the development of TSD as the loading increases while the right vertical axis displays the degree of birefringence associated with the left axis TSD. The blue diamonds represent data for the 90°/90°a sample and yellow squares for the 90°/90°b sample.

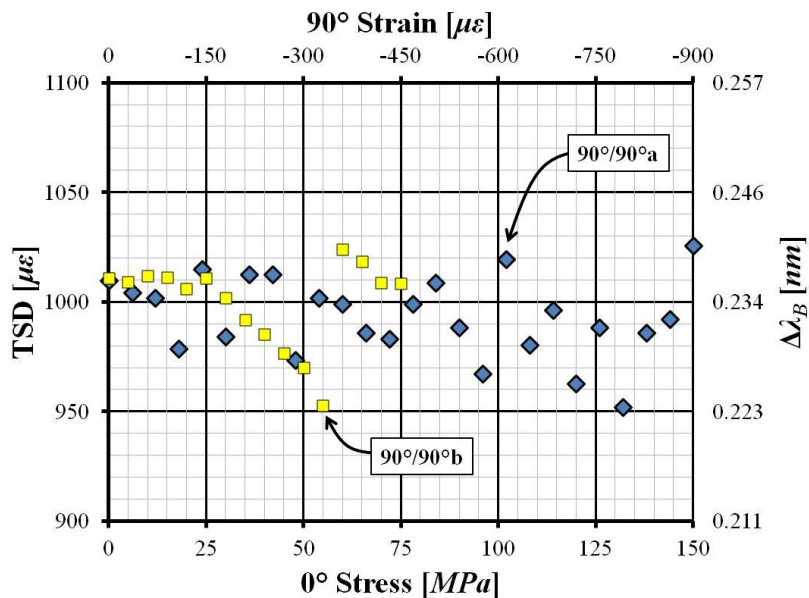


Figure 3-48: Evolution of TSD and birefringence during IPL for FBG-3 in the 90°/90°a and 90°/90°b samples.

The data sets indicate that no increase or decrease in TSD develops in FBG-3 of either composite specimen during loading. This means that both the 90°/90°a and 90°/90°b embedded FBGs behave as a uniaxial strain gauge because the current birefringence is due solely to a

residual TSD developed during curing. This TSD does not significantly change with mechanical loading. This concludes the mechanical load testing performed to collect experimental evidence to help understand the behavior of the embedded FBGs in a $90^\circ/90^\circ$ composite sample. As in the $0^\circ/90^\circ$ sample, the sides of the composite specimens will be polished and observed under an optical microscope to determine if there are any cross-ply cracks.

3.4.3.5 CROSS-PLY CRACKING

The same process of successively sanding the side of the composite sample with finer and finer grit sand paper described for the $0^\circ/90^\circ$ sample was performed again for both $90^\circ/90^\circ$ samples here. In the $0^\circ/90^\circ$ sample, the optical fiber does not intersect the side of the specimen being polished but in the $90^\circ/90^\circ$ samples, the end of the optical fiber will be seen. Figure 3-49 shows four images of the two composite specimens under consideration. The top and bottom rows correspond to the $90^\circ/90^\circ$ a and $90^\circ/90^\circ$ b specimens, respectively. The left column corresponds to a lower microscope magnification while the right column corresponds to a higher magnification. The image is taken at the 15 cm point in the middle of the specimen's side where the optical fiber is embedded. Scratches, resin pockets, and a cross-ply crack are identified.

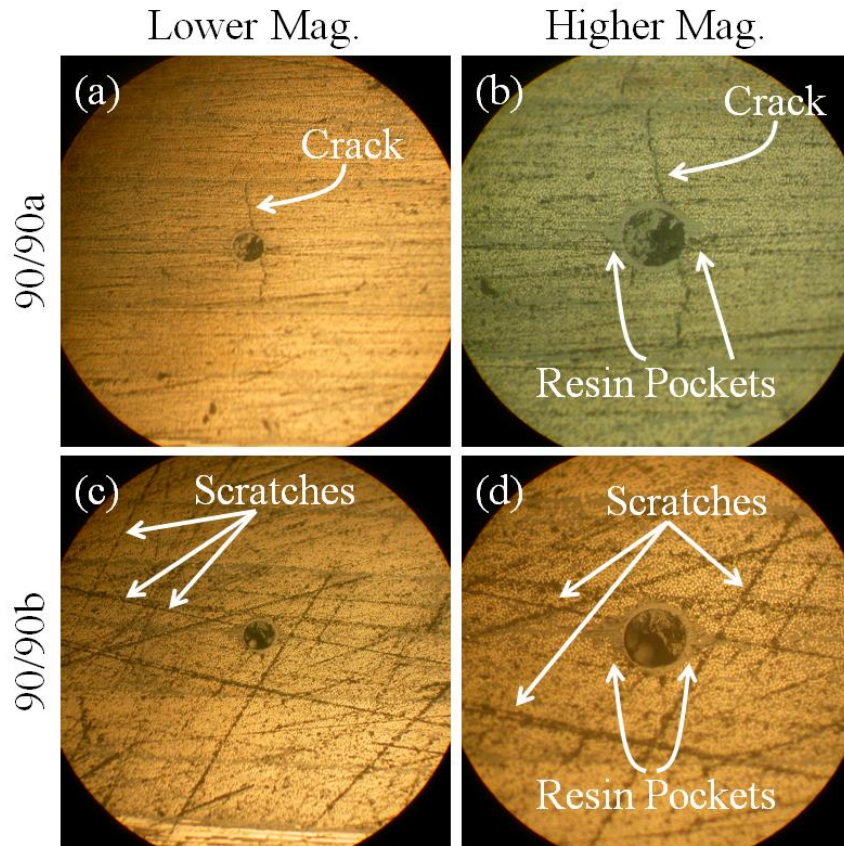


Figure 3-49: Optical microscope images of the region near the optical fibers embedded in the 90°/90° samples.

The optical fiber (with a diameter of $127 \mu\text{m}$) is easily shown along with the $7 \mu\text{m}$ thick polyimide coating. It is clearly seen that a cross-ply crack exists in the 90°/90°a sample which intersects the optical fiber. In the 90°/90°b sample, scratches are seen because the polishing process was not as clean as with the 90°/90°a and 0°/90° samples; however, there is clearly no cross-ply crack. This is consistent with the load histories of the samples with the 0°/90° and 90°/90°a samples being strained up to $6000 \mu\epsilon$ and the 90°/90°b sample only being loaded up to $1500 \mu\epsilon$.

The presence of the cross-ply crack explains why no increase in birefringence was seen in either of the mechanical load tests. Figure 3-50 illustrates why, during IPL and OPL tests, the increasing TSD in the composite is not transferred to the optical fiber. For both loads, the composite will expand in-plane transverse to the optical fiber. However, this strain will not be

sufficiently transferred to the optical fiber because at the crack location, the composite is not stretching; rather, the crack is splitting farther apart. The fiber is therefore effectively surface-mounted onto one of the crack faces. As described earlier, the only direction in which strain is fully transferred from a host to a surface-mounted FBG is in the longitudinal direction of the fiber. This means that, in OPL testing, the main source of strain in the optical fiber is the in-plane Poisson's expansion parallel to the optical fiber. Conversely, for the IPL test, the main source of strain in the optical fiber is in-plane Poisson's compression parallel to the fiber. Hence, the 90°/90°a experimental results make sense that both peaks shift to larger wavelengths in the OPL compression and to smaller wavelengths in the IPL. Additionally, the peaks shift at equal rates as loading increases.

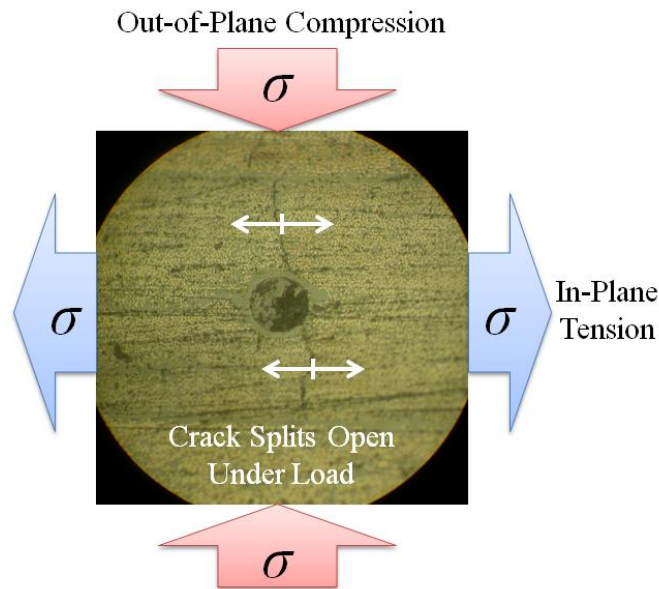


Figure 3-50: Opening of the cross-ply crack during IPL and OPL conditions which effectively creates a FBG surface-mounted to the crack plane.

The 90°/90°b results are more difficult to interpret. Under out-of-plane compression, the TSD was seen to significantly increase which was consistent with the out-of-plane load applied to the 0°/90° sample. However, the in-plane tension did not result in a significant change in TSD. The 90°/90°a sample was explained because the fiber was effectively surface-mounted to a crack

plane. However, the $90^\circ/90^\circ_b$ sample appears to be rigidly attached to the composite host. Figure 3-51 below summarizes these results.

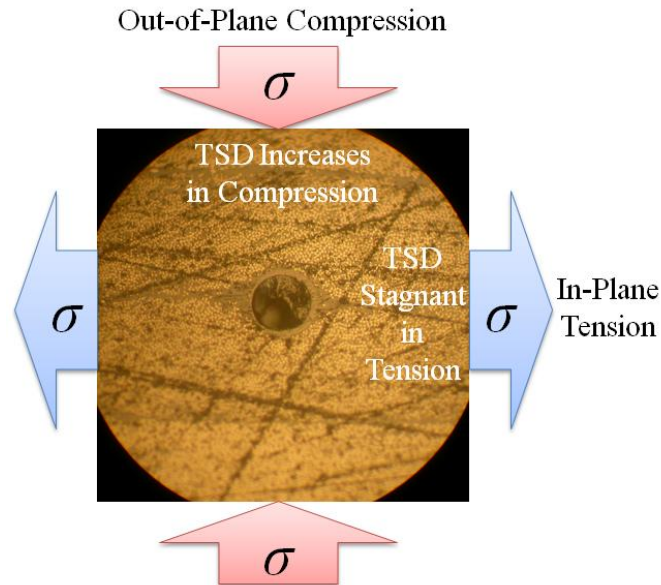


Figure 3-51: Summary of the experimental results observed in IPL and OPL testing.

The reasons for this behavior is found in the geometry of the optical fiber, the local stiffness of the composite in the region of the fiber relative to the macroscopic stiffness of the composite lay-up, and the occurrence of de-adhesion between the embedded fiber and the host. This will become evident in the next section describing finite element analysis (FEA) results.

3.4.4 Concluding Remarks

This concludes the experimental evidence gathered for understanding the behavior of FBGs embedded in composite materials. In the $0^\circ/0^\circ$ sample, excellent agreement was seen between the surface-mounted strain gauges and the embedded FBGs in the far field region. It was established that this type of embedment configuration and load orientation provides uniaxial strain in the far field. Near the tab region, however, the uniaxial assumption breaks down due to the introduction of a TSD from grip pressure.

The $0^\circ/90^\circ$ result fared equally well up to loads inducing a strain value of $3000 \mu\epsilon$. Despite the fact that a rather large residual TSD developed during curing of the composite, subsequent IPL was not seen to exacerbate the birefringence. When loaded to strain levels which induce cross-ply cracking, however, nonuniform strain was seen along the length of the FBG which caused a messy and unreliable reflected wavelength spectrum. Below strains which induce cross-ply cracks, the initial nonlinear results were explained by the varying relative intensity of the split peaks during testing. This problem has been resolved by altering the measurement system in such a way that the peaks will remain constant in intensity relative to one another and the centroid will no longer bounce back and forth between the two peaks. The conclusion of this section is that for in-plane loading in the direction of the optical fiber, changing the orientation of the adjacent structural fibers relative to the direction of the optical fiber will not cause any additional birefringence. The residual TSD from curing may be altered, but the TSD from mechanical loads will not. Note that this conclusion is relevant when cross-ply cracking is not present. Cross-ply cracking will nullify the potential use of a FBG as an effective strain sensor when those cracks run across an embedded optical fiber to create stress concentrations and nonuniform strain. The increase in birefringence during OPL testing indicates that this type of loading should be avoided in any applications of this embedment configuration because the increased TSD breaks down the uniaxial assumption.

The $90^\circ/90^\circ$ samples displayed similar results in the role of residual TSD on the effectiveness of the embedded FBGs as uniaxial strain sensors. As long as the individual peaks can remain at constant relative intensity, birefringence that develops due to residual curing strains will not preclude the FBG from behaving as a uniaxial strain gauge during subsequent mechanical loading. Additionally, the $90^\circ/90^\circ$ results are interesting in that a cross-ply crack was seen to cause a FBG to become immune to any TSD developed in the composite regardless of the direction of loading (IPL or OPL). This implies that a cross-ply crack (which does not significantly affect the structural performance of the composite coupon) aids in the creation of a

well behaved uniaxial strain sensor. This is a unique observation which has not been reported in the literature until Emmons et al. 2009 [197].

The mechanical load test results for the $90^\circ/90^\circ$ sample were quite interesting in that compressive OPL induced further birefringence but tensile IPL did not. The reason for this is unclear based on just the experimental evidence. Thus, a finite element study has been carried out to help understand the transfer of strain from a composite host to an embedded FBG in the $90^\circ/90^\circ$ configuration. The FEA results are presented next.

3.5 Finite Element Analysis Results

The purpose of this section is to supplement the experimental results with theoretical calculations in order to help explain the phenomena observed in the tensile IPL and the compressive OPL tests of the $90^\circ/90^\circ$ samples. Additionally, the FEA will allow for the manipulation of certain embedment parameters, specifically the coating thickness and the size of the lenticular resin rich pocket, in order to determine whether these factors can mitigate the TSD and therefore minimize birefringence.

This section describes the finite element results. Introductory results for a 3-D model of a $90^\circ/90^\circ$ composite sample with an embedded optical fiber will be given. This will introduce the effects of strain transfer from the composite to the optical fiber being dependent upon direction. After this, the use of a 2-D model in the place of a 3-D model will be validated. Subsequently, some parameters of the embedded fiber will be manipulated in order to determine the effects on birefringence. After this, the effect of de-adhesion and a cross-ply crack on TSD will be described. Lastly, these FEA results will be compared with the experimentally obtained results in order to determine whether or not the experimentally observed phenomena are fully or partially explained.

3.5.1 Strain Transfer

This portion of the FEA results compares the strain experienced by the composite versus that by the optical fiber when embedded in a $90^\circ/90^\circ$ sample. This will provide a baseline for the amount of birefringence that could be expected from a pristine sample which is experimentally tested in both IPL and OPL conditions. Figure 3-52 below demonstrates the strain in the loading direction (i.e. the x -direction in the global coordinate system specified in the figure) transverse to the embedded optical fiber. Note that the loading direction is parallel to the 1-direction in the optical fiber coordinate system used throughout this work. The lighter areas correspond to higher strain values while the dark areas correspond to lower values of strain. The aluminum tabs experience little strain due to their high modulus and the boundary conditions laid out in the experimental setup section. Due to the stress concentration where the aluminum tab ends, large strains are seen in the composite just outside the tab region. These high strains quickly die out and approach as steady state value near $1500 \mu\epsilon$. The inset shows a zoomed-in image of the side of the composite. Note the color map corresponding to the isometric view of the composite sample does not correspond to the color map in the inset. The surrounding 90° layer is a fairly dark gray while the polyimide coating (due to its low Young's modulus) becomes very light from the large amount of strain present.

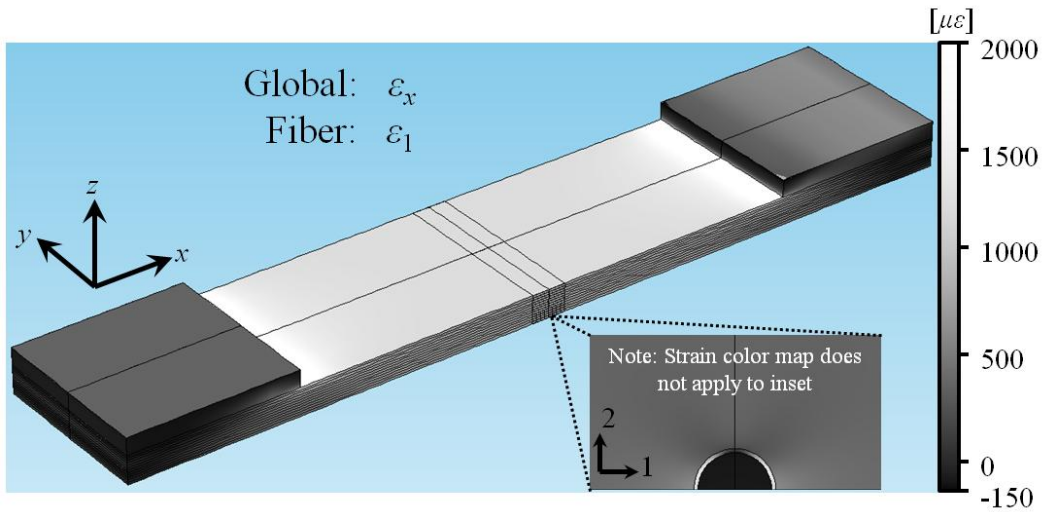


Figure 3-52: FEA strain in the loading direction for a 90°/90° sample under IPL.

The optical fiber itself is significantly darker than the surrounding composite, indicating that strain in the x -direction (i.e. the 1-direction) is diminished. This is due to the fiber geometry having a small length in the loading direction. This is very promising for the use of embedded FBGs as a uniaxial strain sensor. Such results are corroborated further in Figure 3-53 below depicting strain in the out-of-plane direction (i.e. the z -direction of the global coordinate system and in the 2-direction of the optical fiber coordinate system). No structural carbon fibers are oriented in the z -direction; thus, the composite stiffness in the out-of-plane direction is close to the Young's modulus of the epoxy matrix. This means that the pressure applied normal to the tab surface causes much less strain in the stiffer aluminum in comparison to the more compliant composite beneath. Additionally, no surface traction is applied outside of the tab region; thus, no strain is seen normal to the composite surface. Looking at the inset which shows the strain response in the region of the embedded FBG, the surrounding 90° layer is a darker shade of gray than the optical fiber.

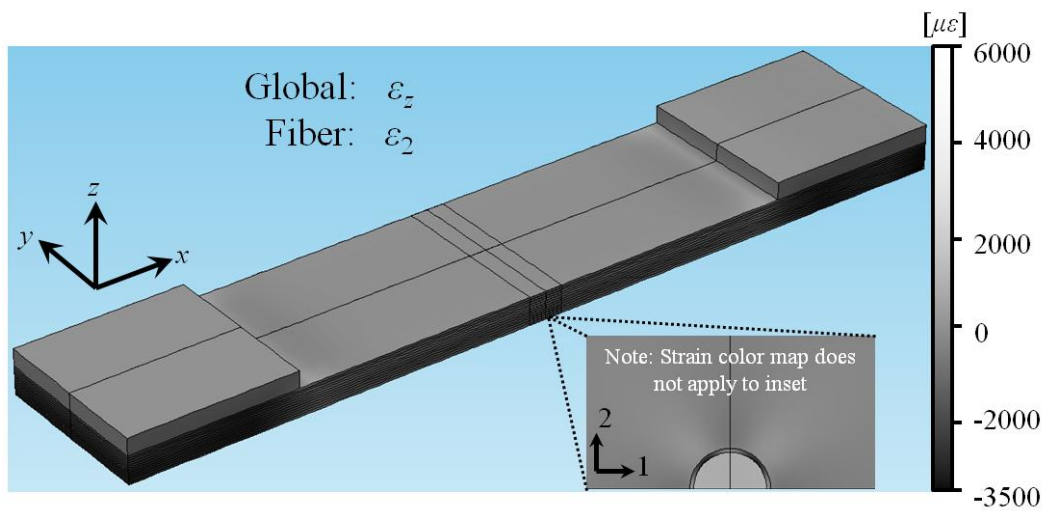


Figure 3-53: FEA strain in the composite's out-of-plane direction for a 90°/90° sample under IPL.

The surrounding composite region is experiencing a Poisson's contraction in the z -direction due to the tensile loading in the x -direction. As noted in Figure 3-52, the x -direction strain in the composite is not completely transferred to the optical fiber. Thus, the degree of Poisson's contraction in the 2-direction of the optical fiber is severely diminished. This further indicates that strain transverse to an optical fiber is not entirely transferred due to the small geometry of the fiber in this dimension. Figure 3-54 shows the strain in the global y -direction which is in-plane and transverse to the loading direction. This is parallel to the optical fiber and thus, aligned with the 3-direction in the fiber coordinate system. Due to the zero displacement boundary condition in the y -direction at the tab-grip interface, the tab surface elicits no strain in the y -direction. In the far field composite region, a consistent gray region is observed and indicates a uniform strain value around $-450 \mu\varepsilon$. Note that edge effects are present near the lateral sides of the composite specimen. The inset shows the optical fiber region and indicates a uniform color across the entire area.

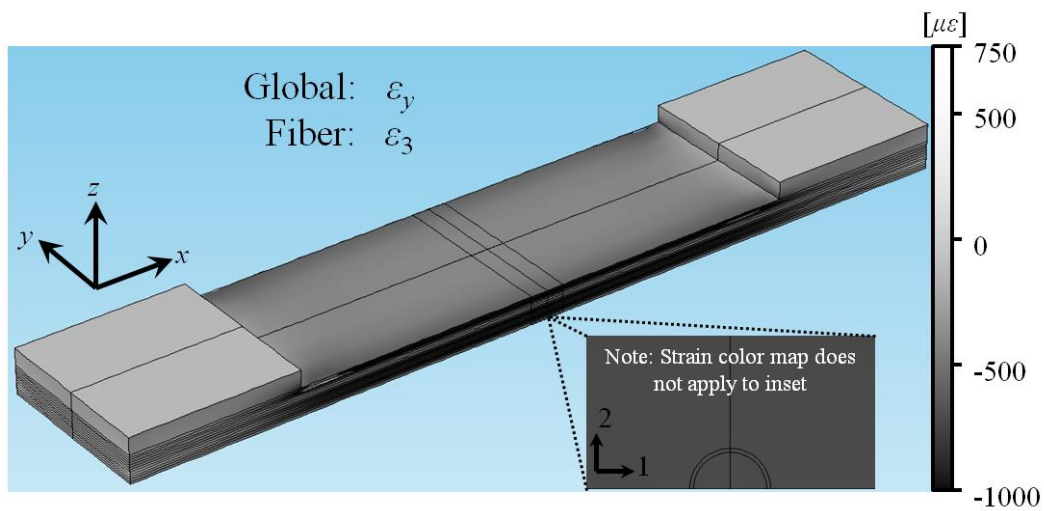


Figure 3-54: FEA strain in the direction of the embedded optical fiber for a 90°/90° sample under IPL.

The uniform color in the inset image specifies the uniformity of strain in the optical fiber’s 3-direction. This is consistent with the argument that strain transfer is greatest in the direction of the fiber’s long dimension. Thus, the present situation is such that strain in the longitudinal direction of the optical fiber is entirely transferred to the FBG while strains in the transverse directions are not. This signifies the potential of using optical fibers as uniaxial strain sensors when embedded within a composite material.

To further quantify the results seen in the inset images in Figure 3-52 through Figure 3-54, strains in the x -, y -, and z -directions of the composite (i.e. 1-, 3-, and 2-directions of the fiber respectively) are plotted along three particular lines cutting through the composite mid-plane. Figure 3-55 below shows the “under-side” of the composite sample shown in Figure 3-52 through Figure 3-54 which, due to the symmetry conditions described earlier, is the mid-plane of the composite. Labeled on the composite mid-plane are the various sample regions of interest which include the tab, edge, near field, and far field regions. Also indicated in the figure are the three cut lines with the first being parallel to the loading direction. The second and third are parallel to the optical fiber direction with the third coinciding with the core of the optical fiber.

The second cut line is within the far field of the composite material but sufficiently far from the optical fiber so as not to be affected by the embedded sensor.

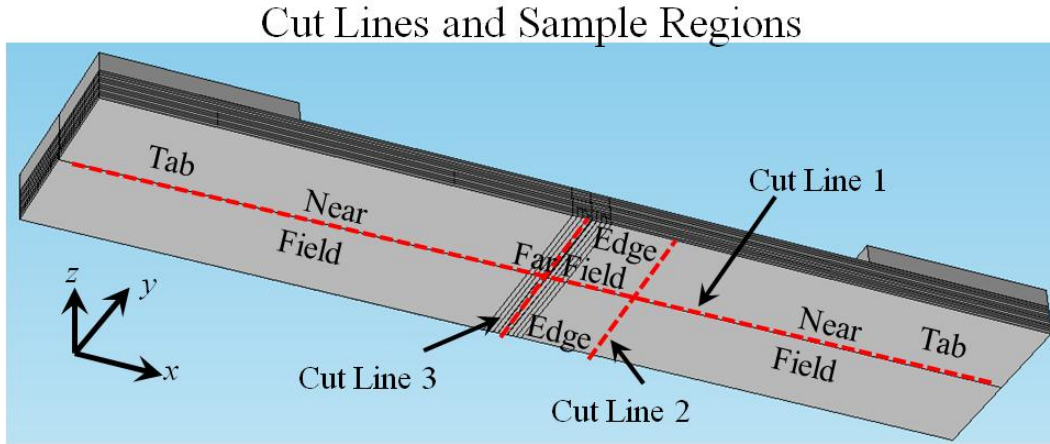


Figure 3-55: Depiction of the three cut lines in the IPL model along with which FEA strains will be plotted.

Strains in the three coordinate directions are plotted in Figure 3-56 along the first cut line which is oriented in the loading direction. The vertical axis corresponds to strain while the horizontal axis corresponds to the various regions of the composite sample. The blue, green, and red curves indicate ε_x , ε_y , and ε_z respectively and are labeled as such. In the tab regions, a large strain is seen in the out-of-plane (z) direction whereas the x - and y -direction strains are inhibited from the grips clamping the composite. The near fields of the composite just outside of the tab regions show transitional strains approaching their steady state values in the far field region. In the far field of the composite, the strain in the loading direction is about $1500 \mu\varepsilon$ whereas the in-plane transverse and out-of-plane transverse strains are near $-450 \mu\varepsilon$ due to a Poisson's contraction.

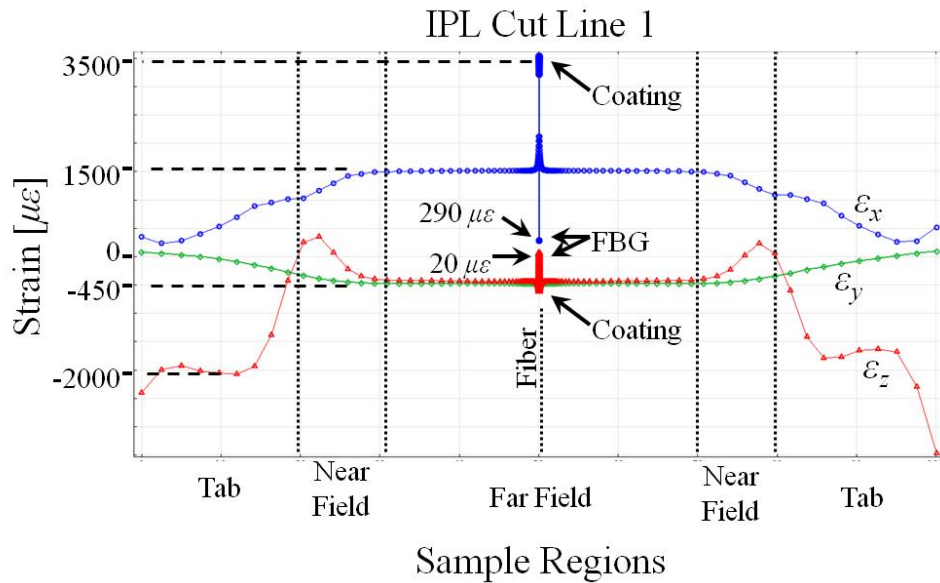


Figure 3-56: Plot of strains in the coordinate directions along Cut Line 1 in the model under IPL conditions.

At the center of the far field, sharp changes in strain are seen in the ε_x and ε_z curves because the cut line is traversing the coating and optical fiber. The ε_y curve, on the other hand, does not change at all because strain in this direction is completely transferred to the optical fiber. A large increase is seen in ε_x when the cut line enters the relatively compliant coating whereas a sharp decrease to $290 \mu\varepsilon$ is seen when the cut line enters the relatively stiff optical fiber. In the ε_z curve, a slight drop-off is seen in strain in the coating and a sharp increase to $20 \mu\varepsilon$ is seen in the fiber. The net effect is a sharp reduction in the TSD of the optical fiber. This provides quantitative evidence that the transverse strain difference in the optical fiber is vastly different than the host material. This is corroborated with the comparison of the strains in the second and third cut lines.

Plotted below in Figure 3-57 are the strains within the composite along the cut line parallel to the optical fiber. The edge effects are responsible for the variation in strain near the periphery of the composite sample. Once the edge effects have died out, steady state strain is achieved which defines the far field region of the composite. Strain in the loading direction (ε_x) matches the $1500 \mu\varepsilon$ value seen in Figure 3-56. Strain parallel to the optical fiber direction (ε_y) is $-470 \mu\varepsilon$ and out-of-plane strain (ε_z) is $-430 \mu\varepsilon$. These are both near the $-450 \mu\varepsilon$ value seen in the first cut line plot.

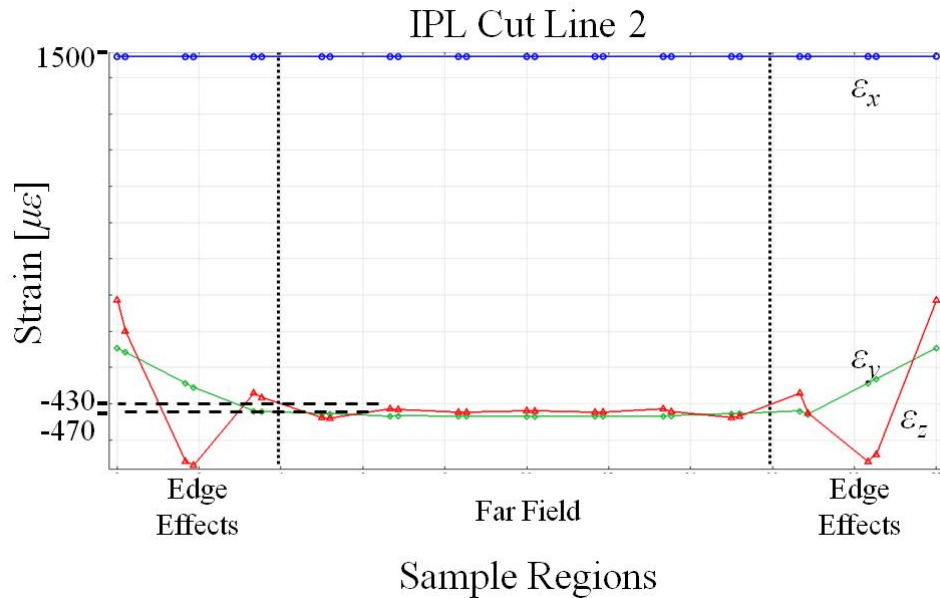


Figure 3-57: Plot of strains in the coordinate directions along Cut Line 2 in the model under IPL conditions.

If strain in every direction transferred perfectly to the optical fiber, the strain along the third cut line would match the strains in Figure 3-57. The result would be a very large transverse strain difference in the optical fiber of $1930 \mu\epsilon$ which would correspond to the reflected wavelengths splitting apart by 0.45 nm . The lack of any further splitting in the peaks due to experimental in-plane tensile loading of the composite indicates that this is not the case. Therefore, the strains along the third cut line will not match those along the second as will be seen next.

Figure 3-58 below shows the strains in the x -, y -, and z -directions (i.e. 1-, 3-, and 2-directions respectively) along the cut line coinciding with the optical fiber core. Similar edge effect behavior is seen in this data as in Figure 3-57 although of a different magnitude. Strain in the longitudinal direction of the optical fiber (ϵ_y or ϵ_3) is $-470 \mu\epsilon$ which matches that in Figure 3-57. This is due to the complete transfer of the Poisson's contraction in the composite to the optical fiber along this direction. The loading direction strain (ϵ_x or ϵ_1) is $290 \mu\epsilon$ which is a value drastically diminished from the surrounding composite material's value of $1500 \mu\epsilon$. The out-of-plane direction strain (ϵ_z or ϵ_2) is $20 \mu\epsilon$ which is also vastly different from the $-430 \mu\epsilon$ seen in the previous figure.

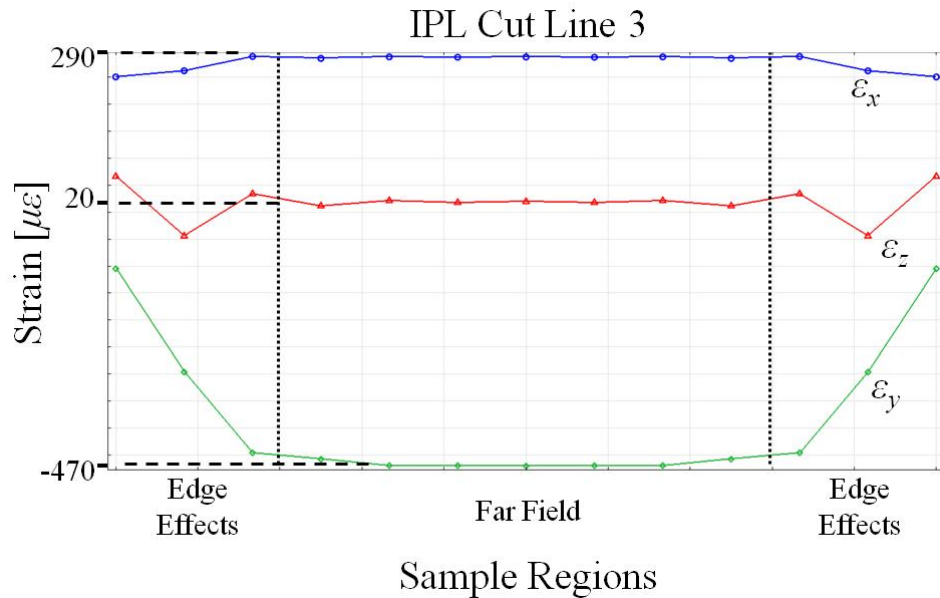


Figure 3-58: Plot of strains in the coordinate directions along Cut Line 3 of the model under IPL conditions.

The out-of-plane strain (ϵ_z or ϵ_2) will be further explained in order to provide a very interesting example of the lack of strain transfer from the host to the optical fiber in the transverse direction. For a positive tensile strain in the loading direction, one would intuitively expect that the $-430 \mu\epsilon$ Poisson's contraction in the composite's out-of-plane direction would partially transfer to the optical fiber and create a diminished, yet still negative strain value in the FBG core. However, a positive $20 \mu\epsilon$ value is seen. This is because the transfer of a negative out-of-plane strain from the composite is the weaker of two contributing factors. The second factor stems from the complete transfer of compressive strain from the composite to the optical fiber in the fiber's longitudinal direction. This contraction results in a Poisson's expansion in the out-of-plane direction transverse to the optical fiber fighting against the compressive strain in the z -direction of the composite host. It turns out that the second factor is stronger than the first and thus, a net expansion in the optical fiber is observed. This is an excellent example providing quantitative results demonstrating the large disparity in strain transfer to the optical fiber from the host material in the various directions. Next, OPL conditions will be used to further demonstrate the strain transfer characteristics in an optical fiber.

Figure 3-59 below shows the result of applying an out-of-plane compressive load to the tab centrally located above the optical fiber. Due to the fixed, zero-displacement boundary condition on the top surface of the tab, no strain is observed. Additionally, the lack of stress traction on the top surface of the composite leads to negligible strain with the exception of near the tab region where stress concentrations occur due to the abrupt change in area. Looking at the side of the composite sample, the region directly beneath the tab is clearly lighter than the darker regions outside the tab. This indicates how quickly the strain in the composite dies out once out from under the tab compression. The inset demonstrates the strain in the optical fiber region. As the grip compresses the tab, the composite will experience a Poisson's expansion in-plane. This Poisson's expansion is highest at the top of the optical fiber due to the higher Young's modulus of the optical fiber relative to the surrounding composite material. The optical fiber is darker than the surrounding 90° layer, thus indicating the tensile strain is not as large. This is consistent with the results of the IPL conditions indicating a diminished strain transfer lateral to the optical fiber.

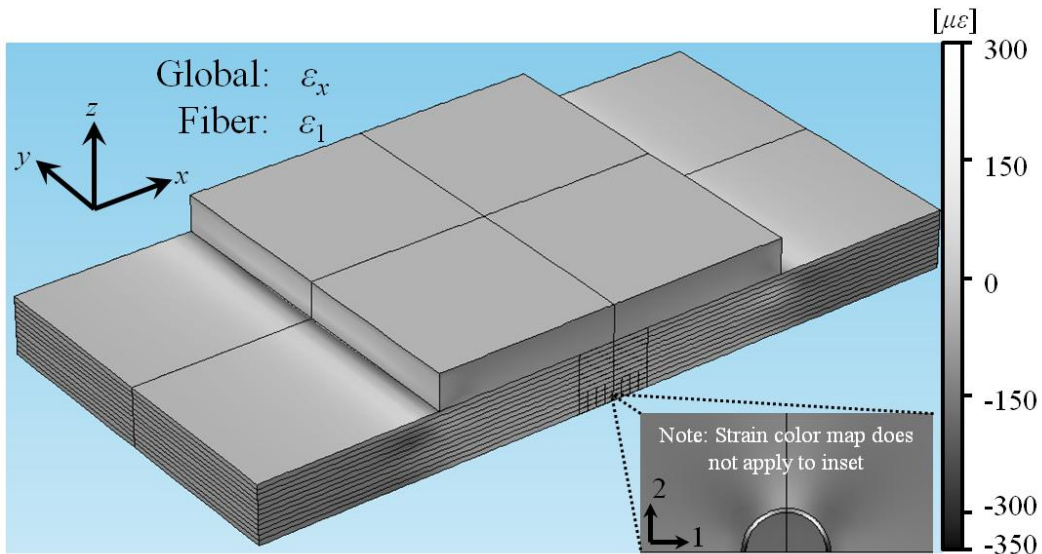


Figure 3-59: FEA strain in the 0° direction for a 90°/90° sample under OPL.

The other in-plane strain which is parallel to the embedded optical fiber direction is plotted in Figure 3-60 below. The zero-displacement boundary conditions and absence of surface traction

leads to no observed strain on the top surface of the tab and composite respectively with the exception of near the stress concentration where the tab region ends. Note that the range of strain values plotted in Figure 3-60 is smaller than that in Figure 3-59; therefore, it is easier to see the variation in strain within the composite as the differently angled plies are traversed. This variation is explained by the fact that the 0° layers are much more compliant in the y -direction compared to the 90° layers. Therefore, the 0° layers elicit a larger Poisson's in-plane expansion which is captured by the lighter area on the side of the composite beneath the tab. The darker regions coincide with the $+45^\circ$, -45° , and 90° layers which do not expand as much in the y -direction. Note that this feature is occurring on the outer surface of the modeled composite. Once away from the edge regions, the strain will be uniform across all of the layers. The inset depicts an image of the optical fiber and the surrounding 90° layer. As in Figure 3-53, the strain parallel to the optical fiber is wholly transferred and thus, the entire region is monochrome.

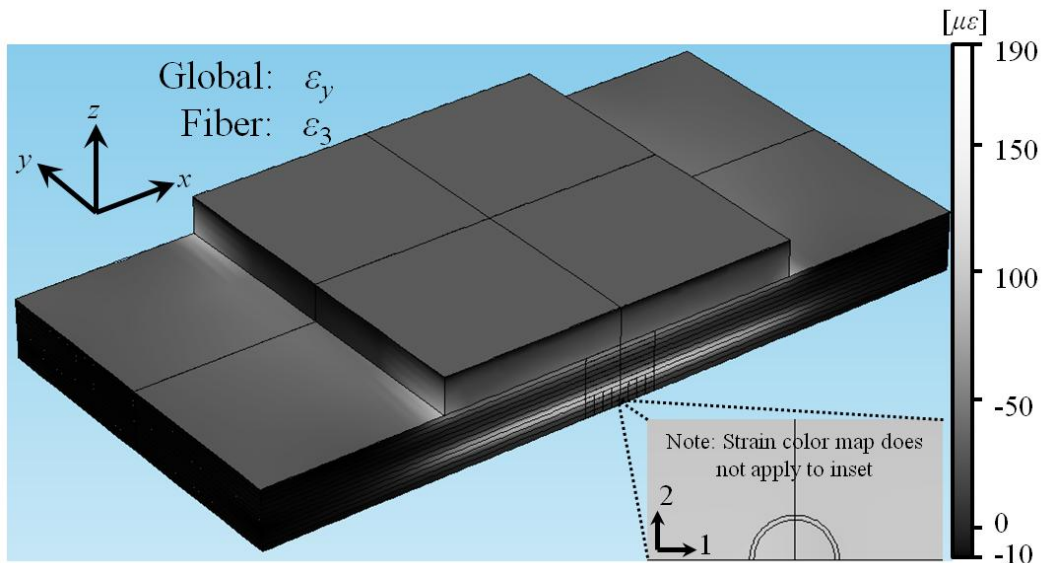


Figure 3-60: FEA strain in the direction of the embedded optical fiber for a $90^\circ/90^\circ$ sample under OPL.

Lastly, the out-of-plane strain is plotted in Figure 3-61 below. The tab is directly loaded with the compressive out-of-plane force, but the large Young's modulus of the tab in comparison with the out-of-plane stiffness of the composite causes the strain in the composite to be much larger.

Thus, the tab surface is light with a slightly negative strain and the composite beneath is very dark with a negative strain much larger in magnitude. Looking at the inset indicating the strains near the embedded optical fiber, the largest stress concentration occurs at the top of the optical fiber, thus creating the darkest region. The optical fiber itself is much lighter than the surrounding 90° layer strain. This again corroborates the notion that a host's strain transverse to the embedded optical fiber direction transfers poorly to the FBG.

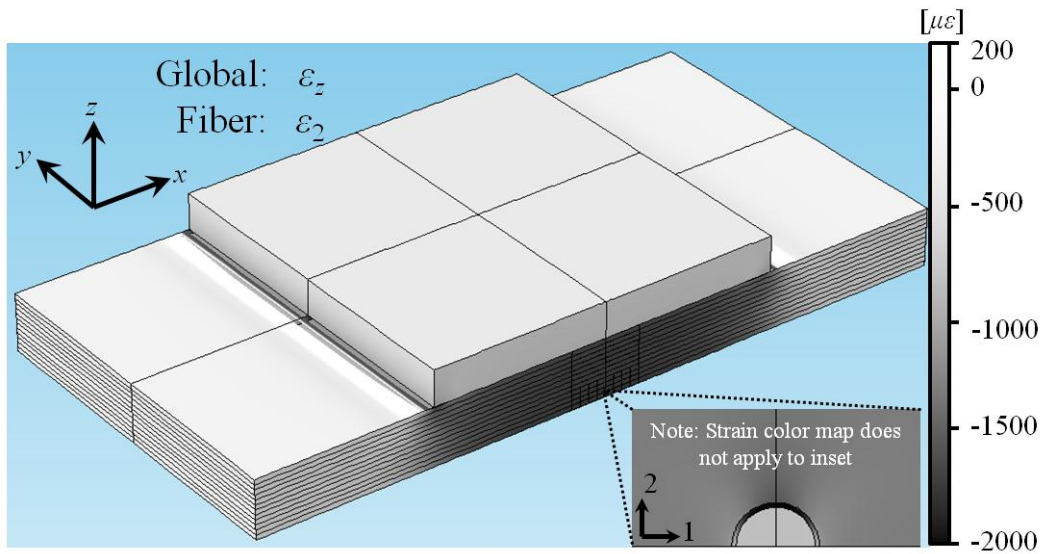


Figure 3-61: FEA strain in the composite's out-of-plane direction for a 90°/90° sample under OPL.

Similar to the IPL results, the strains along three cut lines will be presented next. The three cut lines coincide with the three cut lines of the IPL analysis. The largest difference between the OPL and IPL sample region labels is that in the OPL model, the area directly beneath the tab and far enough away from the edges and the regions outside the tabs is now considered the far field. The cut lines and the various pertinent sample regions are identified and labeled in Figure 3-62.

Cut Lines and Sample Regions

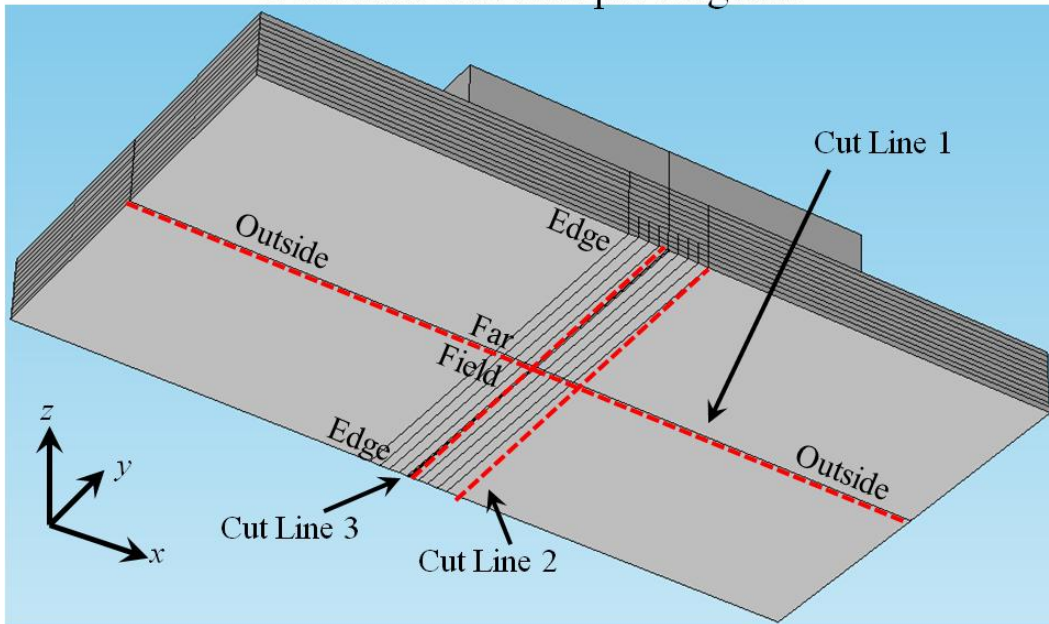


Figure 3-62: Depiction of the three cut lines in the OPL model along with which FEA strains will be plotted.

The strains along the first cut line are presented in Figure 3-63 below. As in Figure 3-56, strain in the y -direction is consistent along the entire far field region and across the optical fiber. The strains in the x - and z -directions, however, experience significant and abrupt changes in magnitude as the cut line crosses the optical fiber. This change in magnitude will be explored in the coming figures, but it is evident from Figure 3-63 that the result is a TSD which significantly reduces birefringence in the embedded optical fiber.

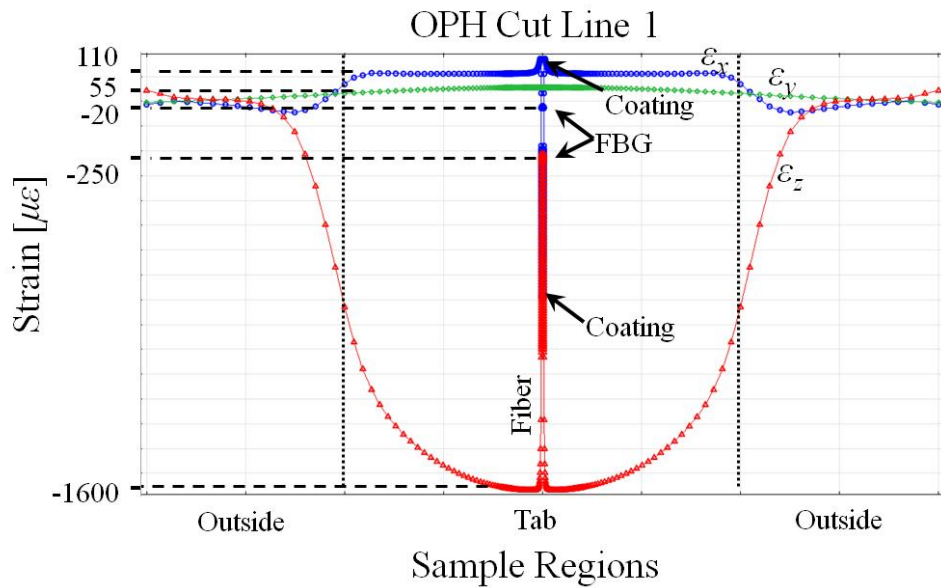


Figure 3-63: Plot of strains in the coordinate directions along Cut Line 1 in the model under OPL conditions.

The strains along the second cut line are shown in Figure 3-64 below. Once far enough away from the edges, steady state values are reached which define the far field region. As expected, the out-of-plane strain (ϵ_z) is negative and -1550 $\mu\epsilon$ in value. The two in-plane strain directions indicate positive strain due to the Poisson's expansion. The slightly different values (110 $\mu\epsilon$ versus 55 $\mu\epsilon$) are the result of the composite layer being stiffer in the y -direction.

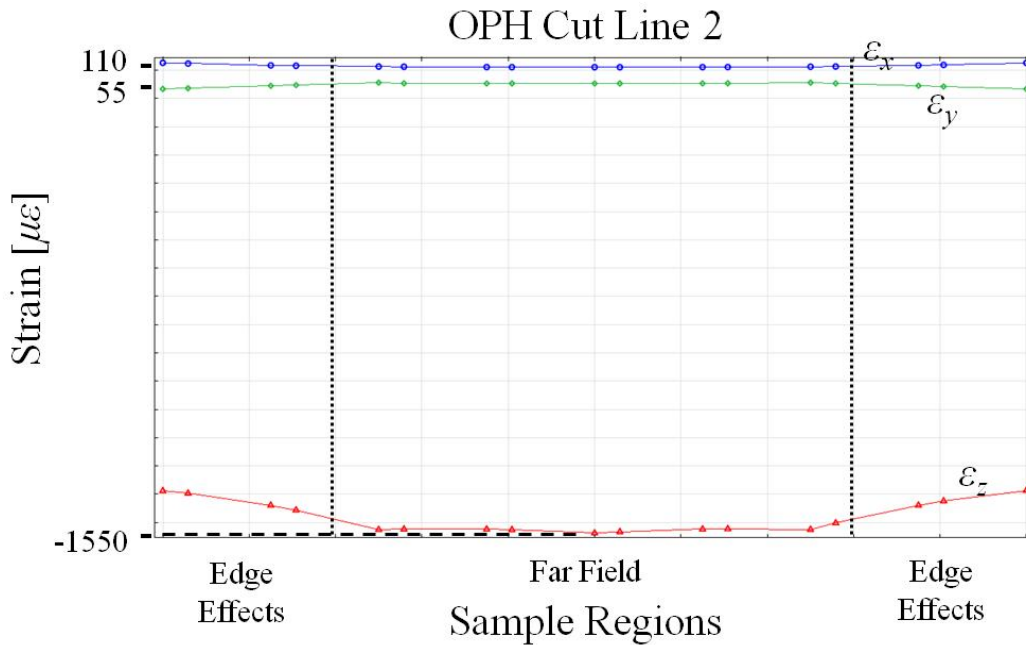


Figure 3-64: Plot of strains in the coordinate directions along Cut Line 2 in the model under OPL conditions.

A comparison of Figure 3-64 above with Figure 3-65 below directly demonstrates the diminished strain transfer in the x - and z -directions. The y -direction strain (ϵ_3 in the fiber) matches that in the composite whereas the z -direction strain (ϵ_2 in the fiber) is reduced from the composite's $-1550 \mu\epsilon$ value to $-250 \mu\epsilon$. Strain transverse to the load and the optical fiber (ϵ_1 in the fiber, ϵ_x in the composite) is altered from $110 \mu\epsilon$ to $-20 \mu\epsilon$.

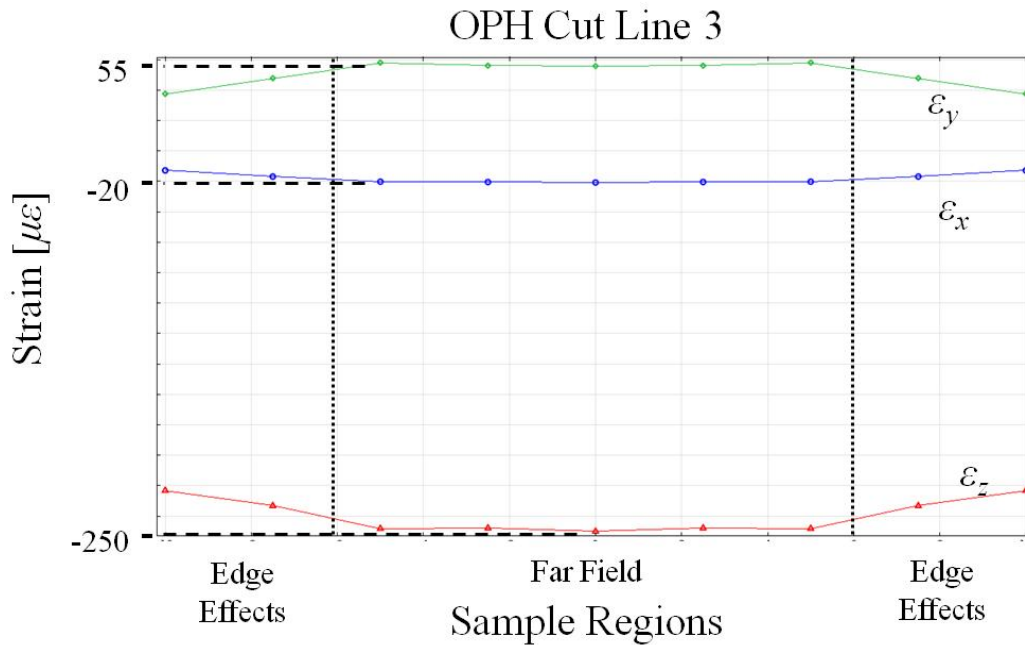


Figure 3-65: Plot of strains in the coordinate directions along Cut Line 3 of the model under OPL conditions.

As in the IPL results, the strain in the direction which is orthogonal to both the load and the optical fiber (ϵ_2 previously for IPL, ϵ_1 here for OPL) is reduced in magnitude and changed sign. This is because of two competing factors having opposite effects on the optical fiber strain in this direction. The out-of-plane compressive load causes the optical fiber to expand in the in-plane transverse direction (1-direction). However, the reduced strain transfer in this direction severely reduces this factor's influence. The Poisson's expansion of the optical fiber in the longitudinal direction (which is the result of a complete strain transfer from the composite) causes the optical fiber to experience a Poisson's contraction in the 1-direction. The stronger of these two factors is Poisson's contraction from the longitudinal expansion of the optical fiber due to the better strain transfer in this direction. This result is consistent with the results of the IPL analysis.

These results demonstrate that while the strain in the optical fiber's longitudinal direction matches that of the host material, strains in the transverse directions do not match the host. This severely complicates any desire to fully resolve the strain state of the surrounding composite material; however, this also promotes the use of optical fibers as uniaxial strain sensors. If the

TSD created in an optical fiber from the host is very weak in comparison to a more dominant longitudinal strain, the FBGs can be utilized as uniaxial strain sensors. At this point, it is clear that the longitudinal strain is dominant, but it is unclear whether it is dominant enough to invoke the uniaxial FBG assumption. This will be explored in the coming FEA results.

3.5.2 2-D Model Validation

The 3-D model created for the strain transfer results just described is relatively simple in comparison to the models which will be explored shortly. This is because the upcoming models involve adjustments to the embedded fiber which drastically increase the required fineness of the mesh along with the size and processing time of the model. In order to get around some of the more complicated models, 2-D models are used instead of 3-D models. The use of 2-D models to represent an experiment which is inherently 3-D and take the place of a 3-D model must be validated. This is accomplished by comparing the strains transverse to the optical fiber (ε_1 and ε_2) and TSD in 2-D models with that in the 3-D models for both the IPL and OPL conditions. The response of the strains transverse to the optical fiber under in-plane loading for increasing applied stress in the 0° direction is plotted in Figure 3-66 below. The vertical axis represents strain in the 1- and 2-directions while the horizontal axis represents the applied 0° stress. Note that the ~ 50 GPa stiffness of the composite means that when the 0° stress is increased from 0 to 150 MPa, the 0° and 90° strains in the composite reach $3000 \mu\varepsilon$ and $-900 \mu\varepsilon$ respectively. The red diamonds, blue squares, yellow circles, and purple triangles correspond to 3-D ε_1 , 2-D ε_1 , 3-D ε_2 , and 2-D ε_2 respectively.

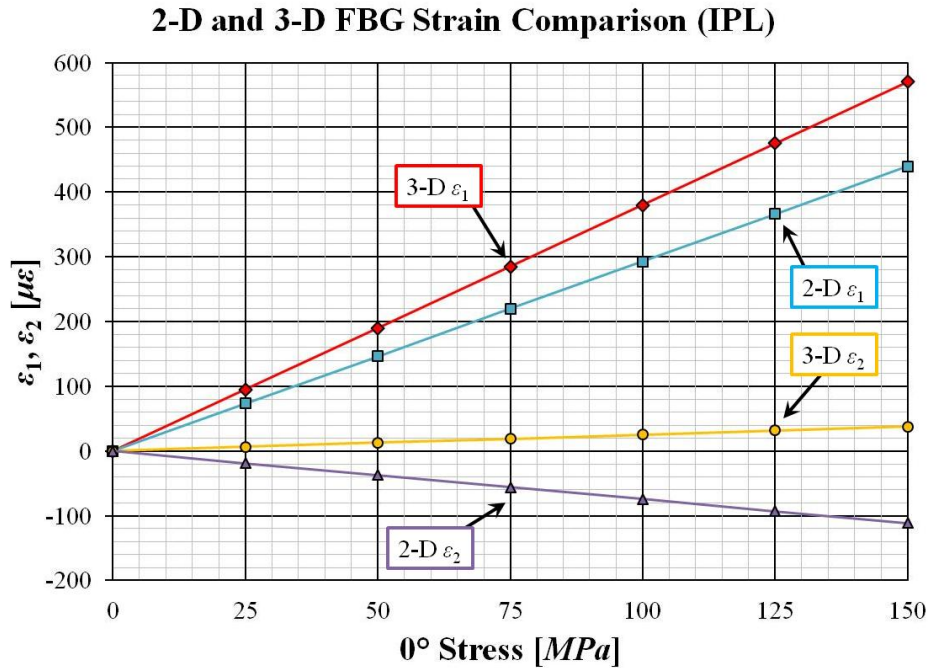


Figure 3-66: Validation of 2-D IPL model by comparing strains transverse to the embedded optical fiber with the 3-D IPL model.

There is an obvious mismatch in the strains which increases proportionately as the load increases. One particularly interesting difference between the 2-D and 3-D results is in the ϵ_2 curves. The 3-D curve goes positive, as previously described due to the negative strain transferred from the composite competing and losing against the positive strain from the Poisson's expansion due to the fiber contracting longitudinally. However, the 2-D curve goes negative. Thus, the competing factors are a 3-D phenomenon which is not captured by the 2-D model. Continuing with the comparison, Figure 3-67 below depicts the TSD for the 2-D and 3-D IPL cases as load increases. The left vertical axis depicts TSD while the right vertical axis represents the size of the peak splitting that is expected to occur due to the derived TSD.

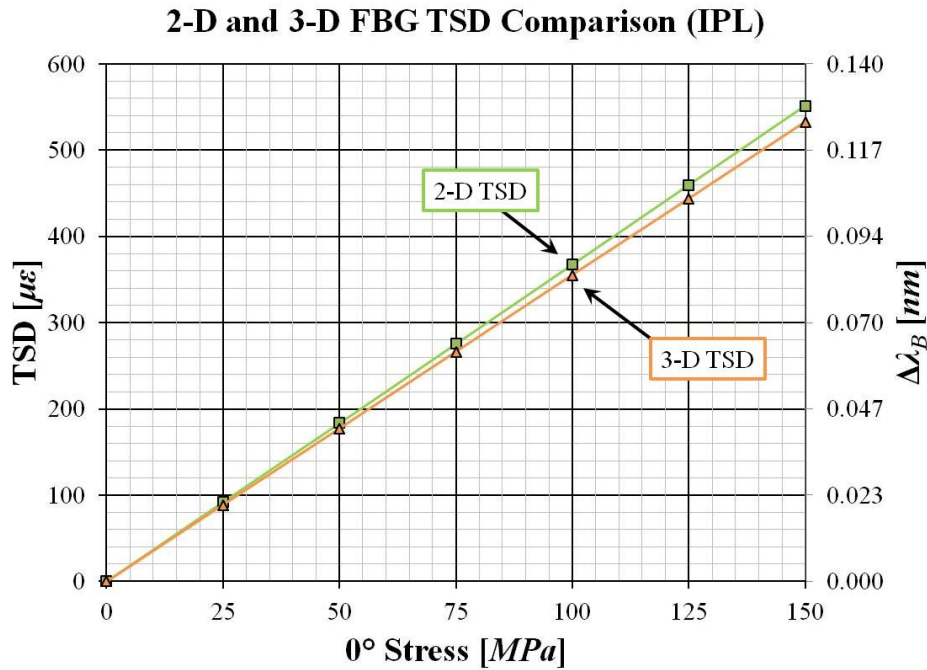


Figure 3-67: Validation of 2-D IPL model by comparing the TSD of the embedded optical fiber with the 3-D IPL model.

Despite the difference in the values of the individual transverse strains, the TSD for the 2-D and 3-D models are strikingly similar. This indicates that while perhaps it is unwise to use the 2-D model to draw conclusions about ϵ_1 and ϵ_2 , the TSD in the 3-D model is satisfactorily captured by the 2-D model. This notion will be explored by comparing 2-D and 3-D models of the OPL condition next. The results for the OPL model are presented in Figure 3-68 below and are analogous to Figure 3-66. The color and symbol combinations are consistent with their correspondence with the various strain directions. However, rather than the horizontal axis representing loading in the 0° direction, it represents stress applied to the tab by the theoretical grips. Note that the values in the horizontal axis correspond to compressive stress.

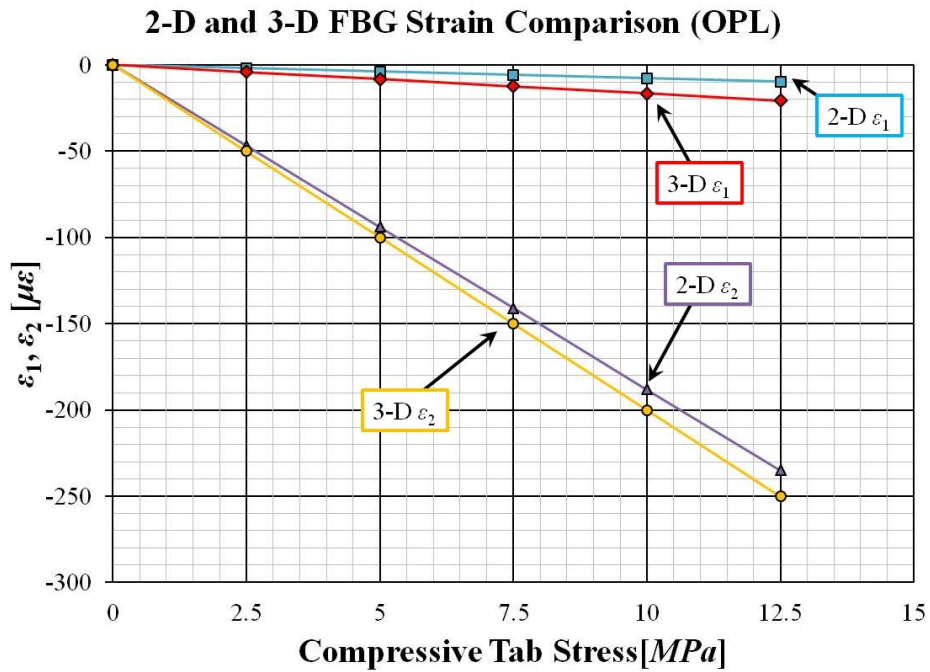


Figure 3-68: Validation of 2-D OPL model by comparing strains transverse to the embedded optical fiber with the 3-D OPL model.

The individual transverse strains in the 2-D and 3-D OPL models are much more closely aligned than those in the IPL models. Next, the difference between the two 2-D and the two 3-D curves will be presented in Figure 3-69 as the TSD. Once again, the left vertical axis corresponds to TSD while the right vertical axis corresponds to the split in the reflected peaks of an FBG associated with the TSD.

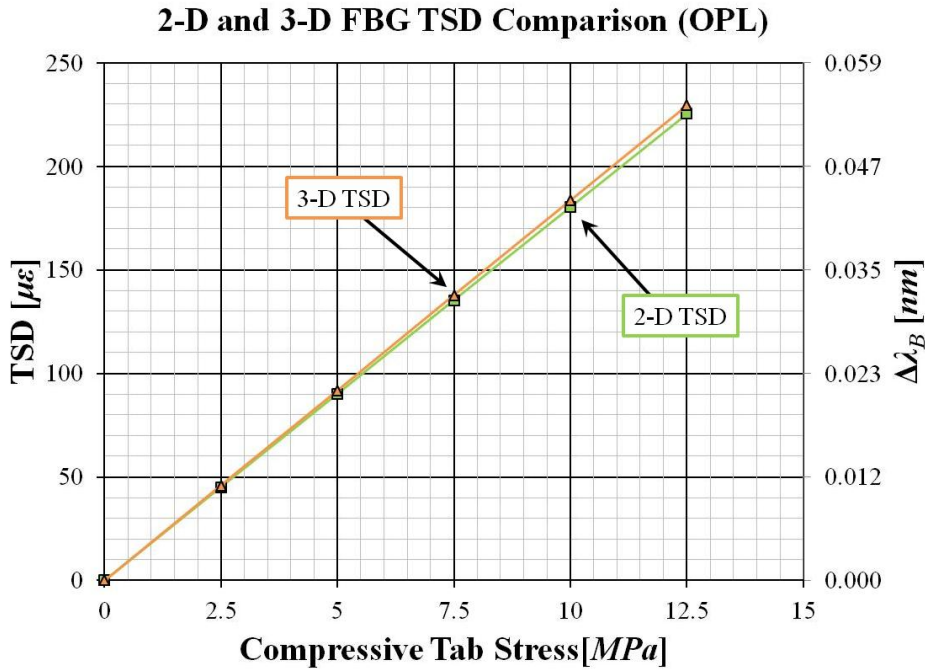


Figure 3-69: Validation of 2-D OPL model by comparing the TSD of the embedded optical fiber with the 3-D OPL model.

The TSD for the 2-D and 3-D models match very closely for the OPL models. This means that usage of a 2-D model in place of a 3-D model has been validated for calculating TSD, but not necessarily the individual transverse strains. It will be seen in the cases where both a 2-D and 3-D model were calculated, the TSD trends and behavior are nearly identical with only slightly different magnitudes. Next, parameters of the geometric configuration of the embedded optical fiber will be altered to demonstrate their effects on TSD and thus, birefringence.

3.5.3 Non-Experimental Parameter Variation

The purpose of this portion of the FEA results is to utilize the freedom and ease of performing theoretical calculations to determine whether or not altering experimental factors would be worth the experimental effort. This first example is whether or not increasing the thickness of the optical fiber coating will result in a significantly reduced TSD under different load conditions. Perhaps the currently experimentally employed $7 \mu\text{m}$ thick polyimide coating partially reduces the TSD, but not enough to utilize the embedded FBGs as uniaxial strain

sensors. Experimentally verifying this would be a lengthy process involving the design and execution of a study measuring the influence of coating thickness on birefringence. This would entail obtaining FBGs with various coating thicknesses, embedding them in composites, performing experimental tests, and analyzing the data. Rather than committing to this path, a proper FEA study can be completed in a much shorter amount of time to determine whether or not the study is worth the effort. This can be accomplished with various parameters, but the fiber coating thickness will be explored first. Figure 3-70 below includes images showing the variation in coating thickness and the values used in the study.

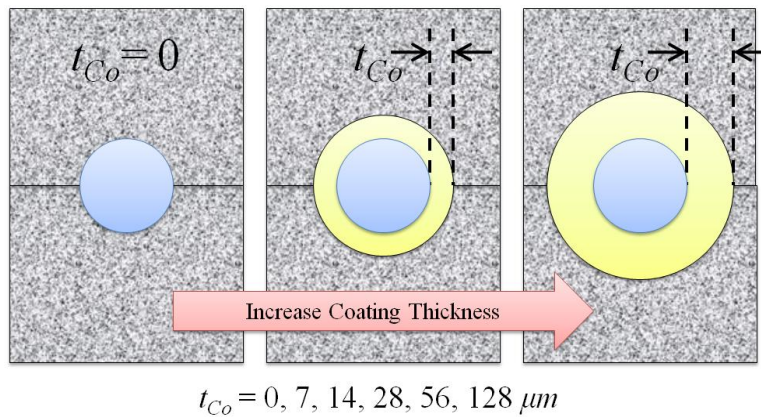


Figure 3-70: Variation of coating thickness in the FEA study.

The TSD was first calculated using 2-D models of both IPL and OPL conditions. The results are plotted in Figure 3-71 below with blue triangles and green squares representing the IPL and OPL data respectively. The left vertical axis corresponds to TSD while the right vertical axis corresponds to the reflected wavelength split associated with the left axis' TSD. Each symbol represents a different coating thickness while the lines connecting the symbols are solely meant for easier interpretation of data trends.

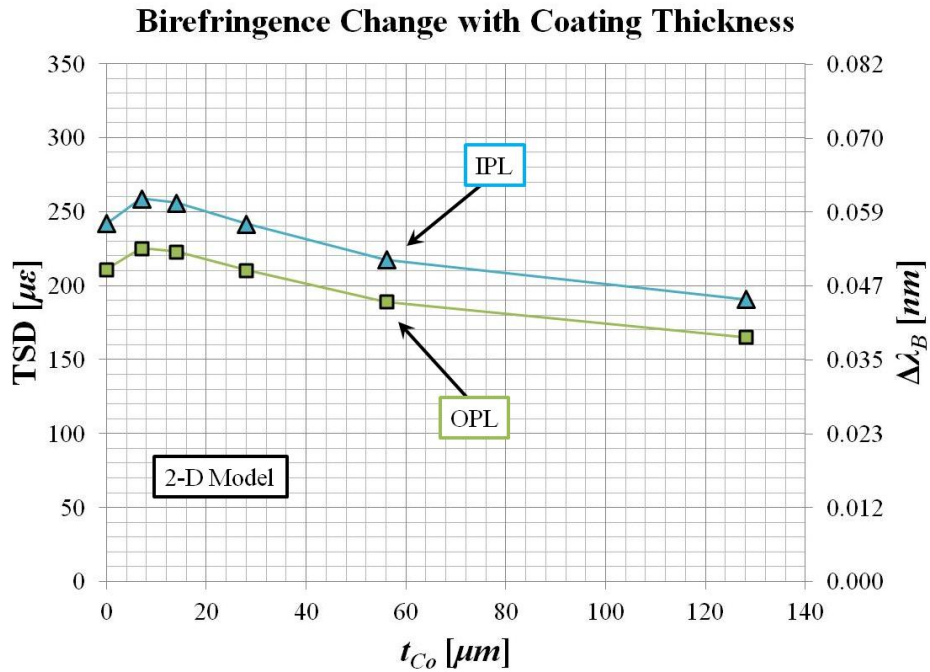


Figure 3-71: Variation of TSD in 2-D IPL and OPL models while varying coating thickness.

The TSD is seen to increase immediately from having no coating ($t_{Co} = 0$) to having a coating. This is followed by a steady drop-off which causes an overall reduction in TSD. The decrease in TSD from the original $7 \mu m$ coating to the largest $128 \mu m$ coating thickness is approximately 25 % ($\sim 260 \mu\epsilon$ to $\sim 190 \mu\epsilon$). This trend is confirmed by processing 3-D models of both IPL and OPL conditions. The results are plotted in Figure 3-72 below. The color and symbol combinations along with the axes are consistent between Figure 3-71 and Figure 3-72.

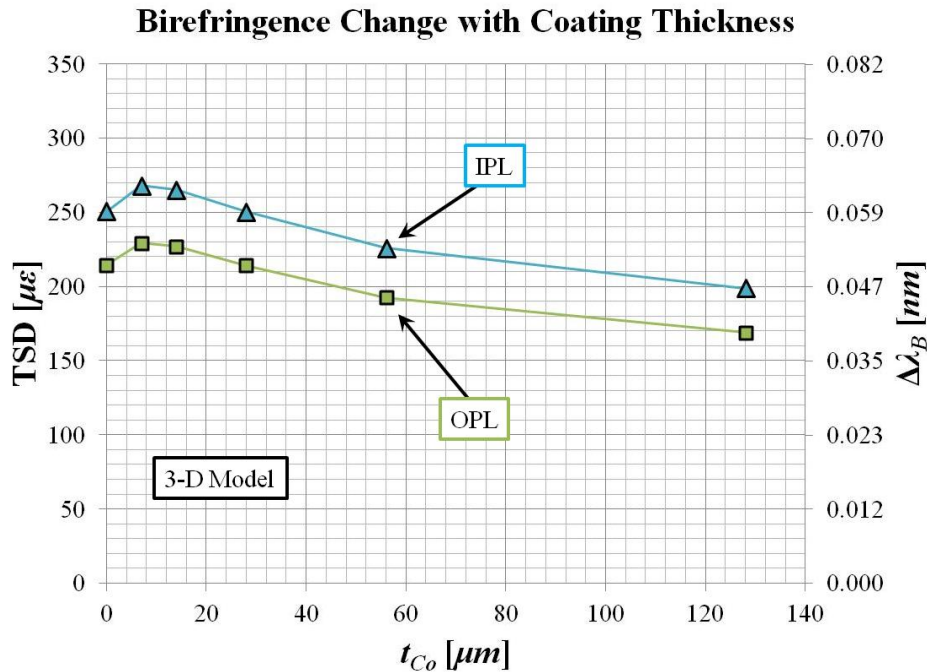


Figure 3-72: Variation of TSD in 3-D IPL and OPL models while varying coating thickness.

It is obvious that the 2-D and 3-D models exhibit nearly identical behavior with the exception being that the 3-D TSD in both the IPL and OPL models are slightly higher in magnitude. The main conclusion from this work is that the ~25 % decrease in TSD is significant, but not enough on its own to completely mitigate the entire TSD. This partial reduction in TSD and birefringence means that other methods must be considered in allaying TSD in an embedded fiber.

One such factor which could contribute to the reduction of a TSD in an embedded optical fiber is the size of the lenticular resin rich pocket adjacent to the fiber optic. As previously mentioned in the literature review, Dasgupta et al. 1990 and Dasgupta et al. 1992 studied the influence of various curing methods on the size of the lenticular resin pocket. If such methods are carried out to increase the size of the pocket, it is possible that the TSD could be further mitigated. Figure 3-73 below shows images demonstrating the variation in the pocket size and what values are utilized.

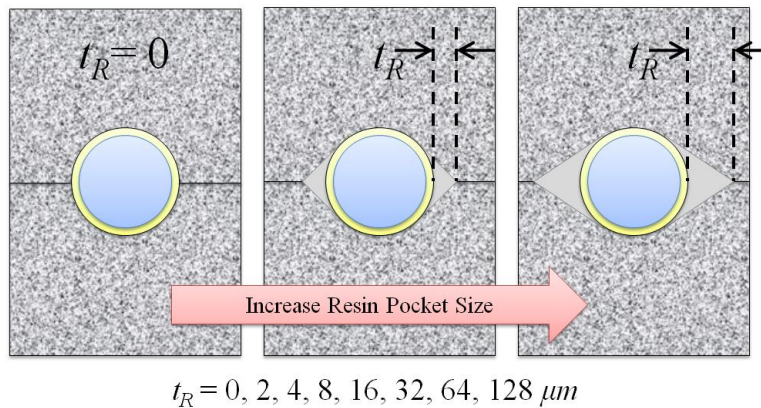


Figure 3-73: Variation of resin pocket length in the FEA study.

The results of 2-D models in both IPL and OPL conditions are shown in Figure 3-74 below. The vertical axes once again correspond to TSD and differences in the two reflected wavelengths while the symbol and color combinations of the data are consistent with Figure 3-71 and Figure 3-72. The horizontal axis corresponds to the length of the resin pocket. As the size of the pocket is increased from 0 to 128 μm , the IPL TSD slowly drops off by 15 % from $\sim 260 \mu\epsilon$ to $\sim 220 \mu\epsilon$. The OPL TSD, on the other hand, exhibits a slight increase in TSD which quickly flattens out.

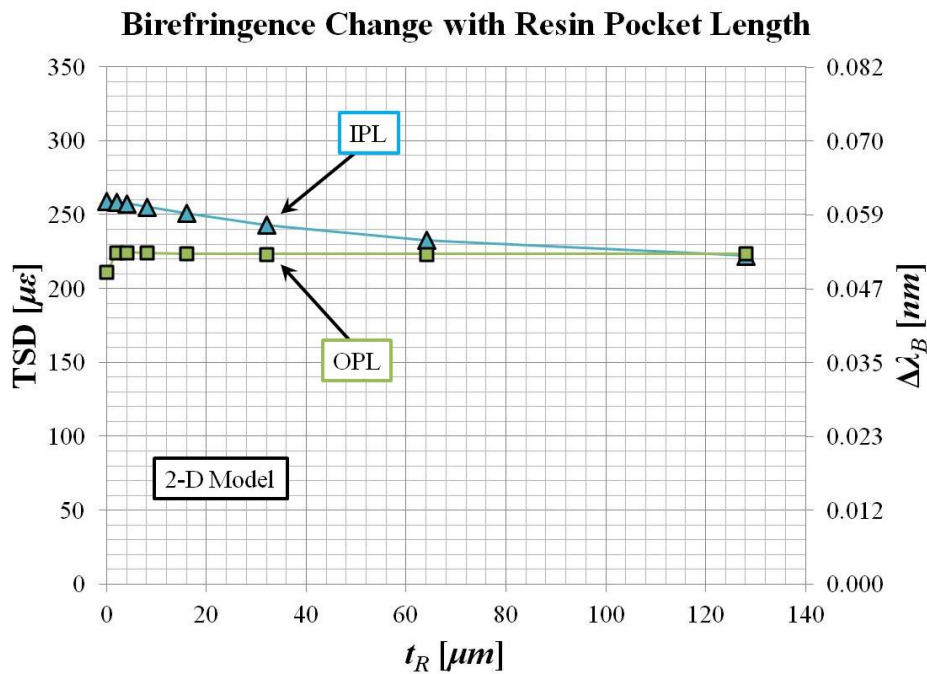


Figure 3-74: Variation of TSD in 2-D IPL and OPL models while varying resin pocket length.

The reason for the TSD reduction in the IPL model and not in the OPL model makes sense when considering the location of the highest stress concentration around the surface of the optical fiber. The stiffness of the optical fiber in the transverse direction is much higher than that of the surrounding 90° composite layer. This is because the Young's modulus of glass is ~70 *GPa* while the Young's modulus of the 90° layer in the directions transverse to the structural fibers is an order of magnitude smaller at ~7 *GPa*. Therefore, the location of the highest stress concentration in the optical fiber will be on the surface whose normal is parallel to the loading direction. This is the 1-direction (*x*-direction) for the IPL model and the 2-direction (*z*-direction) in the OPL model. Increasing the size of the resin pocket will mitigate the magnitude of the stress concentration when they coincide. This coincidence occurs in the IPL model, but not in the OPL model.

Despite the fact that neither the increase in polyimide coating thickness nor the increase in lenticular resin pocket size causes a complete mitigation of TSD in an embedded optical fiber, achievements were still made and lessons still learned from the process. One achievement is that a massive amount of time and money was saved in determining that these factors would only play a minor role in allaying a TSD without performing full experimental studies. A lesson from this work involves prioritizing factors which could eventually be implemented down the road. If a choice is made whether to pursue increasing the coating thickness or the size of the resin pocket, the coating thickness will almost certainly be chosen. The first reason is that the coating will help mitigate TSD in both IPL and OPL conditions. The second is that increasing the coating size exhibited a larger reduction in TSD compared to the lenticular pocket for both loading conditions. Another lesson is that a significant reduction in TSD can be achieved by increasing coating thickness; however, these results indicate that the thicker coating must be implemented in addition to other methods of TSD mitigation to be successful. Now that this study on potential factors to implement experimentally down the road has been completed, factors which are actually occurring and changing in the experiments carried out will be analyzed in order to help explain the experimental results observed.

3.5.4 Experimental Parameter Variation

This portion of the FEA results is meant to explain experimental results observed in the previous section. Specifically, the influence of de-adhesion between the polymer coating and the surrounding composite layer and of cross-ply crack propagation on TSD will be explored. Figure 3-75 demonstrates the evolution of de-adhesion around an optical fiber and the various angles of de-adhesion which will be studied.

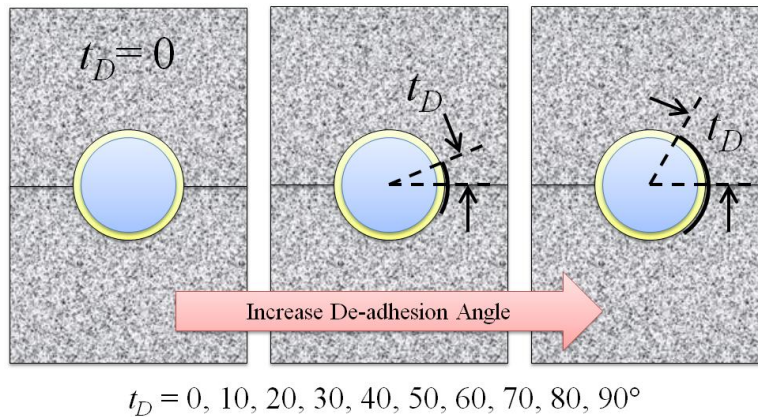


Figure 3-75: Variation of de-adhesion angle in the FEA study.

The advent of de-adhesion is most likely a precursor to cross-ply cracking. Figure 3-77 depicts the three magnitudes of cross-ply cracking considered with the crack height being 0, 50, or 100 % of the ply thickness.

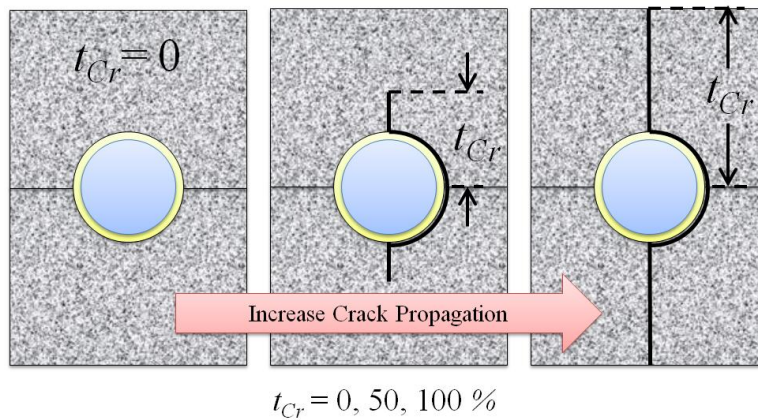


Figure 3-76: Variation of crack propagation in the FEA study.

The results of modeling the de-adhesion progression and the crack propagation in 2-D IPL and OPL models are plotted in Figure 3-77. As in previous IPL and OPL comparisons such as Figure 3-74, the vertical axes as well as the color and symbol combinations remain consistent. The horizontal axis represents the de-adhesion angle or the crack progression as a percent of ply thickness.

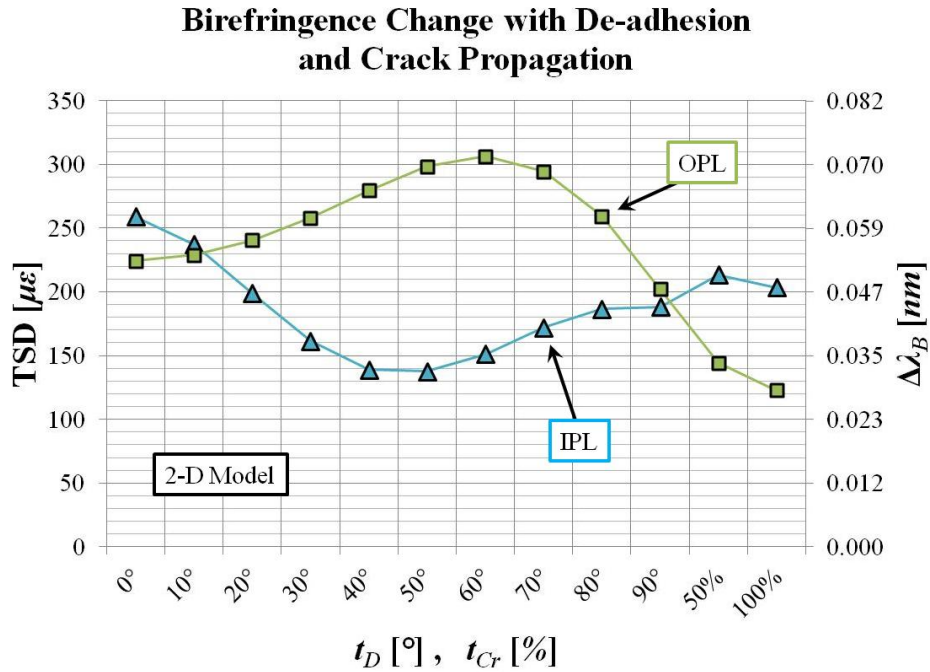


Figure 3-77: Variation of TSD in 2-D IPL and OPL models while varying de-adhesion angle and crack propagation.

These results are very interesting in that neither the IPL nor the OPL models result in monotonic behavior. For the IPL model, the TSD drops off until $\sim 45^\circ$ when the TSD begins to increase again before leveling off as 90° de-adhesion is approached. Once 50 % crack propagation is introduced, the TSD jumps up and then decreases slightly when $t_{Cr} = 100\%$. The OPL model behaves in almost the exact opposite manner. TSD initially increases up until $\sim 60^\circ$ de-adhesion when the TSD decreases. The drop-off in TSD is enhanced by the introduction of a propagating crack. In order to further verify and validate these results, 3-D models of the data

were created with the exception of the OPL crack propagation models which did not converge. The results of the 3-D IPL and OPL models are plotted in Figure 3-78.

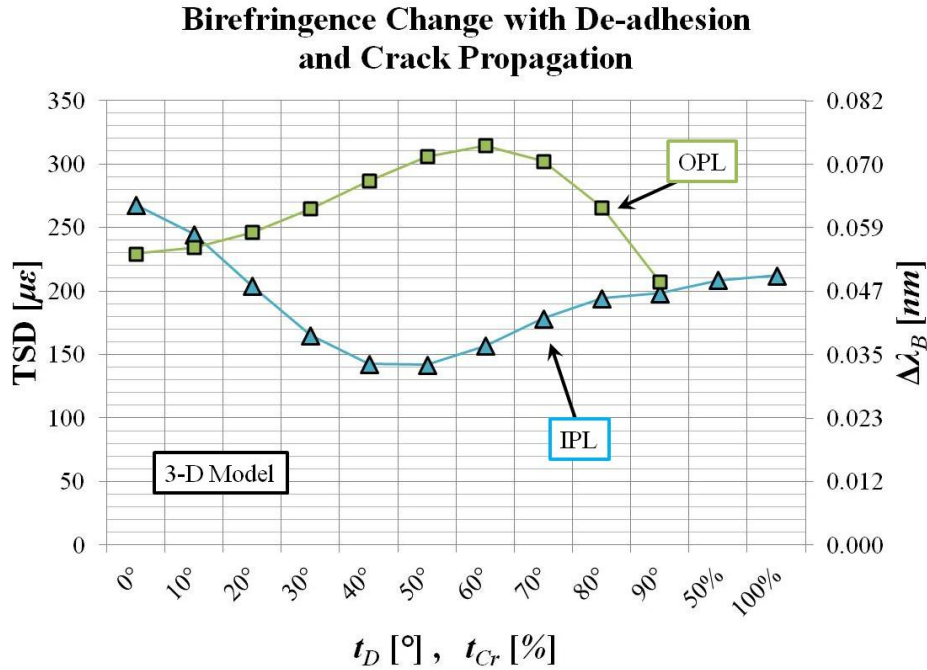


Figure 3-78: Variation of TSD in 3-D IPL and OPL models while varying de-adhesion angle and crack propagation.

The behavior is strikingly similar in Figure 3-77 and Figure 3-78. This establishes further confidence in the 2-D representation of the 3-D experiment. Additionally, the ability to carry out 3-D models allows for the analysis of the individual transverse strains in order to fully understand the TSD behavior. This behavior is plotted in Figure 3-79 below. Blue triangles, red diamonds, green squares, and orange circles represent IPL ϵ_1 , IPL ϵ_2 , OPL ϵ_1 , and OPL ϵ_2 , respectively.

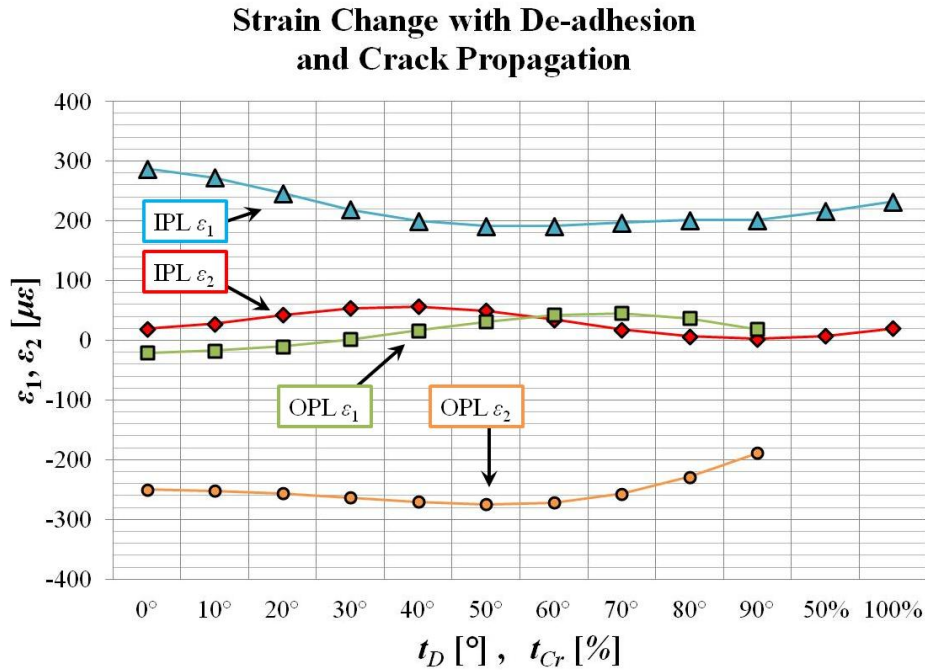


Figure 3-79: Variation of strains transverse to the optical fiber in 3-D IPL and OPL models while varying de-adhesion angle and crack propagation.

As the de-adhesion angle increases, IPL ε_1 initially decreases because the stress concentration at that location is partially mitigated. Therefore, less tensile strain in the 1-direction is transferred from the composite to the fiber. This reduction in IPL ε_1 in turn reduces the associated Poisson's contraction imparted by the composite on the fiber in the 2-direction. Recall that this 2-direction strain originating from the composite is one of two competing factors. The second is the fiber's desire to have a Poisson's expansion due to its longitudinal compression. The initiation of de-adhesion tilts the scales further in favor of the latter factor, thus causing IPL ε_2 to increase. As the de-adhesion wraps farther around the fiber, the location of the stress concentration rotates ahead of the leading edge of the de-adhesion surface. This rotation of the stress concentration closer to the top of the fiber exacerbates the transfer of strain from the composite material to the fiber. Thus, the trend reverses as the composite's positive strain in the 1-direction and negative strain in the 2-direction are more strongly asserted.

As for the OPL model, the initial de-adhesion does not coincide with the location of the stress concentration at the top of the fiber. This results in very little initial change in the

transverse strains. However, as the stress concentration associated with the leading edge of the de-adhesion surface gets closer to the top of the fiber, it compounds with the aforementioned stress concentration. The result is more strain transfer to the optical fiber from the composite and thus, the fiber is compressed more in the 2-direction and expands more in the 1-direction. Eventually at large enough de-adhesion angles, the de-adhesion boundary cuts into the stress concentration region and results in less strain transfer from the host. Thus, the compressive strain in the 2-direction is reduced. Additionally, the balance in the two competing OPL ε_1 factors (positive ε_1 from the Poisson's expansion due to the composite strain transfer versus negative ε_1 from Poisson's contraction due to the fiber elongating in the longitudinal direction) is shifted in favor of the latter effect; thus, the fiber experiences a negative shift in ε_1 .

Now that the role of de-adhesion and crack propagation in the TSD of an embedded optical fiber have been theoretically explored and analyzed, the FEA results will be related back to the experimental results. This will provide perspective on whether or not the observed reduction in TSD in the FEA models provides an adequate explanation of the experimental results.

3.5.5 Comparison with Experimental Results

First, recall Figure 3-48 which plotted the calculated TSD based on the split in the measured difference in the two reflected Bragg wavelengths during IPL. Note that there are two possible sources of birefringence in the data. The first is due to residual strain from the embedment and composite fabrication process and the second is due to the mechanical loading of the optical fiber. The data is re-plotted in the Figure 3-80 below, with the alteration that the residual TSD from the embedment process ($\sim 1000 \mu\varepsilon$) is stripped out of the results to demonstrate the birefringence developing due solely to mechanical testing. This will offer a better comparison because there is no residual strain in the FEA models.

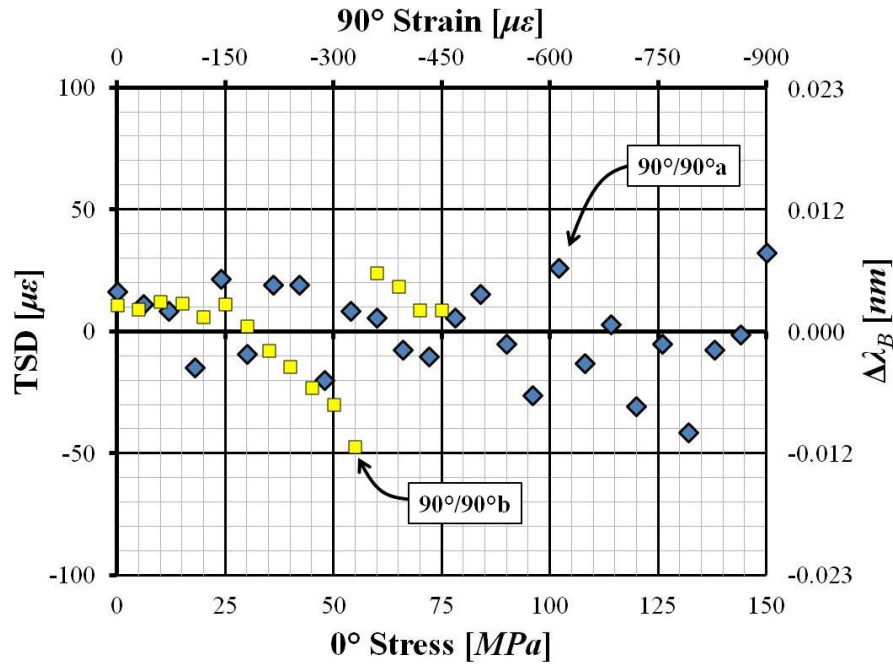


Figure 3-80: Evolution of TSD and birefringence during IPL for FBG-3 in the 90°/90°a and 90°/90°b samples.

As the mechanical load is increased from 0 to 150 *MPa* in the 90°/90°a sample and to 75 *MPa* in the 90°/90°b sample, the TSD is seen to vary between -50 $\mu\epsilon$ and +30 $\mu\epsilon$. Therefore, no significant TSD results from the load. This was explained with a cross-ply crack in the 90°/90°a sample, but the 90°/90°b sample was assumed to be pristine due to its small load history. The notion that a pristine sample results in no TSD under mechanical IPL conditions is in stark contrast with the results of the 3-D IPL model shown in Figure 3-67. The FEA shows that the TSD increases to $\sim 250 \mu\epsilon$ under a 75 *MPa* load which is above the noise level found in experimental results. Thus, something more must be going on which is not captured in the original, unaltered 3-D IPL model. This unknown factor must create a diminished TSD under IPL conditions while still allowing for significant birefringence during OPL conditions. Note that no sign of a cross-ply crack is evident in the 90°/90°b sample while the 7 μm thick coating and slight resin pocket cannot contribute to any significant drop in TSD according to previous FEA results.

It is therefore proposed that de-adhesion is occurring between the fiber optic and the composite. Under this proposed solution, the strain levels experienced by the 90°/90°b sample were not large enough to elicit a cross-ply crack, but were large enough to cause de-adhesion. According to the results in Figure 3-78, a de-adhesion in the 45° to 60° range would cause the TSD to significantly diminish during IPL conditions yet increase in OPL conditions. This type of behavior is qualitatively observed in the 90°/90°b experimental results where peaks were seen to remain the same distance apart during IPL yet move farther apart during OPL. The assumption that the de-adhesion has not gone far beyond the 60° angle (and thus, result in a reversal of the IPL and OPL TSD behavior) is supported by the fiber embedded in the 90°/90°a sample which experienced a cross-ply crack. In studying image (b) of Figure 3-49, the crack does not propagate from the top or bottom of the fiber. Therefore, if de-adhesion is indeed the precursor to a crack, the de-adhesion in the 90°/90°a sample only went up to ~70° in one direction around the fiber and ~45° around the other direction from the mid-plane. Therefore, a 90° de-adhesion angle was not experienced and it can be proposed that the composite matrix will crack well before de-adhesion approaches 90° and the TSD behavior reverses.

The presence of de-adhesion provides a qualitatively consistent explanation to the experimental 90°/90°b results, but the quantitative gap between FEA and experimental results is not entirely closed. De-adhesion would drop the IPL TSD nearly 50 % from ~270 $\mu\epsilon$ to ~140 $\mu\epsilon$, but not all the way into the ± 40 $\mu\epsilon$ noise level experimentally observed. The reason for this discrepancy resides within the method used to model the crack. As described in the experimental setup section, issues with element inversion and overlap were avoided by modeling the crack as a very compliant solid material. Figure 3-81 below demonstrates the change in stress distribution in the region of an embedded optical fiber under IPL conditions with the introduction of a cross-ply crack. As noted in the figure, the Young's modulus of the optical fiber is much larger than that of the fiber coating. The coating stiffness is approximately equal to the x -direction stiffness of the 90° layer. This in turn is much larger than the stiffness used to represent air. In the physical experiment, the absence of any material in the crack region causes a zero surface

traction on the crack surface and the portion of the optical fiber exposed to the crack. This completely negates any stress transfer from one crack surface to the other. This, however, is not the case in the model.

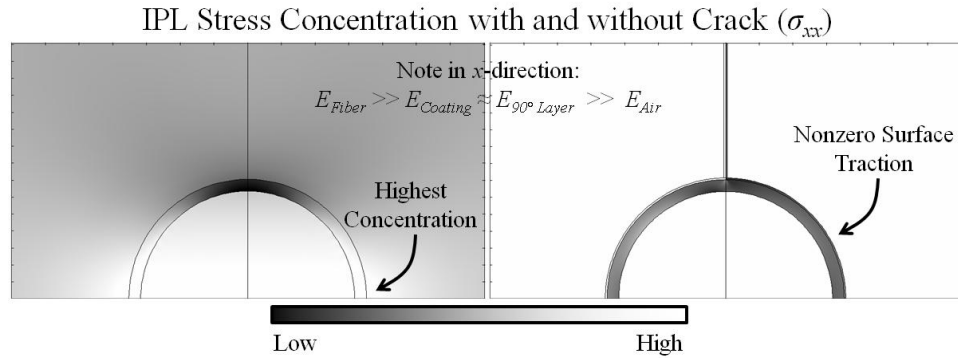


Figure 3-81: Stress transmission across the extremely compliant material used to model the crack.

Modeling the crack as a solid material of reduced stiffness allows the crack medium deformation to be entirely dependent on the surrounding material as is true in the experiment; however, stress is still communicated across the crack material medium which results in a nonzero surface traction on the portion of the optical fiber exposed to the crack. This transmission of stress across the crack surface prevents the optical fiber from being truly surface-mounted on the crack and thus, the modeled fiber will not behave as a uniaxial strain sensor. It is believed that removing this stress transfer across the surface could cause the quantitative gap in TSD between experiment and FEA to close.

3.5.6 Concluding Remarks

This concludes the work done to model the behavior of an optical fiber embedded in the 90°/90° configuration. There are three main outcomes of this section which expands our knowledge of the behavior of embedded optical fibers. The first outcome from modeling the fiber is the determination of strain transfer to an embedded optical fiber. Strain is completely communicated from the host material to the sensor in the longitudinal direction of the fiber optic,

but only a small portion of strain transverse to the optical fiber is transferred. This has major consequences in how FBG strain sensors should be implemented. This result lessens the potential for FBGs to behave as multiaxial strain sensors which can fully resolve the complex strain state of a host material; however, it promotes the potential for utilizing FBGs as effective uniaxial strain sensors.

The second outcome came after validating the use of 2-D models to effectively represent TSD in 3-D models. Two embedded-fiber parameters were altered to understand the role of coating thickness and the lenticular resin rich region size in fiber birefringence. The FEA results found that coating thickness can reduce the TSD by around 25 % for both IPL and OPL conditions. The resin pocket, on the other hand, reduces the IPL TSD by about 20 % but increases the OPL TSD by ~5 %. In conclusion, playing with composite fabrication procedures to alter the size of the resin pocket will most likely not bear worthwhile reductions in fiber birefringence. On the other hand, increasing coating thickness will reduce, but not completely eliminate birefringence in a FBG; therefore, this may be a worthwhile fiber parameter to adjust but it must be carried out in conjunction with other TSD mitigation techniques.

The final outcome is that an explanation has been proposed to explain the experimental results observed in the 90°/90°b IPL and OPL tests. De-adhesion between the fiber and host will result in a drop in TSD during IPL conditions and an increase during OPL conditions. This behavior agrees well qualitatively with the 90°/90°b experimental results. However, a quantitative gap still exists which may possibly be closed with a better model of the crack material as a void rather than an extremely compliant material. This would completely negate any stress transmission from one side of the crack or de-adhesion surface to the other and may drive the IPL TSD smaller while still keeping the OPL TSD larger.

3.6 Summary

The goal of this chapter was to develop the fiber optic strain sensing system by researching the feasibility of embedded FBGs. The ability to reliably embed FBG strain sensors with a structure expands the effectiveness and range of applications for the structural health monitoring system. Internal strain may lead to better characterization of the strain history of structural components in order to more reliably and efficiently determine when replacements and repairs need to be made. Additionally, the detection of internal damage such as cracks among other indicators of imminent failure will provide more information upon which to make decisions. The goal of exploring the feasibility of embedded FBG strain sensors was carried out by fabricating composite samples with embedded FBGs for mechanical load testing, performing a FEA study, and understanding the photoelastic theory which governs the behavior of and dictates the information which can be extracted from the sensors.

One conclusion to take away from this study is that current embedded FBG strain sensors cannot fully resolve the strain state of a host material despite the extensive work in literature on the subject. The first of two reasons behind this conclusion is that not enough information can currently be extracted from the FBG to fully calculate a general, complex strain state. One FBG cannot provide enough information to calculate all six strain components. Even in the relatively simple and controlled testing in this research, the two pieces of information from each FBG (the two reflected wavelengths associated with the principal strain transverse to the optical fiber) in many cases could not be used to calculate the three principal strains in the fiber. The mathematical reasoning behind this assertion was developed in the previous chapter. When a TSD is imparted on an optical fiber, an initial single-peak FBG splits into two or if the peaks are initially split, then the distance between them is altered. Therefore, transverse loading is, in many cases, a debilitating factor which negates the ability to resolve strain. While strains can be used to determine the reflected wavelengths of a FBG, the reverse process is not mathematically possible. The second reasons for this is that strain transfer from a host to an embedded fiber is

very poor in the direction transverse to the fiber optic. Even if one is able to utilize a FBG response to completely calculate the strain state of an optical fiber, it will not match the strain state of the host. Therefore, an added layer of complexity arises in correlating that fiber strain state to the host strain state when the strain transfer characteristics are not consistent in every direction.

Another conclusion from this research is that despite there being several factors which deny the FBG's ability to act as a multi-axial strain sensor, there is plenty of evidence indicating the potential use of embedded FBGs to behave as uniaxial FBG strain sensors and damage detectors. The aforementioned lack of strain transfer in the directions transverse to an optical fiber actually promote this form of sensing. This work was successful in identifying certain embedment configurations which will allow for the minimization of transverse loading. Thus, a range of embedment configurations were determined in which an embedded sensor will respond accurately and reliably. The consistent feature in all situations where the FBG can behave as a uniaxial strain sensor is that the reflected peaks do not shift relative to one another. As described mathematically in the previous chapter, this amounts to no change in TSD in the fiber cross-section. Interestingly enough, it was determined that despite birefringence developing from residual curing strains in the fabrication process, the FBG could still act as a uniaxial strain sensor. The qualifying condition for this is that during any subsequently applied load, the peaks cannot split any farther apart or move closer together.

Additional conclusions were also drawn pertaining to cross-ply cracking. As has been seen in literature on the subject, cross-ply cracks in the $0^\circ/90^\circ$ sample resulted in nonuniform strain which degraded the reflection signal. This result provides a boundary for the applicability of FBG strain sensors embedded perpendicular to adjacent structural fibers. In the $0^\circ/90^\circ$ results, the FBG was a well behaved uniaxial strain sensor up until the advent of cross-ply cracking. Therefore, the uniaxial assumption has not been invalidated for optical fibers embedded perpendicular to structural fibers as long as cross-ply cracking is absent. As for the $90^\circ/90^\circ$ sample, a cross-ply crack was seen to promote and maintain the uniaxial assumption of the

embedded FBGs for both IPL and OPL conditions. This previously unreported characteristic could possibly lead to designing sensor embedment configurations with a very broad range of loads in which the uniaxial assumption remains valid. If a sensor is designed to create a cross-ply crack which does not degrade the strength or stiffness of the composite (as is the case with composite specimen tested here), then a sensor could be created which is completely shielded from any host transverse strain.

This concludes the work on developing the strain sensing and damage detection ability of the FOID system. In the next two chapters, the FBGs will be used to measure phenomena other than strain to expand the capabilities of the optical sensing system.

CHAPTER 4:

FERROIC THIN FILM COATINGS

4.1 Synopsis

The next two chapters describe forays into expanding the sensing capabilities of the fiber optic sensing system. Using a human analogy, the previous chapter on strain sensing equates to perceiving body position, motion, and even pain (in the case of damage detection of cross-ply cracking). By increasing the functionality of the system to detect other physical phenomena such as pressure, temperature, and magnetic fields, a more valuable sensory system can be developed.

This chapter aims to accomplish this by coating the optical fiber Bragg gratings with thin film coatings using a sputtering technique. The two types of coatings will be Nickel-Titanium (NiTi) and Terfenol-D. After a literature review on alternative forms of FBG sensors, the methods of fabricating such sensors will be described and followed with experimental results. A common thread in the FBG sensors considered in this chapter is that strain is used as a thoroughfare to link optical responses to the applied external fields. The work performed in this research coupling shape memory alloy Nickel-Titanium (SMA NiTi) with the optical response of a FBG with a thin film ferroelastic coating is a continuation of work published by the author in Mohan et al. 2008 [198].

4.2 Literature Review

As established by the large number of papers published, strain monitoring with FBGs is a heavily explored area of research. FBG strain monitoring systems are becoming increasingly

advanced and are even available commercially. Therefore, much of the research involves implementation of the technology into important yet specific applications. A more novel and less explored area of FBG research is the expansion of FBG sensors into areas not described solely by photoelasticity. By exploring additional FBG sensing capabilities, opportunities arise to explore the fundamental coupling mechanisms between different physical phenomena. This type of research path allows for a more valuable contribution to the foundation of new classes of FBG sensors rather than simply building upon the well-established foundation of strain sensing FBGs. This section describes the body of literature describing the various ferroic materials commonly used to couple different forms of energy and how those materials have currently been incorporated with FBGs.

4.2.1 Ferroic Materials

Ferroic materials offer the ability to transduce energy from one form to another. Figure 4-1 below demonstrates various forms of energy such as electrical, chemical, and mechanical energy. Though the optical energy could be considered a combination of magnetic and electrical energy, it is treated as its own form for this research. The reason for this is that changes in optical energy are interpreted (i.e. not defined) as changes in the wavelength of light reflected by FBGs.

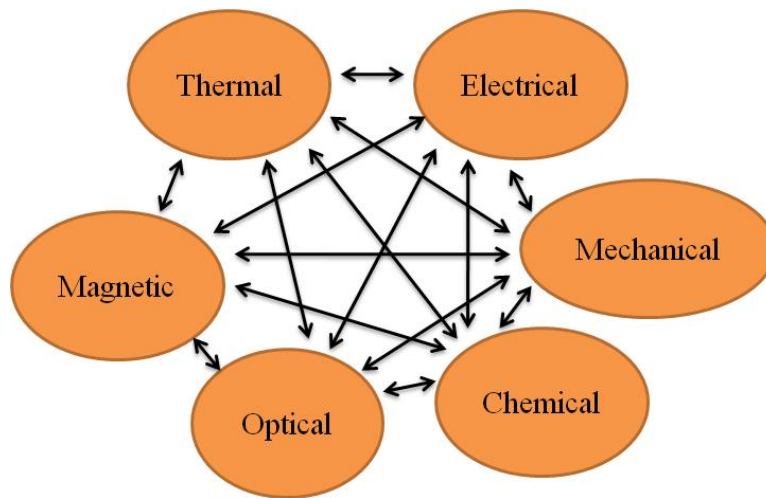


Figure 4-1: Various forms of energy which can be coupled.

The three main types of ferroic materials are ferroelastic, ferroelectric, and ferromagnetic. Ferroelectric materials, for example, spontaneously polarize when an electric field is applied and maintain that polarization when the electric field is removed. By the same token, ferromagnetic materials generate a spontaneous magnetization in the presence of a magnetic field. Two effects associated with ferroelectrics and ferromagnetic are piezoelectricity and magnetostriction, respectively. This simply means that a mechanical response (i.e. strain) occurs with the application of electric or magnetic fields. Alternatively, the application of strain to piezoelectric and magnetostrictive materials leads to spontaneous polarization and magnetization, respectively.

An example of the benefit of combining such materials is described by Fiebig 2005 and Khomskii 2006 [199, 200]. In their research, ferromagnetic and ferroelectric effects have been combined in what is known as a multiferroic material to couple magnetic and electric fields via strain. By creating a laminated composite with one layer ferroelectric and the other layer ferromagnetic, an applied magnetic field will cause the magnetostrictive layer to expand or contract. This strain will transfer to the piezoelectric layer which will produce an associated polarization. This is the direct magnetoelectric (ME) effect whereas the reverse (applying an electric field to create a magnetic response) is the converse ME effect. Research of the behavior of ferromagnetic and ferroelectric has been performed to fully understand the microscopic coupling mechanisms and also to determine optimal methods for applying these materials. For example, Khomskii 2006 describes material properties for combining the ferromagnetic and ferroelectric effects into one single phase material. Chung et al. 2009 explored the behavior of single ferromagnetic domains which make up the macro-scale material when attached to a piezoelectric substrate [201]. Wu et al. 2011 characterized ferromagnetic behavior in thin film nickel under load and electric field bias [202]. Multiferroic systems such as those explored in the referenced papers coupling electric and magnetic fields have applications in antennae, energy harvesting, and computer memory applications.

Nickel-Titanium (NiTi), also known as Nitinol, is a ferroelastic material with interesting properties. Depending on the composition of the alloy, NiTi may be superelastic or a shape memory alloy (SMA). SMAs have been heavily researched to develop and understand their unique properties such as large stress output, strain recovery, biocompatibility, and damping [32]. Some applications involving NiTi include eyeglass frames, antennae, and pipe coupling. At temperatures below the martensite finish (M_f) temperature, SMA NiTi is in a twinned martensitic structure. Upon loading, elastic deformation is followed with plastic deformation involving twin boundary reorientation. If the stress is released, the specimen will not return to its original shape. However, heating the NiTi above the austenite finish (A_f) temperature will result in the crystal structure recapturing its original shape. Miller and Lagoudas 2000 describe the response of shape memory NiTi undergoing a variety of thermomechanical experiments [203].

In addition to macro-scale applications, SMA NiTi has many uses in microelectromechanical system (MEMS) devices. Chun 2009 describes extensive research utilizing thin film superelastic NiTi for a biomedical application involving endovascular stents [204]. Kerrigan et al. 2009 utilized twin boundary motion in thin film NiTi for structural damping of micro-scale structures [205]. In order to create an effective thin film NiTi structure, the desired composition must be obtained during any deposition process and must remain consistent over a large area. This is a particularly important requirement because, as noted before, the behavior of the NiTi (e.g. A_s , A_f , M_s , and M_f temperatures, SMA or superelastic) largely depend on the composition. Ho and Carman 2000 and Ho et al. 2002 describe the necessary steps to obtain consistent Ni to Ti ratios during a sputtering process by using a heated target [206, 207]. These methods are applied in this research toward sputtering a thin film of NiTi onto a FBG. There are very few applications of NiTi involving fiber optics. Therefore, an interesting realm of research is to combine optical signals with ferroelastic behavior.

4.2.2 Alternative FBG Sensors

In this section, existing literature will be described which pertains to the use of ferroic and other active materials to couple optical responses with external phenomena such as strain. Most of the papers include the use of thin film materials which utilize strain as an intermediary between the optical response and the phenomenon of interest.

Lin et al. 1998 surrounded a FBG with a 5 mm outside-diameter layer of soldering lead [208]. The larger thermal expansion coefficient of the lead gave the FBG greater wavelength-shift sensitivity to temperature changes. While most metal coated optical fibers exist in order to protect the fiber from environmental and handling hazards at high temperatures (greater than the glass transition temperature of typical polymer coatings), this paper demonstrates the use of metal coatings to enhance the sensitivity of FBG temperature sensors.

Shelyakov and Terekhov 1995 attached an “L” shaped blinder made from 30 μm thick SMA TiNiCu to the end of an optical fiber [209]. The blinder is closed when cooled and thus, in a martensite phase. The result is a significant amount of light intensity reflected back from the film blinder. Upon heating into the austenite phase, the blinder significantly deforms and allows more light to exit the optical fiber and thus, reduces the reflection intensity. Due to the differing phase transformation temperatures in heating and cooling, a hysteresis in reflection intensity was measured when a thermal cycle was applied. While this demonstrates a coupling of the ferroelastic effect with an optical response, the device relies on capping the end of an optical fiber; thus, no distributed measurement can be made with a single optical fiber. Due to the binary high/low reflection states of the device, an additional limitation exists in determining the start and finish phase transition temperatures of the TiNiCu. This paper demonstrates an early example of incorporating SMAs with optical fibers.

Continuing with additional SMA applications, a 40 μm thick Ti-50.2at.%Ni SMA foil was embedded between 90° layers in a cross-ply CFRP composite laminate by Amano et al. 2005 [210]. When cross-ply cracks were induced upon loading, a stress concentration occurs in the region of the Bragg fiber embedded in a nearby 0° layer. The result was a broadening of the

FBG's wavelength reflection spectrum. The other effect was a local stress-induced twin boundary reorientation in the SMA foil. Upon heating the sample, the SMA foil compressed as it underwent a phase transformation to austenite and recovered the original, unstressed state. This compressive force helped to mitigate the nonuniform strain field and the broadening of the reflection spectrum was reversed. While this research demonstrates an interesting use of the shape memory effect, the overarching purpose is to aid FBGs in successfully monitoring strain in a composite. It does not expand the sensing capabilities of the FBG system into realms beyond mechanical phenomena.

In a similar manner, Balta et al. 2005 embedded a 150 μm diameter SMA NiTiCu wire into a Kevlar composite and monitored the influence of the shape memory effects on the composite's strain with an embedded FBG [211]. Upon stretching the composite, the SMA wire underwent a stress-induced phase transformation. Upon heating the wire with electrical current, a phase transformation took place which applied a compressive force on the composite. The goal was to create a feedback loop such that a mechanical load was counteracted with shape memory compression to achieve zero strain. This demonstrated the utilization of FBGs to monitor the shape memory effect. Such an approach does not develop a novel optical sensor, but instead utilized FBG strain sensors to monitor a novel type of composite material system.

Trouillet et al. 2006 created a hydrogen-sensing FBG using a thin film of Palladium (Pd) deposited on a small section of a Bragg fiber [212]. The film was between 25 and 300 nm thick and was not concentric around the entire surface of the optical fiber. The Pd was thermally evaporated onto a static FBG with a section of coating removed. Pure gaseous nitrogen flowed over the FBG and a shift in reflected wavelength was seen when 4 % hydrogen was added to the gaseous mixture. This was because the Pd expanded when in contact with hydrogen. This is a very good example of using a thin film coating deposited onto a FBG to expand the optical sensor's capabilities. One practical issue in such a device was the lack of repeatability in results when the coated FBG was exposed to the hydrogen enriched gaseous mixture for less than 2

minutes. This could lead to limitations in the sensor's response time and restrict its use in certain applications.

Viegas et al. 2009 used electrostatic self-assembly to create a thin layer of SiO₂ nanospheres coating a long period grating (LPG) [213]. The LPG coupled the fundamental forward propagating mode into forward propagating cladding modes which interacted with the surrounding nanospheres. When the coated optical fiber was exposed to increasing humidity, the hydrophilic spheres pulled water into the interstitial gaps and caused a change in the coating's index of refraction. This index change altered the wavelength of the cladding modes in a measurable manner. This was a clever method for creating a thin film coated optical grating sensor with capabilities beyond typical mechanical applications. However, exposing the surface of an optical fiber to humidity may cause cracks in the fiber. The survivability of the sensor under prolonged exposure was not addressed.

The research presented in this chapter on magnetic coated FBGs was completed in March of 2009. In November of that same year, Yang et al. 2009 published a paper describing successful deposition of thin film Terfenol-D on a FBG [214]. When placed in a magnetic field, the Terfenol-D strained the optical fiber and a shift in the reflected wavelength was seen. This demonstrated the same type of strain-based magnetometer described in this research.

Tien et al. side-polished a 20 *mm* long FBG at the end of an optical fiber and deposited iron onto the tip using electron-beam evaporation [215]. Once the sensor was fabricated, the fiber tip deflected based on its proximity to a NdFeB permanent magnet. The resulting strain-induced wavelength shift was correlated to magnetic flux in order to determine the sensitivity. The "top" and "bottom" of the optical fiber was reduced in thickness during polishing whereas the "left" and "right" were not. Thus, birefringence was induced and exacerbated by the Fe deposition. The peak assumed to be representative of the top-bottom polarization was tracked while the permanent magnet was moved closer to the FBG.

4.2.3 Concluding Remarks

Ferroic materials offer an excellent opportunity to couple optical fiber signals to external phenomena. Examples were provided describing how materials such as hydrogen-absorbing Pd, ferroelastic TiNiCu, and ferromagnetic Terfenol-D and iron have been used for optical coupling. While other papers have described interesting coupling behavior, very few offer the possibility of integration within a distributed, multifunctional sensing network for application in smart structures. One driving motivation in this research is to observe ferroelastic and ferromagnetic material behavior in a FBG in a manner which could expand the capabilities of the FOID measurement system. The fabrication and experimental methods for testing novel FBG sensors developed in this research is described next.

4.3 Fabrication and Experimental Setup

This section describes the methods and processes for fabricating the optical fiber sensor and the experimental setup used to evaluate the sensor. The steps preparing the optical fiber for fabrication will be described first followed by the thin film deposition process. The deposition section consists of a general description of sputtering, the specific setup for sputtering NiTi and Terfenol-D films onto the optical fiber, and the annealing process to crystallize the film. Methods for evaluating the deposition process are presented and followed with the experimental setup for sensor evaluation.

4.3.1 FBG Preparation

The Luna Innovations FBGs from the previous strain sensing research are also used to create alternative FBG sensors here. Thus, the same fiber characterization is carried out as in the previous chapter determining such values as $n_1 = 1.444$, $n_2 = 1.457$, $n = 1.450$, and $(\lambda_B)_0 = 1546.29 \text{ nm}$. The first step in the sensor fabrication is to use the cleaver shown in the previous chapter to obtain an optical fiber approximately 19-20 *cm* (7½-8”) long. The length constraint is

due to the sputtering process because the optical fiber must be long enough to fit in the holding apparatus which spans the 2.5-3” diameter target (which will be defined later). The fiber must also not be so long that too many FBGs will be wasted since only the section of optical fiber above the target will be coated.

Once the optical fiber has been cleaved from the spool, the polyimide coating must be removed so the new coating will be sputtered directly onto the silica fiber. This will provide better adhesion and strain transfer to the fiber optic. The polyimide coating is removed by placing the optical fiber in a dish of sulfuric acid heated to a temperature between 85 and 90 °C for approximately 5 minutes. The polyimide coating along the entire length of the optical fiber is removed. The results of etching the polyimide coating are shown in Figure 4-2 below in microscope images of two optical fibers that were partially immersed in sulfuric acid. The yellow, thicker portion to the right of the dotted line was outside the sulfuric acid and the coating was left intact. The clear, thinner portion to the left of the dotted line was immersed in sulfuric acid and no coating remains.

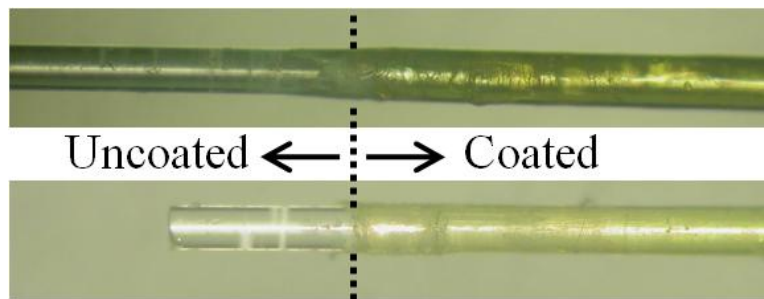


Figure 4-2: Sulfuric acid etching resulting in coated and uncoated regions of fiber.

In contrast with the two optical fibers shown above, the coating in this procedure is removed from the entire fiber optic sample. Next, the optical fiber is cleaned with dry wipes to remove any excess acid and placed on a hotplate at 150 °C for two minutes to drive off any moisture on the fiber and prevent absorption before loading into the sputtering chamber. The optical fiber has

now been fully characterized and prepared for the sputtering process which will be described next.

4.3.2 Thin Film Deposition

This section describes key aspects of sputtering in general and is followed by the specific steps used to sputter NiTi and Terfenol-D onto optical fibers.

4.3.2.1 GENERAL SPUTTERING DEPOSITION

Figure 4-3 below shows the custom-designed Denton DC magnetron sputtering system used for deposition in this research. A Stanford Research residual gas analyzer is used to ensure the chamber contains a proper sputtering environment with negligible amounts of water, carbon dioxide, and carbon monoxide.



Figure 4-3: Custom DC magnetron sputtering system.

The chamber is filled with 99.999 % purity argon (Ar) gas which is ionized with a DC electric field. The ionized atoms move rapidly in the electric field and slam into a heated target, which is the bulk source of NiTi. After impact, the Ni and Ti atoms vaporize and fly up to a substrate which is usually a silicon wafer. In this research, the substrate is the optical fiber. A shutter is typically used to shield the substrate from deposition until the target has had a

sufficient amount of time (~4 minutes) to heat up. The heated target method allows for compositional control less than 0.5 atomic percent (*at.%*) to be achieved [32].

4.3.2.2 FBG SPUTTERING TECHNIQUE

The apparatus inside the sputtering chamber for deposition onto optical fibers is demonstrated in Figure 4-4 below. A rotating holder clamps onto one end of the optical fiber while the opposite end is placed on a metal support. The optical fiber spans across the target material (3" diameter NiTi from SEI Engineering Materials or 2.5" diameter Terfenol-D from Etienne). Due to slight variations between targets, thin film is first sputtered onto a layer of silica topping a silicon substrate placed 4 *cm* above the target. Once a film with satisfactory properties (i.e. displaying the shape-memory effect and acceptable phase transition temperatures) is achieved, the same target and sputtering conditions are used to coat an optical fiber spanning the target at the same height of 4 *cm*.

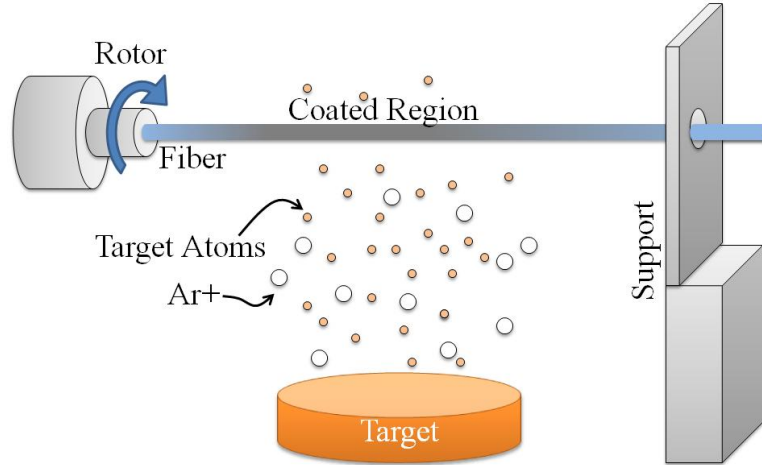


Figure 4-4: Fiber holder and rotator apparatus within the sputtering chamber.

After placing the optical fiber in the sputtering chamber but before sputtering begins, the chamber temperature is increased to 120 °C for 30 minutes in order to prevent moisture absorption by the uncoated optical fiber. Next, a series of steps is carried out to remove a satisfactory amount of air and replace it with Ar gas. This is done by alternating between

pumping out gas from the chamber and purging the chamber with Ar. The final Ar pressure is 2.5×10^{-3} Torr while the base pressure and partial pressure of residual gases are 10^{-8} and 10^{-9} Torr respectively. A sputtering power of 300 W is used while the optical fiber rotates at 40 rpm. The target temperature is maintained at 650 °C, a relatively hot temperature which, as described earlier, reduces the compositional variation of NiTi along the length of the optical fiber. The ferroelastic target composition is 52 at.% Ni and 48 at.% Ti in order to achieve shape memory alloy NiTi at room temperature (as opposed to a superelastic composition). The ferromagnetic target composition is 12 at.% Tb, 65 at.% Fe, and 23 at.% Dy. For NiTi, sputtering is carried out for 24 minutes in order to produce a $\sim 2 \mu\text{m}$ thick coating ($\sim 115 \text{ nm}/\text{min}$). For Terfenol-D, sputtering is carried out for ~ 10 minutes at $\sim 100 \text{ nm}/\text{min}$ to achieve a film thickness of about $1 \mu\text{m}$. Figure 4-5 below demonstrates two pictures of the sputtering chamber during deposition. The picture on the left is for NiTi while the right is for Terfenol-D. Note the rotor and support components of the sputtering apparatus in addition to the target. The glow above the target is the plasma due to ionized argon atoms and is blue for NiTi deposition and purple in Terfenol-D deposition.

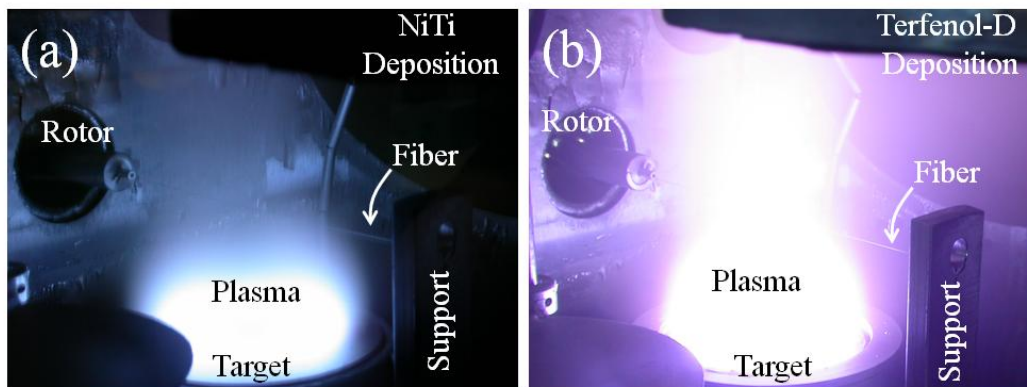


Figure 4-5: Plasmas developing within the sputtering chamber during deposition of NiTi and Terfenol-D.

4.3.2.3 ANNEALING

Individual atoms from the target (nickel and titanium for a NiTi target) land randomly on the optical fiber and silicon wafer in an amorphous crystal state. In order to achieve the desired material properties, an annealing process must take place to crystallize the thin film coating. A crucial factor to consider when determining the annealing process temperature and time is the survivability of fiber Bragg gratings at high temperatures. During FBG fabrication, energy is put into the optical fiber with UV light to alter the germanium dopant bonds in the optical fiber core in a periodic fashion. Exposing FBGs to high temperatures will reverse the effects of the UV light and cause the FBG to effectively “wash out” as the germanium dopants return to their original state and the core index of refraction returns to a constant value. Thus, the annealing process must be completed with the thin film coating modified from a high energy state (amorphous) to a low energy state (crystallized) before the optical fiber core converts from its high energy state (periodic) to a low energy state (constant). Using a few trial and error steps, an annealing temperature and time of 500 °C for 30 minutes was used to crystallize the NiTi and 450 °C for 60 minutes with Terfenol-D without washing out the FBGs. Annealing NiTi at 550 °C for 30 minutes, for example, reduced the FBG reflection signal beyond recognition.

4.3.3 Thin Film Characterization

Before testing the newly fabricated FBG sensors, steps were taken to characterize and assess the thin film deposition process. One method to specifically evaluate the NiTi thin film’s ferroelastic properties is a digital scanning calorimetry (DSC) technique. Before sputtering onto the optical fiber, thin film was deposited onto a silicon dioxide (SiO₂) layer topping a silicon substrate above the target. A piece of film deposited on the wafer 10 *milligram* in mass was removed from the substrate and placed inside a digital scanning calorimeter (DSC). The model of the system is a Shimadzu DSC-50. The reason this was performed on a stand-alone piece of NiTi is that the mass of NiTi sputtered directly onto the optical fiber is too small to obtain a measurable response. The DSC measures the difference between heat flow applied across the

surface of a thin film NiTi sample and a reference sample whose thermal properties such as heat capacity (c_p) are well known. For this research, no specimen was placed in the reference chamber, effectively making the reference material air. Thus, the DSC measures the difference in heat flow required to obtain a desired temperature in the NiTi sample compared to air. Upon initial heating when the thermal properties of the NiTi and reference samples are constant, a steadily increasing differential in heat flow will occur. During phase transformations, exothermic or endothermic reactions take place in the NiTi sample which significantly changes the differential heat flow measured by the DSC. This test, therefore, indicates what temperatures span the phase transition and whether those changes are exothermic or endothermic.

Another method of evaluation is to use a scanning electron microscope (SEM) to get a closer visual of the thin film coating. The SEM picture will tell us the thickness of the coating in addition to confirming whether or not the film is conformal. It may also indicate whether or not the film is well adhered to the optical fiber.

Another method of film characterization is an X-ray diffraction (XRD) technique. With this method, an x-ray beam is aimed at the thin film coated optical fiber and the diffraction of such a beam due to the electron clouds of the specimen's atoms is monitored. This will indicate the thin film's crystallographic structure to determine whether the annealing process was successful in converting the film from its amorphous state to a crystallized state. A Bruker AXS XRD with a greater area diffraction detection system is used to emit Cu K α radiation. The beam's spot size is 0.5 mm and diffraction intensity data in the 2θ range of 27.5° to 62.5° is recorded.

4.3.4 Sensor Testing

Two different types of sensors were created; thus, two different types of tests were performed to evaluate the FBGs. For the NiTi coated FBGs, the temperature was cycled from 10°C to over 109°C and back. For the Terfenol-D coated FBGs, DC and AC currents were run through a coil to create a magnetic field in the direction of the optical fiber.

4.3.4.1 NICKEL TITANIUM COATING

The FBG sensor was placed into an Omega CL-720A thermocouple calibration chamber to apply the thermal cycle. Figure 4-6 below shows the test setup. The FOID system is plugged into the computer and the reflection signal is alternately gathered in Langley and Raw Data mode. The light output travels through a lead-in optical fiber in which no FBGs are written. The lead-in fiber plugs into one end of the mechanical splice held over the opening to the thermal chamber. The NiTi coated optical fiber plugs into the opposite end of the mechanical splice and is lowered into the thermal chamber.

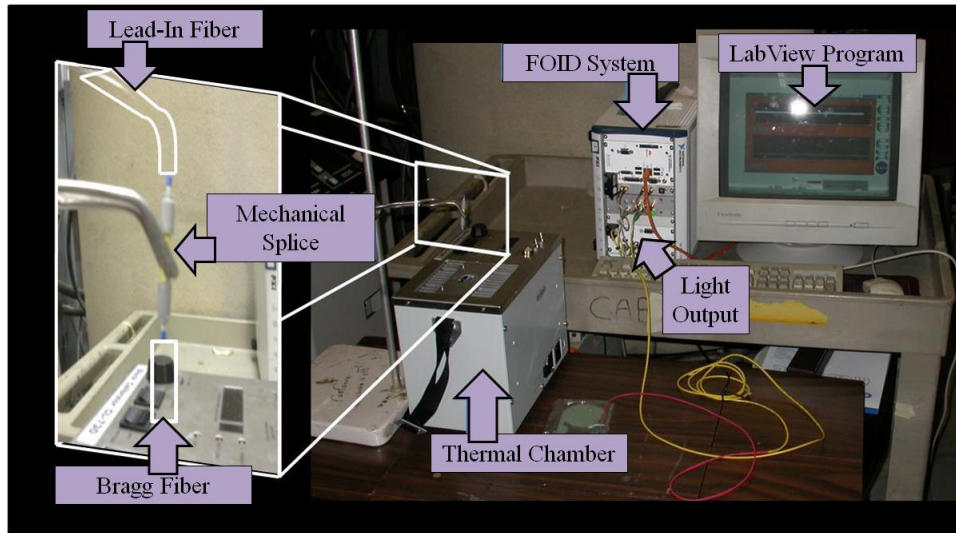


Figure 4-6: Experimental setup for thermal testing of NiTi coated FBGs.

As will be seen in the results, there is a thermal gradient due to conduction and convection which cause the first two FBGs not to match the rest of the FBGs deeper within the chamber where a steady state temperature is present. Five raw data snapshots were taken at each temperature increment to obtain five wavelength measurements in order to establish a mean and a standard deviation (i.e. error) in the Bragg wavelength. Snapshots were initially taken at room temperature for reference. Subsequently, the temperature was set to 10 °C and increased in increments of 2 °C up to 108 °C and then finally to the chamber's maximum value of 109.1 °C. From there, the temperature was decreased in the same incremental values back to 10 °C before

returning to room temperature. Approximately 2-3 minutes elapsed between when the desired temperature was input to the thermal chamber interface and when the optical fiber data was taken. This allowed ample time for the chamber to converge to steady state as corroborated by the thermal chamber's own temperature measurement system and the Langley mode real-time monitoring of the wavelength shifts of the FBGs within the thermal chamber.

For comparison purposes, the same steps were taken with an optical fiber coated with its original polyimide material. This provides a control which allows us to determine the true influence of changing the coating from polyimide to NiTi.

4.3.4.2 TERFENOL-D

A magnetic field was applied parallel to the longitudinal direction of the optical fiber with a Terfenol-D thin film coating as shown in Figure 4-7 below or to a FBG surface-mounted to a bulk Terfenol-D specimen. The magnetic field (labeled "H-Field" in the figure) was created with current running through a coil surrounding the Bragg fiber. An electric signal (AC or DC) was amplified and fed into the coil in order to provide an alternating or static magnetic field. Additionally, a cooling system was used to run liquid through the coil in order to prevent overheating due to the large currents. A magnetometer was inserted in the coil and used to simultaneously measure and record the applied magnetic field. The FOID data was collected in Langley mode for both DC and AC magnetic fields. The magnetic field was measured with a F.W. Bell model 5080 Gauss/Teslameter magnetic probe and recorded with LabView.

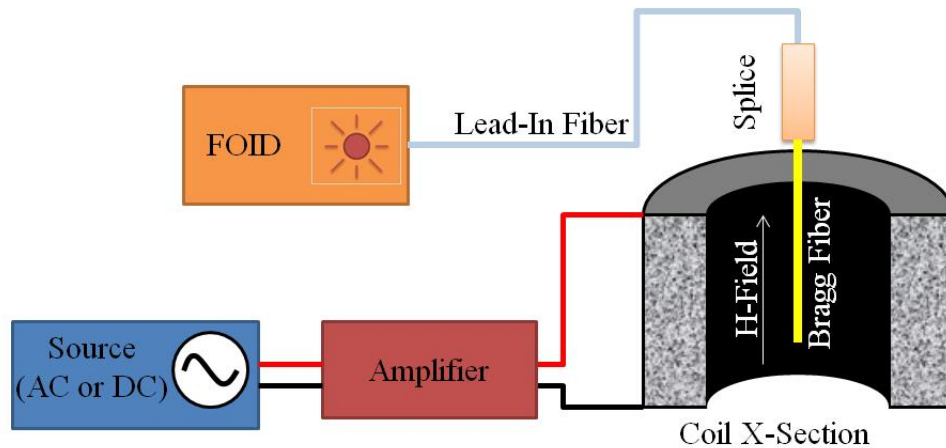


Figure 4-7: Magnetic field test schematic for experiment with Terfenol-D coated FBGs.

Two sets of magnetic field tests were performed with Terfenol-D. The first set involves surface mounting a polyimide-coated Bragg fiber onto a bulk piece of Terfenol-D within the coil while the second set involves the thin film coated Bragg fiber. Due to the small volume fraction of Terfenol-D for the thin-film coated FBG (~5 %), a large, static magnetic field 2 *kiloOersted* (*kOe*) in magnitude did not provide a sufficiently large strain response in the thin film to cause a noticeable shift in λ_B . In order to get around this, an AC magnetic field was applied and a Fourier transform was used to transform the time-domain data (which appears to be composed entirely of noise) into the frequency domain. By doing this, the frequency domain data may show a spike at the applied AC signal frequency if the strain is not “buried” too deeply within the time-domain noise. This process will be demonstrated in the first set with bulk Terfenol-D and replicated with thin film.

In the first set, a DC magnetic field was applied in the range of zero to 2 *kOe* followed by a sinusoidal AC field from 0.6 to 1.6 *kOe* at 0.2 *Hz*. Finally, an AC field from 76 to 95 *Oersted* (*Oe*) at 0.2 *Hz* was applied. The purpose of this first set of tests was to demonstrate the coupling of magnetic fields with a response in λ_B for a FBG. Once this has been demonstrated with a bulk piece of Terfenol-D, the next set of tests involving a Bragg fiber coated with thin film Terfenol-D was performed.

In the second test set, 14 different AC magnetic fields were applied to the thin film coated Bragg fiber – 7 different frequencies each with two wave shapes. The two wave shapes were a sine wave and a square wave while the 7 frequencies were 0.1, 0.2, 0.5, 1.0, 1.2, 1.5, and 2.0 *Hz*. The sine wave varied from 0 to 1.67 *kOe* and the square wave from 0 to 1.55 *kOe* in magnitude.

4.3.5 Concluding Remarks

This concludes the description of the fabrication and experimentation techniques used to create and test the ferroelastic and ferromagnetic FBG sensors. The sputtering parameters for both NiTi and Terfenol-D were carefully chosen to balance achieving substantial ferroic behavior in the thin film coating while not degrading the FBG reflection signal. Methods for evaluating the success of the deposition process and characterizing the film were described. Additionally, methods for testing the ferroelastic and ferromagnetic behavior of the thin film coatings were illustrated with descriptions of thermal and magnetic field testing. The results of this testing as well as the thin film characterization are presented next.

4.4 Results

This describes the results of the thin film characterization and the experimental testing. The thin film NiTi coating results will be shown first demonstrating a successful deposition and followed with observations of ferroelastic phase transitions in the FBG reflection signal. The Terfenol-D results, on the other hand, did not conclusively identify a crystallized film nor a ferromagnetic response in the thin film coating. However, attaching the FBG to a bulk sample did demonstrate the desired coupling and demonstrated the effectiveness of the aforementioned Fourier transform technique to extract sub-noise responses from the data.

4.4.1 NiTi Coated FBG

The successful deposition and demonstration of ferroelastic behavior in a FBG signal are described here. The characterization of the thin film deposition will be provided and followed by a demonstration of the thermal response of a NiTi coated FBG undergoing a temperature cycle.

4.4.1.1 FILM CHARACTERIZATION RESULTS

The results of the previously described characterization procedures for the NiTi thin film will be described first. The DSC results are shown in Figure 4-8 below to demonstrate that the sputtering method and target composition used does indeed provide shape memory behavior in the thin film NiTi. The aforementioned 10 mg piece of thin film NiTi and the reference material (air) are heated in the chamber from 0 °C to ~127 °C and subsequently cooled back to 0 °C. Upon initial heating, the difference in heat capacities of the NiTi sample and air results in a linearly increasing difference in heat flow required to establish the steadily increasing temperatures. At 78 °C, the NiTi begins to undergo an endothermic phase transition from martensite to austenite (hence, this is referred to as the austenite start temperature, or A_s in the figure). The endothermic reaction results in the NiTi absorbing the heat applied and thus, the measured heat flow dips. Once the phase transition is completed at the austenite finish temperature (A_f) of 102 °C, the steady linear increase is recovered. Upon cooling, the linear DSC data is interrupted by an exothermic reaction which results in the film expelling heat into the DSC chamber at 68 °C. Therefore, a spike in the heat flow measured occurs from the martensite start ($M_s = 68$ °C) to the martensite finish ($M_f = 40$ °C) temperatures. Once below the M_f temperature, the entire film is martensite and the linear DSC data trend is recovered. This demonstrates that the film deposition technique should provide a SMA NiTi coating.

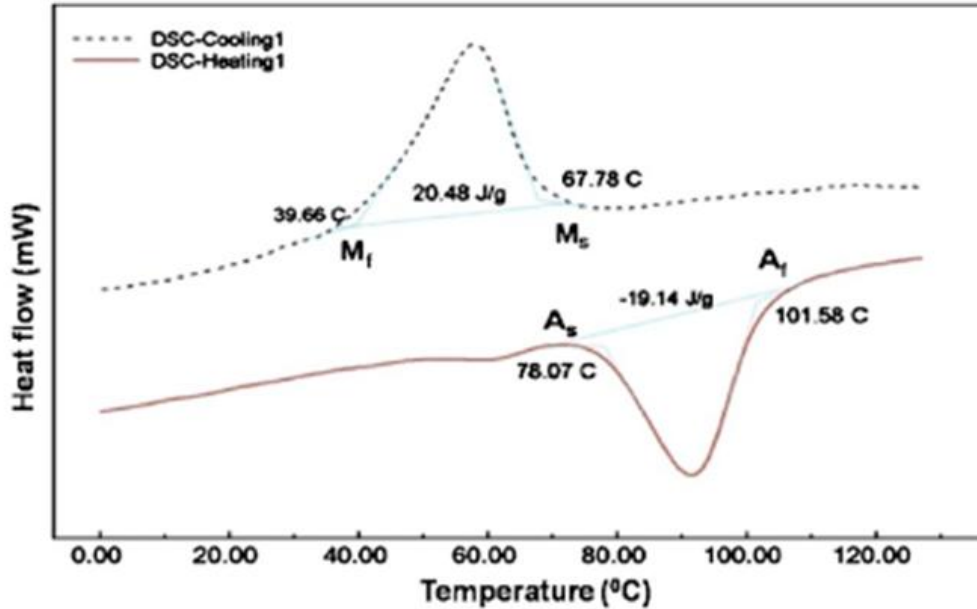


Figure 4-8: DSC results demonstrating phase transition temperatures in thin film NiTi, indicating the deposition parameters are satisfactory for coating an optical fiber.

The images shown in Figure 4-9 below are SEM images of the NiTi coating on the optical fiber. Lateral, cross-section, and zoomed in cross-section views of a NiTi coated FBG are shown in order to demonstrate visual evidence that the coating is both conformal and well-adhered to the optical fiber. The color pattern on the optical fiber cross section is due to the non-conducting nature of silica. Charging is the result of the SEM hitting the optical fiber with electrons. The 127 μm diameter optical fiber has a NiTi coating 2 μm thick. In the center picture depicting the zoomed-out cross-section, the material in the bottom left is a substrate to which the optical fiber is bonded using an epoxy mold. The epoxy holds the fiber in place during polishing in order to get a satisfactorily pristine surface for SEM imaging.

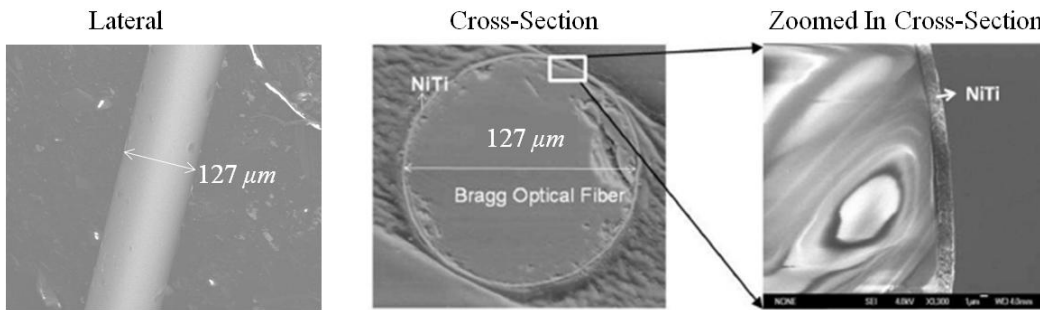


Figure 4-9: Lateral and cross-sectional SEM images of a NiTi coated FBG.

Now that the thin film has passed visual inspection, the next step is to use a XRD system to verify that the thin film is crystalline. The results of the X-ray sweep at 0 °C are shown in Figure 4-10 below. The various peaks indicate that at the low temperature, the NiTi is crystallized in a B19' type crystal structure – also referred to as monoclinic or Martensite. An amorphous crystal structure would lack any peaks because there is no repeated pattern in the atoms to cause a constructively interfering wave reflection. Due to the established crystallinity, we expect that upon heating a phase transition will occur to a B2 type crystal structure – also referred to as body center cubic or Austenite. The last step is to verify that such a phase transformation will occur on a piece of thin film NiTi sputtered onto a layer of silicon dioxide before rotating optical fiber.

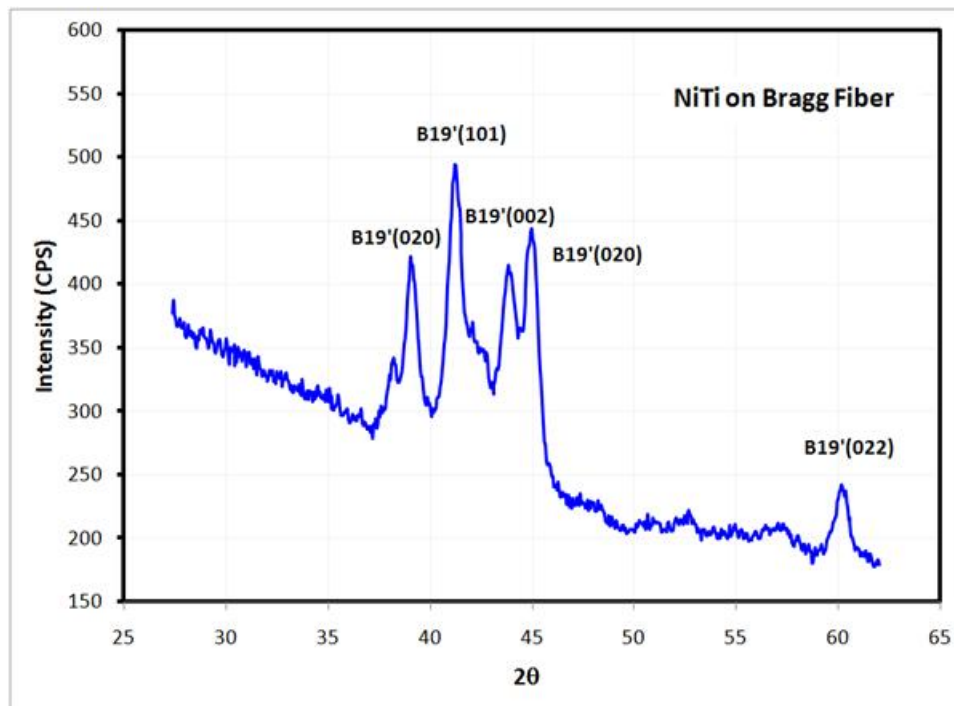


Figure 4-10: XRD data demonstrating the thin film NiTi coating the optical fiber is crystalline.

This completes the results of the thin film characterization for the NiTi deposition. It has been established that the thin film visually is well adhered to the optical fiber, the coating is conformal and crystallized, and we expect a phase transition from martensite at room temperature to austenite at elevated temperatures. We also expect those phase transition temperatures to vary depending on whether the specimen is being heated or cooled. The next step is to place the thin-film NiTi coated FBGs in a thermal chamber and measure the response in comparison to a polyimide coated FBG.

4.4.1.2 THERMAL TESTING RESULTS

The length of the coated optical fiber used in testing is 5.5 *cm*. This includes six FBGs 0.5 *cm* in length each and five regions with no grating also 0.5 *cm* each. This is shown in Figure 4-11 below which plots the reflection intensity along the length of the Bragg fiber. A sharp spike is seen in reflection intensity at the beginning of the fiber where it is spliced with the lead-in optical

fiber and at the end of the fiber due to reflection off the back-end surface. During testing, the narrow peak seen due to the end reflection increases in width and makes the sixth FBG unreadable. Therefore, only the first five FBGs are analyzed.

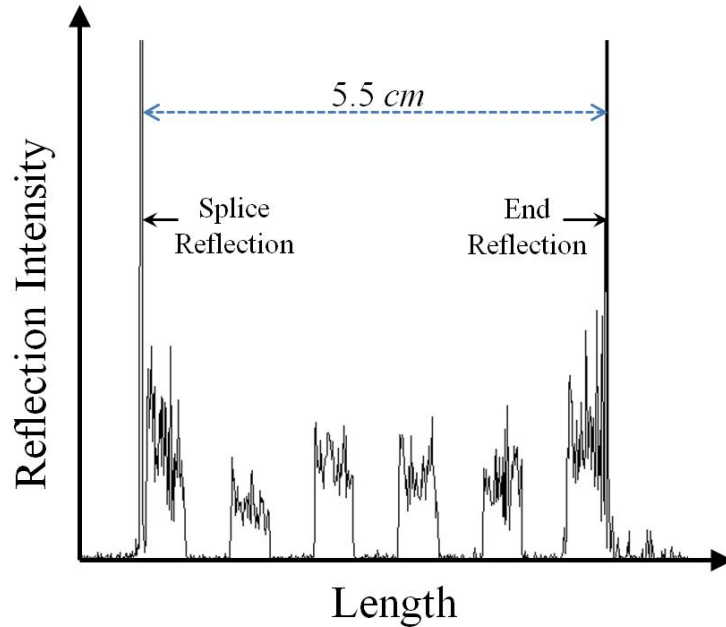


Figure 4-11: Length domain plot of the NiTi coated Bragg fiber reflection signal.

The first set of results presented next is the shift in Bragg wavelength, $\Delta\lambda_B$, for the five FBGs along the length of the Bragg fiber. The temperatures considered (in addition to room temperature) range from 10 °C to 110 °C in increments of 20 °C. (Note that the 110 °C data is rounded from the maximum chamber temperature, 109.1 °C, which does not create any error in the conclusions drawn from the plot). Figure 4-12 shows the $\Delta\lambda_B$ profile along the length of the fiber. The shifts in λ_B are calculated by taking the Bragg wavelength at the specified temperatures and subtracting λ_B at room temperature (thus the room temperature shift is 0 nm). Each symbol represents the average of five data samples whose standard deviations ranged between 0.002 and 0.006 nm. Solid lines used to connect isothermal data sets are for viewing purposes only.

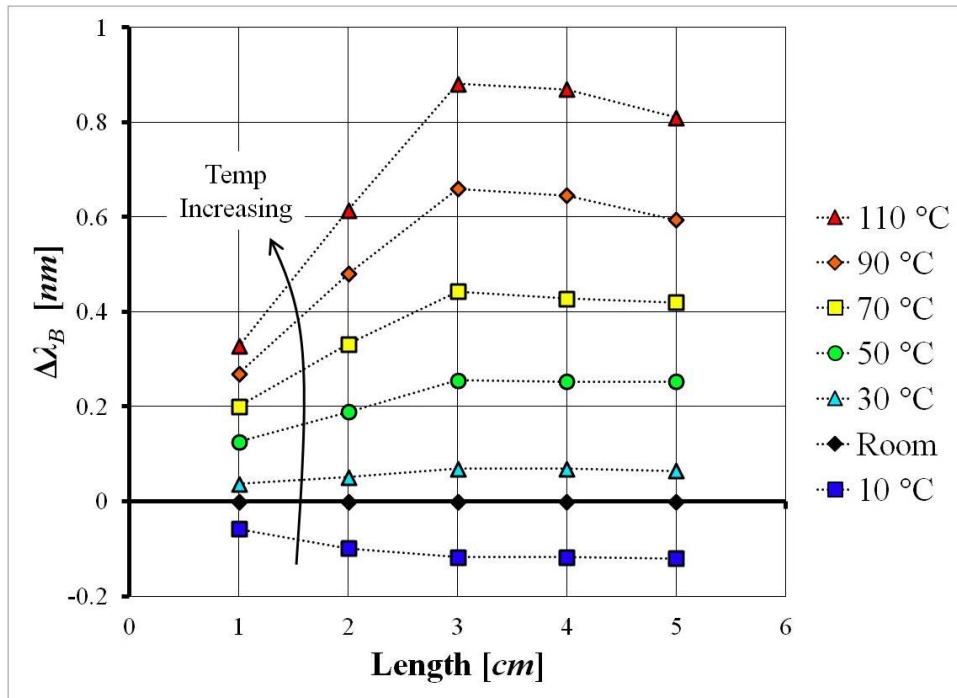


Figure 4-12: Bragg wavelength shift profile along the NiTi coated Bragg fiber at various temperatures.

The first two FBGs lie within the mechanical splice and do not experience the same input temperatures as the other three FBGs. The result is a thermal gradient that exists and levels out after 3 cm. For temperatures 50 °C and below, this conclusion is supported with consistent λ_B shifts for the last three FBGs. However, for temperatures 70 °C and above, there are inconsistent shifts in λ_B for the three FBGs previously concluded to share the same thermal environment. The cause of this inconsistency is that FBGs in the 3-5 cm range are experiencing the same temperature but not exhibiting the same ferroelastic behavior. This will be elaborated upon in the coming results. We will first look at the $\Delta\lambda_B$ data for the FBG at the 3 cm mark in comparison with the $\Delta\lambda_B$ of a polyimide coated FBG undergoing the same temperature change. We will then compare this result with the same NiTi-polyimide data for the FBG at the 5 cm mark.

Figure 4-13 below shows a comparison between shifts in λ_B for a FBG coated in its original polyimide material with $\Delta\lambda_B$ of the FBG coated in NiTi at the 3 cm mark in the previous figure. The red diamond symbols represent polyimide data, yellow circles represent NiTi $\Delta\lambda_B$ data upon heating, and blue triangles represent NiTi data upon cooling. Each symbol represents the average

of five data samples whose standard deviations ranged between 0.002 and 0.006 nm. Note that there is a slight curvature in the polyimide data due to silica's thermo-optic coefficient increasing slightly with increased temperature. The NiTi data follows the polyimide data up until about 50 °C when a nonlinear trend occurs. This kink lasts until about 65 °C when it once again trends parallel to the polyimide data.

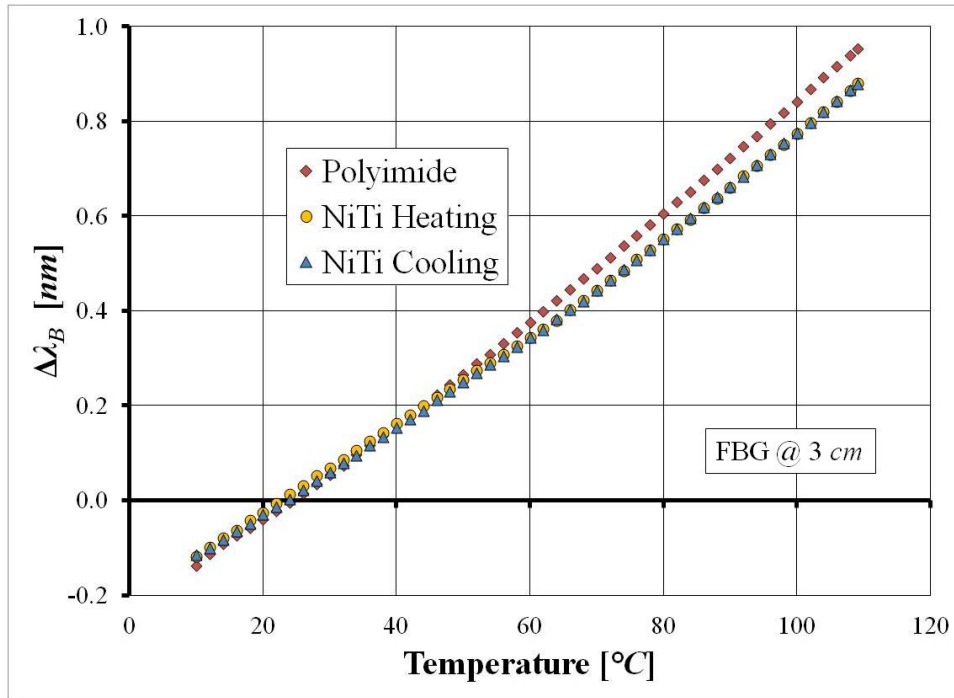


Figure 4-13: Comparison of Bragg wavelength shift in a polyimide coated FBG and the NiTi coated FBG at the 3 cm mark along the fiber.

The reason for the slight difference between polyimide and NiTi data is that during heating, the NiTi undergoes a phase transition from martensite to austenite. Upon cooling, this phase transition is reversed. Note that the small (~3 %) volume fraction of NiTi in the sensor results in a very small difference in thermally induced $\Delta\lambda_B$ between the polyimide and NiTi coated FBGs. This is in spite of the coefficient of thermal expansion (CTE) for the 7 μm thick polyimide being nearly ten times larger than that of the 2 μm thick martensitic NiTi (55 versus 6 $\mu\text{E}/^\circ\text{C}$). The same idea holds true with austenitic NiTi having a CTE of 11 $\mu\text{E}/^\circ\text{C}$ and explains why the NiTi and polyimide $\Delta\lambda_B$ data are parallel at elevated temperatures. During the phase transition

temperatures, however, the NiTi undergoes a strain change on the order of several percent which, despite the small volume fraction, is large enough to cause a split from its agreement with the polyimide data. It has therefore been demonstrated that the NiTi $\Delta\lambda_B$ data runs parallel to the polyimide data except during phase transitions. We expect that the phase transition occurs across a different temperature range in the heating direction than the cooling direction. However, the near identical NiTi heating and cooling data does not demonstrate this. The results shown next for the NiTi coated FBG at the 5 *cm* location will explain why.

Figure 4-14 below is a plot showing the same polyimide-NiTi comparison in Figure 4-13 but this time with the NiTi coated FBG at the 5 *cm* location. Once again, red diamonds, yellow circles, and blue triangles represent polyimide, NiTi heating, and NiTi cooling data respectively. Each symbol represents the average of five data samples whose standard deviations ranged between 0.002 and 0.030 *nm*. The two important discrepancies between the Figure 4-13 and Figure 4-14 are that (1) the Figure 4-14 has a more severe nonlinear kink in the NiTi data results, thus causing a larger departure from the polyimide data and (2) the NiTi heating and cooling data sets are not overlapping in Figure 4-14 as they are in Figure 4-13. This demonstrates a hysteresis characteristic of a ferroelastic material.

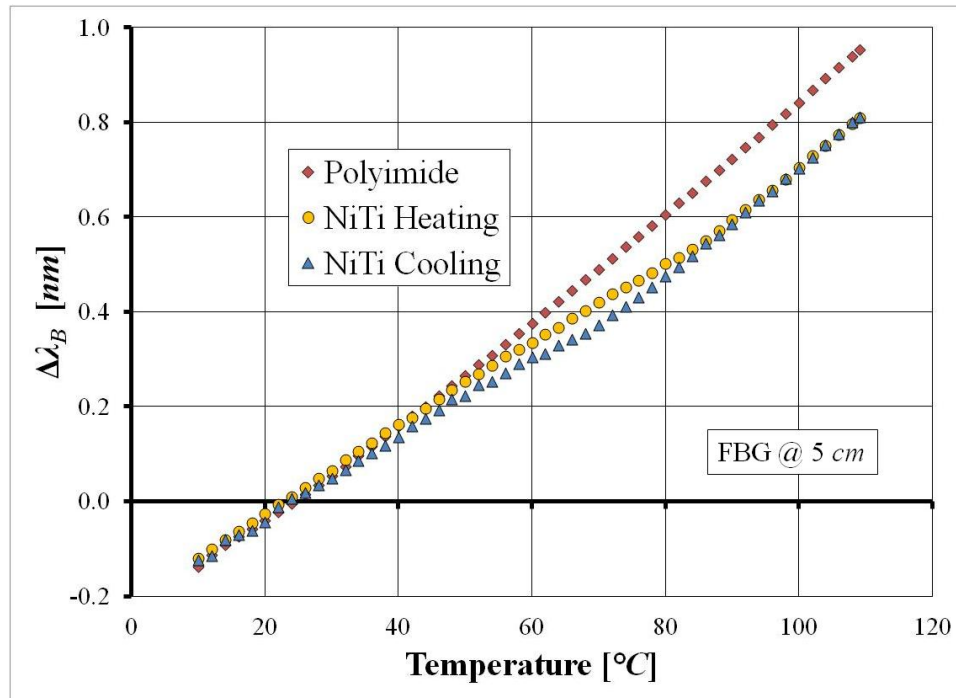


Figure 4-14: Comparison of Bragg wavelength shift in a polyimide coated FBG and the NiTi coated FBG at the 5 cm mark along the fiber.

Pertaining to the first difference between Figure 4-13 and Figure 4-14, we can see that the bigger nonlinear kink due to large NiTi strains in the phase transition region results in a NiTi $\Delta\lambda_B$ which is smaller at the maximum temperature of 109.1 °C. This explains why the $\Delta\lambda_B$ versus length plot indicates a consistent thermal environment over the last three FBGs at below the phase transition temperature but not above it.

As for the second difference, the hysteresis seen in the NiTi heating and cooling data in Figure 4-14 is exactly what we expect from a ferroelastic material. The question of why two NiTi coated FBGs at the same temperature exhibit different phase transition effects is explained with positioning along the fiber. The FBG at the 3 cm location is close to the portion of the Bragg fiber clamped within the mechanical splice whereas the FBG at the 5 cm location is closer to the free end of the fiber. Therefore, the hysteresis and phase transition effects are more constricted in the 3 cm FBG and therefore, do not show up as strongly in the data. An additional reason is that residual strains vary along the length of the fiber. Residual strains can heavily

affect the ferroelastic behavior and in this case, may have inhibited the NiTi phase transition strains at the 3 *cm* mark much more than at the 5 *cm* mark.

The next step is to take a closer look at the hysteretic behavior of the 5 *cm* NiTi FBG using Figure 4-15 below. The plot is the difference between λ_B of the NiTi coated FBG and the polyimide coated FBG. The yellow circles indicate data for the heating process and blue triangles for the cooling process. Each symbol represents the average of five data samples and the error bars represent the standard deviations which ranged between 0.002 and 0.030 *nm*. The two horizontal lines indicate when the difference in data remains stagnant. This is equivalent to parallel NiTi and polyimide data curves in the Figure 4-13 and Figure 4-14.

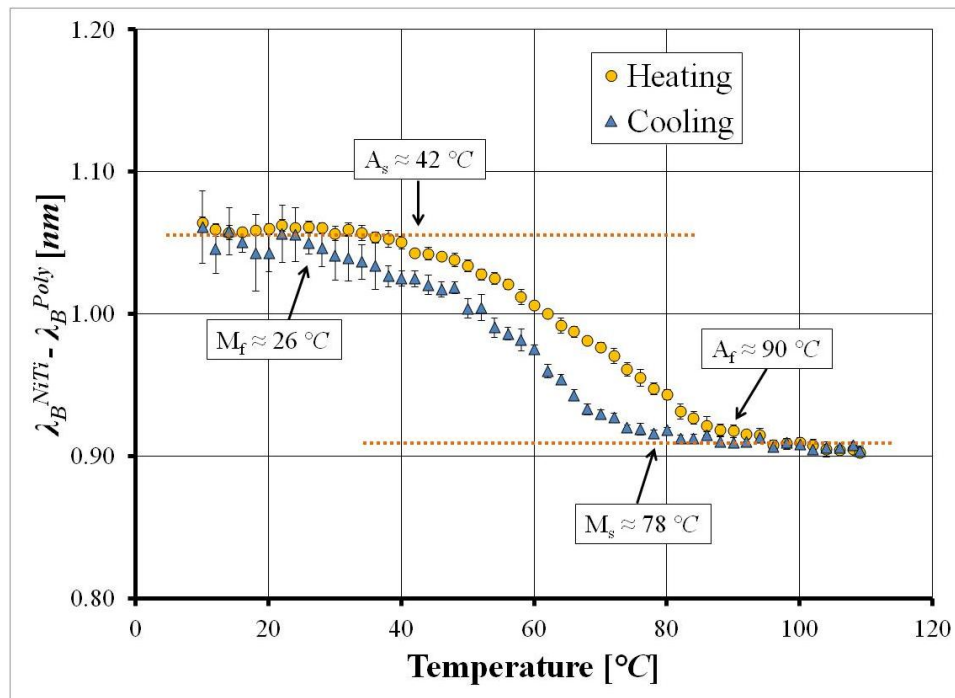


Figure 4-15: Difference between NiTi and polyimide Bragg wavelengths during heating and cooling resulting in a hysteresis characteristic of ferroelastic materials.

Departures from the overlain horizontal lines indicate when the NiTi is undergoing a phase transition. In the heating process, the A_s and A_f temperatures are at 42 and 90 °C respectively. Upon cooling, the M_s and M_f temperatures are 78 and 26 °C respectively. Note that these are different from the phase transition temperatures in the DSC results of Figure 4-8. This is because

the residual strains in a thin film deposited and peeled off of a flat wafer substrate as opposed to film deposited on a rounded optical fiber will be different. This difference in residual strains affects what temperatures the NiTi crystal structure transition starts and finishes.

This concludes the demonstration of ferroelastic behavior in NiTi thin film coating FBGs. Successful film fabrication and characterization was achieved along with solid experimental evidence of SMA NiTi. Next, the results of deposited a thin film of Terfenol-D on FBGs will be explored.

4.4.2 Terfenol-D Coated FBG

In the previous research with NiTi coated FBGs, large strains during phase transitions were required to create a noticeable difference from the polyimide coated FBG. The strains we expect to encounter in Terfenol-D coated optical fiber will not be as large, so we will attempt to use a Fourier transform method to pull the strain signal out of the noise. This method will first be demonstrated with a polyimide coated FBG attached to a bulk piece of Terfenol-D.

4.4.2.1 BULK TESTING

The first step in this process is to understand the strain behavior of the Terfenol-D by bonding a FBG to the bulk sample. A DC magnetic field is applied parallel to the optical fiber and a comparison is made in Figure 4-16 below between a FBG bonded to the bulk Terfenol-D sample and an unattached, free FBG on the same fiber. The horizontal axis depicts the magnetic field applied while both vertical axes depict strain. The two vertical axes are scaled differently to demonstrate the large strain transferred to the bonded FBG (left axis, blue square symbols) and the small drift and error associated with the free FBG (right axis, green circular symbols). The magnetic field was increased from zero to 2 *kOe* in increments of 0.1 *kOe*. At each magnetic field level, 10 strain measurements were taken. The symbols in the graph above represent the average while the error bars represent the standard deviation. Note that the error bars are only

seen in the free FBG because the strain scale is small enough to see. The error in the bonded FBG measurements was much smaller than the strain change between magnetic field levels.

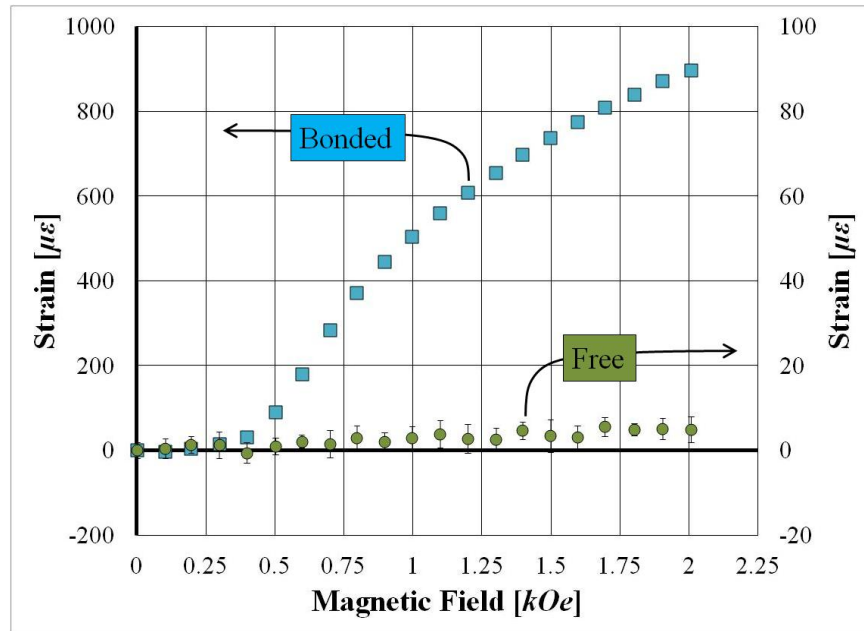


Figure 4-16: Comparison of a free FBG with a FBG surface-mounted to a bulk Terfenol-D sample when a magnetic field is applied.

The behavior of the bonded FBG is as expected for a magnetostrictive material. The low-field strain is small and increases approximately quadratically until around 0.8 kOe where a point of inflection occurs in the data curve and saturation of the Terfenol-D magnetization begins to inhibit further strain. To demonstrate the process of applying a Fourier transform to identify a signal, an AC magnetic field is applied to the bulk Terfenol-D sample between 0.55 and 1.45 kOe at 0.2 Hz . Strain is recorded in both a bonded and free FBG as in the DC test. The time domain test results are shown in Figure 4-17 below. The right vertical axis shows the applied magnetic field (H-Field) as represented by red triangular symbols. The left vertical axis shows the measured strain by the bonded (blue square symbols) and free (green triangular symbols) FBGs. A sampling rate of $\sim 2.4\text{ Hz}$ was used for 505 seconds (though only the first 20 seconds are shown).

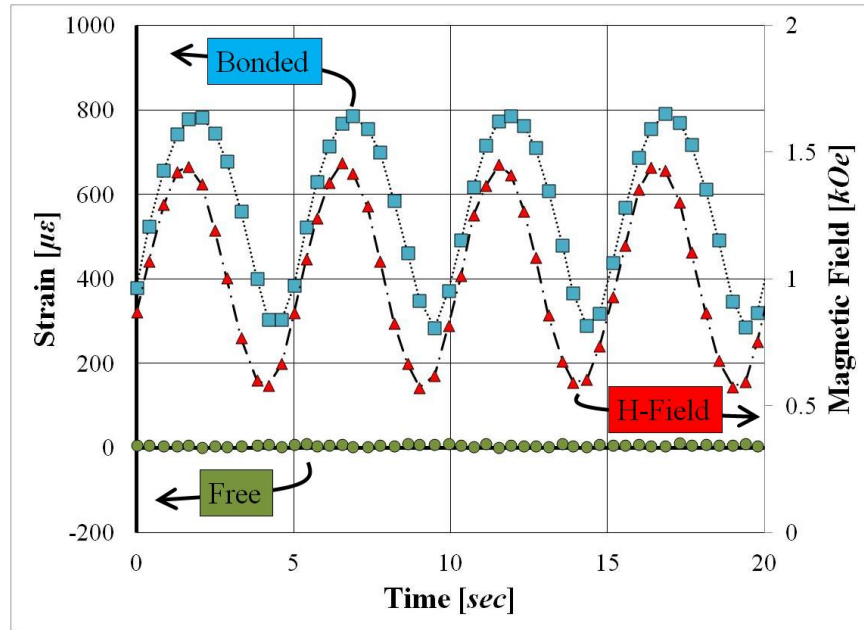


Figure 4-17: Time domain response of a bonded FBG, free FBG, and magnetic field.

The free FBG is seen to have no discernable response while the bonded FBG follows the sinusoidal pattern of the input magnetic field. The next step is to perform a Fourier transform of the data and create a frequency-domain plot. The equation for calculating the frequency domain function, $G(\omega)$, by applying a Fourier transform of a time-domain function, $g(t)$, is as follows:

$$G(\omega) = \int_{-\infty}^{+\infty} g(t) e^{-i\omega t} dt \quad (4.1)$$

However, the data plotted comes from a vector of finite length. Thus, a discrete Fourier transform formula is used to transform a time-domain vector, $\{g\}$, of length N whose entries are denoted g_n into a frequency-domain vector, $\{G\}$, of the same length whose entries are denoted G_k . Note the different subscript letters used to denote the vector entries due to the summation in the transform as shown in the following equation:

$$G_k(\omega) = \sum_{n=0}^{N-1} g_n(t) \cdot e^{-i2\pi \frac{k}{N} n} \quad (4.2)$$

When the sampling rate is consistent, the formula for determining the entries, f_k , of the frequency vector, $\{f\}$, is a simple formula based on the time between samples, Δt , and the length of the vector, N , as follows:

$$f_k = \frac{k-1}{\Delta t(N-1)} \quad (4.3)$$

However, this is not the case in this research. The average sampling rate is $\sim 2.4 \text{ Hz}$ but the minimum and maximum sampling rates during the 505 *second* test are 1.7 Hz and 3.1 Hz respectively. In this situation, we step through a series of formulas in Smith 2007. The sampling rate is defined by the time vector entry, $\Delta t_k = t_k/(k-1)$, and the frequency vector entries are defined by $f_k = (k-1)/(N \cdot \Delta t_k)$. Thus, the frequency vector entries are determined using the following formula:

$$f_k = \frac{(k-1)^2}{t_k \cdot N} \quad (4.4)$$

Note the equations above give units of Hz for frequency when the time units are seconds. Also note that the transformed function is complex. For plotting and comparison purposes, the transformed vector is multiplied by its complex conjugate and divided by that maximum value in the vector. This makes every entry real, unitless, and in the range from 0 to 1. The result of applying this process to the three time domain data sets in Figure 4-17 is plotted below in Figure 4-18. The vertical axis depicts the transformed vector entries multiplied by their complex conjugate to obtain the “power” and divided by the maximum term in the vector to achieve the “normalized power”. The horizontal axis shows the frequency in Hz . The color and symbol combinations of the bonded FBG (blue squares), free FBG (green circles), and magnetic field (red triangles) are consistent with Figure 4-17 and will be through Figure 4-21 in this chapter.

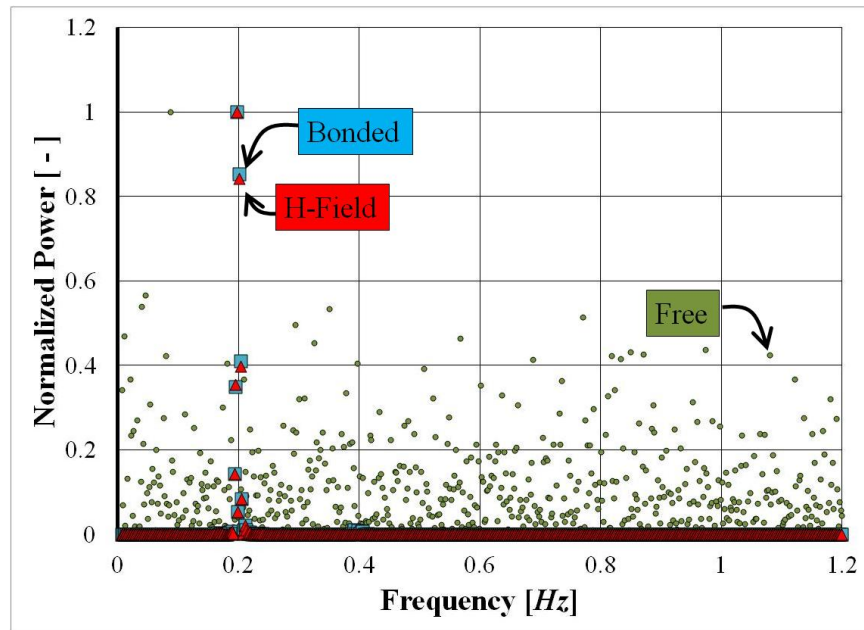


Figure 4-18: Frequency domain response of a bonded FBG, free FBG, and magnetic field.

The Fourier transform of a perfect sine function is a delta function at the frequency of oscillation. Knowing this, seeing a spike in the transformed magnetic field and bonded FBG data at 0.2 Hz makes sense. The transformed free FBG data is simply noise with the maximum being an outlier to that noise arbitrarily located near 0.1 Hz. This demonstrates the process of using a Fourier transform to demonstrate the frequency of oscillation. This is easily demonstrated when the strain response of the FBG is well above the noise, so the next step is to demonstrate that this method works for a strain response below the noise level. This begins the same way with a plot of the strain response in a DC magnetic field of a lower magnitude. This is plotted in Figure 4-19 below, which is analogous to Figure 4-16 but at a lower magnetic field range. The magnetic field was increased from 0 to 0.3 kOe in increments of 0.02 kOe. Each symbol represents the average of 20 strain measurements and the error bars are the standard deviation which indicates error of about $\pm 3 \mu\epsilon$.

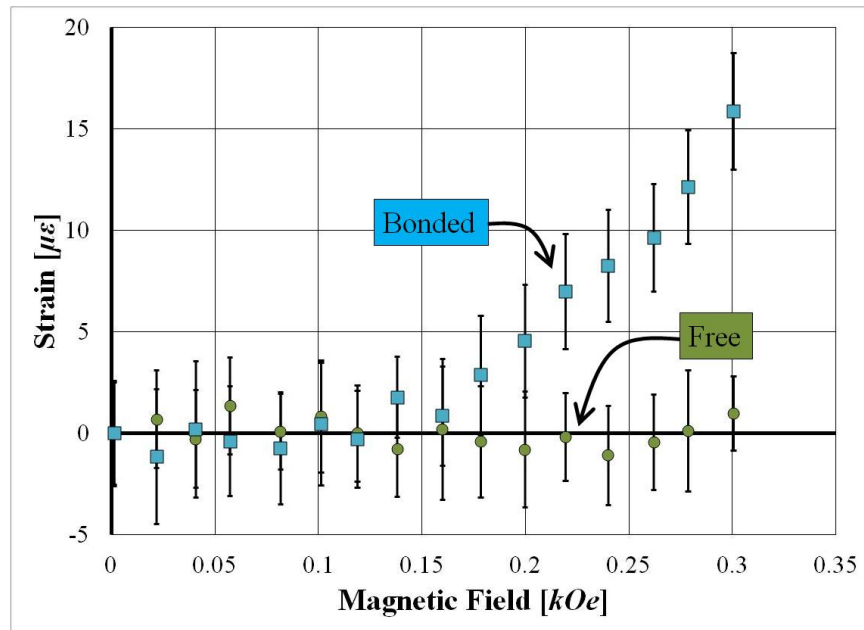


Figure 4-19: Comparison of a free FBG with a FBG surface-mounted to a bulk Terfenol-D sample when a small magnetic field is applied.

The strain of the free FBG (green triangular symbols) once again exhibits no response while the bonded FBG (blue square symbols) has the aforementioned quadratic response. The magnetic field is too small to notice any inflection due to Terfenol-D magnetization saturation effects. Below 0.18 *kOe*, the bonded FBG strain does not increase beyond the noise level. Thus, when the magnetic field is oscillated between 0.076 and 0.094 *kOe*, both the bonded and free FBGs' responses should look like noise. The time domain plot of such a test is shown in Figure 4-20 below. The test ran for 389 seconds but data from the first 20 seconds (four cycles) is shown below. The right vertical axis corresponds to the magnetic field while the left vertical axis corresponds to strain.

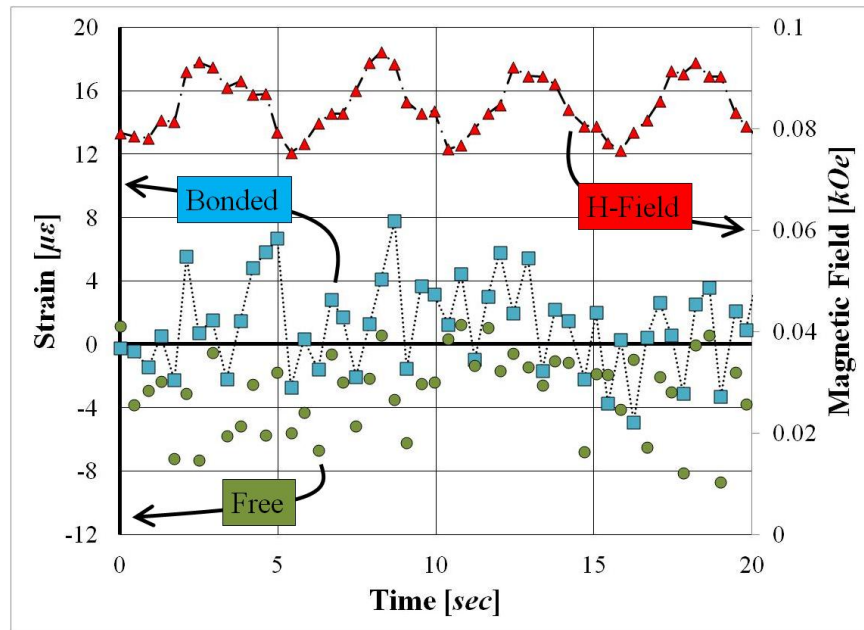


Figure 4-20: Time Domain response of a bonded FBG, free FBG, and magnetic field for low AC magnetic field strength.

The magnetic field oscillates in the aforementioned range at 0.2 Hz . The low amplitude prevented the test setup from creating a nicely shaped sinusoidal signal, but the approximately consistent oscillating frequency should still provide a spike in the frequency domain. As expected, both the free and bonded FBG strain data appears to be simply noise. The question to be answered by the Fourier transform method is whether or not there is a 0.2 Hz oscillating strain signal embedded within the noise of the bonded FBG data. The response of the transformed data is plotted in Figure 4-21 below. The vertical axis corresponds to the normalized “power” previously described. As with all the previous graphs on the transform method, the red triangles, blue squares, and green circles represent the magnetic field, bonded FBG, and free FBG data.

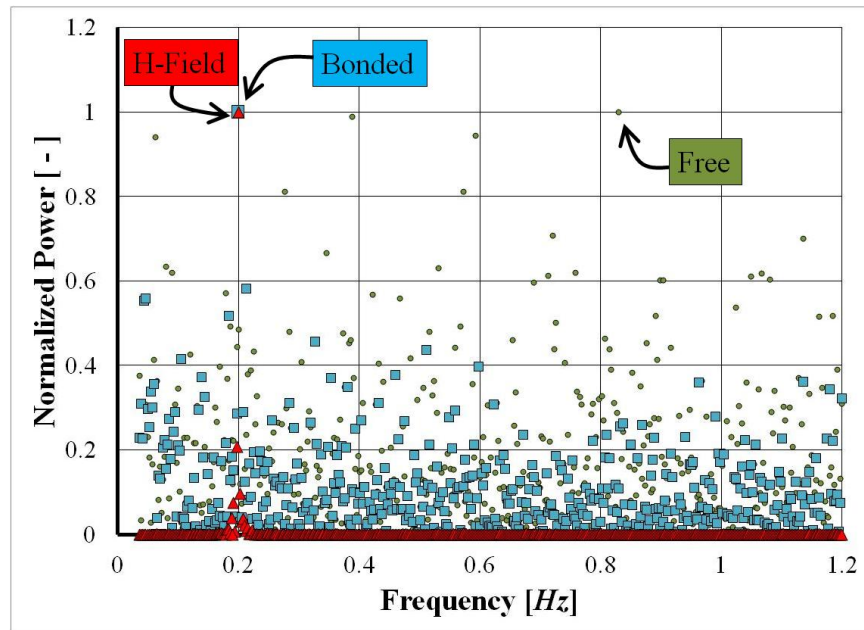


Figure 4-21: Frequency domain response of a bonded FBG, free FBG, and magnetic field at low AC magnetic field strength.

The transformed magnetic field data displays the expected sharp spike at 0.2 Hz while the free FBG data is scattered due to noise with outliers to that noise arbitrarily located near 0.05, 0.4, 0.6, and 0.85 Hz . The bonded FBG data, while showing a much more significant amount of noise compared to the previous large-amplitude AC magnetic field test, still has a spike at 0.2 Hz . Thus, it has been demonstrated that a sub-noise 0.2 Hz strain response that cannot be conclusively recognized in the time domain data has been identified in the frequency domain. This successful approach will now be used with a thin-film coated FBG.

4.4.2.2 THIN FILM TESTING

Rather than jumping right into experimentation, a quick calculation of the expected strain in the optical fiber due to strain in the thin film coating is performed using a rule of mixtures method. Take the optical fiber's Young's modulus and diameter to be 70 GPa and 127 μm respectively and the Terfenol-D's modulus and thickness to be 25 GPa and 1 μm respectively. The optical fiber's volume fraction is therefore 96.9 % and the effective Young's modulus for the coated FBG is 68.6 GPa . If we apply a magnetic field up to 1.3 kOe then, according to the

bulk Terfenol-D sample, the thin film will want to expand to about $650 \mu\epsilon$. Using the 25 GPa Terfenol-D modulus, this results in a 16.3 MPa stress in the fiber direction. Knowing the cross sectional area of the thin film, the mechanical force that must be applied to the free-standing film in order to achieve such a stress is 7 mN . If we assume such a force is now applied to the entire cross section of the coated optical fiber, the resulting stress is 0.5 MPa . Using the calculated 68.6 GPa stiffness, the resulting strain is approximately $7 \mu\epsilon$. Such a strain magnitude is slightly above the expected noise level ($\pm 3 \mu\epsilon$) but is only an approximation. Thus, the Fourier transform method may be able to extract any sub-noise or near-noise level signal in the AC magnetic field testing.

Four different frequency magnetic field signals were applied in four different tests. The first five seconds of the magnetic field oscillating at 0.2, 0.5, 1.0, and 2.0 Hz are shown in Figure 4-22 below. The magnitude of oscillation for all tests was between 0.3 and 1.3 kOe . The length of each test was 50, 22, 11, and 7 seconds with the longest test corresponding to the lowest frequency in order to achieve a sufficient number of cycles.

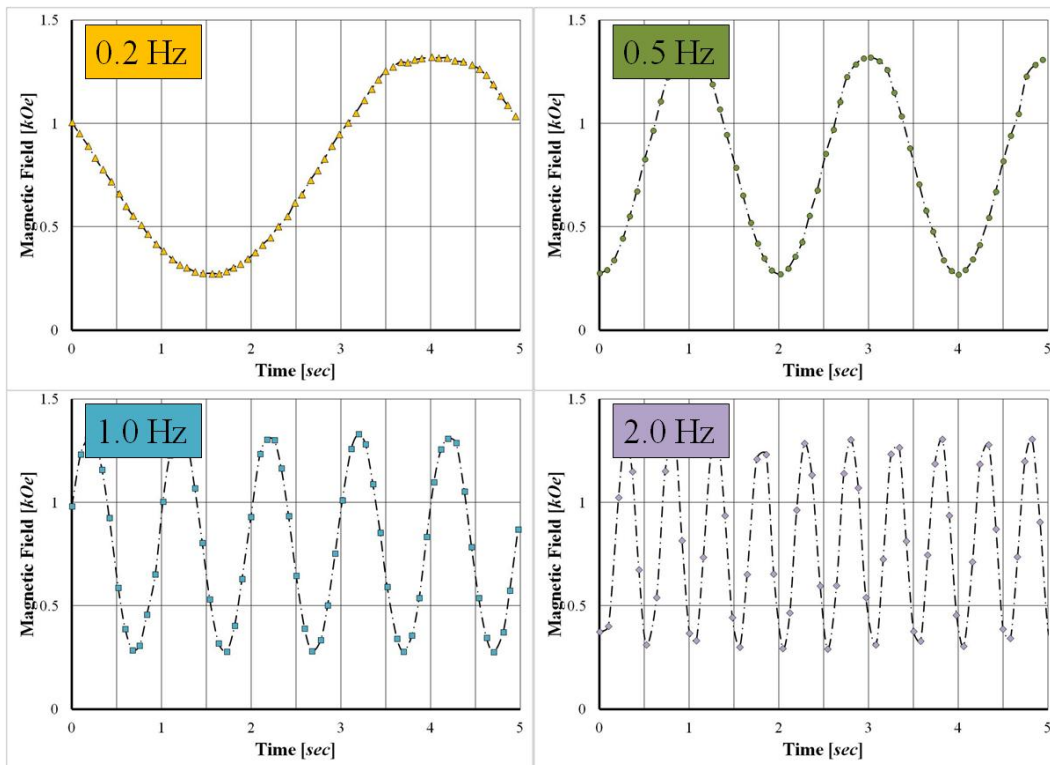


Figure 4-22: Time domain data of four different AC magnetic field frequencies.

The data from in Figure 4-22 through Figure 4-25 will be displayed with consistent color and symbol representation according to magnetic field frequency. Yellow triangles, green circles, blue squares, and purple diamonds correspond to data with a 0.2, 0.5, 1.0, and 2.0 Hz AC magnetic field input respectively. The Fourier transformed data of the plots above are shown in Figure 4-23 below. The vertical axis corresponds to the unitless normalized power term. A spike is seen at the appropriate frequency for each of the data sets as expected.

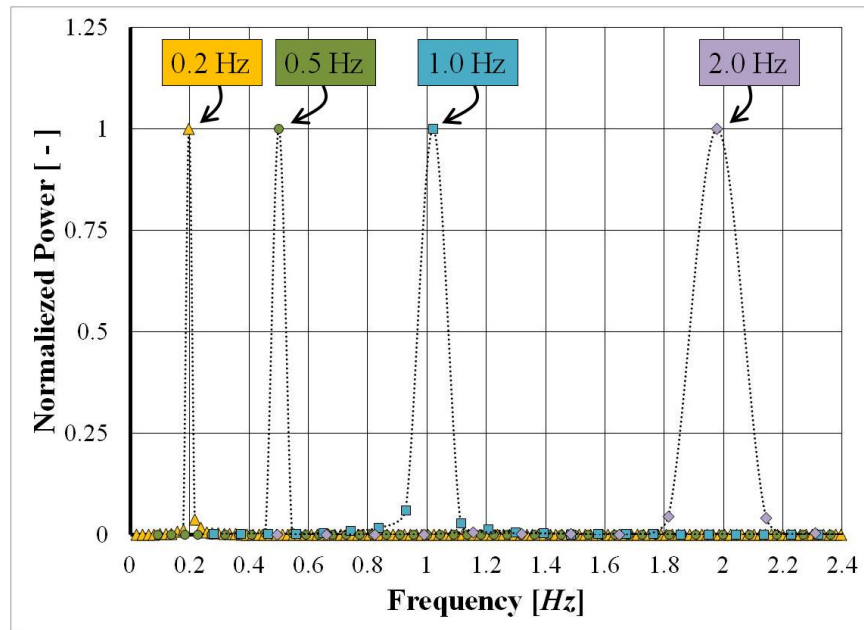


Figure 4-23: Frequency domain data of magnetic fields oscillating with four different frequencies.

Note the width of the spikes increase as the input magnetic field frequency increases. This is because the sampling rate remains the same for each frequency and thus, the total number of data points per cycle is inversely proportional to the magnetic field frequency. Though the result is reduced accuracy in determining the exact location of the spike in the frequency domain at higher magnetic field frequencies, this effect should not fatally inhibit the ability of the Fourier transform method to work on the sub-noise data.

The plot below demonstrates the time-domain strain measurements of a FBG coated in Terfenol-D while the aforementioned AC magnetic fields are applied. Data during the first 5 seconds of each test is plotted in Figure 4-24 below though all tests lasted longer (50, 22, 11, and 7 seconds as reported earlier). As expected, no discernable oscillating strain response is witnessed at every applied magnetic field frequency due to the sub-noise magnitude.

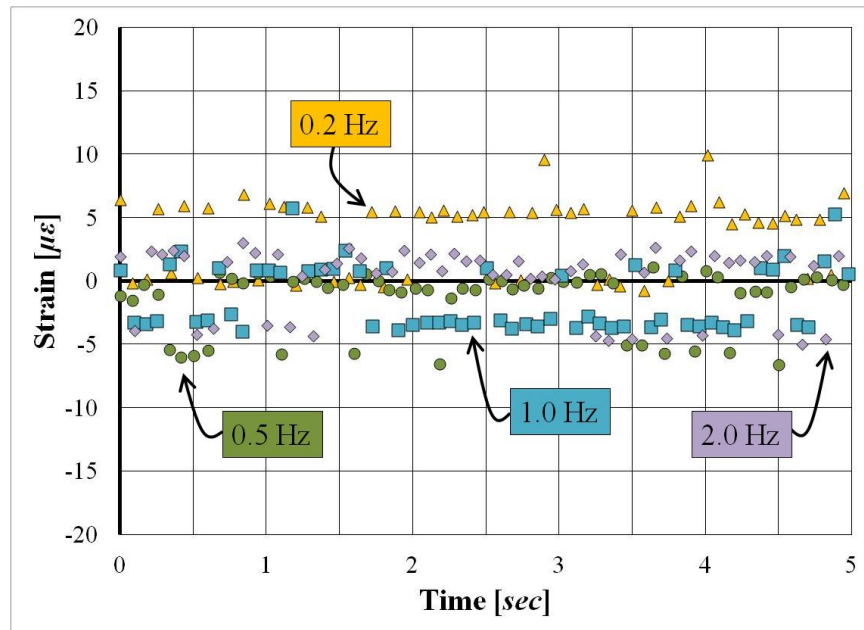


Figure 4-24: Time domain response of the bonded FBG when four different AC magnetic field frequencies are applied.

The next step is to perform the Fourier transform on the data and see whether or not there are spikes at the expected frequency locations. The transformed data is plotted in Figure 4-25 below. The vertical axis corresponds to normalized power.

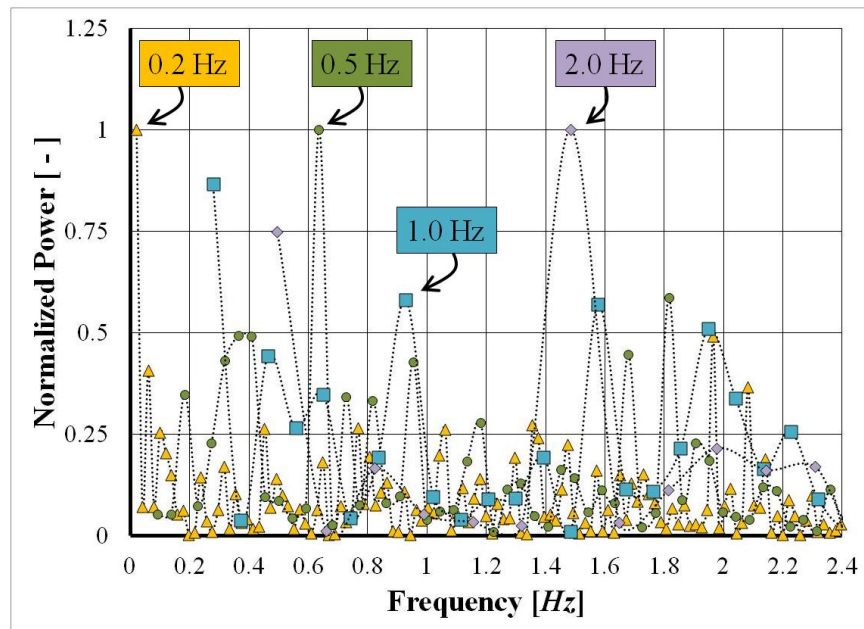


Figure 4-25: Frequency domain response of the bonded FBG when four different AC magnetic field frequencies are applied.

In a successful test, this plot would heavily resemble the frequency domain plot in Figure 4-23 of the input magnetic field signals, but this is obviously not the case. The maxima for each of the frequencies are scattered and located at arbitrary frequencies unequal to that expected. This test was repeated with an AC magnetic field in the form of a square wave rather than a sine wave, but the test remained unsuccessful.

There are several possible reasons why a significant response from the FBG was not seen. The first reason is that unlike the NiTi thin film covered FBG, the crystallinity of the coating was not verified. When the x-ray beam was focused on the Terfenol-D coated FBG, no discernable diffraction pattern was observed. This may have been either due to user error in shining the 500 μm spot size beam on the $\sim 130 \mu\text{m}$ diameter or due to the thin film not being crystallized. Though it was expected that the annealing procedure balanced the objective of crystallizing the coating while not washing out the Bragg grating, there is a possibility that this step was unsuccessful in crystallizing the thin film.

Another possibility is that the strain transferred from the coating to the core of the optical fiber was not adequate enough to cause perceptible strain in the FBG. As mentioned in the rule of mixtures calculation, the strain response is expected to be barely above noise at best. A third possibility is that the ferromagnetic properties and thus, the magnetostrictive strain response of the thin film (if it were free standing) is not as large as that of the bulk Terfenol-D. This would reduce the ability of the thin film to stretch the attached optical fiber.

4.4.3 Concluding Remarks

This concludes the experimentation of deposited thin film ferroic material coatings on FBGs. For the NiTi portion of the results, steps were taken to assess the deposition process and characterize the deposited NiTi film before thermal testing which including using tools such as SEM, XRD, and DSC. The thermal testing provided a $\Delta\lambda_B$ profile along the length of the optical fiber which, along with the explanation of large strains during phase transition, indicates that the FBGs in the 3-5 *cm* range experience equal thermal environments. It was then demonstrated that

the magnitude of the phase transition effect varied along the length of the Bragg fiber with the 3 *cm* FBG exhibiting a nonlinear departure from the polyimide control FBG but no hysteresis. This may have been due to its less constraining position near the end of the fiber as opposed to the more constraining position near the mechanical splice. It may also have been due to variation in residual strains along the length of the FBG inhibiting the ferroelastic response of the NiTi at the 3 *cm* location. Regardless of the reason, the 5 *cm* FBG displayed a significant nonlinear departure from the polyimide coated control FBG and a measurable hysteresis. This hysteresis allowed for the assignment of phase transition temperatures and therefore demonstrated the ferroelastic effect on an optical signal via strain transfer from a thin film to a FBG.

Despite being unable to ascertain any strain response in the Terfenol-D thin film coated FBG portion of the results, there are a few successes to take away from the testing. The first success is in depositing Terfenol-D on an optical fiber and maintaining a reflection signal from the FBGs after an annealing process. Another achievement was using a FBG surface-mounted onto a bulk piece of Terfenol-D to characterize the magneto-elastic strain response of the magnetostrictive material. The notion that a FBG bonded to a bulk Terfenol-D sample can be used as the control to which the more unknown thin film test is compared speaks to the ease of use and reliability of FBGs as surface-mounted strain sensors in general.

4.5 Summary

The goal of this portion of the research was to expand the capabilities of the fiber Bragg grating sensing system beyond its original design of monitoring strain. This would demonstrate the potential of fiber optic based systems in the growing trend of creating smart structures. Such an effort grew out of the foundation provided by NASA Dryden Flight Research Center's development of the fiber optic interrogation system and by the UCLA Active Materials Lab's expertise in materials such as NiTi and Terfenol-D in both bulk and thin film form. The endeavor resulted in successfully observing a thermal hysteresis in the optical signal associated with phase

transformations in the thin film ferroelastic NiTi coating deposited on the FBG. This demonstration of ferroic material behavior in a FBG reflected wavelength shift was then successfully carried over into a ferromagnetic material with bulk Terfenol-D, but not with a thin film coating.

A fork in the road was encountered at this point in the research. On the one hand, measures could be taken to better analyze, fabricate, and test the Terfenol-D thin film coating. This could result in the Fourier transform method successfully identifying a strain response in the ferromagnetic film. Though this would be appealing research, a different option of pursuing a more interesting, novel, and challenging approach to coupling optical and magnetic fields was taken. The new approach would bypass strain as a mechanism for coupling and involve direct magneto-optic effects. The details of this approach are described in the next chapter.

CHAPTER 5:

MAGNETO-OPTIC COUPLING

5.1 Synopsis

The goal of this chapter is to demonstrate a magneto-optic effect in a FBG for the eventual purpose of creating a fiber optic magnetometer capable of making distributed magnetic field measurements. As stated in the previous chapter, the desire is to bypass strain in the magneto-optical coupling process. In order to do this, part of the waveguide material is altered from magnetically inert silica to a magnetically active iron oxide. By applying a magnetic field to the iron oxide through which part of the EM wave propagates, the index of refraction changes. This in turn alters the wavelength reflected by the FBG in a measurable manner.

An introduction will be given first describing the motivation and current research in the area. Then the theoretical work describing EM wave propagation from Chapter 2 will be extended to demonstrate the degree of sensitivity expected from the sensor. Subsequently, the iterations in design and fabrication procedures will be described along with the magnetic field experiments. Lastly, the results will be provided demonstrating the desired magneto-optic coupling.

5.2 Literature Review

The purpose of this portion of the research is to create novel FBG sensors and in doing so, explore the fundamental physical phenomena that define the sensor. Specifically, the influence of magnetic fields on the interaction of light will be explored within FBGs. In the literature review provided here, several motivational examples will be provided which demonstrate the various

applications in which this technology could be utilized. Established methods for coupling optical signals to external phenomena via the fiber's evanescent field will then be described. Lastly, published research in the area of fiber optic magnetic sensors will be described.

5.2.1 Motivation

One particular motivation which has been described throughout this research is the development of sensors that could be used to create smart structures. While the FBG magnetic field sensors could be implemented as a stand-alone sensor system, there is great opportunity in utilizing the multiplexing capabilities of FBGs. The result of pursuing such an opportunity could be the creation of a single fiber optic sensory system which has the ability to interrogate numerous types of FBG sensors (e.g. strain, magnetic field) which are spliced into the same fiber optic neural network. This application represents a possible extrapolation of the results obtained in this research investigating underlying physical phenomena related to magneto-optic coupling.

There are several examples of specific applications for which magnetic sensors on smart structures could be of use. One type of application is in the detection of foreign objects as described by Nicoll et al. 1990 [216]. Incoming objects such as missiles create a magnetic signature which could be rapidly picked up by an optical sensor. Once identified, countermeasures could be taken to avoid or minimize damage due to impact. Another example would be the ability to detect locations of enemy structures such as weapons, tanks, or submarines which may be masked from visible and infrared imaging. A third such example is the ability to detect friendly vehicles such as when two helicopters land to deploy troops in the same location while visibility is reduced from either darkness or the helicopter blades kicking up debris such as sand. The ability of the pilots to see one another could be inhibited visually, but a magnetic sensor could feasibly allow for the helicopters to monitor each other's location and avoid crashing.

Additional motivation stems from biological examples of using ferromagnetic particles for migration and vicinal mapping. Johnsen and Lohmann 2005 explored the use of

superparamagnetic nanoparticles made from magnetite (Fe_3O_4) in biological systems where animals such as sea turtles create a magnetic map to find feeding sites [4]. Lohmann 2010 elaborates on the subject of magnetoreception by describing various other animals in which the effect is seen [5]. Magnetoreception is described to be utilized both for migrational purposes in birds and for vicinal mapping in flies and mole rats. This indicates that small magnetic particles sensitive to the Earth's magnetic field can be used not only in a manner analogous to a compass, but also to determine positioning. Applying these ideas to smart structures, the navigation system in aircrafts, for example, could be determined from the Earth's magnetic field rather than global positioning satellites. This would negate the vulnerability of satellites being shot down or hacked with viruses.

These applications provide ample motivation for demonstrating the integration of ferric oxide nanoparticles into a FBG sensor to detect magnetic fields and open research avenues into the development of new sensors.

5.2.2 Evanescent Field Coupling

In the analysis of Chapter 2 describing the distribution of electromagnetic energy within the optical fiber, it was found that most of the propagating light intensity remains within the core yet some exists in the cladding layer as well. This is a distinct characteristic of the wave nature of light which is not found under a ray representation. This is a very important feature of optical fibers because we wish to access the light in order to directly couple light to external magnetic fields via magneto-optic materials. Thus, the cladding layer is almost entirely removed to reach the propagating light. The cladding layer is then replaced with ferric oxide in order to manipulate the light without exiting the optical fiber.

The portion of the propagating EM wave within the cladding is called the evanescent field due to the fact that light intensity rapidly declines as the distance from the core increases. Evanescent field-based IOR sensors have been previously fabricated and described in literature. Polynkin et al. 2005 embedded a tapered optical fiber in polydimethylsiloxane (PDMS) with a

semicircular notch near the optical fiber [217]. With the IOR of the PDMS (1.402) being less than the optical fiber's fused silica (1.445), the light is still guided through the optical fiber. When the notch is filled with varying concentrations of water ($n = 1.311$) and glycerol ($n = 1.459$), the overall index of the liquid is varied as the transmission through the optical fiber is measured. The transmission percentage is correlated to the index of refraction of the liquid mixture in order to calibrate the IOR sensor. This demonstrates the effective utilization of the evanescent field, but no FBG is used. Fabricating the sensor in this manner prevents possible multiplexing. This work was built upon previous studies by Lacroix et al. 1986 and Villatoro et al. 2004 researching the transmission of tapered multimode fibers which was dependent upon the surrounding material's optical properties [218, 219].

Optical fiber couplers are an excellent example of an optical circuit component which takes advantage of the evanescent field. Input light from an optical fiber propagates through the core of a waveguide within the coupler which has a second waveguide core in close proximity. The evanescent field near the first core is substantial enough at the edge of the second core that the light is able to tunnel through the gap and propagate within the second core. This phenomenon is analogous to quantum tunneling. The rate that light couples from the original core into the secondary core is dependent upon the distance between the two cores running alongside each other. Boucouvalas and Georgiou 1986 and Stadnik and Dybko 2003 used optical fiber couplers as IOR sensors [220, 221]. This was done by simply exposing the coupling region to fluids with different IORs and measuring the amount of light that transferred from one optical fiber to the other.

Further evidence of the effectiveness of utilizing evanescent field manipulation to monitor index of refraction is provided by DeLisa et al. 2000 [222]. In this work, the shift in wavelength where a dip in transmission wavelength occurs was measured while an antibody-antigen reaction occurred in the region surrounding the fiber. Because the index of refraction changed during the interaction, a chemical reaction biosensor was established. This demonstrated an interesting use

of a grating fiber, but the use of LPGs hinders the possibilities of multiplexing because the measurement is in light lost (i.e. no longer propagating in the fiber) rather than light reflected.

Liang et al. 2005 etched a FBG down to $6\ \mu\text{m}$ in diameter and placed the optical fiber in air, isopropyl alcohol (IPA), methanol, and ethanol [223]. The change in surrounding index of refraction altered the effective IOR of the fiber. The relationship between reflected wavelength and surrounding index was plotted and described with a fitted curve. A more quantitatively rigorous relationship between effective index and the surrounding material in an etched FBG was provided by Iadicicco et al. 2004 and Iadicicco et al. 2005 [224, 225]. The authors took the transcendental eigenvalue equation for a three-layer optical fiber and calculated the effective index of refraction. The change in effective index was calculated as the IOR of the outer layer and the diameter of the optical fiber (i.e. the thickness of the cladding layer) were changed. The theoretical section of this chapter uses the same equations to develop a relationship between IOR of the material surrounding the optical fiber and the reflected wavelength. The work presented here extends the analysis further by looking into higher order modes to increase the sensitivity of the sensor.

5.2.3 Magnetic Sensors

FBG sensors are most commonly used to measure strain and temperature. These external stimuli produce an optically based change in index of refraction (described by photoelasticity, thermo-optics) along with a mechanically based change in length (mechanical strain, thermal expansion) which combine to shift λ_B . As demonstrated in the previous chapter, FBG sensors have been developed which utilize strain-based shifts in λ_B to sense other physical phenomena. Tien et al. 2009 deposited iron on the tip of a FBG to cause fiber deflection in the presence of a magnetic field while Yang et al. 2009 successfully demonstrated shifts in λ_B due to a thin-film Terfenol-D coating [214, 215]. Chiang et al. 2003 attached the front and back half of a FBG to Terfenol-D and MONEL 400 respectively [226]. Magnetic fields caused the Terfenol-D (but not the MONEL 400) to expand and thus, split the reflected wavelength for the FBG in two. The

approximately equal coefficients of thermal expansion for the two materials allowed for thermal compensation of the magnetometer.

These examples demonstrate the use of mechanical strain as an avenue for creating a reflected wavelength shift due to an input magnetic field. The purpose of this portion of the research is to create a magnetic sensor based on evanescent field interaction of the propagating EM wave with a magnetically active material. The underlying magneto-optic interaction which causes the index of refraction change has been described as the Faraday Effect by Arce-Diego et al. 1997 and Wu et al. 2009 [227, 228]. Both papers explained theoretical analyses of the originally degenerate eigenvalue (index of refraction value) corresponding to two principal eigenvectors (polarization directions) spanning the cross section of an optical fiber. The degeneracy was broken by the application of a magnetic field and birefringence was concluded to take place because distinct eigenvalues now corresponded to the two eigenvectors. In this analysis, the Faraday Effect involved the addition of imaginary, antisymmetric entries in off-diagonal locations of the fiber's permittivity tensor. Though the eigenvalues (and thus, indices of refraction) were still real, the eigenvectors became complex. Any experiment performed will measure light polarized in a real direction and it is unclear whether the measurement would indicate a change in reflected wavelength associated with a real direction.

More reliable explanations of the magneto-optic effects at play in the sensor to be fabricated were described in Mailfert and Nahounou 1980 and Horng et al. 1999 [229, 230]. In the former, the effect of a magnetic field on the electric susceptibility of superparamagnetic particles was analyzed. It was theoretically determined that the susceptibility (and thus, index of refraction) of light polarized parallel to the applied magnetic field increased while that of light polarized perpendicular decreased. This was experimentally verified with ferrofluid. In the latter publication, a magnetic field was applied through a magnetic fluid containing ferrite particles at a 45° angle to the input light polarization. The magnetic fluid became birefringent which causes input linearly polarized light to exit elliptically polarized. The result was a polarization which rotated at a particular rate over a given distance after exiting the magnetic fluid. As the magnetic

field increased, the birefringence increased as did the rate of polarization rotation in a measurable fashion. The corroborating experimental and theoretical analysis along with the well-established nature of the magneto-optic interaction described in these papers (the Cotton-Mouton Effect) points to this being the underlying magneto-optic phenomenon taking place in the proposed sensor.

Choosing a proper magnetically active material is very important to obtain measurable results. Magnetorheological (MR) fluid was chosen first in this research, but was quickly found to be inadequate. The main reason is that in MR fluid, the magnetically active particles floating in a carrier fluid are several microns in diameter. This is larger than the wavelength of light, so the EM wave is more apt to scattering from the particles. Ferrofluid was analyzed next due to its use of particles tens of nanometers in size. This is orders of magnitude lower than the wavelength which means that the light “sees” the two-phase ferrofluid as a single-phase, homogeneous fluid. Next, we look to literature to determine the magnitude of index of refraction change expected in a ferrofluid when placed in a magnetic field. Yang et al. 2002 created an index of refraction measurement setup of a 200 μm thick film of ferrofluid [231]. The test involved measuring the change in refracted angle of light passing through a prism adjacent to the film. The index of refraction of the magnetic fluid was deduced based on the angle of incidence at which total internal reflection occurs. When placed in a magnetic field parallel to the fluid film’s surface normal, the critical angle changed in a measurable manner. The index of refraction was linearly dependent on particle concentration and also highly dependent on carrier fluid index of refraction. The water-based ferrofluid index was varied between 1.38 and 1.58 while the kerosene-based index was varied between 1.33 and 1.49 by altering the magnetic particle concentration and not magnetic field. For a particular water-based mixture, a 200 *Oe* applied magnetic field increased the index of refraction from 1.435 to 1.452. This work was followed up by Hong et al. 2003 and Horng et al. 2003 [232, 233]. The former paper studied the effects of the angle of applied magnetic field while the latter studied the choice of carrier fluid and magnetic particles on the index of refraction response in a magnetic field. The angle of applied magnetic

field was found to affect the IOR response, but no mention of the angle of applied magnetic field relative to the angle of polarization of the incident EM wave was described. Thus, no birefringence effects were considered. In the other paper, it was found that MnFe_2O_4 had a slightly stronger response than Fe_3O_4 by $\sim 15\%$. From these papers, it can be deduced that the use of Fe_3O_4 particles in water should provide a low enough index of refraction to maintain the waveguide while still allow a suitable shift in index of refraction to obtain a measurable response (as long as we create a thin enough optical fiber as will be seen in the theoretical analysis).

A factor which could negatively affect the efficacy of the proposed sensor is the scattering loss introduced when the ferrofluid is subject to a magnetic field. Pu et al. 2006 demonstrated a thinned optical fiber whose evanescent wave penetrated into the surrounding ferrofluid [234]. When various magnetic field strengths were applied between 0 and 858 Oe , the transmission of light through the tapered region was measured to decrease. The magnetic field was applied perpendicular to the optical fiber direction. The loss in light intensity was due to the forming of ferric oxide chains adjacent to the fiber which caused significant scattering. The effect on transmission was repeatable and followed up with a study on the response time of the sensor in Pu et al. 2007 [235]. The response time was found to be a function applied magnetic field strength and varied between 0.4 and 4.5 seconds. Note that these results indicated that the sensor response time was limited by the particle motion in the fluid (i.e. Hz) rather than the ferromagnetic resonance (GHz). Thus, the potential for a response time several orders of magnitude faster hinges upon a sensor designed to have its magneto-optic interaction dominated by particle magnetization rather than particle motion.

A recent paper published by Yang et al. 2010 utilized a thin film of TbFeCo sputtered onto a FBG which was side-polished to expose the evanescent field [236]. The authors demonstrated that increased coating thicknesses between 84 and 245 nm resulted in increased reflected wavelength shifts when placed in a magnetic field parallel to the optical fiber direction. Though the wavelength shift was attributed to a direct magneto-optic effect, no mention of the magnetostrictive properties of TbFeCo was given. Thus, the influence of magnetically induced

strain stretching the FBG mechanically was not stripped out of the measured reflected wavelength shifts. Additionally, the penetration depth of the light into the TbFeCo was not addressed. Materials typically applied to waveguides are not electrical conductors. This is unlike TbFeCo, so the issue of light penetration, also known as skin depth, becomes important and is not mentioned in the manuscript. The paper also claims that the coupling efficiency is 50 %. This essentially means that for a given change in index of refraction of the TbFeCo, the effective index of the waveguide changes by half this value. This is not realistic in that only a small portion of the total light intensity is present in the TbFeCo. This is because the thin film is only deposited on one side of the fiber (i.e. not concentric) and there is still a 1 μm thick silica cladding region between the core and TbFeCo at minimum. It can be assumed very conservatively that less than 10 % of the light intensity is within the TbFeCo. The claimed change in index for the entire EM wave being 50 % of the index change for only 10 % of the EM wave does not make sense. The reason for such a high value must come from other effects such as magnetostriction causing a larger than expected shift in reflected wavelength.

Other authors have used a fiber grating to observe magneto-optic coupling. Liu et al. 2007 used a long-period grating (LPG) to demonstrate that the wavelength of light which couples into a non-propagating cladding mode shifts depending on the IOR of the surrounding magnetically active material [237]. This was accomplished with a water-based Fe_3O_4 ferrofluid. One notable effect is in contrast to the previously mentioned work of Yang et al. is that the index of refraction of the ferrofluid was measured to be decreasing with an applied magnetic field transverse to the optical fiber rather than increasing. This was attributed to previous publications explaining that the angle between the polarization of the propagating light and the applied magnetic field dictates whether the susceptibility increases or decreases. However, no indication of polarization control was given by the authors.

A few months after the results in this research incorporating a direct magneto-optic effect with a FBG were obtained, Dai et al. 2011 achieved a similar result [238]. The two main differences are that Dai et al. used ferrofluid and observed a negative shift in index of refraction

(and thus, λ_B) whereas this research utilized ferromagnetic particles and observed a positive shift in index of refraction and λ_B .

5.2.4 Concluding Remarks

The purpose of this section has been to establish the usefulness and proposed method of creating a fiber optic magnetometer in the context of currently published literature. Several motivational examples of biological and defense applications were provided to help visualize a tangible goal that could be achieved based on this research. Aside from an application-based impetus, another main driving force behind this work is to research the fundamental physical interactions upon which future magneto-optic sensors could be founded. Such interactions were elucidated with examples of various sensors that utilize evanescent field interactions as a coupling mechanism. Additionally, the ferromagnetic coupling material was explored with examples of previous work in the area on optical interactions with ferrofluid. This work aims to complement the published work on FBG magnetometers (much narrower in scope than the strain-sensing field) in three ways. The first is providing a theoretical foundation for establishing expected λ_B shifts, the second is exploring fabrication techniques for creating a robust sensor, and third is establishing a measurable magneto-optic coupling in a FBG utilizing the same strain-sensing fiber optic interrogation system produced for the purpose of creating smart structures.

5.3 Theoretical Calculations

The purpose behind performing this theoretical work is twofold. The first motivation is to gain familiarity with the behavior of optical fibers when particular parameters are altered. This is achieved by exploring various dependencies of effective IOR such as fiber dimensions and the IOR of the different fiber layers. Parameters which won't be altered in the experimental section were nevertheless altered in the theoretical section. Varying a wide range of parameters regardless of whether or not they will be experimentally implemented will promote a

comprehensive understanding of the behavior of propagating EM waves. This is necessary to understand and explain future experimental behavior. The second reason for this theoretical section is to aid the fabrication procedures and design parameters of the sensor. Using results from the theoretical analysis, predictions can be made as to how sensitive the ensuing sensor will be. This eliminates as much of the guesswork which goes into determining the cladding radius, the surrounding material, and the necessary external magnetic field to elicit a response from the sensor.

This section begins with the theoretical equations describing the propagation of light within an optical fiber. Specifically, the wave equation for a propagating EM wave will be solved with boundary conditions representing the optical fiber sensor that will later be fabricated. The effects of manipulating the geometric and optical characteristics of the fiber will then be explored. This work builds upon introductory material from Chapter 2 describing a 2-layer (i.e. core-cladding) optical fiber. By reducing the diameter of the silica cladding (accomplished later with an etching process) and including an outer layer with an IOR dependent upon magnetic field, a 3-layer, magnetically sensitive fiber is created. This will be seen to complicate the equations from Chapter 2 and a computer program developed for this research will be used to process the analytical calculations.

The central theme in this section is the determination of the effective index for an optical fiber with certain material and geometric properties. Once the behavior of the effective index is understood and mapped out, the feasibility and sensitivity of certain sensor designs can be evaluated and predicted for the subsequent experimental section.

5.3.1 Theoretical Analysis

The process for the development of equations describing the propagation of light through the optical fiber will be analogous to that in Chapter 2. First, the wave equation will be introduced which results in a particular partial differential equation solved by various Bessel and exponential functions. Next, boundary conditions will be introduced based on the fiber geometry

and the result will be a set of equations whose solution will be non-trivial if particular, discrete values of the propagation constant are realized. These propagation constants are the eigenvalues of the previously derived equation and determine the effective IOR of the fiber. The largest constant found will be that of the fundamental mode of propagation. These solutions are a function of fiber radius, surrounding material index, and mode of propagation.

First, recall the electromagnetic wave equation derived from Maxwell's equations defining the behavior of the electric ($\overset{\mathbf{1}}{E}$) and magnetic ($\overset{\mathbf{1}}{H}$) fields.

$$\left(\nabla^2 - \frac{n^2}{c^2} \frac{\partial^2}{\partial t^2} \right) \begin{Bmatrix} \overset{\mathbf{1}}{E} \\ \overset{\mathbf{1}}{H} \end{Bmatrix} = 0 \quad (5.1)$$

The Laplacian operator is carried out in cylindrical coordinates (r, φ, z) rather than Cartesian (x, y, z) coordinates for ease of analysis with the optical fiber's geometry. Recall that for a wave traveling in the z -direction, the φ , z , and t relationships were determined through a separation of variables technique to determine the following:

$$\begin{Bmatrix} \overset{\mathbf{1}}{E}(\overset{\mathbf{r}}{r}, t) \\ \overset{\mathbf{1}}{H}(\overset{\mathbf{r}}{r}, t) \end{Bmatrix} = \begin{Bmatrix} \overset{\mathbf{1}}{E}(r) \\ \overset{\mathbf{1}}{H}(r) \end{Bmatrix} e^{i(l\varphi + \omega t - \beta z)} \quad (5.2)$$

The traveling wave is oscillatory in φ , z , and t at rates of integer value l , propagation constant β , and angular frequency ω respectively. Recall now that the r and φ components of the electric and magnetic fields can be written in terms of the longitudinal components. For example, $E_r = f(E_z, H_z)$. Thus, only the z -components need to be solved in the wave equation. This reduces the wave equation to be a set of two equations involving only E_z and H_z rather than six equations involving all components of the field. After carrying out the Laplacian operator, the resulting wave equation is as follows in a given medium:

$$\left[r^2 \frac{\partial^2}{\partial r^2} + r \frac{\partial}{\partial r} + \left(r^2 (k^2 - \beta^2) - l^2 \right) \right] \begin{Bmatrix} E_z \\ H_z \end{Bmatrix} = 0 \quad (5.3)$$

The scalar term k is the wavenumber for the EM wave if it were traveling solely through one of the multiple media making up the sensor. The solution to the partial differential equation above is a combination of Bessel functions. The forms of the Bessel function solutions depend on whether $k^2 > \beta^2$ or $k^2 < \beta^2$. Thus, the following form of the z -component of the electric field was determined:

$$E_z(r, \varphi, z, t) = \begin{cases} \left[AJ_1\left(r\sqrt{k^2 - \beta^2}\right) + BY_1\left(r\sqrt{k^2 - \beta^2}\right) \right] e^{i(\omega t + l\varphi - \beta z)} & k^2 > \beta^2 \\ \left[CI_1\left(r\sqrt{\beta^2 - k^2}\right) + DK_1\left(r\sqrt{\beta^2 - k^2}\right) \right] e^{i(\omega t + l\varphi - \beta z)} & k^2 < \beta^2 \end{cases}, \quad (5.4)$$

The z -component of the magnetic field takes the same form with different multiplication constants. In the case previously analyzed with only two layers to consider, the propagation constant was always smaller than k_1 (core wavenumber) and larger than k_2 (cladding wavenumber). In the more general case considered here with three layers, the electric field solution becomes more complex. A comparison between the two and three layer approach is outlined Figure 5-1 below. The left image is a two-layer optical fiber with a Ge-doped silica core (of radius a) and silica cladding. The right shows an optical fiber consisting of the original core (radius a), a thinned cladding (radius b) and an additional surrounding material. In this research, air, IPA, and ferric oxide are examples of surrounding layers used. Note that (1) the IOR and thus, k value, decreases as you step from inner to outer materials and (2) the diameter of the outermost layer for both 2- and 3-layer fibers does not need to be specified in the equations because the evanescent field is assumed to decrease in magnitude to essentially zero well before the edge of the outermost layer is reached.

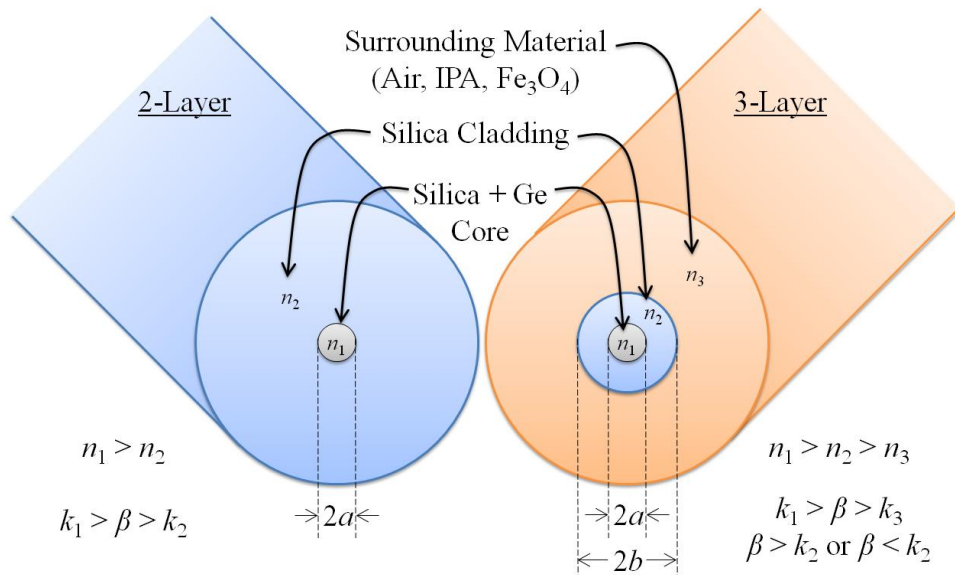


Figure 5-1: Schematic diagram of the 2- and 3-layer fibers analyzed in this research.

In this research, the core layer has a slightly higher index than the cladding layer. Thus, in order to maintain total internal reflection for EM wave propagation, the surrounding material should have a IOR lower than the cladding. In the two-layer example, the propagation constant for any EM wave mode, β , must be between the k values of the core and cladding. In the three-layer setup, β must be between the k values of the core and surrounding material. For a given material configuration, some of the finite number of β values (at least one) will be larger than k_2 while the rest are smaller. This is important in considering the Bessel function solutions for each layer. Table 5-1 summarizes the selection process. Each row represents a different material layer. The two main columns represent the two options for β values being between k_1 and k_2 or between k_2 and k_3 . The sub-columns represent each of the four Bessel function options for solving the wave equation. An entry of “1” indicates that Bessel function is a physically realistic solution to the wave equation. An entry of “0” indicates that the Bessel function either represents a physically unrealistic result (e.g. light intensity approaches infinity as $r \rightarrow 0$ or $r \rightarrow \infty$) or is not a solution based on the whether β is greater than or less than the k value for that layer.

Table 5-1: Demonstration of the Bessel functions that describe the EM wave behavior in the three different fiber layers.

Bessel Function →	$k_1 > \beta > k_2 > k_3$				$k_1 > k_2 > \beta > k_3$			
	J	Y	I	K	J	Y	I	K
Layer 1 ($a > r$)	1	0	0	0	1	0	0	0
Layer 2 ($a < r < b$)	0	0	1	1	1	1	0	0
Layer 3 ($r > b$)	0	0	0	1	0	0	0	1

From Table 5-1, we see that for the i^{th} layer, the modified Bessel functions (I and K) are a solution if $k_i < \beta$ whereas the original Bessel function (J and Y) are a solution if $\beta < k_i$. Layer 1 contains the value of $r = 0$, so Bessel function Y is not physically realistic because it is infinite at $r = 0$. Layer 3 contains the approximation $r \rightarrow \infty$, so Bessel function I is not physically realistic because it is infinite in value as $r \rightarrow \infty$. These “physically realistic” arguments are not applicable in Layer 2 because all four Bessel function remain finite within the region $a < r < b$. With this reasoning, the form of the z -components of the electric and magnetic fields which provide solutions to the wave equation are written as follows:

$$\begin{aligned}
 & r \leq a \\
 & E_z(r, \varphi, z, t) = c_1 J_l(hr) e^{i(\omega t + l\varphi - \beta z)} \\
 & H_z(r, \varphi, z, t) = c_2 J_l(hr) e^{i(\omega t + l\varphi - \beta z)} \\
 & \text{where } h^2 = k_1^2 - \beta^2 = n_1^2 k_0^2 - \beta^2
 \end{aligned} \tag{5.5}$$

$$\begin{aligned}
 & b \geq r \geq a \\
 & E_z(r, \varphi, z, t) = e^{i(\omega t + l\varphi - \beta z)} \begin{cases} c_3 J_l(pr) + c_4 Y_l(pr) & \text{if } \beta < k_2 \\ c_3 I_l(pr) + c_4 K_l(pr) & \text{if } \beta > k_2 \end{cases} \\
 & H_z(r, \varphi, z, t) = e^{i(\omega t + l\varphi - \beta z)} \begin{cases} c_5 J_l(pr) + c_6 Y_l(pr) & \text{if } \beta < k_2 \\ c_5 I_l(pr) + c_6 K_l(pr) & \text{if } \beta > k_2 \end{cases} \\
 & \text{where } p^2 = \begin{cases} \beta^2 - k_2^2 = \beta^2 - n_2^2 k_0^2 & \text{if } \beta < k_2 \\ k_2^2 - \beta^2 = n_2^2 k_0^2 - \beta^2 & \text{if } \beta > k_2 \end{cases}
 \end{aligned} \tag{5.6}$$

$r \geq b$

$$\begin{aligned}
E_z(r, \varphi, z, t) &= c_7 K_1(qr) e^{i(\omega t + l\varphi - \beta z)} \\
H_z(r, \varphi, z, t) &= c_8 K_1(qr) e^{i(\omega t + l\varphi - \beta z)} \\
\text{where } q^2 &= \beta^2 - k_2^2 = \beta^2 - n_2^2 k_0^2
\end{aligned} \tag{5.7}$$

We now have 8 unknown constants (c_1 through c_8) which are solved for by using 8 boundary conditions. Namely, the electric and magnetic field components transverse to the interface surface (E_φ , E_z , H_φ , and H_z) must be continuous across the interface. This gives four boundary conditions for the layer 1-2 (core-cladding) interface and four boundary conditions for the layer 2-3 (cladding-surrounding material) interface. Explicitly stated, the boundary conditions take the following form:

$$\begin{aligned}
E_\varphi(a^-, \varphi, z, t) &= E_\varphi(a^+, \varphi, z, t) & E_\varphi(b^-, \varphi, z, t) &= E_\varphi(b^+, \varphi, z, t) \\
E_z(a^-, \varphi, z, t) &= E_z(a^+, \varphi, z, t) & E_z(b^-, \varphi, z, t) &= E_z(b^+, \varphi, z, t) \\
H_\varphi(a^-, \varphi, z, t) &= H_\varphi(a^+, \varphi, z, t) & H_\varphi(b^-, \varphi, z, t) &= H_\varphi(b^+, \varphi, z, t) \\
H_z(a^-, \varphi, z, t) &= H_z(a^+, \varphi, z, t) & H_z(b^-, \varphi, z, t) &= H_z(b^+, \varphi, z, t)
\end{aligned} \tag{5.8}$$

The relationships between the z -components of the electric and magnetic fields and the r - and φ -components are relisted from Chapter 2 as follows:

$$\begin{aligned}
E_r &= \frac{-i\beta}{k^2 - \beta^2} \left(\frac{\partial E_z}{\partial r} + \frac{\omega\mu}{r\beta} \frac{\partial H_z}{\partial \phi} \right) \\
E_\phi &= \frac{-i\beta}{k^2 - \beta^2} \left(\frac{1}{r} \frac{\partial E_z}{\partial \phi} - \frac{\omega\mu}{\beta} \frac{\partial H_z}{\partial r} \right) \\
H_r &= \frac{-i\beta}{k^2 - \beta^2} \left(\frac{\partial H_z}{\partial r} - \frac{\omega e}{r\beta} \frac{\partial E_z}{\partial \phi} \right) \\
H_\phi &= \frac{-i\beta}{k^2 - \beta^2} \left(\frac{1}{r} \frac{\partial H_z}{\partial \phi} + \frac{\omega e}{\beta} \frac{\partial E_z}{\partial r} \right)
\end{aligned} \tag{5.9}$$

In the same manner as Chapter 2, a matrix equation can be set up as follows:

$$[\Omega_{ij}] \{c_i\} = 0, \quad i, j = 1, 2, \dots, 8 \tag{5.10}$$

The adjustment from Chapter 2 is that in the three-layer setup, i and j vary from 1 to 8 rather than 1 to 4 in the two-layer setup. There are two possible $[\Omega]$ matrices depending on whether $k_2 > \beta$ or $\beta > k_2$. The components (Ω_{ij}) of both possible forms of the matrix are shown in the appendix. Once again, we end up with an equation that will have a null solution (i.e. all $c_i = 0$) unless the determinant of the matrix equals zero (i.e. $|\Omega| = 0$). Unlike the two-layer system whose 4x4 matrix determinant can be easily factored and explicitly written as in Chapter 2, the three-layer system is much more complicated. Despite having 28 of its 64 entries equal zero, explicitly writing out the determinant would provide over 300 terms. Setting the determinant of $[\Omega]$ equal to zero creates a massive transcendental equation used to find the finite number of propagation constant solutions (i.e. β_{lm}) and would be extremely lengthy to solve analytically. Rather than finding the propagation constants explicitly, a MATLAB computer program was written in order to numerically solve the transcendental equation. Once the propagation constants are determined, the kernel of the 8x8 matrix after plugging in the calculated value of β_{lm} is determined. This dictates relative values of all the c_i terms which allows for the determination of all the c_i terms to within a multiplicative factor. Assuming that multiplicative factor is the first constant, c_1 , the z -components of the electric and magnetic fields can be determined. These are plugged into Equation (5.9) to determine the r - and φ -components in terms of the constant c_1 for all three layers. The expressions for the field components in the core layer are as follows:

$$\boxed{\boxed{r \leq a}}$$

$$E_r(r, \varphi, z, t) = c_1 \left[-\frac{i\beta}{h} J_1'(hr) + \left(\frac{c_2}{c_1}\right) \frac{\omega\mu_1 l}{h^2 r} J_1(hr) \right] e^{i(\omega t + l\varphi - \beta z)} \quad (5.11)$$

$$E_\varphi(r, \varphi, z, t) = c_1 \left[\frac{\beta l}{h^2 r} J_1(hr) + \left(\frac{c_2}{c_1}\right) \frac{i\omega\mu_1}{h} J_1'(hr) \right] e^{i(\omega t + l\varphi - \beta z)} \quad (5.12)$$

$$E_z(r, \varphi, z, t) = c_1 \left[J_1(hr) \right] e^{i(\omega t + l\varphi - \beta z)} \quad (5.13)$$

$$H_r(r, \varphi, z, t) = c_1 \left[-\frac{\omega e_1 l}{h^2 r} J_1(hr) - \left(\frac{c_2}{c_1}\right) \frac{i\beta}{h} J_1'(hr) \right] e^{i(\omega t + l\varphi - \beta z)} \quad (5.14)$$

$$H_\varphi(r, \varphi, z, t) = c_1 \left[-\frac{i\omega e_1}{h} J'_l(hr) + \left(\frac{c_2}{c_1}\right) \frac{\beta l}{h^2 r} J_l(hr) \right] e^{i(\omega t + l\varphi - \beta z)} \quad (5.15)$$

$$H_z(r, \varphi, z, t) = c_1 \left[\left(\frac{c_2}{c_1}\right) J_l(hr) \right] e^{i(\omega t + l\varphi - \beta z)} \quad (5.16)$$

In the cladding layer, the electric and magnetic fields are dependent on whether $\beta < k_2$ or $\beta > k_2$. For the former case, the cladding field components are:

$$\boxed{a < r \leq b}, \quad \underline{\beta < k_2}$$

$$E_r(r, \varphi, z, t) = c_1 \left[\begin{aligned} & -\left(\frac{c_3}{c_1}\right) \frac{i\beta}{p} J'_l(pr) - \left(\frac{c_4}{c_1}\right) \frac{i\beta}{p} Y'_l(pr) \dots \\ & \dots + \left(\frac{c_5}{c_1}\right) \frac{\omega\mu_2 l}{p^2 r} J_l(pr) + \left(\frac{c_6}{c_1}\right) \frac{\omega\mu_2 l}{p^2 r} Y_l(pr) \end{aligned} \right] e^{i(\omega t + l\varphi - \beta z)} \quad (5.17)$$

$$E_\varphi(r, \varphi, z, t) = c_1 \left[\begin{aligned} & \left(\frac{c_3}{c_1}\right) \frac{\beta l}{p^2 r} J_l(pr) + \left(\frac{c_4}{c_1}\right) \frac{\beta l}{p^2 r} Y_l(pr) \dots \\ & \dots + \left(\frac{c_5}{c_1}\right) \frac{i\omega\mu_2}{p} J'_l(pr) + \left(\frac{c_6}{c_1}\right) \frac{i\omega\mu_2}{p} Y'_l(pr) \end{aligned} \right] e^{i(\omega t + l\varphi - \beta z)} \quad (5.18)$$

$$E_z(r, \varphi, z, t) = c_1 \left[\left(\frac{c_3}{c_1}\right) J_l(pr) + \left(\frac{c_4}{c_1}\right) Y_l(pr) \right] e^{i(\omega t + l\varphi - \beta z)} \quad (5.19)$$

$$H_r(r, \varphi, z, t) = c_1 \left[\begin{aligned} & -\left(\frac{c_3}{c_1}\right) \frac{\omega e_2 l}{p^2 r} J_l(pr) - \left(\frac{c_4}{c_1}\right) \frac{\omega e_2 l}{p^2 r} Y_l(pr) \dots \\ & \dots - \left(\frac{c_5}{c_1}\right) \frac{i\beta}{p} J'_l(pr) - \left(\frac{c_6}{c_1}\right) \frac{i\beta}{p} Y'_l(pr) \end{aligned} \right] e^{i(\omega t + l\varphi - \beta z)} \quad (5.20)$$

$$H_\varphi(r, \varphi, z, t) = c_1 \left[\begin{aligned} & -\left(\frac{c_3}{c_1}\right) \frac{i\omega e_2}{p} J'_l(pr) - \left(\frac{c_4}{c_1}\right) \frac{i\omega e_2}{p} Y'_l(pr) \dots \\ & \dots + \left(\frac{c_5}{c_1}\right) \frac{\beta l}{p^2 r} J_l(pr) + \left(\frac{c_6}{c_1}\right) \frac{\beta l}{p^2 r} Y_l(pr) \end{aligned} \right] e^{i(\omega t + l\varphi - \beta z)} \quad (5.21)$$

$$H_z(r, \varphi, z, t) = c_1 \left[\left(\frac{c_5}{c_1}\right) J_l(pr) + \left(\frac{c_6}{c_1}\right) Y_l(pr) \right] e^{i(\omega t + l\varphi - \beta z)} \quad (5.22)$$

For the latter case where $\beta > k_2$, the cladding field components are:

$$\boxed{a < r \leq b}, \quad \underline{\underline{\beta > k_2}}$$

$$E_r(r, \varphi, z, t) = c_1 \left[\begin{array}{l} \left(\frac{c_3}{c_1}\right) \frac{i\beta}{p} I'_l(pr) + \left(\frac{c_4}{c_1}\right) \frac{i\beta}{p} K'_l(pr) \dots \\ \dots - \left(\frac{c_5}{c_1}\right) \frac{\omega\mu_2 l}{p^2 r} I_l(pr) - \left(\frac{c_6}{c_1}\right) \frac{\omega\mu_2 l}{p^2 r} K_l(pr) \end{array} \right] e^{i(\omega t + l\varphi - \beta z)} \quad (5.23)$$

$$E_\varphi(r, \varphi, z, t) = c_1 \left[\begin{array}{l} -\left(\frac{c_3}{c_1}\right) \frac{\beta l}{p^2 r} I_l(pr) - \left(\frac{c_4}{c_1}\right) \frac{\beta l}{p^2 r} K_l(pr) \dots \\ \dots - \left(\frac{c_5}{c_1}\right) \frac{i\omega\mu_2}{p} I'_l(pr) - \left(\frac{c_6}{c_1}\right) \frac{i\omega\mu_2}{p} K'_l(pr) \end{array} \right] e^{i(\omega t + l\varphi - \beta z)} \quad (5.24)$$

$$E_z(r, \varphi, z, t) = c_1 \left[\left(\frac{c_3}{c_1}\right) I_l(pr) + \left(\frac{c_4}{c_1}\right) K_l(pr) \right] e^{i(\omega t + l\varphi - \beta z)} \quad (5.25)$$

$$H_r(r, \varphi, z, t) = c_1 \left[\begin{array}{l} \left(\frac{c_3}{c_1}\right) \frac{\omega e_2 l}{p^2 r} I_l(pr) + \left(\frac{c_4}{c_1}\right) \frac{\omega e_2 l}{p^2 r} K_l(pr) \dots \\ \dots + \left(\frac{c_5}{c_1}\right) \frac{i\beta}{p} I'_l(pr) + \left(\frac{c_6}{c_1}\right) \frac{i\beta}{p} K'_l(pr) \end{array} \right] e^{i(\omega t + l\varphi - \beta z)} \quad (5.26)$$

$$H_\varphi(r, \varphi, z, t) = c_1 \left[\begin{array}{l} \left(\frac{c_3}{c_1}\right) \frac{i\omega e_2}{p} I'_l(pr) + \left(\frac{c_4}{c_1}\right) \frac{i\omega e_2}{p} K'_l(pr) \dots \\ \dots - \left(\frac{c_5}{c_1}\right) \frac{\beta l}{p^2 r} I_l(pr) - \left(\frac{c_6}{c_1}\right) \frac{\beta l}{p^2 r} K_l(pr) \end{array} \right] e^{i(\omega t + l\varphi - \beta z)} \quad (5.27)$$

$$H_z(r, \varphi, z, t) = c_1 \left[\left(\frac{c_5}{c_1}\right) I_l(pr) + \left(\frac{c_6}{c_1}\right) K_l(pr) \right] e^{i(\omega t + l\varphi - \beta z)} \quad (5.28)$$

And finally, the surrounding material's electric and magnetic fields are:

$$\boxed{r > b}$$

$$E_r(r, \varphi, z, t) = c_1 \left[\left(\frac{c_7}{c_1}\right) \frac{i\beta}{q} K'_l(qr) - \left(\frac{c_8}{c_1}\right) \frac{\omega\mu_2 l}{q^2 r} K_l(qr) \right] e^{i(\omega t + l\varphi - \beta z)} \quad (5.29)$$

$$E_{\varphi}(r, \varphi, z, t) = c_1 \left[-\left(\frac{c_7}{c_1}\right) \frac{\beta l}{q^2 r} K_l(qr) - \left(\frac{c_8}{c_1}\right) \frac{i\omega\mu_2}{q} K_l'(qr) \right] e^{i(\omega t + l\varphi - \beta z)} \quad (5.30)$$

$$E_z(r, \varphi, z, t) = c_1 \left[\left(\frac{c_7}{c_1}\right) K_l(qr) \right] e^{i(\omega t + l\varphi - \beta z)} \quad (5.31)$$

$$H_r(r, \varphi, z, t) = c_1 \left[\left(\frac{c_7}{c_1}\right) \frac{\omega e_2 l}{q^2 r} K_l(qr) + \left(\frac{c_8}{c_1}\right) \frac{i\beta}{q} K_l'(qr) \right] e^{i(\omega t + l\varphi - \beta z)} \quad (5.32)$$

$$H_{\varphi}(r, \varphi, z, t) = c_1 \left[\left(\frac{c_7}{c_1}\right) \frac{i\omega e_2}{q} K_l'(qr) - \left(\frac{c_8}{c_1}\right) \frac{\beta l}{q^2 r} K_l(qr) \right] e^{i(\omega t + l\varphi - \beta z)} \quad (5.33)$$

$$H_z(r, \varphi, z, t) = c_1 \left[\left(\frac{c_8}{c_1}\right) K_l(qr) \right] e^{i(\omega t + l\varphi - \beta z)} \quad (5.34)$$

The term c_1 is the final value that must be determined in order to fully resolve the EM field in the fiber. This term is calculated by knowing the intensity of light and using the following equation:

$$I = \frac{cne_0}{2} |E|^2 \quad (5.35)$$

This concludes the theoretical description of the equations used to derive the propagation constant as well as the electric and magnetic field values. Next, the computer program used to calculate β and all of the c_i values will be described.

5.3.2 Computational Program

A series of MATLAB computational programs were written in order to determine approximate solutions to the equations above. The three main tasks of the programs are as follows:

- (1) Create an effective index versus V parameter plot similar to that shown in Chapter 2. This provides a visualization of the relationship between the effective IOR of propagating light and

input variables such as the properties of the fiber (e.g. radius and IOR of each layer) and light (e.g. wavelength).

(2) Calculate the reflected wavelength or wavelengths of light. Given the pitch of the core index of refraction oscillation, Λ , the fiber properties, and a wavelength range in which you expect the laser to tune, the reflected wavelength(s) can be calculated.

(3) Calculate mode shapes. Given the effective index, wavelength of light, and the fiber properties, the program calculates the magnitudes of the electric and magnetic fields (both real and imaginary). Thus, a spatial distribution of light intensity can be visualized.

The steps taken in the three tasks above will now be described in more detail.

5.3.2.1 EFFECTIVE INDEX RELATIONSHIP

A MATLAB computational program was written in order to provide estimates of the propagation constant solutions to the 2- and 3-layer transcendental equations. The program calculates the determinant of $[\Omega]$ in Equation (5.10) as a function of effective index and input light wavelength. Using the nomenclature from Chapter 3, the term $Z(\lambda_0, n)$ is used to represent the determinant's value for each wavelength and index value. Note that for given values of a , n_1 , and n_2 , the following equation describes the relationship between the V parameter and wavelength, λ_0 .

$$V = \frac{2\pi}{\lambda_0} a \sqrt{n_1^2 - n_2^2} \quad (5.36)$$

With this relationship, $Z(\lambda_0, n)$ can be reparameterized to $Z(V, n)$. A 3-dimensional surface plot is created with V and n being the independent variables and the height represented by Z values. The locus of points where $Z = 0$ determines the coupled values of λ_0 and n which satisfy the transcendental equation (i.e. the determinant of $[\Omega]$ is equal to zero).

Table 5-2 below summarizes the input parameters for the program and gives examples of 2- and 3-layer inputs. The first step of the program is to input the necessary fiber

parameters which include the number of layers, IORs, core and cladding radii, and FBG index oscillation pitch. Additionally the three sweep parameters are also set. The first sweep setting is the range of mode numbers which determine the Bessel function orders to consider. Second, the choice of sweeping through a range of wavelengths or V parameter values is given. Note that Equation (5.36) allows for easily going back and forth between the two variables; however, the inverse, nonlinear relationship between the two means that choosing consistent, equal increments of λ in the sweep will lead to changing increments of V . Therefore, the user is given the choice of which independent variable gets equal increments. Once the type of sweep is set, the range of wavelengths or V parameter values is input along with the resolution (i.e. the number of λ or V points). Thirdly, the sweep range and resolution of the effective IOR is chosen.

Table 5-2: Input parameters for calculating and plotting the n - V relationship in an optical fiber.

Input Parameter	Value	2-Layer Example	3-Layer Example
# of Layers	2 or 3	2	3
IORs	$n_1, n_2,$ and n_3^*	1.457, 1.444	1.457, 1.444, 1.300
Layer Outer Radii	a and b^*	2.7e-6	2.7e-6, 3.75e-6
FBG Oscillation Pitch	Λ	533.23e-9	533.23e-9
Mode Number Sweep	l	[0:1:4]	[0:1:4]
Choose Wavelength or V Sweep	1 for λ_0 , 2 for V	2	2
(if 1) Wavelength Sweep Range	$\lambda_{0start}, \lambda_{0end}$	(2196e-9, 659e-9)	(1647e-9, 1318e-9)
(if 2) V Parameter Sweep Range	V_{start}, V_{end}	1.5, 5.0	2, 2.5
λ or V Resolution (pts.)	length($\{\lambda_0$ or $V\}$)	250	200
Effective IOR Sweep Range	n_{start}, n_{end}	1.4441, 1.4569	1.4000, 1.4569
Effective IOR Resolution (pts.)	length($\{n\}$)	200	250

From the inputs, the program builds the V parameter, $\{V\}$, wavelength, $\{\lambda_0\}$, effective index, $\{n\}$, and wavenumber, $\{k_0\}$, vectors and calculates pertinent values such as layer permittivity (ϵ_i) and permeability (μ_i). Next, the determinant of $[\Omega]$ is calculated for each combination of V (or λ_0), n , and l . The values are compiled into entries of $[Z(V,n)]$ matrices with the number of $[Z]$ matrices equal to the number of l values considered. A plot is created by replacing the entries of

$[Z]$ simply with +1 or -1 when the value is positive or negative respectively. The $\text{sign}([Z])$ matrices are each array-multiplied (as opposed to matrix-multiplied) by calculating an element-by-element product. For instance, the row 5, column 3 entries of all of the $\text{sign}([Z])$ matrices are multiplied. The feature of each matrix in which we are interested is when the sign changes. Thus, combining the multiple $\text{sign}([Z])$ matrices into one using the array-multiplication technique maintains these features. Figure 5-2 below shows the 3-D plot indicating what combinations of n and V values give positive or negative Z values. The sweep ranges and fiber parameters are those listed in the “2-Layer Example” column in Table 5-2Table 5-2 above.

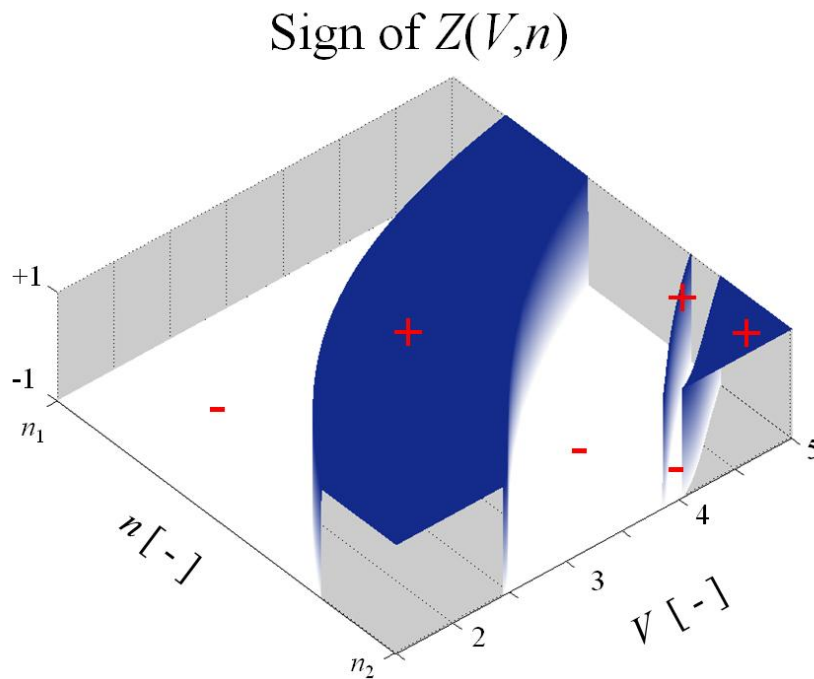


Figure 5-2: Plot indicating combinations of effective IOR and V parameter values which cause the sign of the determinant of $[\Omega]$ to be positive and negative.

The particular feature of interest in the plot above is not the regions of negative (light) or positive (dark) Z values, but rather where changes in sign occur. These are the locations numerically closest to the combinations of n and V which cause the determinant of $[\Omega]$ to be zero. The locations are shown in the graphs in Figure 5-3 below. The top graph depicts a top-

view of Figure 5-2 with the locus of $Z = 0$ points represented by the curves. Each curve is assigned a mode name such as HE_{11} , EH_{11} , and TM_{01} . The two lower graphs depict portions of the upper graph magnified to show that what look like single curves in the upper graph are actually two or three curves (each representing a different mode) closely spaced. This simply means that for given fiber characteristics and input wavelength, the HE_{21} , TE_{01} , and TM_{01} modes have similar effective IOR values (and thus, propagation constants, β).

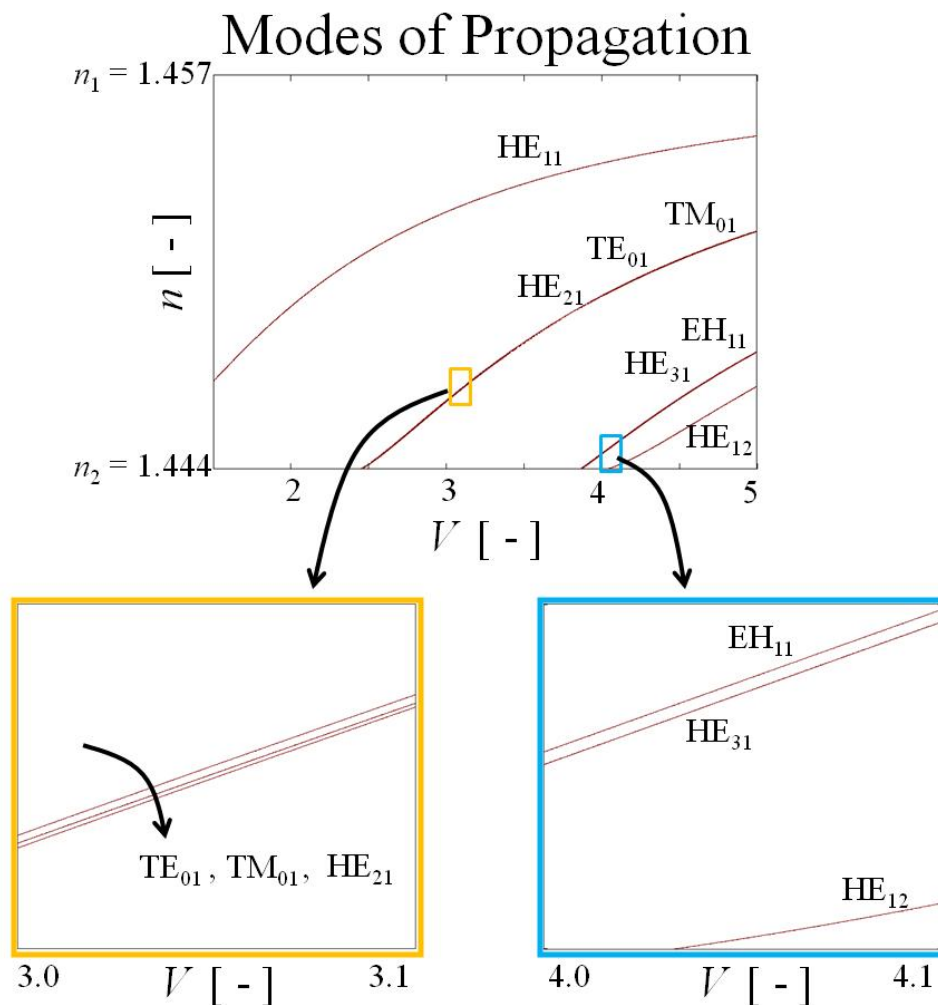


Figure 5-3: Plots showing the curves representing the dependence of effective IOR on V parameter.

Now that the program describing the creation of the effective IOR graphs above has been described, the method for calculating reflected wavelengths will be described next.

5.3.2.2 REFLECTED WAVELENGTH DETERMINATION

This next task determines the reflected wavelengths of the FBG using a methodology based on that just described to calculate the effective index plots. The first step in the process of understanding how the program works is to rescale the effective IOR variable by multiplying by 2Λ . Figure 5-4 demonstrates the rescaling of the vertical axis. The graph on the left is identical to the upper plot in Figure 5-3. The graph on the right alters the scale from $[n_2 \rightarrow n_1]$ to $[2n_2\Lambda \rightarrow 2n_1\Lambda]$. Additionally, the graph on the right zooms-in to the V parameter range of $2.0 \rightarrow 2.5$ from the original $1.5 \rightarrow 5.0$.

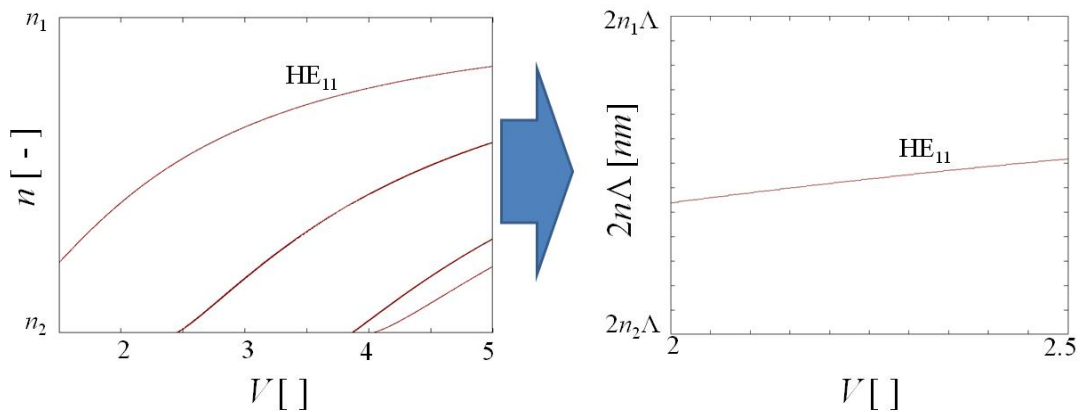


Figure 5-4: Re-parameterization of the effective IOR scale.

The only remaining mode in the new range is the fundamental HE_{11} mode. The next step is to reparameterize the horizontal axis from V to λ_0 using Equation (5.36). This step is shown in Figure 5-5 below. Note the inverse relationship between λ_0 and V leads from a monotonically increasing curve in the left graph of Figure 5-5 to a monotonically decreasing curve in the right graph. Recall that the red curve describing the HE_{11} mode represents the combinations of n and λ_0 values which are supported by the fiber. Overlaid on the right graph is a $\lambda_0 = 2n\Lambda$ curve in blue which represents all of the wavelengths of light which satisfy the Bragg condition. The intersection of these two curves represents the simultaneous satisfaction of light propagating through the fiber in the HE_{11} mode and the Bragg condition. Thus, projecting this intersection point to either axis provides the Bragg wavelength, λ_B , indicated by the black dotted lines.

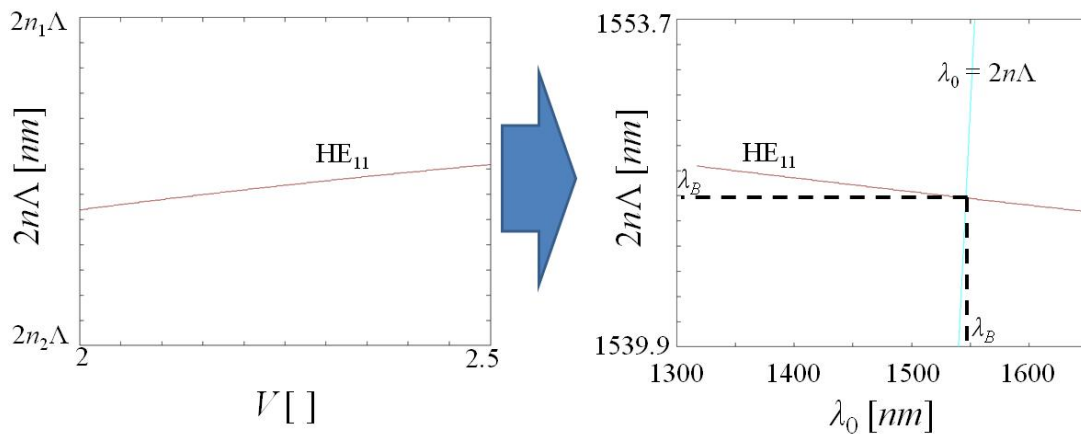


Figure 5-5: Re-parameterization of the V parameter which leads to two curves representing a supported fiber mode and the satisfaction of the Bragg condition. The intersection of the curves represents the FBG reflected wavelength.

The program takes the same fiber characteristics as the effective index program (i.e. a , b , n_1 , n_2 , n_3) and sweeps through the blue Bragg condition curve in the right graph above. At each point along the curve, the determinant of $[\Omega]$ is calculated and the locations where $\text{sign}(Z)$ changes its sign is where the blue curve crosses the red curve and a Bragg reflection will occur in the fiber.

An additional layer of complexity is added to this program in that the user can specify certain fiber characteristics to alter. This calculates the relationship between λ_B and fiber characteristics such as core or cladding radius. For example, Figure 5-6 below demonstrates the n - V relationship for the case when the cladding radius, b , is 63.5 (upper left graph) and $3.75 \mu\text{m}$ (lower left graph). Note the surrounding material index is that of air, 1.00 . The regions of positive and negative Z values are seen to shift. When the two plots are overlaid to create the graph on the right side of the figure, regions associated with blue or yellow keep their color while overlapping regions are now colored green.

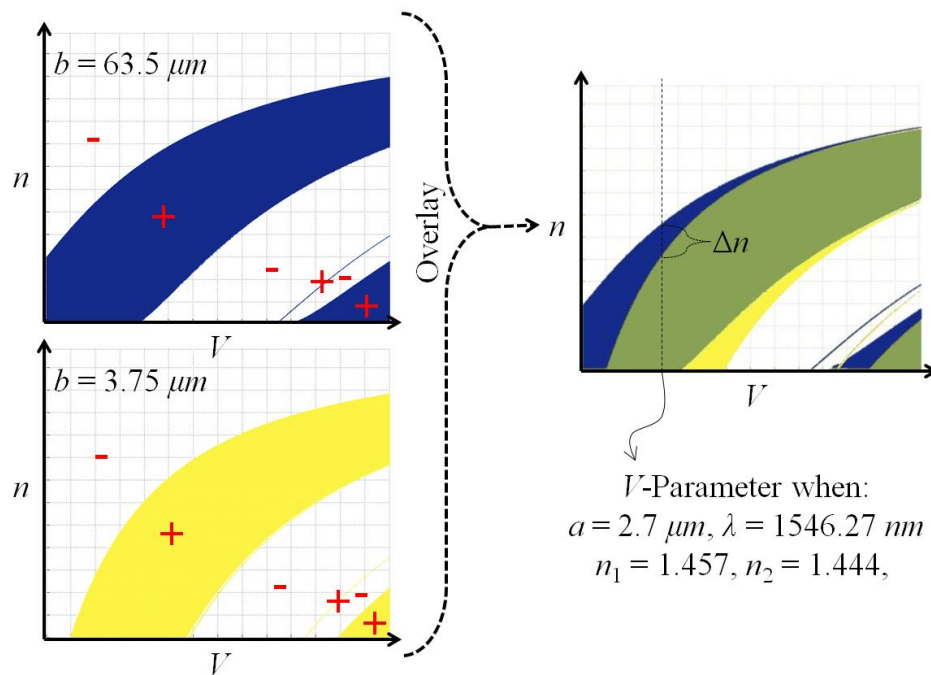


Figure 5-6: Change in the n - V relationship when the cladding radius is altered.

For a particular set of fiber characteristics listed in the lower-right of the figure above, the locus of points where the switch from a positive to negative Z -value region for the fundamental mode changes by a value Δn . The reflected wavelength calculation program will therefore find that the wavelength satisfying the Bragg condition when $b = 63.5 \mu\text{m}$ ($1546.27 \text{ nm} = 2n\Lambda$) does not satisfy the condition when $b = 3.75 \mu\text{m}$ due to the shift, Δn ($1546.27 \text{ nm} \neq 2(n+\Delta n)\Lambda$). Thus, the program will find a Bragg wavelength where the curve describing light propagation in the fiber (red HE_{11} curve in Figure 5-5 which has shifted due to the change in cladding radius) intersects the curve satisfying the Bragg condition (blue $\lambda_0 = 2n\Lambda$ curve in Figure 5-5). Now that the effective index has been determined for a particular mode and set of fiber characteristics (a , b , n_1 , n_2 , n_3), the mode shape can be calculated. This is described next.

5.3.2.3 MODE SHAPE CALCULATION

This program takes as an input the number of layers considered, refractive indices and outer radii of each layer, FBG oscillation pitch (Λ), mode number (l), and effective index previously

calculated. A cylindrical coordinate mesh is created in r and φ and the electric and magnetic field magnitudes and EM wave intensities are calculated at each mesh node point using Equations (5.11) through (5.32). Note the program does not calculate the determinant of the $[\Omega]$ matrix, but instead calculates the constant ratios c_i/c_1 . Additionally, an arrow plot is created to indicate the magnitude and intensity of the EM wave at various rectangular coordinates in the plane transverse to the optical fiber. As an example, the fundamental HE_{11} mode shape calculated from the program is shown in Figure 5-7. The input parameters are for a 2-layer fiber where $a = 2.7 \mu m$, $n_1 = 1.457$, $n_2 = 1.444$, $\Lambda = 533.23 \text{ nm}$, $l = 1$, and $n = 1.44914$ (calculated from the effective index program). The magnitude of the intensity has been normalized to its maximum value.

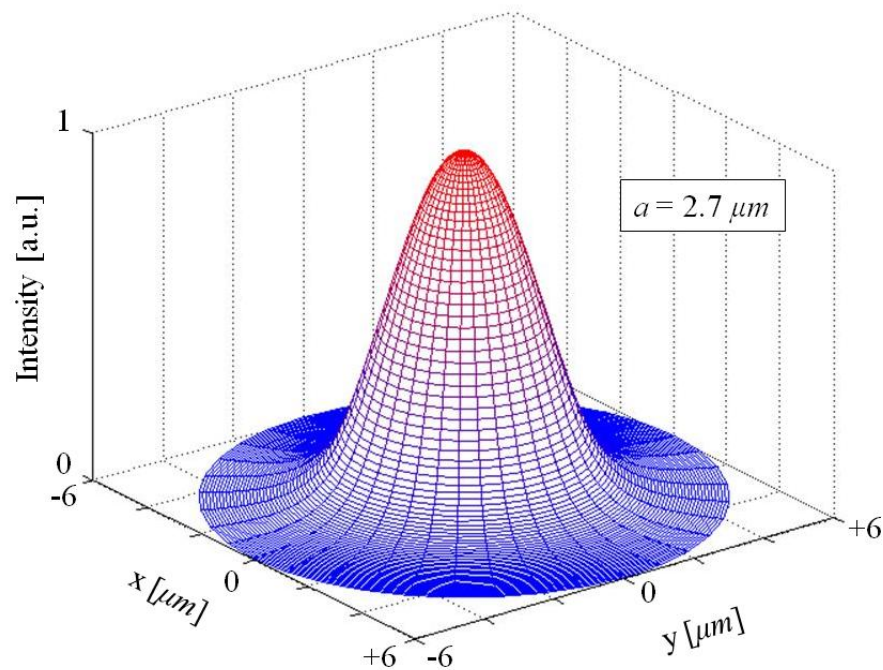


Figure 5-7: Mode shape of the fundamental HE_{11} mode.

In addition to the mode plot above, an arrow plot is calculated and shown in Figure 5-8 below to demonstrate the direction of the electric field in the cross section of the optical fiber. The figure below has arrows every $0.25 \mu m$ in both the x- and y-directions. The lengths of the

arrows are proportional to the magnitude of the field. Additionally, a red circle has been drawn to indicate the core of the optical fiber.

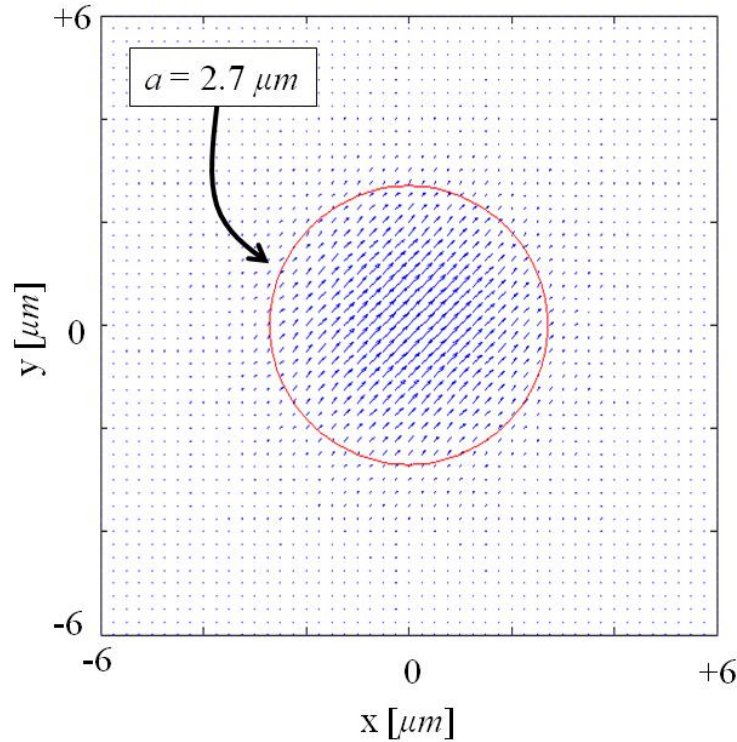


Figure 5-8: Arrow plot indicating the direction of the electric field in the cross-section of the optical fiber for the HE_{11} mode.

Note that the field is largely aligned at a 45° angle from the x-axis. This supports the notion that the fundamental mode's electric field is linearly polarized and validates our treatment of the propagating EM wave as such in previous birefringence analysis. In the next subsection, the programs just described will be applied to specific examples of a propagating EM wave when certain fiber characteristics are manipulated. The behavior will aid in designing and fabricating the magnetic sensor.

5.3.3 Examples

In this section, the MATLAB programs just described will be applied to calculate the response of effective IOR and thus, of λ_B , when various fiber parameters are manipulated. The

first change will be to the core and cladding radii. The second will be to cladding and surrounding material IOR. After exploring the effects of each variable on its own, two combinations of parameters will be altered to gain further insight into the behavior of optical fibers. These variations will then be expanded from originally studying how the fundamental mode responds to alterations in fiber parameters to studying how higher order modes respond. The sensitivities of three different modes will be explored to compare sensitivities.

5.3.3.1 RADIUS

First, the effect of core and cladding radius will be explored. In a 2-layer fiber with a cladding radius of $63.5 \mu\text{m}$, the core radius is varied between 1.5 and $8.0 \mu\text{m}$. The core and cladding layer indices are maintained at 1.457 and 1.444 throughout. The graph in Figure 5-9 plots the relationship. The left vertical axis represents the effective index for the propagating wave while the horizontal axis represents the core radius. The right vertical axis shows where the core and cladding indices are in relation to the effective index. The blue circles represent the calculated effective IOR data for the fundamental mode while the orange dotted vertical line indicates the original core radius value of $2.7\mu\text{m}$. Note the inset table indicating constant parameters such as b , n_1 , n_2 , and n_3 .

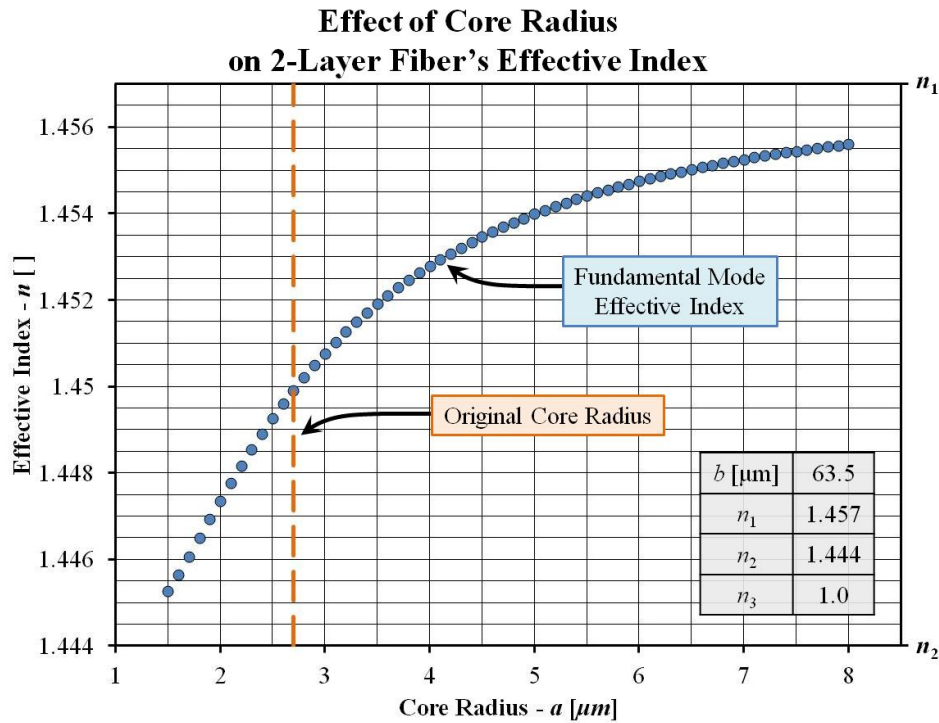


Figure 5-9: Relationship between core radius and effective IOR in a 2-layer fiber.

As expected, the effective index is between the core and cladding index. As stated in Chapter 3, the effective index for at the original core radius is 1.450. Note that as the core radius increases, the effective index increases as well. The reason for this can be explained with Figure 5-10 demonstrating the mode shapes for the two extremes. The plot on the left shows a side-profile of the light intensity distribution within the optical fiber when the core radius is $1.5 \mu\text{m}$. The vertical axis represents light intensity while the horizontal axis represents distance from the center of the fiber ($r = 0$) scaled in units of core radius (a) for comparison purposes. The vertical red lines indicate the core-cladding interface.

Distribution of Light Intensity in Optical Fiber

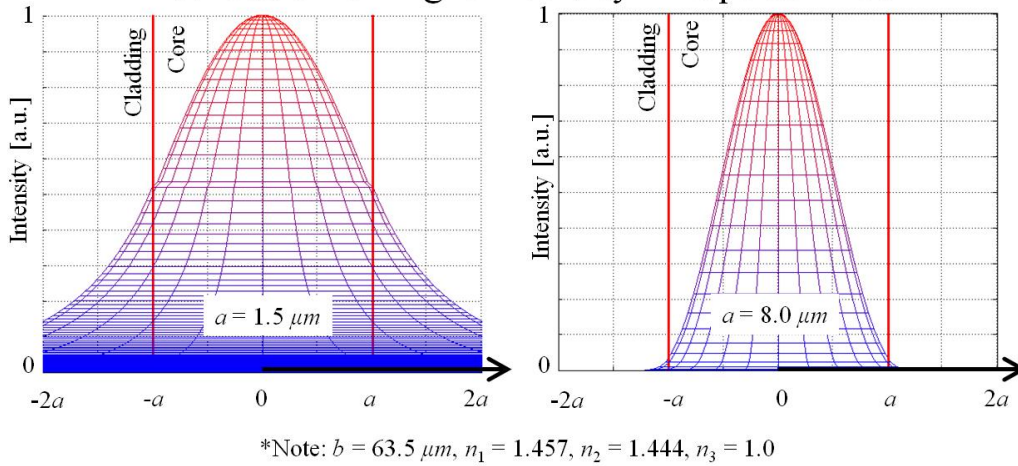


Figure 5-10: Change in mode shape when core radius is altered in a 2-layer fiber.

It can easily be seen that there is a stark difference in the ratio of light intensity within the core to that within the cladding when the core radius is changed. This explains the behavior seen in the previous figure in that when the core radius is smaller, a larger portion of light is within the cladding and thus, the effective index will be closer to the refractive index of the cladding. As the core radius increases, the proportion of light within the core will also increase and thus, the effective IOR will approach the IOR of the core material.

In fabricating the eventual magnetic sensor, a portion of the cladding layer will be removed and surrounded with a magnetically active material. Thus, tracking the behavior of the effective IOR when reducing the cladding radius, b , is an endeavor more relevant to this research. This relationship is shown in Figure 5-11. The left vertical axis represents the effective index while the horizontal axis is a logarithmic scale of the cladding radius. The range of cladding radii considered is between 3.0 and $70 \mu\text{m}$. Just as in Figure 5-9, the right vertical axis shows where the core and cladding indices are in relation to the effective index. The red circles represent the calculated effective IOR values of the fundamental mode and the green dotted line indicates the original cladding radius of $63.5 \mu\text{m}$. Note the inset table indicating constant parameters such as a , n_1 , n_2 , and n_3 .

Effect of Cladding Radius on 3-Layer Fiber's Effective Index

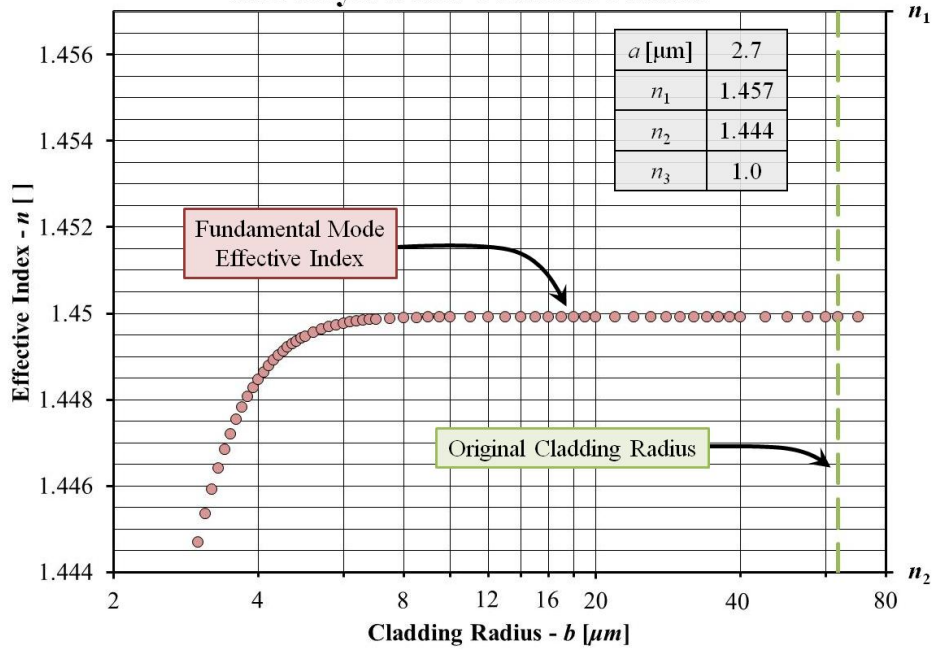
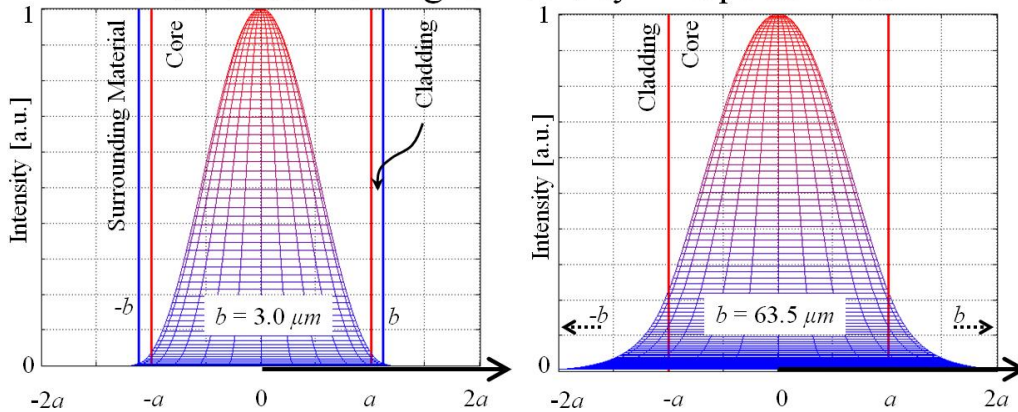


Figure 5-11: Relationship between cladding radius and effective IOR in a 3-layer fiber.

At higher cladding radii, the effective index remains at the original 1.450 value stated earlier. However, as the cladding radius decreases, a larger and larger portion of the EM wave's evanescent field is present in the low-index surrounding material. This can be seen in Figure 5-12 demonstrating the mode shapes when the cladding radius is set to $3.0 \mu\text{m}$ and $63.5 \mu\text{m}$. The vertical axis represents intensity normalized to the peak intensity while the horizontal axis represents distance from the fiber center. The common properties in both fibers are that $a = 2.7 \mu\text{m}$, $n_1 = 1.457$, $n_2 = 1.444$, and $n_3 = 1.0$. The red vertical lines indicate the extent of the core while the blue lines indicate that of the cladding. Note the absence of blue lines in the graph on the right because the cladding is beyond the range displayed.

Distribution of Light Intensity in Optical Fiber



*Note: $a = 2.7 \mu\text{m}$, $n_1 = 1.457$, $n_2 = 1.444$, $n_3 = 1.0$

Figure 5-12: Change in mode shape when cladding radius is altered in a 3-layer fiber.

Two qualitative factors can be used to assign an effective IOR value for the two distributions shown. The first is the relative amount of light intensity (or volume under the mesh in the plots above) within the different fiber layers. The second is the refractive index of those layers. Comparing the two graphs, the distribution on the left has a higher percentage of its intensity within the higher-index core compared to the right distribution. This would indicate that the mode on the left has a higher index, but this is not the case as seen from Figure 5-11. The more significant factor is the presence of a small portion of the light in the left graph within the low-index surrounding material ($n_3 = 1.0$). This feature of the mode on the left indicates that the effective IOR will shift down to a lower value than the mode on the right which essentially has none of its distribution in the surrounding material because of the large cladding radius. Thus, having even a small portion of light within the surrounding material is seen to significantly influence the effective index of the propagating light. This indicates that the second qualitative factor is stronger than the first. Next, the influence of the IOR of the individual layers of an optical fiber will be explored.

5.3.3.2 OUTER INDEX

The first relationship to be explored is the role of the cladding index in a 2-layer optical fiber. With the core index and radius set to 1.457 and $2.7 \mu\text{m}$ respectively and the cladding radius set to $63.5 \mu\text{m}$, the change in effective index is calculated when the cladding index is varied between 1.0 and 1.454. Figure 5-13 demonstrates the relationship with the left vertical axis representing effective IOR and the horizontal axis representing cladding IOR. The blue circles represent the effective index of the fundamental mode while the orange dotted line represents the original cladding index value of 1.444. The right vertical axis demonstrates where the core index and original cladding index lay on the effective index scale. The effective index is seen to increase at a faster and faster pace as the cladding index increases. Note the inset table indicating constant parameters such as a , b , n_1 , and n_3 .

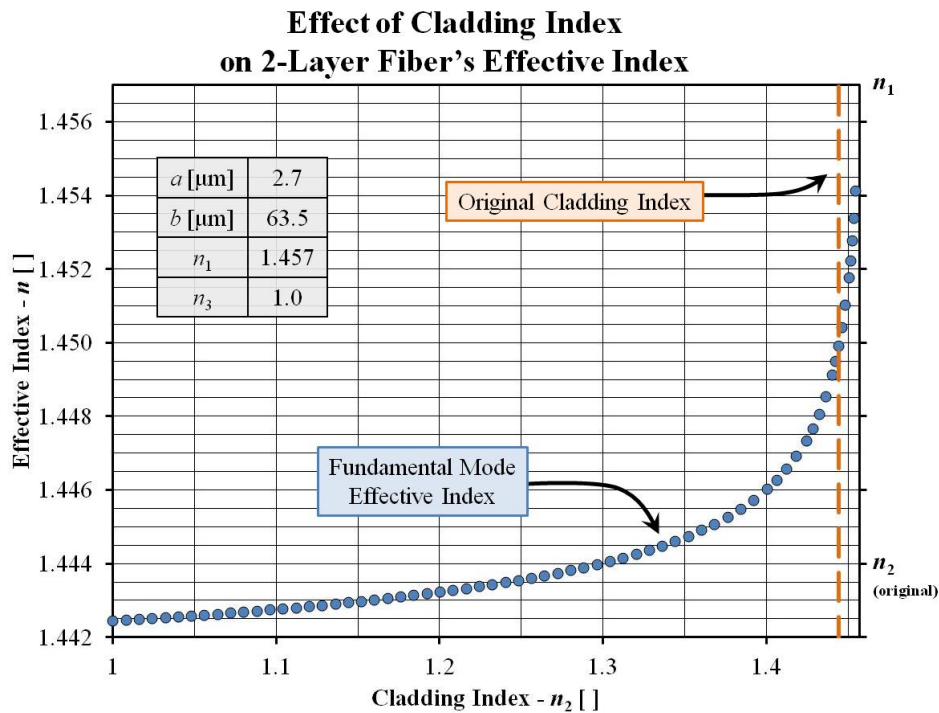


Figure 5-13: Relationship between cladding IOR and effective IOR in a 2-layer fiber.

The behavior of the effective index can be explained in a manner similar the effect of cladding radius, b , on effective index. Figure 5-14 below shows the intensity distribution within

the optical fiber for the two extreme cases in the plot above where $n_2 = 1.0$ and 1.454 . Note that values of $a = 2.7 \mu\text{m}$, $b = 63.5 \mu\text{m}$, $n_1 = 1.457$, and $n_3 = 1.0$ were used to create both mode shapes.

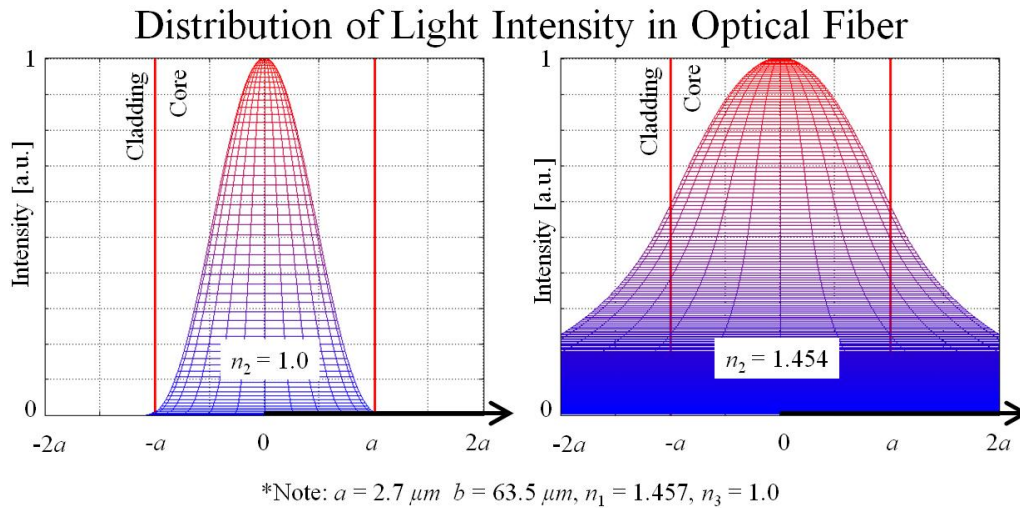


Figure 5-14: Change in mode shape when cladding IOR is altered in a 2-layer fiber.

In the graph on the left, a large portion of the light intensity is in the core whereas in the graph on the right, a significant portion now exists in the cladding. Once again, this would intuitively indicate that the effective IOR of the left mode is greater than the right mode, but according to our data, this is not the case. The reason is that even though only a small portion of the distribution on the left is in the cladding, the very low value of $n_2 = 1.0$ pulls the effective index down much farther than the graph on the right with a much higher cladding index of 1.454 . Next, the surrounding material IOR will be manipulated.

The idea behind the magnetic sensor to be created is to replace a portion of the cladding material with a magnetically active material. This magnetic surrounding material will experience a change in IOR when a magnetic field is applied. Thus, theoretically analyzing the shift in effective index resulting from changes in the surrounding material's index is a relevant effort. The influence of taking an optical fiber with a cladding diameter reduced to $3.75 \mu\text{m}$ and manipulating the surrounding material IOR between 1.0 and 1.444 is presented in Figure 5-15.

The left vertical axis represents effective index while the horizontal axis represents the surrounding material index. The red circles indicate the effective index values while the green dotted line indicates the cladding index. The right vertical axis indicates where the core and cladding index values are located in the effective index range. The effective index increases at a faster rate as the surrounding material index increases. Note the inset table indicating constant parameters such as a , b , n_1 , and n_2 .

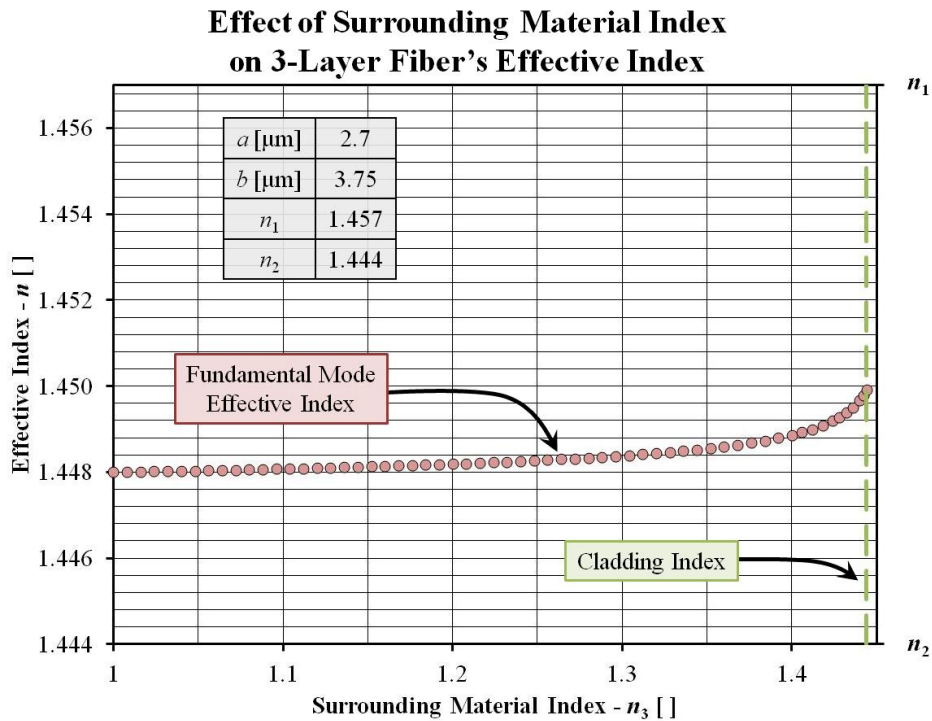


Figure 5-15: Relationship between surrounding material IOR and effective IOR in a 3-layer fiber.

The behavior of the effective index resembles that of the previous study manipulating the cladding index but to a smaller magnitude. This is because the remaining cladding material prevents full access of the surrounding material to the evanescent field for manipulation by changes in IOR. The change in mode shape is shown in Figure 5-16 to demonstrate this. In the two graphs, the distribution of intensity within the optical fiber is shown for the extreme cases in

the previous figure with $n_3 = 1.0$ and 1.444 . The red vertical lines indicate the core-cladding interface while the blue lines indicate the cladding-surrounding material interface.

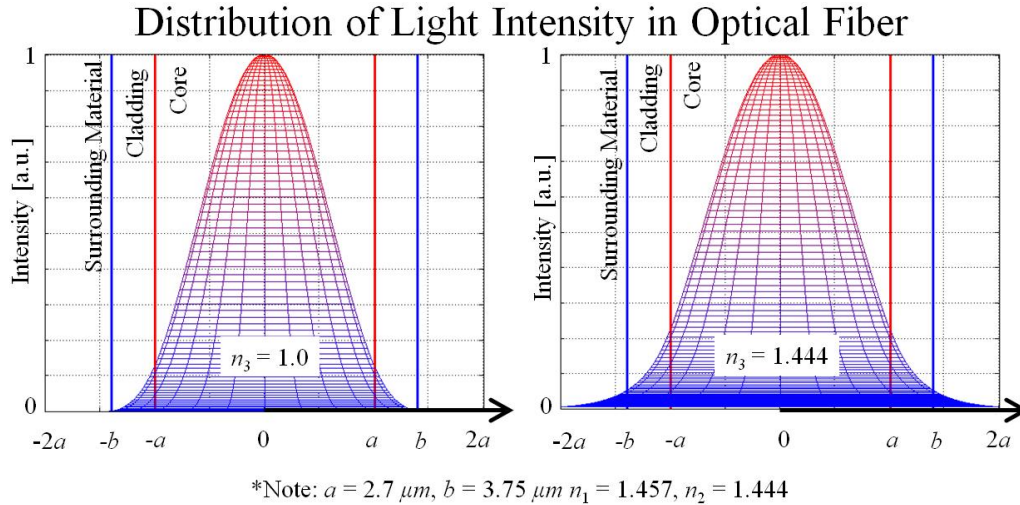


Figure 5-16: Change in mode shape when surrounding material IOR is altered in a 3-layer fiber.

Once again, despite the fact that a smaller proportion of the light intensity remains within the higher-index core when the surrounding material IOR is increased, the effective IOR increases. This is because the magnitude of the lower-index cladding and surrounding material in the left distribution (1.444 and 1.0 respectively) drive the effective index value down farther than the right distribution (1.444 and 1.444).

The theme developing in the four cases studied so far (varying a , b , n_2 , and n_3) indicates that two factors are at play in analyzing the link between mode shape and effective index. The weaker factor is the proportion of light intensity within each layer. In the case of manipulating the core radius, a , when a larger portion of the light intensity is in the higher-index material, the overall effective index is increased. This was not true, however, in the cases of manipulating b , n_2 , and n_3 . This is because in the latter 3 cases, the stronger of the two factors comes into play. This stronger factor is the magnitude of the refractive indices of each layer. It was seen that having even very small portions of the evanescent field within a very low index material drastically decreased the effective index. This work described the variation of a single parameter.

In the next section, the manipulation of two sets of two parameters will be explored. The first set of parameters will be a and n_2 while the second set will be b and n_3 .

5.3.3.3 COMBINATION

In designing and implementing the optical fiber sensor to measure magnetic fields, two characteristics of the original optical fiber will be manipulated. The first is the cladding radius and second is the surrounding material index of refraction. Thus, extrapolating the single-parameter manipulation in the previous two subsections to a dual-parameter manipulation can provide insight into the necessary fabrication and the ensuing functionality of the sensor.

The first set of characteristics manipulated is the core radius and the cladding index of refraction. Though not representative of the sensor to be fabricated in this work, the response of the optical fiber to manipulating these parameters still provides insight into how the fiber behaves. In Figure 5-17 below, the effective IOR is plotted and represented by the vertical axis when the cladding index is varied between 1.0 and 1.451 and the core radius is varied between $1.5 \mu\text{m}$ and $8.0 \mu\text{m}$. The graph on the left shows the 3-dimensional surface plot while the two graphs are side-views of the surface to further demonstrate the multivariate dependence of effective index. Note the similarities between the upper right graph and Figure 5-9 and the bottom right graph and Figure 5-13. Also note that for all the data in this figure, the cladding radius is $63.5 \mu\text{m}$, core index is 1.457, and surrounding material index is 1.0.

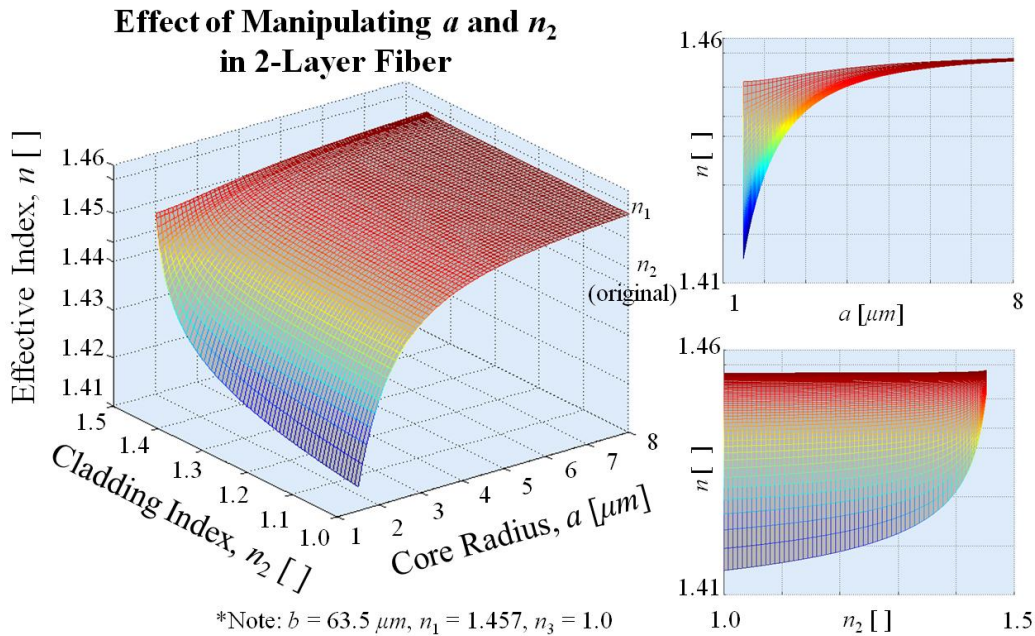


Figure 5-17: Variation of effective IOR with change in core radius and cladding IOR in a 2-layer fiber.

It is easily seen that the thinner the fiber, the more responsive the effective IOR is to changes in the cladding IOR. By the same token, a lower cladding IOR creates a stronger response in effective IOR when the core radius is altered. Using this as a starting point, we now look to create an analogous figure with the exception that the effective index will be plotted against cladding radius, b , and surrounding material index, n_3 . This is shown in Figure 5-18 below with the cladding radius varied between $3.0 \mu\text{m}$ and $70 \mu\text{m}$ and with the surrounding material index varied between 1.0 and 1.444. Note the cladding radius is plotted using a logarithmic scale. Also note that for all the data in this figure, the core radius is $2.7 \mu\text{m}$, core index is 1.457, and cladding index is 1.444.

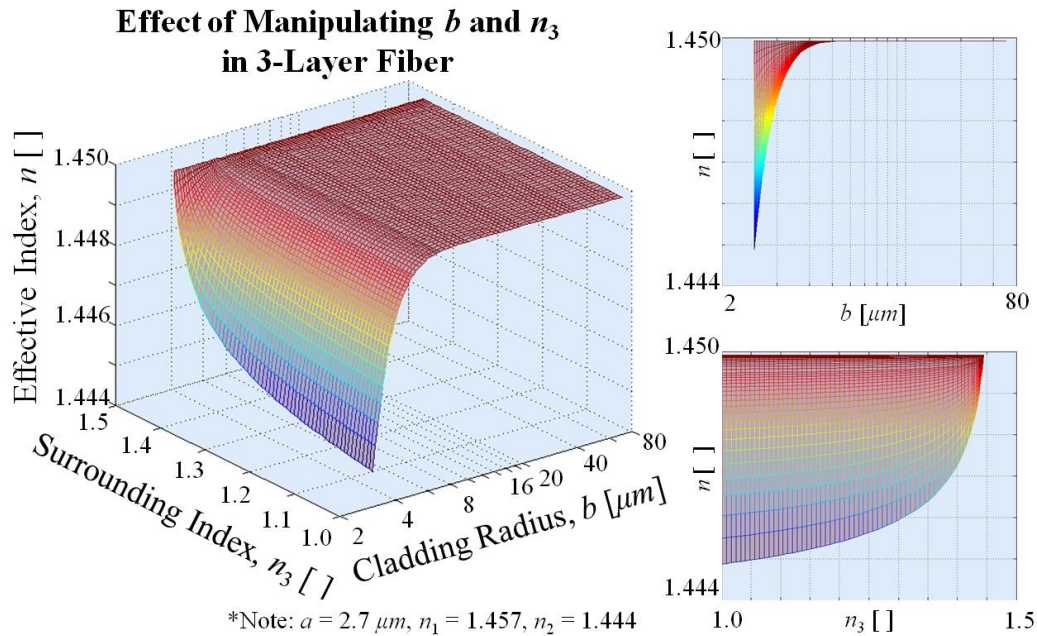


Figure 5-18: Variation of effective IOR with change in cladding radius and surrounding material IOR in a 3-layer fiber.

The plot showing the dependence of effective IOR on surrounding IOR and cladding radius is similar in shape to the previous figure. However, note the smaller effective index scale used. This indicates that even though changing the surrounding index for a small enough cladding radius can have a significant effect, it does not match the sensitivity of a sensor based on manipulating the cladding index for a given core radius. Despite this, manipulation of the second set of parameters is deemed to be sensitive enough and thus, will be pursued in designing the fiber sensor.

The main reason why it was chosen in this research to pursue a response in the optical fiber when manipulating the surrounding index and cladding radius (b - n_3) as opposed to the cladding index and core radius (a - n_2) is that the laboratory resources were already in place to pursue the former but not the latter. The a - n_2 manipulation involves changing the drawing procedure already set in place by the fiber manufacturer whereas the b - n_3 manipulation involves etching the optical fiber for an appropriate duration of time in the laboratory. Additionally, the b - n_3 manipulation provides an adequate response that should be measurable by the FOID system.

Next, an additional variable is added to the study of the optical fiber response by considering multiple modes of light propagation.

5.3.3.4 MODES

This section describes the effect of the previously described $b-n_3$ manipulation on three different modes propagating through an optical fiber. Due to the characteristics of the off-the-shelf fiber Bragg gratings, the FBG sensors fabricated and tested in this research only utilize the fundamental mode of propagation. However, the theoretical response of effective IOR for higher order modes will be explored here. Two different theoretical changes will be made from the characteristics of the currently used FBGs to access higher order modes. The first change involves doubling the optical fiber core radius from $2.7 \mu\text{m}$ to $5.4 \mu\text{m}$ while the second involves extending the wavelength range through which the FOID laser scans from a lower bound of 1535 nm to 1495 nm .

The manner in which increasing the core radius from $2.7 \mu\text{m}$ to $5.4 \mu\text{m}$ creates multiple modes of propagation will be described first using Figure 5-19. The plot shows $n-V$ curves for various modes in red. The blue curve represents the points within the $n-V$ domain which satisfy the Bragg condition when $a = 2.7 \mu\text{m}$. By doubling the core radius, you are effectively doubling the V parameter of a given propagating wave when all other parameters remain constant. Thus, doubling the core radius effectively shifts the range of V parameter values covered by the blue curve to a range now covered by the green curve. Note that the intersection of the red mode curves with the blue and green Bragg condition curves represents a reflected wavelength for the FBG. Thus, we can see that the initial blue curve only intersects one red mode curve whereas the green curve intersects more.

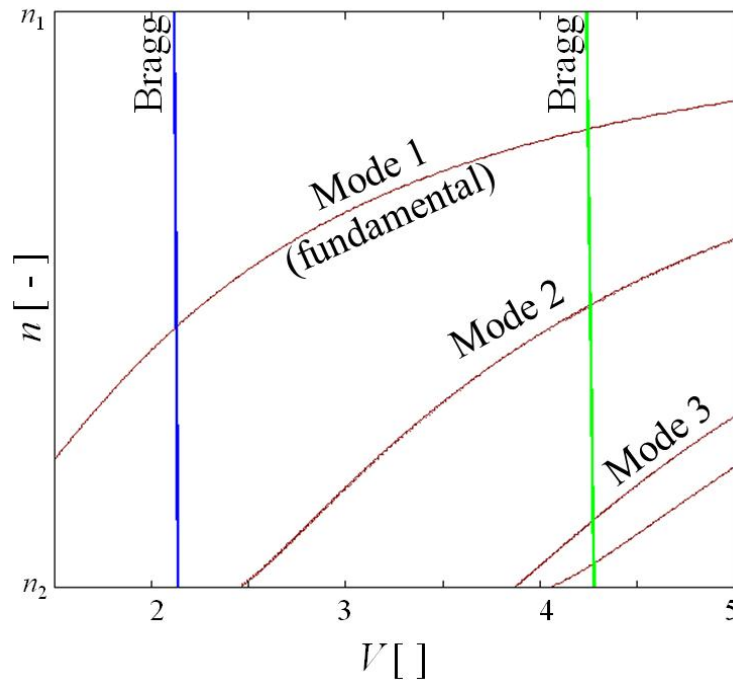


Figure 5-19: Altering the core radius to shift the V parameter to a higher value in order to have more modes intersect the Bragg condition curve.

When the cladding radius, b , and the surrounding material index, n_3 , change, the mode curves will shift in relation to the Bragg condition curves. However, each mode curve is not expected to shift equally with $b-n_3$ manipulation. Therefore, the effective IOR and thus, λ_B will not shift equally for each mode. Therefore, the purpose of this portion of the theoretical work is to reveal whether or not higher order modes are more responsive to manipulation than the fundamental mode.

The result of the $b-n_3$ manipulation on effective index for three different modes is shown in Figure 5-20 below. This figure is similar to the left graph in Figure 5-18 with the exception that the vertical axis represents change in effective IOR rather than the value itself. The zero location is taken to be when the surrounding material index is 1.0. Another difference is that the cladding radius range is abbreviated to between $5.5 \mu\text{m}$ and $8.0 \mu\text{m}$ (since the core has been increased to $5.4 \mu\text{m}$). The three surfaces represent the three modes with Mode 3 clearly being more sensitive to $b-n_3$ manipulation than Modes 1 and 2.

Effect of Manipulating b and n_3 in 3-Layer Fiber

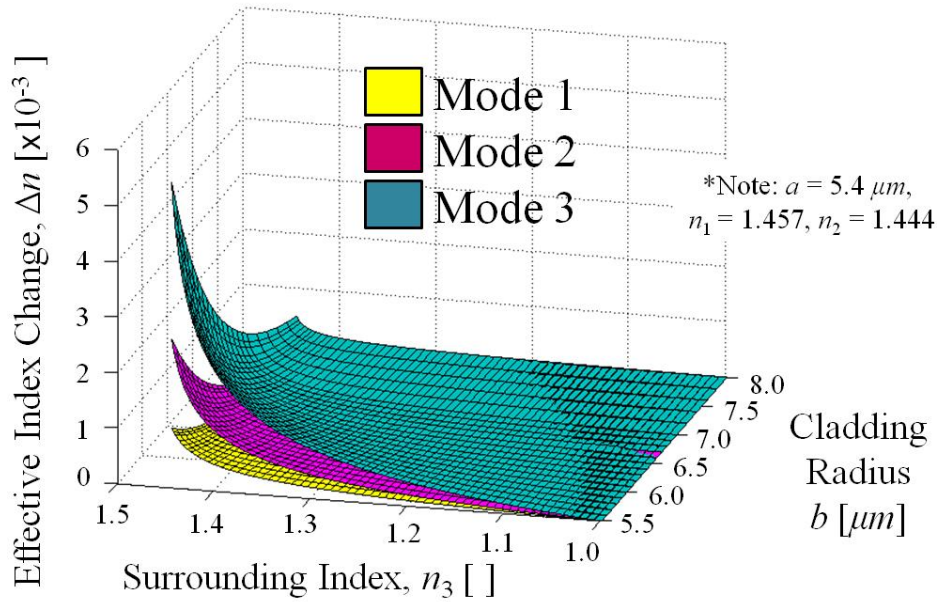
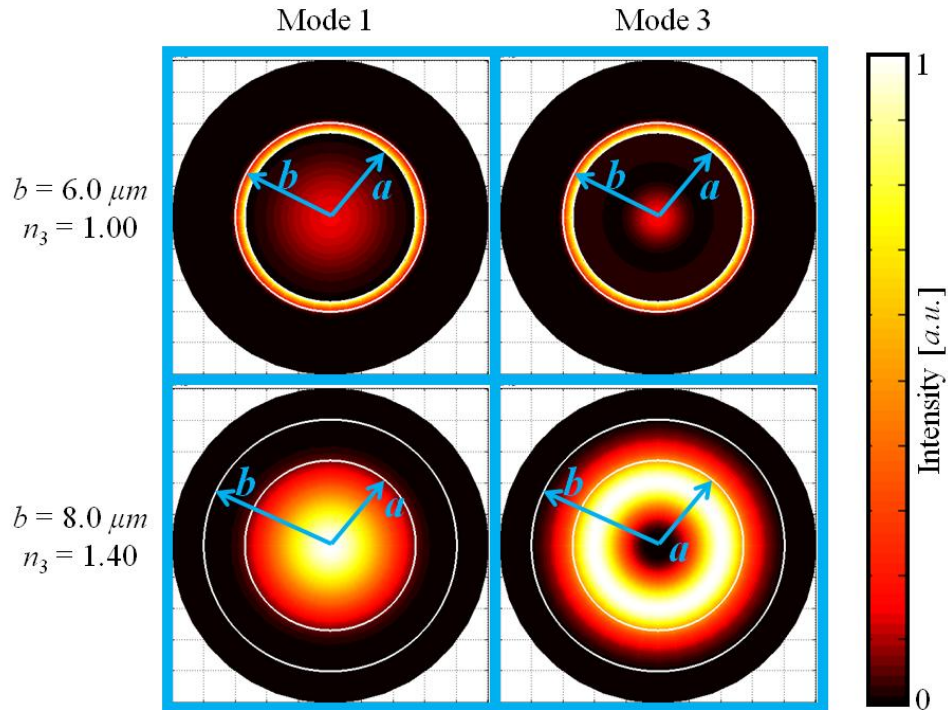


Figure 5-20: Variation of effective IOR for three different modes with change in cladding radius and surrounding material IOR in a 3-layer fiber.

The result that higher order modes are more responsive to b - n_3 manipulation is promising for future work in sensor development. Ample room is given for improvement upon the sensitivity of the currently fabricated sensor. The next step is to gain an understanding of why these modes provide increased sensitivity. This is done by plotting the intensity distribution within the various layers of the optical fiber in Figure 5-21. Four different cases are shown taking the extreme values in Modes 1 and 3. The left column indicates intensity distribution for Mode 1 and the right column for Mode 3. The upper row corresponds to the case where the cladding radius and surrounding material index are set to the lower end of the range at $6.0 \mu\text{m}$ and 1.0 respectively. The bottom row is for the upper portion of the ranges with $b = 8.0 \mu\text{m}$ and $n_3 = 1.40$. Darker regions indicate a lower intensity while brighter regions indicate higher intensity. White circles are overlaid onto the distribution with arrows and labels indicating they represent the core-cladding (a) and the cladding-surrounding material (b) interfaces. The intensity is plotted between the values of $0 \leq r \leq 10 \mu\text{m}$.



*Note for all of the above: $a = 5.4 \mu m$, $n_1 = 1.457$, $n_2 = 1.444$

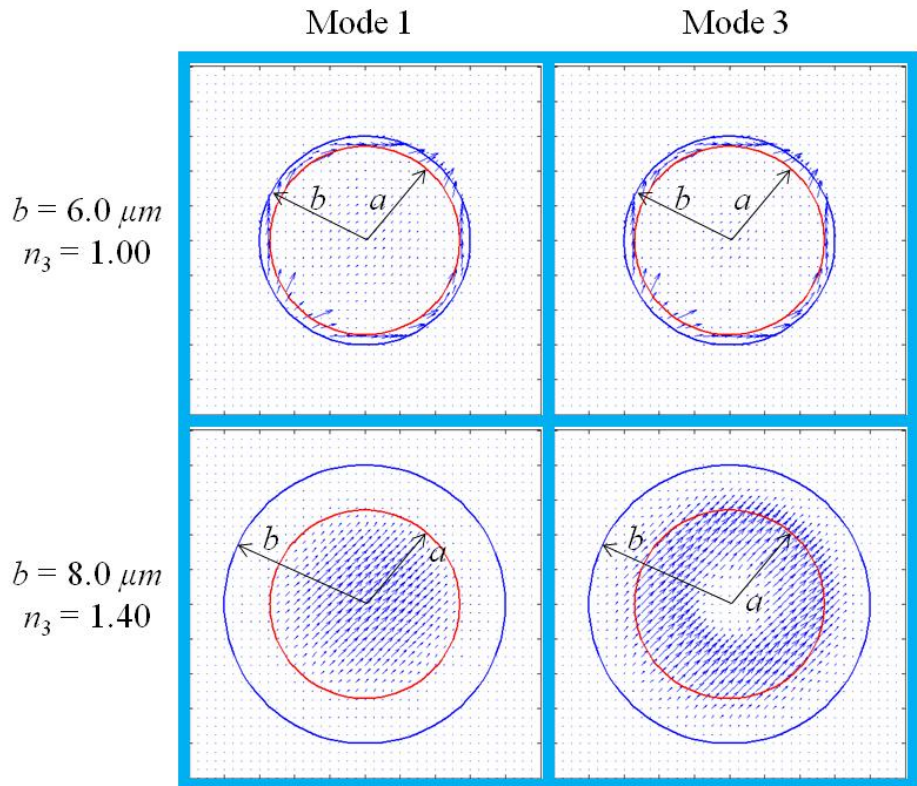
Figure 5-21: Mode shape for two different modes under two sets of cladding radius and surrounding material IOR values.

Comparing the two Mode 1 distributions, the upper case indicates that a majority of the light intensity is within the cladding with some spilling over into the low-index surrounding material. In the lower case, the majority of the intensity is within the core with very little extending into the surrounding material. Thus, the upper distribution should have (and does have according to Figure 5-20) a smaller effective index of refraction than the lower distribution due to a larger portion of the evanescent field being present in the low-index surrounding material. Similar reasoning applies when comparing the two Mode 3 distributions.

Comparing Mode 1 to Mode 3, we can see that the light intensity distribution is more tightly held to the center of the fiber in Mode 1. This is easily seen when comparing the two lower graphs. In the lower-left graph, a single-peak intensity distribution is present with the maximum (brightest region) at the center of the core. In the lower right distribution, a minimum is seen at the core center with the neighboring bright ring representing a “smearing” of the intensity

distribution over a larger area. With a more spread-out intensity distribution, the evanescent field within the surrounding material is more abundant and thus, manipulating the surround material index has a greater influence. The smearing is more difficult to see in comparing the two upper graphs. Both upper graphs have the brightest area within the small cladding region, but comparing the two core regions demonstrates the smearing effect. The upper left distribution has a single peak with the brightest region at the center of the core. In the upper right graph, the brightest region in the core is still at the center but it quickly dies out to a dark region and, unlike the upper left distribution, begins to increase slightly before the cladding region. This is indicated by the slightly lighter ring as $r \rightarrow a$ compared to the darker ring when $r \approx a/2$. Thus, the smearing effect is seen when comparing Mode 1 with Mode 3 and explains why the surrounding material plays a larger role in the modes with a more expansive intensity distribution.

An additional feature which is interesting to note is the local polarization field of the propagating wave for the four cases just considered. Figure 5-22 below plots the same four cases but rather than an intensity distribution, an arrow plot is created which indicated the local direction of the electric field in the cross section of the optical fiber. The red circle indicates the value $r = a$ and the blue circle indicates the value $r = b$. Longer arrows indicate a greater magnitude.



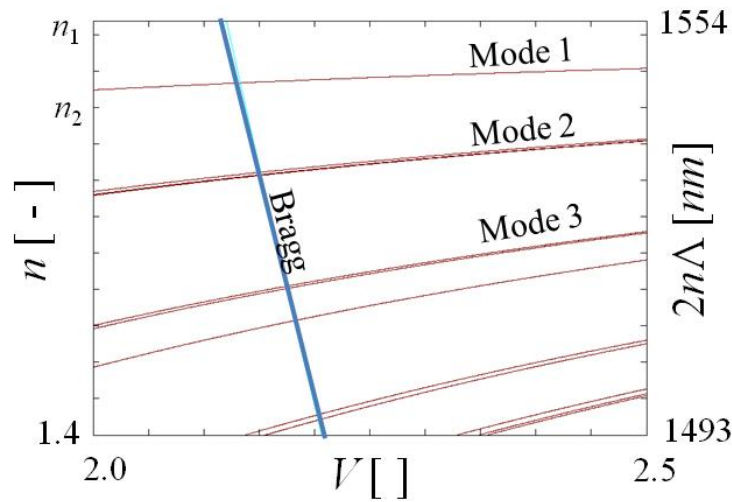
*Note for all of the above: $a = 5.4 \mu m$, $n_1 = 1.457$, $n_2 = 1.444$

Figure 5-22: Arrow plot indicating the approximately linearly polarized nature of the propagating light for the given mode and fiber parameter combinations.

Comparing the arrow plots with the intensity distribution, it makes sense that brighter regions in Figure 5-21 are the same regions with the longer arrows in Figure 5-22. The most interesting aspect of this figure is that all four cases maintain a semblance to a linearly polarized mode with the arrows mostly oriented in the upper-right direction. This means that the modes can be treated as linearly polarized modes which can be analyzed in a similar manner to the fundamental mode in the presence of birefringence.

Next, higher order modes will be accessed by expanding the wavelength range of the tuning laser down from a lower bound of approximately 1535 nm to 1495 nm . This idea is demonstrated in Figure 5-23. The n - V plot below shows several red curves, each representing a different supported mode within the optical fiber. The left axis represents effective index while the right axis is simply the effective IOR multiplied by the factor 2Λ . The purpose of this variable

transformation is to help demonstrate the method for creating the blue curve which represents the locus of points in the n - V space (or $2n\Lambda$ - λ space since $V = f(\lambda)$) which satisfy the Bragg condition. For this particular set of modes, the parameters are $a = 2.7 \mu\text{m}$, $b = 3.75 \mu\text{m}$, $n_1 = 1.457$, $n_2 = 1.444$, and $n_3 = 1.3$.



Note: $b = 3.75 \mu\text{m}$, $n_3 = 1.3$

Figure 5-23: Altering the lower bound of the wavelength sweep in order to have more modes intersect the Bragg condition curve.

When considering only a 2-layer fiber, it was determined that the effective IOR must be higher than the IOR of the cladding layer. If this were not true, total internal reflection would not occur and the light would not propagate. This means that the only fiber modes in the graph above which could exist are those in the $n > n_2$ region. The value of n_2 is very close to that of n_1 , so lower extent of the Bragg condition curve was very limited. However, in the case of a 3-layer fiber with the cladding thinned to a sufficiently small radius, ($b = 3.75 \mu\text{m}$ for the data in Figure 5-23), the surrounding material's index ($n_3 = 1.3$ above) now becomes the lower bound for a propagating wave's effective IOR. Thus, the blue line in the figure above can be extended below the original lower limit n_2 value and intersect with higher order mode curves. Thus, more reflected wavelengths are supported by the FBG.

As noted in the previous example, each mode curve will not shift equally with respect to the Bragg condition curve and thus, the intersection points will not change at the same rate. This paves the way for different modes to have different sensitivities to surrounding material IOR changes. The intersections of the Bragg curve in Figure 5-23 with the Mode 1, 2, and 3 curves are tracked as the cladding radius and surrounding index are changed. Figure 5-24 below plots the results with the vertical axis representing the change in effective index from the zero-point taken to be when $n_3 = 1.0$. The lowest surface represents the Mode 1 response with the middle and upper surfaces representing Mode 2 and 3 respectively. Mode 3 is clearly the most sensitive.

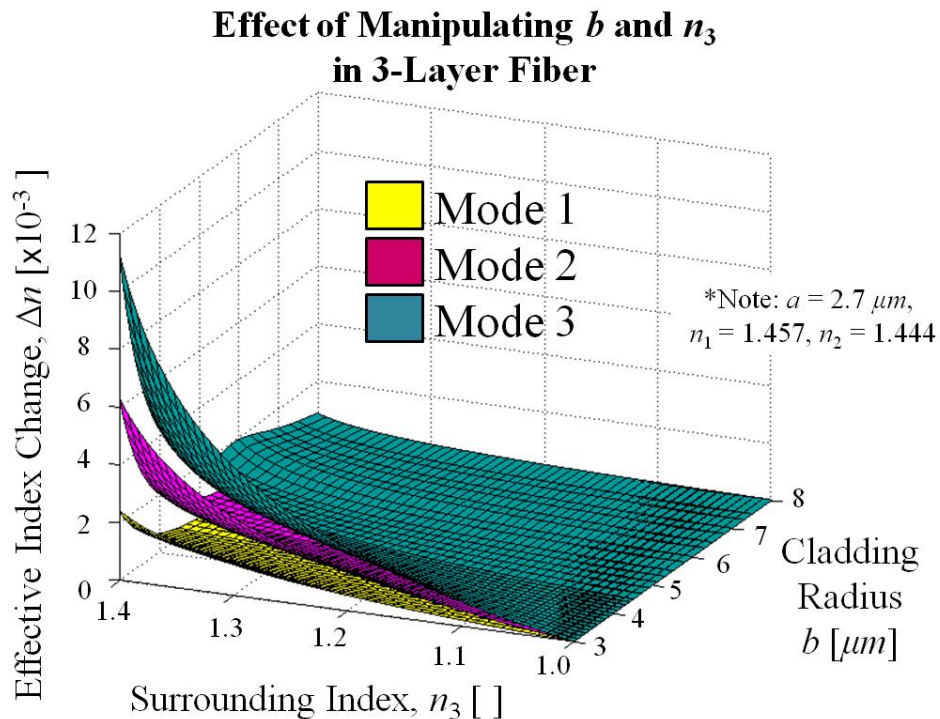


Figure 5-24: Variation of effective IOR for three different modes with change in cladding radius and surrounding material IOR in a 3-layer fiber.

The results are strikingly similar to the previous example altering the core radius. We see that the effective index and in turn, λ_B experiences larger shifts for higher order modes and with smaller cladding radius. To extend the argument in the same manner as the previous example, the intensity distributions of Mode 1 and 3 are shown in Figure 5-25 for two extreme cases to

compare low cladding radius and surrounding material index with high b and n_3 values. Brighter areas represent higher intensity and darker areas lower intensity. Two white circles (labeled with arrows and either “ a ” or “ b ”) are overlaid to represent the core-cladding and cladding-surrounding material interfaces.

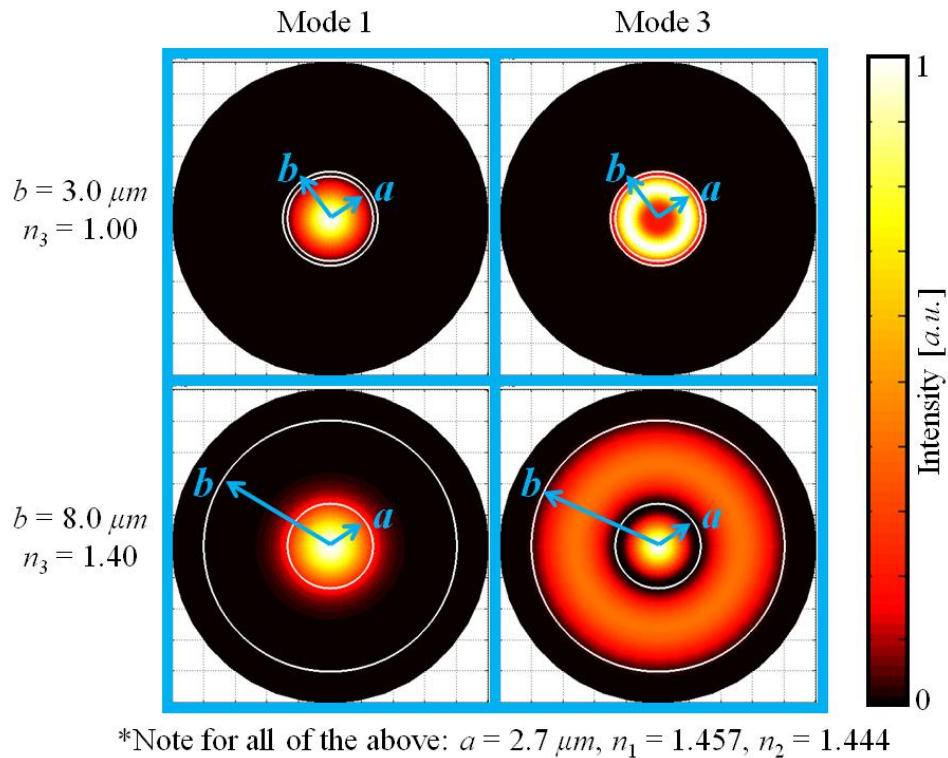
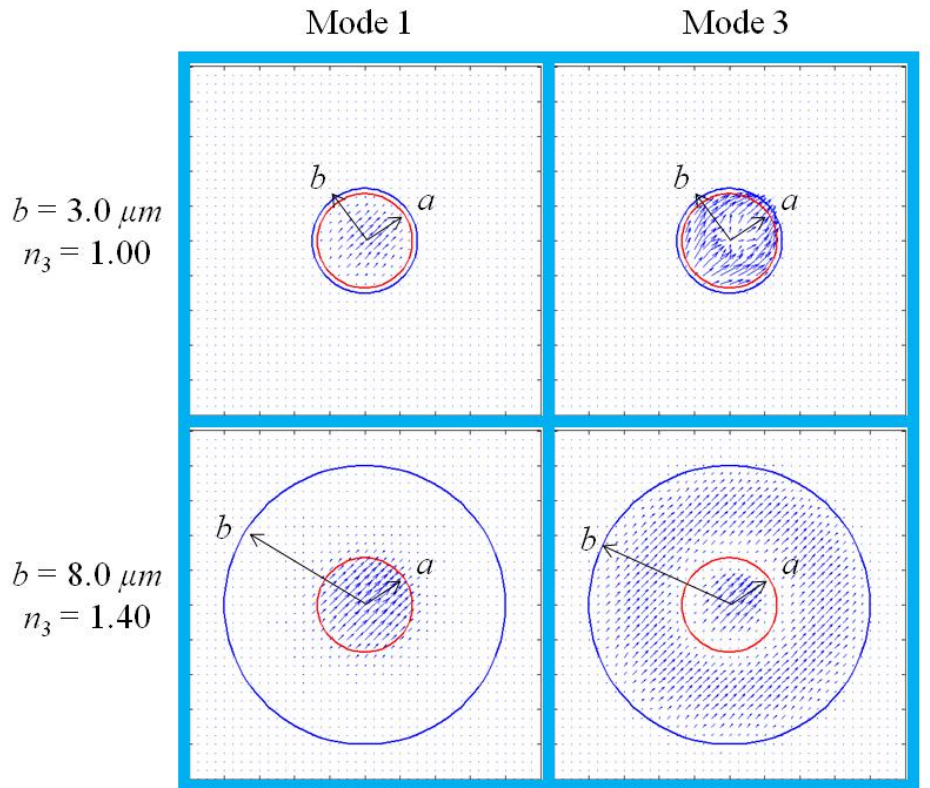


Figure 5-25: Mode shape for two different modes under two sets of cladding radius and surrounding material IOR values.

The comparisons for this example are nearly identical to those in the previous example. The lower b and n_3 values have more of their evanescent field present in the low-index surrounding material compared to the higher b and n_3 values. This is largely due to the small thickness of the cladding. Additionally, the distribution of light intensity is more densely packed toward the center of the core for the light propagating in Mode 1 compared to the more smeared distributions in Mode 3. Thus, the more expansive distribution of light makes the higher order mode more susceptible to changes in the refractive index of the surrounding material.

An arrow plot is provided analogous to that in Figure 5-22 in order to demonstrate that the modes presented in Figure 5-25 exhibit the same approximately linearly polarized behavior as the modes observed when doubling the core radius.



*Note for all of the above: $a = 2.7 \mu m$, $n_1 = 1.457$, $n_2 = 1.444$

Figure 5-26: Arrow plot indicating the approximately linearly polarized nature of the propagating light for the given mode and fiber parameter combinations.

This work demonstrates that higher order modes offer the potential for making the fiber optic sensor more sensitive to changes fiber characteristics. In the context of this research, higher order EM wave modes reflecting from a FBG will exhibit more sensitivity to changes in the surrounding material IOR and thus to magnetic field. This type of theoretical work paves the way for increasing the sensor's potential in future design iterations.

5.3.4 Experimental Sensitivity

The purpose of this next set of theoretical calculations is to determine minimum fiber design parameters which will exhibit a measurable change in λ_B . The central theme of this theoretical work has been to determine the effective index behavior of an optical fiber undergoing certain material property and geometric changes. The behavior of particular interest which is most applicable to the sensor fabricated and experimentally tested is the change in effective index when the parameters b and n_3 are manipulated. Since this relationship has been calculated, the results will be compared to noise levels in the measurement system. This will help determine how thin the fiber must be and how much the surrounding material IOR must change in order to induce a shift in λ_B above the noise level. At this point, consider that the noise level of the reflected wavelength for the interrogation system is approximately $\pm 2 \text{ pm}$ under favorable testing conditions. The following equation describes the calculation for the effective IOR noise level based on the noise in measuring λ_B :

$$\Delta n = \frac{\Delta \lambda_B}{2\Lambda} = \frac{2 \text{ pm}}{2(533.23 \text{ nm})} = 1.9 \times 10^{-6} \quad (5.37)$$

Thus, we need to etch the fiber to a cladding radius small enough to elicit a 1.9×10^{-6} change in effective IOR when a magnetic field is applied. Now that the minimum change in effective IOR has been calculated, the expected change in surrounding IOR will be determined. This is done by studying the work of Yang et al. 2002, Hong et al. 2003, and Horng et al. 2003, and figuring that an index change around 5×10^{-3} is feasible. The next step in the process is to create a 3-D surface plot similar to that of Figure 5-24 which shows the variation in effective index with b and n_3 . Figure 5-27 below is the resulting plot. Just as in Figure 5-24, the vertical axis represents change in effective IOR while the right horizontal axis represents the cladding radius. The left horizontal axis, however, represents the initial IOR of the surrounding material from which a positive shift 5×10^{-3} in magnitude is applied in order to obtain the calculated Δn . The

black plane indicates the cutoff where all points on the meshed surface above the black plane can be measured above noise level while all those below cannot.

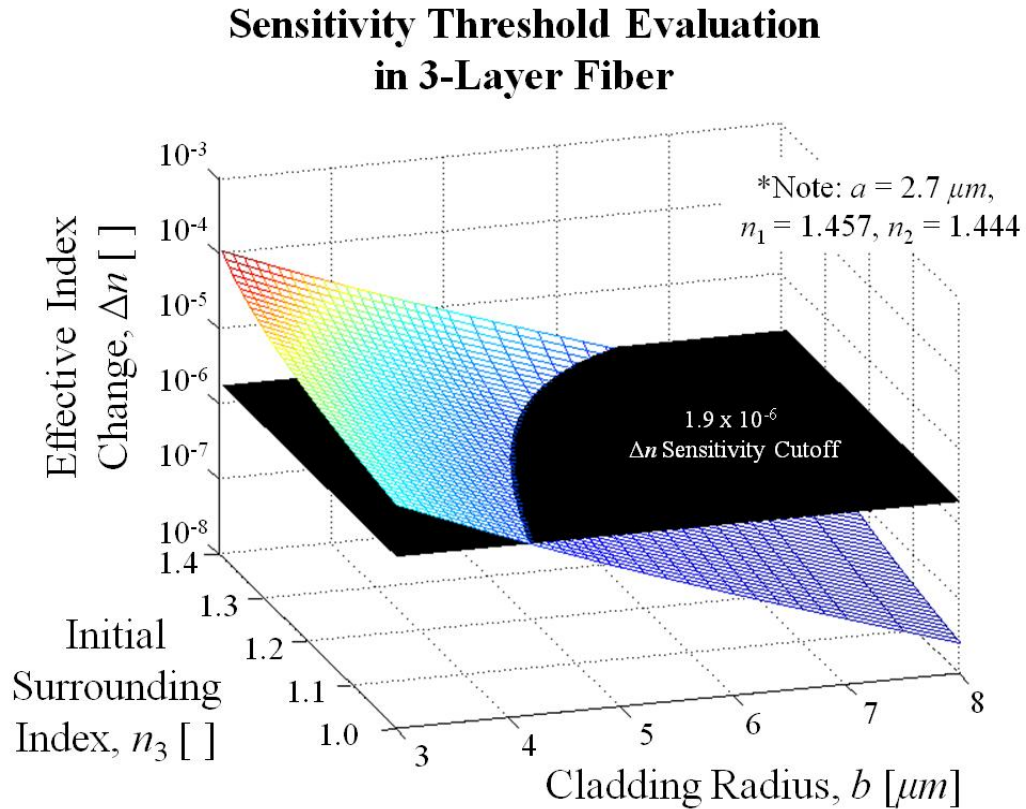


Figure 5-27: Shift in effective IOR due to a +0.005 change in surrounding material IOR as a function of initial surrounding material IOR and cladding radius. The noise level cutoff is represented with the black plane.

As an example, the $[b, n_3]$ point corresponding to $[4 \mu m, 1.2]$ defines the change in effective index of a 3-layer optical fiber of cladding radius $4 \mu m$ undergoing a magnetically induced change in surrounding material index from 1.2 to 1.205 (or $1.2 + 5 \times 10^{-3}$). This point on the meshed surface is above the sensitivity cutoff, so the change in effective index should be measurable.

In this research, small magnetic particles of high index are mixed with a carrier fluid of lower index to create a composite surrounding material. The index of the composite surrounding material depends on the concentration of magnetic particles and the index of refraction of the

carrier fluid. Thus, the initial surrounding index can be tailored depending on the strength of response required. Assuming that the least responsive initial surrounding material index of 1.0 is utilized, the cladding radius must be less than $4.2 \mu\text{m}$. This gives us a maximum cladding radius for the fabrication process.

5.3.5 Concluding Remarks

This concludes the theoretical work done in preparation for the fabrication and experimentation of a FBG magnetometer. In order to create a sensor out of a fiber optic, some parameter must be changed due to an external phenomenon. The theoretical equations developed in this section aid in understanding the rules governing an optical fiber so that when changes to various fiber parameters are implemented, the behavior can be predicted and understood. The various examples changing parameters such as core radius and cladding IOR provided opportunities to implement the theoretical equations and fully understand the accompanying changes in effective IOR.

In addition to understanding the behavior of FBGs, developing a solid theoretical foundation helps to determine how the sensor should be designed. The expected shifts effective IOR were compared with expected noise levels in order to determine design constraints such as maximum fiber thickness. The theory also helps to guide future design iterations of the FBG sensor. It was seen that changing the core radius and decreasing the minimum wavelength in the FOID's laser sweep opens up the possibility of monitoring higher order modes. These higher order modes have sensitivities which are higher than the fundamental mode; thus, demonstrating potential methods for increased sensitivity in future magnetometer designs. In the next section, the fabrication of the FBG sensor will be described along with the magnetic field experiments performed to instigate a response in the FBG sensor.

5.4 Fabrication and Experimental Setup

This section describes the work done to fabricate a sensor which responds to a magnetic field. Several design iterations were required to achieve a successful sensor. The progression of iterations is meant to develop suitable design constraints and create a reliable FBG reflection signal. The etching process will then be defined and the methods for monitoring the reflected wavelength shift in the thinned FBG will be explained. Next, a characterization procedure will be described which evaluates the success of the fabrication process. Specifically, the reflected wavelength spectrum of the thinned FBG will be assessed and the sensitivity to changes in surrounding material IOR will be quantified. Lastly, the characterization of the magnetic particles used in the surrounding material and the method for applying an external magnetic field will be illustrated.

5.4.1 Design Iterations

The overall goal in the initial design considerations was to etch an optical fiber and surround it with a magnetically active material. As more and more iterations were created, additional design constraints were added in order to increase structural integrity, fabrication consistency, and reduce noise in the FBG signal. In the descriptions of the various iterations to follow, it will be seen that the fabrication steps must incorporate (1) control of the fiber's directionality, (2) exposure to a large reservoir of hydrofluoric acid for consistent etching (where "large" will be defined later), (3) a surrounding magnetic material which does not create too much loss in the optical signal, and (4) a post-fabrication test to evaluate the sensor. The rest of this section describes, in order, the various design iterations, lessons learned, and conclusions about the data collected with the early sensor designs.

5.4.1.1 ITERATION 1: TAPERED FIBER

The first iteration involved taking two Bragg fibers each 18 *cm* long (i.e. containing 18 FBGs) and using hot sulfuric acid to remove the polyimide coating from 7 of the FBGs for subsequent HF etching. The optical fiber was held at a certain height to allow all 7 uncoated FBGs to be submerged within the 24 % by volume HF. After predetermined time intervals, the position of the optical fiber was raised in 1 *cm* increments. The 7 FBGs of the first fiber were etched for 44, 84, 94, 104, 110, 114, and 118 minutes while those of the second fiber were etched for 22, 42, 47, 52, 55, 57, and 59 minutes. The stark difference in the times for the two fibers is meant to provide enough data to determine the etch rate in addition to hedge the estimated etch rate range (somewhere between 0.5 and 1.0 $\mu\text{m}/\text{min}$) to create an etched FBG whose evanescent EM wave is exposed to the surrounding material.

The reflected wavelengths of the FBGs were not monitored during the etching process for this iteration. Instead, pre- and post-etch snapshots were taken and the shift in λ_B was calculated. The results for the two fibers are shown in Figure 5-28 below. The shift in Bragg wavelength is plotted against the FBG# with the green diamonds representing Fiber-1 data and yellow squares representing Fiber-2 data. The vertical purple dotted line displays the boundary between etched and unetched portions of the optical fibers. Note the increase in wavelength in the etching region. Also note that the Fiber-1 FBGs have a larger λ_B shift at lower FBG# values due to the longer exposure. For example, FBG#14 on Fiber-1 and Fiber-2 was exposed to HF for 94 and 47 minutes respectively. Wavelength shifts in FBG#16-18 on Fiber-1 are not displayed because the etching time was long enough for the entire FBG to be etched away. Thus, no post-etch signal was obtained. Etched FBGs on Fiber-2 display the same increase as Fiber-1 with the exception of FBG#18 which has a negative shift.

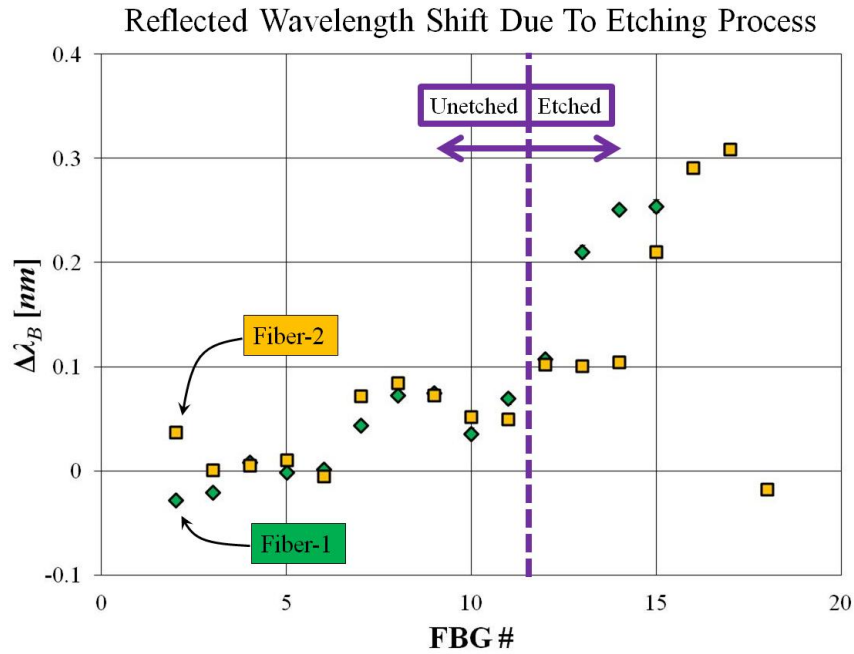


Figure 5-28: Shift in reflected wavelength for FBGs which were etched for different times along two different fibers.

The positive shift in reflected wavelength is most likely due to a release in residual compressive strains within the optical fiber that accrued during the fiber drawing process. When the optical fiber gets thin enough, the evanescent field is exposed to the surrounding material. Thus, for FBG#18 on Fiber-2, the surrounding material changes from silica to air. The result is a negative change in surrounding material index and in turn, a negative shift in Bragg wavelength. To test this conclusion that the evanescent field in FBG#18 is exposed to the surrounding material, the optical fiber is dipped in isopropyl alcohol (IPA) with an index greater than air but less than silica. The fiber is also dipped in benzene which has a refractive index greater than silica. In the IPA case, the Bragg wavelength should increase whereas in the benzene case, the wave will no longer be bound and the signal should disappear. The Bragg wavelength shift resulting from dipping Fiber-2 in these fluids is shown in Figure 5-29. Each data point represents the average of 10 measurements with the error bars representing the standard deviation of those measurements. The blue Air-IPA data is seen to not shift significantly with the exception of FBG #18 which exhibits a +0.06 nm shift that is well above noise. The positive shift matches the

aforementioned prediction. The red Air-Benzene data shows no discernable change in the etched region, but a consistent increase throughout the unetched region which can be explained simply with a shift in the fiber positioning. For FBG#18, a larger +0.52 *nm* shift is seen but an incredibly large error of 1.46 *nm* is also measured. The reason for this odd result is found by studying the inset graph which shows the length domain reflection signal for the final 3 FBGs on Fiber-2 in the three cases of the surrounding material being air, IPA, and benzene. The air and IPA reflection signals are nearly equivalent with a strong reflection seen in both cases. However, the benzene reflection is seen to exist for FBG#16 and 17, but FBG#18 disappears. This is due to the propagating EM wave no longer being bound within the optical fiber. Therefore, no reflection occurs in FBG#18 because no light from the optical source reaches the grating. Thus, the large error in the FBG#18 reflected wavelength is due to the fact that there is no reflection. The FBG#18 data essentially represents noise.

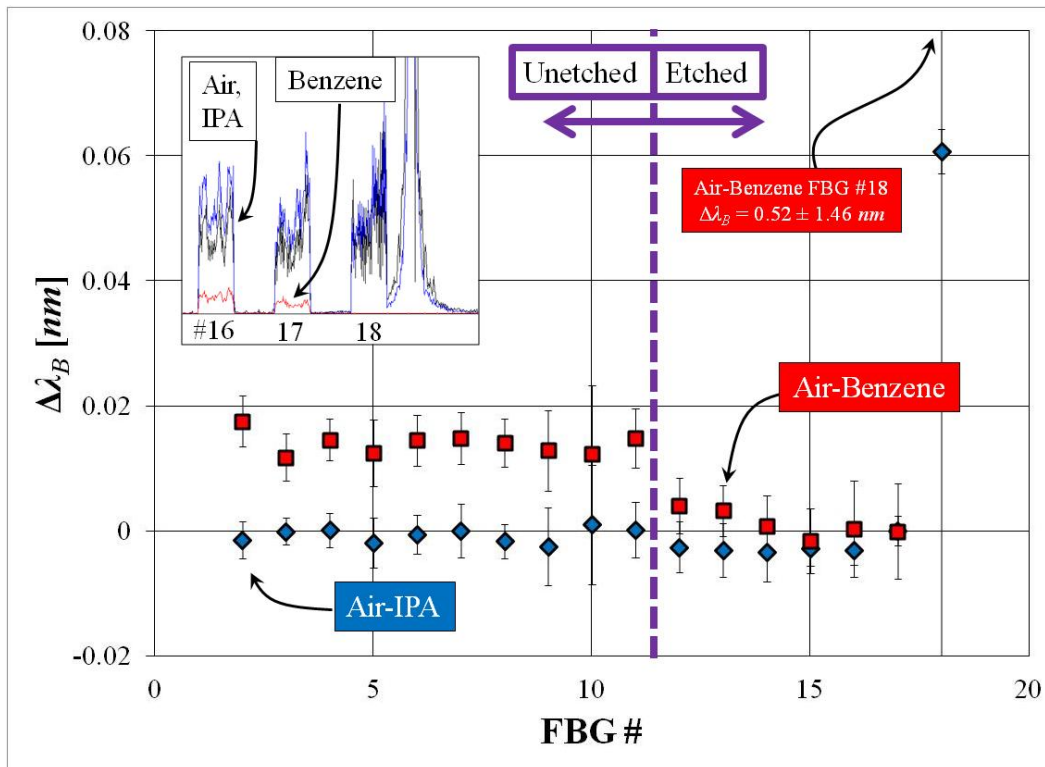


Figure 5-29: Response of the FBGs along Fiber-2 when moved from air to either IPA or benzene.

This demonstrates the successful achievement of experimentally verifying the findings in the theoretical analysis that when the optical fiber is thin enough to have a significant amount of its evanescent wave exposed to the surrounding material, the surrounding index heavily affects the reflected wavelength. In the case of IPA, the wavelength is seen to shift whereas in benzene, the reflection disappears.

Before the next iteration is created, greater control of the etching process is desired. Fiber-1 was etched too much but Fiber-2 was not etched enough to eventually elicit a magnetic response when surrounded by a magnetically active material. This means FBG#18 should be etched longer, but it is not clear how much longer. Thus, the next step is to more accurately characterize the etching process.

5.4.1.2 ETCH RATE CHARACTERIZATION

An attempt to calculate and predict the etch rate of an optical fiber in hydrofluoric acid (HF) was performed. This initial characterization would indicate how long the FBG must be placed within a bath of HF to achieve a desired cladding radius. If an accurate radius could consistently be attained from a preliminary etching characterization, then fabrication process would be fairly simple and automated. If the reliability of the etch rate becomes an issue, then the optical fiber needs to be actively monitored throughout the etching process which takes between 30 minutes and 3 hours depending on the HF concentration.

To characterize the etch rate, two arrays of 10 Bragg fibers are dipped in HF (after the initial polyimide coating is completely removed by dipping the fiber in 80 °C sulfuric acid for ~5 min). All fibers were approximately 1 cm and each set of 10 fibers is attached to a metal substrate held above a HF bath. A portion of each fiber's length is submerged within the HF bath for etching. Figure 5-30 depicts the setup for 5 fibers. Note that the fiber is not directly taped to the metal substrate. The reason is that after a predetermined amount of time has passed, the optical fiber is removed from the HF bath by rotating the fiber as indicated by the black arrow. The tape's adhesive is used to stick to the underside of the metal substrate in order to hold the optical fiber outside of the HF.

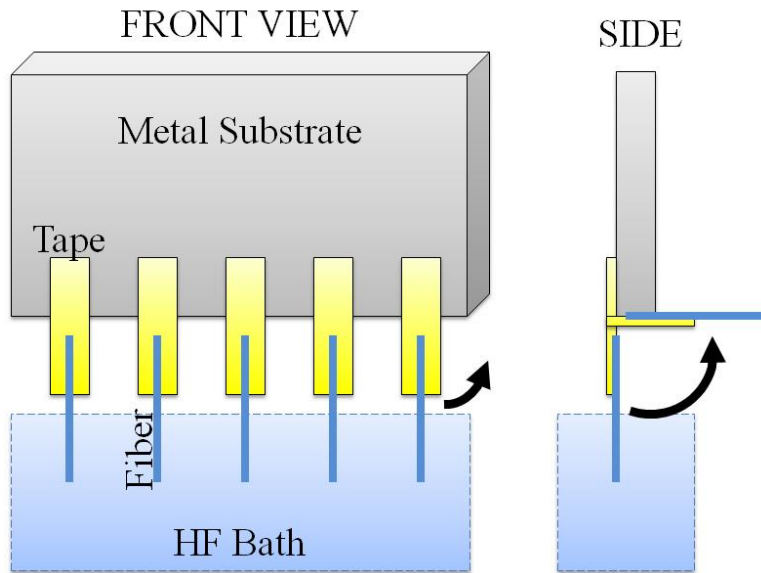


Figure 5-30: Schematic of the removal of optical fibers dipped in HF acid for etch rate characterization.

Using a scanning electron microscope (SEM), the radius of each fiber is measured. The different exposure times for each fiber should result in different radii. Thus, the etch rate can be calculated using a least squares regression calculation and used for future sensor fabrication. The results of the two sets of 10 fibers are shown in Figure 5-31. The blue diamonds represent the time and radius for each of the 10 fibers in the first set and the red squares represent the second set. Circled with a red dotted line are two outliers in the first set. The blue and red lines represent trendlines when any outliers are taken out of consideration. The trendline slopes are used to calculate the etch rate for future use. A separate HF bath was used for each set and the concentration of HF was 49 % by volume.

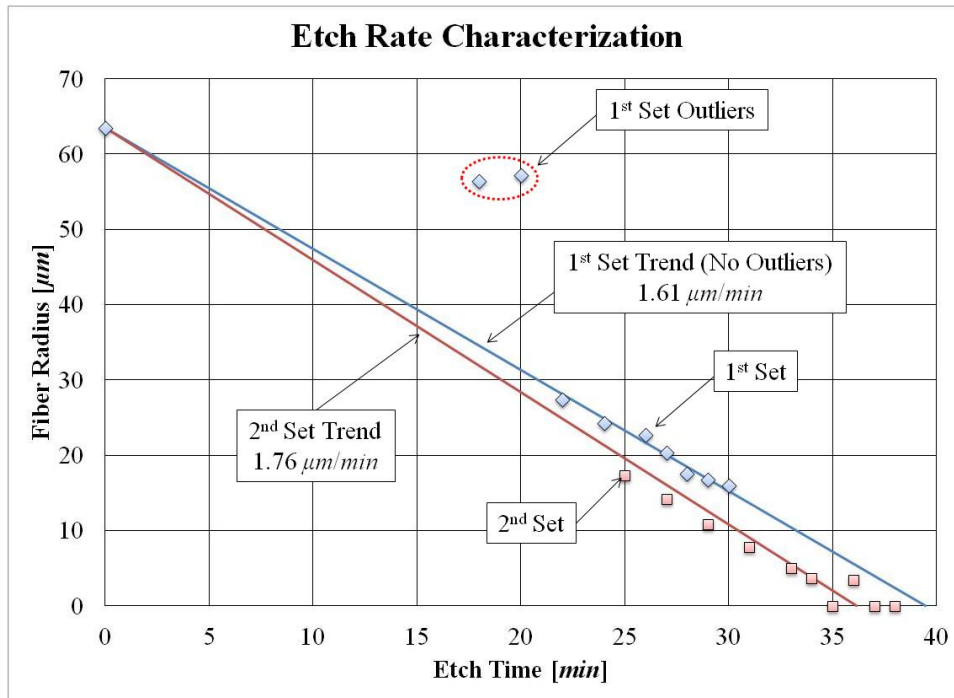


Figure 5-31: Dependence of fiber radius on etching time for two sets of 10 fibers.

From the first set of fibers, it was determined that the etch rate is $1.61 \mu\text{m}/\text{sec}$ when the two outliers were ignored. The cause of the outliers is unclear but may have been due to residual polyimide coating preventing etching or error in recorded time. The fiber submerged in HF the longest was etched 30 min which only brought the radius down to $16 \mu\text{m}$. The etch rate calculated using the first set was used to determine appropriate removal times for the second set of fibers. It was intended that all fibers in the second set would be removed before the entire fiber was etched away. However, three of the fibers were completely gone by the time they were removed from the HF bath. The trendline indicates an etching rate of $1.76 \mu\text{m}/\text{sec}$. This is faster than the first set despite the fact that the same approximate concentration of 50 % HF was used for both sets. Thus, too much error is found to occur to be able to accurately etch the fiber to a desired radius within a few micrometers; thus, the etching process must be monitored during etching. This lesson will be applied by taking measurements of the optical fiber's reflected wavelengths throughout the etching process.

5.4.1.3 ITERATION 2: MONITORED TAPERED FIBER

A tapered Bragg fiber was created in the same manner as the first iteration. An optical fiber 12 *cm* in length with the polyimide coating removed from FBG#5-12. All uncoated FBGs were dipped in 49 % HF acid by volume and the fiber was removed 1 FBG at a time to taper the fiber. In this process, the FOID's Langley method is used to continuously monitor the Bragg wavelength shifts of the FBGs during the etching process. The results are shown in Figure 5-32 below. The vertical axis represents the shift in the Bragg wavelength from its original unetched value while the horizontal axis represents time in minutes. The various colored data sets represent the reflected wavelength in time for all etched FBGs with the exception of FBG#12. FBG#5-9 were removed at 12.5, 20, 25, 29, and 31 minutes while both FBG#10 and 11 were removed at 32 minutes. The peak created in the length domain data due to reflection off the end of the fiber broadens as the fiber is etched. This broadening tends to corrupt the signal from the last one or two FBGs, making it impossible to discern the FBG reflection signal from the noise. This is the reasoning behind omitting data from FBG#12 and for the messy data for FBG#11 in the 14-22 minute timeframe. Note that small, abrupt shifts in the FBGs tend to occur all simultaneously due to handling of the optical fiber when a portion is removed from the HF bath.

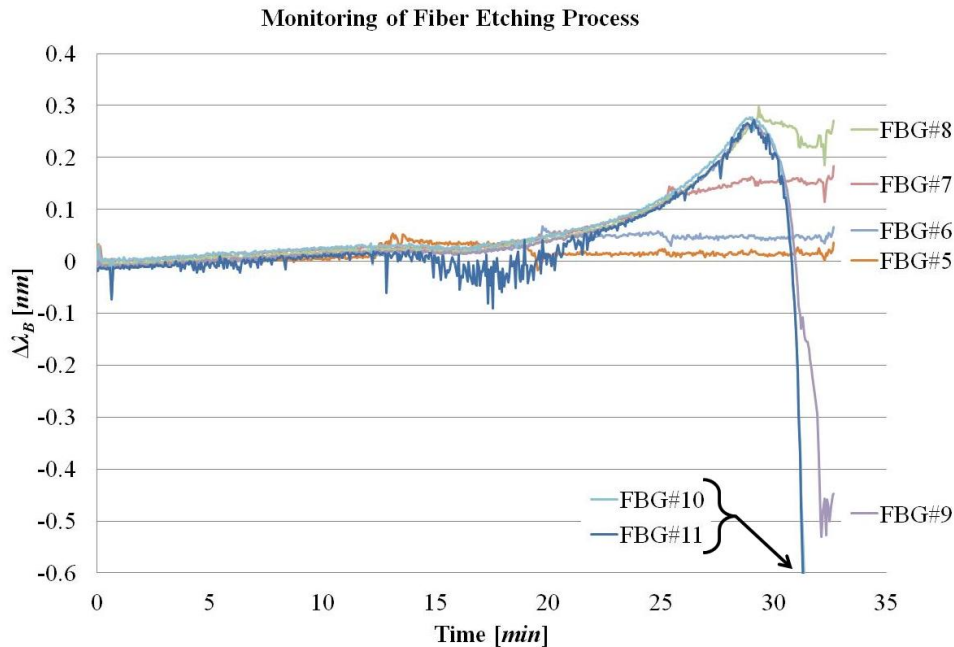


Figure 5-32: Shift in λ_B during the etching process for 11 FBGs etched for various amounts of time.

As seen in the previous tapered fiber results, the reflected wavelength increases until a critical time when the trend reverses and the reflected wavelength rapidly decreases. Iadicicco et al. 2005 reported this trend and attributed it to the optical fiber heating up during the etching process. However, as the graph above shows, once the fiber is removed from the HF bath, the reflected wavelength remains nearly constant. Thus, if the etching were to cause the fiber to heat up, then removing the fiber from HF would result in a cooling and a negative shift in the reflected wavelength. This does not occur, thus ruling out thermal influence. An alternative explanation is that the optical fiber is under residual strain due to the fiber drawing process with the center of the fiber compressed by the outer portion. Thus, as the cladding is etched, the outer portion of the fiber residually compressing the center is removed and the core is able to elongate. When the FBG is removed from the HF, the etching process stops and no more residual strain is released.

The effect that the residual compressive strain release has on the reflected wavelength shift during the first ~29 minutes of etching is quickly dominated by a second effect brought about by

the etching process. When the optical fiber becomes thin enough, the evanescent EM field is exposed to the surrounding HF which has a lower index of refraction than silica. Due to the increasing influence of the HF refractive index as the optical fiber gets thinner, the effective index rapidly decreases. FBG#8 is removed just before the evanescent field interaction becomes the dominant effect, but FBG#9 is removed a few minutes after. When FBG#8 is removed from the HF, the reflected wavelength remains fairly stable. The evanescent field outside the silica cladding is still insignificant, so whether HF or air is the surrounding material makes no difference. On the other hand, when FBG#9 is removed, a drastic drop from a -0.1 nm shift to -0.5 nm is measured. This is because the evanescent field exposed to HF becomes exposed to air upon removal and air has a lower IOR than HF.

Continuously monitoring the etching progress of the FBGs shown here is a crucial step in creating an accurately thinned optical fiber. However, the tapered form of the FBG results in weaknesses which must be overcome in the next iteration. The first weakness is the lack of maintained directionality of the optical fiber. When the optical fiber is thinned to such a small diameter, there is very little control over the position of the end of the fiber. The end of the fiber moves drastically even in the small air currents of a quiet room. Combining this with the increased difficulty in seeing the end of such a thin fiber poses great difficulties in handling the sensor. Additionally, it will be necessary to know the direction of the externally applied magnetic field relative to the etched FBG's direction. The second weakness in the tapered fiber design is the continued etching of the fiber once removed from the HF bath. In order to maintain the positional accuracy of removing 1 cm at a time, the portion removed from HF bath must be rinsed by squirting the fiber with a water bottle or not rinsing at all. This is a very unclean method for rinsing the fiber which can result in slightly uneven etching of the fiber once removed from the HF. This will cause poor results in the reflection signal due to scattering off the locations of the fiber's etching defects. Attempts to resolve these issues will be handled in the coming iterations.

5.4.1.4 ITERATIONS 3-5: DIRECTIONALITY WITH BUCKLING

In order to maintain directional control of the optical fiber, an apparatus was created to firmly hold two ends of an uncoated Bragg fiber. Figure 5-33 below shows the setup. The mechanical splice joining the Bragg fiber with the FOID's lead-in fiber is on the far left of the image. A different mechanical splice was cut in two small pieces for the Bragg fiber to attach to at Fixed Point 1 and 2 which were $\sim 3.5\text{ cm}$ apart. Two white strips of plastic material were used to rigidly connect the two fixed points. 5-minute epoxy was used to glue everything together. Plastic materials were used rather than metal or glass in order for the entire apparatus to survive when immersed within the HF bath. When removed, the entire apparatus is submerged in deionized (DI) water in order to rinse the HF off of the fiber.

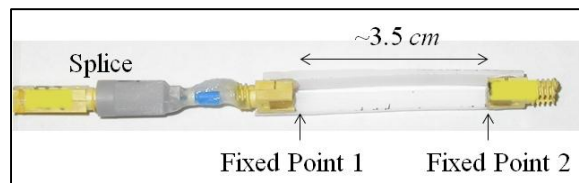


Figure 5-33: Apparatus for maintaining the directionality of an etched fiber.

Once thinned, the optical fiber was seen to buckle into a large curve from one fixed point to the other. The curve was so drastic that the fiber came in contact with the white plastic strips. This contact between the fiber and plastic will increase the noise in the signal as well as undermine the desire to maintain a straight and constant directionality in the fiber. Thus, the design was altered by creating a shorter segment of fiber to etch. This is shown in Figure 5-34 below. Five fixed points are used in this design rather than two and a smaller distance is provided between points (0.8 cm as opposed to 3.5 cm).

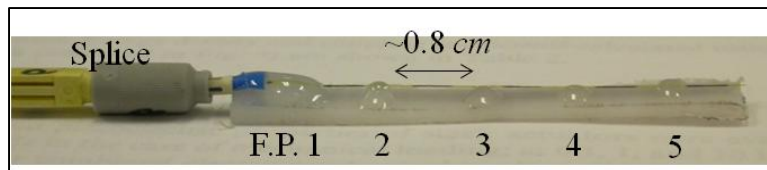


Figure 5-34: Fiber with directionality maintained at closer fixed points.

It was hoped that the smaller distance between fixed points would not allow for the large buckling seen in the previous design. However, buckling was still seen to be a factor even with the smaller distance between fixed points. In order to counteract the buckling, the fixed point was changed from being rigidly glued to the white plastic strip to being taped. This is shown in a microscope image in Figure 5-35. The plastic strip is the white background while the tape is the yellow area on the right side with the fiber emerging from the tape.

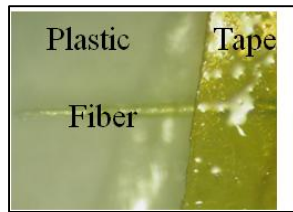


Figure 5-35: Tape used to loosely fix the fiber in place to avoid the problem of buckling.

It was hoped that the tape would secure the fiber's position enough to keep the fiber relatively straight but would allow for the etched fiber to be pulled taut after etching in order to remove any buckling. However, the tape provided a messy etching and rinsing process and was quickly discarded. In order to satisfy the directionality design constraint for the sensor and cope with the buckling problem, a new design iteration was created.

5.4.1.5 ITERATION 6: DIRECTIONAL DROP ETCHING

The new iteration is shown in Figure 5-36. The splice is still glued to a white plastic strip for rigidity. Rather than gluing or taping the optical fiber directly to the plastic strip at fixed point 1 and 2, the optical fiber is guided through two small glass tubes. These tubes are taken from the inside of a mechanical splice and the glass tube itself is glued to the plastic strip, allowing for a ~1.2 *cm* fiber span to etch. The optical fiber must be uncoated in order to fit within the tubes. The glass tubes would disintegrate if immersed within HF so the entire apparatus cannot be placed in a HF bath. Instead, a drop of HF is placed on a plastic surface and the fiber is lowered

within the droplet. After the etching process is complete, the apparatus is dipped in DI water to rinse the HF off the fiber and abruptly terminate the etching progress.

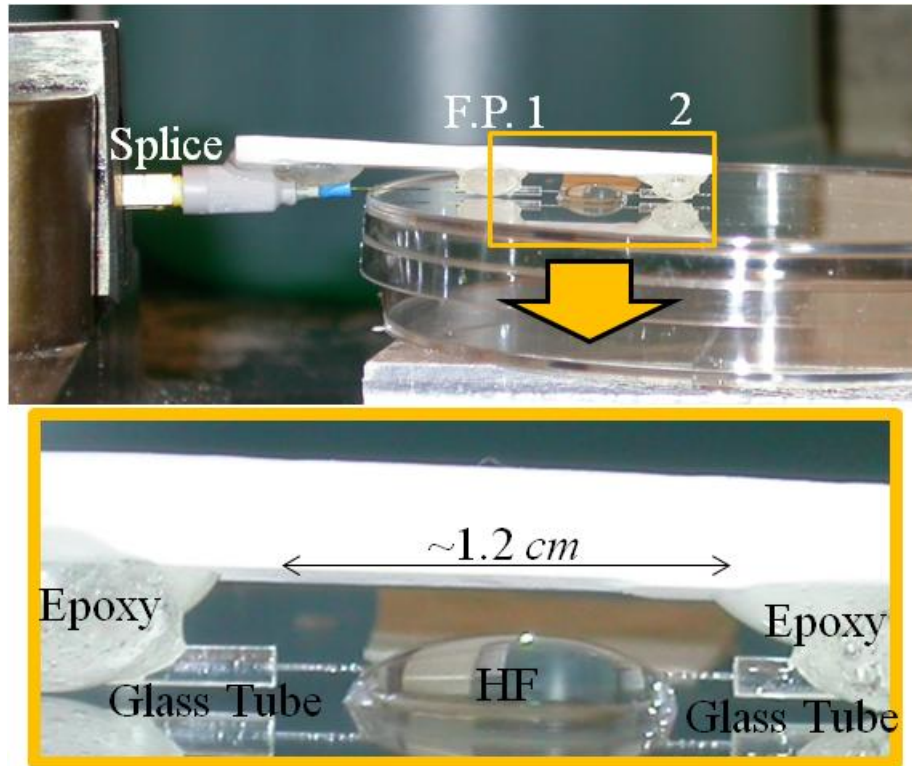


Figure 5-36: Iteration for maintaining the directionality of the thinned optical fiber while allowing for the buckling problem to be resolved.

This design is capable of maintaining the directionality of a FBG and when the optical fiber is seen to buckle, the fiber can simply be pulled through the glass tube (since it is not rigidly attached in any way) to remove any curvature. The size and placement of the droplet is important in order to have a consistent fiber diameter along the entire length of the 5 mm long FBG. The microscope image in Figure 5-37 shows that the fiber takes about 1 mm to taper from the original 127 μm diameter down to $\sim 15 \mu\text{m}$. This means that the diameter of the droplet must be larger than 7 mm in order to accommodate two tapers 1 mm in length each and the 5 mm long FBG.

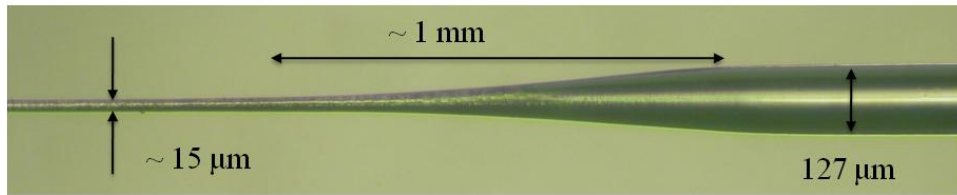


Figure 5-37: Microscope image demonstrating the length required to taper down to the final fiber diameter.

Several thinned FBGs were fabricated using this setup. An optical microscope image provides a decent approximation of the fiber radius, but is not very exact. A SEM image would provide a much more accurate measurement, but takes more time and money. Therefore, an alternative cheap, efficient metric is used to evaluate the degree of etching across various fabrication attempts. This metric is the shift in Bragg wavelength when the etched FBG is immersed in IPA from air. This provides a consistent test used to evaluate the degree of sensitivity the FBG has to the surrounding material's index of refraction.

This metric is demonstrated in 4 successive etchings of a single FBG using the design iteration just described. The results are plotted in Figure 5-38 with the vertical axis representing the Bragg wavelength shift when immersed from air into IPA and the horizontal axis representing the number of etching processes the FBG has undergone. Each symbol represents the average of 10 Bragg wavelength measurements while the error bars represent the standard deviation of those measurements. As the number of etches increases, the exposure of the evanescent EM field to the surrounding material also increases. This causes an increased sensitivity to the surrounding material's refractive index and thus, a larger shift in Bragg wavelength when immersed in IPA. The four etches lasted for 119 minutes, 45 seconds, 30 seconds, and 15 seconds respectively. The insets in the graph represent the reflected wavelength spectrum after each etching process. It is easily seen that as more etching takes place, the reflection signal becomes noisier as it splits from a single peak into multiple peaks. This accounts for the large increase in error in the measurements.

Shift in Bragg Wavelength When Immersed in IPA

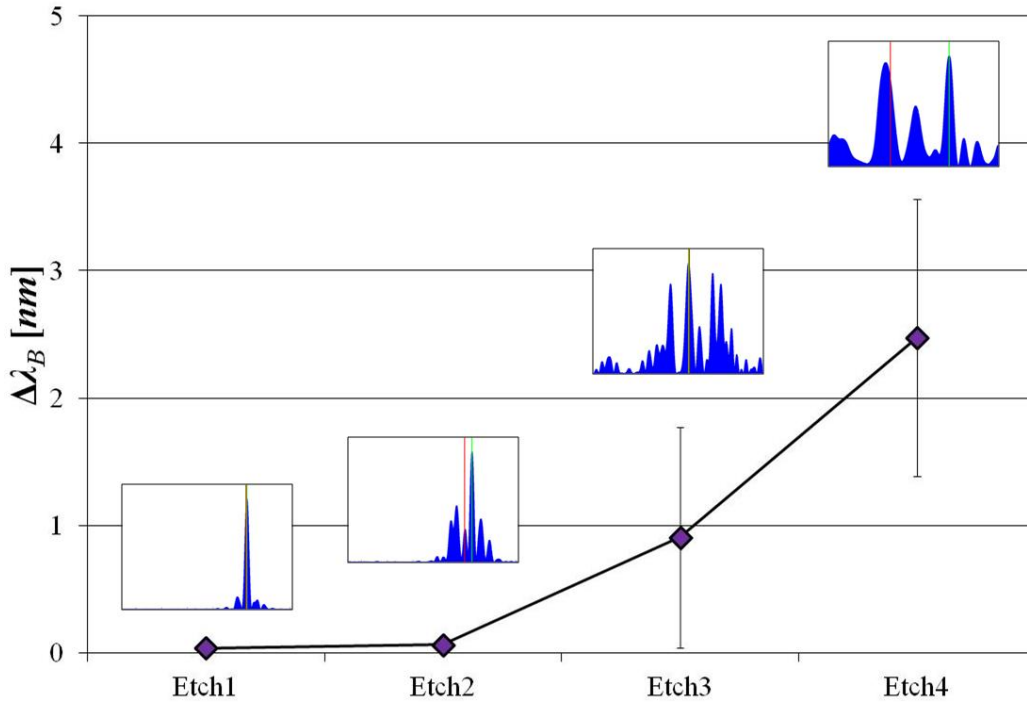


Figure 5-38: Change in λ_B when the FBG is immersed in IPA from air and evolution of reflected wavelength spectrum as the number of etches increases.

This clearly demonstrates the balance that must be struck between etching the fiber long enough to achieve the greatest sensitivity to the surrounding material index while not etching the fiber so much that the signal degrades and the noise becomes too large to discern any sensor response. One source of the noise could be a messy etching process. This could stem from the fact that only a small drop of HF acid is used to etch the fiber. HF molecules which have reacted with the silica may not be able to move away from the etch location so that fresh HF molecules are unable to move in and continue etching the fiber uniformly. Additionally, the fume hood which protects from inhalation of any HF molecules causes the acid to evaporate during etching. This is not significant for a bath of HF, but it is for a single drop. Thus, the HF must be replenished during the etching process. The last source of noise may come from the repeated etching processes. If the desired radius can be achieved in a single etching process rather than re-etching, the diameter may be more uniform and free of defects.

Taking these factors into account, the etching process is more closely monitored with any evaporated HF quickly replenished and the final radius achieved in two etches rather than four. By doing this, the signal to noise ratio is increased for a FBG etched to achieve a 1 *nm* shift in reflected wavelength when immersed in IPA from air. Due to the success in getting a relatively steady air-IPA shift, the next step of carrying out a magnetic field test was taken. The test will be described in more detail later with the final and successful iteration but an abbreviated description will be given here. A thinned FBG is taken from air and immersed in IPA. From there it is then immersed in a bath of ferrofluid. Next, five magnetic fields of increasing strength (1, 2, 3, 4, and 5 *kOe*) are applied to the submerged sensor. Lastly, the magnetic field is shut off. The results are plotted in Figure 5-39. The horizontal axis represents the nine different states while the vertical axis represents the shift in Bragg wavelength from when the fiber is initially surrounded by air. Several measurements are taken at each of the nine states (1 air, 1 IPA, 1 ferrofluid no magnetic field, 5 ferrofluid with magnetic field, 1 ferrofluid no magnetic field) and the standard deviation is used to create the error bars. The green diamonds represent the data for an etched FBG while the blue squares represent data for an unetched FBG on the same fiber and therefore in the same state as the etched FBG.

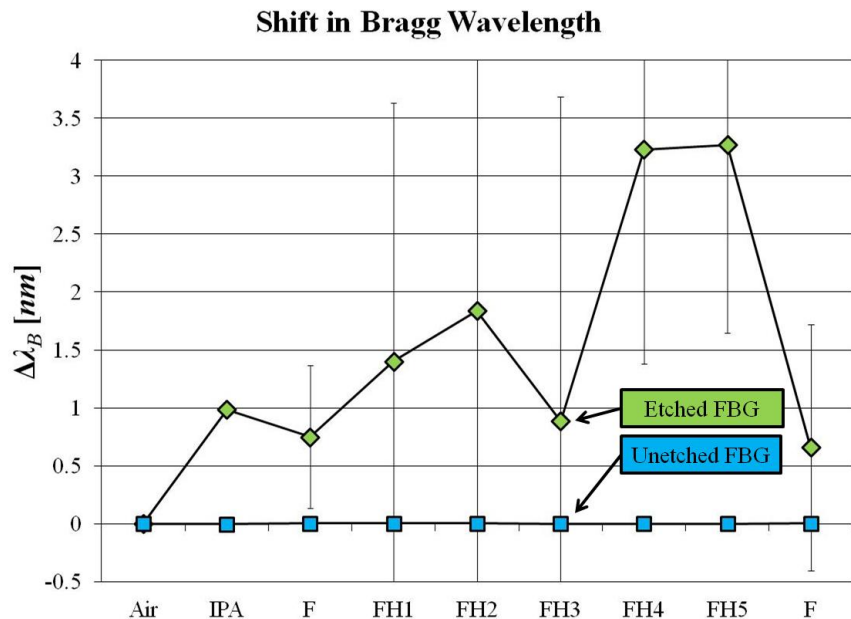


Figure 5-39: Response of an etched FBG when immersed in IPA and then ferrofluid with a magnetic field applied.

Note the +1 nm shift when immersed in IPA. When immersed in ferrofluid (F) the wavelength is not as long as in IPA, but the error is significantly higher. When the successive magnetic fields are applied (FH1-FH5), the wavelength averages increase with the exception of FH3, but the error is so large, the shifts cannot be concluded to be accurate. When the magnetic field is shut off, the wavelength nearly recovers (F) with still a significant amount of error. The unetched FBG is seen to have no shift regardless of the state as expected. Unfortunately, this test does not provide conclusive evidence of a Bragg wavelength shift due to a magnetic field. However, the application of a magnetic field is seen to increase the error in the Bragg wavelength measurements. This is demonstrated in the Figure 5-40 with the horizontal axis remaining the same as the previous figure and the vertical axis now representing the error in the measurements on a logarithmic scale.

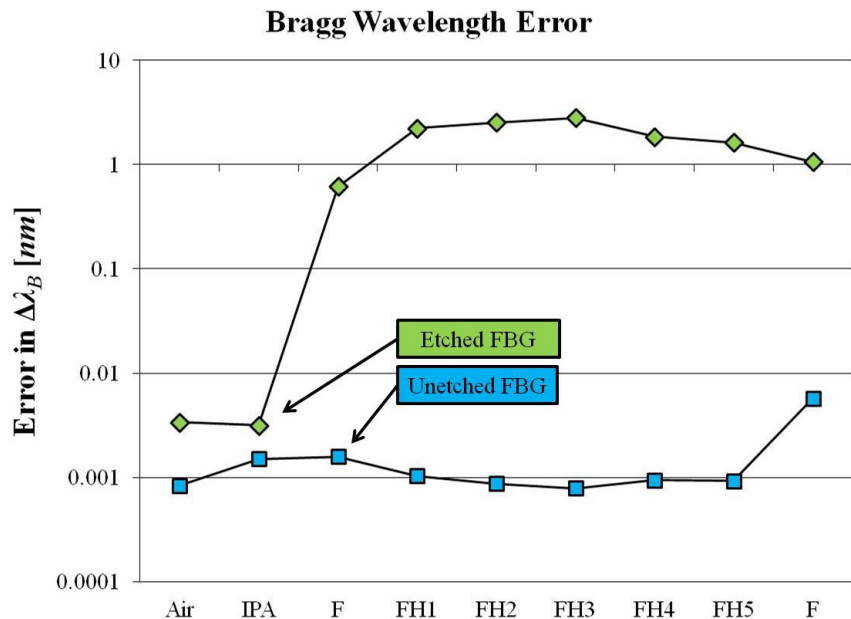


Figure 5-40: Progression of error in the λ_B measurement for the various states.

It is easily seen that dipping the fiber in ferrofluid greatly increases the error by a couple orders of magnitude. Applying a magnetic field is seen to increase the error even further with a slight decrease in error when the magnetic field is shut off. The unetched FBG maintains its small error throughout the test. A major reason for the failure of this test can be seen when the sensor is removed from the ferrofluid as shown in the digital camera and SEM images in Figure 5-41 below. The top-left picture (a) shows the apparatus covered in black ferrofluid. The bottom-left picture (b) bordered in blue shows a SEM image of the fiber emerging from the glass tube. The scale shown in the bottom-right corner of the SEM image represents a length of $200\ \mu\text{m}$. The particle coverage is so comprehensive that the glass tube and fiber look like one entity. The top-right picture (c) bordered in red shows a SEM image of the fiber near the middle of its span with a $20\ \mu\text{m}$ scale. The bottom-right image (d) bordered in green shows a zoomed in version of SEM image (c). The scale of image (d) is $4\ \mu\text{m}$ which indicates that the diameter of the thinned portion of the fiber is about $5.8\ \mu\text{m}$.

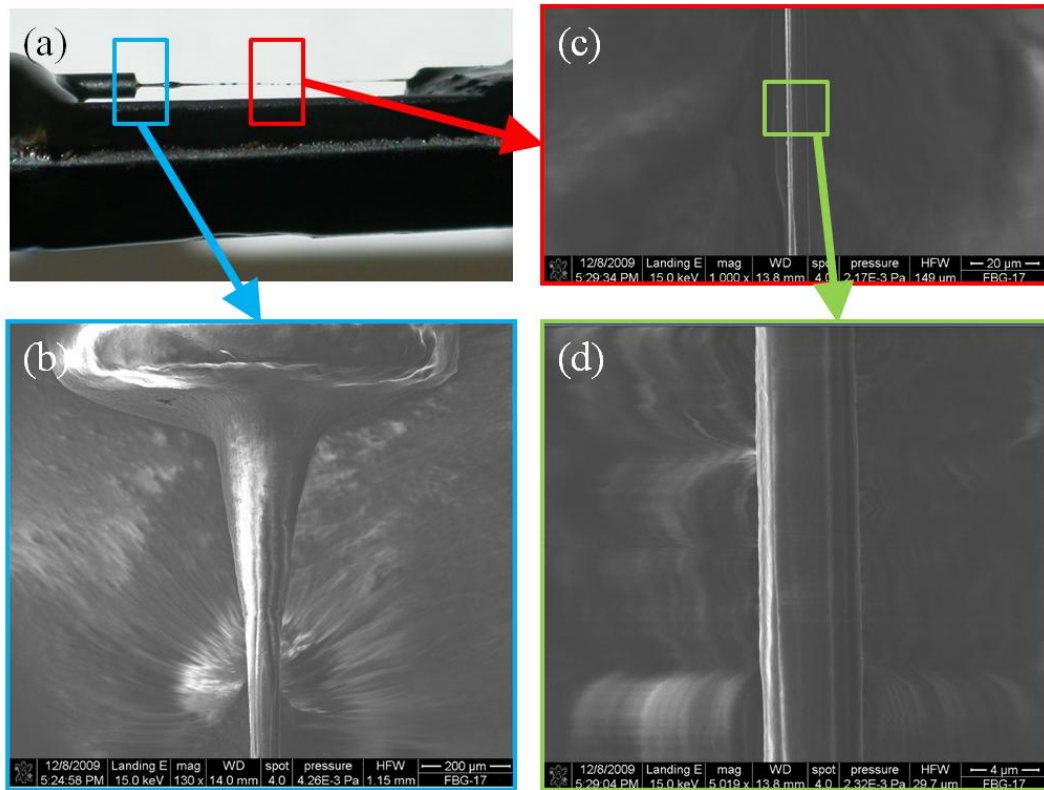


Figure 5-41: Images depicting the ferrofluid sticking to the fiber apparatus and the uneven surface of the thinned fiber.

As indicated at the end of the theoretical section, the obtained diameter is much smaller than is necessary to achieve a magnetic field response. However, the large error due to uneven etching with only a drop of HF rather than a bath and the sticking of ferromagnetic particles to the surface of the fiber results in a nonresponsive sensor. Attempts to immediately rinse the thinned FBGs in DI water or IPA help remove a portion of the ferrofluid, but many particles still remain. The SEM images in Figure 5-42 below show the rinsing results of a different fiber from the one in Figure 5-41. Image (a) shows a zoomed-out picture whose scale in the bottom-right corner is $20\ \mu\text{m}$. Image (b) shows a zoomed-in image whose scale is $4\ \mu\text{m}$. It is evident that the coverage of ferrofluid is no longer as comprehensive and conformal. However, significant amounts of ferric oxide particles remain attached to the fiber.

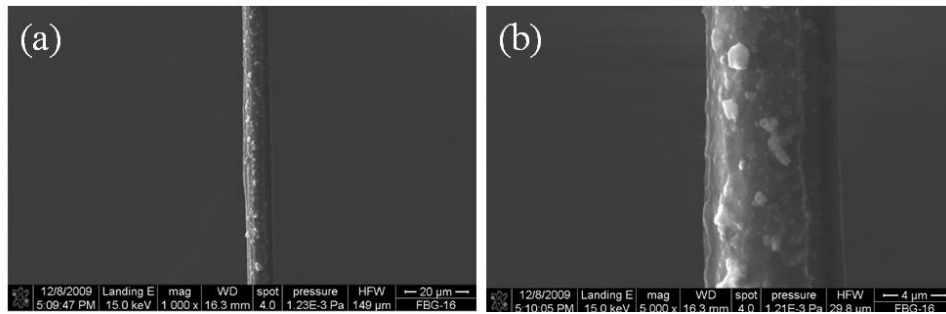


Figure 5-42: SEM images of a fiber dipped in ferrofluid and subsequently rinsed in IPA in an attempt to remove the ferric oxide particles.

A minor adjustment that may help resolve these issues corresponds to limiting the amount of thinned fiber exposed to the ferrofluid. This is accomplished by creating a more rapid taper in the fiber diameter. This will minimize the length of thinned fiber before the FBG whose evanescent field is exposed to the noise-magnifying ferrofluid. This is accomplished by placing within the HF drop a small portion of fiber which still has its polyimide coating. This allows for a rapid taper due to undercutting of the etchant beneath the coating as shown in Figure 5-43. The drawing represents the different components of the design with the optical fiber spanning between two glass tubes. The red circled etching region includes an uncoated FBG along with a portion of polyimide coated fiber. The SEM images just below the drawing show the end of the glass tube along with the two tapered regions. Both tapered region SEM images are taken at the same magnification in order to compare feature sizes. Note the SEM is taken after the polyimide coating is completely removed from the tapered region in a post-HF etch coating removal process. The two optical microscope images below the SEM images show before and after the coating has been removed from the etched fiber. In the upper microscope image, the polyimide/silica boundary is far to the right with obvious signs of undercutting. After more of the coating is removed, the polyimide/silica boundary is shifted to the left.

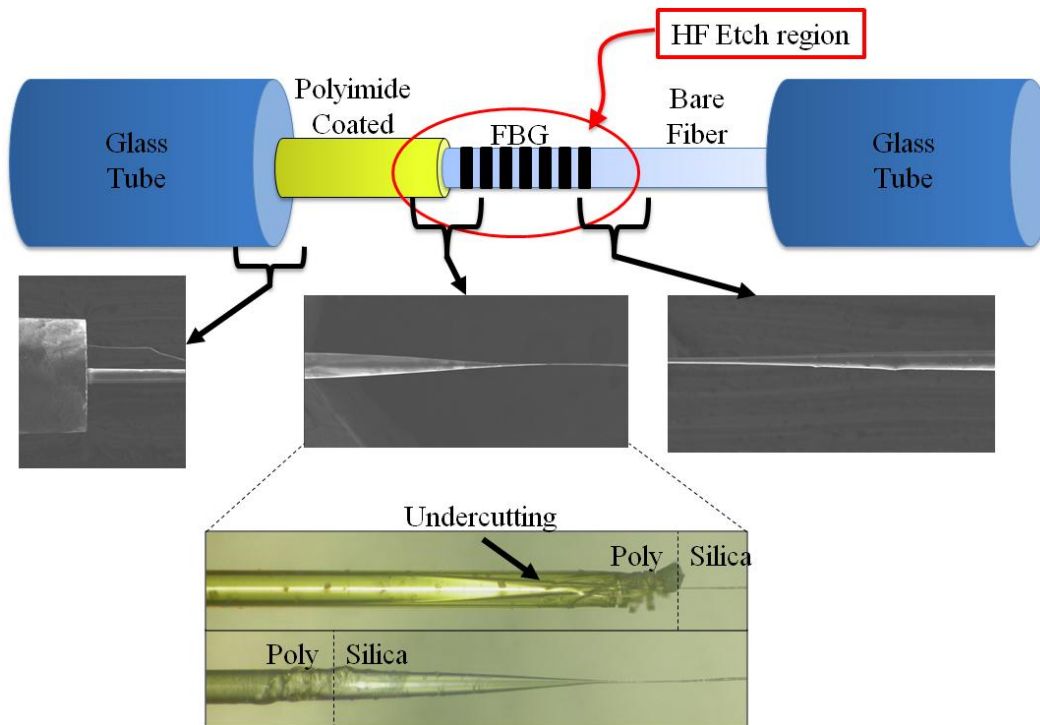


Figure 5-43: Increased taper rate by immersing part of the optical fiber which is still coated within the HF droplet.

In comparing the two tapered regions, it is obvious to see that the polyimide coated region resulted in a taper lasting over a shorter distance than the bare fiber. This minimizes the region of thinned fiber whose evanescent EM field is exposed to the ferrofluid before reflection takes place at the FBG. Despite this adjustment, however, the noise from submerging the etched FBG in ferrofluid remained too large. In addition to the issue with ferric oxide particles sticking to the fiber, the other reason for a large amount of noise can be seen with the SEM images in Figure 5-44 below showing etched optical fibers. Note all three images are taken before immersion in ferrofluid. Image (a) shows a thinned optical fiber whose scale shown in the bottom-right of the image is $10\ \mu\text{m}$. The etching process was not conformal and resulted in a non-circular cross section. Image (b) is a $100\ \mu\text{m}$ scale picture of a different location along the thinned fiber shown in (a). Certain locations appear to have been shielded during the etching process, resulting in an uneven surface that resembles craters. Image (c) is a $10\ \mu\text{m}$ scale picture of a separate fiber etched with the same process and shows long ridges long the fiber length. The lack of

smoothness and the unevenness of the etching process results in a nonuniform surface that in turn leads to a poor reflection signal.

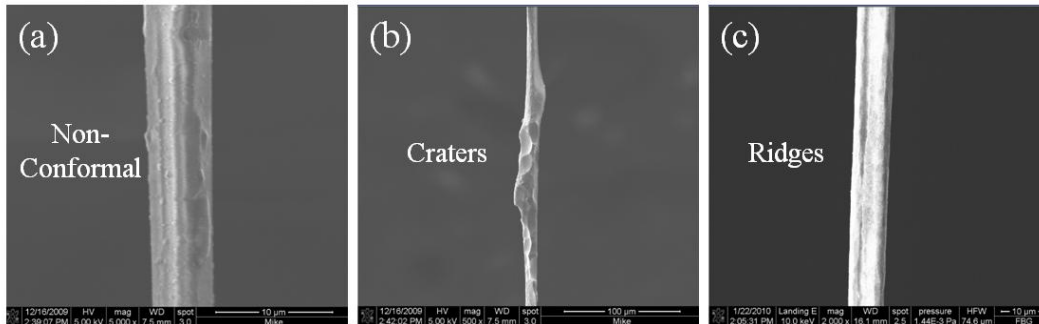


Figure 5-44: Poor etching results due to the small volume of HF used for thinning the fiber.

In order to achieve a smooth, conformal etching process, it is determined that a HF bath must be used rather than a drop. This will allow for better replacement of reacted HF with fresh HF at the etching site. Additionally, the problem of needing to replenish the HF droplet due to evaporation is eliminated. The next iteration describes how the sensor is changed to create a apparatus which can survive the HF bath.

5.4.1.6 ITERATION 7: DIRECTIONAL BATH ETCHING

Recall that the main reason for switching from a HF bath in the initial iterations to a droplet was that glass tubes were used to control the directionality of the thinned FBG. Glass tubes would not survive the etching process if they were dipped in a HF bath. These tubes provide enough rigidity to maintain the fiber orientation while allowing for the fiber to be manually pulled through the second tube in order to keep the fiber taut and counteract the buckling phenomenon previously observed during etching. In order to dip the apparatus in a HF bath, the glass tube is replaced with a Teflon tube. Changing the material will allow for the tube holding the fiber to survive the etching process; however, the Teflon tubes available have a much larger inside diameter than the glass tubes (which are specifically designed to snugly fit a bare optical fiber). Thus, the ability to achieve a more even etch with a HF bath is counteracted with a less

rigidly held fiber. It will be seen that this is a worthwhile trade-off and that the drop-off in rigidity simply means the handler of the fiber during the etching process must be even more cautious.

In addition to switching the second glass tube to Teflon, the fiber is no longer rinsed in a bath of DI water immediately after removal from the HF. Instead, a bath of IPA is used. It was qualitatively observed that the reflection signal from a thinned FBG improved when immersed in IPA from air. Therefore, it was determined to be a simple and worthwhile endeavor to try rinsing with IPA and the results were quite good. It is unclear why IPA works better than DI water, but the sensor signal remains well maintained with the new rinsing fluid.

The final change in the design is to abandon the use of ferrofluid and instead use dry ferric oxide nanoparticles. The massive amount of loss seen when dipping etched FBGs in ferrofluid led to the conclusion that using ferrofluid as a surrounding material would not provide a magnetic coupling which could overcome the increased noise levels. One possible reason for this is the degradation of or the optical interaction with the surfactant which is used to keep the particles from agglomerating in the carrier fluid. Rather than dipping the thinned FBG apparatus in a bath of ferrofluid, the apparatus is lowered into a small glass container and commercially purchased nanoparticles are used to fill the container and bury the sensor.

With these changes, the final design takes the form shown in Figure 5-45. A picture is shown of the setup along with a drawing to indicate the various components. The total length of Bragg fiber is 4 *cm* with the four FBGs along the length of the fiber indicated with labels and dotted black lines. The splice connecting the Bragg and lead-in fiber is on the far left. The red regions indicate locations where glue is used. The optical fiber is glued at the egress point from the splice and enters a glass tube which is in turn glued to the white plastic structure. The tight fit of the fiber within the glass tube firmly holds the position of the fiber as it traverses to the Teflon tube. Note the FBG to be etched is FBG#3 and is entirely contained in the portion of fiber spanning from the glass to Teflon tube. Also note that after FBG#3 has ended, the uncoated fiber region

ends and the last ~ 1.3 cm remains coated. This shields the end of the fiber from the HF bath so the portion of fiber containing FBG#3 is the only length that is etched.

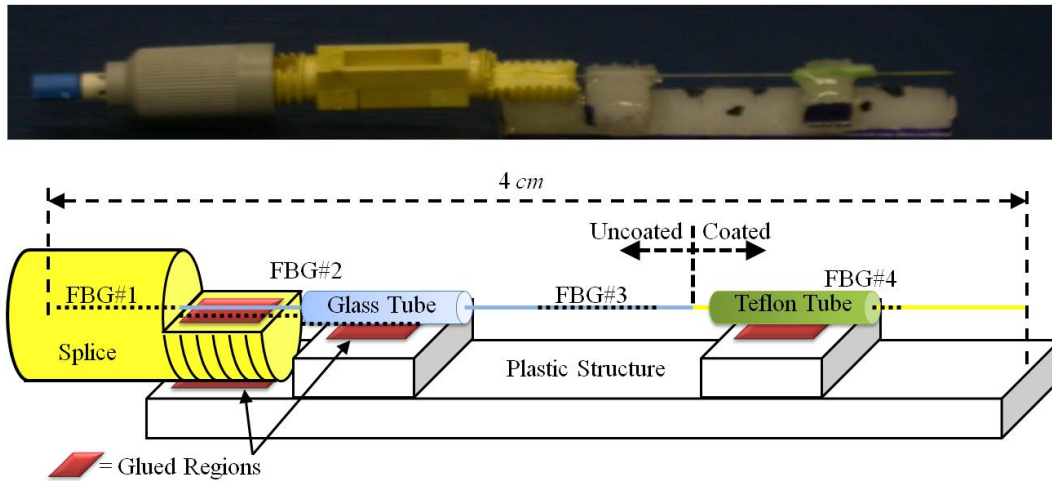


Figure 5-45: Final design of the fiber holding apparatus.

This concludes the progression of iterations which leads to the final, successful design that demonstrates a magneto-optic coupling signal greater than the noise caused by the fabrication and testing process. In the next section, the employment of this final design iteration in experimental testing will be described in detail.

5.4.2 Experimental Setup

Now that a final design has been decided upon, the experimental setup will be described. First, the steps for fabricating the fiber apparatus will be explained as well as the HF acid etching process. Subsequently, methods for evaluating the success of the etch procedure and for applying magnetic fields to demonstrate magneto-optic coupling in the thinned FBG will be illustrated.

5.4.2.1 APPARATUS

The 7th iteration provided the final design used in this research. The step-by-step process to creating the structure is described here. The Bragg fiber used in this research is commercially obtained from Luna Innovations. It has a $5.4 \mu\text{m}$ core diameter, $127 \mu\text{m}$ cladding diameter, and 7

μm polyimide thickness. The gratings are 5 mm in length and the centers of the gratings are spaced 1 cm apart. The FBGs are designed to reflect light at 1546 nm. The regions of fiber between gratings will be referred to as “basic” fiber. A 4 cm specimen is cut from the Bragg fiber spool such that exactly 4 Bragg gratings and 4 regions of basic fiber are contained within the specimen. With this cut, the first 5 mm of the fiber is all grating and the last 5 mm of fiber is all basic. Using this orientation, the Bragg gratings will be labeled FBG#1 through FBG#4.

Next, the first 2.7 cm of the specimen (which entirely contains FBG#1-3) is dipped in hot sulfuric acid (~80 °C) for several minutes. When dipped in sulfuric acid, the polyimide coating will be visible and turn from yellow to orange and eventually brown. When the coating is completely removed, the optical fiber will be essentially invisible because the refractive index of H₂SO₄ is nearly equal to silica.

In order to minimize the number of Bragg gratings used in each specimen, the mechanical splice bringing together the lead-in fiber from the FOID system to the Bragg fiber is altered. The change is shown in Figure 5-46 below. One of the gray screw-on fasteners on the splice purchased from Fiber Instrument Sales Inc. is removed and discarded. Next, a portion of the remaining splice is cut away. The fiber which is inside the mechanical splice cannot be used for any meaningful purpose other than connecting to the lead-in fiber. Thus, performing this step minimizes the amount of fiber which must be placed within the mechanical splice.

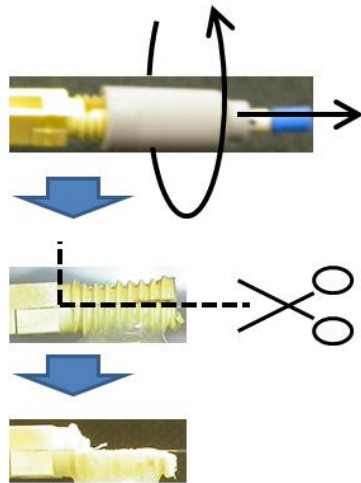


Figure 5-46: Alteration of the mechanical splice.

After removing the polyimide coating from most of the fiber specimen, a glass tube is removed from a second, unaltered mechanical splice. The bare end of the fiber specimen is slid through that tube. Next, the bare end of the fiber is inserted into the glass tube encased within the altered mechanical splice. At this point, the plastic structure is created as shown in Figure 5-47 below. The base of the structure is a strip of plastic $3.5 \times 0.5 \times 0.2 \text{ cm}^3$ in dimensions. From there, two mounts are attached in the form of smaller pieces of plastic $0.5 \times 0.5 \times 0.2 \text{ cm}^3$ in size. These two pieces are glued 0.6 cm and 0.75 cm from the edges and are meant for mounting the glass and Teflon tubes.

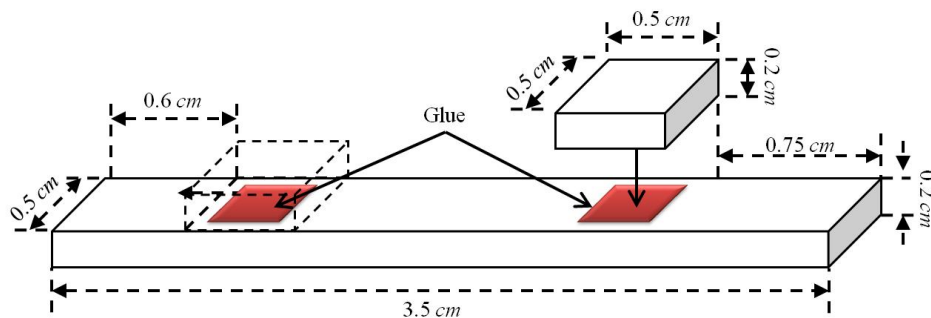


Figure 5-47: Schematic of the plastic structure of the apparatus.

Next, the splice and fiber will be attached to the plastic structure. The splice is glued so that approximately 0.5 cm of overlap occurs between the splice and plastic base. When using the

epoxy, sure the splice should be held at a vertical height such that the fiber remains level. The glass tube should lay flat on the plastic mount which was glued to the plastic base. Figure 5-48 below demonstrates three cases where (1) too much glue is used and thus, the splice is too high, (2) too little glue is used so the splice is too low, and (3) just enough glue is used and the splice is at the correct height.

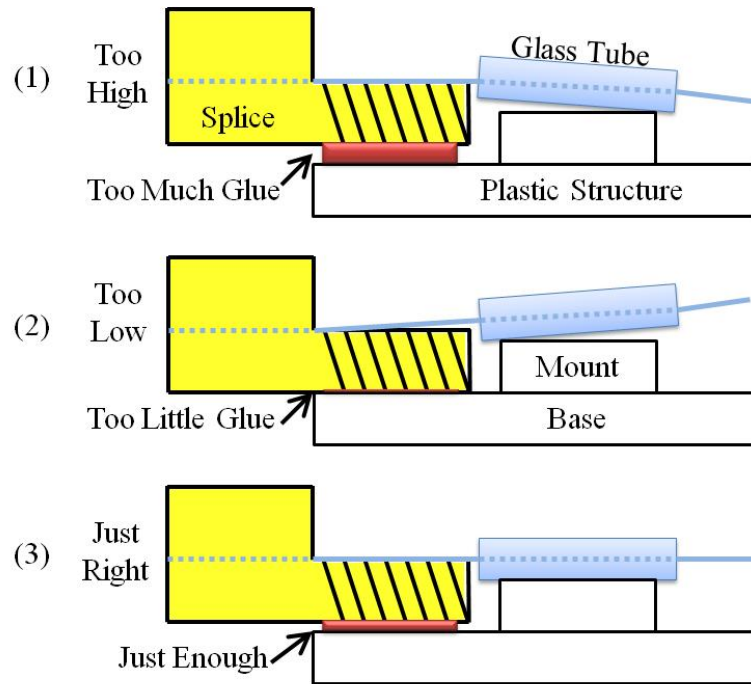


Figure 5-48: Schematic demonstrating that the amount of glue used should give the fiber enough height so that the glass tube will lay flat on the plastic mount.

Figure 5-49 below demonstrates the next step in positioning the fiber. At this point, the fiber is not rigidly attached to anything. Thus, it can easily translate by sliding out of or farther into the mechanical splice. The location of the fiber is determined by lining up the end of the fiber with the end of the plastic structure. Once this alignment is achieved, the fiber is glued to the splice at the location specified in the figure.

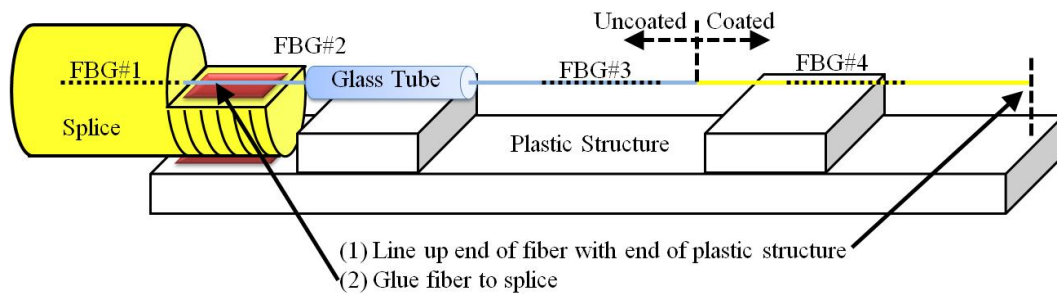


Figure 5-49: Translational positioning of the fiber relative to the apparatus.

The final steps of the apparatus fabrication are now completed. First, the glass tube is glued to the plastic structure. Next, the Teflon tube is slid onto the end of the optical fiber and glued to the plastic mount as shown in Figure 5-50.

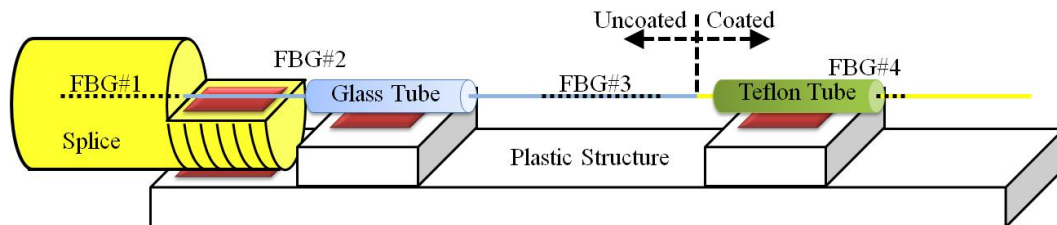


Figure 5-50: Final steps of gluing the glass tube and Teflon tube in place.

This completes the detailed steps used to create the apparatus used to give the fiber directionality. Three separate fiber apparatuses were created in the aforementioned manner for subsequent magnetic field testing. Next, the etching process will be described.

5.4.2.2 HYDROFLUORIC ACID ETCHING PROCESS

A portion of the apparatus is dipped within the HF bath for etching. The entire apparatus shown in Figure 5-51 is rotated clockwise 90° and lowered into a plastic container filled with HF. The concentration of the acid is 24 % by volume. This concentration allows for a slower etch compared to the 49 % by volume concentration and thus, should provide a smoother surface. Using an external holder to position the apparatus at the proper height, the plane indicated by the dotted lines (drawn with a 3-D perspective) represents the surface of the HF bath; therefore, everything to the right is beneath the surface and immersed in the HF bath while

everything to the left is above the surface. A dotted line is drawn on the plastic structure and a cross is drawn on the fiber to help indicate where the air-HF interface plane intersects the apparatus and fiber respectively.

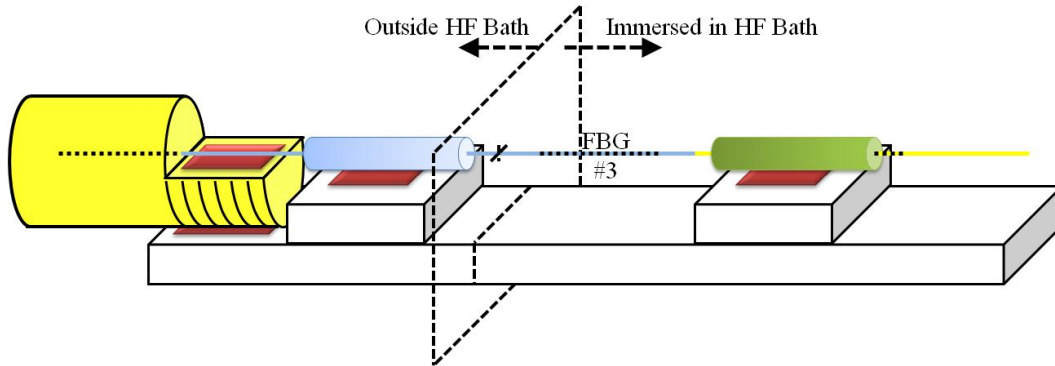


Figure 5-51: Drawing depicting how far the fiber apparatus should be dipped in a bath of HF.

During the etching process, the optical fiber is actively monitored by the FOID system. The original intent of the system was to measure uniaxial strain in an optical fiber. The output of the system, therefore, comes in units of microstrain. However, the strain reading can easily be converted to Bragg wavelength shifts by a multiplication factor as follows:

$$\Delta\lambda_B = \varepsilon(1 - p_e)(\lambda_B)_0 \quad (5.38)$$

The term p_e is the strain-optic coefficient which equals 0.1667 for the Bragg fiber used in this research and $(\lambda_B)_0$ is the original Bragg wavelength defined at the beginning of the etching process. For example, if the original Bragg wavelength is 1546 nm, then a +200 $\mu\varepsilon$ output corresponds to a Bragg wavelength shift of +0.258 nm.

The amount of etching time depends on the desired diameter of the optical fiber. The previously demonstrated inconsistency in etch rate means that the time at which the apparatus should be removed from the HF bath is determined by whether or not the real-time strain readings output by the FOID system (and hence, the Bragg wavelength shifts) have achieved a desired value.

Note that as it stands, nothing is protecting the end of the fiber after FBG#4 from getting etched. The acid will therefore undercut beneath the polyimide coating as it shortens the fiber. The length that the fiber shortens is negligible during the etching process, but the uneven etching causes an expansion of the end reflection spike seen in the length domain. Figure 5-52 below shows plots before and during the etching process to demonstrate the increase in noise due to this end etching effect. The vertical axes represent reflected intensity and the horizontal axes represent length. Each of the four FBGs is labeled along with the start and end of the fiber. Note the large increase in noise during etching in graph (b) due to a broadening of the end reflection signal. Though this may not affect the peak reflection wavelength as much, the real-time monitoring of the centroid of the reflected wavelength distribution will exhibit an increase in noise.

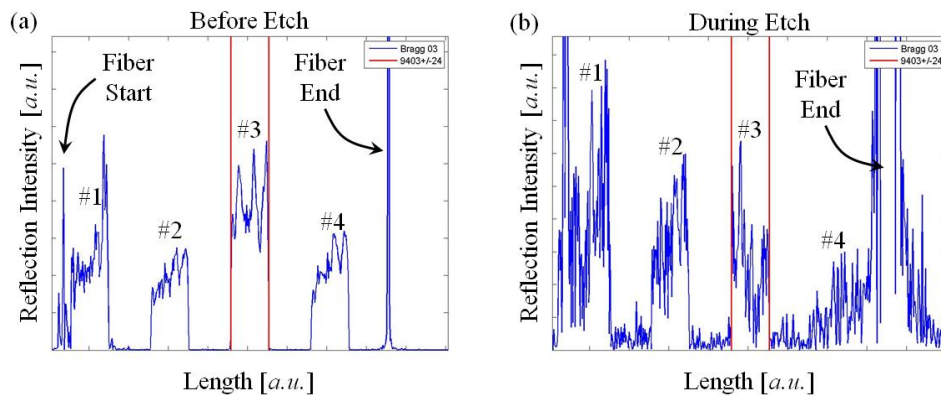


Figure 5-52: Broadening of the end reflection peak during the etching process.

Three fiber apparatuses were used to obtain the results which will be presented in the next section. Two of the FBGs were etched so that the evanescent field will interact with the surrounding material. These etching processes lasted for 140 and 143 minutes in order for the strain reading to be approximately $-1200 \mu\epsilon$ at the time of removal from the HF bath. This corresponded to shifts in reflected wavelengths of roughly -1.55 nm . The third FBG was etched to a diameter just before the evanescent field has a measurable interaction with the surrounding material. The motivation for this is to create a control FBG for comparison purposes. This

control FBG will be in the same realm of diameter as the two previously etched FBGs but the etching will terminate before the influence of any evanescent field interaction becomes significant. This point in the etching process occurs at the maximum strain reading (or highest wavelength shift). This represents the turning point when the release of residual compressive strains becomes outweighed by the evanescent field interaction. This point is reached with a 130 minute etch and resulted in a $+190 \mu\epsilon$ reading which corresponded to a $+0.245 \text{ nm}$ wavelength shift.

Once the etching process has finished, the fiber apparatus is removed from the HF bath and placed in a bath of IPA. After approximately one minute, the measured reflected wavelength signal will have stabilized and any residual HF will have been removed from the fiber and apparatus. At this point, the apparatus is removed from the IPA bath and placed on a table to allow any residual IPA on the apparatus to evaporate.

Once on the table after the IPA rinse, it is typical to observe the buckling phenomenon described previously in the section describing the fiber design iterations. This nonlinear orientation of the optical fiber is exacerbated by the fiber being loosely held in place by the Teflon tube. A typical post-etch fiber position is shown in Figure 5-53 below. Note the large deflection of the fiber which is not exaggerated in the drawing. In order to counteract this, the fiber is pulled at its end as indicated with the arrow in the drawing. The user must be careful not to pull too hard because the fiber is very fragile now that it has been thinned. To quantify this, the tensile strength of fused silica is about 50 MPa . If the fiber is etched down to a diameter of $7.5 \mu\text{m}$, then the total force required to break the fiber is about 1.3 mN or $3 \times 10^{-4} \text{ lbs}$. The result of a careful pull is the bottom drawing with a straight, taut optical fiber. In order to maintain the straight, taut position, the fiber is glued at the Teflon tube egress point.

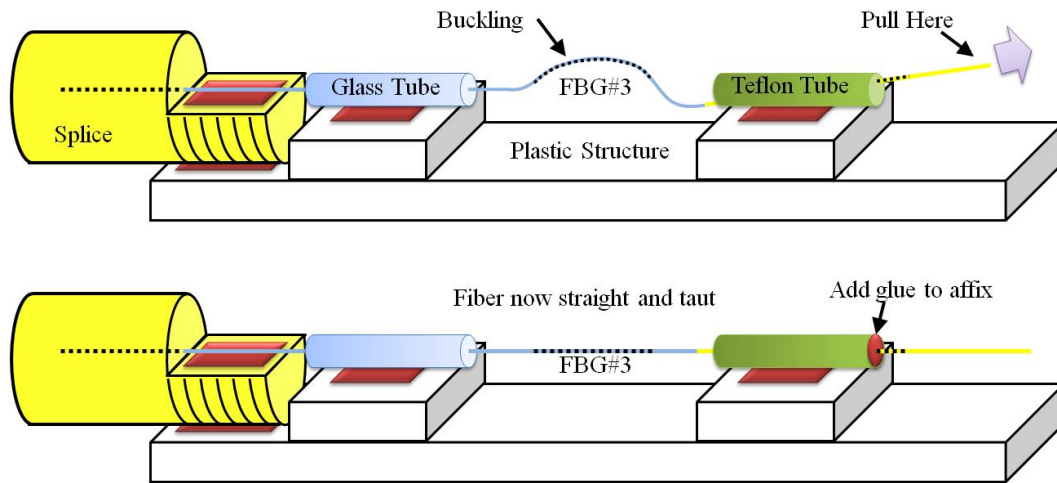


Figure 5-53: Mitigation of the buckling problem by pulling the fiber taut after etching and gluing the fiber to the Teflon tube egress point.

This concludes the description of the etching process. Next, a characterization of the fabrication is conducted in order to evaluate the fiber reflection signal and sensitivity.

5.4.2.3 ETCHING EVALUATION

Now that the fiber is etched, the sensitivity of the signal is measured. This provides an indirect measurement of the diameter of the optical fiber which dictates how sensitive the thinned FBG will be to changes in the surrounding material IOR. Six different states are measured in order to evaluate the entire etching process. In each state, five raw data snapshots are taken of the fiber. This provides the ability to find the peak corresponding to the Bragg wavelength in addition to evaluating the reflected wavelength spectrum to see if there are multiple peaks or if excessive noise is present. The six states are as follows:

BEFORE – The 4 cm Bragg fiber specimen is measured after cutting the fiber from the spool but before it is attached to the apparatus.

PRE – After fastening the fiber specimen to the apparatus, the device is oriented vertically in order to replicate the position it will be in during the etching process. Measurements are taken of the FBGs and the apparatus is then moved into the HF bath while minimizing any change in the lead-in fiber's position.

POST – After the post-etch rinse of the etched FBG in IPA, the apparatus is placed on the table. Before fixing any buckling problems, measurements are taken of the fiber.

AIR – After getting the etched fiber straight, taut, and glued to the Teflon tube, the apparatus is once again turned vertical and placed in an empty vial. Measurements are taken with the surrounding material being ambient air.

IPA – The empty vial is filled with fresh IPA (not the same solution used in the post-etch rinse). Once the signal stabilizes, measurements are taken to determine the air-IPA shift.

AFTER – The apparatus is removed from the vial full of IPA and placed on the table. After any IPA still on the sensor is given time to evaporate, the final measurements are taken.

This characterization is performed to obtain data for evaluating the success of the fabrication process. The two main metrics of success are a satisfactorily large air-IPA Bragg wavelength shift and a clean, single peak reflection signal under all of the above states. An additional step in the characterization process is taking SEM pictures to accurately measure the diameter of the optical fiber. In this work, SEM images were captured after the magnetic testing for the control FBG and one of the thinner experimental FBGs. Once it has been determined that the fabrication process was successful, the apparatus is surrounded with ferromagnetic particles and placed in an external magnetic field. The magnetic field testing will be described next.

5.4.2.4 MAGNETIC FIELD TESTS

The first step before performing any magnetic field testing is to characterize the ferric oxide nanoparticles using SEM images to verify the size of the particles. The ferromagnetic nanoparticles used in this study are 98+% Fe_3O_4 (iron oxide) nanoparticles approximately 10-20 nm in size according to their manufacturer, SkySpring Nanomaterials Inc. Additionally, a superconducting quantum interference device (SQUID) is used to demonstrate the magnetic properties of the particles. The response of the index of refraction of the particles to an external magnetic field will be analogous to its magnetization response. Therefore, a magnetization versus magnetic field plot will help develop a prediction for what magnetic field range will elicit

a response in the FBG. The specific machine used in this research was a Quantum Design MPMS XL-5 SQUID magnetometer. The magnetic field was cycled from +10 *kOe* to -10 *kOe* and back over a 3 hour period.

Next, the FBG apparatuses are surrounded by the ferromagnetic particles and placed in an externally applied magnetic field. To do this, each apparatus (the experimental and the control) are placed in their own empty vial. The vial is then filled with ferromagnetic particles. Figure 5-54 below shows two pictures of a FBG apparatus placed within a vial surrounded by particles.

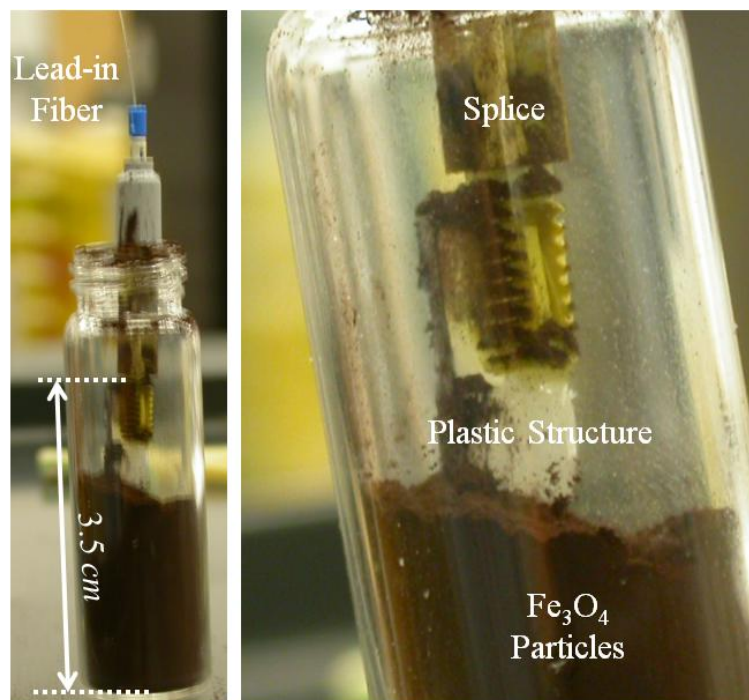


Figure 5-54: Pictures of the fiber apparatus placed in a vial containing ferric oxide particles.

Before loading the vials into the electromagnet used to apply the external magnetic field, double-sided tape is wrapped around the glass vial for padding. When large magnetic fields are applied, large forces can be imparted on the particles which press up against the sides of the vial. This pushes the vial up against the metal yokes and could possibly lead to the vial's glass cracking. After taping the vials, the FBGs are placed between the yokes of a Varian current-controlled electromagnet. The magnetic field is measured with a F. W. Bell Model 6010

Gauss/Teslameter positioned within the magnetic field adjacent to the vials. The setup is shown in Figure 5-55 which shows a zoomed-out side-view picture of the electromagnet on the left and a zoomed-in top-view picture of the apparatuses placed between the yokes on the right. The direction of the magnetic field is indicated with dotted arrows. The Gaussmeter probe is also identified along with the aforementioned tape padding. Masking tape is used to hold the lead-in fibers in place as well as the fiber apparatuses within the vials. This is done to prevent any response in the reflected wavelength to be caused by movement of the apparatus. A source of apparatus movement is the aforementioned force imparted on the apparatus by the particles when the magnetic field is applied.

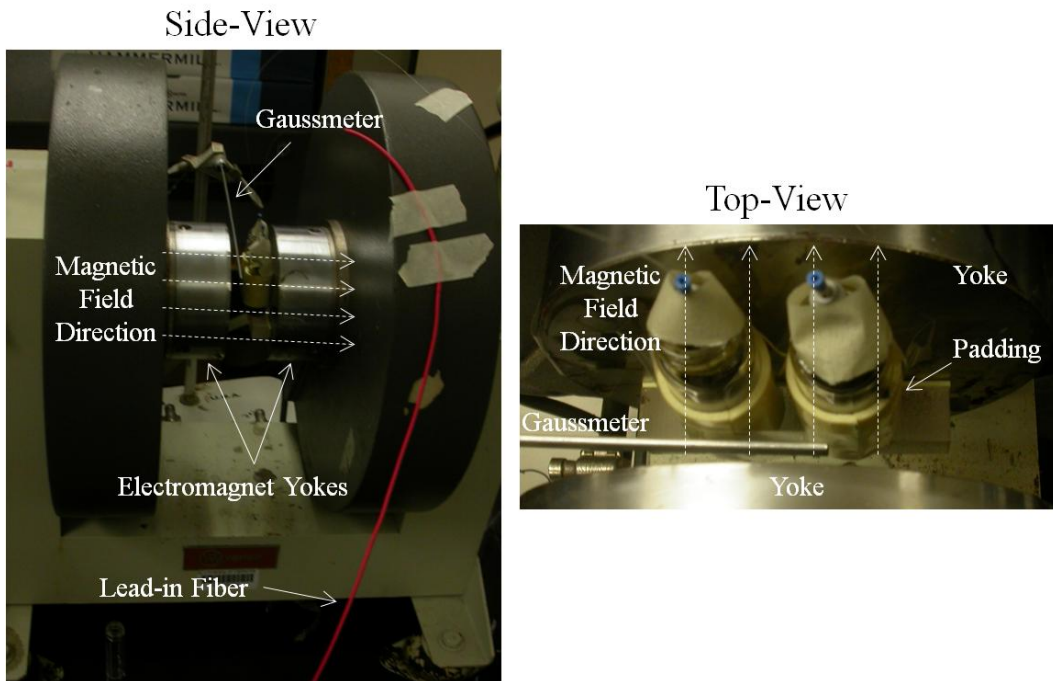


Figure 5-55: Pictures of the electromagnet used to apply the magnetic field during testing and a close-up image of the fiber apparatuses between the electromagnet's yokes.

Note that the picture above is for the case when two apparatuses are tested simultaneously. In this work, one of the experimental FBGs is tested first on its own. From the results of this initial magnetic field test, it was determined that the electromagnet's cooling system played a role in the measurements. The purpose of the cooling system is to keep the electromagnet from

overheating due to the large amount of current running through the coils that produce the magnetic field. Despite the cooling system working well to prevent overheating, it did not prevent the apparatus and thinned FBG from slightly heating up. In order to discern the true influence from a magneto-optic interaction from the aggregate shift stemming from both magnetic and thermal factors, a magnetic field test involving the control FBG and the second experimental FBG was performed.

An illustration of the magnetic test setup involving both an experimental and a control fiber is shown in Figure 5-56 for further clarification. The magnetic field (H-field) is applied between the yokes and through the vials. The apparatus maintains the etched FBG direction to be orthogonal to the magnetic field. The experimental fiber and control fiber are labeled “E-Fiber” and “C-Fiber” respectively. FBG#3 and FBG#4 are identified on both fibers. FBG#4 for both fibers is unetched with a diameter of $127\ \mu\text{m}$. The FBG#3 diameters for the E-fiber and C-fiber are $7.5\ \mu\text{m}$ and $23\ \mu\text{m}$ respectively. Note these diameters were determined using SEM images after all magnetic field testing was completed. Both fibers are simultaneously plugged into and monitored by the FBG interrogation system. Also note that FBG#3 and #4 on both Fibers (4 FBGs total) are completely surrounded with ferromagnetic particles.

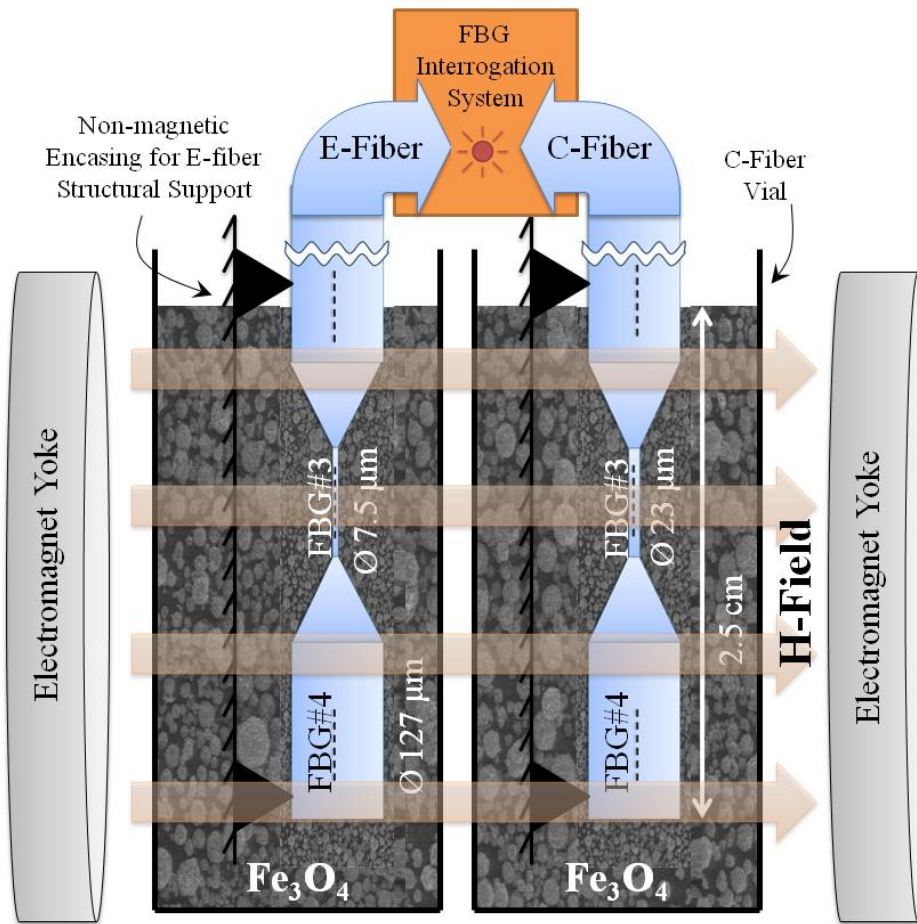


Figure 5-56: Schematic diagram showing the application of an external magnetic field and how much of the fiber apparatus is buried in ferric oxide particles.

The initial E-fiber tested on its own did not survive all magnetic testing and thus, the diameter had not been verified with a SEM image. The distance between yokes is set by the user with large cranks on either side of the electromagnet. However, there is a slight amount of slack in the yoke positioning. In the fatal test, the yokes were positioned with one touching the glass vial and the other nearly touching it. Once a large magnetic field was applied, the small amount of slack in the yoke positioning allowed for the yokes to attract and both came into contact with the glass vial. The yokes eventually applied enough compressive force to crack the glass and allow particles to escape the vial. This rapid movement in the glass vial, the apparatus, and the particles caused the thinned optical fiber to break. This explains the logic behind using tape for

padding and to help hold the glass vial in one piece if a crack should occur. Additionally, the yokes were positioned farther apart so that only one would remain in contact with the vial after accounting for the positioning slack. Fortunately, significant data was collected from this fiber before it broke. Now that the test setup has been explained, the types of magnetic fields that will be applied during the experiments will be described.

Two types of tests are performed on the optical fibers. The first type is an “On/Off” test. This involved simply switching the magnetic field on and off several times. The results from this test demonstrate the magneto-optic coupling in addition to evaluating the ability of the signal to recover its original, zero magnetic field value. The sensor response is binary in nature whereby the reflected wavelength should switch between two different values. The second type is a step test where the magnetic field is incrementally increased to higher and higher values. This type of test provides a more detailed response which should allow the nonlinear magnetization behavior of the ferric oxide particles to be observed.

In addition to the two types of magnetic field tests, two methods of data collection are used. The first method is to monitor in real time the FOID system output while manipulating the magnetic field. This is the Langley mode of the interrogation system. This provides measurements of shifts in the centroid of the reflected wavelength distribution which is output in units of strain. This data, as described earlier, is converted to wavelength shifts in post-processing after the test is completed. The second method is to take a finite number of raw data snapshots while the magnetic field is held constant. The disadvantage of how this method was applied in the experiment is that temporal sensor behavior such as signal drift and magnetic field response time were not picked up. However, this allows for analysis to be performed on the shape of the reflected wavelength spectrum in order to evaluate whether or not a single peak is present and if that peak is well above the noise level.

5.4.3 Concluding Remarks

This concludes the description of steps taken to set up a test which will demonstrate magneto-optic coupling in an optical fiber Bragg grating. The sensor underwent several iterations in order to finalize an apparatus design which would provide a clean wavelength reflection signal and maintain a constant directionality with respect to the externally applied magnetic field. The apparatus was designed to survive being dipped in a HF acid bath while etching only one of the FBGs on the fiber. The observed buckling phenomenon and uneven etching rates were accounted for in the design and etch monitoring process. A detailed description of the etching and rinsing procedures along with the method for evaluating the fabrication process was described. Finally, the steps for characterizing the magnetically active material used to surround the thinned FBG were described along with the magnetic field tests with respect to the type of applied field and the method of data collection. Now that the details of setting up the experiments have been illustrated, the results will be shown.

5.5 Experimental Results

The experimental results will be provided in this section. First, the behavior of pertinent FBGs will be demonstrated during the etching process with real-time data which was collected. Subsequently, etch evaluations will be performed to determine how sensitive the thinned FBGs are to changes in the surrounding material IOR and how well the reflected wavelength spectra survived the fabrication process. Next, SEM photographs will be shown of the ferric oxide particles to determine their size and a SQUID magnetometer will be used to measure the magnetization response of the particles when an external magnetic field is applied.

Once the sensors have been deemed ready for magnetic field testing and the expected behavior of the sensors as indicated by the ferric oxide particle characterization has been determined, magnetic field tests are performed. The first step of the tests is to turn on the cooling system and monitor how this affects the FBG reflection signals. Once this has been

accomplished, the On/Off magnetic field test will be performed to study the binary response of the thinned FBG sensors. Lastly, the Magnetic Saturation test will be performed to study the nonlinear behavior of the thinned FBGs when a broad range of magnetic fields is applied.

5.5.1 Etch Results

The etching results of the three fibers used in the final design iteration will be presented first. The graph below demonstrates the real-time monitoring of FBG#2 and #3 during the etching and rinsing process for the first fiber, denoted “Fiber-1.” Note as explained earlier that during etching, noise is created due to a broadening of the end reflection peak in the length domain. Thus, the data may become erratic over certain periods of time. A MATLAB program was created to filter out noisy data hiding the diameter reduction-induced wavelength shifts. The smoother curves shown in Figure 5-57 below are the result. The vertical axis represents reflected wavelength shift (after transforming from the FOID system’s strain output) and the horizontal axis represents time in minutes. Data recording begins immediately after placing the optical fiber in the HF bath. Red FBG#2 and blue FBG#3 data are identified in the graph.

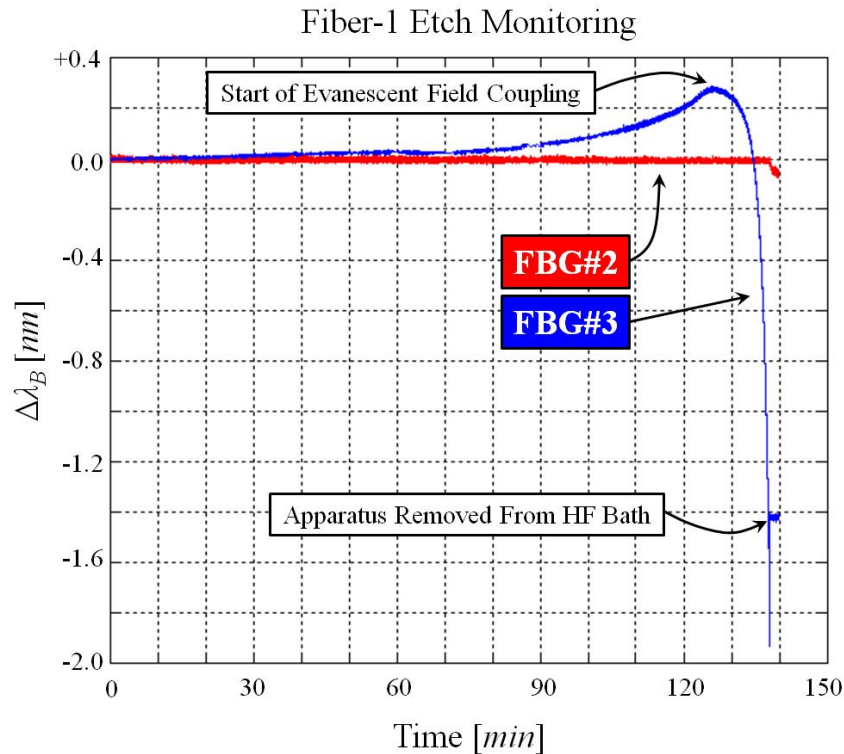


Figure 5-57: Change in reflected wavelength of FBG#2 and #3 on Fiber-1 during etching.

FBG#2 data remains flat throughout the process because it is not inside the HF and therefore is not being etched. FBG#3 data rises due to the aforementioned release of compressive residual strain until the commencement of evanescent field coupling with the surrounding HF. The coupling begins after 126 minutes of etching and results in an accelerating decrease in reflected wavelength. After 138 minutes, the apparatus is removed from the HF bath. An elaboration of the data near the conclusion of the etching process is shown in Figure 5-58 below. Both graphs plot reflected wavelength versus time in minutes but the ranges of values plotted in the graphs are not the same. The graph on the left once again shows that FBG#2 is nonresponsive as expected. FBG#3, on the other hand, experiences a decrease in reflected wavelength until approximately the 138 minute mark when the apparatus is removed from the HF bath and rinsed in an IPA bath. The graph on the right shows the FBG#3 data as the surrounding material is changed. HF is the surrounding material until the apparatus is removed near the 138 minutes

mark. At this point, air becomes the surrounding material and a rapid drop is seen in the Bragg wavelength. This is due to the decrease in refractive index of the surrounding material. Once the apparatus is placed in the IPA bath, the reflected wavelength jumps up to a higher value and remains steady because any remaining HF has been washed away and the FBG is no longer being etched.

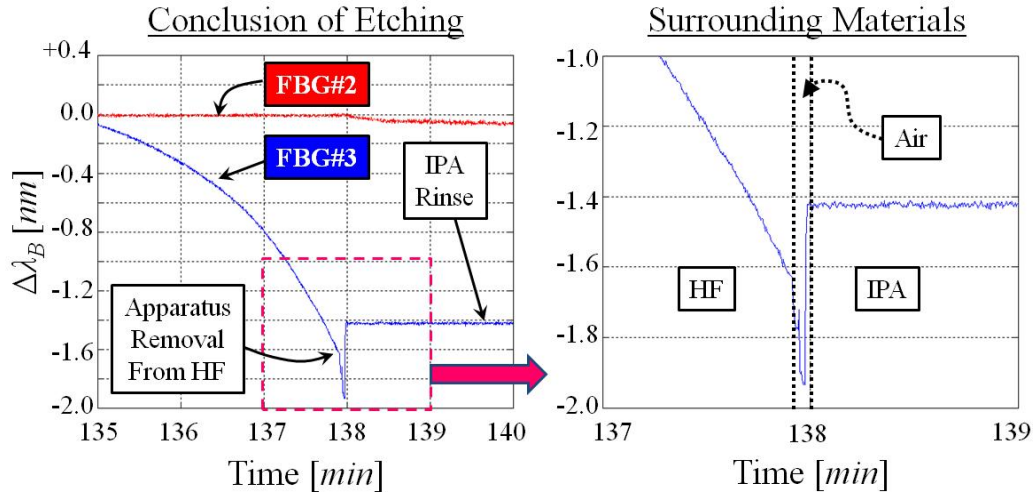


Figure 5-58: Shift in λ_B of FBG#2 and #3 on Fiber-1 toward the end of etching and when the apparatus is removed from the HF bath and rinsed in IPA.

This demonstrates a clean, successful etching process which behaves as expected. While the FBG#2 data remains approximately flat especially in comparison to FBG#3, there is a slight decrease in reflected wavelength that can be noticed when the apparatus is removed from the HF bath. This is because shifting the apparatus position can slightly alter the FBG reflection signal. This demonstrates the necessity to keep the fiber apparatus very still during experimentation. Though the response of FBG#4 will be important for future analysis, the etch-monitoring data is not presented here. This is because the broadening of the length-domain end reflection signal introduces too much noise to draw any meaningful conclusions from the etching data. FBG#1 data is also excluded because it is entirely within the mechanical splice and thus, the response is

not of interest. It is expected that the λ_B of FBG#1 and #4 should remain stagnant through the etching process just as FBG#2 since they are not being etched.

Next, Fiber-2 undergoes the etching procedure to attain a FBG thinned to a similar diameter as FBG#3 in Fiber-1. The data from the etching process is shown in Figure 5-59 below. The vertical and horizontal axes once again represent Bragg wavelength shift and etching time. FBG#2 data in red essentially remains flat while FBG#3 data in blue displays a similar trend as Fiber-1. The inset graph zooms in closer to the data around the time when the apparatus is removed from the HF bath. Notice that the time at which the Fiber-2 apparatus was removed from the HF bath is just after 143 minutes rather than 138 minutes as with Fiber-1. This 5 minute difference is simply due to the aforementioned variability in etch-rate. The same etch-rate influence is observed with the maximum change in reflected wavelength occurring in Fiber-2 after 131 minutes as opposed to 126 minutes for Fiber-1. Additionally, note that the Bragg wavelength shift goes to a much more negative value when removed from the HF acid bath.

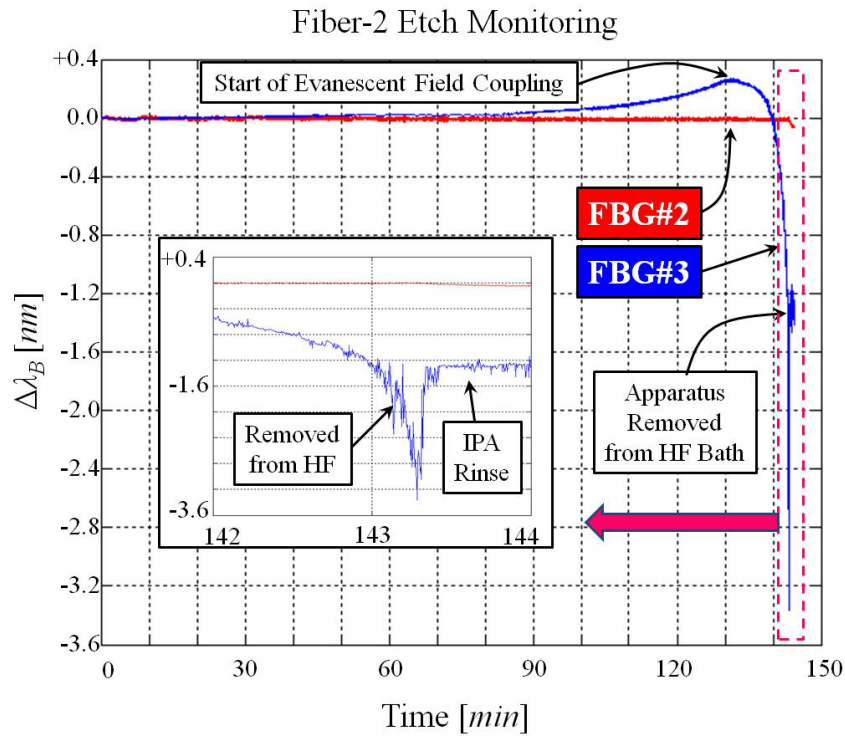


Figure 5-59: Change in reflected wavelength of FBG#2 and #3 on Fiber-2 during etching.

It will later be seen in the etching evaluations of these fibers that FBG#3 on Fiber-1 exhibits a larger air-IPA wavelength shift compared to the Fiber-2 FBG#3. This fact seems to contradict the etching results that the negative Bragg wavelength shift is larger in the Fiber-2 etching process (compare -1.95 nm in Fiber-1 with -3.4 nm in Fiber-2). Two feasible reasons for such a discrepancy are as follows. Firstly, the end reflection signal broadening may have been greater in Fiber-2; therefore, more noise is created in the Bragg wavelength shifts. The excess noise becomes the source of the large negative shifts rather than a reduction in fiber diameter. Note that even though both fibers seem to have a steady, smooth $\Delta\lambda_B$ response, this is because both fiber data sets have been put through a filtering program. The purpose was to discard any data creating excessive noise which distracts from the response that stems from diameter changes. However, this may not have been completely successful. It was not shown in any figure, but the Fiber-2 data shown in Figure 5-59 had much more pre-filter noise compared to the Fiber-1 data in figure 57 due to the end reflection broadening.

Another reason why a contradictory response is observed stems from the buckling phenomenon previously noticed. The fiber will buckle and will not be kept taut due to the Teflon tube only loosely keeping the fiber in place. The result is that the etched FBG undergoes a relatively large change in position. As seen in the response of FBG#2 in both fibers, fiber motion stemming from removal of the apparatus from the HF bath can result in significant Bragg wavelength shifts. In the process of moving the fiber from the HF bath to the IPA bath, the buckled fiber may have undergone enough motion to cause the excessive negative shift in reflected wavelength. The conclusion from these two explanations for the discrepancy is that real-time monitoring provides fairly accurate information for deciding when to remove the optical fiber to achieve a desired radius, but it is not an exact science. A fair amount of artistry is required by the user in monitoring and interpreting data from the etching process.

The etching process for Fiber-3 is presented next in Figure 5-60. Vertical and horizontal axes again represent Bragg wavelength shifts and time in minutes respectively. Red FBG#2 and blue FBG#3 data are identified. The inset graph shows a zoomed-in view of the time around when the

fiber apparatus is pulled from the HF bath. The apparatus for this test was removed from the HF bath after only 131 minutes, a significantly shorter time than the previous two fibers. This is because Fiber-3 will be used as a control for future magnetic field experiments. FBG#3 in this fiber is etched so it has a diameter fairly comparable to both FBG#3s in Fiber-1 and -2 but it will not interact with any surrounding material. Therefore, the time when the apparatus is removed from the HF bath is chosen to match the start of the evanescent field coupling. This occurs at the maximum $\Delta\lambda_B$ between +0.25 and +0.30 nm. There is already an indication of no surrounding material interaction in the data because no abrupt negative shift is seen in the FBG#3 data when removed from the HF bath and no abrupt positive shift follows when rinsed in IPA.

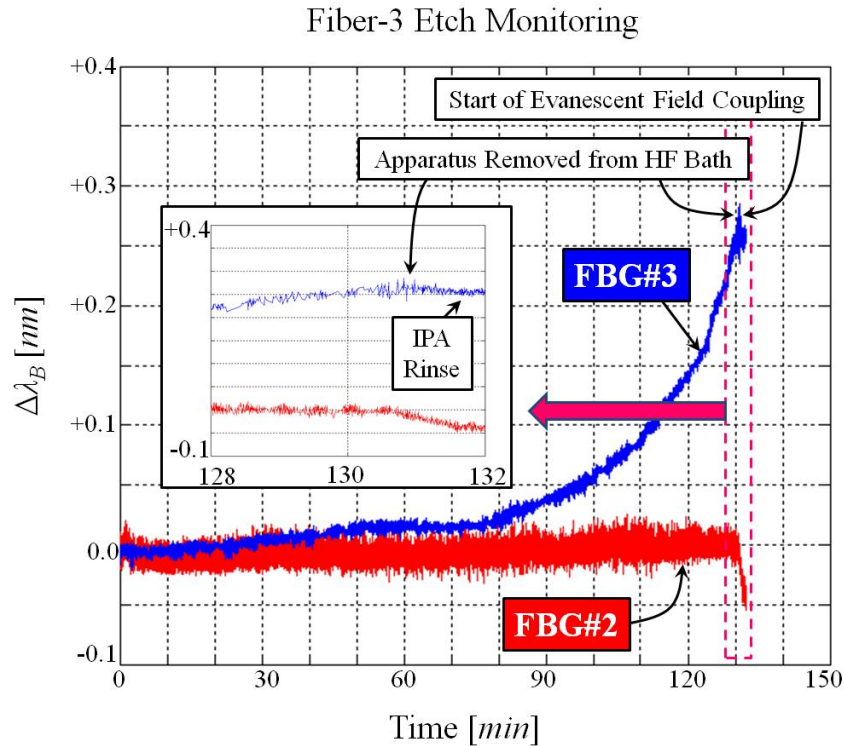


Figure 5-60: Change in reflected wavelength of FBG#2 and #3 on Fiber-3 during etching.

This concludes the presentation of real-time etch monitoring data. All three fibers exhibit similar features with FBG#2 essentially being nonresponsive while FBG#3 displays a steady

increase in $\Delta\lambda_B$ until the start of evanescent field coupling when λ_B plunges. Next, the etching processes will be evaluated by studying data when the fibers are in the six aforementioned states.

5.5.2 Etch Evaluation

The next step in the process of testing the fibers is the evaluation of the etching procedure. This is done by measuring the reflected wavelength at six different states. The Fiber-1 results are shown in the graph in Figure 5-61 below with the vertical axis representing reflected wavelength and horizontal axis corresponding to the various states. Each data point corresponds to an average of 10 measurements. The maximum error in these measurements was 0.01 nm , so error bars were not included. Lines connecting the data points are for viewing purposes only. Data for FBG#2, 3, and 4 are shown in blue, red, and green respectively. Three combinations of wavelength shifts between two states are identified. These include the shift from PRE to POST, from AIR to IPA, and from BEFORE to AFTER.

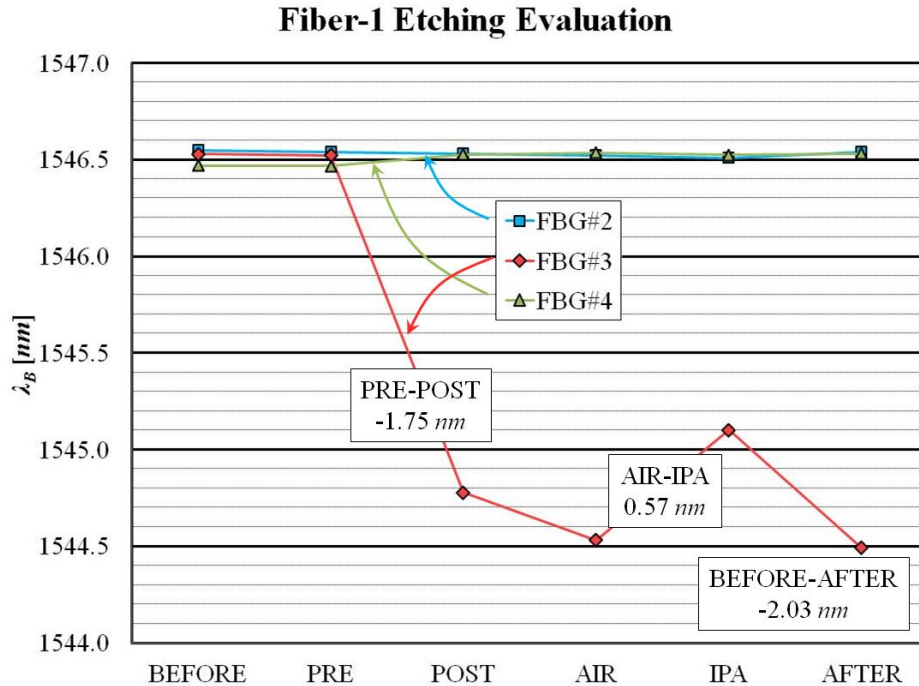


Figure 5-61: Reflected wavelength at each of the six etch evaluation states for FBG#2-4 in Fiber-1.

As expected, the data from FBG#2 and #4 show no significant shift compared to the thinned FBG#3. Before etching, FBG#3 has a reflected wavelength near 1546.5 nm, but the etching process drops this value down to around 1544.8 nm. After gluing the optical fiber to the Teflon tube to counteract the buckling phenomenon and placing the apparatus in an empty vial, λ_B shifts farther down to 1544.5 nm. When the vial is filled with IPA, λ_B shifts up to 1545.1 nm. After removal from the IPA filled vial, the apparatus is placed on a table and any remaining IPA is given time to evaporate. After plenty of time to allow for the signal to stabilize, the final reflected wavelength is 1544.5 nm. This corroborates what was seen in the etch monitoring that λ_B has a net decrease in λ_B (-1.75 nm) due to the etching process. When surrounded with IPA, the wavelength has a positive shift in λ_B of 0.57 nm. This confirms that the fiber's evanescent field is interacting significantly with the surrounding material and provides a quantitative metric to evaluate that interaction. The overall λ_B shift from when the fiber was cut from the Bragg fiber spool to the final state when the apparatus is ready for magnetic field testing is -2.03 nm. In addition to the shift in λ_B , the reflected wavelength spectrum can be viewed and analyzed to evaluate how far the reflection signal is above noise level. Figure 5-62 below shows the reflected wavelength spectrum for FBG#3 in each of the six states. The vertical axes represent light reflection intensity in arbitrary units and the horizontal axes correspond to wavelength (in the range of 1540 to 1548 nm).

Fiber-1, FBG#3 – Reflected Wavelength Spectrum

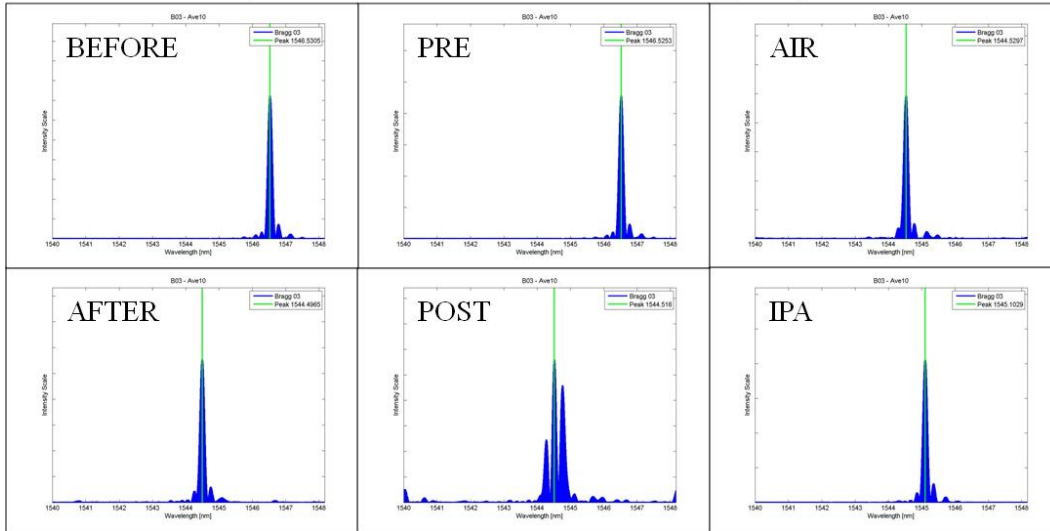


Figure 5-62: Reflected wavelength spectra in each of the six etch evaluation states for FBG#3 on Fiber-1.

Every state indicates that the FBG is behaving nicely with a single peak well above noise level with the exception of the POST state. This is most likely an artifact of the buckling phenomenon. This distortion seems to be a chirping effect spreading out the single peak into multiple peaks. Once the FBG is straightened out and the fiber is glued to the Teflon tube, the FBG changes from the POST to AIR state and the single peak distribution is recovered.

This process is repeated for Fiber-2 and -3 for evaluation of their respective etching processes. Figure 5-63 below shows the graphs from Fiber-2 and -3 analogous to Figure 5-61 above for Fiber-1. The vertical axes represent reflected wavelength and horizontal axes correspond to the etch evaluation state. FBG#2, #3, and #4 data are identified in blue, red, and green respectively. In both of these fibers, each data point corresponds to an average of 5 measurements. The error bars were too small to warrant inclusion in the graph because the maximum error in the average as calculated with the standard deviation was 0.012 nm (for the FBG#3 AFTER state of Fiber-2). Fiber-2 was etched to a similar degree as Fiber-1 and thus, exhibits similar trends in λ_B from one state to another with the magnitudes being slightly different. For example, the AIR-IPA shift was 0.51 nm for Fiber-2 compared to 0.57 nm in Fiber-

1. Fiber-3, on the other hand, was only etched until the evanescent field interaction with the surrounding material was just starting. This means that the apparatus was pulled from the HF bath before the sharp decrease in λ_B occurred. Thus, the post-etching reflected wavelengths are all greater than the original value of 1546.6 nm in the BEFORE and PRE states. Note that there is no significant shift in λ_B when changing from the AIR state to IPA. This confirms that no evanescent field interaction occurs with the surrounding material as desired.

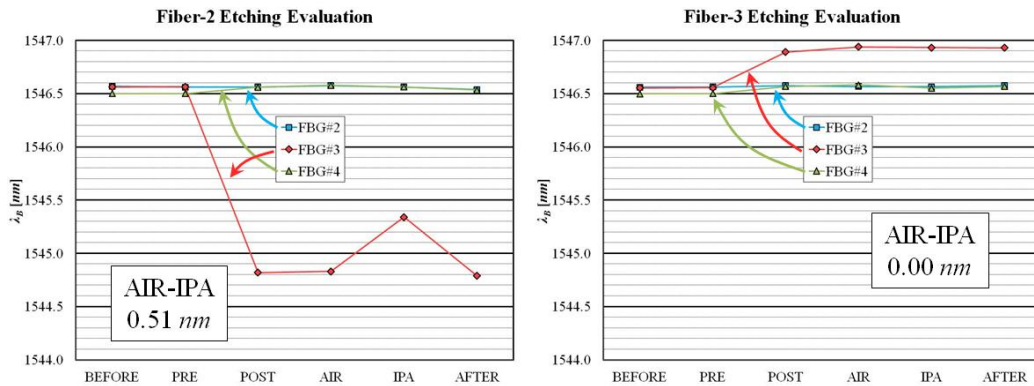


Figure 5-63: Reflected wavelength at each of the six etch evaluation states for FBG#2-4 in Fiber-2 and -3.

As with Fiber-1, the reflected wavelength spectrum for FBG#3 in each state is analyzed to identify the influence of noise in the signal. Data from the thinned fiber in Fiber-2 is shown in Figure 5-64 below analogous to Figure 5-62 above. The BEFORE, PRE, POST, and IPA states all have a very clean, single peak well above noise. The AIR state still maintains a single peak, but the noise levels are seen to decrease heavily. The AFTER state again maintains the peak seen in all other states, but the noise is substantially higher with one particular peak amongst the noise nearly equaling the magnitude of the λ_B peak. This second, large peak in the AFTER state is confirmed later to be noise because in future test results, it has disappeared. In this data, the noise is not due to any end reflection peak broadening. For each state below, the end reflection signal was narrowed by placing index-matching gel on the end of the fiber. The length domain end reflection signal is very similar to that in image (a) of Figure 5-52 above.

Fiber-2 Etching Evaluation

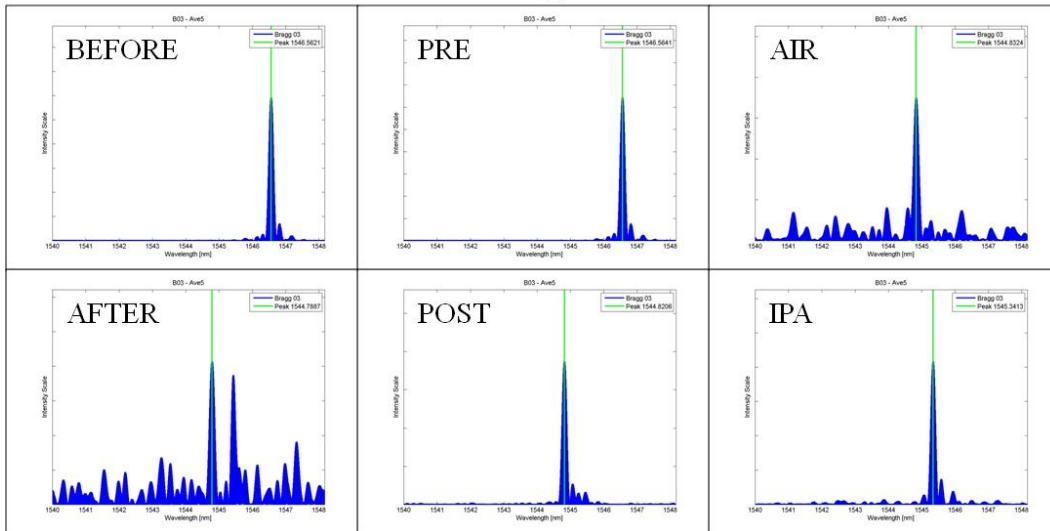


Figure 5-64: Reflected wavelength spectra in each of the six etch evaluation states for FBG#3 on Fiber-2.

The reflected wavelength spectra for FBG#3 in Fiber-3 are analyzed next. Figure 5-65 shows the spectrum for each state and, as expected, the signal is very clean with a single-peak well above noise. Due to the smaller etching time, the evanescent field experiences a negligible interaction with the surrounding material and the fiber's etched surface. Therefore, the reflected wavelengths of the BEFORE and PRE states are at a smaller wavelength than all other states.

Fiber-3, FBG#3 – Reflected Wavelength Spectrum

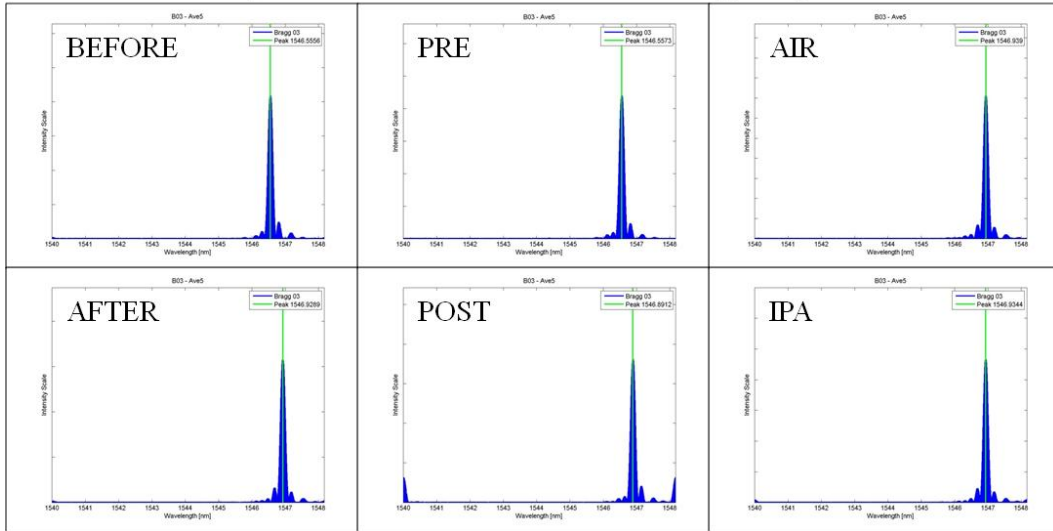


Figure 5-65: Reflected wavelength spectra in each of the six etch evaluation states for FBG#3 on Fiber-3.

The final analysis performed on the data collected for the etching evaluation is to look at the change in λ_B between particular pairs of states. Specifically, the difference in λ_B between BEFORE and AFTER, PRE and POST, and AIR and IPA are shown for FBG#3 and #4 in Table 5-3 below for all three fibers. All quantities are in units of *nm*. The AIR-IPA shifts are highlighted with a red dotted line because this shift is the most important quantitative factor in evaluating the potential for magneto-optic interaction.

Table 5-3: Bragg wavelength shifts between relevant pairs of states in the etch evaluation process.

State Change	Bragg Wavelength Shift, $\Delta\lambda_B$ [nm]					
	Fiber-1		Fiber-2		Fiber-3	
	FBG#3	FBG#4	FBG#3	FBG#4	FBG#3	FBG#4
BEFORE-AFTER	-2.03	+0.06	-1.77	+0.04	+0.38	+0.07
PRE-POST	-1.75	+0.06	-1.74	+0.06	+0.33	+0.07
AIR-IPA	+0.57	-0.01	+0.51	-0.02	0.00	-0.03

The shifts in λ_B amongst all pairs of states are very small for FBG#4. This is expected because FBG#4 is not etched and therefore, the only change in λ_B should be due to movement of the apparatus during the etch evaluation. In contrast, FBG#3 experiences a large negative shift in λ_B from BEFORE to AFTER and from PRE to POST when etched to a diameter that allows for evanescent field interaction with the surrounding material (as in Fiber-1 and -2). The shift in λ_B is positive for these state changes in Fiber-3 because it is removed after compressive residual strains are released but before the evanescent field interacts with the surrounding material. For the same reasons, the AIR-IPA shift is positive for Fiber-1 and -2 but negligible for Fiber-3.

The AIR-IPA shift is identified as the most important quantity in the table above because it is the best metric for comparing how one FBG interacts with a surrounding material to another FBG. According to the data, Fiber-3 FBG#3 will not interact, Fiber-2 FBG#3 will, and Fiber-1 FBG#3 should experience an interaction greater than that of Fiber-2. This metric strips out other differences between FBGs such as the original λ_B , etching time, noise due to end reflection signal during etch monitoring, and degree of buckling from the etching process. The AIR-IPA shift provides the most fundamental quantity which predicts how responsive the FBG will be when surrounded with a magnetic material and placed in a magnetic field.

The final component of the etch evaluation is the analysis of SEM images of the etched fibers. Unfortunately, Fiber-1 broke during testing and therefore, no SEM images were taken. However, images were taken of Fiber-2 and -3 after magnetic testing had occurred. Figure 5-66

below shows four images of Fiber-2. Image (a) shows the optical fiber emerging from the Teflon tube. Note that because this was after the fiber was removed from the ferromagnetic particles, many Fe_3O_4 particles remain on the fiber and apparatus. Also note the large inside diameter of the tube which corroborates that the fiber is not firmly held in place until the fiber is glued to the Teflon tube after the etching process is complete. Image (b) shows part of the tapered region, (c) shows an anomalous, large Fe_3O_4 particle sticking to the fiber, and (d) is a close-up image which shows that the diameter of the optical fiber in the FBG#3 vicinity is $7.5 \mu\text{m}$.

Fiber-2 Post Magnetic Test SEM Images

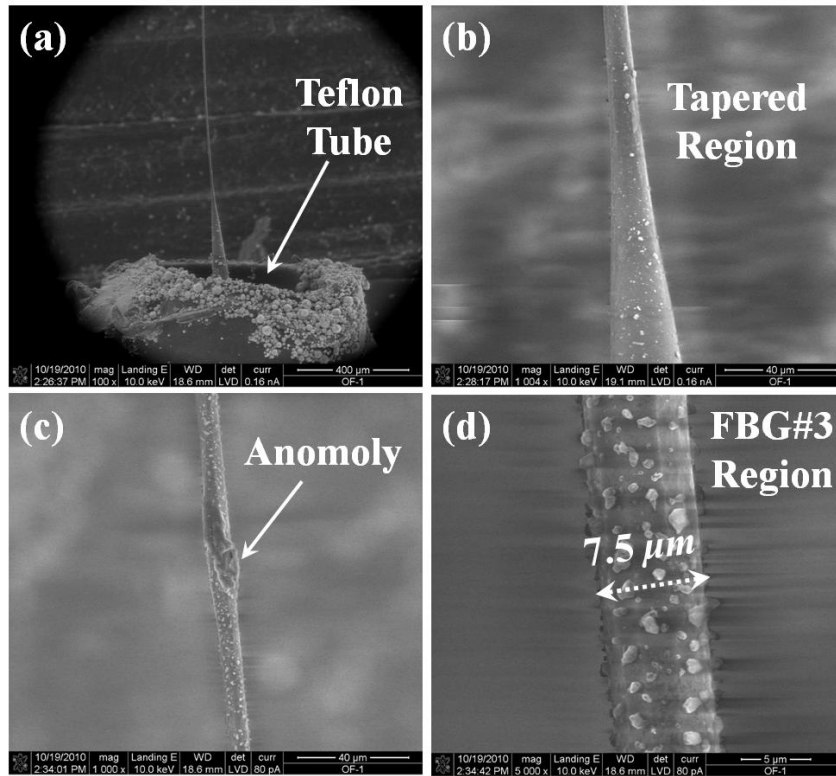


Figure 5-66: SEM images of Fiber-2 after magnetic field testing used to determine the diameter of the optical fiber.

Next, SEM images of Fiber-3 are shown in Figure 5-67 below. Image (a) shows the optical fiber with polyimide coating remaining. If the images were extended farther down, one could see the Teflon tube. Note that the reason the polyimide portion of the optical fiber is outside the Teflon tube in Fiber-3 but inside the Teflon tube in Fiber-2 (image (a) in the Figure 5-66) is that

the buckling phenomenon was much less prevalent in the fiber that was etched for a smaller amount of time. Therefore, Fiber-3 did not need to be pulled as much as Fiber-2 to get the fiber straight and taut. Image (b) shows the fiber emerging from the glass tube while images (c) and (d) are in the vicinity of FBG#3, showing the diameter of the thinned FBG to be $23\ \mu\text{m}$.

Fiber-3 Post Magnetic Test SEM Images

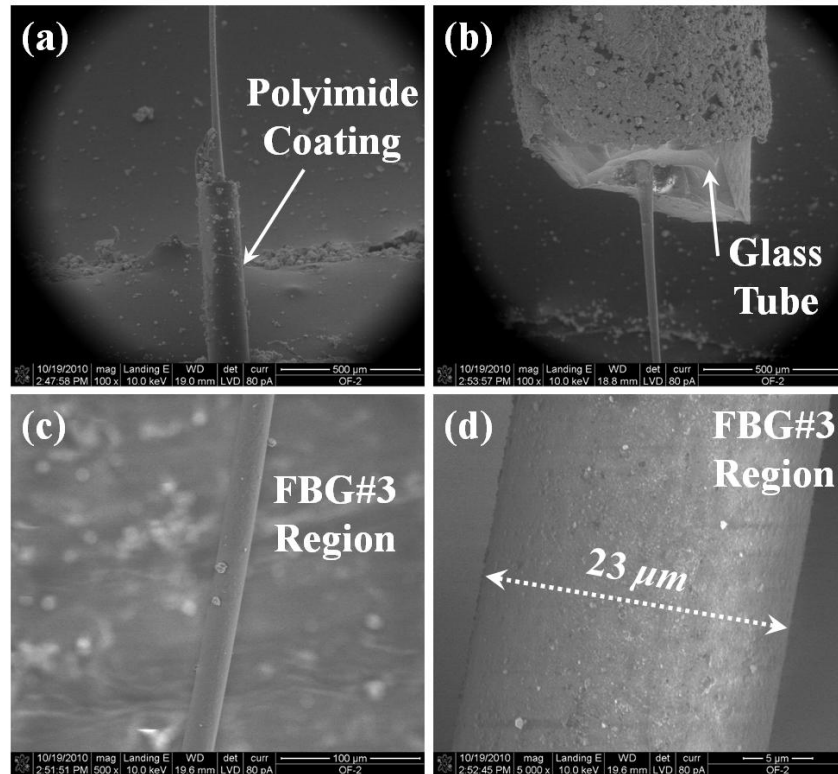


Figure 5-67: SEM images of Fiber-3 after magnetic field testing used to determine the diameter of the optical fiber.

Now that the etch evaluation has been carried out, the results of characterizing the ferromagnetic particles with SEM images and a SQUID magnetometer are shown next.

5.5.3 Ferromagnetic Particles Evaluation

The first action taken to characterize the ferric oxide particles was to take SEM images and view the particles. The images in Figure 5-68 show a small sample of particles from the commercially purchased batch. Each row corresponds to a set of successively magnified images.

The scales in each image are (a) $200\ \mu\text{m}$, (b) $10\ \mu\text{m}$, (c) $1\ \mu\text{m}$, (d) $100\ \text{nm}$, (e) $500\ \mu\text{m}$, (f) $10\ \mu\text{m}$, (g) $2\ \mu\text{m}$, and (h) $1\ \mu\text{m}$. As seen in images (d) and (h), many of the particles remain in the 10-20 nm range; however, particles have also agglomerated into much larger particles. A range of particles sizes on the orders of $100\ \text{nm}$, $1\ \mu\text{m}$, and $10\ \mu\text{m}$ have been created. It is hoped that once placed in the vicinity of the thinned FBG, scattering off of larger particles will not dominate the FBG reflection signal measuring the magneto-optic change in IOR.

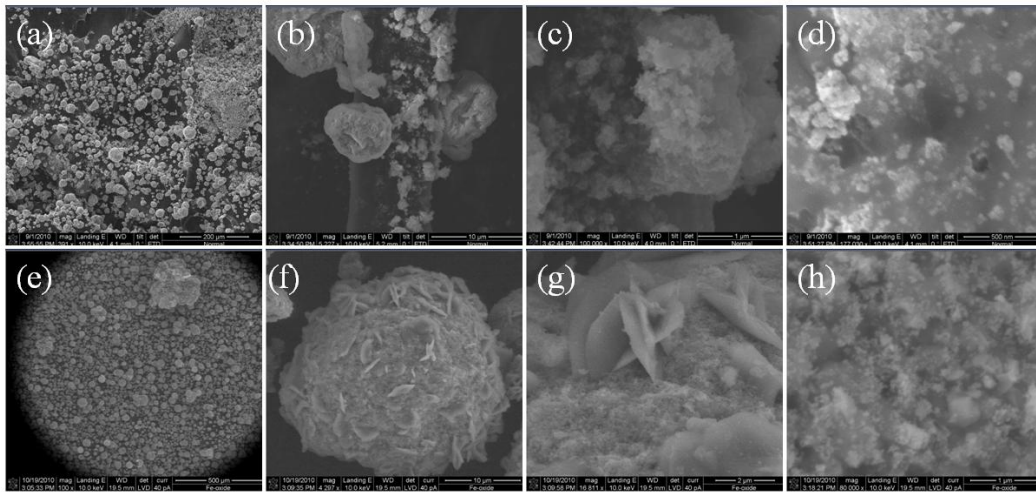


Figure 5-68: SEM images of the ferric oxide particles to determine their size.

The next step in the ferromagnetic particle characterization is to place a sample of particles through a magnetic field cycle while measuring the magnetization change of the particles. A SQUID magnetometer will be used to collect this data. This is important because the IOR of the iron oxide will follow the behavior of the magnetization. The result of exposing a $1.9\ \text{mg}$ sample of Fe_3O_4 particles to a magnetic field cycling from $+10\ \text{kOe}$ to $-10\ \text{kOe}$ and back over approximately 3 hours is shown in Figure 5-69. The vertical axis represents the magnetization normalized to mass (emu/g) and the horizontal axis represents applied external magnetic field. The inset graph shows a zoomed-in view of the data over a narrower range of magnetization and magnetic field values.

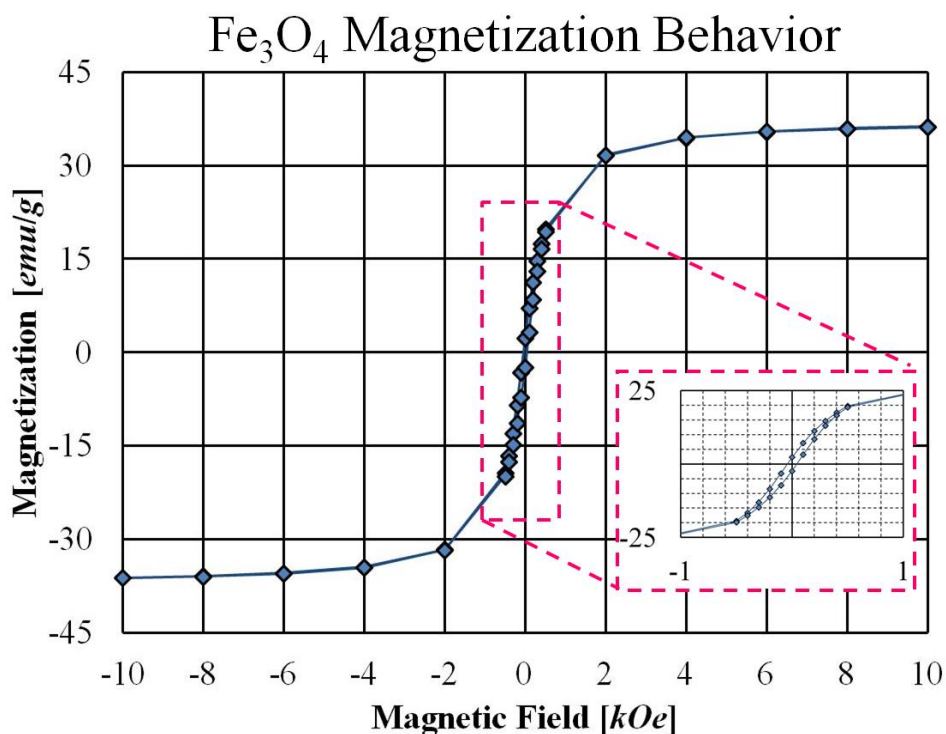


Figure 5-69: SQUID magnetometer results for a sample of ferric oxide particles.

The iron oxide exhibited an expected nonlinear dependence of magnetization on magnetic field with a magnetization saturation (M_s) of $\pm 36.2 \text{ emu/g}$ at field strengths greater than $\pm 3 \text{ kOe}$ and a slight remnant magnetization of $\pm 2.3 \text{ emu/g}$. The amount of remnant magnetization is largely dependent on the size of particles. When the size of the particles is reduced to a small enough value (on the order of 10 nm) the material becomes superparamagnetic and thermal fluctuations cause the magnetization (in the absence of an external magnetic field) to move in any direction. The result would be 0 emu/g of magnetization at 0 kOe . Since this is not the case, we see that the particles are ferromagnetic but nearly superparamagnetic since the hysteresis in the magnetic field loop is so small. This tells us that the index of refraction of the iron oxide particles will nonlinearly increase with applied magnetic field until values between 3 and 4 kOe are achieved. At 4 kOe and beyond, the magnetization is saturated and the index of refraction should no longer increase.

Now that the thinned FBGs have been fabricated, the etching process has been evaluated, and the surrounding material to be used has been characterized, the magnetic field tests can commence.

5.5.4 Magnetic Field Test Results: Fiber-1

The outcome of performing a cooling procedure, a magnetic On/Off test, and a Magnetic Saturation test in Fiber-1 is presented here first. The results will indicate that the magneto-optic effect is influencing observed shifts in λ_B ; however, thermal effects are also influencing the results. Despite the success of observing the desired magneto response, the ability to strip out the thermal influence from the magneto-optic influence is necessary in order to satisfactorily demonstrate magneto-optic coupling.

After the fiber and apparatus are placed in a glass vial and surrounded with Fe_3O_4 particles, the vial is placed between the electromagnet's yokes and the cooling system is turned on. This process cools the fiber and therefore, causes a negative shift in the reflected wavelength. This shift is tracked in time and shown in Figure 5-70 to show that after nearly 80 minutes, the system has reached a steady state. The vertical axis represents the shift in λ_B while the horizontal axis represents time in minutes. The blue and red data are labeled for FBG#2 and FBG#3 respectively.

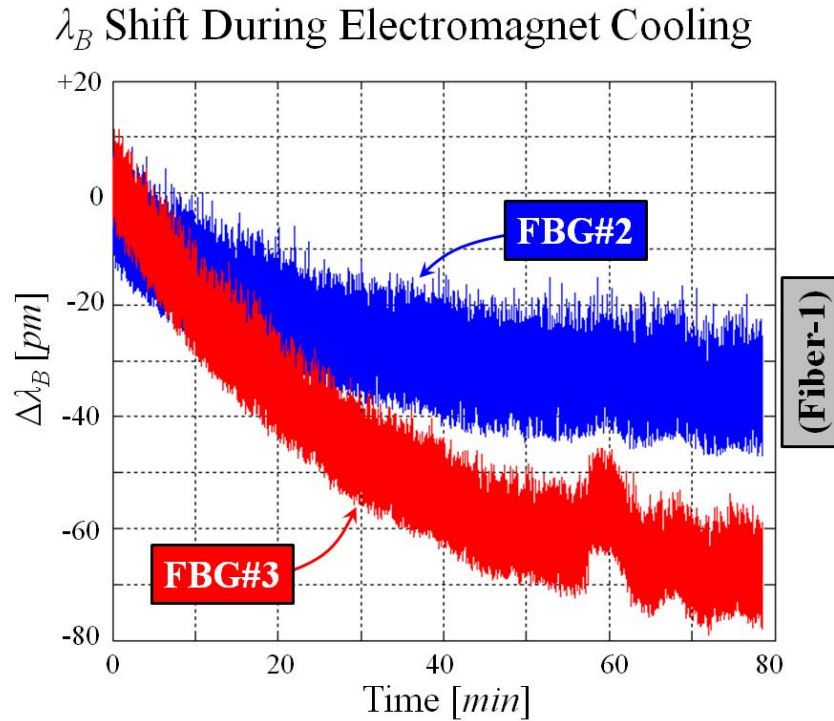


Figure 5-70: Shift in reflected wavelength for FBG#2 and #3 for Fiber-1 while the electromagnet test setup is being cooled.

The decrease in reflected wavelength leveled off, indicating that the temperature of the system is stable. Note that the shift in FBG#3 is greater than FBG#2. Two factors may be causing the difference. The first is that a thermal gradient probably exists along the fiber. This is due to the imbalance of heat flow from the cooled yoke via conduction through the ferric oxide particles to FBG#3 and via convection through air to FBG#2. The second is that the responses of FBG#2 and #3 to temperature changes may be significantly different. If a thinned FBG and a thick FBG undergo the exact same change in temperature, the thermo-optic properties of the former may not be completely identical to the latter, thus, resulting in different shifts in reflected wavelength.

The influence of these two factors in the varying responses of the FBGs means that in future magnetic tests, other FBGs on the fiber (FBG#1, #2, and #4) will not necessarily have the same thermal response. Therefore, they will not adequately work as a control fiber. The magneto-optic

effect may still be observed and be the more dominant phenomenon during testing, but the thermal influence cannot be adequately quantified without a proper control.

The data from FBG#4 was not included in the cooling data because a large amount of noise from the end reflection was present during testing. This can be seen in Figure 5-71 below showing the length domain plot of the Fiber-1 reflection signal. FBG#1-4 are labeled along with the reflection peaks from the start and end of the fiber. Note that the end reflection is much broader than the start and penetrates into the FBG#4 reflection signal. Centroid calculations of the FOID system to obtain data like that shown in Figure 5-70 will be significantly thrown off by the noise created by the end reflection, but the peak data is still reliable and will be presented in later results.

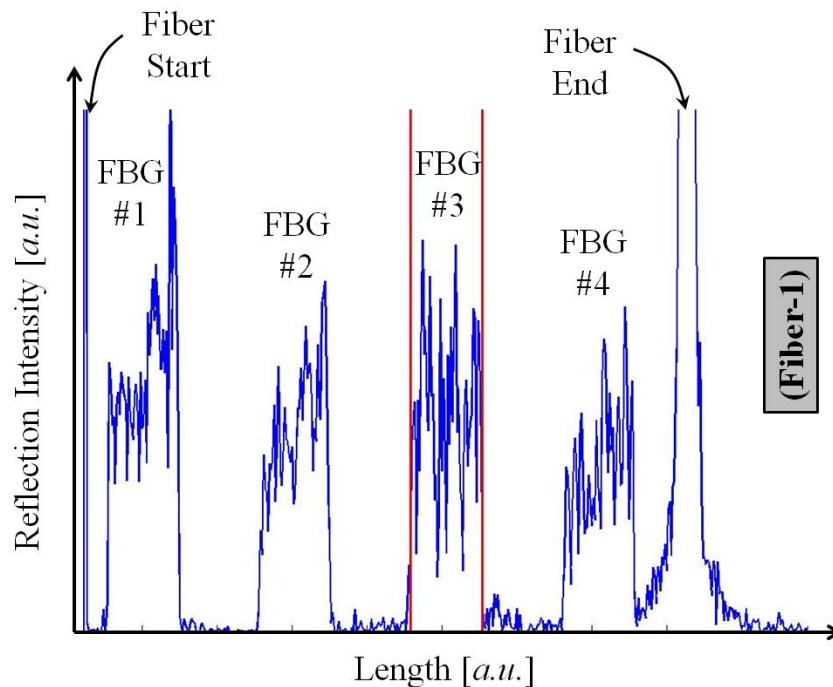


Figure 5-71: Penetration of the end reflection peak into the reflection signal of FBG#4 on Fiber-1.

The first test performed is the On/Off magnetic field test. In this test, the electromagnet is turned on and off every 30-45 seconds while monitoring the FBG#2 and 3 wavelength shifts. Figure 5-72 below shows a graph of the results. The vertical axis represents the shift in λ_B from

the initial λ_B when $t = 0$ while the horizontal axis represents time in minutes. FBG#2 and 3 data are identified and plotted in blue and red respectively. When turned off, a residual 80 *Oe* magnetic field is present but when turned on, the field is 1 *kOe*. The periods of time when the electromagnet is turned on are labeled “EM On” while the opposite are labeled “EM Off.”

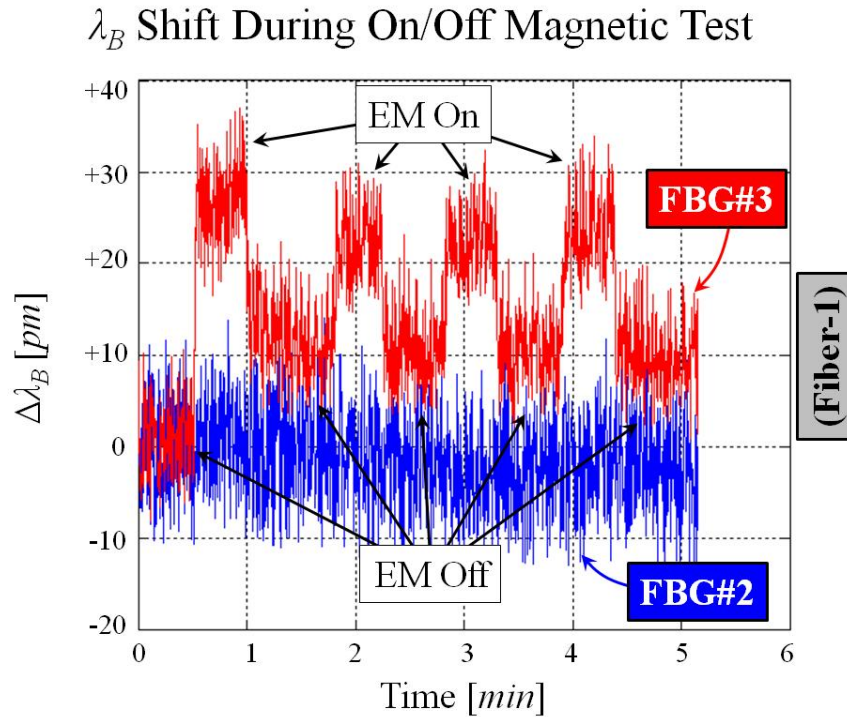


Figure 5-72: Real-time monitoring of the reflected wavelength shift of FBG#2 and #3 on Fiber-1 during the On/Off magnetic field test.

Turning the magnetic field off and on results in uneven shifts during the first period. This is most likely due to a small shift in the positioning of the apparatus as it settles into a stable position within the surrounding Fe_3O_4 particles. Once the settling is complete, an approximately 12 *pm* shift is seen between the two magnetic field levels which is consistent and recoverable. This exact same test is continued in Raw Data collection mode and processed to track the peaks of the FBG reflections as opposed to the Langley centroid tracking method in the previous figure. The results are shown in Figure 5-73 below. The vertical axis again represents shift in reflected wavelength from the first state while the horizontal axis corresponds to the state of the

electromagnet being off (labeled OFF) or on (labeled ON). The peak data for FBG#2, 3, and 4 are shown. Each data point represents the average of 10 measurements and the error bars represent the standard deviation of those measurements.

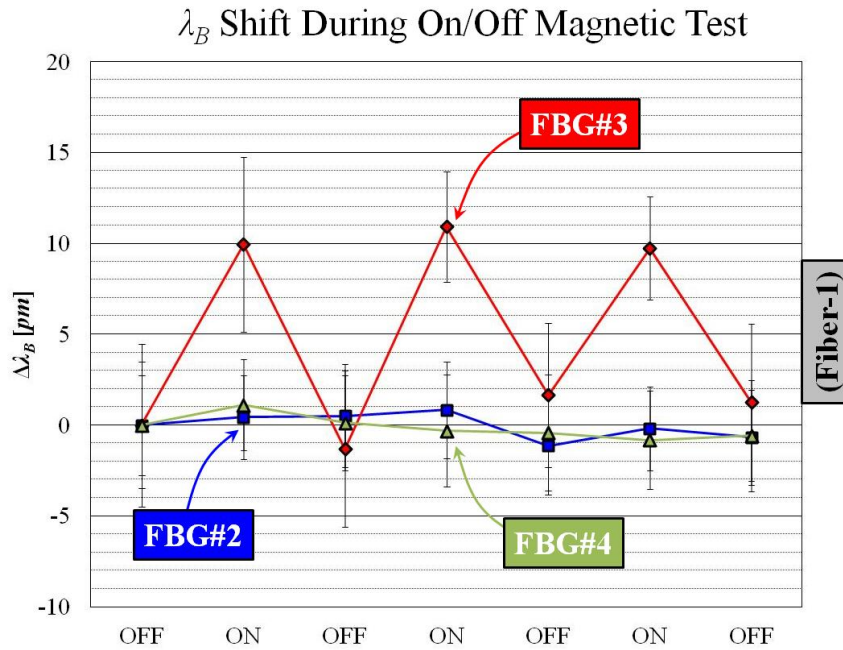


Figure 5-73: Shifts in reflected wavelength of FBG#2-4 on Fiber-1 calculated from peaks of the reflected wavelength spectra during the On/Off magnetic field test.

Note the similar magnitude of shifts seen between the two methods of data collection. Also note that FBG#2 and 4 do not exhibit any significant shift in λ_B . It is clear that the response of FBG#3 is vastly different from the nonresponsive FBG#2 and 4. The lack of shift in FBG#2 and 4 indicates that the thermal environment does not change significantly. This indicates that the shifts seen in FBG#3 (after settling) are entirely due to the magneto-optic effect. However, as noted earlier, the expected variation in response to a change in temperature along the length of the fiber does not allow for the quantization of thermal influence in the observed shifts in λ_B of FBG#3.

An important factor to consider in testing the thinned FBG is whether or not the signal degrades or if noise has increased. Figure 5-74 below plots the reflected wavelength spectra of FBG#3 during three OFF states and three ON states.

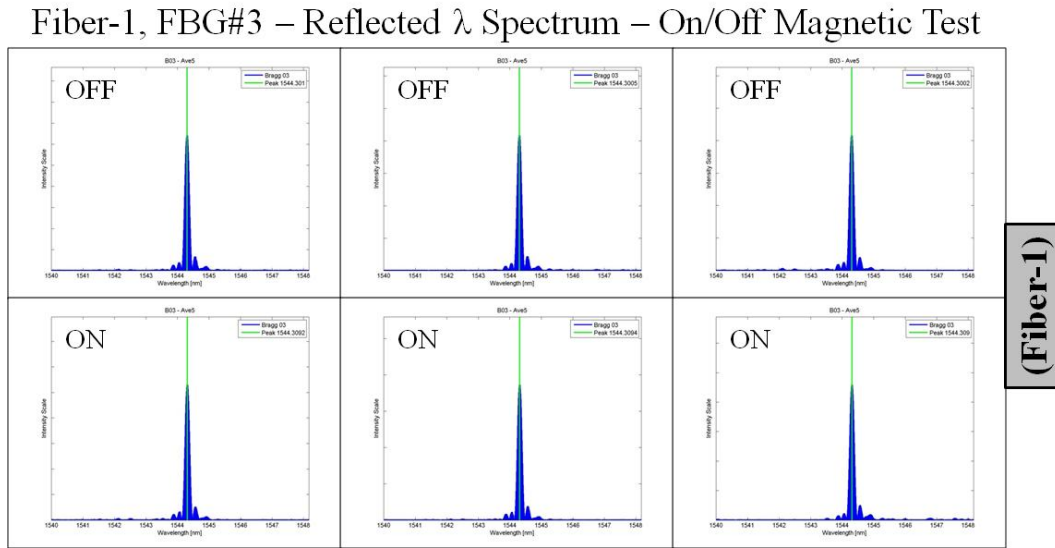


Figure 5-74: Reflected wavelength spectra of FBG#3 on Fiber-1 during the On/Off magnetic field test to evaluate how far the signal is above noise.

A single peak is seen throughout the test; therefore, noise is not a significant factor during testing. At this point, a test will be performed where magnetic fields large enough to saturate the magnetization of the Fe_3O_4 particles are applied. This involves increasing the initial zero field up in increments of 1 *kOe* every 20 seconds up to 4 *kOe* and then turning the field back down to zero. This is repeated twice while monitoring the centroid in real-time. The results are plotted in Figure 5-75 below. The vertical axis represents shifts in λ_B and horizontal axis represents time in minutes. For the first cycle, the periods when the field is at 0, 1, 2, 3, and 4 *kOe* are identified. Blue and red data represent FBG#2 and 3 results, respectively.

λ_B Shift During Magnetic Saturation Test

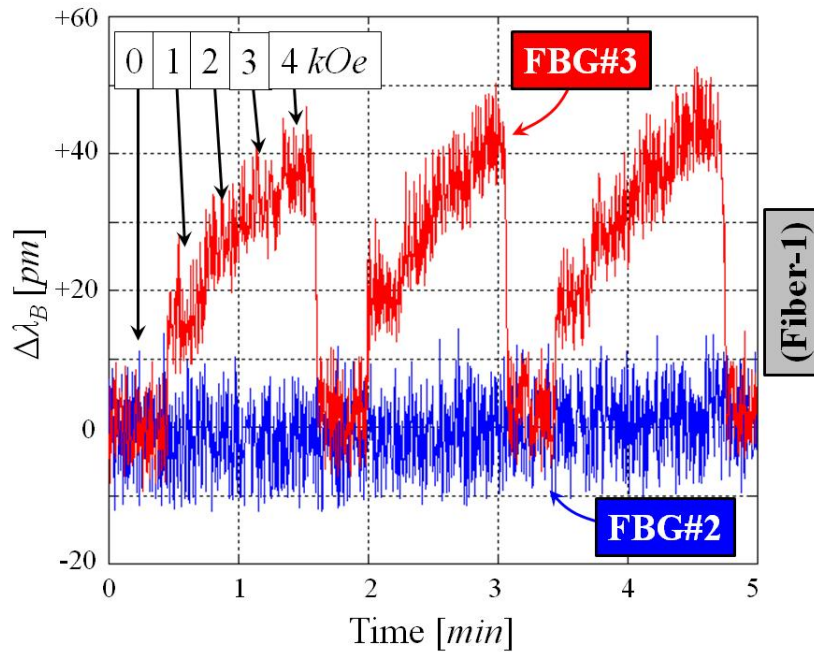


Figure 5-75: Real-time monitoring of the reflected wavelength shift of FBG#2 and #3 on Fiber-1 during the Magnetic Saturation test.

The λ_B of FBG#2 remains essentially stagnant throughout the entire test; however, FBG#3 experiences a nonlinear increase which appears to begin leveling off at higher magnetic fields. Note that because this test was performed after the On/Off test and without changing the position of the fiber apparatus, no settling period was necessary. The same test was performed again using the Raw Data peak tracking method. The shift in λ_B is plotted for FBG#2-4 in Figure 5-76. The vertical axis represents shift in λ_B while the horizontal axis shows the various magnetic field values applied. The blue, red, and green data represent shifts for FBG#2, 3, and 4 respectively. Each data point is the average of 10 measurements and the error bars represent the standard deviation of those measurements.

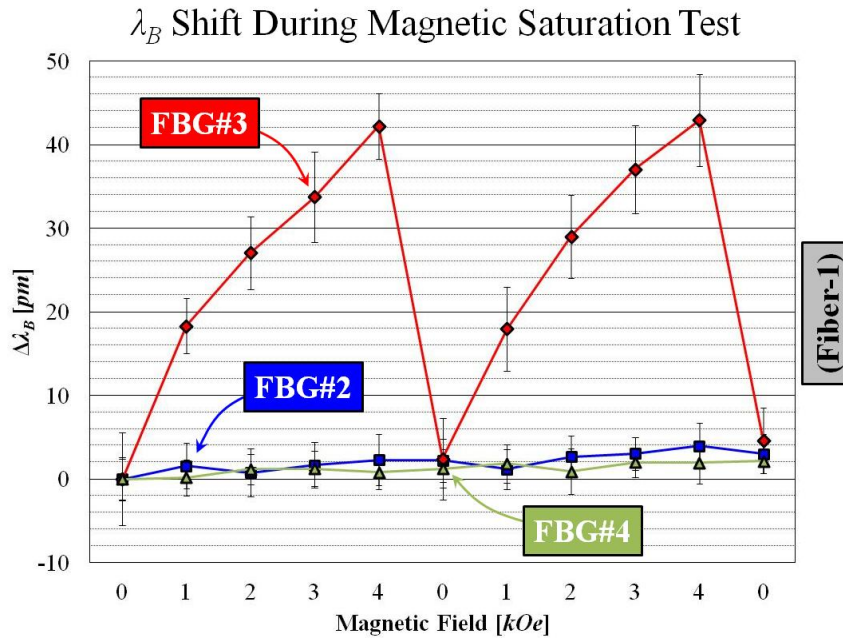


Figure 5-76: Shifts in reflected wavelength of FBG#2-4 on Fiber-1 calculated from peaks of the reflected wavelength spectra during the Magnetic Saturation test.

The unetched FBGs exhibit nearly no response with the exception that a slight increase in λ_B is seen over the entire length of the test. A similar trend and magnitude in the $\Delta\lambda_B$ of FBG#3 is observed between the two data collection methods for the Magnetic Saturation test; however, note that rather than completely leveling off at 4 kOe, λ_B looks as though it will continue to increase. This indicates that either the magnetization has not saturated or the temperature of FBG#3 is increasing during the tests. The characterization of the Fe₃O₄ particles demonstrated a saturation magnetic field between 3 and 4 kOe. Therefore, an increase in temperature throughout the test is the most likely reason for the continuing increase in λ_B .

The mismatch between the observed response in FBG#3 and the magnetization behavior of the iron oxide particles is presented in Figure 5-77 showing the FBG#3 and Fe₃O₄ data normalized to their maximum values. The red data represents the shift in reflected wavelength divided by the maximum shift seen at the highest magnetic field. The yellow data represents the Fe₃O₄ magnetization divided by the saturation magnetization (M_s). The vertical axis is a unitless scale and the horizontal axis represents the applied magnetic field value.

$\Delta\lambda_B$ and Fe_3O_4 Magnetization Normalized

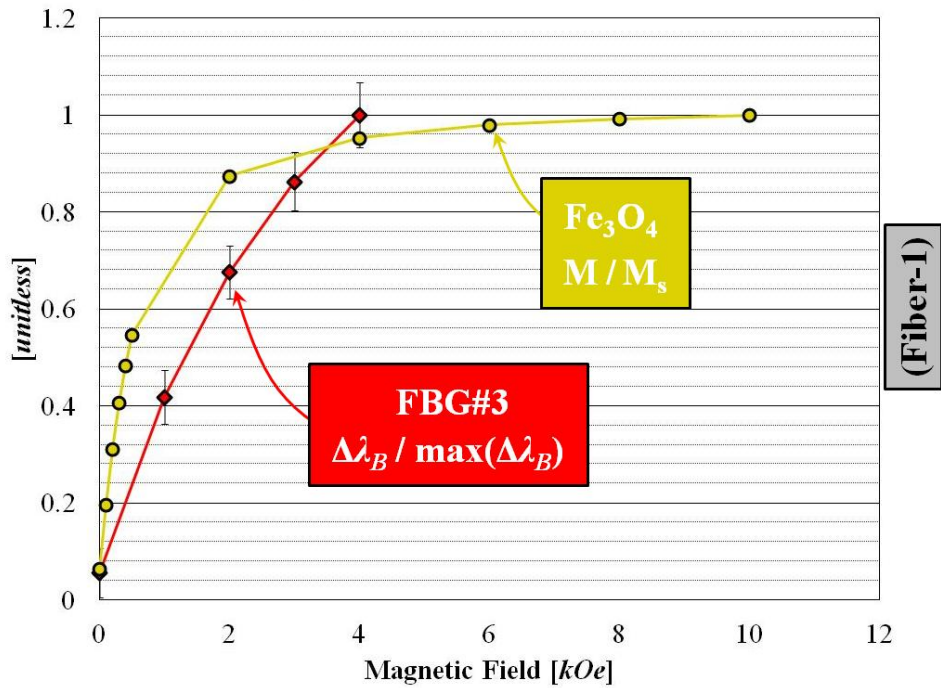


Figure 5-77: Normalized behavior of ferric oxide particles and of λ_B shifts in FBG#3 on Fiber-1 during the Magnetic Saturation test.

The rise in Fe_3O_4 data does not match that of the FBG#3 data. This is most likely because the temperature increase in FBG#3 is causing an exaggerated maximum $\Delta\lambda_B$; thus, causing the normalized FBG#3 data to be lower than if only magneto-optic effects were in play. This will be confirmed with a subsequent test using fields up to 8 kOe; however, the reflected wavelength spectra of FBG#3 during the magnetic field test will be shown first in Figure 5-78 below for analysis.

Fiber-1, FBG#3 – Reflected λ Spectrum – Magnetic Saturation Test

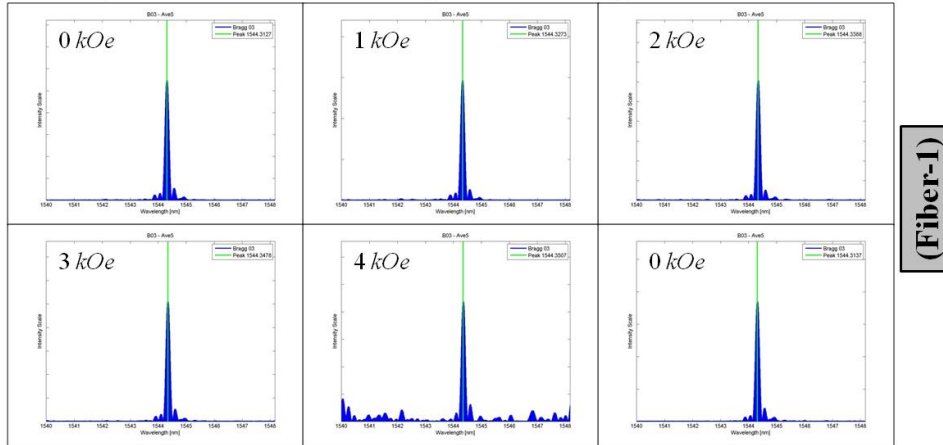


Figure 5-78: Reflected wavelength spectra of FBG#3 on Fiber-1 during the Magnetic Saturation test to evaluate how far the signal is above noise.

The reflection spectrum maintains its single peak response throughout the test. This is an excellent result indicating all of the previously described work developing a robust apparatus and consistent etching procedure to achieve a large signal to noise ratio has worked. This also strips any noise effects from contributing to the observed shifts in λ_B .

The results of the Magnetic Saturation test performed with fields up to 8 kOe are measured with the real-time centroid tracking method. The shifts in λ_B are shown in Figure 5-79 below. The vertical axis represents shifts in λ_B and horizontal axis represents time in minutes. The magnetic field is increased in increments of 1 kOe from 0 to 8 kOe and repeated twice. Points in time when the magnetic field is at 0, 1, 2, 4, and 8 kOe are identified for the first cycle. Blue and red data represent the results from FBG#2 and 3 respectively.

λ_B Shift During Magnetic Saturation Test

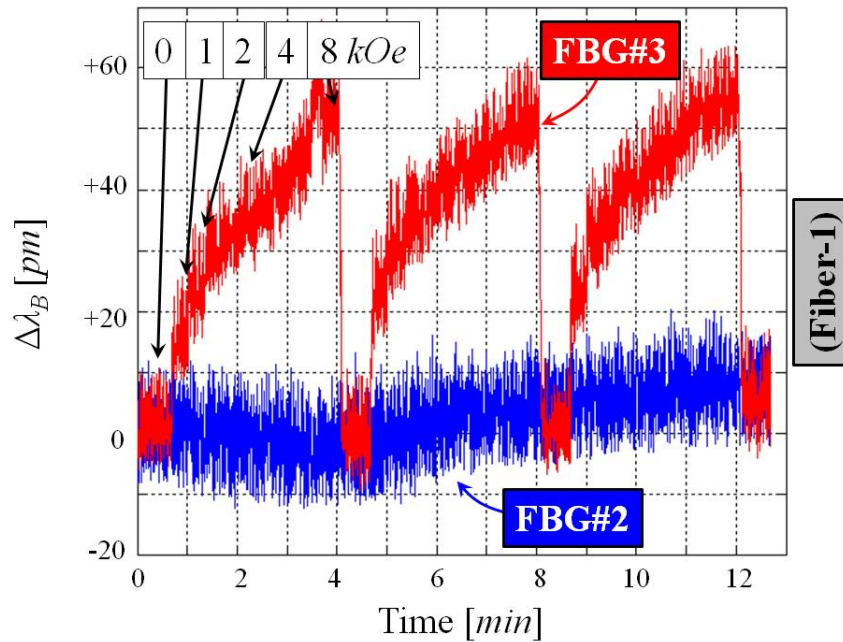


Figure 5-79: Real-time monitoring of the reflected wavelength shift of FBG#2 and #3 on Fiber-1 during the Magnetic Saturation test at higher magnetic field values.

A similar trend is seen compared to Figure 5-75 where the shift in λ_B for FBG#3 is ~ 40 pm at 4 kOe. When the field is increased to 8 kOe, λ_B continues to increase to ~ 55 pm rather than saturating, but the Fe_3O_4 characterization indicates that the magnetization of the ferric oxide has saturated well before the 8 kOe magnetic field is applied. Therefore, the continued increase in λ_B beyond the saturation field is most likely due to a temperature increase in FBG#3. This is partially corroborated with the slight increase over time in the response of FBG#2. Before any further testing could be completed on Fiber-1, the fiber broke due to the previously describe cracking in the glass vial used to hold the ferromagnetic particles around the apparatus.

Judging by the magnitude and shape of the response of FBG#3 in comparison to FBG#2 and #4, there seems to be a significant magneto-optic response in $\Delta\lambda_B$. However, due to the gradient in thermal environment and thermal response along the length of the fiber, the magnitude of the magneto-optic response relative to the thermal response cannot be quantified. This is because

FBG#2 and #4 cannot be adequately used as a control sensor. This necessitates the simultaneous testing of a thinned experimental fiber and a thinned control fiber which is carried out with Fiber-2 and 3.

5.5.5 Magnetic Field Test Results: Fiber-2 & 3

The results of applying an external magnetic field to Fiber-2 and 3 will be shown next. The shift in Bragg wavelength during the cooling process is presented first in Figure 5-80. The graph on the left plots data from Fiber-2 while the graph on the right plots data collected simultaneously for Fiber-3. The vertical axes represent shift in λ_B while the horizontal axes represent time. Blue and red data correspond to FBG#2 and #3 respectively.

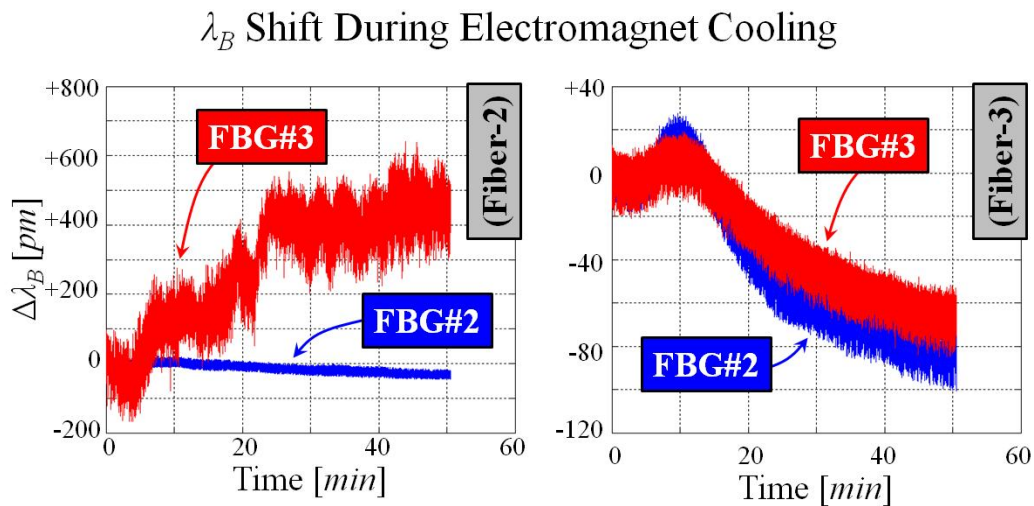


Figure 5-80: Shift in reflected wavelength for FBG#2 and #3 of Fiber-2 and -3 while the electromagnet test setup is being cooled.

All data exhibits the expected decrease in λ_B which levels off in time, indicating steady state is achieved with the exception of FBG#3 on Fiber-2. This FBG actually demonstrates an increase in reflected wavelength which is counterintuitive. Recall this is the experimental etched fiber thinned down to $7.5 \mu m$ in diameter. Therefore, it is important to obtain a reliable signal to demonstrate magneto-optic coupling. The reason for the stark contrast in behavior can be seen by looking at the length domain and the reflected wavelength spectra. The length domain of Fiber-2

and 3 are shown in the two graphs in Figure 5-81. Vertical axes represent reflection intensity and horizontal axes represent length. Each of the four FBGs along with the fiber start and end locations are identified.

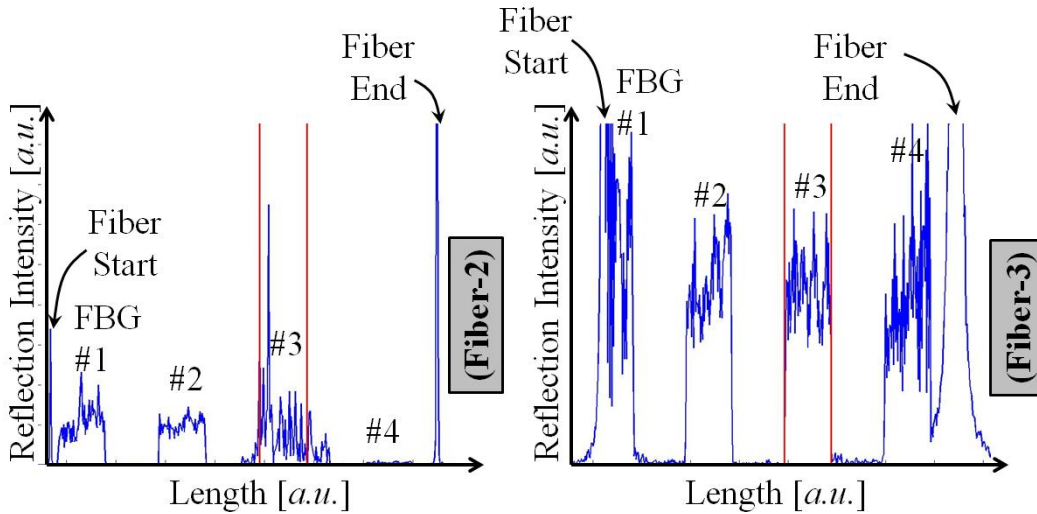


Figure 5-81: Length domain reflection signals of Fiber-2 and -3 to determine the influence of noise.

There is clearly a considerable amount of noise in FBG#3 of Fiber-2 in comparison with all the other FBGs. This is the result most likely of a slightly uneven etching process. The effects of this noise can be seen in the reflected wavelength spectra shown in Figure 5-82 below. The plots compare the reflection spectrum for FBG#3 on Fiber-2 and 3 before and after cooling.

Fiber-2 & 3, FBG#3 – Electromagnet Cooling

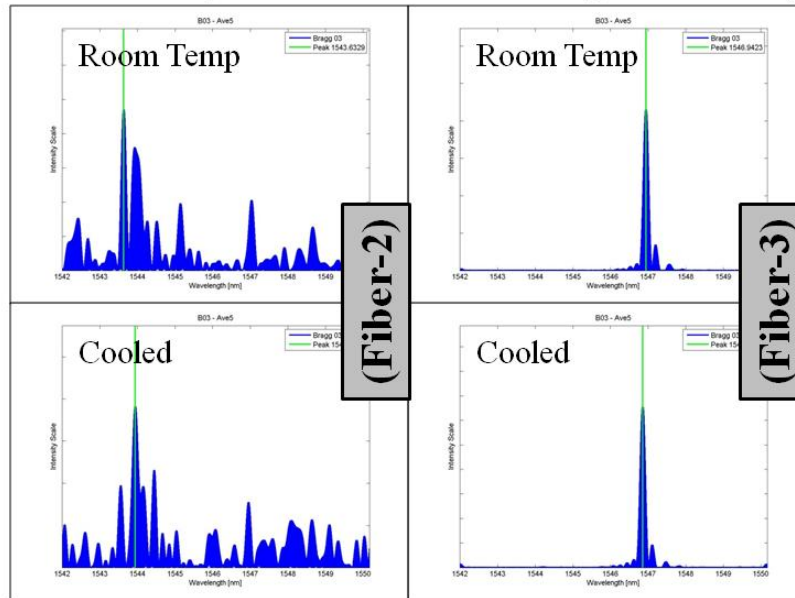


Figure 5-82: Reflected wavelength spectra of FBG#3 on Fiber-2 and -3 before and after cooling the electromagnet test setup.

FBG#3 in Fiber-3 exhibits a clean, single peak with very little noise. FBG#3 in Fiber-2, on the other hand, has considerable noise, corroborating the results seen in the length domain plot. In the “Room Temp” plot, the peak marked in green is simply due to noise which has randomly created a fluctuation in reflection intensity eclipsing the peak just to its right at a higher wavelength. By the time the fiber has cooled to steady state, this noise peak has subsided and the true reflection peak from the grating becomes dominant. Therefore, the positive shift observed during the cooling is representative of a lower-wavelength noise peak subsiding to allow the true peak at a higher wavelength to become dominant. If the true peak had been tracked the whole time rather than the centroid, the behavior would be similar to the other FBGs exhibiting the expected cooling response.

The conclusion from observing the cooling response of FBG#3 is that throughout this test, it is essential to make sure that any measured shift in λ_B in future magnetic testing is due to shifts in the reflected peak and not any noise behavior. This verification will be carried out by monitoring the reflected wavelength spectrum of FBG#3 throughout each test. It will be found that unlike in

the cooling portion of the test, the application of magnetic fields will result in consistent peak shapes and noise will not become a dominating factor.

The first magnetic test is the On/Off magnetic field test. The electromagnet will be switched on and off several times, alternating the field between 0 and 5 kOe. Each state is held for approximately one minute for data collection. Magneto-optic effects will be essentially instantaneous, but thermal effects will be much slower. Figure 5-83 plots the response of FBG#2-4 in both Fiber-2 (graph on the left) and Fiber-3 (graph on the right). Blue, red, and green data are labeled as representing FBG#2, 3, and 4 respectively. The vertical axis corresponds to shifts in λ_B while the horizontal axis indicates the state of the electromagnet (OFF or ON). Each data point represents the average of 5 measurements and the error bars represent the standard deviation of those measurements.

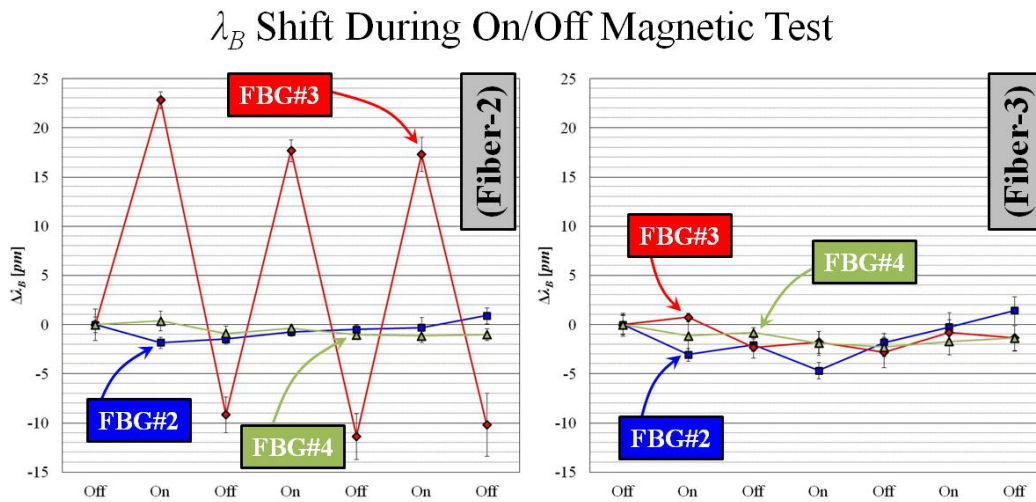


Figure 5-83: Shifts in reflected wavelength of FBG#2-4 on Fiber-2 and -3 calculated from peaks of the reflected wavelength spectra during the On/Off magnetic field test.

The results for FBG#3 in Fiber-2 are nearly the same as those in Fiber-1. After settling into the surrounding Fe_3O_4 particles during the first cycle, a consistent shift of approximately 27 pm is observed. The shift is seen to be consistent and recoverable. In contrast, every other FBG considered on both fibers is seen to have no discernable shift in λ_B . This also corresponds well

with the pattern observed in the Fiber-1 results. The difference here is that we now have a satisfactory control grating (FBG#3 on Fiber-3) which experiences a nearly identical thermal environment and is thinned to a diameter fairly close to that of the experiment grating (FBG#3 on Fiber-2). This verifies that the instantaneous magneto-optic effect was able to dominate during the ~1 minute while the magnetic field was applied but the thermal effects due to the large currents did not have time to influence the results. To verify that the response was not due to any noise effects, the reflected wavelength spectra of FBG#3 on Fiber-2 during three of the OFF and ON states are shown in Figure 5-84.

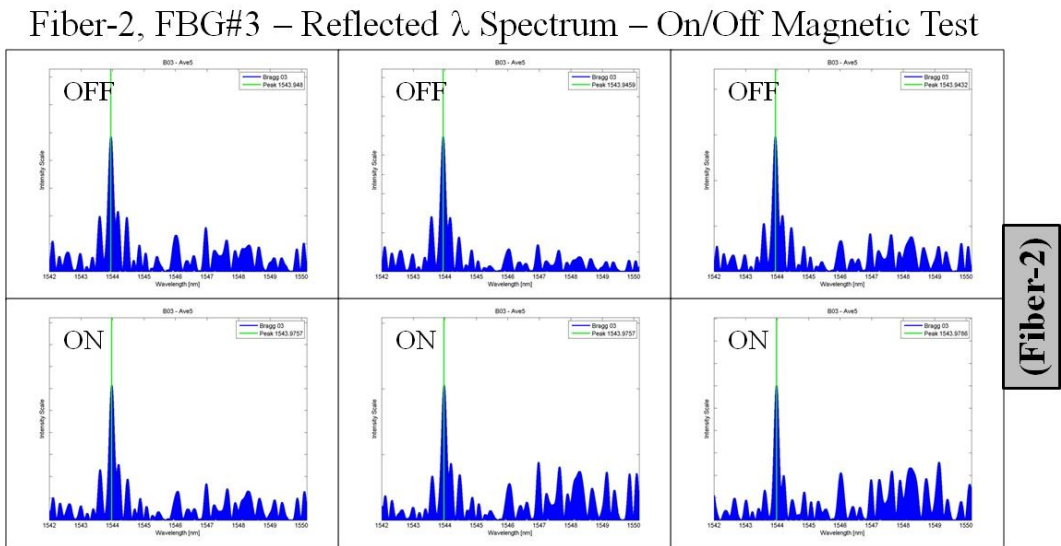


Figure 5-84: Reflected wavelength spectra of FBG#3 on Fiber-2 during the On/Off magnetic field test to evaluate how far the signal is above noise.

The noise is clearly more abundant than in FBG#3 in Fiber-1 as demonstrated in Figure 5-74; however, it is less than what was observed during the electromagnet’s cooling process shown in Figure 5-82. The shape of the dominant peak along with the position and height of many of the nearby noise peaks are seen to remain consistent throughout the test. This demonstrates in a much more conclusive manner than in Fiber-1 that FBG#3 in Fiber-2 is shifting entirely due to magneto-optic coupling except during the settling period.

The results continue with the measured wavelength shifts during a saturation magnetic field test. Figure 5-85 demonstrates the shift in reflected wavelength for FBG#3 and #4 in Fiber-2 and -3. Each magnetic field value (with the exception of the final, 0 *kOe* field) was held for sufficient time for the shifts to stabilize and the system to reach thermal equilibrium before measurements were taken. The vertical axis corresponds to shifts in λ_B and the horizontal axes indicate the magnetic field value. Each data point represents an average of 5 measurements and the error bars represent the standard deviation of those measurements.

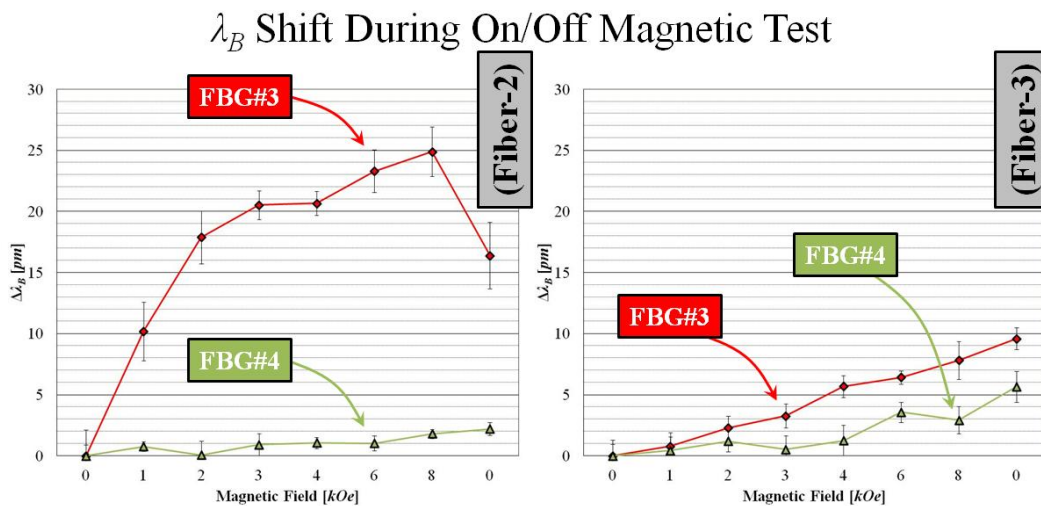


Figure 5-85: Shifts in reflected wavelength of FBG#2-4 on Fiber-2 and -3 calculated from peaks of the reflected wavelength spectra during the Magnetic Saturation test.

All of the gratings exhibit a nearly linear increase in reflected wavelength with the exception of the experiment FBG (FBG#3 in Fiber-2) which displays a nonlinear trend. The nonlinear result is similar to the behavior seen in Fiber-1 data shown in Figure 5-76 where the λ_B rapidly increases until it settles into a consistent linear increase rather than leveling off as would be expected with the magneto-optic effect. This time an adequate control fiber has been simultaneously tested for comparison. The purpose of displaying the data for FBG#4 of both Fiber-2 and -3 is to further validate the assumption that Fiber-3 experiences the same thermal environment as Fiber-2, thus cementing Fiber-3's status as an adequate control fiber.

Measurements were taken immediately after shutting off the 8 kOe field and are represented with the last data point for each FBG. This means that enough time passed for a magneto-optic effect to occur but not for the temperature to significantly change. The result is that every FBG experiences a positive shift in λ_B from the 8 kOe to 0 kOe field except for FBG#3 in Fiber-2. This indicates that the magneto-optic effect is influencing the observed shifts in λ_B for FBG whose evanescent field is exposed to the surrounding ferromagnetic particles.

Before using the control fiber is used to strip out the thermal influence in the experiment fiber's response, the reflected wavelength spectra of FBG#3 on Fiber-2 during the Magnetic Saturation test will be studied. Figure 5-86 below shows the spectra at various applied magnetic fields.

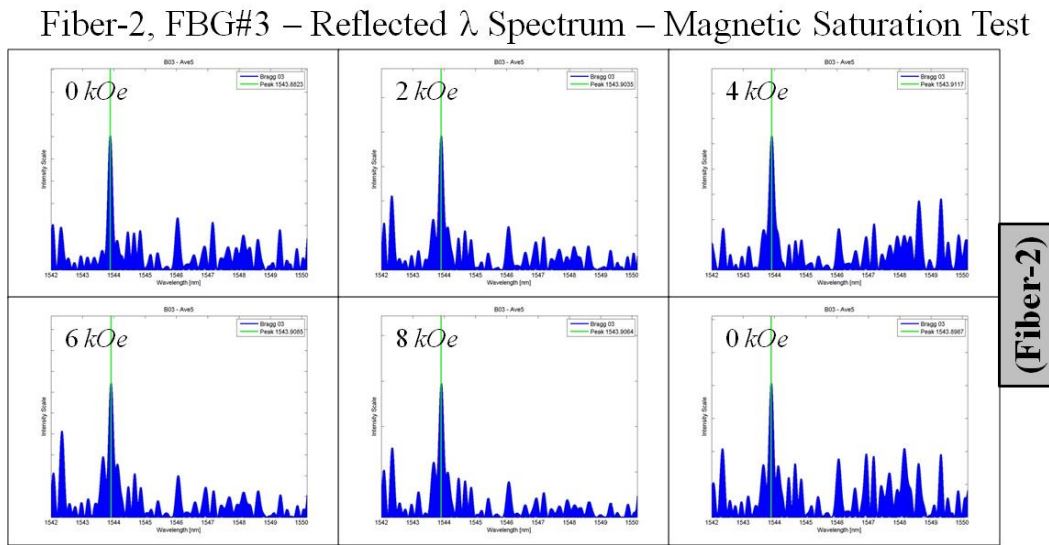


Figure 5-86: Reflected wavelength spectra of FBG#3 on Fiber-2 during the Magnetic Saturation test to evaluate how far the signal is above noise.

Just as in the On/Off test, the noise is large compared to the other FBGs but it is not large enough to influence the results. The peak keeps a consistent shape throughout the test and no peaks from noise are seen to be dominant or near enough to the true peak to sway the results. The shifts in λ_B will now be corrected to strip out the influence of changes in temperature by

subtracting the response of FBG#3 and #4 in Fiber-3 from that in Fiber-2. The results are shown in Figure 5-87 below.

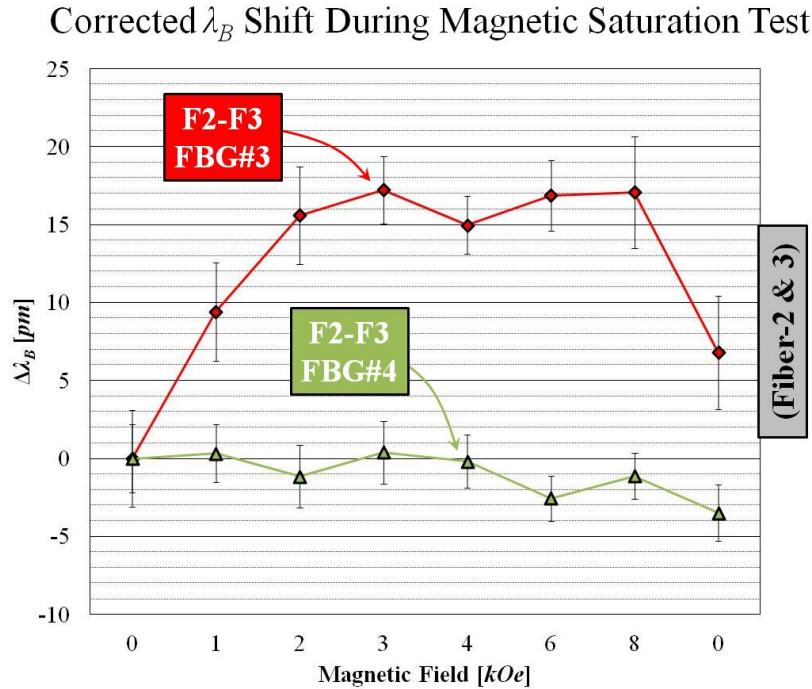


Figure 5-87: Shift in λ_B for FBG#3 and #4 in Fiber-2 corrected by subtracting the shifts measured in FBG#3 and #4 in Fiber-3.

After correcting for thermal effects, FBG#4 is seen to remain essentially stagnant throughout the entire test. FBG#3, on the other hand, increases rapidly before leveling off and essentially remaining flat for fields greater than 4 kOe. This behavior is in line with the saturation magnetization properties of the surrounding ferromagnetic particles. A comparison is made between the corrected response of FBG#3 in Fiber-2 and the iron oxide SQUID magnetization results by normalizing the two sets of data. The result is shown in Figure 5-88. The vertical axis represents a unitless scale for the two sets of data. The FBG#3 data is calculated by taking the corrected shifts in λ_B for FBG#3 in Figure 5-87 ($\Delta\lambda_B^{(2-3)}$) and dividing by the corrected shift at the maximum magnetic field value of 8 kOe ($\max(\Delta\lambda_B^{(2-3)})$). The magnetization (M) is normalized to the large-field saturation magnetization value (M_s).

Corrected $\Delta\lambda_B$ and Fe_3O_4 Magnetization Normalized

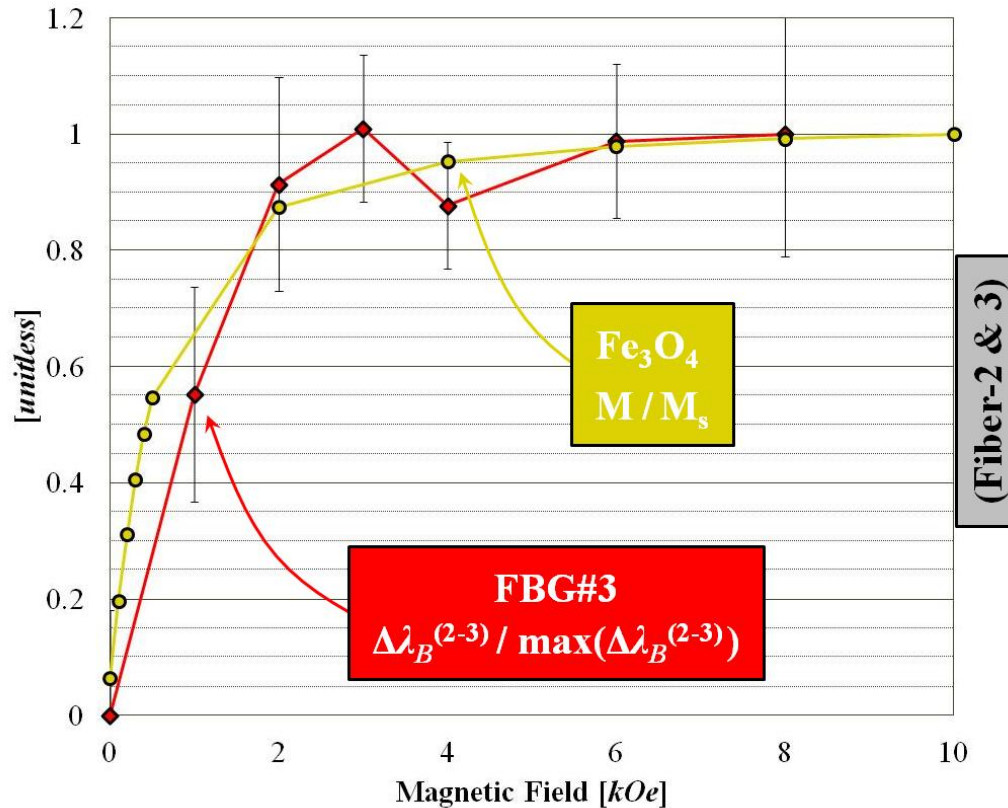


Figure 5-88: Normalized behavior of ferric oxide particles and of the corrected λ_B shifts in FBG#3 on Fiber-2 during the Magnetic Saturation test.

The behavior of the two sets of data is very similar. This result is better than what was found in Fiber-1 because in this set of data, thermal effects when the magnetic field is turned up to high values is accounted for with the control FBG and filtered out of the results. The nonlinear increase in λ_B occurs at a similar rate and levels off in the 3-4 *kOe* range. This conclusively demonstrates that a magneto-optic coupling has been achieved in the FBG.

5.5.6 Concluding Remarks

This concludes the experimental results section. Three fibers were etched using the designed apparatus with the evanescent field of two thinned FBGs able to interact with the surrounding material and one thinned FBG unable to interact because it was barely too thick. The etch

evaluation was carried out to help determine that the etching process was indeed successful in that the chosen FBGs had enough sensitivity to the IOR of the surrounding material and the signal did not degrade too much from the fabrication process. The final step presented before testing was to characterize the size and magnetization response of the ferromagnetic particles used to surround the thinned FBG sensors.

The magnetic field test results demonstrate the desired magneto-optic coupling in a FBG via evanescent field interaction. The shift in Bragg wavelength and the reflected wavelength spectra were reported in thinned FBGs during the initial cooling of the electromagnet test setup and during the two magnetic field tests. It was seen that once the apparatus settled into a stable position within the ferromagnetic nanoparticles, consistent, recoverable shifts in reflected wavelength were observed. The results of Fiber-1 indicated that magneto-optic coupling took place, but without a satisfactory control sensor, the magnitude of the magnetic effect relative to thermal effects could not be quantified. This issue was resolved with simultaneous testing of Fiber-2 and -3.

5.6 Summary

The goal set forth at the beginning of this chapter to demonstrate a magneto-optic effect in a FBG using the FOID system has been met. This enhances the potential of the optical measurement system by expanding the capabilities and in turn the range of applications for FBG sensors. Additionally, the demonstration of a fundamental magneto-optic interaction with a Bragg grating is quite new for the field of fiber optic magnetic sensors. The magneto-optic coupling in a FBG was predicted by rigorously developing the theoretical equations governing the behavior of the optical fiber and was carried out experimentally replacing most of the cladding layer with a magnetically active material. The result was an interaction between the evanescent field of light propagating down the fiber optic and the changing optical properties of the surrounding ferric oxide due to the magnetization being altered by an external magnetic field.

These results offer a proof of concept demonstrating the potential for future utilization of FBGs as magnetic field sensors. However, there is still a large amount of work which must be performed in order to increase the sensitivity of the FBG to magnetic fields, optimize the apparatus design to maintain a rugged structural sensor mount, and minimize the loss in order to obtain a reliable sensor signal which can be multiplexed for distributed magnetic field sensing. Such undertakings will be described in more detail in the future work section of the next chapter.

CHAPTER 6:

CONCLUSION

6.1 Summary

The purpose of this research was to develop the strain sensing abilities of embedded FBGs in addition to designing and fabricating novel FBG sensors for smart structure applications. This coincided with the goal of expanding the capabilities and the potential applications for the FOID system designed and created by NASA Dryden Flight Research Center. Background and motivation was provided in Chapter 1 to establish worthwhile applications of the technology under development.

In Chapter 2, a foundation was laid out for understanding the behavior of optical fiber Bragg gratings and what mechanisms would be used to couple external phenomena such as strain and magnetic field to a shift in the FBG's reflected wavelength. This included forays into Maxwell's equations, photoelasticity, thermo-optics, and magneto-optics. The purpose of this material was to provide the reader with a solid background in the behavior of FBGs to understand how subsequent chapters would branch out from the established foundation.

The aim of Chapter 3 was to tackle the strain sensing aspects of this research by studying the response of the FBG once embedded in a composite material and subsequently loaded. The extensive body of FBG literature which pertains to this research was then described and followed with a description of the embedment process. Next, experimental results were shown relating measured shifts in λ_B in the FBG to composite host strain stemming from curing residual strains and external loading. Specific results were then compared to a finite element analysis study to gain further understanding of the observed behavior. The lessons to take away from this portion

of the research pertain to the validity of the uniaxial assumption in FBG strain sensing. Under circumstances where the two reflected wavelengths move apart or closer together, it was demonstrated that the strain state of the optical fiber could not be resolved. Additionally, the difficulty was established in relating the sensor's strain to that in the host when the strain transfer is complete in the longitudinal direction of the fiber yet severely reduced transverse to the fiber. These mountainous barriers made it necessary to demonstrate embedment and loading configurations which allow for the FBG to behave as a uniaxial strain sensor. A few embedment configurations were fabricated and tested to experimentally demonstrate what types of loading would maintain the uniaxial assumptions and which would invalidate it. Additionally, the effects of cross-ply cracking on the sensor response were studied and it was found that some cracks cause nonuniform strain along the length of a FBG while other cracks completely dissociate the fiber from host transverse strains. When dissociated from the host transverse strains, the applicability of the FBG as a uniaxial strain sensor was augmented.

In Chapter 4, thin film NiTi and Terfenol-D were deposited onto a FBG to replace the inert polyimide coating with an active material that would couple various phenomena to the FBG reflection signal. Previously published methods for linking fiber optic sensors to external phenomena with active materials was described and followed with the fabrication procedure and the process for evaluating the film deposition. This was followed with a thermal cycle of the NiTi coated FBG to demonstrate the hysteresis associated with the NiTi ferroelastic properties. Subsequently, a magnetic field test was performed on the Terfenol-D coated FBG in an unsuccessful attempt to demonstrate the magnetostrictive properties of the coating. This work demonstrated an interesting method for linking external phenomena to the FBG reflection signal in order offer possible options for expanding the capabilities of the FOID system.

Chapter 5 implemented the concept of expanding the FOID system capabilities by creating a magnetically sensitive whose mechanism would be entirely different from that described in Chapter 4. Rather than using strain as the middle step in the coupling between magnetism and optical signals, the sensor was redesigned to have the magnetic field directly alter the optical

properties of the waveguide material. This direct coupling was explored theoretically by expanding the 2-layer fiber analyzed in Chapter 2 to a 3-layer fiber. The theoretical equations aided in determining future designs of the sensor as well as whether or not current designs would be sensitive enough to elicit a measurable response in the FBG. The various iterations in sensor designs were described as was the pre-experimental characterization steps for determining the success of the sensor fabrication process. The results of the different magnetic field tests were then shown in order to demonstrate that the desired magneto-optic coupling in the FBG had been achieved. This work represented a novel sensor design which expands the potential applications of the FOID system by allowing the FBGs to become sensitive to magnetic fields.

6.2 Future Work

This work represents one of the many steps along the road to developing current FBG sensors and designing new ones. In the strain-sensing branch of this work, NASA is currently performing experiments on composite overwrapped pressure vessels with embedded FBGs. This represents the implementation of lessons learned from the coupon-level experiments described in this research into more complicated composite structures which are used in flight applications. This is most likely one of many future experiments involving the FOID system and embedded FBGs utilized as uniaxial strain sensors.

In addition to experimental developments, future work in the analytical realm of strain sensing FBGs involves the development of algorithms which study the reflected wavelength spectra of embedded FBGs. In the research presented here, the decision of whether or not the FBG is behaving as a uniaxial strain sensor was very fragile in that any change in TSD was taken to completely nullify a FBG strain measurement. The aforementioned algorithms aim to create a metric whereby the introduction of birefringence represents a quantifiable error in uniaxial strain measurements rather than invalidation. Additionally, the algorithms will develop methods for

identifying chirping seen in a reflected wavelength spectrum which is indicative of cracks or some form of imminent failure.

As for the thin film sensors described in Chapter 4, the two biggest issues are lack of sensitivity due to the small volume fraction of the thin film coating and fragility of the sensor (i.e. easily broken when bent) caused by the film deposition process. In the NiTi coated FBG, a slight hysteresis was observed but it was not large. In the Terfenol-D coated FBG, no response was observed. The straightforward method for fixing this issue is to increase the volume fraction of the thin film coating either by increasing the thickness of the coating or by decreasing the diameter of the glass fiber. The decrease in fiber diameter can be attained either by changing the drawing process used by the fiber manufacturer or by etching the fiber as was done in Chapter 5. Sources of the increased fragility of the optical fiber due to the deposition process should be identified and must either be eliminated or compensated for, perhaps by attaching the coated FBG to a support structure.

The biggest issue with the FBG magnetometer fabricated in Chapter 5 is the lack of sensitivity. If the FBG is to perceive changes in Earth's magnetic field, the sensor must be responsive to magnetic field changes on the order of 1 Oe and below. Drastic changes must be made to the current sensor design because the sensitivity is on the order of $k\text{Oe}$. Despite the gap being several orders of magnitude, there is plenty of room for improvement in the sensor design as learned from experimental tests and from theoretical analysis. For instance, it was found that manipulating the properties of the fiber core alter the wave propagation characteristics much more heavily than the cladding and surrounding material. Thus, if the core of the fiber is replaced with a magnetically active material rather than the cladding, sensitivity should see a large change for the better. Additionally, the type of magnetic material chosen can be altered. While Fe_3O_4 particles were chosen in this research, other ferromagnetic materials may elicit a stronger magneto-optic coupling. Examples of alternative materials which could be explored are other forms of ferric oxide such as Fe_2O_3 , chromium dioxide, or barium-based magnetic materials known as BaM (BaFeO) materials. Loss in the fiber optic signal caused noise in the measured λ_B


value to increase. This loss was due in part to the opaque nature of the ferromagnetic material used and in part by the etching process. Choosing a single-phase or composite magneto-optic material with more favorable loss properties and further development of a cleaner etching process will help push the sensitivity to better values. Lastly, it was found in the theoretical section of Chapter 5 that higher order modes are more sensitive to changes in fiber properties. Thus, the sensitivity can be improved if the measurements system or the optical fiber itself were altered so that the λ_B of higher order modes can be tracked.

There is a tremendous amount of promise in utilizing FBGs and the FOID system developed by NASA Dryden Flight Research Center for creating smart structures. This research demonstrates the potential of FBG sensors and a few of the many avenues of research that can be taken with this technology.

CHAPTER 7:

APPENDIX

7.1 Appendix A: Luna FBG Specifications



LUNA

*Ideas
taking
flight*

2851 Commerce Street Blacksburg, VA 24060
 voice: (540) 552-5128 / fax: (540) 552-0760
 email: solutions@lunainnovations.com
 www.lunainnovations.com

Distributed Sensing System Sensor Array Specification


Description
 The Luna Innovations Distributed Sensing System (DSS) Sensor Array incorporates embedded fiber Bragg grating (FBG) sensors in a very compact, flexible and light weight assembly with an industry standard fiber optic interface. Using Luna's unique DSS interrogation system these sensor cables allow high accuracy high spatial density measurements of temperature and strain in a wide variety of environments and applications. The system can accommodate thousands of sensors per cable assembly making real time simultaneous measurements.

Features

- 1000 sensors, 1 fiber.
- Wide operational temperature range
- High sensor spatial density
- Ultra light and flexible
- Low per sensor cost
- Easy installation (embeddable)

Applications

- Harsh environment sensing
- High density strain measurements
- High density thermal measurements



Optical Specifications

Sensor Array Fiber:	Min.	Typ.	Max.	Units
Numerical Aperture ($\pm 0.01^{\circ}$)		0.2		°
Cutoff Wavelength		1290		nm
Attenuation * (per 360° loop)	@ 1/2" radius	0.00		dB
	@ 1/4" radius	< 0.05		dB
	@ 1/8" radius	1.2		dB
	@ 1/16" radius	6.0		dB
Tensile strength		> 50		kpsi
Apparent strain / °C		9.2		µε
Fiber diameter		141		µm
Fiber cladding diameter		127		nm
Fiber core diameter		5.4		nm
Buffer Thickness		14		µm
Buffer type	Polyimide			
Material	Silica cladding, Ge-doped silica core			

* Measured by wrapping one loop of fiber around an object with stated radius and then measuring the loss relative to no bend.

Luna Innovations, Inc. / (540) 552-5128 / www.lunainnovations.com
Document Revision LI06/1.2
1

Figure 7-1: Page 1 of the FBG specifications sheet.

Optical Specifications (CONTINUED)

Bragg Gratings:

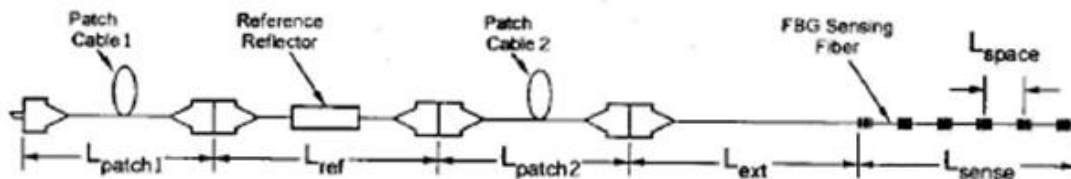
	Min	Typ	Max	Units
Length		5.0		mm
Spacing (center-to-center)		1.0		cm
Center wavelength		1546		nm
Bandwidth		< 0.5		nm
Reflectivity (per grating)		-34		dB

Absolute Maximum Ratings

		Min	Typ	Max	Units
Storage Temperature:	Sensor fiber *	-200		300	°C
Operating Temperature:	Sensor fiber *	-40		300	°C
	Reference reflector	-40		100	°C
	Patch cable	-40		100	°C
Strain				20,000	µε

* Ratings are for bare sensing fiber alone. For temperature sensing applications when using some type of sensing fiber sheathing temperature ratings will be reduced (see Luna DSS Application Notes).

Sensor Cable Configuration



L_{patch1}	Length of patch cable between DSS measurement instrument and reference reflector
L_{ref}	Length of reference reflector cable
L_{patch2}	Length of patch cable between reference reflector and sensor array assembly
L_{ext}	Length of sensor array lead-in fiber
L_{sense}	Length of sensor array sensing fiber
L_{space}	Spacing between sensors on sensing fiber (center-to-center)

Ordering Information

Patch Cable 1 (L_{patch1})

Fiber Optic Patch Cable with 900µm jacket

Part Number: Patch-900-X

Fiber Optic Patch Cable with braided steel jacket

Part Number: Patch-steel-X

Fiber Optic Patch Cable with 3mm jacket

Part Number: Patch-3mm-X

X = Length of patch cable 1. Standard lengths are 1, 3, 5, 10 & 30 meters. The patch cable between the DSS measurement instrument and the reference reflector can be up to 2 kilometers in length.

Reference Reflector (L_{ref})

Reference Reflector

Part Number: Reflector-001

The typical reference reflector cable is less than 1/2 meter in total length. The reflectivity of the reference reflector is -14 dB return.

Figure 7-2: Page 2 of the FBG specifications sheet.

Ordering Information (CONTINUED)

Patch Cable 2 ($L_{patch\ 2}$)

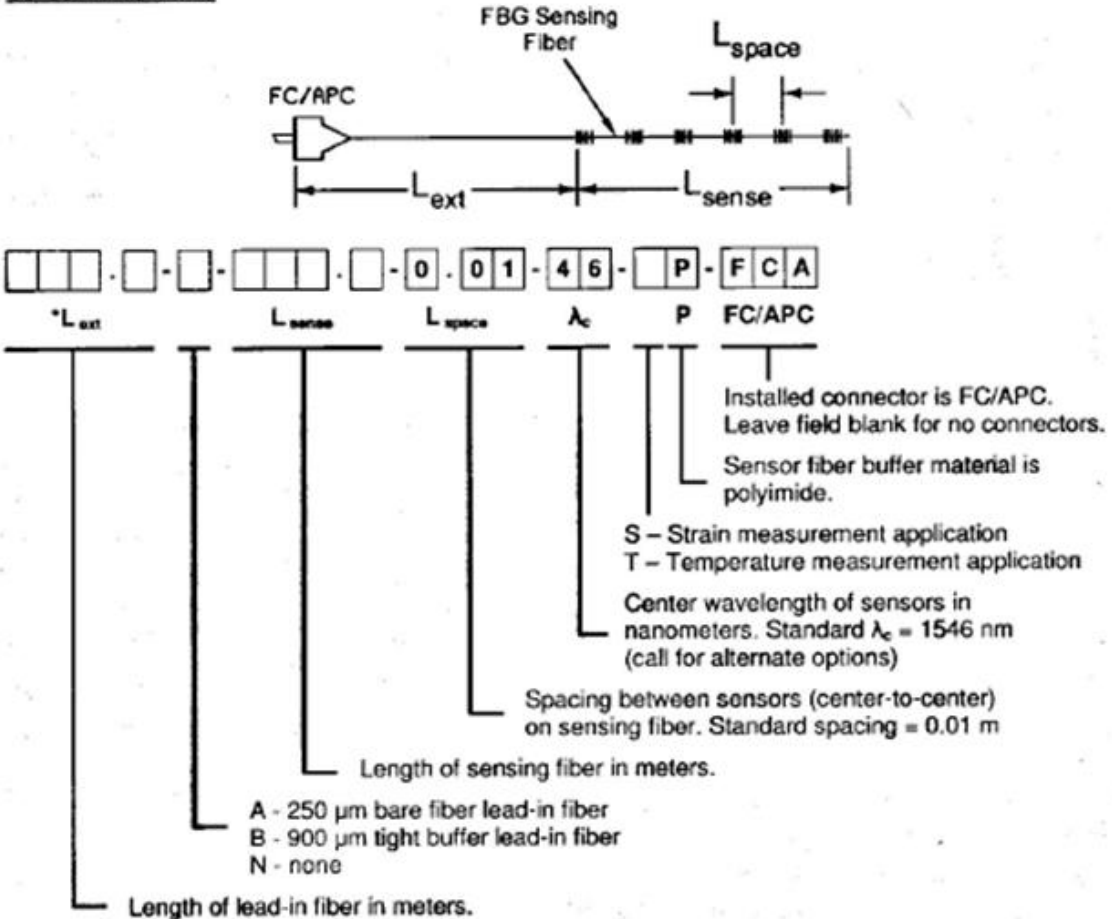
Fiber Optic Patch Cable with 900 μ m jacket
 Fiber Optic Patch Cable with braided steel jacket
 Fiber Optic Patch Cable with 3mm jacket

Part Number: Patch-900-X
 Part Number: Patch-steel-X
 Part Number: Patch-3mm-X

X = Length of patch cable 2. Standard lengths are 1, 3, 5 & 10 meters.

* The choice of the length of the input patch cable ($L_{patch\ 2}$) must be made in conjunction with the choice of the length of the sensor array lead-in fiber (L_{ext}). **BOTH** of the following length constraints **MUST** be met for proper system operation: $L_{patch\ 2} + L_{ext} + L_{sense} \leq 19$ meters **AND** $L_{sense} < L_{patch\ 2} + L_{ext}$

Sensor Array Cable



Note: For technical assistance such as determining the applicability of particular sensor configurations to your system consult the Luna Innovations DSS Application Notes or email questions to solutions@lunainnovations.com.

Information furnished by Luna Innovations is believed to be reliable, accurate and is subject to change without notice. No risk or liability is assumed for use of the products and applications. Luna Innovations reserves the right to change without notice the design, specifications, form, fit or function relating to products herein. Copyright 2006 Luna Innovations. All rights reserved.

Figure 7-3: Page 3 of the FBG specifications sheet.

7.2 Appendix B: Hexcel Composite Material Properties

7.2.1 AS4 Carbon Fiber Properties



Hexcel AS4 carbon fiber is a continuous, high strength, high strain, PAN based fiber available in 3,000 (3K), 6,000 (6K) and 12,000 (12K) filament count tows. The fiber has been surface treated and can be sized to improve its interlaminar shear properties, handling characteristics, and structural properties, and is suggested for use in weaving, prepregging, filament winding, pultrusion, and molding compounds. Sizing compatible with various resin systems are available to improve handling characteristics and structural properties.

Typical Fiber Properties	U.S. Units	SI Units
Tensile strength	620,000 psi	4,278 MPa
Tensile modulus		
Chord 8000-1000	39.1 x 10 ³ psi	228 GPa
Ultimate elongation ^{a)}	1.87%	1.87%
Carbon content	94.0%	94.0%
Density	0.0646 lb/in ³	1.79 g/cm ³
Specific heat		
at 167°F (75°C)	0.22 Btu/lb, °F	0.22 cal/g, °C
at 347°F (175°C)	0.27 Btu/lb, °F	0.27 cal/g, °C
Electrical resistance, 12K	9.6 ohms/ft	0.32 ohm/cm
Electrical resistivity, 12K	5.09 x 10 ⁴ ohm-ft	1.53 x 10 ⁻⁴ ohm-cm

a) Calculated from tow test data.

Typical Epoxy Composite Properties (at Room Temperature)	U.S. Units	SI Units
Tensile strength	322,000 psi	2,221 MPa
Tensile modulus	20.5 x 10 ³ psi	141 GPa
Flexural strength	250,000 psi	1,725 MPa
Flexural modulus	18.5 x 10 ³ psi	128 GPa
Short-beam shear strength	18,000 psi	124 MPa
Fiber volume	62%	62%

Yarn/Tow Characteristics	U.S. Units	SI Units
Filament diameter	0.281 mil	7.1 microns
Filament shape	Round	Round
Twist	None	None
Tow cross-sectional area		
3K	1.82 x 10 ⁻⁴ in ²	0.12 mm ²
6K	3.70 x 10 ⁻⁴ in ²	0.24 mm ²
12K	7.43 x 10 ⁻⁴ in ²	0.48 mm ²
Approximate yield		
3K	7,100 ft/lb	4.76 m/g
6K	3,500 ft/lb	2.34 m/g
12K	1,750 ft/lb	1.17 m/g
Weight/length		
3K	11.8 x 10 ⁻² lb/in	0.210 g/m
6K	23.9 x 10 ⁻² lb/in	0.427 g/m
12K	48.0 x 10 ⁻² lb/in	0.858 g/m

Carbon Fiber Certification

This carbon fiber is manufactured to Hexcel aerospace specification HS-CP-5000. A copy of this specification is available upon request. A Certificate of Analysis will be provided with each shipment.



Figure 7-4: Page 1 of the AS4 carbon fibers material properties.

Available Sizing

Epoxy compatible sizes for prepregging, filament winding, braiding, and weaving are available on request.

Other resin compatible sizes are also available to satisfy customer needs.

Packaging

A standard package of 12K fiber contains 8 lb; 3K fiber and 6K fiber packages contain 4 lb; other package sizes are available on request. The fiber is wound on a 3 in. ID by 11 in. long cardboard cylinder and overwrapped with plastic film.

Safety Information

Obtain, read, and understand the Material Safety Data Sheet (MSDS) before use of this product.

Important

Hexcel Corporation believes, in good faith, that the technical data and other information provided herein is materially accurate as of the date this document is prepared. Hexcel reserves the right to modify such information at any time. The performance values in this data sheet are considered representative but do not and should not constitute specification minima. The only obligations of Hexcel, including warranties, if any, will be set forth in a contract signed by Hexcel or in Hexcel's then current standard Terms and Conditions of Sale as set forth on the back of Hexcel's Order Acknowledgement.

© Copyright Hexcel Corporation March 2002
 ® Magnamite, Hexcel and the Hexcel logos are registered trademarks of Hexcel Corporation, Stamford, Connecticut

For more Information

Hexcel Composites is a leading worldwide supplier of composite materials to aerospace and other demanding industries. Our comprehensive product range includes:

- Carbon Fiber
- Carbon, glass, aramid and hybrid prepregs
- Honeycomb cones
- Structural film adhesives
- Honeycomb sandwich panels
- Special process honeycombs
- RTM materials

For further information, please contact your nearest sales office, or visit our website at www.hexcelcomposites.com

<p>Australia Suite 2, 86 Grimshaw Street Geelong, Victoria 3088 Tel: 61 3 9432 7100 Fax: 61 3 9432 7200</p>	<p>France ZI La Plaine, B.P.27 Dagneux 01121 Montlual CEDEX Tel: 33 (0)4 72 25 20 27 Fax: 33 (0)4 72 25 27 30</p>	<p>Spain Bruselas, 10 - 10 Polig. Ind. "Ciudad de Parla" 28060 Parla, Madrid Tel: 34 91 604 4900 Fax: 34 91 608 4914</p>	<p>USA 42705 Grand River Suite 201 Novi, MI 48375 Tel: 1 248 344 8668 Fax: 1 248 305 9780</p>
<p>Austria Industriestrasse 1, A-4061 Rasching Tel: 43 (0)7229 7720 Fax: 43 (0)7229 772299</p>	<p>Germany Am Wiespark 1-3 61373 München Tel: 49 89 743 5250 Fax: 49 89 743 52520</p>	<p>United Kingdom Duxford, Cambridge CB2 4QD Tel: 44 (0)1223 853141 Fax: 44 (0)1223 859808</p>	<p>USA 2350 Airport Freeway, Suite 550 Bedford, TX 76022-5027 Tel: 1 817 315 3659 Fax: 1 817 571 8609</p>
<p>Belgium Rue Trois Bourgeois, 54 B-4040 Walfersegem Tel: 32 87 307 4111 Fax: 32 87 862 896</p>	<p>Italy Via San Cristoforo, 44 21047 Saronno (VA) Tel: 39 02 95705052 Fax: 39 02 9500609</p>	<p>USA 11711 Dublin Blvd. Dublin, CA 94568-2832 Tel: 1 925 551 4000 Fax: 1 925 928 9202</p>	<p>USA 10310 NE 80th Street, Suite 102 Redmond, WA 98052 Tel: 1 425 558 4400 Fax: 1 425 861 5847</p>
<p>China Room B707, Yin Hai Bldg. 250 Cao Xi Rd Shanghai 200233 Tel: 86 21 6483 674-1/2 Fax: 86 21 6483 6744</p>	<p>Japan - Joint Venture DIC • Hexcel Limited Room 603, San-tsu-Mori Bldg. 2-22-1 Nishi • Shimizu-shi Minato-Ku, Tokyo 105 Tel: 81 3 5401 0271 Fax: 81 3 5401 0270</p>	<p>USA 101 East Ridge Drive, Suite 100 Danbury, CT 06810 Tel: 1 203 798 8311 Fax: 1 203 798 8101</p>	<p>USA P.O. Box 18748 Salt Lake City, UT 84119-0748 Tel: 1 801 987 0568 1 801 252 2400 Fax: 1 801 508 8103</p>

Figure 7-5: Page 2 of the AS4 carbon fibers material properties.

7.2.2 3501-6 Epoxy Matrix Properties

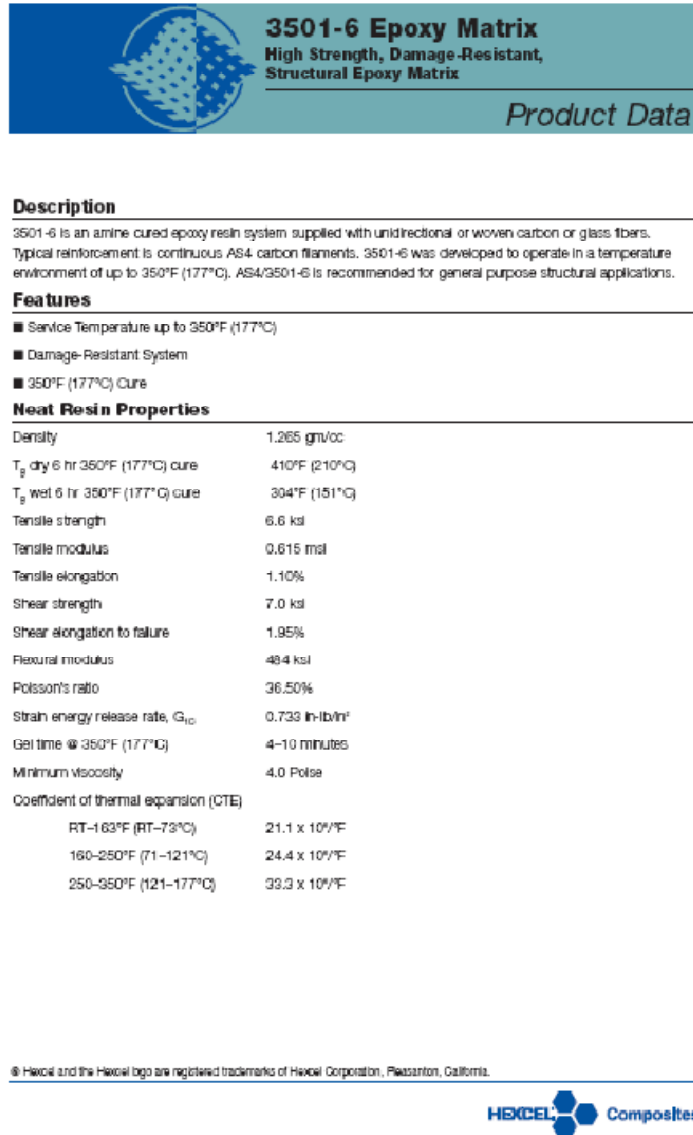


Figure 7-6: Page 1 of the 3501-6 epoxy matrix material properties.



3501-6 Epoxy Matrix *Product Data*

Physical Properties

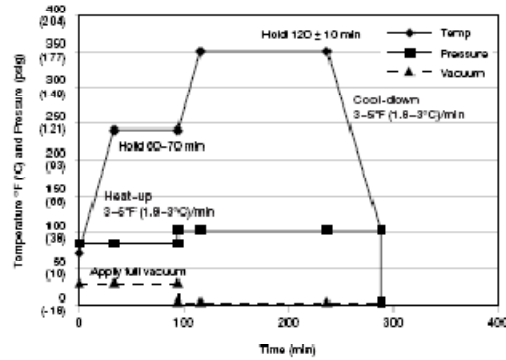
		AS4	A185C8W	A193P	A280-5H	A370-8H
Prepreg	% Resin content	32-45	32-45	32-45	32-45	32-45
	Areal weight, GSM	150	185	193	280	370
	% Volatiles	1.5 max	1.5 max	1.5 max	1.5 max	1.5 max
	% Flow	12-32	12-32	12-32	12-32	12-32
	Gel time @ 350°F (177°C)	6-12	6-12	6-12	6-12	6-12
Laminate	Cured thickness per ply (in)	5.2 mils	7.5 mils	7.7 mils	10.0 mils	14.0 mils
	Fiber volume	62%	58%	58%	58%	58%

Mechanical Properties

Property	Temp °F (°C)	Condition	AS4	A185C8W	A193P	A280-5H	A370-8H
0° Tensile strength, ksi	RT	Dry	310.0	120.0	110.0	120.0	120.0
0° Tensile modulus, msi	RT	Dry	20.5	10.0	10.0	10.0	10.0
0° Compression strength, ksi	RT	Dry	250.0	120.0	125.0	130.0	125.0
0° Flexural strength, ksi	RT	Dry	250.0	10.0	9.0	9.0	9.0
0° Flexural strength, ksi	350 (177)	Dry	185.0	-	-	150.0	130.0
0° Flexural modulus, msi	RT	Dry	18.5	-	-	-	-
0° Flexural modulus, msi	350 (177)	Dry	18.0	-	-	10.0	9.0
Short beam shear, psi	RT	Dry	18,500	-	-	-	-
Short beam shear, psi	350 (177)	Dry	9,500	12,000	12,000	12,000	12,000

Figure 7-7: Page 2 of the 3501-6 epoxy matrix material properties.

Cure Cycle



Cure Procedure

Auto-clave

1. Apply full vacuum and 85 psig pressure.
2. Heat at 3-5°F (1.8-3°C)/minute to 240°F (116°C).
3. Hold at 240°F (116°C) for 60-70 minutes.
4. Raise pressure to 100 psig; vent vacuum.
5. Raise temperature to 350°F (177°C) at 3-5°F (1.8-3°C)/minute.
6. Hold at 350°F (177°C) for 120 ± 10 minutes.
7. Cool at 3-5°F (1.8-3°C) to 100°F (38°C) and vent pressure.

Note: Straight-up cure cycle may be used.

Figure 7-8: Page 3 of the 3501-6 epoxy matrix material properties.



3501-6 Epoxy Matrix *Product Data*

Handling and Safety Precautions

Hexcel recommends that customers observe established precautions for handling resins and the fibrous materials. Operators working with this product should wear clean, impervious gloves to reduce the possibility of skin contact and to prevent contamination of the material.

Material Safety Data Sheets (MSDS) have been prepared for all Hexcel products and are available to company safety officers on request from your nearest Hexcel Sales Office.

Storage

3501-6 prepreg should be sealed in a polyethylene bag and refrigerated, preferably below 32°F (0°C). Following removal from refrigerated source, allow the prepreg to reach room temperature before opening the polyethylene bag to prevent moisture condensation.

Shelf Life

12 months at 0°F (-18°C)

4 months at 40°F (4°C)

10 days at 70°F (21°C)

Shipping

Prepreg is generally shipped in a sealed polyethylene bag in refrigerated transportation or in containers with dry ice.

Disposal of Scrap

Disposal of the material should be in a landfill in accordance with state and federal regulations.

Important

Hexcel Corporation makes no warranty, whether expressed or implied, including warranties of merchantability or of fitness for a particular purpose. Under no circumstances shall Hexcel Corporation be liable for incidental, consequential or other damages arising out of a claim from alleged negligence, breach of warranty, strict liability or any other theory through the use or handling of this product or the inability to use the product. The sole liability of Hexcel Corporation for any claims arising out of the manufacture, use, or sale of its products shall be for the replacement or the quantity of this product which has proven to not substantially comply with the data presented in this bulletin. Users should make their own assessment of the suitability of any product for the purposes required. The above supercedes any provision in your company's forms, letters, or other documents.

For technical assistance, applications and procedures, or further information please contact:

**Administrative Office and
Customer Service Center**
5704 West Las Posas Blvd.
P.O. Box 8181
Pleasanton, CA 94566-8181
Tel: (925) 947-4600
Fax: (925) 734-4070

Hexcel Composites
Duxford, Cambridge CB2 4JD
United Kingdom
Tel: 44 (0) 1223 833444
Fax: 44 (0) 1223 833838

Sales Offices
2350 Airport Frey, Suite 550
Forth Worth, TX 76120-8077
Tel: (817) 315-3030
Fax: (817) 571-8820

Sales Offices (continued)
101 East Ridge Drive, Suite 102
Danbury CT 06810-4140
Tel: (203) 706-8311
Fax: (203) 706-8168

11410 Northeast 122nd Way, Suite 320
Kirkland, WA 98034-6027
Tel: (425) 821-7411
Fax: (425) 823-6437

Printed on recycled paper.
Copyright © 1996 - Hexcel - All Rights Reserved.

B-089

Figure 7-9: Page 4 of the 3501-6 epoxy matrix material properties.

7.3 Appendix C: MATLAB Program for Rotation Matrices

```
clear all

%% Enter the angle of rotation for the composite ply of interest
% For example, 0, +pi/4, -pi/4, pi/2
Theta = -pi/4;

%% Calculate the 6x6 rotation matrix symbolically in VOIGT and COMSOL
syms A11 A12 A13 A21 A22 A23 A31 A32 A33;
A = [A11 A12 A13; A21 A22 A23; A31 A32 A33];
At = conj(A');
Vo = [1 1; 2 2; 3 3; 2 3; 1 3; 1 2]; % Voigt notation
Co = [1 1; 2 2; 3 3; 1 2; 2 3; 1 3]; % Comsol notation
for ii = 1:6
    i=Vo(ii,1); j=Vo(ii,2);
    k=Co(ii,1); l=Co(ii,2);
    E=zeros(3,3); F=zeros(3,3);
    if i==j
        E(i,j)=1; F(k,l)=1;
    else
        E(i,j)=1; E(j,i)=1;
        F(k,l)=1; F(l,k)=1;
    end
    Rv = A*E*At; Rc = A*F*At;
    for jj=1:6
        RV(jj,ii) = Rv(Vo(jj,1),Vo(jj,2));
        RC(jj,ii) = Rc(Co(jj,1),Co(jj,2));
    end
end
```

```

end

%% Calculate the elasticity matrix in the 1-2-3 coordinate system
E1 = 138.51e9; E2 = 7.48e9;
v12 = 0.26; v23 = 0.4; %=vm
G12 = 3.88e9;

%Compliance matrix using VOIGT notation
SV = zeros(6,6);
SV(1,1:3) = [1/E1 -v12/E1 -v12/E1];
SV(2,1:3) = [-v12/E1 1/E2 -v23/E2];
SV(3,1:3) = [-v12/E1 -v23/E2 1/E2];
SV(4,4) = 2*(1+v23)/E2;
SV(5,5) = 1/G12;
SV(6,6) = 1/G12;

%Compliance matrix using COMSOL notation
SC = zeros(6,6);
SC(1,1:3) = [1/E1 -v12/E1 -v12/E1];
SC(2,1:3) = [-v12/E1 1/E2 -v23/E2];
SC(3,1:3) = [-v12/E1 -v23/E2 1/E2];
SC(4,4) = 1/G12;
SC(5,5) = 2*(1+v23)/E2;
SC(6,6) = 1/G12;

%Elasticity Matrix
DV = SV^-1;
DC = SC^-1;

%% Create 3x3 rotation matrix to evaluate 6x6 rotation matrix.
%Create 3x3 rotation matrix for 2D and for 3D
for Dim = 2:3

```



```

if Dim==2
    %2D: Rotate about 2-dir
    AD = [cos(Theta) 0 sin(Theta); 0 1 0; -sin(Theta) 0 cos(Theta)];
elseif Dim==3
    %3D: Rotate about 3-dir
    AD = [cos(Theta) -sin(Theta) 0; sin(Theta) cos(Theta) 0; 0 0 1];
end

A11=AD(1,1); A12=AD(1,2); A13=AD(1,3);
A21=AD(2,1); A22=AD(2,2); A23=AD(2,3);
A31=AD(3,1); A32=AD(3,2); A33=AD(3,3);
if Dim==2
    RV2 = eval(RV); RC2 = eval(RC);
elseif Dim==3
    RV3 = eval(RV); RC3 = eval(RC);
end

end

DVrot2 = RV2*DV*RV2';
DVrot3 = RV3*DV*RV3';
DCrot2 = RC2*DC*RC2';
DCrot3 = RC3*DC*RC3';

```

7.4 Appendix D: Creation of the 8x8 $[\Omega]$ Components

7.4.1 Electric and Magnetic field components

Firstly, the φ - and z -components of the electric and magnetic fields for the three layers are explicitly stated below:

Layer 1 ($r \leq a$):

$$\begin{aligned}
 k_1 > \beta &\Rightarrow h^2 = k_1^2 - \beta^2 = n_1^2 k_0^2 - \beta^2 \\
 E_\varphi(r, \varphi, z, t) &= \left[c_1 \left(\frac{\beta l}{h^2 r} J_l(hr) \right) + c_2 \left(\frac{i\omega\mu_1}{h} J_l'(hr) \right) \right] e^{i(\omega t + l\varphi - \beta z)} \\
 E_z(r, \varphi, z, t) &= c_1 J_l(hr) e^{i(\omega t + l\varphi - \beta z)} \\
 H_\varphi(r, \varphi, z, t) &= \left[c_1 \left(-\frac{i\omega e_1}{h} J_l'(hr) \right) + c_2 \left(\frac{\beta l}{h^2 r} J_l(hr) \right) \right] e^{i(\omega t + l\varphi - \beta z)} \\
 H_z(r, \varphi, z, t) &= c_2 J_l(hr) e^{i(\omega t + l\varphi - \beta z)}
 \end{aligned} \tag{7.1}$$

Layer 2 ($b \geq r \geq a$):

$$\begin{aligned}
 k_2 > \beta &\Rightarrow p^2 = k_2^2 - \beta^2 = n_2^2 k_0^2 - \beta^2 \\
 E_\varphi(r, \varphi, z, t) &= \left[c_3 \left(\frac{\beta l}{p^2 r} J_l(pr) \right) + c_4 \left(\frac{\beta l}{p^2 r} Y_l(pr) \right) \dots \right. \\
 &\quad \left. \dots + c_5 \left(\frac{i\omega\mu_2}{p} J_l'(pr) \right) + c_6 \left(\frac{i\omega\mu_2}{p} Y_l'(pr) \right) \right] e^{i(\omega t + l\varphi - \beta z)} \\
 E_z(r, \varphi, z, t) &= \left[c_3 J_l(pr) + c_4 Y_l(pr) \right] e^{i(\omega t + l\varphi - \beta z)} \\
 H_\varphi(r, \varphi, z, t) &= \left[c_3 \left(-\frac{i\omega e_2}{p} J_l'(pr) \right) + c_4 \left(-\frac{i\omega e_2}{p} Y_l'(pr) \right) \dots \right. \\
 &\quad \left. \dots + c_5 \left(\frac{\beta l}{p^2 r} J_l(pr) \right) + c_6 \left(\frac{\beta l}{p^2 r} Y_l(pr) \right) \right] e^{i(\omega t + l\varphi - \beta z)} \\
 H_z(r, \varphi, z, t) &= \left[c_5 J_l(pr) + c_6 Y_l(pr) \right] e^{i(\omega t + l\varphi - \beta z)}
 \end{aligned} \tag{7.2}$$

$$\begin{aligned}
\beta > k_2 &\Rightarrow p^2 = \beta^2 - k_2^2 = \beta^2 - n_2^2 k_0^2 \\
E_\varphi(r, \varphi, z, t) &= \left[c_3 \left(-\frac{\beta l}{p^2 r} I_l(pr) \right) + c_4 \left(-\frac{\beta l}{p^2 r} K_l(pr) \right) \dots \right. \\
&\quad \left. \dots + c_5 \left(-\frac{i\omega\mu_2}{p} I_l'(pr) \right) + c_6 \left(-\frac{i\omega\mu_2}{p} K_l'(pr) \right) \right] e^{i(\omega t + l\varphi - \beta z)} \\
E_z(r, \varphi, z, t) &= [c_3 I_l(pr) + c_4 K_l(pr)] e^{i(\omega t + l\varphi - \beta z)} \\
H_\varphi(r, \varphi, z, t) &= \left[c_3 \left(\frac{i\omega e_2}{p} I_l'(pr) \right) + c_4 \left(\frac{i\omega e_2}{p} K_l'(pr) \right) \dots \right. \\
&\quad \left. \dots + c_5 \left(-\frac{\beta l}{p^2 r} I_l(pr) \right) + c_6 \left(-\frac{\beta l}{p^2 r} K_l(pr) \right) \right] e^{i(\omega t + l\varphi - \beta z)} \\
H_z(r, \varphi, z, t) &= [c_5 I_l(pr) + c_6 K_l(pr)] e^{i(\omega t + l\varphi - \beta z)} \\
(7.3)
\end{aligned}$$

Layer 3 ($r \geq b$):

$$\begin{aligned}
\beta > k_3 &\Rightarrow q^2 = \beta^2 - k_3^2 = \beta^2 - n_3^2 k_0^2 \\
E_\varphi(r, \varphi, z, t) &= \left[c_7 \left(-\frac{\beta l}{q^2 r} K_l(qr) \right) + c_8 \left(-\frac{i\omega\mu_3}{q} K_l'(qr) \right) \right] e^{i(\omega t + l\varphi - \beta z)} \\
E_z(r, \varphi, z, t) &= c_7 K_l(qr) e^{i(\omega t + l\varphi - \beta z)} \\
H_\varphi(r, \varphi, z, t) &= \left[c_7 \left(\frac{i\omega e_3}{q} K_l'(qr) \right) + c_8 \left(-\frac{\beta l}{q^2 r} K_l(qr) \right) \right] e^{i(\omega t + l\varphi - \beta z)} \\
H_z(r, \varphi, z, t) &= c_8 K_l(qr) e^{i(\omega t + l\varphi - \beta z)} \\
(7.4)
\end{aligned}$$

7.4.2 Boundary Conditions

Next, each of the components listed above will be bound as continuous across the interfaces at $r = a$ and at $r = b$. There are two different possibilities to the explicit forms of the boundary conditions. One in the case that $\beta > k_2$ and the other case that $k_2 > \beta$. The results of applying the boundary conditions in the former case is shown first.

$$\boxed{\beta > k_2} \tag{7.5}$$

$$\boxed{r = a} \tag{7.6}$$

$$\begin{aligned}
\underline{E_\varphi(a^-, \varphi, z, t) = E_\varphi(a^+, \varphi, z, t)} \\
c_1 \left[\frac{\beta l}{h^2 a} J_l(ha) \right] + c_2 \left[\frac{i\omega\mu_1}{h} J_l'(ha) \right] \dots \\
\dots = c_3 \left[\frac{-\beta l}{p^2 a} I_l(pa) \right] + c_4 \left[\frac{-\beta l}{p^2 a} K_l(pa) \right] + c_5 \left[\frac{-i\omega\mu_2}{p} I_l'(pa) \right] + c_6 \left[\frac{-i\omega\mu_2}{p} K_l'(pa) \right]
\end{aligned}
\tag{7.7}$$

$$\begin{aligned}
\underline{E_z(a^-, \varphi, z, t) = E_z(a^+, \varphi, z, t)} \\
c_1 [J_l(ha)] = c_3 [I_l(pa)] + c_4 [K_l(pa)]
\end{aligned}
\tag{7.8}$$

$$\begin{aligned}
\underline{H_\varphi(a^-, \varphi, z, t) = H_\varphi(a^+, \varphi, z, t)} \\
c_1 \left[\frac{-i\omega e_1}{h} J_l'(ha) \right] + c_2 \left[\frac{\beta l}{h^2 a} J_l(ha) \right] \dots \\
\dots = c_3 \left[\frac{i\omega e_2}{p} I_l'(pa) \right] + c_4 \left[\frac{i\omega e_2}{p} K_l'(pa) \right] + c_5 \left[\frac{-\beta l}{p^2 a} I_l(pa) \right] + c_6 \left[\frac{-\beta l}{p^2 a} K_l(pa) \right]
\end{aligned}
\tag{7.9}$$

$$\begin{aligned}
H_z(a^-, \varphi, z, t) = H_z(a^+, \varphi, z, t) \\
c_2 [J_l(ha)] = c_5 [I_l(pa)] + c_6 [K_l(pa)]
\end{aligned}
\tag{7.10}$$

$$\boxed{r = b}
\tag{7.11}$$

$$\begin{aligned}
\underline{E_\varphi(b^-, \varphi, z, t) = E_\varphi(b^+, \varphi, z, t)} \\
c_3 \left[\frac{-\beta l}{p^2 b} I_l(pb) \right] + c_4 \left[\frac{-\beta l}{p^2 b} K_l(pb) \right] + c_5 \left[\frac{-i\omega\mu_2}{p} I_l'(pb) \right] + c_6 \left[\frac{-i\omega\mu_2}{p} K_l'(pb) \right] \dots \tag{7.12} \\
\dots = c_7 \left[\frac{-\beta l}{q^2 b} K_l(qb) \right] + c_8 \left[\frac{-i\omega\mu_3}{q} K_l'(qb) \right]
\end{aligned}$$

$$\begin{aligned}
\underline{E_z(b^-, \varphi, z, t) = E_z(b^+, \varphi, z, t)} \\
c_3 [I_l(pb)] + c_4 [K_l(pb)] = c_7 [K_l(qb)]
\end{aligned}
\tag{7.13}$$

$$\begin{aligned}
H_\varphi(b^-, \varphi, z, t) &= H_\varphi(b^+, \varphi, z, t) \\
c_3 \left[\frac{i\omega e_2}{p} I'_l(pb) \right] + c_4 \left[\frac{i\omega e_2}{p} K'_l(pb) \right] + c_5 \left[\frac{-\beta l}{p^2 b} I_l(pb) \right] + c_6 \left[\frac{-\beta l}{p^2 b} K_l(pb) \right] \dots & \quad (7.14) \\
\dots = c_7 \left[\frac{i\omega e_3}{q} K'_l(qb) \right] + c_8 \left[\frac{-\beta l}{q^2 b} K_l(qb) \right] &
\end{aligned}$$

$$\begin{aligned}
H_z(b^-, \varphi, z, t) &= H_z(b^+, \varphi, z, t) \\
c_5 [I_l(pb)] + c_6 [K_l(pb)] &= c_8 [K_l(qb)] \quad (7.15)
\end{aligned}$$

Next, the boundary conditions under the second case will be stated.

$$\boxed{k_2 > \beta} \quad (7.16)$$

$$\boxed{r = a} \quad (7.17)$$

$$\begin{aligned}
E_\varphi(a^-, \varphi, z, t) &= E_\varphi(a^+, \varphi, z, t) \\
c_1 \left[\frac{\beta l}{h^2 a} J_l(ha) \right] + c_2 \left[\frac{i\omega \mu_1}{h} J'_l(ha) \right] \dots & \\
\dots = c_3 \left[\frac{\beta l}{p^2 a} J_l(pa) \right] + c_4 \left[\frac{\beta l}{p^2 a} Y_l(pa) \right] + c_5 \left[\frac{i\omega \mu_2}{p} J'_l(pa) \right] + c_6 \left[\frac{i\omega \mu_2}{p} Y'_l(pa) \right] & \\
(7.18) &
\end{aligned}$$

$$\begin{aligned}
E_z(a^-, \varphi, z, t) &= E_z(a^+, \varphi, z, t) \\
c_1 [J_l(ha)] &= c_3 [J_l(pa)] + c_4 [Y_l(pa)] \quad (7.19)
\end{aligned}$$

$$\begin{aligned}
H_\varphi(a^-, \varphi, z, t) &= H_\varphi(a^+, \varphi, z, t) \\
c_1 \left[\frac{-i\omega e_1}{h} J'_l(ha) \right] + c_2 \left[\frac{\beta l}{h^2 a} J_l(ha) \right] \dots & \\
\dots = c_3 \left[\frac{-i\omega e_2}{p} J'_l(pa) \right] + c_4 \left[\frac{-i\omega e_2}{p} Y'_l(pa) \right] + c_5 \left[\frac{\beta l}{p^2 a} J_l(pa) \right] + c_6 \left[\frac{\beta l}{p^2 a} Y_l(pa) \right] & \\
(7.20) &
\end{aligned}$$

$$\begin{aligned}
H_z(a^-, \varphi, z, t) &= H_z(a^+, \varphi, z, t) \\
c_2 [J_l(ha)] &= c_5 [J_l(pa)] + c_6 [Y_l(pa)] \quad (7.21)
\end{aligned}$$

$$\boxed{r = b} \quad (7.22)$$

$$\begin{aligned} \underline{E_\varphi(b^-, \varphi, z, t) = E_\varphi(b^+, \varphi, z, t)} \\ c_3 \left[\frac{\beta l}{p^2 b} J_l(pb) \right] + c_4 \left[\frac{\beta l}{p^2 b} Y_l(pb) \right] + c_5 \left[\frac{i\omega\mu_2}{p} J_l'(pb) \right] + c_6 \left[\frac{i\omega\mu_2}{p} Y_l'(pb) \right] \dots \\ \dots = c_7 \left[\frac{-\beta l}{q^2 b} K_l(qb) \right] + c_8 \left[\frac{-i\omega\mu_3}{q} K_l'(qb) \right] \end{aligned} \quad (7.23)$$

$$\begin{aligned} \underline{E_z(b^-, \varphi, z, t) = E_z(b^+, \varphi, z, t)} \\ c_3 [J_l(pb)] + c_4 [Y_l(pb)] = c_7 [K_l(qb)] \end{aligned} \quad (7.24)$$

$$\begin{aligned} \underline{H_\varphi(b^-, \varphi, z, t) = H_\varphi(b^+, \varphi, z, t)} \\ c_3 \left[\frac{-i\omega e_2}{p} J_l'(pb) \right] + c_4 \left[\frac{-i\omega e_2}{p} Y_l'(pb) \right] + c_5 \left[\frac{\beta l}{p^2 b} J_l(pb) \right] + c_6 \left[\frac{\beta l}{p^2 b} Y_l(pb) \right] \dots \\ \dots = c_7 \left[\frac{i\omega e_3}{q} K_l'(qb) \right] + c_8 \left[\frac{-\beta l}{q^2 b} K_l(qb) \right] \end{aligned} \quad (7.25)$$

$$\begin{aligned} \underline{H_z(b^-, \varphi, z, t) = H_z(b^+, \varphi, z, t)} \\ c_5 [J_l(pb)] + c_6 [Y_l(pb)] = c_8 [K_l(qb)] \end{aligned} \quad (7.26)$$

7.4.3 Matrix Assembly

The boundary conditions can be collected into a matrix equation in the following form:

$$[\Omega_{ij}] \{c_i\} = 0 \quad (7.27)$$

$$\boxed{\beta > k_2} \quad (7.28)$$

$$\begin{bmatrix} \Omega_{11} & \Omega_{12} & \Omega_{13} & \Omega_{14} \\ \Omega_{21} & \Omega_{22} & \Omega_{23} & \Omega_{24} \\ \Omega_{31} & \Omega_{32} & \Omega_{33} & \Omega_{34} \\ \Omega_{41} & \Omega_{42} & \Omega_{43} & \Omega_{44} \end{bmatrix} = \begin{bmatrix} \frac{\beta l}{h^2 a} J_1(ha) & \frac{i\omega\mu_1}{h} J_1'(ha) & \frac{\beta l}{p^2 a} I_1(pa) & \frac{\beta l}{p^2 a} K_1(pa) \\ J_1(ha) & 0 & -I_1(pa) & -K_1(pa) \\ \frac{-i\omega e_1}{h} J_1'(ha) & \frac{\beta l}{h^2 a} J_1(ha) & \frac{-i\omega e_2}{p} I_1'(pa) & \frac{-i\omega e_2}{p} K_1'(pa) \\ 0 & J_1(ha) & 0 & 0 \end{bmatrix} \quad (7.29)$$

$$\begin{bmatrix} \Omega_{15} & \Omega_{16} & \Omega_{17} & \Omega_{18} \\ \Omega_{25} & \Omega_{26} & \Omega_{27} & \Omega_{28} \\ \Omega_{35} & \Omega_{36} & \Omega_{37} & \Omega_{38} \\ \Omega_{45} & \Omega_{46} & \Omega_{47} & \Omega_{48} \end{bmatrix} = \begin{bmatrix} \frac{i\omega\mu_2}{p} I_1'(pa) & \frac{i\omega\mu_2}{p} K_1'(pa) & 0 & 0 \\ 0 & 0 & 0 & 0 \\ \frac{\beta l}{p^2 a} I_1(pa) & \frac{\beta l}{p^2 a} K_1(pa) & 0 & 0 \\ -I_1(pa) & -K_1(pa) & 0 & 0 \end{bmatrix} \quad (7.30)$$

$$\begin{bmatrix} \Omega_{51} & \Omega_{52} & \Omega_{53} & \Omega_{54} \\ \Omega_{61} & \Omega_{62} & \Omega_{63} & \Omega_{64} \\ \Omega_{71} & \Omega_{72} & \Omega_{73} & \Omega_{74} \\ \Omega_{81} & \Omega_{82} & \Omega_{83} & \Omega_{84} \end{bmatrix} = \begin{bmatrix} 0 & 0 & -\frac{\beta l}{p^2 b} I_1(pb) & -\frac{\beta l}{p^2 b} K_1(pb) \\ 0 & 0 & I_1(pb) & K_1(pb) \\ 0 & 0 & \frac{i\omega e_2}{p} I_1'(pb) & \frac{i\omega e_2}{p} K_1'(pb) \\ 0 & 0 & 0 & 0 \end{bmatrix} \quad (7.31)$$

$$\begin{bmatrix} \Omega_{55} & \Omega_{56} & \Omega_{57} & \Omega_{58} \\ \Omega_{65} & \Omega_{66} & \Omega_{67} & \Omega_{68} \\ \Omega_{75} & \Omega_{76} & \Omega_{77} & \Omega_{78} \\ \Omega_{85} & \Omega_{86} & \Omega_{87} & \Omega_{88} \end{bmatrix} = \begin{bmatrix} \frac{-i\omega\mu_2}{p} I_1'(pb) & \frac{-i\omega\mu_2}{p} K_1'(pb) & \frac{\beta l}{q^2 b} K_1(qb) & \frac{i\omega\mu_3}{q} K_1'(qb) \\ 0 & 0 & -K_1(qb) & 0 \\ \frac{-\beta l}{p^2 b} I_1(pb) & \frac{-\beta l}{p^2 b} K_1(pb) & \frac{-i\omega e_3}{q} K_1'(qb) & \frac{\beta l}{q^2 b} K_1(qb) \\ I_1(pb) & K_1(pb) & 0 & -K_1(qb) \end{bmatrix} \quad (7.32)$$

$$\boxed{k_2 > \beta} \quad (7.33)$$

$$\begin{bmatrix} \Omega_{11} & \Omega_{12} & \Omega_{13} & \Omega_{14} \\ \Omega_{21} & \Omega_{22} & \Omega_{23} & \Omega_{24} \\ \Omega_{31} & \Omega_{32} & \Omega_{33} & \Omega_{34} \\ \Omega_{41} & \Omega_{42} & \Omega_{43} & \Omega_{44} \end{bmatrix} = \begin{bmatrix} \frac{\beta l}{h^2 a} J_1(ha) & \frac{i\omega\mu_1}{h} J_1'(ha) & \frac{-\beta l}{p^2 a} J_1(pa) & \frac{-\beta l}{p^2 a} Y_1(pa) \\ J_1(ha) & 0 & -J_1(pa) & -Y_1(pa) \\ \frac{-i\omega e_1}{h} J_1'(ha) & \frac{\beta l}{h^2 a} J_1(ha) & \frac{i\omega e_2}{p} J_1'(pa) & \frac{i\omega e_2}{p} Y_1'(pa) \\ 0 & J_1(ha) & 0 & 0 \end{bmatrix} \quad (7.34)$$

$$\begin{bmatrix} \Omega_{15} & \Omega_{16} & \Omega_{17} & \Omega_{18} \\ \Omega_{25} & \Omega_{26} & \Omega_{27} & \Omega_{28} \\ \Omega_{35} & \Omega_{36} & \Omega_{37} & \Omega_{38} \\ \Omega_{45} & \Omega_{46} & \Omega_{47} & \Omega_{48} \end{bmatrix} = \begin{bmatrix} \frac{-i\omega\mu_2}{p} J_1'(pa) & \frac{-i\omega\mu_2}{p} Y_1'(pa) & 0 & 0 \\ 0 & 0 & 0 & 0 \\ \frac{-\beta l}{p^2 a} J_1(pa) & \frac{-\beta l}{p^2 a} Y_1(pa) & 0 & 0 \\ -J_1(pa) & -Y_1(pa) & 0 & 0 \end{bmatrix} \quad (7.35)$$

$$\begin{bmatrix} \Omega_{51} & \Omega_{52} & \Omega_{53} & \Omega_{54} \\ \Omega_{61} & \Omega_{62} & \Omega_{63} & \Omega_{64} \\ \Omega_{71} & \Omega_{72} & \Omega_{73} & \Omega_{74} \\ \Omega_{81} & \Omega_{82} & \Omega_{83} & \Omega_{84} \end{bmatrix} = \begin{bmatrix} 0 & 0 & \frac{\beta l}{p^2 b} J_1(pb) & \frac{\beta l}{p^2 b} Y_1(pb) \\ 0 & 0 & J_1(pb) & Y_1(pb) \\ 0 & 0 & \frac{-i\omega e_2}{p} J_1'(pb) & \frac{-i\omega e_2}{p} Y_1'(pb) \\ 0 & 0 & 0 & 0 \end{bmatrix} \quad (7.36)$$

$$\begin{bmatrix} \Omega_{55} & \Omega_{56} & \Omega_{57} & \Omega_{58} \\ \Omega_{65} & \Omega_{66} & \Omega_{67} & \Omega_{68} \\ \Omega_{75} & \Omega_{76} & \Omega_{77} & \Omega_{78} \\ \Omega_{85} & \Omega_{86} & \Omega_{87} & \Omega_{88} \end{bmatrix} = \begin{bmatrix} \frac{i\omega\mu_2}{p} J_1'(pb) & \frac{i\omega\mu_2}{p} Y_1'(pb) & \frac{\beta l}{q^2 b} K_1(qb) & \frac{i\omega\mu_3}{q} K_1'(qb) \\ 0 & 0 & -K_1(qb) & 0 \\ \frac{\beta l}{p^2 b} J_1(pb) & \frac{\beta l}{p^2 b} Y_1(pb) & \frac{-i\omega e_3}{q} K_1'(qb) & \frac{\beta l}{q^2 b} K_1(qb) \\ J_1(pb) & Y_1(pb) & 0 & -K_1(qb) \end{bmatrix} \quad (7.37)$$

Despite the number of zero-entries in the 8x8 Ω matrix, performing a determinant results in over 300 terms! Rather than explicitly writing this out, a numerical calculation will be performed.

CHAPTER 8:

LIST OF REFERENCES

- [1] T. E. Noll, J. M. Brown, M. E. Perez-Davis *et al.*, *Investigation of the helios prototype aircraft mishap*, NASA Internal Report, 2004.
- [2] R. M. Measures, *Structural monitoring with fiber optic technology*: Academic, 2001.
- [3] N. Hiroshi, U. Hideki, D. Taishi *et al.*, "Application of a distributed fibre optic strain sensing system to monitoring changes in the state of an underground mine," *Measurement Science and Technology*, vol. 18, no. 10, pp. 3202, 2007.
- [4] S. Johnsen, and K. J. Lohmann, "The physics and neurobiology of magnetoreception," *Nat Rev Neurosci*, vol. 6, no. 9, pp. 703-712, 2005.
- [5] K. J. Lohmann, "Q&A: Animal behaviour: Magnetic-field perception," *Nature*, vol. 464, no. 7292, pp. 1140-1142, 2010.
- [6] E. Udd, "Fiber optic smart structures," *Proceedings of the IEEE*, vol. 84, no. 6, pp. 884-894, 1996.
- [7] L. Byoung-ho, "Review of the present status of optical fiber sensors," *Optical Fiber Technology*, vol. 9, no. 2, pp. 57-79, 2003.
- [8] W. L. Richards, "Validation of fibre optic smart structures for monitoring the structural health of aerospace vehicles," Engineering, University of Wales Swansea, 2006.
- [9] A. W. Snyder, and J. D. Love, *Optical waveguide theory*: Chapman and Hall, 1983.
- [10] J. Blyler, Lee L, and F. V. DiMarcello, "Fiber Drawing, Coating, and Jacketing," *Proceedings of the IEEE*, vol. 68, no. 10, pp. 1194-1198., 1980.
- [11] H. Huang, R. M. Miura, and J. J. Wylie, "Optical Fiber Drawing and Dopant Transport," *SIAM Journal on Applied Mathematics*, vol. 69, no. 2, pp. 330-347, 2008.
- [12] K. O. Hill, Y. Fujii, D. C. Johnson *et al.*, "Photosensitivity in optical fiber waveguides: Application to reflection filter fabrication," *Applied Physics Letters*, vol. 32, no. 10, pp. 647-649, 1978.
- [13] B. S. Kawasaki, K. O. Hill, D. C. Johnson *et al.*, "Narrow-band Bragg reflectors in optical fibers," *Opt. Lett.*, vol. 3, no. 2, pp. 66-68, 1978.
- [14] K. O. Hill, "Aperiodic Distributed-Parameter Waveguides for Integrated Optics," *Appl. Opt.*, vol. 13, no. 8, pp. 1853-1856, 1974.

- [15] J. Stone, "Photorefractivity in GeO₂-doped silica fibers," *Journal of Applied Physics*, vol. 62, no. 11, pp. 4371-4374, 1987.
- [16] D. K. W. Lam, and B. K. Garside, "Characterization of single-mode optical fiber filters," *Appl. Opt.*, vol. 20, no. 3, pp. 440-445, 1981.
- [17] A. Othonos, "Fiber Bragg gratings," *Review of Scientific Instruments*, vol. 68, no. 12, pp. 4309-4341, 1997.
- [18] G. Meltz, W. W. Morey, and W. H. Glenn, "Formation of Bragg gratings in optical fibers by a transverse holographic method," *Opt. Lett.*, vol. 14, no. 15, pp. 823-825, 1989.
- [19] M. J. Yuen, "Ultraviolet absorption studies of germanium silicate glasses," *Appl. Opt.*, vol. 21, no. 1, pp. 136-140, 1982.
- [20] C. G. Askins, M. A. Putnam, G. M. Williams *et al.*, "Stepped-wavelength optical-fiber Bragg grating arrays fabricated in line on a draw tower," *Opt. Lett.*, vol. 19, no. 2, pp. 147-149, 1994.
- [21] C. G. Askins, T. E. Tsai, G. M. Williams *et al.*, "Fiber Bragg reflectors prepared by a single excimer pulse," *Opt. Lett.*, vol. 17, no. 11, pp. 833-835, 1992.
- [22] J. L. Archambault, L. Reekie, and P. S. J. Russell, "100% reflectivity Bragg reflectors produced in optical fibres by single excimer laser pulses," *Electronics Letters*, vol. 29, no. 5, pp. 453-455, 1993.
- [23] K. O. Hill, B. Malo, F. Bilodeau *et al.*, "Bragg gratings fabricated in monomode photosensitive optical fiber by UV exposure through a phase mask," *Applied Physics Letters*, vol. 62, no. 10, pp. 1035-1037, 1993.
- [24] L. Dong, J. L. Archambault, L. Reekie *et al.*, "Single pulse Bragg gratings written during fibre drawing," *Electronics Letters*, vol. 29, no. 17, pp. 1577-1578, 1993.
- [25] A. Yariv, *Optical electronics in modern communications*: Oxford University Press, 1997.
- [26] J. T. Verdeyen, *Laser electronics*: Prentice Hall, 1995.
- [27] A. Yariv, *Quantum electronics*: Wiley, 1989.
- [28] W. Eickhoff, and R. Ulrich, "Optical frequency domain reflectometry in single-mode fiber," *Applied Physics Letters*, vol. 39, no. 9, pp. 693-695, 1981.
- [29] J. F. Nye, *Physical properties of crystals*: Clarendon Press, 1957.
- [30] T. S. Narasimhamurty, *Photoelastic and electro-optic properties of crystals*: Plenum Press, 1981.
- [31] J. M. Liu, *Photonic Devices*: Cambridge, 2005.
- [32] S. Zhang, *Nanostructured Thin Films and Coatings: Functional Properties*: CRC Press, 2010.
- [33] M. Froggatt, "Distributed measurement of the complex modulation of a photoinduced Bragg grating in an optical fiber," *Appl. Opt.*, vol. 35, no. 25, pp. 5162-5164, 1996.

- [34] S. A. Kingsley, and D. E. N. Davies, "OFDR diagnostics for fibre and integrated-optic systems," *Electronics Letters*, vol. 21, no. 10, pp. 434-435, 1985.
- [35] T. Amano, H. Hiro-Oka, D. Choi *et al.*, "Optical frequency-domain reflectometry with a rapid wavelength-scanning superstructure-grating distributed Bragg reflector laser," *Appl. Opt.*, vol. 44, no. 5, pp. 808-816, 2005.
- [36] E. Udd, *Fiber optic sensors: an introduction for engineers and scientists*: Wiley, 1991.
- [37] J. H. Cole, R. L. Johnson, and P. G. Bhuta, "Fiber-optic detection of sound," *The Journal of the Acoustical Society of America*, vol. 62, no. 5, pp. 1136-1138, 1977.
- [38] C. D. Butter, and G. B. Hocker, "Fiber optics strain gauge," *Appl. Opt.*, vol. 17, no. 18, pp. 2867-2869, 1978.
- [39] A. Wang, M. S. Miller, D. Sun *et al.*, "Advances in the extrinsic Fabry-Perot interferometric optical fiber sensors," in *SPIE Fiber Optic Smart Structures and Skins V*, 1993, pp. 32-41.
- [40] C. A. Paul, G. P. Sendeckyj, and G. P. Carman, "Detection of the onset of damage using an extrinsic Fabry-Perot interferometric strain sensor (EFPI-SS)," Albuquerque, NM, USA, 1993, pp. 154-164.
- [41] D. C. Betz, G. Thursby, B. Culshaw *et al.*, "Acousto-ultrasonic sensing using fiber Bragg gratings," *Smart Materials and Structures*, vol. 12, no. 1, pp. 122, 2003.
- [42] D. Schmadel, W. H. Culver, and G. Gould, *Fiber optic energy sensor and optical demodulation system and methods of making same*, United States 4568408, to Optelecom Inc., 1986.
- [43] W. H. Glenn, G. Meltz, and E. Snitzer, *Method for impressing gratings within fiber optics*, United States 4725110, to United Technologies Corporation, 1988.
- [44] W. H. Glenn, G. Meltz, and E. Snitzer, *Method for impressing gratings within fiber optics*, United States 4807950, to United Technologies Corporation, 1989.
- [45] G. Meltz, W. H. Glenn, and E. Snitzer, *Distributed, spatially resolving optical fiber strain gauge*, United States 4761073, to United Technologies Corporation, 1988.
- [46] G. Meltz, W. H. Glenn, and E. Snitzer, *Distributed, spatially resolving optical fiber strain gauge*, United States 4806012, to United Technologies Corporation, 1989.
- [47] S. M. Melle, A. T. Alavie, S. Karr *et al.*, "A Bragg grating-tuned fiber laser strain sensor system," *Photonics Technology Letters, IEEE*, vol. 5, no. 2, pp. 263-266, 1993.
- [48] A. D. Kersey, and W. W. Morey, "Multi-element Bragg-grating based fibre-laser strain sensor," *Electronics Letters*, vol. 29, no. 11, pp. 964-966, 1993.
- [49] M. A. Davis, A. D. Kersey, J. S. Sirkis *et al.*, "Fiber optic Bragg grating array for shape and vibration mode sensing," Orlando, FL, USA, 1994, pp. 94-102.
- [50] M. A. Davis, D. G. Bellemore, A. D. Kersey *et al.*, "High-sensor-count Bragg grating instrumentation system for large-scale structural monitoring applications," San Diego, CA, USA, 1996, pp. 303-309.

- [51] S. LaRochelle, V. Mizrahi, K. D. Simmons *et al.*, "Photosensitive optical fibers used as vibration sensors," *Opt. Lett.*, vol. 15, no. 7, pp. 399-401, 1990.
- [52] A. M. Vengsarkar, J. A. Greene, and K. A. Murphy, "Photoinduced refractive-index changes in two-mode, elliptical-core fibers: sensing applications," *Opt. Lett.*, vol. 16, no. 19, pp. 1541-1543, 1991.
- [53] J. A. Greene, K. A. Murphy, B. R. Fogg *et al.*, "Optical fiber, vibration-mode filters incorporating photoinduced refractive-index gratings," *Smart Materials and Structures*, vol. 1, no. 3, pp. 243, 1992.
- [54] S. Melle, K. Liu, and R. M. Measures, "Strain sensing using a fiber-optic Bragg grating," Boston, MA, USA, 1991, pp. 255-263.
- [55] S. M. Melle, K. Liu, and R. M. Measures, "Practical fiber-optic Bragg grating strain gauge system," *Appl. Opt.*, vol. 32, no. 19, pp. 3601-3609, 1993.
- [56] A. D. Kersey, and T. A. Berkoff, "Fiber-optic Bragg-grating differential-temperature sensor," *Photonics Technology Letters, IEEE*, vol. 4, no. 10, pp. 1183-1185, 1992.
- [57] V. Arya, D. W. Sherrer, A. Wang *et al.*, "Application of thin-film optical filters to the temperature compensation of optical fiber grating-based devices," *Instrumentation and Measurement, IEEE Transactions on*, vol. 46, no. 5, pp. 1173-1177, 1997.
- [58] A. Wang, and K. A. Murphy, "Optical-fiber temperature sensor based on differential spectral reflectivity," *Smart Materials and Structures*, vol. 1, no. 1, pp. 5, 1992.
- [59] A. Henriksson, S. Sandgren, and A. Asseh, "Temperature insensitivity of a fiber optic Bragg grating sensor," Denver, CO, USA, 1996, pp. 20-33.
- [60] S. W. James, M. L. Dockney, and R. P. Tatam, "Simultaneous independent temperature and strain measurement using in-fibre Bragg grating sensors," *Electronics Letters*, vol. 32, no. 12, pp. 1133-1134, 1996.
- [61] L. A. Ferreira, A. B. Lobo Ribeiro, J. L. Santos *et al.*, "Simultaneous measurement of displacement and temperature using a low finesse cavity and a fiber Bragg grating," *Photonics Technology Letters, IEEE*, vol. 8, no. 11, pp. 1519-1521, 1996.
- [62] T. Liu, G. F. Fernando, Y.-J. Rao *et al.*, "Simultaneous strain and temperature measurements in composites using a multiplexed fiber Bragg grating sensor and an extrinsic Fabry-Perot sensor," San Diego, CA, USA, 1997, pp. 203-212.
- [63] Y. J. Rao, P. J. Henderson, D. A. Jackson *et al.*, "Simultaneous strain, temperature and vibration measurement using a multiplexed in-fibre-Bragg-grating/fibre-Fabry-Perot sensor system," *Electronics Letters*, vol. 33, no. 24, pp. 2063-2064, 1997.
- [64] M. Song, S. B. Lee, S. S. Choi *et al.*, "Simultaneous Measurement of Temperature and Strain Using Two Fiber Bragg Gratings Embedded in a Glass Tube," *Optical Fiber Technology*, vol. 3, no. 2, pp. 194-196, 1997.
- [65] H. D. Simonsen, R. Paetsch, and J. R. Dunphy, "Fiber Bragg grating sensor demonstration in glass-fiber reinforced polyester composite," in European Conference on Smart Structures and Materials, Glasgow, United Kingdom, 1992, pp. 73-76.

- [66] S. Magne, S. Rougeault, M. Vilela *et al.*, "State-of-strain evaluation with fiber Bragg grating rosettes: application to discrimination between strain and temperature effects in fiber sensors," *Appl. Opt.*, vol. 36, no. 36, pp. 9437-9447, 1997.
- [67] J. S. Sirkis, and J. H. W. Haslach, "Complete phase-strain model for structurally embedded interferometric optical fiber sensors," San Jose, USA, 1990, pp. 248-259.
- [68] C. T. Mathews, and J. S. Sirkis, "Interaction mechanics of interferometric optical fiber sensors embedded in a monolithic structure," San Jose, USA, 1990, pp. 142-153.
- [69] J. S. Sirkis, and H. W. Haslach, "Complete Phase-Strain Model for Structurally Embedded Interferometric Optical Fiber Sensors," *Journal of Intelligent Material Systems and Structures*, vol. 2, no. 1, pp. 3-24, 1991.
- [70] S. S. J. Roberts, and R. Davidson, "Mechanical properties of composite materials containing embedded fiber-optic sensors," Boston, MA, USA, 1991, pp. 326-341.
- [71] G. P. Carman, C. A. Paul, and G. P. Sendekyj, "Transverse strength of composites containing optical fibers," Albuquerque, NM, USA, 1993, pp. 307-316.
- [72] G. Carman, and K. Reifsnider, "Analytical Optimization of Coating Properties for Actuators and Sensors," *Journal of Intelligent Material Systems and Structures*, vol. 4, no. 1, pp. 89-97, 1993.
- [73] J. S. Sirkis, and A. Dasgupta, "Optimal coatings for intelligent structure fiber optic sensors," San Jose, USA, 1990, pp. 129-140.
- [74] A. Dasgupta, Y. Wan, J. S. Sirkis *et al.*, "Micromechanical investigation of an optical fiber embedded in a laminated composite," San Jose, USA, 1990, pp. 119-128.
- [75] A. Dasgupta, W. Ying, and J. S. Sirkis, "Prediction of resin pocket geometry for stress analysis of optical fibers embedded in laminated composites," *Smart Materials and Structures*, vol. 1, no. 2, pp. 101, 1992.
- [76] H. Singh, J. S. Sirkis, and A. Dasgupta, "Microinteraction of optical fibers embedded in laminated composites," Boston, MA, USA, 1991, pp. 76-85.
- [77] M. de Vries, M. Nasta, V. Bhatia *et al.*, "Performance of embedded short-gage-length optical fiber sensors in a fatigue-loaded reinforced concrete specimen," *Smart Materials and Structures*, vol. 4, no. 1A, pp. A107, 1995.
- [78] M. de Vries, V. Arya, S. Meller *et al.*, "Implementation of EFPI-based optical-fiber sensor instrumentation for the NDE of concrete structures," *Cement and Concrete Composites*, vol. 19, no. 1, pp. 69-79, 1997.
- [79] V. Bhatia, C. A. Schmid, K. A. Murphy *et al.*, "Optical fiber sensing technique for edge-induced and internal delamination detection in composites," *Smart Materials and Structures*, vol. 4, no. 3, pp. 164, 1995.
- [80] J. A. Greene, T. A. Tran, V. Bhatia *et al.*, "Optical fiber sensing technique for impact detection and location in composites and metal specimens," *Smart Materials and Structures*, vol. 4, no. 2, pp. 93, 1995.

- [81] M. L. Dockney, I. J. Read, P. D. Foote *et al.*, "Embedded optical fibre Bragg gratings for aerospace monitoring," in *Optical Techniques for Smart Structures and Structural Monitoring* (Digest No. 1997/033), IEE Colloquium on, 1997, pp. 8/1-8/6.
- [82] K. Levin, and S. Nilsson, "Examination of reliability of fibre optic sensors embedded in carbon/epoxy composites," Lyon, France, 1996, pp. 222-229.
- [83] N. C. Eaton, R. C. Drew, and H. Geiger, "Finite element stress and strain analysis in composites with embedded optical fiber sensors," *Smart Materials and Structures*, vol. 4, no. 2, pp. 113, 1995.
- [84] P. D. Foote, "Optical fibre Bragg grating sensors for aerospace smart structures," in *Optical Fibre Gratings and Their Applications*, IEE Colloquium on, 1995, pp. 14/1-14/6.
- [85] Y. J. Rao, D. A. Jackson, L. Zhang *et al.*, "Strain sensing of modern composite materials with a spatial/wavelength-division multiplexed fiber grating network," *Opt. Lett.*, vol. 21, no. 9, pp. 683-685, 1996.
- [86] D. E. Bullock, J. R. Dunphy, and G. H. Hufstetler, "Embedded Bragg grating fiber optic sensor for composite flexbeams," Boston, MA, USA, 1993, pp. 253-261.
- [87] P. Ferdinand, D. Chauvel, E. Toppan *et al.*, "Concrete strain measurements and crack detection with surface-mounted and embedded Bragg grating extensometers," 1997, pp. OFA2.
- [88] M. A. Davis, D. G. Bellemore, and A. D. Kersey, "Distributed fiber Bragg grating strain sensing in reinforced concrete structural components," *Cement and Concrete Composites*, vol. 19, no. 1, pp. 45-57, 1997.
- [89] M. Le Blanc, S. Y. Huang, M. M. Ohn *et al.*, "Tunable chirping of a fibre Bragg grating using a tapered cantilever beam," *Electronics Letters*, vol. 30, no. 25, pp. 2163-2165, 1994.
- [90] M. LeBlanc, S. Y. Huang, and R. M. Measures, "Fiber optic Bragg intra-grating strain gradient sensing," San Diego, CA, USA, 1995, pp. 136-147.
- [91] S. Huang, M. LeBlanc, M. M. Ohn *et al.*, "Bragg intragrating structural sensing," *Appl. Opt.*, vol. 34, no. 22, pp. 5003-5009, 1995.
- [92] S. Huang, M. M. Ohn, and R. M. Measures, "Phase-based Bragg intragrating distributed strain sensor," *Appl. Opt.*, vol. 35, no. 7, pp. 1135-1142, 1996.
- [93] M. LeBlanc, S. Y. Huang, M. Ohn *et al.*, "Distributed strain measurement based on a fiber Bragg grating and its reflection spectrum analysis," *Opt. Lett.*, vol. 21, no. 17, pp. 1405-1407, 1996.
- [94] L. Bjerkan, K. Johannessen, and X. Guo, "Measurements of Bragg grating birefringence due to transverse compressive forces," 1997, pp. OTuC7.
- [95] C. M. Lawrence, D. V. Nelson, and E. Udd, "Measurement of transverse strains with fiber Bragg gratings," San Diego, CA, USA, 1997, pp. 218-228.
- [96] J. R. Dunphy, G. Meltz, F. P. Lamm *et al.*, "Multifunction, distributed optical fiber sensor for composite cure and response monitoring," San Jose, USA, 1990, pp. 116-118.

- [97] E. J. Friebele, C. G. Askins, and M. A. Putnam, "Distributed strain sensing with fiber Bragg grating arrays embedded in CRTM composites," in Second European Conference on Smart Structures and Materials, Glasgow, United Kingdom, 1994, pp. 338-340.
- [98] E. J. Friebele, C. G. Askins, M. A. Putnam *et al.*, "Distributed strain sensing with fibre Bragg grating arrays embedded in CRTM composites," *Electronics Letters*, vol. 30, no. 21, pp. 1783-1784, 1994.
- [99] U. J. Sennhauser, R. Broennimann, and P. M. Nellen, "Reliability modeling and testing of optical fiber Bragg sensors for strain measurements," Denver, CO, USA, 1996, pp. 64-75.
- [100] E. Udd, D. V. Nelson, C. M. Lawrence *et al.*, "Three-axis strain and temperature fiber optic grating sensor," San Diego, CA, USA, 1996, pp. 104-109.
- [101] C. M. Lawrence, D. V. Nelson, and E. Udd, "Multiparameter sensing with fiber Bragg gratings," Troutdale, OR, USA, 1996, pp. 24-31.
- [102] E. Udd, C. M. Lawrence, and D. V. Nelson, "Development of a three-axis strain and temperature fiber optic grating sensor," San Diego, CA, USA, 1997, pp. 229-236.
- [103] D. V. Nelson, A. Makino, C. M. Lawrence *et al.*, "Determination of the K-matrix for the multiparameter fiber grating sensor in AD072 fibercore fiber," Troutdale, OR, USA, 1998, pp. 79-85.
- [104] E. Udd, W. L. Schulz, and J. M. Seim, "Measurement of multidimensional strain fields using fiber grating sensors for structural monitoring," Boston, MA, USA, 1999, pp. 24-34.
- [105] M. G. Xu, J. L. Archambault, L. Reekie *et al.*, "Discrimination between strain and temperature effects using dual-wavelength fibre grating sensors," *Electronics Letters*, vol. 30, no. 13, pp. 1085-1087, 1994.
- [106] H. J. Patrick, G. M. Williams, A. D. Kersey *et al.*, "Hybrid fiber Bragg grating/long period fiber grating sensor for strain/temperature discrimination," *Photonics Technology Letters, IEEE*, vol. 8, no. 9, pp. 1223-1225, 1996.
- [107] L. Yuan, and L. Zhou, "Sensitivity coefficient evaluation of an embedded fiber-optic strain sensor," *Sensors and Actuators A: Physical*, vol. 69, no. 1, pp. 5-11, 1998.
- [108] L. Tang, X. Tao, and C.-I. Choy, "Effectiveness and optimization of fiber Bragg grating sensor as embedded strain sensor," *Smart Materials and Structures*, vol. 8, no. 1, pp. 154, 1999.
- [109] G. Duck, and M. LeBlanc, "Arbitrary strain transfer from a host to an embedded fiber-optic sensor," *Smart Materials and Structures*, vol. 9, no. 4, pp. 492, 2000.
- [110] X. Tao, L. Tang, W.-c. Du *et al.*, "Internal strain measurement by fiber Bragg grating sensors in textile composites," *Composites Science and Technology*, vol. 60, no. 5, pp. 657-669, 2000.
- [111] F. Bosia, P. Giaccari, J. Botsis *et al.*, "Characterization of the response of fibre Bragg grating sensors subjected to a two-dimensional strain field," *Smart Materials and Structures*, vol. 12, no. 6, pp. 925, 2003.

- [112] C.-C. Ye, S. E. Staines, S. W. James *et al.*, “A polarization-maintaining fibre Bragg grating interrogation system for multi-axis strain sensing,” *Measurement Science and Technology*, vol. 13, no. 9, pp. 1446, 2002.
- [113] M. Prabhugoud, and K. Peters, “Finite element model for embedded fiber Bragg grating sensor,” *Smart Materials and Structures*, vol. 15, no. 2, pp. 550, 2006.
- [114] L. G. Melin, K. Levin, S. Nilsson *et al.*, “A study of the displacement field around embedded fibre optic sensors,” *Composites Part A: Applied Science and Manufacturing*, vol. 30, no. 11, pp. 1267-1275, 1999.
- [115] J. M. Menendez, and J. A. Guemes, “Strain measurements inside thick CFRP laminates at the vicinity of bolted joints,” Newport Beach, CA, USA, 1999, pp. 184-194.
- [116] J. M. Menendez, and J. A. Guemes, “Bragg-grating-based multiaxial strain sensing: its application to residual strain measurement in composite laminates,” Newport Beach, CA, USA, 2000, pp. 271-281.
- [117] J. A. Guemes, and J. M. Menéndez, “Response of Bragg grating fiber-optic sensors when embedded in composite laminates,” *Composites Science and Technology*, vol. 62, no. 7–8, pp. 959-966, 2002.
- [118] K. S. C. Kuang, R. Kenny, M. P. Whelan *et al.*, “Residual strain measurement and impact response of optical fibre Bragg grating sensors in fibre metal laminates,” *Smart Materials and Structures*, vol. 10, no. 2, pp. 338, 2001.
- [119] H.-K. Kang, D.-H. Kang, H.-J. Bang *et al.*, “Cure monitoring of composite laminates using fiber optic sensors,” *Smart Materials and Structures*, vol. 11, no. 2, pp. 279, 2002.
- [120] H.-K. Kang, D.-H. Kang, C.-S. Hong *et al.*, “Simultaneous monitoring of strain and temperature during and after cure of unsymmetric composite laminate using fibre-optic sensors,” *Smart Materials and Structures*, vol. 12, no. 1, pp. 29, 2003.
- [121] D. H. Kang, C. S. Hong, and C. G. Kim, “Characteristics of fiber Bragg grating sensors with various grating lengths embedded in composite materials,” *Key Engineering Materials*, vol. 321-323, pp. 152-155, 2006.
- [122] K. Jung, and T. Jin Kang, “Cure Monitoring and Internal Strain Measurement of 3-D Hybrid Braided Composites using Fiber Bragg Grating Sensor,” *Journal of Composite Materials*, vol. 41, no. 12, pp. 1499-1519, 2007.
- [123] K. Jung, T. Kang, B. Lee *et al.*, “Estimation of residual strain and stress in interply hybrid composite using fiber bragg grating sensor,” *Fibers and Polymers*, vol. 8, no. 4, pp. 438-442, 2007.
- [124] Y. Okabe, S. Yashiro, R. Tsuji *et al.*, “Effect of thermal residual stress on the reflection spectrum from fiber Bragg grating sensors embedded in CFRP laminates,” *Composites Part A: Applied Science and Manufacturing*, vol. 33, no. 7, pp. 991-999, 2002.
- [125] E. Chehura, A. A. Skordos, C. C. Ye *et al.*, “Strain development in curing epoxy resin and glass fibre/epoxy composites monitored by fibre Bragg grating sensors in birefringent optical fibre,” *Smart Materials and Structures*, vol. 14, no. 2, pp. 354, 2005.

- [126] L. Sorensen, T. Gmür, and J. Botsis, “Residual strain development in an AS4/PPS thermoplastic composite measured using fibre Bragg grating sensors,” *Composites Part A: Applied Science and Manufacturing*, vol. 37, no. 2, pp. 270-281, 2006.
- [127] J.-R. Lee, H. Tsuda, and B.-Y. Koo, “Single-mode fibre optic Bragg grating sensing on the base of birefringence in surface-mounting and embedding applications,” *Optics & Laser Technology*, vol. 39, no. 1, pp. 157-164, 2007.
- [128] K. Wood, T. Brown, R. Rogowski *et al.*, “Fiber optic sensors for health monitoring of morphing airframes: I. Bragg grating strain and temperature sensor,” *Smart Materials and Structures*, vol. 9, no. 2, pp. 163, 2000.
- [129] K. S. C. Kuang, R. Kenny, M. P. Whelan *et al.*, “Embedded fibre Bragg grating sensors in advanced composite materials,” *Composites Science and Technology*, vol. 61, no. 10, pp. 1379-1387, 2001.
- [130] J. Matrat, and K. Levin, “Embedded optical fiber strain rosette for in-plane measurements,” San Diego, CA, USA, 2002, pp. 187-194.
- [131] F. Bosia, J. Botsis, M. Facchini *et al.*, “Deformation characteristics of composite laminates—part I: speckle interferometry and embedded Bragg grating sensor measurements,” *Composites Science and Technology*, vol. 62, no. 1, pp. 41-54, 2002.
- [132] F. Bosia, M. Facchini, J. Botsis *et al.*, “Through-the-thickness distribution of strains in laminated composite plates subjected to bending,” *Composites Science and Technology*, vol. 64, no. 1, pp. 71-82, 2004.
- [133] D. C. Betz, L. Staudigel, M. N. Trutzel *et al.*, “Structural Monitoring Using Fiber-Optic Bragg Grating Sensors,” *Structural Health Monitoring*, vol. 2, no. 2, pp. 145-152, 2003.
- [134] Y. Fan, and M. Kahrizi, “Characterization of a FBG strain gage array embedded in composite structure,” *Sensors and Actuators A: Physical*, vol. 121, no. 2, pp. 297-305, 2005.
- [135] G. Luyckx, W. De Waele, J. Degrieck *et al.*, “Three-dimensional strain and temperature monitoring of composite laminates,” *Insight - Non-Destructive Testing and Condition Monitoring*, vol. 49, no. 1, pp. 10-16, 2007.
- [136] M. Mulle, R. Zitoune, F. Collombet *et al.*, “Embedded FBGs and 3-D DIC for the stress analysis of a structural specimen subjected to bending,” *Composite Structures*, vol. 91, no. 1, pp. 48-55, 2009.
- [137] M. C. Emmons, S. Karnani, S. Trono *et al.*, “Strain Measurement Validation of Embedded Fiber Bragg Gratings,” *International Journal of Optomechatronics*, vol. 4, no. 1, pp. 22-33, 2010/03/31, 2010.
- [138] M. C. Emmons, S. Karnani, K. P. Mohanchandra *et al.*, “Characterization of Optical Fiber Bragg Gratings as Strain Sensors Considering Load Direction,” in *ASME Smart Materials, Adaptive Structures and Intelligent Systems*, Ellicott City, 2008, pp. 1-5.
- [139] G. Luyckx, E. Voet, W. D. Waele *et al.*, “Multi-axial strain transfer from laminated CFRP composites to embedded Bragg sensor: I. Parametric study,” *Smart Materials and Structures*, vol. 19, no. 10, pp. 105017, 2010.

- [140] E. Voet, G. Luyckx, W. D. Waele *et al.*, “Multi-axial strain transfer from laminated CFRP composites to embedded Bragg sensor: II. Experimental validation,” *Smart Materials and Structures*, vol. 19, no. 10, pp. 105018, 2010.
- [141] Y. Okabe, S. Yashiro, T. Kosaka *et al.*, “Detection of transverse cracks in CFRP composites using embedded fiber Bragg grating sensors,” *Smart Materials and Structures*, vol. 9, no. 6, pp. 832, 2000.
- [142] K. Satori, K. Fukuchi, Y. Kurosawa *et al.*, “Polyimide-coated small-diameter optical fiber sensors for embedding in composite laminate structures,” Newport Beach, CA, USA, 2001, pp. 285-294.
- [143] N. Takeda, “Characterization of microscopic damage in composite laminates and real-time monitoring by embedded optical fiber sensors,” *International Journal of Fatigue*, vol. 24, no. 2-4, pp. 281-289, 2002.
- [144] Y. Okabe, T. Mizutani, S. Yashiro *et al.*, “Detection of microscopic damages in composite laminates,” *Composites Science and Technology*, vol. 62, no. 7-8, pp. 951-958, 2002.
- [145] Y. Okabe, N. Tanaka, and N. Takeda, “Effect of fiber coating on crack detection in carbon fiber reinforced plastic composites using fiber Bragg grating sensors,” *Smart Materials and Structures*, vol. 11, no. 6, pp. 892, 2002.
- [146] Y. Okabe, R. Tsuji, and N. Takeda, “Application of chirped fiber Bragg grating sensors for identification of crack locations in composites,” *Composites Part A: Applied Science and Manufacturing*, vol. 35, no. 1, pp. 59-65, 2004.
- [147] M. Prabhugoud, and K. Peters, “Efficient simulation of Bragg grating sensors for implementation to damage identification in composites,” *Smart Materials and Structures*, vol. 12, no. 6, pp. 914, 2003.
- [148] M. Ussorio, H. Wang, S. L. Ogin *et al.*, “Modifications to FBG sensor spectra due to matrix cracking in a GFRP composite,” *Construction and Building Materials*, vol. 20, no. 1-2, pp. 111-118, 2006.
- [149] J. Palaniappan, H. Wang, S. L. Ogin *et al.*, “Prediction of the reflected spectra from chirped fibre Bragg gratings embedded within cracked crossply laminates,” *Measurement Science and Technology*, vol. 17, no. 6, pp. 1609, 2006.
- [150] A. D. Kersey, M. A. Davis, T. A. Berkoff *et al.*, “Progress toward the development of practical fiber Bragg grating instrumentation systems,” Denver, CO, USA, 1996, pp. 40-63.
- [151] P. Ferdinand, S. Magne, V. Dewynter-Marty *et al.*, “Applications of Bragg grating sensors in Europe,” 1997, pp. OTuB1.
- [152] K. O. Hill, and G. Meltz, “Fiber Bragg grating technology fundamentals and overview,” *Lightwave Technology, Journal of*, vol. 15, no. 8, pp. 1263-1276, 1997.
- [153] A. D. Kersey, M. A. Davis, H. J. Patrick *et al.*, “Fiber grating sensors,” *Lightwave Technology, Journal of*, vol. 15, no. 8, pp. 1442-1463, 1997.

- [154] T. Erdogan, "Fiber grating spectra," *Lightwave Technology, Journal of*, vol. 15, no. 8, pp. 1277-1294, 1997.
- [155] R. Yun-Jiang, "In-fibre Bragg grating sensors," *Measurement Science and Technology*, vol. 8, no. 4, pp. 355, 1997.
- [156] E. J. Friebele, "Fiber Bragg Grating Strain Sensors: Present and Future Applications in Smart Structures," *Opt. Photon. News*, vol. 9, no. 8, pp. 33, 1998.
- [157] W. Du, X. M. Tao, H. Y. Tam *et al.*, "Fundamentals and applications of optical fiber Bragg grating sensors to textile structural composites," *Composite Structures*, vol. 42, no. 3, pp. 217-229, 1998.
- [158] R. Y.J, "Recent progress in applications of in-fibre Bragg grating sensors," *Optics and Lasers in Engineering*, vol. 31, no. 4, pp. 297-324, 1999.
- [159] C. Y. Wei, S. W. James, C. C. Ye *et al.*, "Application Issues Using Fibre Bragg Gratings as Strain Sensors in Fibre Composites," *Strain*, vol. 36, no. 3, pp. 143-150, 2000.
- [160] K. T. V. Grattan, and T. Sun, "Fiber optic sensor technology: an overview," *Sensors and Actuators A: Physical*, vol. 82, no. 1-3, pp. 40-61, 2000.
- [161] G. Zhou, and L. M. Sim, "Damage detection and assessment in fibre-reinforced composite structures with embedded fibre optic sensors-review," *Smart Materials and Structures*, vol. 11, no. 6, pp. 925, 2002.
- [162] K. S. C. Kuang, and W. J. Cantwell, "Use of conventional optical fibers and fiber Bragg gratings for damage detection in advanced composite structures: A review," *Applied Mechanics Reviews*, vol. 56, no. 5, pp. 493-513, 2003.
- [163] Y. Zhao, and Y. Liao, "Discrimination methods and demodulation techniques for fiber Bragg grating sensors," *Optics and Lasers in Engineering*, vol. 41, no. 1, pp. 1-18, 2004.
- [164] N. Mrad, "Potential of Bragg grating sensors for aircraft health monitoring," *Transactions of the CSME*, vol. 31, no. 1, pp. 1-17, 2007.
- [165] Y. Wang, "Review of long period fiber gratings written by CO₂ laser," *Journal of Applied Physics*, vol. 108, no. 8, pp. 081101-081101-18, 2010.
- [166] G. Luyckx, E. Voet, N. Lammens *et al.*, "Strain Measurements of Composite Laminates with Embedded Fibre Bragg Gratings: Criticism and Opportunities for Research," *Sensors*, vol. 11, no. 1, pp. 384-408, 2011.
- [167] M. A. Davis, D. G. Bellemore, M. A. Putnam *et al.*, "High-strain monitoring in composite-wrapped concrete cylinders using embedded fiber Bragg grating arrays," San Diego, CA, USA, 1996, pp. 149-154.
- [168] R. C. Foedinger, D. L. Rea, J. S. Sirkis *et al.*, "Embedded fiber optic sensor arrays for structural health monitoring of filament wound composite pressure vessels," Newport Beach, CA, USA, 1999, pp. 289-301.
- [169] J. Degrieck, W. De Waele, and P. Verleysen, "Monitoring of fibre reinforced composites with embedded optical fibre Bragg sensors, with application to filament wound pressure vessels," *NDT & E International*, vol. 34, no. 4, pp. 289-296, 2001.

- [170] H.-K. Kang, J.-S. Park, D.-H. Kang *et al.*, “Strain monitoring of a filament wound composite tank using fiber Bragg grating sensors,” *Smart Materials and Structures*, vol. 11, no. 6, pp. 848, 2002.
- [171] J. Grant, R. K. Kaul, S. L. Taylor *et al.*, “Distributed sensing of carbon-epoxy composites and composite wound pressure vessels using fiber Bragg gratings,” San Diego, CA, USA, 2003, pp. 187-196.
- [172] D. H. Kang, C. U. Kim, and C. G. Kim, “The embedment of fiber Bragg grating sensors into filament wound pressure tanks considering multiplexing,” *NDT & E International*, vol. 39, no. 2, pp. 109-116, 2006.
- [173] R. M. Measures, A. T. Alavie, R. Maaskant *et al.*, “Bragg grating fiber optic sensing for bridges and other structures,” Glasgow, United Kingdom, 1994, pp. 162-167.
- [174] R. Maaskant, A. T. Alavie, R. M. Measures *et al.*, “Fiber optic Bragg grating sensor network installed in a concrete road bridge,” Orlando, FL, USA, 1994, pp. 457-465.
- [175] R. Maaskant, T. Alavie, R. M. Measures *et al.*, “Fiber-optic Bragg grating sensors for bridge monitoring,” *Cement and Concrete Composites*, vol. 19, no. 1, pp. 21-33, 1997.
- [176] H. Storøy, J. Sæther, and K. Johannessen, “Fiber Optic Condition Monitoring during a Full Scale Destructive Bridge Test,” *Journal of Intelligent Material Systems and Structures*, vol. 8, no. 8, pp. 633-643, 1997.
- [177] P. M. Nellen, A. Frank, R. Broennimann *et al.*, “Fiber optical Bragg grating sensors embedded in CFRP wires,” Newport Beach, CA, USA, 1999, pp. 440-449.
- [178] P. L. Fuhr, D. R. Huston, M. Nelson *et al.*, “Fiber Optic Sensing of a Bridge in Waterbury, Vermont,” *Journal of Intelligent Material Systems and Structures*, vol. 10, no. 4, pp. 293-303, 1999.
- [179] Y. M. Gebremichael, W. Li, W. J. O. Boyle *et al.*, “Integration and assessment of fibre Bragg grating sensors in an all-fibre reinforced polymer composite road bridge,” *Sensors and Actuators A: Physical*, vol. 118, no. 1, pp. 78-85, 2005.
- [180] C. Barbosa, N. Costa, L. A. Ferreira *et al.*, “Weldable fibre Bragg grating sensors for steel bridge monitoring,” *Measurement Science and Technology*, vol. 19, no. 12, pp. 125305, 2008.
- [181] M. Bugaud, P. Ferdinand, S. Rougeault *et al.*, “Health monitoring of composite plastic waterworks lock gates using in-fibre Bragg grating sensors,” *Smart Materials and Structures*, vol. 9, no. 3, pp. 322, 2000.
- [182] K. Schroeder, W. Ecke, J. Apitz *et al.*, “A fibre Bragg grating sensor system monitors operational load in a wind turbine rotor blade,” *Measurement Science and Technology*, vol. 17, no. 5, pp. 1167, 2006.
- [183] N. Takeda, Y. Okabe, and T. Mizutani, “Damage detection in composites using optical fibre sensors,” *Proceedings of the Institution of Mechanical Engineers, Part G: Journal of Aerospace Engineering*, vol. 221, no. 4, pp. 497-508, 2007.

- [184] C. R. Dennison, P. M. Wild, D. R. Wilson *et al.*, “A minimally invasive in-fiber Bragg grating sensor for intervertebral disc pressure measurements,” *Measurement Science and Technology*, vol. 19, no. 8, pp. 085201, 2008.
- [185] C. R. Dennison, P. M. Wild, D. R. Wilson *et al.*, “An in-fiber Bragg grating sensor for contact force and stress measurements in articular joints,” *Measurement Science and Technology*, vol. 21, no. 11, pp. 115803, 2010.
- [186] J. M. Lee, and Y. Hwang, “A novel online rotor condition monitoring system using fiber Bragg grating (FBG) sensors and a rotary optical coupler,” *Measurement Science and Technology*, vol. 19, no. 6, pp. 065303, 2008.
- [187] J.-R. Lee, C.-Y. Yun, and D.-J. Yoon, “A structural corrosion-monitoring sensor based on a pair of prestrained fiber Bragg gratings,” *Measurement Science and Technology*, vol. 21, no. 1, pp. 017002, 2010.
- [188] G. R. C. Possetti, L. C. Côcco, C. I. Yamamoto *et al.*, “Application of a long-period fibre grating-based transducer in the fuel industry,” *Measurement Science and Technology*, vol. 20, no. 3, pp. 034012, 2009.
- [189] S. He, X. Dong, K. Ni *et al.*, “Temperature-insensitive 2D tilt sensor with three fiber Bragg gratings,” *Measurement Science and Technology*, vol. 21, no. 2, pp. 025203, 2010.
- [190] X.-f. Huang, Y. Liu, D. Luo *et al.*, “Wavelet analysis on vibration modal frequency measurement at a low level of strain of the turbine blade using FBG sensors,” *Measurement Science and Technology*, vol. 21, no. 1, pp. 015305, 2010.
- [191] I. H. Malitson, “Interspecimen Comparison of the Refractive Index of Fused Silica,” *J. Opt. Soc. Am.*, vol. 55, no. 10, pp. 1205-1208, 1965.
- [192] P. D. Soden, M. J. Hinton, and A. S. Kaddour, “Lamina properties, lay-up configurations and loading conditions for a range of fibre-reinforced composite laminates,” *Composites Science and Technology*, vol. 58, no. 7, pp. 1011-1022, 1998.
- [193] R. M. Jones, *Mechanics of composite materials*, Second ed.: Taylor & Francis, 1999.
- [194] M. A. Slawinski, *Waves and Rays in Elastic Continua*: World Scientific, 2010.
- [195] S. Karnani, “Characterizing the reliability of embedded Bragg grating optical sensors,” Mechanical Engineering, University of California, Los Angeles, 2007.
- [196] S. Trono, “Characterisation of the response of a Bragg grating fiber optic sensor embedded in an aerospace grade composite,” Mechanical Engineering, University of California, Los Angeles, 2008.
- [197] M. C. Emmons, G. P. Carman, K. P. Mohanchandra *et al.*, “Characterization and birefringence effect on embedded optical fiber Bragg gratings,” San Diego, CA, USA, 2009, pp. 72950C-11.
- [198] K. P. Mohanchandra, S. Karnani, M. C. Emmons *et al.*, “Thin film NiTi coatings on optical fiber Bragg sensors,” *Applied Physics Letters*, vol. 93, no. 3, pp. 031914-031914-3, 2008.

- [199] M. Fiebig, "Revival of the magnetoelectric effect," *Journal of Physics D: Applied Physics*, vol. 38, no. 8, pp. R123, 2005.
- [200] D. I. Khomskii, "Multiferroics: Different ways to combine magnetism and ferroelectricity," *Journal of Magnetism and Magnetic Materials*, vol. 306, no. 1, pp. 1-8, 2006.
- [201] T.-K. Chung, S. Keller, and G. P. Carman, "Electric-field-induced reversible magnetic single-domain evolution in a magnetoelectric thin film," *Applied Physics Letters*, vol. 94, no. 13, pp. 132501-3, 2009.
- [202] T. Wu, A. Bur, J. L. Hockel *et al.*, "Electrical and Mechanical Manipulation of Ferromagnetic Properties in Polycrystalline Nickel Thin Film," *Magnetics Letters, IEEE*, vol. 2, pp. 6000104-6000104, 2011.
- [203] D. A. Miller, and D. C. Lagoudas, "Thermomechanical characterization of NiTiCu and NiTi SMA actuators: influence of plastic strains," *Smart Materials and Structures*, vol. 9, no. 5, pp. 640, 2000.
- [204] Y. J. Chun, "Thin film nickel-titanium endovascular stent grafts for cerebral and aortic aneurysms," Mechanical Engineering, University of California, Los Angeles, 2009.
- [205] C. A. Kerrigan, K. K. Ho, K. P. Mohanchandra *et al.*, "Sputter deposition and analysis of thin film Nitinol/Terfenol-D multilaminate for vibration damping," *Smart Materials and Structures*, vol. 18, no. 1, pp. 015007, 2009.
- [206] K. K. Ho, and G. P. Carman, "Sputter deposition of NiTi thin film shape memory alloy using a heated target," *Thin Solid Films*, vol. 370, no. 1-2, pp. 18-29, 2000.
- [207] K. K. Ho, K. P. Mohanchandra, and G. P. Carman, "Examination of the sputtering profile of NiTi under target heating conditions," *Thin Solid Films*, vol. 413, no. 1-2, pp. 1-7, 2002.
- [208] L. Gang-Chih, L. Wang, C. C. Yang *et al.*, "Thermal performance of metal-clad fiber Bragg grating sensors," *Photonics Technology Letters, IEEE*, vol. 10, no. 3, pp. 406-408, 1998.
- [209] A. V. Shelyakov, and A. Y. Terekhov, "Fiber-optic thermosensor based on shape memory effect," *Journal de physique. IV*, vol. 5, no. 2, pp. C8.1183-C8.1186, 1995.
- [210] M. Amano, Y. Okabe, and N. Takeda, "Evaluation of Crack Suppression Effect of TiNi SMA Foil Embedded in CFRP Cross-Ply Laminates with Embedded Small-Diameter FBG Sensor," *JSME International Journal Series A Solid Mechanics and Material Engineering*, vol. 48, no. 4, pp. 443-450, 2005.
- [211] J. A. Balta, F. Bosia, V. Michaud *et al.*, "Smart composites with embedded shape memory alloy actuators and fibre Bragg grating sensors: activation and control," *Smart Materials and Structures*, vol. 14, no. 4, pp. 457, 2005.
- [212] A. Trouillet, E. Marin, and C. Veillas, "Fibre gratings for hydrogen sensing," *Measurement Science and Technology*, vol. 17, no. 5, pp. 1124, 2006.

- [213] D. Viegas, J. Goicoechea, J. M. Corres *et al.*, “A fibre optic humidity sensor based on a long-period fibre grating coated with a thin film of SiO₂ nanospheres,” *Measurement Science and Technology*, vol. 20, no. 3, pp. 034002, 2009.
- [214] M. Yang, J. Dai, C. Zhou *et al.*, “Optical fiber magnetic field sensors with TbDyFe magnetostrictive thin films as sensing materials,” *Opt. Express*, vol. 17, no. 23, pp. 20777-20782, 2009.
- [215] C.-L. Tien, H.-W. Chen, C.-C. Hwang *et al.*, “Magnetic field sensor based on double-sided polished fibre-Bragg gratings,” *Measurement Science and Technology*, vol. 20, no. 7, pp. 075202, 2009.
- [216] J. F. Nicoll, B. Balko, and K. K. Garcia, *Central research project report on superconductivity (FY 1988). Part 2. Magnetic-field gradiometer tank seeker. Final report, Sep 88-Sep 89*, AD-A-234901/7/XAB; IDA-P--2312 United States Wed Feb 06 22:19:55 EST 2008 NTISGRA; GRA-91-10350; EDB-91-126812 English, 1990.
- [217] P. Polynkin, A. Polynkin, N. Peyghambarian *et al.*, “Evanescent field-based optical fiber sensing device for measuring the refractive index of liquids in microfluidic channels,” *Opt. Lett.*, vol. 30, no. 11, pp. 1273-1275, 2005.
- [218] S. Lacroix, R. Bourbonnais, F. Gonthier *et al.*, “Tapered monomode optical fibers: understanding large power transfer,” *Appl. Opt.*, vol. 25, no. 23, pp. 4421-4425, 1986.
- [219] J. Villatoro, D. Monzon-Hernandez, and D. Talavera, “High resolution refractive index sensing with cladded multimode tapered optical fibre,” *Electronics Letters*, vol. 40, no. 2, pp. 106-107, 2004.
- [220] A. C. Boucouvalas, and G. Georgiou, “External refractive-index response of tapered coaxial couplers,” *Opt. Lett.*, vol. 11, no. 4, pp. 257-259, 1986.
- [221] D. Stadnik, and A. Dybko, “Fibre optic coupler as a detector for microfluidic applications,” *Analyst*, vol. 128, no. 6, 2003.
- [222] M. P. DeLisa, Z. Zhang, M. Shiloach *et al.*, “Evanescent Wave Long-Period Fiber Bragg Grating as an Immobilized Antibody Biosensor,” *Analytical Chemistry*, vol. 72, no. 13, pp. 2895-2900, 2000/07/01, 2000.
- [223] W. Liang, Y. Huang, Y. Xu *et al.*, “Highly sensitive fiber Bragg grating refractive index sensors,” *Applied Physics Letters*, vol. 86, no. 15, pp. 151122-3, 2005.
- [224] A. Iadicicco, A. Cusano, A. Cutolo *et al.*, “Thinned fiber Bragg gratings as high sensitivity refractive index sensor,” *Photonics Technology Letters, IEEE*, vol. 16, no. 4, pp. 1149-1151, 2004.
- [225] A. Iadicicco, A. Cusano, S. Campopiano *et al.*, “Thinned fiber Bragg gratings as refractive index sensors,” *Sensors Journal, IEEE*, vol. 5, no. 6, pp. 1288-1295, 2005.
- [226] K. S. Chiang, R. Kancheti, and V. Rastogi, “Temperature-compensated fiber-Bragg-grating-based magnetostrictive sensor for dc and ac currents,” *Optical Engineering*, vol. 42, no. 7, pp. 1906-1909, 2003.

- [227] J. L. Arce-Diego, R. López-Ruisánchez, J. M. López-Higuera *et al.*, “Fiber Bragg grating as an optical filter tuned by a magnetic field,” *Opt. Lett.*, vol. 22, no. 9, pp. 603-605, 1997.
- [228] B.-J. Wu, X. Liu, and K. Qiu, “Characteristics of magneto-optic fiber Bragg gratings for use in optical signal processing,” *Optical Fiber Technology*, vol. 15, no. 2, pp. 165-171, 2009.
- [229] A. Mailfert, and B. Nahounou, “Dielectric behaviour of a ferrofluid subjected to a uniform magnetic field,” *Magnetics, IEEE Transactions on*, vol. 16, no. 2, pp. 254-257, 1980.
- [230] H. E. Horng, C.-Y. Hong, H. C. Yang *et al.*, “Magnetic field dependence of Cotton–Mouton rotation for magnetic fluid films,” *Journal of Magnetism and Magnetic Materials*, vol. 201, no. 1–3, pp. 215-217, 1999.
- [231] S. Y. Yang, Y. F. Chen, H. E. Horng *et al.*, “Magnetically-modulated refractive index of magnetic fluid films,” *Applied Physics Letters*, vol. 81, no. 26, pp. 4931-4933, 2002.
- [232] C.-Y. Hong, S. Y. Yang, H. E. Horng *et al.*, “Control parameters for the tunable refractive index of magnetic fluid films,” *Journal of Applied Physics*, vol. 94, no. 6, pp. 3849-3852, 2003.
- [233] H. E. Horng, C.-Y. Hong, S. Y. Yang *et al.*, “Designing the refractive indices by using magnetic fluids,” *Applied Physics Letters*, vol. 82, no. 15, pp. 2434-2436, 2003.
- [234] S. Pu, X. Chen, Y. Chen *et al.*, “Fiber-optic evanescent field modulator using a magnetic fluid as the cladding,” *Journal of Applied Physics*, vol. 99, no. 9, pp. 093516-4, 2006.
- [235] S. Pu, X. Chen, Z. Di *et al.*, “Relaxation property of the magnetic-fluid-based fiber-optic evanescent field modulator,” *Journal of Applied Physics*, vol. 101, no. 5, pp. 053532-5, 2007.
- [236] M. Yang, J. Dai, X. Li *et al.*, “Side-polished fiber Bragg grating refractive index sensor with TbFeCo magnetoptic thin film,” *Journal of Applied Physics*, vol. 108, no. 3, pp. 033102-4, 2010.
- [237] T. Liu, X. Chen, Z. Di *et al.*, “Tunable magneto-optical wavelength filter of long-period fiber grating with magnetic fluids,” *Applied Physics Letters*, vol. 91, no. 12, pp. 121116-121116-3, 2007.
- [238] J. Dai, M. Yang, X. Li *et al.*, “Magnetic field sensor based on magnetic fluid clad etched fiber Bragg grating,” *Optical Fiber Technology*, vol. 17, no. 3, pp. 210-213, 2011.